Modeling of liquid film and breakup phenomena in Large-Eddy Simulations of aeroengines fueled by airblast atomizers

Geoffroy Chaussonnet

▶ **To cite this version:**

Geoffroy Chaussonnet. Modeling of liquid film and breakup phenomena in Large-Eddy Simulations of aeroengines fueled by airblast atomizers. Fluids mechanics [physics.class-ph]. Institut National Polytechnique de Toulouse - INPT, 2014. English. NNT : . tel-01006179v1

HAL Id: tel-01006179

https://theses.hal.science/tel-01006179v1

Submitted on 16 Jun 2014 (v1), last revised 27 Oct 2023 (v2)

HAL is a multi-disciplinary open access archive for the deposit and dissemination of scientific research documents, whether they are published or not. The documents may come from teaching and research institutions in France or abroad, or from public or private research centers.

L'archive ouverte pluridisciplinaire **HAL**, est destinée au dépôt et à la diffusion de documents scientifiques de niveau recherche, publiés ou non, émanant des établissements d'enseignement et de recherche français ou étrangers, des laboratoires publics ou privés.

THÈSE

En vue de l'obtention du

DOCTORAT DE L'UNIVERSITÉ DE TOULOUSE

Délivré par :
Institut National Polytechnique de Toulouse (INP Toulouse)

Discipline ou spécialité :
Mécanique des fluides / Combustion

Présentée et soutenue par :
Geoffroy Chaussonnet

le : 13 Mai 2014

Titre :

Modeling of liquid film and breakup phenomena in Large-Eddy Simulations of aeroengines fueled by airblast atomizers

---

Ecole doctorale :
Mécanique, Energétique, Génie civil et Procédés (MEGeP)

Unité de recherche :
CERFACS

Directeur(s) de Thèse :
Thierry Poinsot
Olivier Vermorel

Rapporteurs :

Amsini Sadiki
Mikhael Gorokhovski

Membre(s) du jury :

Alain Berlemont
Stéphane Jay
Rainer Koch
Stéphane Richard

Abstract / Résumé

Aeronautical gas turbines need to satisfy growingly stringent demands on pollutant emission. Pollutant emissions are directly related to the quality of fuel air mixing prior to combustion. Therefore, their reduction relies on a more accurate prediction of spray formation and interaction of the spray with the gaseous turbulent flow field. Large-Eddy Simulation (LES) seems an adequate numerical tool to predict these mechanisms. The objectives of this thesis is to develop phenomenological models describing the liquid phase, in particular the film and its atomization at the injector atomizing lips, in the context of LES. These models are validated or calibrated on the academic experiment performed at Institut für Thermische Strömungsmaschinen (ITS) from the Karlsruhe Institute of Technology (KIT), and applied to a helicopter engine real configuration. In a first step, the thin liquid film is described by a Lagangian approach. Film particles represent an elementary volume of liquid at the wall surface. The equation of motion is given by integrating the Saint-Venant equations over the film thickness. The film dynamics derives from the pressure gradient, the interfacial shear and gravity. In a second step, the film breakup is characterized by the drop size distribution of the spray. The former one is described by a Rosin-Rammler distribution, whose coefficients depend on the gas velocity, the liquid surface tension and the atomizing edge thickness of the injector. The model, labelled PAMELA, is calibrated from the KIT-ITS experiment. The simulation of the KIT-ITS experiment allows to validate the film model, to check PAMELA robustness, and to compare qualitatively the spray angle. The application of these models in a real configuration allows to check PAMELA robustness without constants modification, and to study their impact on the flame structure, in comparison with usual methods of liquid injection.

Les turbines à gaz doivent satisfaire des normes d'émission polluantes toujours en baisse. La formation de polluants est directement liée à la qualité du mélange d'air et de carburant en amont du front de flamme. Ainsi, leur réduction implique une meilleure prédiction de la formation du spray et de son interaction avec l'écoulement gazeux. La Simulation aux Grandes Échelles (SGE) semble un outil numérique approprié pour étudier ces mécanismes. Le but de cette thèse est de développer des modèles phénoménologiques décrivant la phase liquide notamment le film et son atomisation en bout de lèvre d'injecteur, dans un contexte SGE. Ces modèles sont validés ou calibrés sur l'expérience académique réalisée par l'Institut für Thermische Strömungsmaschinen (ITS) de l'université technologique de Karlsruhe (KIT), et appliqués dans une configuration réelle de moteur d'hélicoptère. Dans un premier temps, le film liquide mince est décrit par une approche Lagrangienne. Les particules de film représentent un volume élémentaire de liquide adhérent à la paroi. L'équation du mouvement est donnée par l'intégration des équations de Saint-Venant sur l'épaisseur du film. La dynamique du film est donnée par le gradient de pression longitudinal, le cisaillement interfacial du gaz et la gravité. Dans un second temps, l'atomisation du film est caractérisée par la distribution de taille de gouttes du spray généré. Celle-ci est décrite par une distribution de Rosin-Rammler dont les coefficients sont paramétrés par la vitesse du gaz, la tension superficielle du liquide et l'épaisseur de la lèvre de l'injecteur. Les constantes de ce modèle, baptisé PAMELA, sont calibrées sur l'expérience du KIT-ITS. La simulation de l'expérience KIT-ITS permet de valider le modèle de film, de vérifier la robustesse du modèle PAMELA, et de comparer qualitativement l'angle du spray généré. L'application de ces modèles dans une configuration réelle partiellement instrumentée permet de valider PAMELA sans modification de ses constantes, et d'étudier leur impact sur la structure de flamme, comparé aux méthodes traditionnelles d'injection liquide.

Contents

PART I TWO-PHASE FLOW PHENOMENA FROM INJECTION TO ATOMIZATION

Chapter 2: Spray / Wall interaction

Chapter 3: Thin liquid film flow

Remerciements

Ça y est, j'y suis ! J'écris mes remerciements, signe que ma thèse est finie et bien finie : manuscrit écrit, thèse soutenue et acceptée par le jury, youpi ! Je vais commencer par les professeurs qui m'ont donné le goût de la science tout au long de ma scolarité (je n'ai jamais eu l'occasion de le faire et ici semble être le bon endroit) : Roland Guilmain, professeur de Mathématiques au Lycée Fabert de Metz, Régis Doutres, professeur de Sciences Physiques en classe préparatoire du Lycée Fabert, Patrick Chassaing, professeur de Mécanique des Fluides à l'ENSEEIHT, et Lars Davidson, professeur de Mécanique des Fluides à l'université de Chalmers.

Merci ensuite aux membres du jury pour avoir assister à ma soutenance de thèse et notamment aux rapporteurs pour leur retour positif et leur relecture dans un temps imparti relativement court. Merci à Thierry Poinsot et Bénédicte Cuénot pour m'avoir accepté dans l'équipe CFD du CERFACS. Pour ce qui est de l'encadrement plus régulier, merci à Bénédicte Cuénot et Olivier Vermorel pour leur remarques constructives ainsi que leur relecture éclairée et éclairante du manuscrit. Merci aux autres chercheurs de l'équipe CFD, notamment Gabriel Staffelbach pour ses conseils et sa gentillesse. Pour leur disponibilité quant aux problèmes administratifs, un grand merci à Chantal & Michèle, Nicole et bien-sûr à Marie Labadens. Merci à Séverine pour les livres et articles et pour m'avoir laisser régulièrement faire la sieste sur le canapé de la bibliothèque. N'oublions pas l'équipe CSG (Nicolas, Patrick, Gérard, Fabrice, Maurice & Isabelle) pour leur bonne humeur, leurs bonbons et leur efficacité à gérer le parc informatique (qui constitue l'outil principal du CERFACS).

Un grand merci aussi à tous les thésards et les post-docs que j'ai connu au CERFACS. Les anciens qui m'ont accueilli dans leur groupe : Benedetta pour ta bonne humeur et ton rire tonitruant :-), Marta pour avoir forger le lagrangien et m'avoir enseigné les "trucs et astuces" du code, Jorge, Matthias, Patricia & Victor, Alexandre (Eyssartier), Anthony & Thomas. Merci à Olivier (Cabrit) et JF Parmentier pour leurs conseils pertinents et leur intérêt spontané. Merci à Jérôme pour avoir "industrialisé" mes modèles dans une version stable et avoir démontré leur applicabilité à de nouvelles configurations. Ceux de ma génération : Stéphane, Jean-Phi, Ignacio, Rémy, Alexandre (Neophytou), Pierre et David. Pour les (plus si) nouveaux, merci à Corentin, Raph, Lucas, Antony, Thomas (Livebardon), Michael, Abdullah. Pour les amis du CERFACS, merci à Basti pour les conseils zen ("T'inquiètes pas, ça ira") et les micro-cours d'Allemand, Sandrine pour avoir été co-captain à bord du Bavaria 51 au large du Stromboli, Damien pour toutes ces conversations sur les régimes de combustion, le suivi de particule, le Takeno diphasique, et j'en passe. Merci à Mario pour m'avoir expliqué la différence fondamentale entre "la pasta cousiné par des françaises et la pasta bien cousiné par les ritals" ainsi que pour avoir barré le Bavaria 51 la nuit par Beaufort 9 ! Enfin un grand merci à Greg pour avoir partagé mon bureau, supporté mes état d'âmes (et les autres), écouté mes histoires ;-) et tous les bons délires qu'on s'est tapé !

Du côté, de Karlsruhe, merci à Sebastian Gepperth et Rainer Koch du KIT-ITS pour leur accueil, et surtout le généreux partage inconditionnel de leur données expérimentales, vielen Dank !

De retour à Toulouse, merci à mes colocataire successifs qui, grâce à leur bonne humeur, m'ont fait respirer lorsque la mécanique des fluides commençait à m'étouffer : Giacomo pour ton ampli et ta gratte électrique, Benedetta pour me montrer qu'on pouvait bien se marrer devant "Cauchemar en Cuisine", Maite pour m'avoir initié au caractère catalan, Nele pour ta vision joyeuse de la vie, Julie pour tes conseils sur la course à pied, Julio pour tes cours

d'Espagnol-Colombien, Sophia pour tes brunchs et Clothilde pour les conversations aux sujets multiples, tes cours d'anatomie et pour Epson le chat ;-).

Et merci à tous les potes, les Klauschie de Metz (Pat, Tom, Max, Drej, Baldrik, Mat, Ben, Marco, AnneSo, K-ro, Cap'tain Kerso (respect Dude), Flou, Allison, Charlotte, Jerem, Charles), ceux de Toulouse : Thomas pour les conseils de mode et les conversations/debrieffing pendant le footing, PR pour les découvertes musicales, Al' pour les conseils de Snow Board, Elsa & Mouche pour les motivations rando/rando-raquettes dans les Pyrénées, Mi pour la découverte de cette belle culture aveyronnaise et ce beau paysage de Decazeville, Marina pour ta bonne humeur indéfectible et tes gâteaux gourmands avec plein de petits trucs dessus ;-), Isabel pour m'accompagner au Lindy Hop et aux autres danses, Géraldine pour, entre autre, ce joli voyage à Barcelone.

Enfin, merci à ma famille, et tout particulièrement mes parents et ma grand-mère qui sont venus à Toulouse pour ma soutenance, gros bisous à vous !

Roman letters

Symbol	Description	Units	Reference
A	Area	[m^2]	
a	Acceleration	[m/s^2]	Eq. 4.21
b	Characteristic length of accelerated wave	[m]	Eq. 7.5
b	Width of the film	[m]	Eq. 6.42
C_d	Drag coefficient	[$-$]	Eq. B.10
c	Speed of sound	[m/s]	
c_p	Mass heat capacity at constant pressure	[J/K/kg]	Eq. A.7
c_v	Mass heat capacity at constant volume	[J/K/kg]	Eq. A.9
D_{10}	Arithmetic mean diameter (also abreviated AMD)	[m]	Eq. 1.16
D_{30}	Volume mean diameter (also abreviated VMD)	[m]	Eq. 1.16
D_{32}	Sauter mean diameter (also abreviated SMD)	[m]	Eq. 1.16
D_{V10}	Diameter representing 10% of the spray	[m]	Eq. 7.46a
D_{V90}	Diameter representing 90% of the spray	[m]	Eq. 7.46b
D_h	Hydraulic diameter	[m]	Eq. 8.2
d_p	Particle diameter	[m]	Eq. 2.1
f	Frequency	[Hz]	
G	Group combustion number	[$-$]	Eq. 1.3
g	Geometrical projector	[$-$]	Eq. 5.17
g_i	Component i of gravity	[m/s^2]	
h	Film thickness	[m]	Eq. 3.5
h_a	Atomizing edge thickness	[m]	Eq. 7.10
I_t	Turbulent intensity	[$-$]	Eq. 7.52
$J_{i,k}$	Component i of the diffusive flux of specie k	[kg/m^2/s]	Eq. A.11
K	Longitudinal pressure gradient	[Pa/m]	Eq. 6.26
K_c	Disintegration parameter	[$-$]	Eq.2.2
$\overrightarrow{k}$	Wave vector	[1/m]	Eq. 4.4
k	Turbulent Kinetic Energy (TKE)	[m/s]	Eq. 6.45
L	Latent heat of vaporization	[J^2/kg^2]	Eq. B.24
L_b	Breakup length	[m]	Eq. 4.35
L_c	Local characteristic length	[m]	
l_c	Capillarity length	[m]	Eq. 7.29
M	Momentum flux ratio (also referred to as *dynamic pressure ratio*)	[$-$]	Eq. 4.34
m	Mass	[kg]	
m	Scale parameter of the Rosin-Rammler function	[m]	Eq. 1.17a
N_p	Parcel number	[$-$]	Eq. 5.16a
n_i	Component i of the normal vector	[$-$]	Fig. 3.1
n_l	Particle volume density	[1/m^3]	Eq. 5.32

p	Pressure	[Pa]	
Q	Volume flow rate	[m^3/s]	Eq. 6.36
Q	Q criterion	[1/s^2]	Eq. 8.4
q	Shape parameter of the Rosin-Rammler function	$[-]$	Eq. 1.17a
q	Fragmentation spectrum	[m]	Eq. 4.41
R^*	Dimensionless surface roughness	$[-]$	Eq. 2.8
R_1, R_2	Two principal radii of a surface	[m]	Eq. 3.9
r	Viscosity ratio	$[-]$	Eq. 3.25
r_ρ	density ratio parameter	$[-]$	Eq. 7.12
s_{ij}	Symmetric part of the velocity gradient tensor	[1/s]	Eq. A.3
T	Temperature	[K]	
T_L	Leidenfrost temperature	[K]	Fig. 2.6
T_{sat}	Saturation temperature	[K]	Fig. 2.6
T^*	Dimensionless impacting droplet temperature	$[-]$	Eq. 2.7
t_i	Component i of the tangential vector	$[-]$	Fig. 3.1
U	Velocity magnitude	[m/s]	Eq. 2.1
$\vec{u}$/u_i	Velocity vector / component i	[m/s]	
u, v, w	First, second, third velocity component	[m/s]	
u_{70}	Velocity seen by liquid accumulation	[m/s]	Eq. 7.36
u_τ	Shear velocity	[m/s]	Eq. 7.37
$X_{[0,1]}$	Equipossible random draw between 0 and 1	$[-]$	Eq. 7.59
y_{70}	Thickness related to u_{70}	[m]	Eq. 7.43

Greek letters

Symbol	Description	Units	Reference
α_l	Liquid volume fraction	$[-]$	Eq. 1.1a
Γ_{ij}	Component i,j of the liquid stress tensor	[kg/m/s^2]	Eq. 3.7
γ	Angle between the local referential and Earth gravity	$[-]$	Fig. 3.1
Δ	Laplacian operator	$[-]$	
Δ	Local filter/cell characteristic size	$[m]$	
δ	Boundary layer thickness	[m]	Eq. 7.24a
δ_{ij}	Component i,j of the Kronecker delta	$[-]$	
δq_p^2	Random Uncorrelated Energy (RUE)	[m^2/s^2]	Eq. 5.37
δ_ν	Viscous sublayer	[m]	Eq. 7.38
δ_ω, δ_g and δ_l	Total, gaseous and liquid vorticity thickness	[m]	Fig. 4.17
ϵ	Film size ratio	$[-]$	Eq. 3.16
η	Dimensionless film thickness	$[-]$	Eq. 2.6a
η_N	Secondary-to-incident droplet number ratio (wall impact)	$[-]$	Eq. 2.18

η_s	Secondary-to-incident droplet mass ratio (wall impact)	$[-]$	Eq. 2.17
θ_C	Droplet/wall contact angle	$[-]$	Fig. 2.7
θ_0	Momentum thickness of turbulent boundary layer	[m]	Eq. 7.35
κ	Von Kármánn constant	$[-]$	Eq. 7.39
κ	Normalized vertical coordinate	$[-]$	Eq. 6.35
Λ_f	Film 2D flow rate	[m^2/s]	Eq. 6.42
λ	Thermal conductivity	[W/K/m]	Eq. A.13
λ	Instability wavelength	[m]	Eq. 4.21
μ	Dynamic viscosity	[po]	
μ_p	Liquid mass fraction	$[-]$	Eq. 1.1b
$\Xi(f)$	Uncertainty of quantity f	[dim(f)]	Eq. 8.15
ξ	Thickness of ligaments at breakup time	[m]	Eq. 4.31
ρ	Density	[kg/m^3]	
Σ	Surface area per volume unit	[1/m]	Eq. 4.40
σ	Surface tension	[N/m]	Eq. 2.1
τ	Characteristic time	[s]	
τ_{ij}	Component i,j of the stress tensor	[kg/m/s^2]	Eq. A.2
τ_w	Wall shear stress	[Pa]	Eq. 3.12
τ_{fg}	Film/gas interfacial shear stress	[Pa]	Eq. 3.12
ν	Kinematic viscosity	[m^2/s]	
ϕ	Equivalence ratio	$[-]$	
χ	Cross spectrum	[(Pa s)^2]	Eq. 8.11
ψ	Stream function	[1/s]	Eq. 4.10
Ω_i	Component i of the vorticity	[1/s]	Eq. 8.5
ω	Temporal pulsation	[rad/s]	Eq. 4.4
$\aleph$	Ratio of the numerical time step to the particle relaxation time	$[-]$	Eq. 5.9
∇	Space derivation	[1/m]	

Non-dimensional numbers

Symbol	Description	Reference
At	Atwood number	Eq. 7.33
B_M	Spalding number for mass transfer	Eq. B.19
B_T	Spalding number for heat transfer	Eq. B.31
Eu	Euler number	Eq. 3.16
Fr	Froude number	Eq. 3.16
Ja	Jacob number	Eq. 2.24
Le	Lewis number	Eq. B.32
Nu	Nusselt number	Eq. 2.21

Oh	Ohnesorge number	Eq. 2.3
Pr	Prandtl number	Eq. 2.23
Re	Reynolds number	Eq. A.26
Re_p	particle Reynolds number	Eq. B.7
St	Stokes number	Eq. 1.2
Sc	Schmidt number	Eq. A.24
Sh	Sherwood number	Eq. B.20
We	Weber number	Eq. 2.1

Subscripts

Symbol	Description
0	Initial / reference state
bu	Breakup quantity
f	Film quantity
g	Gaseous quantity
l	Liquid quantity
n	Normal to wall surface
p	Particle quantity
res	Filtered contribution
rms	Root Mean Square quantity
sat	Saturation point
sgs	Subgrid scale contribution
t	Tangential to wall surface
w	Wall quantity

Superscripts

Symbol	Description
$\overline{f}$	Filtered quantity
$\langle f \rangle$	Averaged quantity
$\tilde{f}$	Density weighted filter average quantity
$\breve{f}$	Fluid quantity undisturbed by the particle
f'	Fluctuation in the sense of filtering
f''	Fluctuation in the sense of averaging
$\hat{f}$	Modulus of f''
f^*	Normalized quantity
f^+	Quantity in terms of wall unit
$\dot{f}$	Time derivative of f

Abreviations

Acronym	Description
AFR	Air / Fuel mass Ratio
CFD	Computational Fluid Dynamics
CFL	Courant-Friedrichs-Lewy
CHF	Critical Heat Flux
CTRZ	Central Toroidal Recirculation Zone
DNS	Direct Numerical Simulation
FN	Flow Number
HIT	Homogeneoud Isotropic Turbulence
HR	Heat Release
ITS	Institüt for Thermische Strömungsmaschinen
KH	Kelvin-Helmholtz (instability)
KIT	Karlsruhe Institut of Technology
LES	Large Eddy Simulation
LDA	Laser Doppler Anemometry
LFDM	Laser Focal Displacement Meter
LW	Lax-Wendroff convective scheme
MEF	Mesoscopic Eulerian Formalism
PDA	Phase Doppler Anemometry
PDF	Probability Density Function
PMD	Puissance Maximale Décollage
PVC	Precessing Vortex Core
RANS	Reynolds Averaged Navier-Stokes
RT	Rayleigh-Taylor (instability)
SPH	Smoothed-Particle Hydrodynamics
SWI	Spray/Wall Interaction
TTGC	Two-step Taylor-Galerkin 'C' convective scheme
VOF	Volume Of Fluid

Chapter 1

General introduction

1.1 Earth resources depletion

1.1.1 The Limits to Growth and the World3 *model*

Earth resources are limited and decrease continuously due to mankind energy consumption. It significantly started with the industrial revolution, when engineers and scientists rationalized and standardized the transformation processes of Earth raw substance into high quality materials or energy. In those time the natural reserves were so large compared to the demand that very few raised the question of resource availability. In addition to the resource shortage comes the impact of the human modern life activity onto the primary natural system: pollution. In 1866, Ernest Haeckel labeled the *science of interaction of organisms with their environment* as *'oekologie'* [129]. Although this term was originally cast to describe natural eco-systems, when applied to the human race, the main topic of 'ecology' is the impact of pollution onto nature. Furthermore, as pollution is directly linked to industry and economics, those fields must be taken into account in order to describe the global frame of ecology.

The first computer model (named *World*) to assess the complex interactions between human activities and our planet was created in 1970 by Jay W. Forester [89], from MIT[1] [277]. In 1972, a team of analysts from MIT published "The Limits to Growth" [230], commissioned by the Club of Rome. This report (hereafter referred to as LtG) analyses the sustainability of modern human activity through the *World3* model. This is a system dynamics model of the world's socioeconomic system that describes the interactions between five subsystems, namely: population, food production, industrial production, pollution and consumption of non-renewable resources. The model was run with several earth-scale scenarios (birth or pollution control, doubled resources, improved technology, etc), based on data collected from 1900 and predicted trends until 2100. All scenarios lead to an exponential growth, followed by a dramatic depression. The novelty of this report was double: it was the first time that numerical simulation was applied to a world-scale sustainability study, and it was a formal proof that the modern socioeconomic system was not a sustainable paradigm.

Figure 1.1 illustrates three scenarios investigated by Meadows *et al.* [230]. In the standard run, due to resource depletion, the industrial base collapses first, entraining the services and agricultural system, that in turn increase death rate and lower the population. When doubling the natural reserves (in 1972, the authors thought about the nuclear power as the ultimate answer to the energy production issue), the collapse comes from pollution that has a major impact on agricultural outputs and leads to famine. The third scenario assumes unlimited resource reserves and

[1] Massuchetts Institute of Technology

an enhanced pollution control. In this case the collapse comes from food shortage due to an overshoot of population compared to available agricultural outputs.

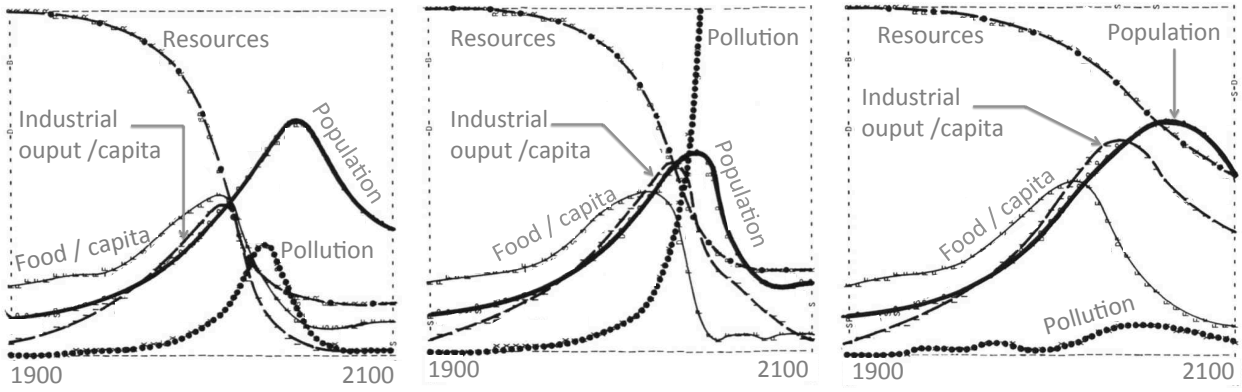

Figure 1.1 : *Output from the LtG modeling for the three scenarios that span the technological and social response explored in LtG. Left: standard run. Middle: doubled natural resource reserves assumption. Right: unlimited resources and pollution control assumption. Adapted from [230]*

1.1.2 Comparison of the predictions with 30 years of global data

In 2008, Turner [348] used 30 years of observed data covering the period (1970-2000) for comparison with the predictions made in 1974 for several scenarios [229]. In addition to the standard run, a "Comprehensive technology" and a "Stabilized world" scenarios were presented. They corresponded respectively to a more sustainable development through technological solutions (recycling, world-wide controlled pollution and birth) and a development entirely devoted to sustainability (two children per family, maintenance of agricultural land, preference for consumption of services and health facilities more than material goods, etc). Although not realistic, these additional scenarios allowed to settle margins to the standard run. Some of the model outputs are displayed on Fig. 1.2. The standard run is in best agreement with observed data compared to the other scenarios. This study must not be taken as an absolute validation of the *World3* model, but it confirms its robustness in predicting trends. Therefore a collapse of our socioeconomic system and resulting major changes are to be expected within the XXI century.

1.1.3 What can be done ?

In the *World3* model, the rate of resource depletion is diminished by technological advances. Even in the standard run, the authors assumed that the extraction and the transformation of raw materials as well as the consumption of final products would require less energy and less industrial output. This assumption partly explains the plateau of the *resources* curves after the depression on Fig. 1.1. This means that even with the perspective of a global collapse, it is still required to improve the energetic efficiency of all technological products, from energy plants to smartphones, in order to minimize the fall of the industrial output and to preserve our minimum life standards.

A clear conclusion is that efforts must be made in all possible directions to push our socioeconomic system towards sustainability. Due to the thousands of different aspects of the *sustainability* concept, such an evolution requires many research projects, each one focusing on a little part of the overall problem. This picture of small projects feeding a big cause (like small streams feed large rivers) coincides with the global human knowledge fueled by single and small discoveries, illustrated by Might [232] and adapted on Fig. 1.3.

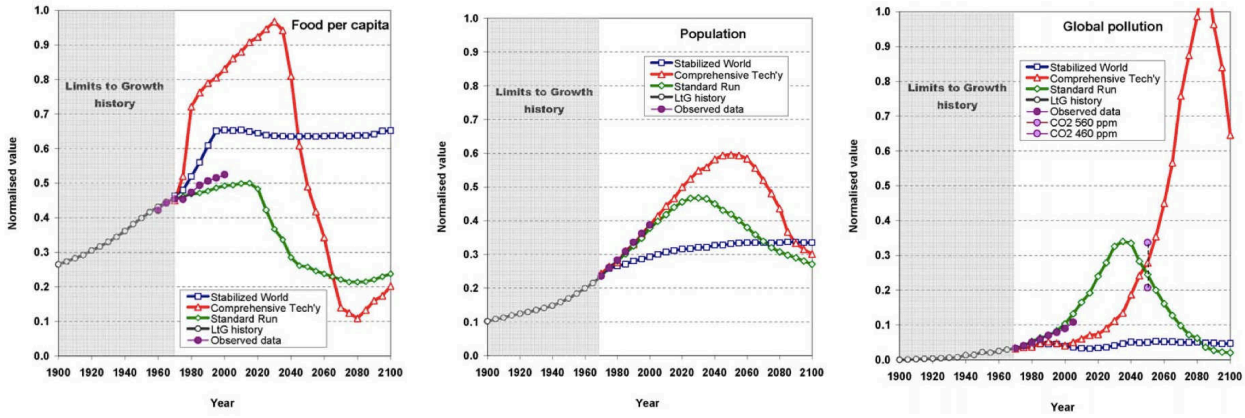

Figure 1.2 : *Comparison of data collected between 1970 and 2000 (solid circles •) with* World3 *predictions for several scenarios. ◇: standard run. △: comprehensive technology. □: stabilized world. ◯: calibrated model output over 1900 -1970. Adapted from [348]*

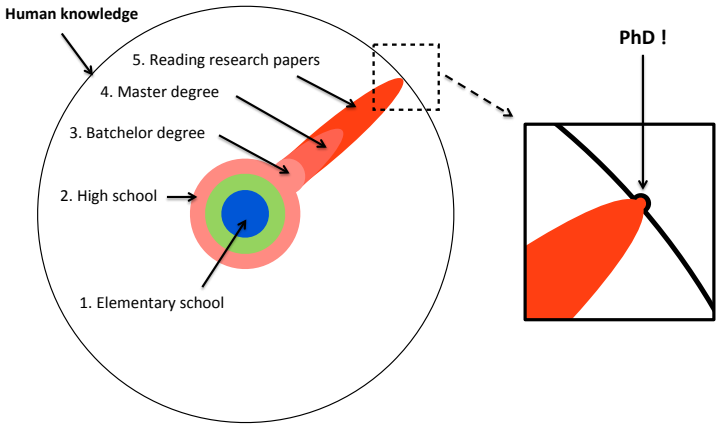

Figure 1.3 : *Topology of the knowledge levels acquired from educational units in a global scope, adapted from [232]*

1.2 The case of Gas Turbines

In this thesis, the aspect of sustainability is treated through the improvement of gas turbine efficiency. The massive use of fuel powered devices, in transportation and energy plants, imposes a high extraction rate of oil from the natural reserves. This trend is worsen by the rise of the population and the overuse of motored-transportation in modern societies. In addition to Earth resources depletion, gas turbines emit pollutants through the combustion process. This pollution has two major effects:

- It impacts the climate by increasing the global earth temperature (global warming) due to the emissions of green house effect gases. One of the major combustion product is carbone dioxide (CO_2) which represents more than 70% of the world's total green house gas emission. The scientific community agrees upon the fact that the global warming over the last decade is mainly due to human activity [263]. The easiest measurable consequence of global warming is the increase of sea level due to the melting ice cap [48]. Other consequences such as extreme climate events (hurricanes, droughts, floods, etc) are more controversed [77, 177].

- It has poisonous effects onto living species: carbon monoxide (CO) reduces the oxygen carrying capacity of the blood, nitrogen oxides (NO_x) induce respiratory difficulties and fine particles (such as soot) deposit in bronchies and damage lungs.

In the *World3* model, the increase of combustion device performance could lead to the decrease of the resource consumption rate as well as slowing down the pollution growth.

1.2.1 Principle of a gas turbine

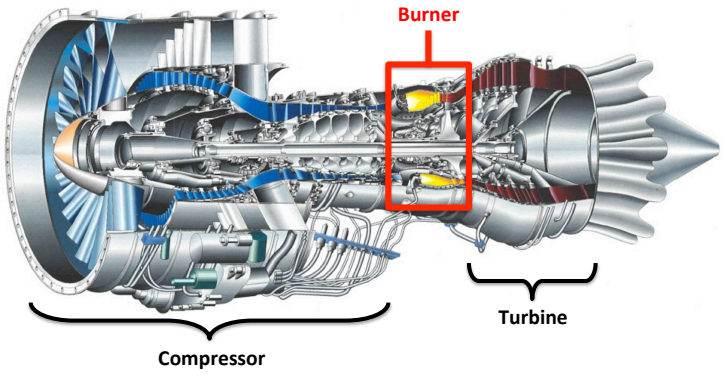

Figure 1.4 : *Mid-plane cut of an aircraft engine. (Source http://web.engr.oregonstate.edu).*

A mid-plane cut of a gas turbine is displayed on Fig. 1.4. It generates power as follow: a large amount of air enters the engine through a compressing stage, where the pressure is increased in order to inject higher combustive concentration. It enters the burner where it is first mixed with the fuel injected as a liquid spray. Fuel droplets evaporate, mix with the gas and burn. Thanks to thermal expansion, the burnt gases accelerate and create thrust. Fresh air is added to the burnt gases in order to decrease the temperature and reduce the fatigue of mechanical parts. The mixture finally go through a turbine that converts the flow energy into work.

In this work, only the processes taking place in the combustion chamber are studied, and more precisely the phenomena related to liquid fuel spray. For this reason, the compressor and the turbine will not be described.

1.2.2 Strategies for the reduction of fuel consumption and pollutant emissions

In aeronautical applications, the reduction of emissions mainly concerns the nitric oxides and carbon monoxides. Unfortunately, the nitric oxides production increases with temperature whereas carbon monoxide decreases. Therefore a tradeoff temperature must be found in order to minimize both pollutant emission. Such temperature may be obtain from a lean combustion but it turns out that lean combustion devices are prone to combustion and thermo-acoustics instabilities. Note that lean combustion also implies a lower fuel consumption. It is then necessary to fully understand combustion mechanisms in real engines to propose improved technologies.

In these engines, the liquid spray interaction with the ambient gas and the flame front is of primary importance in combustion dynamics. The size distribution of the spray is one of the key element that needs to be well understood as it drives the fuel vapour distribution and therefore the flame structure. Due to their larger evaporation time, large droplets can reach the flame front without being totally evaporated and change the combustion regime. On the contrary, small droplets evaporate and mix quickly with the gas, leading to a more homogeneous mixture at the

flame, and a higher efficiency. Liquid injection is therefore a challenging subsystem whose ideal aim would be to *generate the finest spray over the minimum distance*.

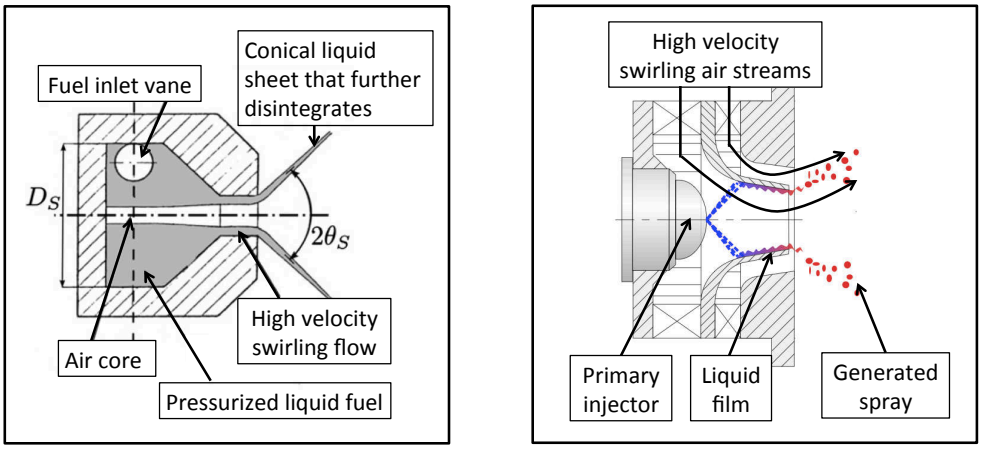

Figure 1.5 : *Left: schematics of a pressure swirl atomizer, adapted from [196]. Right: schematics of an airblast atomizer, adapted from [313]*

There are two main categories of fuel injection systems in gas turbines: pressure swirl atomizers and airblast atomizers [196]. In pressure swirl atomizers the liquid is pressurized in a swirling chamber and enters the combustion chamber where the ambient pressure is smaller. It forms a conical liquid sheet that disintegrates due the velocity differential of the two phases (Fig. 1.5 left). In airblast atomizers, the liquid is injected at a low velocity and is fragmented by the means of a high speed air stream. In this type of atomizers, the liquid forms a thin film that increases the interface area and promotes the momentum transfer from gas to liquid, leading to an efficient atomization (Fig. 1.5 right). Airblast atomizers present very stable performances on a wide range of operating parameters [198]. This thesis focuses on this second type of atomizers.

1.3 Description of liquid phase phenomena

In real combustors the fuel is injected in a liquid state and proceeds through many steps before reaching the flame front together with air. Figure 1.6 illustrates the various phenomena that occur sequentially after the injection via an airblast atomizer.

The proportion of liquid compared to gas is a key parameter that gauges what phenomenon is preponderant in the liquid phase dynamics. It is expressed in terms of volume fraction α_l and mass fraction μ_p:

$$\alpha_l = \frac{V_l}{V_{tot}} \tag{1.1a}$$

$$\mu_p = \frac{m_l}{m_{tot}} \tag{1.1b}$$

where V_l, V_{tot}, m_l and m_{tot} are the liquid and total volume, the liquid and total mass respectively. Fede [82] distinguishes several regimes:

- $\alpha_l > 10^{-1}$: very dense sprays. Inter-particle collisions are the most important contribution to particle motion, and coalescence is responsible for large blob sizes.

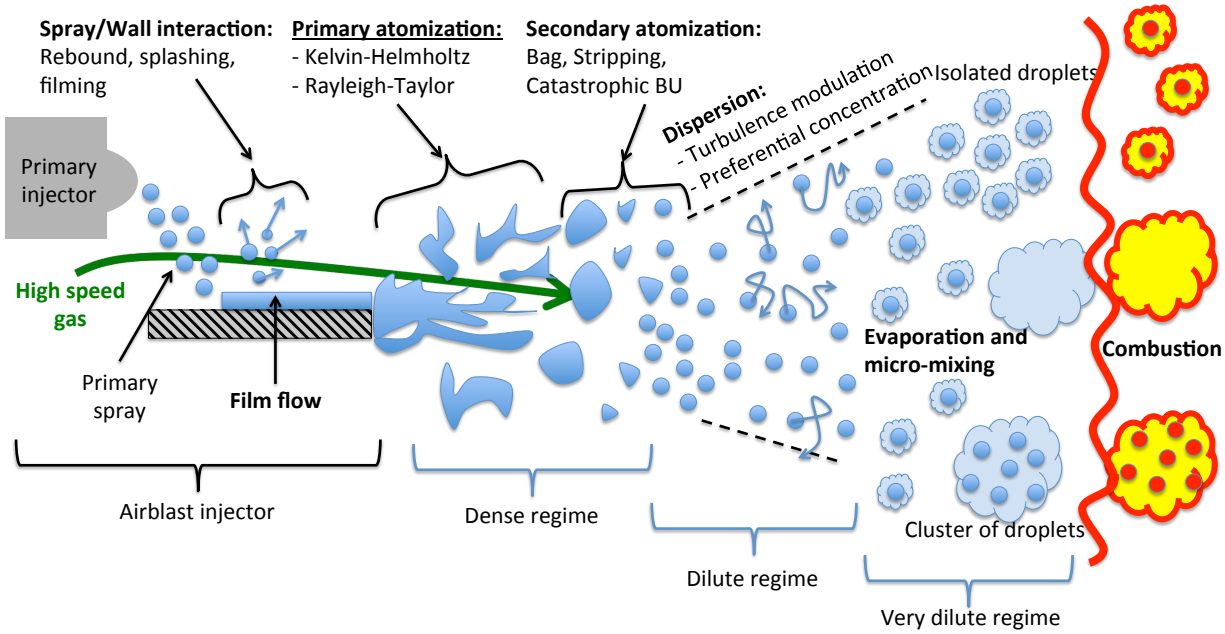

Figure 1.6 : *Main sequential phenomena related to the liquid phase in a combustion chamber supplied by an airblast atomizer*

- $10^{-4} < \alpha_l < 10^{-1}$: moderately dense sprays. Inter-particle collisions become less important. The carrier phase flow begins to be the main contribution to particle motion.
- $\alpha_l < 10^{-4}$ and $\mu_p > 10^{-2}$: dilute sprays. Inter-particle phenomena can be neglected. However, the influence of liquid phase onto the carrier phase must be taken into account.
- $\alpha_l < 10^{-4}$ and $\mu_p < 10^{-2}$: very dilute sprays. Inter-particle collisions and effects of particles on the carrier phase can be neglected due to the low inertia of particles.

The different phenomena illustrated on Fig. 1.6 are described in the following.

Liquid injection

The liquid is primarily injected in the center of the airblast atomizer cavity, often through pressure swirl atomizers. At the exit of the pressure swirl atomizer, the liquid forms a conical liquid sheet that disintegrates due the velocity differential of the two phases. The main interest of experimental studies on pressure swirl atomizers is to determine correlations for the distributions of droplet size [346] and velocity [109, 293], breakup length [251] and film thickness inside the nozzle [94, 237]. Due to the combined action of the large spray opening angle and the centrifugal effect of the flow swirling motion, most of the spray droplets impact the wall of the airblast injector, namely the prefilmer.

Spray/wall interactions

Spray/wall interactions are classified depending on the impact energy and the wall temperature: droplets can rebound on the wall, fragment into smaller droplets (splashing), or aggregate on the wall to form a liquid film. Droplets that

splash and rebound are reemitted in the cavity and either directly enter the combustion chamber, or re-impact the wall, depending on the flow topology or centrifugal effects. Research on spray wall interaction is an active topic and chapter 2 is dedicated to it.

Film flow

The film formed by the multiple impacts is sheared by the high speed air stream. Some interface instabilities may arise, leading to rolling or solitary waves, and finally to film stripping: some liquid blobs are detached from the film and entrained by the gas. When the film is thin, viscosity effects stabilize the film flow and no stripping is observed. Chapter 3 focuses on thin film flows and section 4.2 deals with film instabilities.

Primary breakup

Primary atomization denotes the liquid phase transition from a coherent connected shape to separated elements. It is discussed in details in chapter 4.

In an airblast atomizers, the liquid film reaching the atomizing edge may enter two different regimes, depending on the inertia of the film and the thickness of the atomizing edge[2] . A film with high inertia continues its trajectory and forms a liquid sheet that propagates in the combustion chamber. The large aerodynamic stresses generate longitudinal Kelvin-Hemoltz instabilities, followed by transversal Rayleigh-Taylor instabilities. This instability cascade ends up in the creation of filiform structures elongated in the streamwise direction. These structures, called *ligaments*, are then torn away from the liquid core into blobs. A film with a lower inertia accumulates in the wake region of the atomizing edge. This liquid accumulation is sheared by air and some liquid blobs are torn from it through a transverse instability. A deeper study and modeling of this particular process is provided in chapter 7.

Secondary breakup

Secondary atomization occurs for large liquid blobs that are immersed in a high velocity air stream. The large aerodynamic stresses act as the destabilizing phenomena and is counterbalanced by the liquid surface tension. As large droplets have a large streamwise front area, they undergo a strong aerodynamic force that disintegrates them.

For smaller droplets, the surface tension effect being proportional to the surface curvature, it becomes predominant over the aerodynamic stresses and the droplets do not undergo secondary atomization. In addition, when the droplets become smaller, they become lighter and they are more easily dragged by air, leading to a relative velocity close to zero, that in turn decreases the aerodynamic stress. The competition between drag and surface tension leads to different secondary atomization regimes (bag breakup, stripping breakup, catastrophic breakup). Additional details are brought in section 4.6.

Dispersion

At this stage, due to the swirling motion of the flow and the opening of jet, the liquid volume fraction decreases to reach a *dilute regime*. In this regime, droplet/droplet interactions can be neglected and the droplet dynamics are driven by a competition between inertia and drag. The Stokes number (St) is the dimensionless number that estimates the outcome of this competition. It compares the particle response timescale τ_p to the characteristic timescale of the gas phase τ_f:

$$\mathrm{St} = \frac{\tau_p}{\tau_f} \tag{1.2}$$

[2] S. Gepperth, personal communication, May 22, 2013

When the Stokes number is negligible compared to 1, the particle is called a *tracer*: it is instantaneously in equilibrium with the flow and its trajectory constitutes a pathline of the flow. Inversely, for a Stokes number larger than one, the particle inertia dominates the flow momentum transfer and the particles follow a ballistic trajectory, like a cannonball. The particle velocity can be seen as the output of a low pass filter excited by the gas velocity. It can be shown that the transfer function depends on the Stokes number only [38]. However, whereas the particle response time is well defined, multiple gaseous timescales exist and may evolve with time (Kolmogorov timescale, Taylor timescale, the integral timescale, etc). As a consequence, the same particle may be inertial for some scales and a tracer for others in the same flow.

The interaction between the turbulent gas flow and the particles is not straightforward and can locally leads to enhancement or attenuation of turbulence [375]. Experimental investigations over the last two decades [271] have identified the main responsible mechanisms: (i) damping due to larger droplets leading to enhanced dissipation, (ii) transfer of kinetic energy from the droplets to the gaseous phase, and (iii) formation of wake and vortex shedding behind particles of large particle Reynolds number [17, 166].

An important consequence of turbulence / particles interaction is the *preferential concentration*. It corresponds to the aggregation of particles of Stokes number around unity, in particular zones of the vortical flow. When a 'low-Stokes' particle is immersed in a vortex, as a tracer it follows the helicoidal streamlines of the flow, whatever the distance to the center of the eddy. 'Large-Stokes' particles, driven by their own inertia independently of the flow, follow a trajectory that is uncorrelated to the vortex structure. Preferential concentration is then due to 'moderate-Stokes' particles ($\mathrm{St} = 1$ with Kolmogorov timescale [363] or $\mathrm{St} = 0.15$ with integral turbulent timescale [331, 332]), with low enough inertia to be dragged by the vortex in a circular motion, but large enough to be ejected out of the vortex once they gain sufficient kinetic energy. This results in a higher concentration of intermediate particles between the vortices, in high strain regions [206]. The disparity in droplets concentration leads to evaporation rate inhomogeneities and locally modify the combustion regime.

Evaporation and Micro-mixing

Droplet evaporation and micro-mixing occur approximately at the same time as turbulent dispersion. This process allows the liquid fuel to be vaporized and properly mixed with air before combustion. Vaporization results from a liquid-vapour equilibrium whose parameters are the ambient pressure, the liquid temperature and the concentration of the vaporized species. It leads to an exchange of mass, momentum and energy between the two phases. Vaporization has been extensively studied in the case of complex spray flows (experimentally [203, 329] and theoretically [32, 78]). The vaporization of a single droplet is an interesting approach that provides an ideal framework for theoretical models in the dilute region of the spray. The derivation of such models are available in many textbooks [183, 324, 367].

If there were no micro-mixing at the droplet surface when it evaporates, the vicinity of the droplet would be rapidly saturated of gaseous fuel, and the vaporization would stop. Micro-mixing is therefore an essential transport phenomenon that diffuses the fuel vapour from the droplet surface, and it is therefore strongly related to vaporization. It has been studied by Mastorakos [223] (experimentally and theoretically), and some DNS of evaporating sprays were performed by Reveillon & Vervisch [286, 287]. Three regimes of evaporation and micro-mixing can be distinguished [166, 285]: (i) quick vaporization of isolated droplets in dilute spray regions, (ii) clustered vaporization when the inter-droplets distance is small, leading to a drastic reduction of the evaporation rate in the center of the cluster, and (iii) the turbulent mixing convects isolated droplets into dense droplet clusters and *vice versa*.

Two-phase combustion

Two-phase flames exhibit marked differences compared to gaseous flames [316]. As mentioned, the vaporization rate and mixing are additional key features that bring a new classification of combustions regimes. Chiu [49, 50] developed group combustion models where a spherically symmetric droplet cloud is completely or partially surrounded by

a diffusion flame [166]. One can distinguish four regimes in the model, depending on a group number G defined as the ratio of the droplet evaporation rate to the diffusion rate of hot gases within the droplet cloud. When convective effects are large compared to diffusive effects, G can be approximated as :

$$G \approx \frac{5N_p^{2/3}}{S} \tag{1.3}$$

where N_p represents the number of drops in the cloud and S a mean droplet spacing parameter defined by the ratio of the average distance between droplets to a characteristic diffusion flame radius.

Figure 1.7 by Réveillon & Vervisch [287], based on former studies of Chiu *et al.* [50] illustrates the four regimes. When G is greater than one, the spray region is saturated with fuel vapour, the flame is thus located around the cloud and burns in a diffusion regime; it is referred to as *external sheath* combustion and can be split in two distinct regimes: (i) when $G \gg 1$ the spray is so dense that its core is saturated with fuel vapour that inhibits further vaporization and (ii) when G decreases (but keeps greater than one), droplets of the spray core are sufficiently distant to allow vaporization. When $G < 1$, a first ring of individual burning droplets envelops the droplet cloud surrounded by a diffusion flame. For dilute spray regimes ($G << 1$), droplets are far from each other and the evaporation rate increases due to hot gases diffusion. Separated flames surround each droplet, which burn individually.

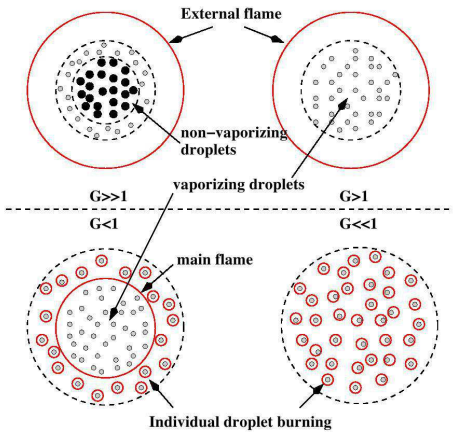

Figure 1.7 : *Classification of different spray combustion regimes, from Réveillon & Vervisch [287]*

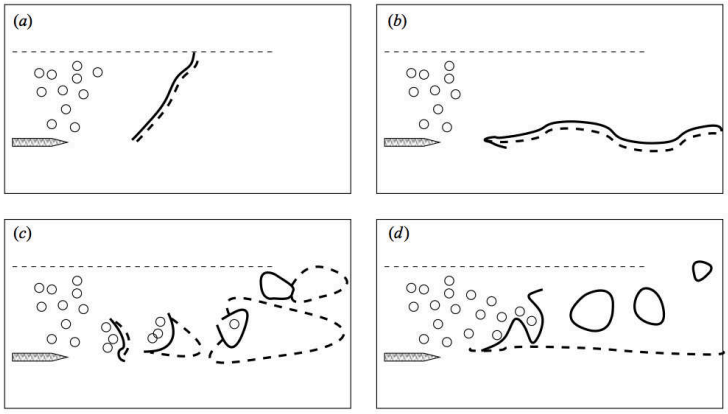

Figure 1.8 : *Classification of different spray combustion regimes, from Réveillon & Vervisch [287]. Continuous and dashed lines stand for a premixed and a diffusion flame, respectively.*

Réveillon & Vervisch [287] added the equivalence ratio as an additional parameter to determine the flame structure. The local equivalence ratio in a spray can show a very complex behaviour due to the relative timescales of evaporation and volume expansion of combustion products. They found out that the flame structure can be categorized into 3 classes, as depicted on Fig. 1.8: for the case of an axisymmetric turbulent jet flame, where a mixture of fuel droplets and air is surrounded by coflowing preheated air. The bold continuous and dashed lines stand for premixed and diffusion flames, respectively. The *external combustion* mode is defined by a continuous flame front in which two sub-regimes may be observed: (i) for a very low equivalence ratio the flame front engulfs the whole fuel-air system and all the fuel is burnt. This is called the *closed external* combustion regime (Fig. 1.8 (a)). For a large equivalence ratio (ii), due to the large amount of fuel to react, the flame front is streamwisely oriented (Fig. 1.8 (b)). This sub-regime is called *open external* combustion regime. The second category is the *group* combustion in which some clusters of droplets burn independently. A rich premixed flame is located directly downstream of the clusters, and the remaining unburnt fuel reacts with additional oxidizer available further downstream (Fig. 1.8 (c))

with a diffusion flame. The last class is a combination of case (i) and (ii), namely the *hybrid* combustion regime. Pockets of very rich mixture are burning in premixed regime, but the inter-cluster environment is too rich to allow for diffusion flames. The flammability domain is only reached by addition of oxidizer at the interface of the coflow where an external diffusion flame can develop (Fig. 1.8 (d)).

1.4 Numerical simulation of two-phase turbulent combustion

Due to the rise of computer power during these last two decades, it has been possible to increase the space and time resolution of numerical simulation, and many efforts have been oriented towards the development of numerical methods to increase the predictive capacities of simulations. The advantage of numerical simulation is the possibility to have access to any physical quantity, at any time, under any conditions. This is not the case with real experiments of complex geometries, with difficult optical access, in extreme conditions of pressure and temperature. However due to the use of models, numerical simulation describes only a part of reality, and its predictive quality relies on its ability to recover the predominant phenomena. Experiments are thus still necessary to validate new models. Note that even if the overall cost of a supercomputer, including power supply, cooling and maintenance, is quite expensive, numerical simulation is by far cheaper than experiments. Nowadays, Computational Fluid Dynamics (CFD) has reached a certain maturity: industry uses it for combustor designs, while it stays a very efficient tools for fundamental sciences.

1.4.1 Modeling gaseous turbulence

The nonlinearity of the Navier-Stokes equations is one of their main characteristics, that gives birth to turbulence. In many combustion devices, turbulence is a desired feature since it promotes atomization, mixing process and evaporation, and finally increases the specific heat release. However turbulence also promotes thermal losses through the walls and local extinction, decreasing the overall performances of the device. Turbulence is characterized by the existence of coherent vortical structures in the flow, over a wide range of length and time scales [274]. There are three main strategies to describe turbulence in numerical simulation:

- Resolving all the energetic length and time scales of turbulence is called Direct Numerical Simulation (DNS). Because of the full scale resolution, no model is required and provided that a low dissipative numerical scheme is used, results are very similar to reality. The drawback of this method is a tremendous computational cost even for a small configuration in time and space: nowadays DNS barely succeeds to handle the cold simulation (non reactive gas phase) of a real burner [241]. Adding more physics such as multiphase flows and combustion is out of reach with this method. However its 'numerical experiment' aspect provides useful databases in the case of canonical flows, and helps to validate lower order models.

- Reynolds-Averaged Navier-Stokes method (RANS) performs an ensemble averaging of the governing equations and model the effects of all turbulence scales through a diffusive term: the turbulent viscosity. This promotes numerical stability and allows to use a coarser mesh. The overall result is a low computational cost that allows to handle complex geometries. The drawback of this method is that it describes only mean values of the flow, so that singular events deviating from the mean are totally out of reach, which is a serious limitation to study combustion instabilities, for example. In addition, complex interaction of any other physics with turbulence is difficult to describe. Contrary to a common preconceived belief, RANS is not limited to steady state configurations and can handle the *statistical average* of transient states.

- Applying a low pass spatial filter to the governing equations helps limiting the required space and time resolution of DNS while directly resolving the largest (and most significant) energetic scales. This method is called Large Eddy Simulation (LES) and stands as the intermediate solution between the two previous ones.

A turbulence model is still required to describe the statistics of the turbulent quantities smaller than the filter size. However due to their universal behaviour, those quantities are easier to model than for the RANS approach. It is sufficiently efficient, robust and accurate to capture unsteady turbulence and transient phenomena in complex industrial flows. Its use tends to widespread as the power of actual computers growths. Being the approach used in this work, LES concept is detailed in Appendix A.2.

1.4.2 Modeling single-phase turbulent combustion

For complex hydrocarbons such as kerosene, combustion is a chemical process that involves hundreds of intermediate species and thousands of chemical reactions. The resolution of the whole system is prohibitive in terms of CPU cost and memory requirement. A first approach consists in filtering out the most important reactions and intermediate species of the reactions [92, 367], in order to build a *simplified chemistries*: reaction rates are ruled by Arrhénius law whose coefficients are adjusted to recover macroscopic values. Hence the flame speed, the adiabatic flame temperature, and the pollutant levels (if modeled) are predicted over a wide range of equivalence ratios, temperature and pressure to cover the whole range of combustor operating points. A second approach is to build chemistry tables from numerical simulation of simple flame configurations (laminar 1D flames) using a detailed chemistry and transport description [108, 214]. The reaction rates of the canonical flames are then tabulated over influent variables described by the simulation, such as the mixture fraction and the progress variable. One weak point of this method is to find the canonical flame that will reproduce the proper physics in complex geometries.

When the flame is immersed in a turbulent flow field, it interacts with the vortical structures, leading to a wrinkling of the flame front and possibly local extinction. As premixed flames are usually thinner than the mesh size used in combustors, they cannot be directly resolved and require modeling. Many models of turbulent combustion are available in the literature [273], but only major families are presented here, and a focus is made on the thickened flame model:

- geometrical description: the G-equation approach considers the flame as a surface that is described via a transport equation with an additional term that accounts for the turbulent flame front propagation [270]. Also using the idea of surface tracking, the flame surface density approach applies a spatial filter to a progress variable to build a filtered flame surface that is then propagated at the correct velocity [140].

- statistical approaches are based on probability density functions. They can be either presumed [204] or conditioned by the progress variable or the mixture fraction [222].

Butler & O'Rourke [39] proposed to thicken the flame front to allows for its resolution: the thermal diffusivity is multiplied by a so-called *thickening factor* F and the pre-exponential constant of the reaction rate is divided by the same factor. Consequently, the flame thickness is multiplied by F, allowing its resolution, and the laminar flame speed is kept unchanged. When the turbulent time scale is far larger than the chemical time scale, this modification can induce an error on the flame/turbulence interaction. In addition, the wrinkling of the flame front by subgrid vortices is neglected, leading to an artificial reduction of the flame surface that, in turn, decrease the reaction rate (Fig. 1.9). To counteract this effect, an efficiency function $\mathcal{E}$ based on DNS results was introduced by Colin *et al.* [54].

Note that to ensure the right mixing properties of the mixture, the thermal and molecular diffusivities should be multiplied by F *only* in reactive zones. A *dynamic* thickening procedure was thus developed [199]: F varies continuously from 1 in non-reactive zones to F_{max} in reactive zones, according to a sensor based on the local temperature and the mass fraction of reactants.

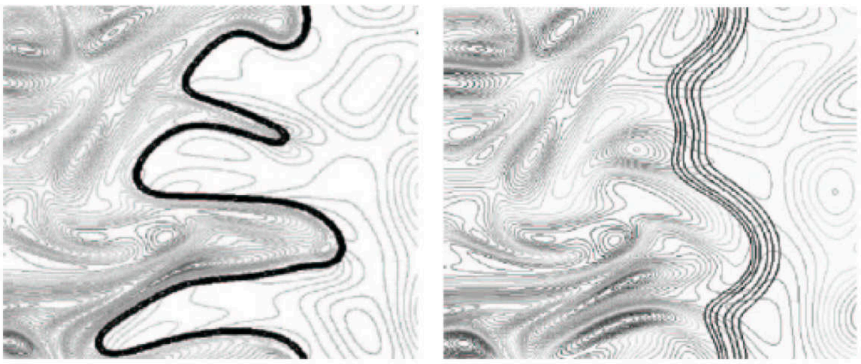

Figure 1.9 : *Influence on the thickened flame model on the flame wrinkling, from [273]. Left: Non thickened flame. Right: thickened flame*

1.4.3 Numerical description of two-phase flows

Due to the different time and length scales encountered in such a complex geometry, the numerical treatment of the liquid phase, from the very dense spray of the primary injection to the dilute spray in the combustion chamber, with the same formalism is challenging. Depending on the ratio of the liquid characteristic length scale over the mesh size, different numerical approaches can be considered. Figure 1.10 illustrates the evolution of this ratio in a combustion chamber.

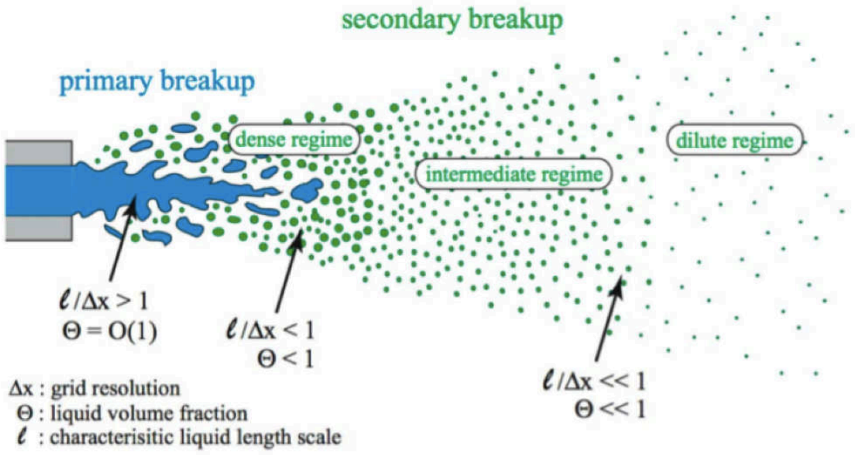

Figure 1.10 : *Grid requirements related to characteristic length scales of the spray. (Source: M. Hermann, Summer Program of the CTR, Stanford).*

In regions where the liquid remains coherent such as film flows and liquid sheets ($l_c \approx 1mm$), the interface undergoes critical phenomena such as instabilities, that require specific methods. *Resolved interface* methods like the Level-Set approach, or *diffuse interface* methods like Volume of Fluid (VOF) allow to describe accurately the interface behaviour [117]. During primary atomization, the liquid length scales decrease to the size of ligaments and liquid blobs ($\approx$ 0.5 mm). In this dense regime, coalescence may occur [256] and the use of Level-Set or VOF approaches needs a very fine mesh that considerably increases the CPU cost of the simulation.

After secondary atomization, the liquid phase enters a diluted regime in which driving phenomena are aerodynamics and particle inertia, so the interface is less critical. In addition the characteristic size of liquid elements (≈ 50 µm) is so small that the use of VOF or Level set in totally out of reach for nowadays computers: with a requirement of two to five cells per droplet [117] leading to a space discretization $\Delta x \approx 10$ µm, a combustion chamber of 1 cm^3 would be made of 10^{13} cells. Therefore diluted regimes are treated with specific methods that take advantage of the low volume occupation of the liquid phase to use simplifying assumptions. Two main approaches exist for dilute regimes: Lagrangian approach and Eulerian approach:

- The Lagrangian approach tracks independent particles (or clusters of particles) individually. The behaviour laws are derived from conservation principles applied on the particle (mass, momentum and energy) with different levels of complexity. Usually, droplets can be considered like local inclusions through the point-source approximation [207].

- In the Eulerian approach, the spray population is described through a Probability Density Function (PDF) depending on time, space, droplet size, droplet velocity and droplet temperature, and whose evolution is ruled by a Boltzmann equation. Solving this equation in the whole phase space (size, velocity, temperature) is out of reach for nowadays computers. Hence in order to decrease the computational overheads, the equation is multiplied by the phase variables and integrated to obtain transport equations of the first-order moments (number of particles, mass, momentum, energy) that still depend on time and space. This method is known as the Method of Moments (MOM) and can be applied in different ways: (i) the transport equations can be directly solved (Quadrature MOM or Direct Quadrature MOM), (ii) a spatial or ensemble average can be performed (mesoscopic Eulerian formulation), or (iii) the Boltzmann equation is integrated over some of the phase space variables and the remaining ones are split into several constant classes (sectional method or multifluid approach).

The numerical methods mentioned in this paragraph are presented in the following.

1.4.3.a) Volume of Fluid method

Volume of Fluid (VOF) methods are useful for free surface flows and have originally be developed by Hirt *et al.* [149]. These methods are efficient to handle complex interfaces as internal moving boundaries. It is based on a marker function that represents the liquid fraction inside each control volume:

$$\psi(\overrightarrow{x}) = \frac{1}{V_c} \int_{V_c} H(||\overrightarrow{x} - \overrightarrow{x_f}||)\, \mathrm{d}V \tag{1.4}$$

where $H(\cdot)$ denotes the Heaviside function.

From mass conservation at the interface, in absence of phase change, the interface motion is described by an advection equation of the marker function:

$$\frac{\partial \psi}{\partial t} + u_{f,i} \frac{\partial \psi}{\partial x_i} = 0 \tag{1.5}$$

where $u_{f,i}$ represents the interface displacement velocity. Equation 1.5 ensures mass conservation naturally and this is one of the main advantages of VOF methods. The main drawback is the implicit formulation of the interface. Equation 1.5 requires the interface velocity and position, to be reconstructed from the marker function. This reconstruction can be computationally costly, and may be difficult when the interface is highly deformed and subject to large strain rates (see Fig. 1.11). Finally, the discretization of Eq. 1.5 can induce a numerical diffusion and smooth a sharp interface [379].

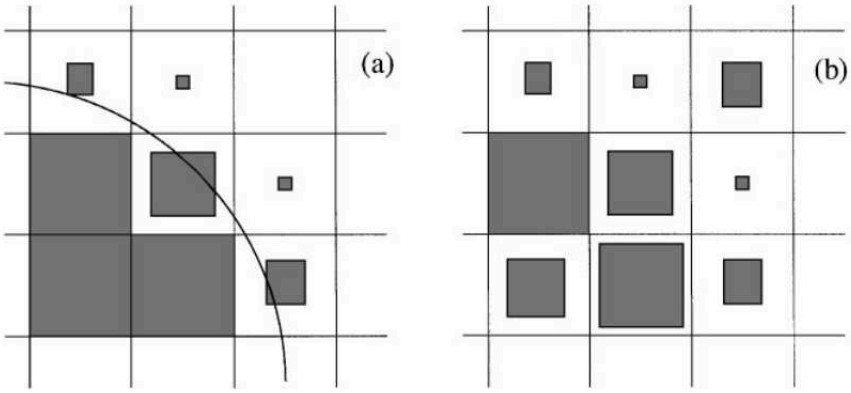

Figure 1.11 : *Interace reconstruction in Volume Of Fluid methods. The liquid volume fraction is represented by shaded squares. Left: Straightforward reconstruction of the interface. Right: No clear determination of the interface. From Scardovelli & Zaleski [308]*

1.4.3.b) Level Set method

The level set method has been originally introduced by Osher & Sethian [261] and actively developed during the nineties. Interested readers can consult the review works by Osher & Fedkiw [260] and Sethian & Smereka [318] for a detailed theoretical understanding.

The level set method describes the interface as the isosurface of a continuous function ϕ. It is usually initialized (at $t = 0$) by the algebraic distance d to the interface:

$$\phi(x_i, t = 0) = \pm d \tag{1.6}$$

The interface motion is described by a scalar advection equation:

$$\frac{\partial \phi}{\partial t} + u_{f,i} \frac{\partial \phi}{\partial x_i} = 0 \tag{1.7}$$

One of the advantage of the Level set methods id to avoid interface reconstruction and to give direct access to detailed interface geometry features, in particular, the surface curvature that is mandatory to compute surface tension forces.

Finally, level set methods suffer from mass loss in under-resolved regions. Given the fact that VOF methods are naturally mass conservative, attempts have been made to couple both methods. Among others, Ménard *et al.* [231] succeeded in applying coupled methods to primary atomization of a liquid jet.

1.4.3.c) Mesoscopic Eulerian Formalism

The Mesoscopic Eulerian Formalism (MEF) was introduced by Février *et al.* [87] for inertial particles suspended in a Homogeneous Isotropic Turbulence (HIT), and applies to dilute sprays. In this approach, the description of the history of each particle is replaced by the description of the sprays mean properties, regarding it as a continuous fluid. The averaging procedure may be carried out in a volumetric or statistical sense, leading to two different formulations for the dispersed phase, whose systems of equations are however very similar [174].

Considering a particle whose velocity $u_{p,i}$, temperature T_p, mass m_p, and position x_p at time t can be equal to $c_{p,i}$, ζ_p, μ_p and x_p in the phase space. The function $\mathcal{P}_p(c_{p,i}, \zeta_p, \mu_p, x_i, t)$ represents the probability for the particle p

to be characterized by the set $(c_{p,i}, \zeta_p, \mu_p, x_i)$ at time t in the phase space:

$$\mathcal{P}_p(c_{p,i}, \zeta_p, \mu_p, x_i, t) = \delta(c_{p,i} - u_{p,i}(t)) \cdot \delta(\zeta_p - T_p(t)) \cdot \delta(\mu_p - m_p(t)) \cdot \delta(x_p - X(t)) \tag{1.8}$$

with δ the Dirac delta function. The realization $\mathcal{H}_p$ of the spray is defined as the ensemble of functions $\mathcal{P}_p$ describing the motion of all the particles composing the spray. The probability density function f_p is defined as the statistical average of realizations $\mathcal{H}_p$ conditioned by one realization $\mathcal{H}_f$ of the fluid phase:

$$f_p(c_{p,i}, \zeta_p, \mu_p, x_i, t, \mathcal{H}_f) = \langle \mathcal{P}(c_{p,i}, \zeta_p, \mu_p, x_i, t) | \mathcal{H}_f \rangle \tag{1.9}$$

The Eulerian probability density function verifies a Boltzmann-type equation for the chosen state space variables. The phase average of any particle function $\psi(c_{p,i}, \zeta_p, \mu_p)$, such as velocity or temperature, is defined as its integration over the entire phase space, *i.e.* the entire possible realizations of this given function. The phase average is weighted by the particle mass, which allows to simplify the resulting set of equations. One obtains:

$$\breve{\psi} = \langle \psi \rangle_l = \frac{1}{\rho_l \breve{\alpha}_l} \int \psi(c_{p,i}, \zeta_p, \mu_p) f_p(c_{p,i}, \zeta_p, \mu_p, x_i, t, \mathcal{H}_f) dc_{p,i} d\zeta_p d\mu_p \tag{1.10}$$

with:

$$\rho_l \breve{\alpha}_l = \int \mu_p f_p(c_{p,i}, \zeta_p, \mu_p, x_i, t, \mathcal{H}_f) dc_{p,i} d\zeta_p d\mu_p \tag{1.11}$$

Eq. 1.10 yields the instantaneous local mean value of a given particle quantity conditioned by the given carrier phase, referred to as the mesoscopic quantity. The deviation from this mean, denoted by the superscript $(\cdot)''$, is the random uncorrelated part. In particular, replacing ψ with the particle velocity $u_{p,i}$ gives access to an Eulerian part, the mesoscopic velocity $\breve{u}_{l,i}$, and to a Lagrangian random part, the random uncorrelated velocity $u''_{p,i}$ [87], as depicted on Fig. 1.12:

$$u_{p,i} = \breve{u}_{l,i} + u''_{p,i} \tag{1.12}$$

This random motion leads to an isotropic redistribution of droplets which is enhanced in zones of shear and com-

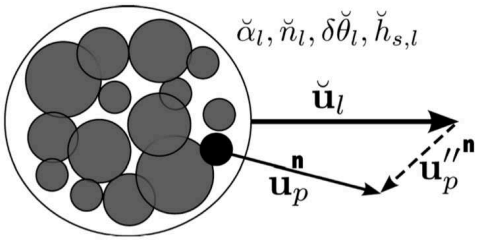

Figure 1.12 : *Schematic of mesoscopic averaged and uncorrelated Lagrangian velocities, from [134]*

pressibility effects of the mesoscopic motion [322]. Filtering the Naviers-Stokes equations of the dispersed phase with the $\breve{\cdot}$ operator leads to second-order terms. Among theses are the uncorrelated velocity tensor $\delta\breve{R}_{l,ij}$ and the uncorrelated energy $\delta\breve{\theta}_l$:

$$\delta\breve{R}_{l,ij} = \langle u''_{p,i}\, u''_{p,j} \rangle \tag{1.13a}$$

$$\delta\breve{\theta}_l = \frac{1}{2} \langle u''_{p,i}\, u''_{p,i} \rangle \tag{1.13b}$$

Those terms are solved through another Boltzmann-type equation [174, 322]. As it will be seen in section 1.4.4, this methods showed promising results in the application of spray combustion.

1.4.3.d) QMOM / DQMOM

Quadrature Method Of Moments (QMOM) and Direct Quadrature Method Of Moments (DQMOM) are sophisticated and more general techniques to use the method of moments. One difficulty when integrating the Boltzmann equation in the phase space is to evaluate the integral of the source terms. In the original MOM introduced by Hulburt & Katz [159] in 1964, the source terms were decomposed on a basis of *Laguerre* polynomials which impose restrictive conditions on their form. The QMOM proposed by McGraw [228] approximates the source terms integral through n points Gaussian quadrature, decomposing the distribution of the associated value (probability of presence, droplet size, velocity and temperature) onto an appropriate base. This approximation requires to solve a $2n \times n$ linear system to determine the weights and abscissas of the Gaussian quadrature from the known moments. Marchisio & Fox [217] proposed the DQMOM by directly expressing the weights and abscissas through Dirac delta functions, decomposing the spray PDF onto delta functions.

1.4.3.e) Sectional method or Multifluid approach

The Boltzmann equation is integrated over some phase space variables and the other one are split into several constant classes. Greenberg *et al.* [123] originally used this method only with different classes of droplet size and Laurent & Massot [188] provided a theoretical basis for the sectional model in a more general case, and named this approach *Multifluid Approach*. Later, de Chaisemartin *et al.* [61] proposed a modification to account both for different diameters and trajectories in the same cell. After ten years of development, those methods begins to be applied in aeronautical chambers, as seen in section 1.4.4.

1.4.3.f) Lagrangian

Lagrangian approaches track individually each particle. As the droplets travel in the domain, they do not necessary coincide with the mesh nodes and an interpolation procedure is used to evaluate the gaseous variables seen by the particle. When the scales of the gaseous flow are not all resolved (LES and RANS), the effect of the unresolved flow fields on particles should be modeled [83] for a rigorous treatment. However effects of subgrid terms are generally neglected in LES of two-phase flows [9, 290] as the subgrid fluid velocity seen by the particles is negligible for preferential concentration [84]. Contrary to Eulerian approaches, no averaging is applied, so that polydispersity as well as crossing trajectories are naturally handled. This last property is interesting for spray/wall interaction modeling: the wall vicinity contains impacting and reemitted droplets (*i.e.* velocities in opposite direction) and the average velocity (classical Eulerian approach) would be close to zero whereas the Lagrangian approach independently treats each trajectory. As the Lagrangian approach is the extensively used in this work, it is presented in details in Appendix B.

1.4.3.g) Smoothed-Particle Hydrodynamics

Smoothed-Particle Hydrodynamics (SPH) was originally developed by Gingold & Monaghan [110] and Lucy [212] to solve Navier-Stokes equations in the context of astrophysical fluid dynamics, this formalism fits well with multiphase flow simulations [157] such as the collapse of a dam [236] or river ice dynamics [319]. One numerical particle represents a volume of fluid and a high number of particles is required to model a continuous flow. This model particularity is that it takes into account particle/particle interactions, and all surface effects that apply to a particle (pressure and viscosity) are computed from its neighbouring particles. The interface is thus naturally defined by the location of the particles for each phase. This way, capillarity effects, that are related to the liquid-gas distribution, are naturally recovered through the heterogeneity of the particles location. Particle/particle interaction is taken into

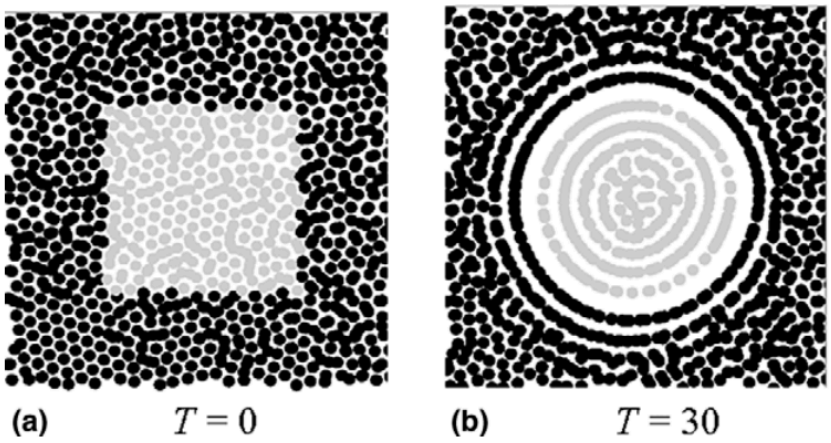

Figure 1.13 : *Visualization of surface tension effect with SPH approach. Black and grey particles represent gas and liquid particles, respectively. a) Initial condition presents a non-equilibrium: particles located at the square corners undergo a stronger attraction towards the interior than particles located at the middle of faces. b) Equilibrium is reached when all interface particles are subject to the same attraction. From Tartakovsky & Meakin [338]*

account through a convolution product between a continuous field A and a weighting function W:

$$A_s(\overrightarrow{r}) = \int_{-\infty}^{+\infty} A(\overrightarrow{r'}) W(\overrightarrow{r} - \overrightarrow{r'}, h)\, \mathrm{d}\overrightarrow{r'} \tag{1.14}$$

where A_s is the smoothed field and h is the support scale of W such as its integral is equal to one. Properties associated to a particle i are expressed by approximating the integral in Eq. 1.14 by the sum:

$$A_i = \sum_j V_j A_j W(\overrightarrow{r_i} - \overrightarrow{r_j}, h) \tag{1.15}$$

where V_j is the volume occupied by the particle j. At any position $\overrightarrow{r}$ mass, momentum or energy are reconstructed from particles space distribution. With this formalism, the interface location does not need to be reconstructed to take surface tension into account: its effects on a liquid particle is reproduced by the attractive force with the other liquid particles present in the liquid phase (see Fig. 1.13). Consequently no mesh is needed, each phase being solved by particle/particle interactions, even for boundary conditions.

The SPH method has recently been applied to thin film flows and atomization in the context of gas turbine by Hoefler *et al.* [150] and showed promising results.

1.4.4 State of this art: LES of two-phase flow combustion in gas turbines

This last decade, computational methods have reached a maturity that allows the simulation of reactive two-phase flows in gas turbine configurations. As this type of simulation describes many complex physical phenomena, their number is still limited in literature.

1.4.4.a) Lagrangian approach

Ham *et al.* [131] and Moin & Apte [235] performed a LES of a Pratt & Whitney combustor (PW6000) fueled by an airblast atomizer (Fig. 1.14 *left*) with the Charles solver [215], in a low-Mach, variable density formulation with a liquid phase described through a Lagrangian approach, validated [11] against Sommerfeld & Qiu experiment [327, 328]. The liquid film inside the airblast atomizer was not explicitly resolved but was approximated by large drops of the size of the atomizing edge thickness. Primary breakup was neglected and the drops started secondary atomization directly, using a stochastic secondary breakup model [9] prior validated in the case of a Diesel-engine configuration of Hiroyasu & Kadota [147]. The final result of this simulation was in good agreement with measurements of the temperature profile at the outlet of the combustion chamber (Fig. 1.14 *right*). In 2009, Apte *et al.* [10] performed a

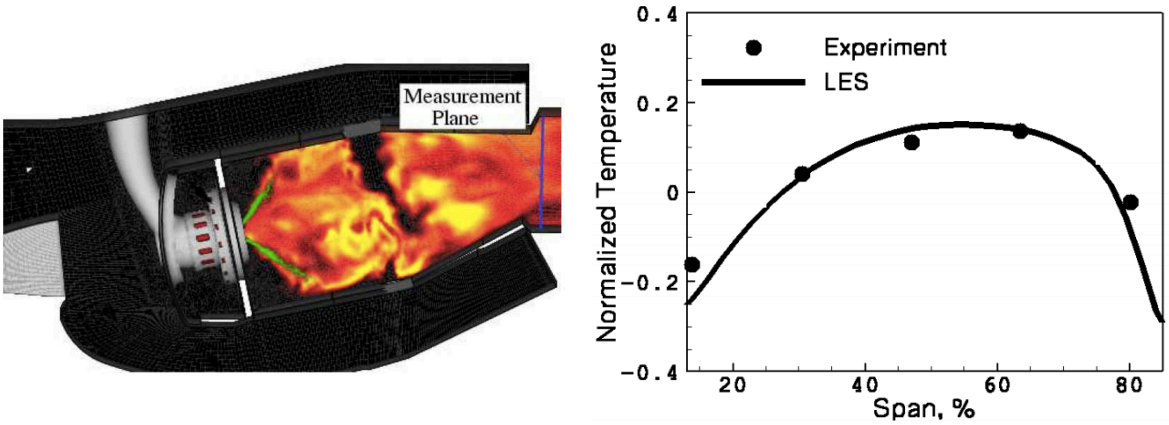

Figure 1.14 : *LES of the PW6000 combustor from [235]. Left: instantaneous snapshot of temperature in a mid-cut plane, superimposed with droplet locations. Right: prediction of mean temperature at the measurement plane of PW combustor. Span represents the normalized vertical distance in the measurement plane*

non-reactive LES on the same geometry with a finer mesh and an improved secondary breakup model. They focused on the prediction of the spray statistics and found out an accurate prediction of the axial mass flow rate but a large deviation of the dropsize distribution.

In 2009, Jaegle [162] performed a LES simulation of an evaporating polydisperse spray in a real geometry, the TLC[3] configuration [189]. In this configuration, the spray is injected through two separate circuits: (i) a piezo-type pilot injector, featuring a ring of very small orifices, and (ii) a multipoint injection system made of 24 holes located on the inner wall of a swirler. This was done with the AVBP code, presented in section 1.5.2, and no film nor breakup models was applied. The comparison of the liquid velocity and diameter proved a good description of the interactions between the carrier and dispersed phase, allowing to identify regions suitable for ignition [163]. Senoner [316] studied the secondary breakup of an evaporating spray on the MERCATO[4] test rig, designed to provide a better physical understanding of ignition sequences in realistic combustion chamber with liquid fuel injection [99]. This configuration is fueled by a pressure-swirl atomizer. Recently, Hannebique [134] and Paulhiac [265] studied the two-phase flame structure in the MERCATO configuration (Fig. 1.15). A LES of a real SNECMA combustor was also performed by Paulhiac [265], without film nor breakup models.

[3]Towards Lean Combustion
[4]Moyen d'Étude et de Recherche en Combustion Aérobie par Techniques Optiques

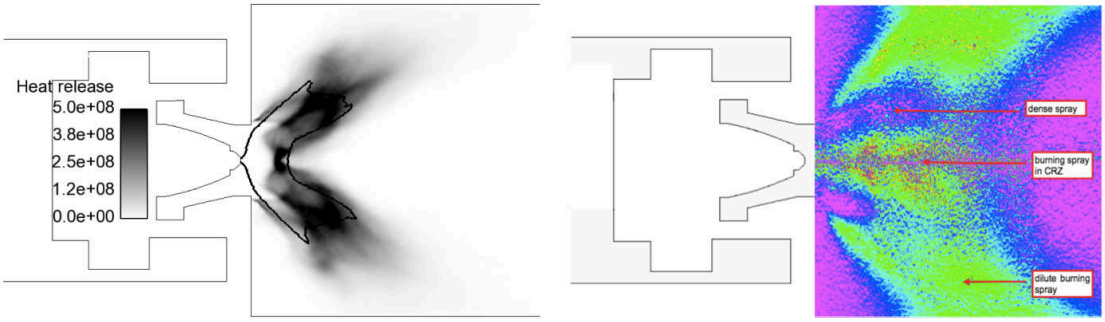

Figure 1.15 : *Left: Average heat release of a flame fed with a polydisperse spray in a mid-cut plane superimposed with the iso line $\alpha_l = 10^{-5}$), from [134]. Right: Direct flame visualization, from [191]*

1.4.4.b) Eulerian approaches

In 2008, Boileau *et al.* [28] applied the MEF in a real configuration with the reactive LES of one sector of a combustion chamber, and soon later, they performed a LES of an ignition sequence of a full annular combustion chamber [29]. Hannebique *et al.* [135] performed a reactive LES of the multipoint TLC configuration in take-off conditions. Recently, Vié *et al.* [356] coupled the multifluid approach with a MEF closure on each diameter class and applied it to a vaporizing kerosene spray in the MERCATO test rig.

1.4.4.c) Conclusion

Up to now, the liquid film as well as the primary breakup were never taken into account in reactive studies of aeronautical combustion chambers fueled by airblast atomizers. The liquid breakup was studied only once through secondary atomization.

As the liquid film is the source of the fuel spray feeding the flame, it can be foreseen that its behaviour has an impact on the spray and in turn, the flame structure. In addition, when the flame front is located close to the atomizing edge, secondary atomization has no time to occur and the flame is fed by a spray generated by primary breakup only. Therefore taking the primary breakup into account may significantly alter the flame structure.

1.5 Objectives of the present work

1.5.1 Thesis objectives

The aim of the present work is to develop a film model and a primary breakup model for airblast atomizers in order to provide a realistic drop size distribution at the atomizer exit, and then to study the impact of this enhanced description onto (i) the liquid distribution inside the chamber and (ii) the flame structure. The film model is derived by simplification of Navier-Stokes equations, and the primary breakup model is of phenomenological type: a part of the physics is not resolved but embedded into the model constants that require to be calibrated onto an academic configuration. The applicability of those models in complex configuration relies on the assumption that the described phenomenon is based on the same physics than in academic configuration. This approach allows to employ much coarser mesh grids and larger time steps that make suitable for the simulation of realistic industrial configurations. As the film and primary breakup phenomena involve a solid wall, and due to its advantages in spray/wall interaction (see section 1.4.3.f)), the Lagrangian formulation of the spray is exclusively chosen for this work.

This work was done in the framework of the european project FIRST ('**F**uel **I**njectors **R**esearch for **S**ustainable **T**ransports') in an effort to enhance the atomization process, decrease pollutant emissions and improve combustion efficiency, and in collaboration with Turbomeca and the KIT-ITS[5].

1.5.2 Lagrangian developments available in the AVBP solver before this work

The numerical tool used during this work is the code AVBP. This cell-vertex unstructured hybrid solver has been jointly developed by CERFACS and IFP-EN (Institut Francais du Pétrole - Energies Nouvelles) over the last twenty years. AVBP is a massively parallel code that explicitly solves both DNS and LES Navier-Stokes equations in compressible form. High-order numerical schemes [122] and characteristic boundary conditions [272] are available. More information on AVBP can be found in [185]. This code is mainly dedicated to aeronautical combustors and internal combustion engines, but it is also used for aerodynamic studies on complex geometries.

The Lagrangian solver was originally written by García [98] in 2009. García demonstrated the competitiveness of the Euler-Largrange solver compared to the Euler-Euler solver in terms of both accuracy and computational cost on canonical tests such as DNS of a Homogeneous Isotropic Turbulence (HIT) flows and a LES of a bluff body flow both laden with particles. Jaegle [162] extended the Lagrangian solver to handle evaporation and performed a LES of evaporating two-phase flow in a complex combustor with fuel staging. Senoner [316] worked on liquid injection and implemented the FIMUR model [305] that mimics fuel injection through a pressure swirl atomizer without accounting for primary and secondary breakups. Senoner also implemented a secondary atomization model called FAST (for Fast Atomization Stochastic Treatment) from the work of Gorokhovski *et al.* [9, 118, 117] and validated it on a diesel spray configuration [147] and a liquid jet in a turbulent gaseous crossflow [22]. It was shown that after calibrating the two model constants, the drop size distribution and the penetration length were in good agreement with the experiments. Hannebique [134] improved the FIMUR model. Recently, Paulhiac [265] implemented a more robust particle tracking algorithm, presented in section 5.1.4.

1.5.3 Thesis outline

The manuscript is organized as follows:

- The first part is dedicated to the description of physical phenomena encountered in prefilming airblast atomizers. Chapter 2 presents the spray/wall interactions and their influencing parameters. It is based on several fundamental experiments, and the correlations derived out of them are detailed. In chapter 3, the thin film flows are described and their equation set is derived and expressed in a non dimensional form. An overview of the numerical strategies to model film flows is presented. Chapter 4 focuses on the liquid instabilities at the film surface that trigger primary atomization process.
- The second part is details the Lagrangian solvers and physical and numerical development performed in this thesis. Chapter 5 describes the Lagrangian solver of AVBP, and the method to project Lagrangian fields onto the mesh grid and convert them into Eulerian quantities. The chapter ends with the details of the spray/wall interaction model implemented by Habchi [128]. Chapter 6 details the development, implementation in AVBP and first validation of the liquid film model. Chapter 7 proposes a mechanism for the particular case of liquid accumulation breakup. A model describing the drop size distribution of the generated spray is built out of this mechanism and calibrated from the KIT-ITS experiment. A quantification of the model error is proposed, and the chapter concludes with implementation details.
- In the third part, the implemented models are confronted with a real academic configuration. Chapter 8 presents the LES of the KIT-ITS experiment that provides deeper insights into the fragmentation process of a

[5] Karlsruhe Institute of Technology - Institüt for Thermische Strömungsmaschinen

liquid film downstream of an atomizing edge. Comparison is made in terms of gaseous velocity profiles, film thickness, drop size distribution and spray angle.

All calculations presented in this thesis were performed on CERFACS supercomputers HP Proliant (Corail) and Bullx B510 (Neptune), and on the SGI Altix ICE 8200 (Jade) from CINES (Centre Informatique National de l'Enseignement Supérieur) under the allocation 2013- x20132b5031 made by GENCI (Grand Equipement National de Calcul Intensif).

Part I

Two-phase flow phenomena from injection to atomization

The three following chapters aim to collect experimental results of academic experiments, highlighting influent parameters that may be inputs for future phenomenological models. Each academic experiment focuses on a particular phenomenon of the liquid phase, from injection to atomization, and their sequential combination leads to describe the overall liquid phase behaviour. As an introduction of this bibliographic part, airblast atomizers and their characteristics are briefly presented.

Airblast atomizers were originally studied by Nukiyama & Tanasawa in 1939 [252] and more recently by Lefebvre and co-workers during the seventies. In 1980, Lefebvre [197] published a review on airblast atomizers, briefly summarized here. Lefebvre highlighted the advantages of airblast atomizers over pressure-swirl atomizers: (i) lower fuel pressure, (ii) thorough mixing between air and fuel, (iii) low soot formation and (iv) sensibly constant fuel distribution over the entire range of fuel flows.

There are two main families of airblast atomizers. First, *plain jet atomizers* inject liquid into the high-velocity airstream in the form of discrete jets, that fragment due to the aerodynamic stresses. The second family is made of *prefilming atomizers* that first spread out liquid into a thin, continuous sheet that is subjected to the atomizing action of high velocity air. The superiority of prefilming airblast atomizers to produce a fine spray was observed [93], especially under adverse conditions of low air/liquid ratio and/or low air velocity [197]. Consequently this work focuses on prefilming airblast atomizers only.

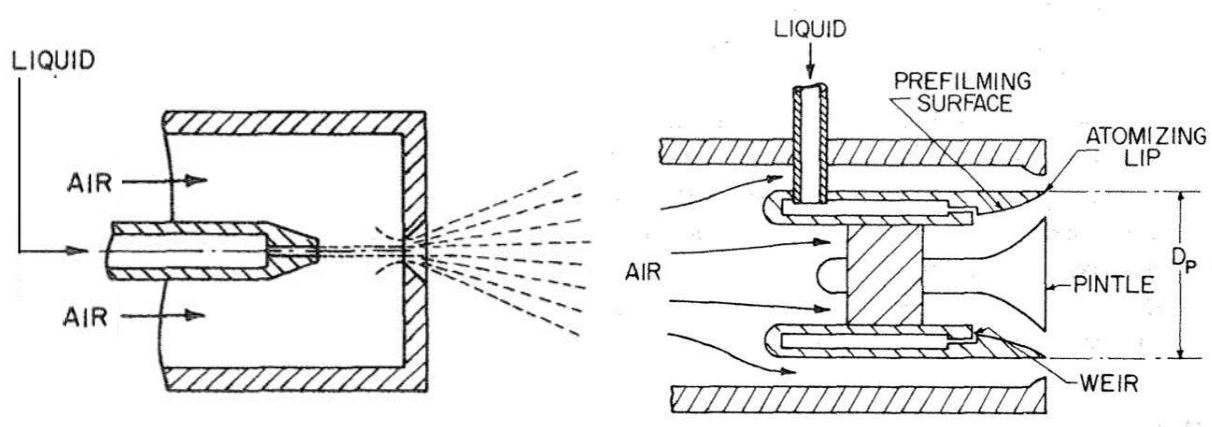

Figure 1.16 : *Sketch of plain jet (left) and prefilming (right) airblast atomizer, from [197]*

Performances of airblast atomizers are characterized by the quality of the spray they produce. First quantities that characterize a spray are mean diameters. Their general form $D_{a,b}$ is expressed as:

$$D_{a,b} = \left(\frac{\sum_{i=1}^{N_{sample}} d_i^a}{\sum_{i=1}^{N_{sample}} d_i^b} \right)^{1/(a-b)} \tag{1.16}$$

where d is the diameter of the collected droplet, N_{sample} is the number of collected droplets, and a,b are integers defining the type of mean diameter. Common mean diameters are (i) the Arithmetic Mean Diameter (AMD) D_{10}, (ii) the Volume Mean Diameter (VMD) D_{30} that recovers the spray volume ($N_{sample}\, D_{30}^3 \propto V_{spray}$ where V_{spray} is the spray volume), and (iii) the Sauter Mean Diameter (SMD) D_{32} that represents the mean volume-to-surface ratio of the spray, and is appropriate for combustion.

Second quantities to characterize sprays are the drop size PDFs that gives an accurate characterization and theoretically allow to find all mean diameters. There are commonly two type of spray PDF: (i) the Number PDF (NPDF) f_0 that describes the probability to find a droplet in a diameter range, *e.g.* the probability to find a droplet of diameter comprised between d_i and $d_i + \Delta d$ is $f_0(d_i)\,\Delta d$, and (ii) the Volume PDF (VPDF) f_3 that quantifies the proportion of the spray volume in a diameter range, *e.g.* the proportion of the spray volume accounted by droplets of diameter comprised between d_i and $d_i + \Delta d$ is $f_3(d_i)\,\Delta d$. The number and volume PDF are linked by $f_3(d) \propto d^3\, f_0(d)$.

Spray PDF are usually described by analytical functions, the most popular being the Rosin-Rammler (Eq. 1.17a), the Nukiyama-Tanasawa (Eq. 1.17b), the Log-Normal (Eq. 1.17c) and the Upper Limit (Eq. 1.17d) functions:

$$f_3(d) = C_{RR}\, d^{q-1} \exp\left[-\left(\frac{d}{m}\right)^q\right] \tag{1.17a}$$

$$f_0(d) = C_{NT}\, d^p \exp\left(-m\, d^q\right) \tag{1.17b}$$

$$f_0(d) = \frac{C_{LN}}{d} \exp\left[-\frac{1}{2}\left(\frac{\ln d/m}{\ln q}\right)\right] \tag{1.17c}$$

$$f_3(d) = \frac{C_{UL}}{d\,(p-d)} \exp\left\{-\frac{1}{2\ln^2 q}\left[\ln\left(\frac{p\,d}{m(p-d)}\right)\right]^2\right\} \tag{1.17d}$$

where m, p and q are parameters that must be fitted on experiments and C_{RR}, C_{NT}, C_{LN}, and C_{UL} are normalizing constants that fulfill $\int_0^\infty f(d)\,\mathrm{d}d = 1$ and depend on m, p and q, see [14] for further details. Figure 1.17 shows the influence of m, p and q on these distributions.

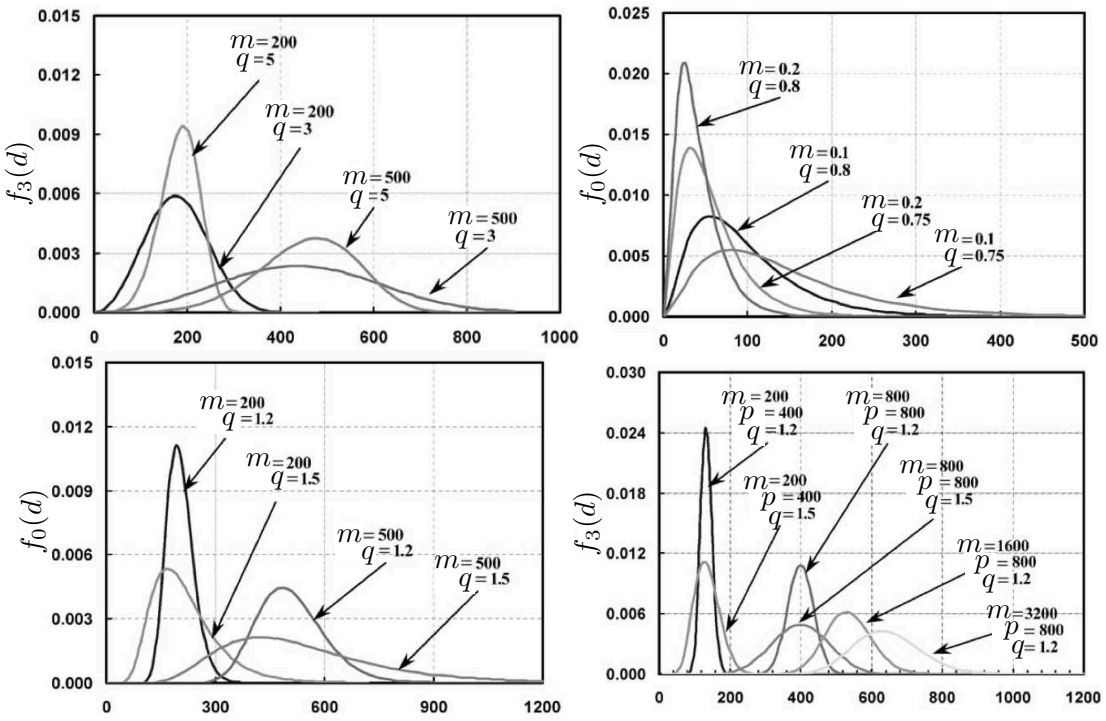

Figure 1.17 : *Typical functions to describe spray PDF, x axis: d in µm and y axis in µm^{-1}. Top left: Rosin-Rammler. Top right: Nukiyama-Tanasawa. Bottom left: Log-Normal. Bottom right: Upper Limit. Adapted from [14]*

In prefilming airblast atomizers, influent parameters are, sorted by decreasing influence: gas velocity U_g, air/fuel mass flux ratio AFR, surface tension σ, gas density ρ_g, liquid viscosity μ_l, injector dimension L_c and the film thickness h. Note that some of these parameters can combine into another influent parameter, *e.g.* the gas dynamic pressure $\rho_g\, U_g^2$.

Lefebvre [review 80] proposed a generic correlation on the SMD:

$$\frac{SMD}{L_c} = A\sqrt{\frac{\sigma}{\rho_g\, U_g^2\, D_p}}\,(1+AFR) + B\sqrt{\frac{\mu_l^2}{\sigma\,\rho_l\, D_p}}\,(1+AFR) \tag{1.18}$$

where D_p is the diameter of the atomizer exit, and A and B are constants depending on the atomizer design. The right-hand side of Eq. 1.18 shows the sum of two terms that Lefebvre & co-workers attribute to two modes of atomization: for low viscosity liquids, the second term can be neglected, and atomization is mainly the result of aerodynamic stresses on the liquid sheet. For viscous liquid, the second term becomes preponderant and the SMD mainly depends on liquid viscosity. The form of Eq. 1.18 is found by many other authors, see [197] for an extensive comparison of different correlations. Rizk & Lefebvre [292] found an influence of the film thickness upstream the atomizing lip, with $h^{0.4}$. It is also found that increasing the atomizing lip diameter D_p leads to a finer spray. This is explained by the fact that a larger D_p increases the film/gas contact area and decrease the film thickness.

In nowadays airblast atomizers, liquid is injected through a pressure-swirl atomizer (Fig. 1.5 *right*) under the form of a hollow cone spray that impacts the injector wall and creates a film. The impact of the spray droplets onto the wall is a complex phenomenon that needs to be understood, bringing additional complexity to the overall behaviour.

To conclude, there are three categories of physical phenomena corresponding to the different steps of the liquid phase in a prefilming airblast atomizer: (i) spray/wall interaction when droplets of the primary spray impact the injector wall (the so-called prefilmer), (ii) thin film flow, sheared by a high-speed airstream and (iii) atomization of liquid by aerodynamic stresses. Each phenomena is presented in a chapter. Chapter 2 details the main experimental studies of spray/wall interaction during those last two decades. A particular attention is made on the mechanisms leading to different regimes. The dimensionless numbers that distinguish the different regimes as well as their threshold value is discussed. Correlations on the number, diameter and velocity of reemitted droplets (secondary droplets) are summarized in order to derive phenomenological models. In chapter 3, general film equations are derived from Navier-Stokes equations via comparison of dimensionless numbers. A summary of modeling strategies for film flows is then presented. Chapter 4 presents the general mechanisms leading to different types of atomization encountered in aeroengines. Parallel flows stability is first theoretically studied, highlighting the presence of two dimensional instabilities. The particular case of film instability is discussed and a corresponding regime map is displayed. Then the instability transition from 2D to 3D (the so-called secondary instability) and the ligament breakup are tackled. More practically, the different flow configurations encountered in aeroengines are connected to academic studies of primary breakup, and they are presented with their main mechanisms and characteristics. The chapter ends with an overview of numerical methods to model primary breakup.

Chapter 2

Spray / Wall interaction

This chapter provides a phenomenological description of the interaction between a spray and wall. An overview of the impact outcomes is first proposed, followed by a description of influent parameters, and the resulting regimes map built from experimental observations. Each outcome (splashing, rebound and filming) and their associated phenomena is then tackled in details for modeling purposes. Finally macroscopic correlations derived from real sprays experiments are presented.

2.1 Overview

In some injection systems, the spray impacts inner walls, leading to rebound, splashing or possibly forming a liquid film. Those different regimes result in various distributions of the liquid phase inside the injector that in turn, may lead to different chemical reactions. In addition, heat transfer may occur and modify the gas, liquid and wall temperatures.

2.1.1 Phenomenology

When a spray impinges a wall, two families of phenomena occurs in the wall vicinity: isolated droplets and clustered droplets phenomena. The former family corresponds to the interaction between a single droplet and the wall while the later presents additional droplet/droplet interactions.

When an isolated droplet impacts a wall, several types of outcome are observed:

- sticking: the droplet sticks on the wall and conserves a spherical shape;
- filming: the droplet spreads on the wall and forms a liquid film (Fig. 2.1 *left*);
- rebound: the droplet does not stick nor spread on the wall, but is reemitted (Fig. 2.1 *right*);
- splashing: the droplet disintegrates and reemits so-called secondary droplets. A fraction of the droplet can spread on the wall (Fig. 2.2).

When a real spray impact a wall, the mechanisms involved are a combination of isolated droplet/wall and droplet/droplet interactions. One difficulty when studying spray/wall interaction is that no superposition principle

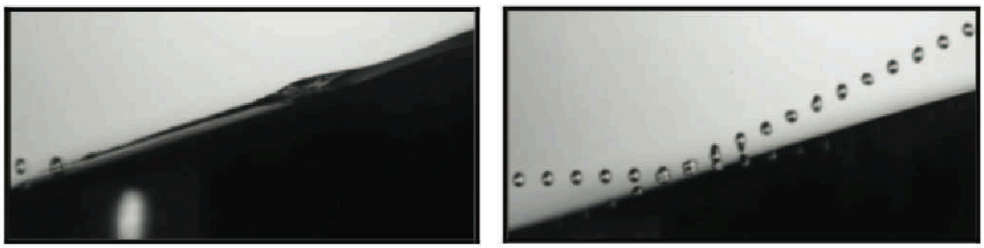

Figure 2.1 : *Photograph of isolated droplet/wall interaction in filming (left) and rebound (right) regimes, from [6]*

can be applied to the spray droplets: the overall spray does not behave as the superposition of single droplets. This is partly explained by droplet/droplet interaction that becomes predominant in the dense spray close to the wall [133]. As the proportion of droplet/droplet interaction is not well characterized in real spray/wall impact phenomena, it will not be tackled in this chapter, the first modeling step being to assimilate spray/wall interaction to multiple single droplet/wall interactions.

2.1.2 Experiments

As pointed by Moreira *et al.* [238], experiments on spray/wall interaction are numerous and present various boundary conditions and measurements techniques. The goal of this section is to describe a generic picture of this type of experience. For an extensive list of experiments and their characteristics, the reader is addressed to Table 1 of [238]. Two types of experiment are presented in the following: (i) isolated droplet/wall interaction and (ii) spray/wall interaction.

2.1.2.a) Isolated droplet

The study of isolated droplet/wall interactions is useful to derive elementary models based on experimental observation. The typical experiment consists in a flat plate on which is projected single droplets of controlled diameter. The plate is characterized by several parameters: temperature, roughness, presence of a liquid film, hydrophilic/hydrophobic properties (explained in section 2.1.3.d)). The droplet characteristics are the liquid type, its diameter, its velocity magnitude and direction. The velocity direction is usually perpendicular to the wall surface but some authors investigated oblique impacts. As the droplet characteristics are controlled, it is possible to repeat exactly the same impact several times and perform an ensemble average, as displayed on Fig. 2.2 (*left*). This allow sto filter out singularities, to study global mechanisms and to derive statistical correlations. The use of high-speed cameras allows to produce time series that give insights into the splashing mechanisms, as shown on Fig. 2.2 (*right*). The outcome of the impact is monitored in term of mass deposited (amount of liquid sticking to the surface), secondary droplet characteristics (number, diameter, velocity, temperature) and extracted heat flux.

2.1.2.b) Real sprays

In the optic of deriving macroscopic laws, some authors perform experiment with a real impinging spray. In addition to the parameters of isolated droplets are the shape of the plate (*e.g.* curved surface to mimic spray/piston interaction in internal combustion engine), the drop size distribution, the mass flux and the angle of the spray. As displayed on Figs. 2.3 and 2.4, determining secondary droplets characteristics is not possible. Therefore in such experiments, only macroscopic values (global heat transfer, global liquid deposition or global mass flux) and statistical data (mean diameters, mean deviation angles) are extracted.

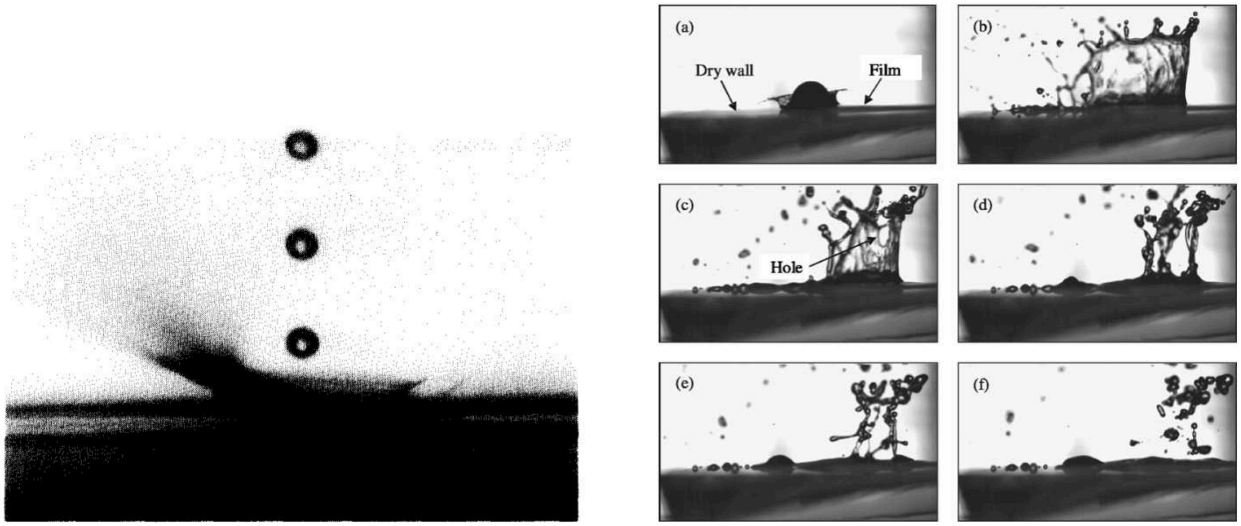

Figure 2.2 : *Illustration of isolated droplet interaction. Left: Photograph of droplet splashing, averaged over many individual events at the same phase, from [245]. Right: time sequence of single normal drop impact onto a non uniform film, from [295]*

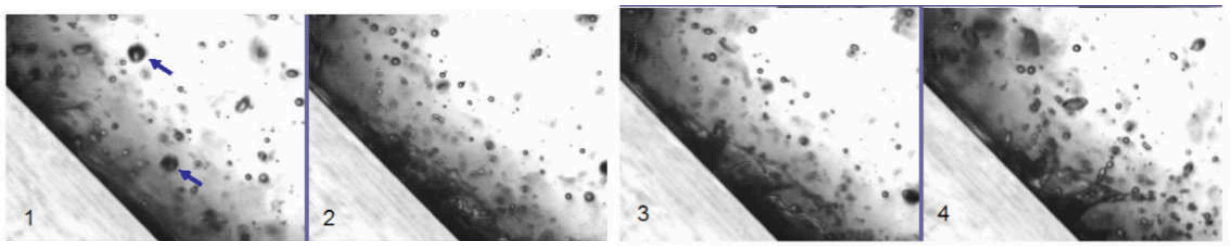

Figure 2.3 : *Spray impact onto a wall inclined at 45°, from [20]*

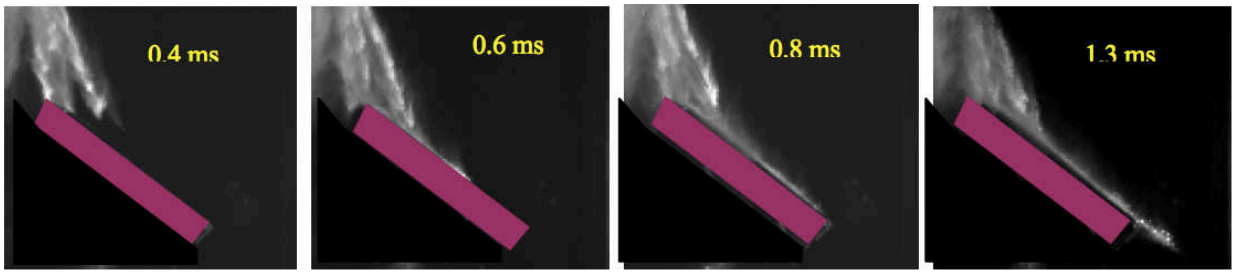

Figure 2.4 : *Impinging spray development on an inclined wall (60°) at 381 K in a pressurized (3 bars) atmosphere, from [1]*

2.1.3 Influent parameters

The impact energy and the wall temperature are first order parameters which are used to characterize different regimes. Second order parameters are the presence of a liquid film, the surface roughness and the system wettability.

2.1.3.a) Impact energy

It represents the amount of kinetic energy of the impacting droplet that acts as a destabilizing effect. At the impact, the droplet kinetic energy is dissipated into heat through viscosity and converted into surface energy through droplet deformation. When the impact energy increases, the droplet is more likely to disintegrates, as depicted on Fig. 2.5. An important stabilizing effect expresses through surface tension which tends to minimize the droplet surface and therefore keep a spherical shape. The competition between stabilizing and destabilizing effects is quantified by the Weber number:

$$\mathrm{We} = \frac{\rho_l d_p u_{n,p}^2}{\sigma} \tag{2.1}$$

where ρ_l is the liquid density, d_p the droplet diameter, $u_{n,p}$ the normal (to the impacted surface) component of the droplet velocity and σ the surface tension of the liquid/gas system. The Weber number is representative of the balance between impact and surface tension energy, and as it is of primary importance to determine the droplet impact regime, other parameters in the literature are based on it [128, 245, 335, 370]. Note that some authors express the Weber number with the droplet velocity magnitude U_p instead of the normal component $u_{n,p}$. In this chapter, such a Weber number is superscripted with a star $(*)$: We^*.

Similarly to the Weber number, a disintegration parameter estimating balance between stabilizing and destabilizing forces is used to quantity the impact energy. It was originally introduced by Stow & Hadfield [335] as:

$$K_c = A \cdot \mathrm{We}^a \cdot \mathrm{Oh}^b \tag{2.2}$$

where A, a and b are constants fitted from experiments. Equation 2.2 is another definition of the impact energy which uses the Ohnesorge number in addition to the Weber number:

$$\mathrm{Oh} = \frac{\mu_l}{\sqrt{\rho_l \, \sigma \, d_p}} \tag{2.3}$$

where μ_l is the liquid viscosity. The Ohnesorge number evaluates the importance of three effects linked to the liquid properties: the viscosity, the density and the surface tension. Note that the Ohnesorge number can be expressed as $\mathrm{Oh} = \sqrt{\mathrm{We}}/\mathrm{Re}$ where Re is the Reynolds number:

$$\mathrm{Re} = \frac{\rho_l \, d_p \, u_{n,p}}{\mu_l} \tag{2.4}$$

As well as for the Weber number in this chapter, the Reynolds number expressed with the velocity magnitude U_p is written Re^*.

The form of the disintegration parameter (Eq. 2.2) was later confirmed by Mundo *et al.* [245] and its constants set (A, a, b) depends on authors:

$$K_c = \mathrm{We}^{5/8} \, \mathrm{Oh}^{-1/4} \qquad \text{from Mundo } \textit{et al.} \text{ [245]} \tag{2.5a}$$

$$K_c^* = \mathrm{We}^* \, \mathrm{Oh}^{-2/5} \qquad \text{from Cossali } \textit{et al.} \text{ [56] and García-Rosa } \textit{et al.} \text{ [297]} \tag{2.5b}$$

$$K_c = \mathrm{We}^{5/4} \, \mathrm{Oh}^{-1/2} \qquad \text{from Han } \textit{et al.} \text{ [133]} \tag{2.5c}$$

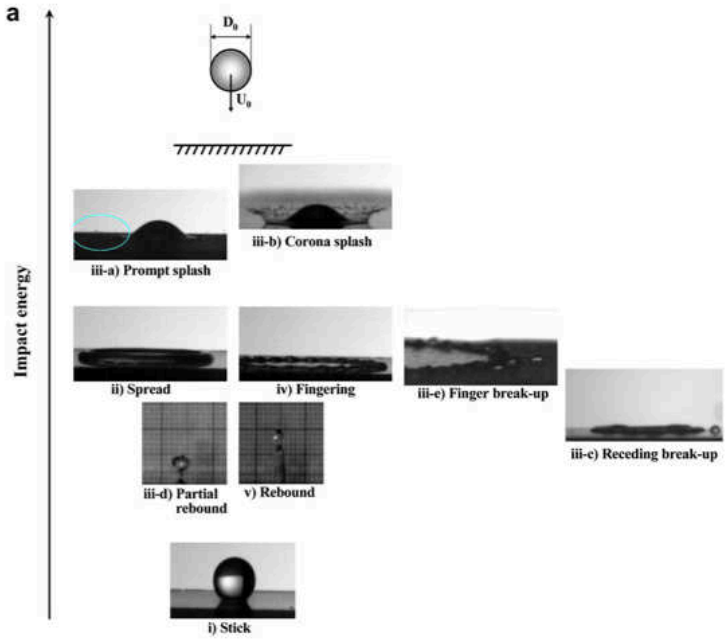

Figure 2.5 : *Outcome of single droplets impacting non-heated dry surface, classified according to the impact energy as in Bai & Gosman [15], from [238]*

In Eq. 2.5b the disintegration parameter is written K_c^* to remind the fact that the Weber number is expressed with the velocity magnitude. Although these disintegration parameters have different expressions, they can be compared among themselves by elevating them to an adequate power. For instance elevating Eqs. 2.5a and 2.5c to the power of $8/5$ and $4/5$ respectively allows to turn their expression into the one of Eq. 2.5b ($K_c = \mathrm{We}\,\mathrm{Oh}^{-2/5}$). Finally, K_c is sometimes referred to as the *Mundo number* Mu.

2.1.3.b) Wall temperature

When the wall temperature is different (usually higher) from the air and liquid temperatures, is has a major influence on the impact outcome, and additional thermal transfers must be taken into account. In the context of boiling films and spray impingement onto heated surface, several characteristic temperatures are introduced, separating different regimes (Fig. 2.6):

- The saturation temperature T_{sat} represents the temperature at which the liquid phase begins to boil. It depends on the ambient pressure via the Clausius-Clapeyron law.
- The Nukiyama temperature T_N is the temperature at which the heat flux withdrawn from the wall is maximum [57]. This flux is also called Critical Heat Flux (CHF) and its associated temperature may also be referred to as T_{CHF} (Fig. 2.6).
- The Leidenfrost temperature T_L is defined as the wall surface temperature when the heat flux is minimum, due to the presence of an insulating vapor layer. It is also called $T_{Leidenfrost}$ or T_{Leiden} in the literature.

T_{CHF} is reported to be insensitive to impact conditions whereas T_L varies with the impacting droplet diameter and velocity (magnitude and impact angle) and surface roughness. The droplet diameter is reported to have negli-

gible effects on T_L [182] while Nishio & Hirata [250] observe an increase of T_L with drop size. Depending on its magnitude, the impact velocity decreases [44] or increases [25] T_L.

Different heat transfer regimes are experimentally observed by a gently deposition of a droplet onto a hot surface at temperature T_w. The evolution of both the resulting extracted heat flux and the droplet lifetime defines several regimes. Four regimes have been listed [81, 238], as summarized on Fig. 2.6:

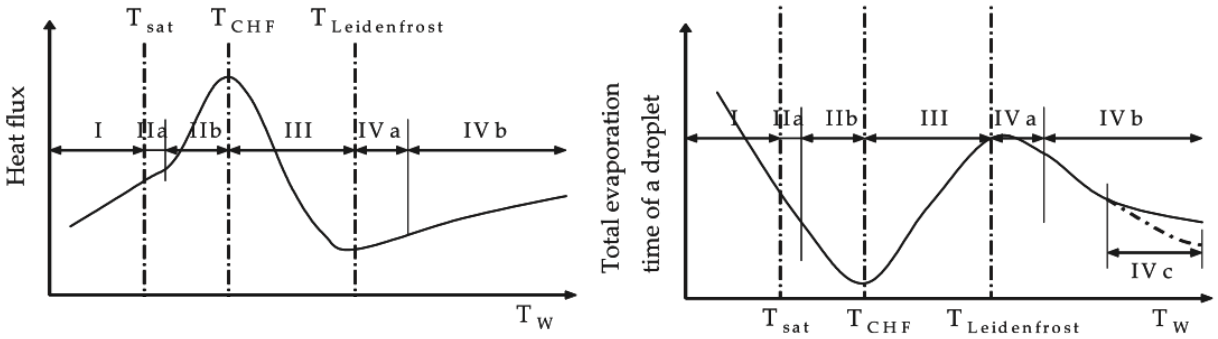

Figure 2.6 : *Boiling (left) and lifetime (right) curves of a droplet gently deposited onto a heated surface as a function of the wall temperature T_w, from [238]*

I) single phase/film-evaporation ($T_w < T_{sat}$): heat transfer is driven by conduction and free convection

II) nucleate boiling ($T_{sat} < T_w < T_{CHF}$): bubbles of vapour are created close to the wall (*region IIa*) and move towards the liquid/air interface under buoyancy effect (*region IIb*). This flow induced by the uprising bubbles enhances the wall heat flux, until it reaches the CHF.

III) transition ($T_{CHF} < T_w < T_{Leidenfrost}$): the generated vapor forms an insulating layer between the wall and the liquid. The heat flux decreases and reaches a minimum at the Leidenfrost temperature.

IV) film boiling / Leidenfrost regime ($T_w > T_{Leidenfrost}$): the layer of vapour is stable and prevents any contact between the surface and the liquid. Heat transfer is driven by conduction and radiation at higher temperatures (*region IVb*). In the case of fuel droplets, the high temperature triggers droplet ignition, lowering its lifetime (*region IVc*).

Wang *et al.* [362] showed that heat transfer regimes and impact regimes are mostly independent. However, for the ease of modeling, Naber & Farrel [246] proposed to consider the evaporation and nucleate boiling regimes as a wetting surface regime, and film boiling as a non-wetting regime. A hybrid approach is adopted in the transition regime: droplets are intermittently in contact with the heated wall.

2.1.3.c) Presence of a liquid film

The film thickness becomes an additional parameter that is accounted for through two non-dimensional parameters: the ratio of film thickness h by the impinging droplet diameter d_p and the ratio of the film thickness to the roughness amplitude R_a, as qualitatively investigated by Vander Wal *et al.* [352]:

$$\delta = h/d_p \tag{2.6a}$$

$$\varphi = h/R_a \tag{2.6b}$$

Kalantari & Tropea [170] built a classification of impact regimes on a wetted surface depending on the parameter δ only, as depicted in Table 2.1. For each regime, the onset of splashing phenomenon depends on a different threshold value as detailed later.

δ	$\delta \leq 0.1$	$0.1 < \delta \leq 1$	$1 < \delta \leq 2$	$\delta > 2$
Impact regime	Wetted wall	Thin liquid film	Shallow liquid film	Deep liquid layer

Table 2.1 : *Film regime classification depending on dimensionless film thickness δ, from [170]*

2.1.3.d) Surface wettability

It is defined as the ability of a surface to be homogeneously covered by a liquid, and is quantified by the contact angle between the wall surface and the gas/liquid interface (Fig. 2.7). Wettability is not an individual solid surface property but a characteristic of the liquid/gas/wall interaction, as it depends on the three surface tensions (gas/solid, solid/liquid, liquid/gas). Hence a wetting system should be rigorously defined as the combination of the three phases, but as the surrounding gas is always air, it is commonly defined by the liquid/solid couple. Wetting systems are qualified as *hydrophilic* when the contact angle θ_C is lower than 90 degrees and *hydrophobic* otherwise. For a moderate impact kinetic energy, hydrophilic systems result in a film creation while hydrophobic systems lead to rebound or splashing. The wall surface roughness significantly alters the wettability of the system: when the surface presents asperities, some tiny pockets of gas can be trapped between the surface and the liquid, and the overall contact angle is increased, making the system more hydrophobic. This effect is also know as the lotus flower effect [97].

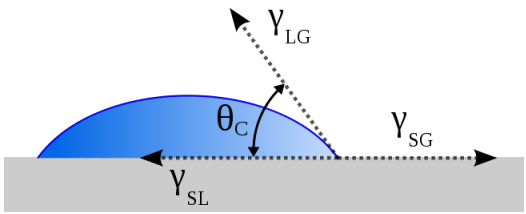

Figure 2.7 : *Definition of the contact angle in the simple case of a flat surface. γ represents the surface energy between two phases. Subscripts $_L$, $_G$ and $_S$ mean liquid, gas and solid, respectively.*

2.1.4 Regimes maps

An overall map has been proposed by several authors [15, 193, 282] in a two-dimensional space, coordinates being the Weber number and the wall surface temperature, as depicted on Fig. 2.8. Three regions are visible depending on the wall temperature. Cold regimes ($T \lesssim T_B$) are (sorted by increasing energy) *sticking*, *rebound*, *spreading* and *splashing*. Hot regimes ($T > T_N$) present *rebound*, *rebound with breakup*, *breakup* and *splashing*. According to [193], the regime between criteria A and B stands as a transition regime between rebound and breakup. In addition, no clear correlation between breakup and splashing was reported for hot impact, due to the very similar behaviour of the droplet in those two regimes. When the temperature lies in the thermal transition state, *i.e.* between $\approx T_B$ and T_N, the regimes are *boiled induced breakup*, *breakup* and *splashing*.

Other authors use maps simpler than Fig. 2.8 with a reduced number of regimes. For instance, García-Rosa *et al.* [297] use different coordinates: the impact energy is expressed with the disintegration parameter K_c (Eq. 2.2) and

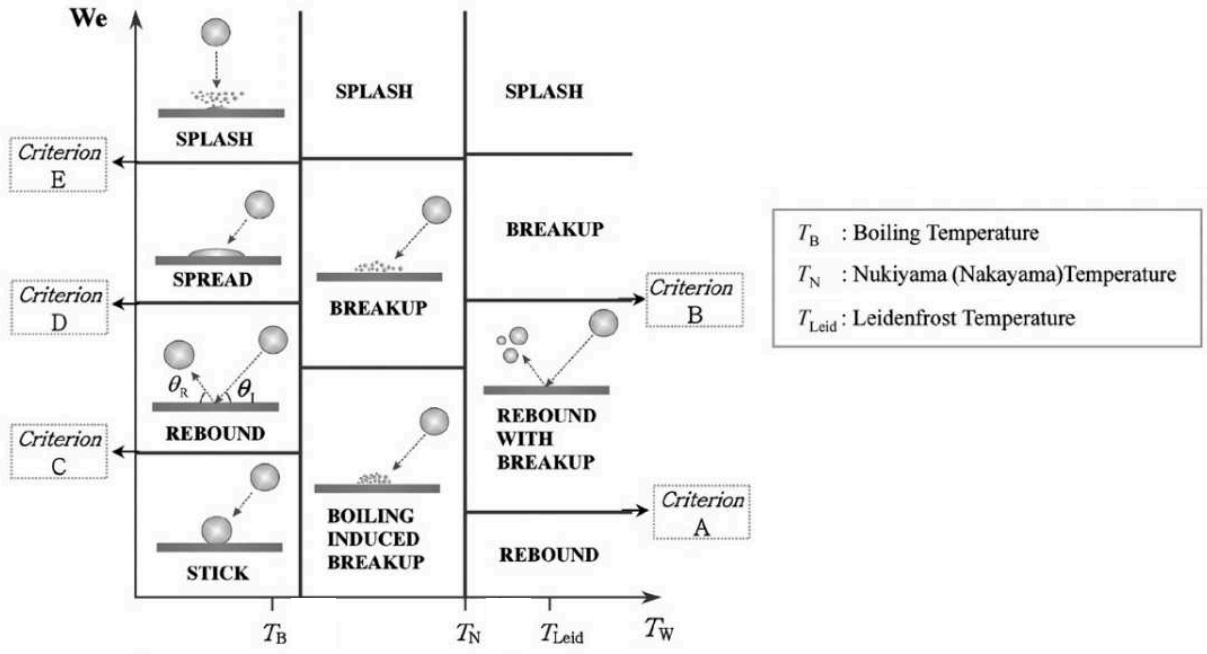

Figure 2.8 : *Map of impact regimes based on [15], adapted from [193]*

the wall surface temperature is transformed into a non-dimensional form, as also done by [43, 283]:

$$T^* = \frac{T - T_B}{T_L - T_B} \tag{2.7}$$

T^* is negative for conduction and free convection regimes and larger than one for film boiling regime. The regime map derived by García-Rosa *et al.* [297] is displayed on Fig. 2.9. For $T^* < 0$ the regimes are simplified to deposition and splashing only, and to rebound and splashing for $T^* > 1$, as done by [283]. For T^* between 0 and 1, as a thermal transition state, the presence of three regimes was identified: rebound, deposition and splashing. In this range of temperature, contrary to other authors, the regimes thresholds continuously vary with the temperature.

2.2 Splashing

The impact energy is large enough to trigger a disintegration mechanism. The impacting droplet (mother drop) fragments into several droplets of lower diameter (daughter droplets). On dry surfaces, five disintegration mechanisms are identified and illustrated on Fig. 2.5:

- prompt splash: the droplet disintegrates within the first instants after impact. This regime is promoted by surface roughness over two different scales: small roughness amplitudes enhance lamella destabilization while large amplitudes drive the disintegration mechanism.
- corona splash: in complete wetting systems, ($\theta_C \approx 0$), disintegration occurs after the formation of a crown that fragments into secondary droplets.

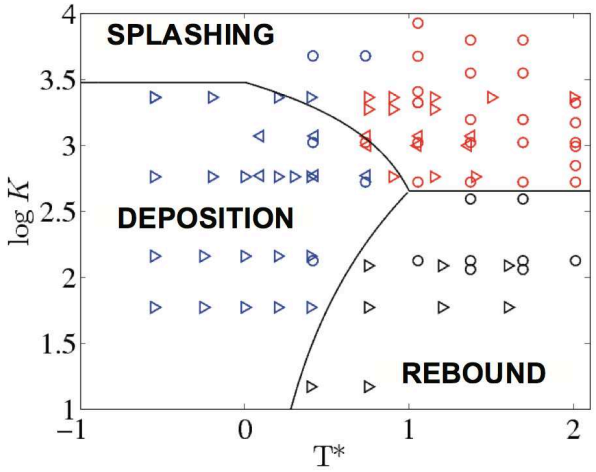

Figure 2.9 : *Experimental conditions from [57] (left-oriented triangles and circles), [65] (right-oriented triangles) and [297]: deposition (blue), splashing (red) and rebound(black) regime, from [297]*

- receding breakup: in the spreading regime, when the lamella (or the fingers) have reached their maximal size and there is still energy to dissipate, a recoiling phase occurs and the spread structure shrinks. At this stage, the surface tension forces are not able to maintain the retracting lamella, and breakup may occur. This effect is enhanced by surface roughness as small amount of liquid cannot cross the surface asperities while the main structure continues to recede.

- partial rebound: at the end of the receding stage, if a significant amount of energy is still available, a part of the liquid may detach from the surface, leading to a partial rebound.

The different outcomes of a droplet impacting a liquid film have been described by Roisman *et al.* [295]. As the impact energy increases, the droplet splashes and secondary droplets are created from both the mother drop and the film liquid. If the film is not too thick and the wall surface is hydrophobic, a crater can be formed due to the acceleration tangential to the surface of the liquid constitutive of the droplet. When the film gets thicker, the droplet only interacts with the film and an uprising central jet breakup can be observed. Possible scenarios for a droplet impinging a wet surface are illustrated on Fig. 2.10 as listed in [295]:

(i) *corona breakup* corresponds to a lamella that destabilizes in an azimuthal pattern.

(ii) *symmetric uprising sheet* follows a corona breakup when the droplet initial velocity is not normal to the wall.

(iii) *prompt splash* is the regime where the droplet disintegrates just after the impact.

(iv) *destruction of the crown* appears in the presence of a fluctuating film.

(v) *uprising central jet* is generated at the center of the impact location. It appears for thick films and is the consequence of air entrainment by the impinging droplet.

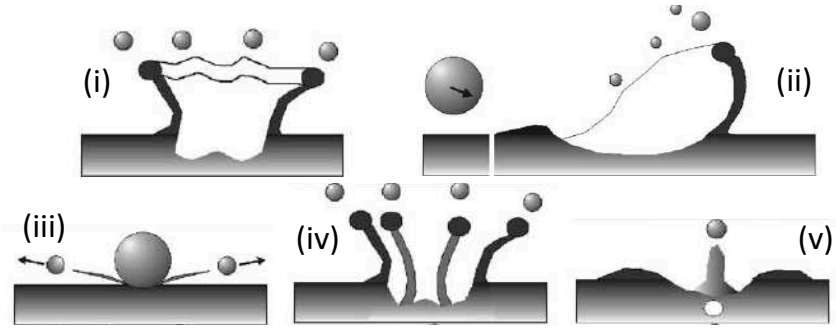

Figure 2.10 : *Outcome of single droplets impacting onto a film, from Roisman et al. [295]*

2.2.1 Criterion threshold

On Fig. 2.8, splashing is observed when the impact energy increase above the criterion E (labeled K_c^E) for 'cold' impacts and to criterion B (labeled K_c^B) for impact on a heated wall. Criterion E is modulated by some authors to take the surface roughness into account, and in the presence of a liquid film.

2.2.1.a) Cold dry surface

Some results of the literature are summarized in Table 2.2, additional values may be found in [238]. Cossali *et al.*

Authors	Disintegration parameter	K_c^E
Mundo *et al.* [245]	$K_c = \mathrm{We}^{5/8}\,\mathrm{Oh}^{-1/4}$	57.7
Cossali *et al.* [56]	$K_c^* = \mathrm{We}\,\mathrm{Oh}^{-2/5}$	$649 + 3.76/R^{*\,0.63}$
García-Rosa *et al.* [297]	$K_c^* = \mathrm{We}\,\mathrm{Oh}^{-2/5}$	3000
Han *et al.* [133]	$K_c = \mathrm{We}^{5/4}\,\mathrm{Oh}^{-1/2}$	$1500 + 650/R^{*\,0.42}$

Table 2.2 : *Summary of disintegration parameters expressions and associated critical values for the spreading/splashing limit* ***(criterion E)***

[56] included the surface roughness effect by defining a critical disintegration parameter K_c^E that depends on the dimensionless surface roughness:

$$R^* = \frac{R_a}{d_p} \tag{2.8}$$

They derived the expression for the critical value:

$$K_c^{*E} = 649 + \frac{3.76}{R^{*\,0.63}} \tag{2.9}$$

with R^* between $3{\cdot}10^{-5}$ and 5. In the same manner, Han *et al.* [133] derived a threshold for a dry surface with regards to the disintegration parameter expressed by Eq. 2.5c:

$$K_c^E = 1500 + \frac{650}{R^{*\,0.42}} \tag{2.10}$$

Equation 2.10 was derived on the same database as Cossali *et al.* [56] and consequently the variation range of R^* is the same as for Eq. 2.9.

2.2.1.b) Wetted wall

The disintegration parameter (Eq. 2.2) is still relevant in the presence of an initial liquid film on the surface, and the regimes identified for the dry wall impact still arise [15, 56, 333]. However, thresholds are different and depend on the liquid film thickness. Two examples are given below for the splashing/spreading criterion, but more extensive results are available in [193, 238]. Cossali *et al.* [56] modified Eqs. 2.9 when the film thickness is larger than the roughness amplitude to obtain:

$$K_c^{*,E} = 2100 + 5880\,\delta^{1.44} \tag{2.11}$$

Han *et al.* [133] added a correcting factor to account for both the roughness and the film thickness at the same time:

$$K_c^E = \left[1500 + \frac{650}{R^{*\,0.42}}\right] \cdot \left[1 + 0.1\,\sqrt{\mathrm{Re}} \cdot \min(\delta, 0.5)\right] \tag{2.12}$$

In their classification depending on δ (see Table 2.1), Kalantari & Tropea [170] did not use the disintegration parameter (Eq. 2.2) but an impact Weber number (Eq. 2.1). They associated to each regime a critical Weber number characterizing the onset of splashing (We_c^E) as summarized in Table 2.3.

δ	$\delta \leq 0.1$	$0.1 < \delta \leq 1$	$1 < \delta \leq 2$	$\delta > 2$
$\mathbf{We}_c^E$	$\approx 480 - 500$	$136\,\delta + 354$	$\approx 1657\,\delta^{-0.54}$	≈ 1100

Table 2.3 : *Critical Weber number for the onset of splashing (We_c^E) depending on dimensionless film thickness δ, from [170]*

2.2.1.c) Hot surface

As previously mentioned, the regime between criteria A and B on Fig. 2.8 is a transition regime between rebound and breakup and can be assimilated to splashing. Therefore criteria A and B are presented in this subsection. In 1966, Watchers & Westerling [360] expressed criteria A and B with a constant critical Weber number of 30 and 80 respectively, for wall temperatures larger than T_N. The order of magnitude of these results were later confirmed by Araki & Moriyama [12] with $\mathrm{We}_c^A \approx 60$ and $\mathrm{We}_c^B \approx 100$. Yao & Cai [369] noticed an influence of the impact angle on the critical disintegration criterion. They interpreted this effect as the dependence of the dynamic Leidenfrost temperature on the impact velocity.

In their regime map (Fig. 2.9), García-Rosa *et al.* [297] found:

$$K_c^B = 3000 - 2550\,T^* \quad \text{for} \quad 0 < T^* < 1 \tag{2.13a}$$

$$K_c^B = 450 \quad \text{for} \quad T^* > 1 \tag{2.13b}$$

Equation 2.13b was later confirmed by Castanet *et al.* [43] who found $K_c^B \approx 400$ for $T^* > 1$.

2.2.2 Mass deposition of splashed droplets

On cold surfaces, some liquid remains on the wall while the complementary amount is splashed. Many authors agree upon the fact that the maximum splashed mass ratio, defined as the ratio of the splashed mass and the impacting droplet mass $\eta_s = m_s/m_0$, is limited to 0.75. This implies that, in case of splashing, some liquid always sticks to the surface. On a cold wet surface, a ratio larger than one is possible: the splashed mass comes from both the impacting drop and the liquid film. Correlations predicting the splashed mass are generally expressed as a function

of Re^*, Oh and the impact angle [303], or solely as a function of $H = We\sqrt{Re}$ [133]. Roisman *et al.* [295] used a semi-empirical relation depending on K_c, Re, the impacting mass flux $\dot{m}_0$ and the impacting velocity U_0. Bai & Gosman [15] expressed this ratio as a pure random function $\eta_s = 0.2 + A \cdot X_{[0,1]}$ where A is equal to 0.6 and 0.9 in case of dry and wet wall respectively, and $X_{[0,1]}$ is an equiprobable random draw between 0 and 1.

In case of impact on a hot surface, the total mass is splitted into deposition (which is subject to boiling in the transition regime), splash and vaporization (Fig. 2.12). In the film boiling regime, the deposited mass vaporizes almost instantaneously. The amount of splashed liquid is therefore larger with higher temperature and the ratio η_s is close to one. From this observation, Habchi [128] stated that in the splashing regime with $T > T_N$, the whole droplet mass is splashed. García-Rosa *et al.* [297] derived a general criterion for η_s that depends on K_c^* and T^*. In their derivation, they limited η_s to 0.75 to both a liquid deposition in case of cold impact and liquid vaporization in case of hot impact, in agreement with the measurements of Amiel *et al.* [6].

2.2.3 Secondary droplets

Secondary droplets are different from the initial impinging droplets and need to be characterized in terms of number, diameter, temperature as well as velocity magnitude and direction. The prediction of these values must be in accordance with the conservation laws of mass, momentum and energy.

2.2.3.a) Number of drops

Among the experiments described in the literature, the number of generated drops is an increasing function of the impact energy. It is expressed with the impact Weber number [4, 15, 194], the disintegration number K_c [245], and the film thickness [253, 254], or the Reynolds number [374]. It may also be calculated from volume conservation after the determination of the splashed mass and the secondary droplets diameter [295, 303, 315]. It is always expressed by a deterministic function except in [15, 16] where it is drawn from an equiprobable law and in [333] where the random draw follows a Probability Density Function (PDF) parametrized by secondary droplets diameter and splashed mass.

2.2.3.b) Diameter

A simple way to determine secondary droplets diameter is to use volume conservation after the preliminary determination of the splashed mass and the number of secondary droplets [15, 374]. However this method is not often applied. It can also be

The diameter of secondary droplets can be predicted following the same methodology as for the number of droplets. It can be expressed as a deterministic function of the disintegration parameter [245], for 'high energy impacts' [315], of the Weber number [4, 170] or the film thickness in case of wetted surface with low energy impact [315]. Samenfink *et al.* [303] used an expression depending on Re^*, Oh and the impact angle.

Using a deterministic law for the droplet diameter produces a monodisperse spray if impacting conditions are constant. A more sophisticated approach is to use a diameter randomly drawn from a distribution. In practice, a PDF is determined experimentally and its coefficients are expressed with influent parameters. This method has been adopted in [16] with the PDF coefficients determined by volume conservation and in [333] with a Weibull function depending on the impacting Weber number. Roisman *et al.* [295] modulated their Weibull function by the diameter of the impacting drop and its associated Reynolds number, Han *et al.* [133] used a Nukiyama-Tanasawa distribution with constant coefficients and a mean diameter determined from the disintegration criterion and density ratio. Finally García-Rosa *et al.* [297] used a LogNormal function with a mean diameter depending on K_c^* and a constant variance.

2.2.3.c) Velocity

The velocity characterization of the secondary droplets requires to predict both the velocity magnitude and direction. The velocity magnitude can be determined by energy conservation. In a first approach, only kinetic and surface energy are accounted for, as in [15] and [315] for a high energy impact. Then, the energy dissipated at the impact can be also considered [16, 374]. Roisman *et al.* [295] found that the ratio of mechanical energy (*i.e.* the sum of surface and kinetic energy) before and after splashing η_e is a function of the splashed mass ratio η_s.

To predict the velocity direction, one may first assume that the secondary droplets velocity vector belongs to the impacting plane, *i.e.* the plane defined by $(\overrightarrow{u_p^{old}}, \overrightarrow{n_w})$ on Fig. 2.11. Stanton & Rutland [333] used a PDF depending on α to determine the tangential velocity. The normal velocity was found by a random drawn on a deflection angle. Mundo *et al.* [245] expressed the components by empirical correlations depending on the secondary droplet diameter. Samenfink *et al.* [303] used correlations depending on multiple parameters (Re^*, Oh and the impact velocity) to determine normal and tangential components. For low impact energy, Senda *et al.* [315] expressed the velocity components with the film thickness. In a more complete approach, an azimuthal angle is added, determined from a random process. It was used by Han *et al.* [133] where the normal velocity follows a Nukiyama-Tanasawa function, the tangential velocity a normal distribution and the azimuthal angle a Weibull function. Yoon & DesJardins [374] used energy conservation to determine the velocity magnitude, then splitted one third to the normal velocity and the rest to the other components, randomly distributed. García-Rosa *et al.* [297] used a Weibull function to determine the normal velocity, set the tangential velocity as a portion $(5/7)$ of the original tangential velocity, and chose randomly the elevation and azimuthal angles, providing a splashed cloud symmetric with respect to the impacting plane.

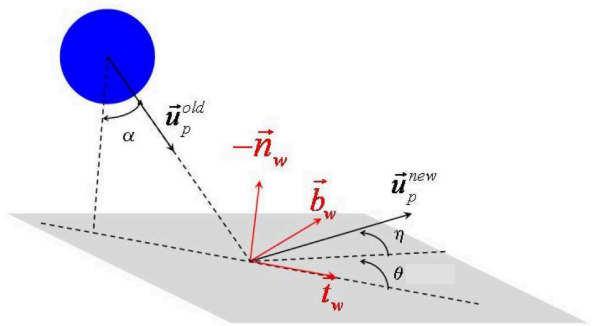

Figure 2.11 : *Notations and definition of the local referential in droplet/wall interaction, from [128]*

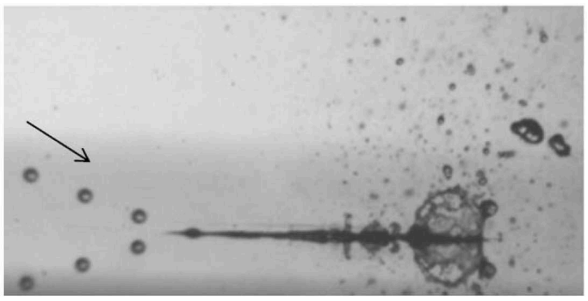

Figure 2.12 : *Illustration of splashing regime above the boiling temperature, from [43]*

2.2.3.d) Temperature

Few studies on the secondary droplet temperature are available in the literature. Recently, Castanet *et al.* [43] conducted a study where they noticed that the impact angle was the main parameter to determine secondary droplet temperature. They also observed that the wall temperature (as soon as it is far above the boiling temperature) has little influence on the droplet temperature. For instance they monitored the same temperature variation of 18 K for an impact angle of 17° and wall temperatures ranging from 240 to 440°C.

2.3 Other isolated droplet regimes

The two other isolated droplet regimes are the filming (or spreading) phenomenon and the rebound (or bouncing) phenomenon.

2.3.1 Filming/Spreading

This regime occurs when the impact energy is sufficiently low to avoid splashing, but sufficiently large to counteract the surface tension effect which cannot maintain a spherical shape anymore. A spreading lamella (a circular extent of liquid) is thus formed on the surface, and after its maximal extent, recoils until the impact energy is totally dissipated. Filming is not observed for high surface temperatures because the film boils and vaporizes quickly. On a wet surface, if the impact energy is low, the droplet is 'deposited' on the film and coalesces with it.

2.3.1.a) Criterion threshold

The threshold between spreading and rebound (criterion D on Fig. 2.8) was originally given by Yoon & DesJardin [374] from an energy analysis. The current form is taken from [193] as:

$$\frac{\mathrm{We}^*}{\sqrt{\mathrm{Re}^*}} = \frac{3}{4}\left(1-\cos\theta_C\right) \tag{2.14}$$

Converting Eq. 2.14 into the generic form of Eq. 2.2 leads to the following disintegration parameter and limit:

$$K_c^* = \mathrm{We}^{*3/4}\,\mathrm{Oh}^{1/2} \tag{2.15}$$

$$K_c^{*D} = \frac{3}{4}\left(1-\cos\theta_C\right) \tag{2.16}$$

2.3.2 Rebound

The droplet remains as a whole, and detaches from the surface. A stage of spreading and receding may occur on wettable surfaces.

2.3.2.a) Criterion threshold

Criterion C on Fig. 2.8 is not precisely determined. It is only stated that the impact energy must be very low $(\mathrm{We} \ll 1)$ to switch from rebound to stick [193].

2.3.2.b) Velocity

In the case of elastic rebound, the velocity computation is straightforward from momentum conservation: the normal velocity component of the secondary droplet is the opposite of the impacting droplet, and tangential components are equal. When energy dissipation due to the impact is accounted for (non elastic rebound), García-Rosa *et al.* [297] take the wall temperature dependence on the restitution factor, and the tangential velocity is damped to 0.8 time the impacting tangential velocity.

2.3.2.c) Diameter

In the case of rebound on hot surface, García-Rosa *et al.* [297] took the evaporation rate into account. As they did for the splashed mass, they defined η_r as the ratio of the droplet mass after and prior to the bounce and expressed it as a function of K_c and T^*. Volume conservation led to a diameter decrease.

2.3.2.d) Temperature

García-Rosa *et al.* [297] stated in their model that the secondary droplet temperature was constant during bouncing onto hot walls, the excess of temperature being converted into vapour.

2.4 Macroscopic effects of real sprays

As previously mentioned, a real spray/wall impact cannot be accurately extrapolated by summing the behaviour of several single droplet impacts. Non linearities brought to the spray/wall impact by drop/drop interaction prior to the impact (mainly coalescence), during the impact (lamellas interaction, leading to uprising jets), and after the impact (secondary droplets coalescence) make the process very complex and macroscopic models are used to recover the global spray/wall interaction.

The main values of interest when considering spray/wall interaction are the deposited mass, secondary drop size distribution and extracted heat from the surface in case of hot walls [238].

2.4.1 Deposited mass

Few experiments explicitly describe the liquid deposition in case of a full impinging spray. Kalantary & Tropea [170] conducted a statistical study from a water spray. They found a strong dependence of the liquid deposition on the impacting Weber number, depending on the impact angle. They correlated the secondary-to-incident mass and number ratio, respectively η_s and η_N in the case of normal impact:

$$\eta_s = 6.74 \times 10^{-3} \cdot \mathrm{We} - 0.204 \tag{2.17}$$

$$\eta_N = 2.16 \times 10^{-3} \cdot \mathrm{We} + 8.96 \times 10^{-2} \tag{2.18}$$

In the case of oblique rebound, they found a different dependency on the Weber number:

$$\eta_s = 35 \cdot \mathrm{We}^{-1.63} \tag{2.19}$$

$$\eta_N = 7.1 \cdot \mathrm{We}^{-1.14} \tag{2.20}$$

2.4.2 Thermal transfer

The thermal effect of a cold spray impinging a hot surface is a common process in industry (metallurgy, etc) and has been widely studied [ref de review]. The main goal of such studies is to use the spray to cool down the surface. In the present case, studying fuel spray impact is important for the heating of the film and the secondary droplets. From a macroscopic point of view, energy conservation gives the global heating of the secondary spray knowing the extracted heat from the surface and the evaporation rate. In order to quantify the heat extracted from the wall and transferred to the secondary droplets, many researchers derived a correlation for the Nusselt number defined as the convective-to-conductive heat fluxes ratio:

$$\mathrm{Nu} = \frac{\phi_{conv}}{\phi_{cond}} = \frac{h\, L_c}{\lambda} \tag{2.21}$$

where h is the convection coefficient, L_c a characteristic length and λ the heat conductivity. The generic form of the Nusselt correlation found in [238] is:

$$\mathrm{Nu} = a\,\mathrm{Pr}^b\,\mathrm{Re}^c\,\mathrm{We}^d\,\mathrm{Ja}^e \tag{2.22}$$

where Pr and Ja are the Prandtl and Jacob numbers respectively, defined by:

$$\mathrm{Pr} = \frac{\mu\, c_p}{\lambda} \tag{2.23}$$

$$\mathrm{Ja} = \frac{c_p\, \Delta T_{wb}}{L_{vap}} \tag{2.24}$$

The term c_p is the mass heat capacity, $\Delta T_{wb} = T_w - T_{sat}$ is called the superheating degree of the wall and L_{vap} is the latent heat of vaporization of the liquid. Table 2.4 summarizes the constants used in various experiments.

Authors	a	b	c	d	e	Remarks
Eckhause & Reitz [74]	2	0	0	0	0	Non-wetting regime
Eckhause & Reitz [74]	3.32	0.33	0	0	0	Wetting regime
Rybicki & Mudawar [298]	4.7	0.32	0.61	0	0	-
Arcoumanis & Chang [13]	0.34	-0.33	-0.53	0.94	0	-
Panao & Moreira [264]	3.4 10^{-5}	0	1.51	0	0.254	-

Table 2.4 : *Nusselt number correlation coefficients*

2.5 Conclusion

Real spray/wall interaction is the combination of droplet/wall and droplet/droplet interactions. The former type allows to give insights into the basic mechanisms and constitutes the first step of spray/wall interaction modeling. The latter type of interaction is more complicated to study, and is useful to derive macroscopic correlations. The main regimes of single droplet/wall interaction are (i) filming, (ii) rebound and (ii) splashing. As highlighted by [238] many experiments are available in the literature. However as no standard protocol was settled, almost each experiment provides unique boundary conditions, which makes it difficult for general comparison.

The two majors influent parameters are the impact energy and the wall surface temperature. The impact energy is expressed through the Weber and/or the Ohnesorge numbers and their relative influence depends on the authors. The wall surface temperature influences the impact through liquid vaporization and film boiling effects. Influent parameters of lower importance are (i) the presence of a liquid film on the surface, (ii) the surface roughness and (iii) the wettability of the liquid/solid/gas system. A map of impact regimes is built in a 2D space, the coordinates being the impact energy and the wall surface temperature. The boundary between different regimes is derived from experimental observation. Based on this map, several authors built isolated droplet/wall interaction models for numerical simulation.

In the filming regime the droplet spreads on the wall, creating or feeding a liquid film. In the rebound regime the droplet deforms on the wall and is reemitted, with a different velocity direction and magnitude (in case of damping effect). Some author account for possible partial vaporization during the rebound, modifying the droplet diameter. The splashing regime is the most complex one as it is a combination of the two previous ones: some liquid can stick on the surface and secondary droplets are emitted. Secondary droplets are characterized through their velocity direction and magnitude, their temperature, their number and their diameter. Finally, as real spray/wall interaction cannot be considered as a superposition of single droplet/wall interactions, some authors derived macroscopic correlation for real sprays impact, in term of liquid mass deposited on the surface and thermal transfer coefficient.

Chapter 3

Thin liquid film flow

3.1 Introduction

3.1.1 Definition and applications

Films can be defined as a thin layer of a given material that lies at the interface of two other different media. The *thin* aspect is to be compared to geometrical length scales of the surrounding media as well as its aspect ratio. From this definition, films can be sorted in two categories : static films and dynamic films. The formers are made of solid material and are mainly used in the industry of optics (anti-reflective glasses) [161], electronics (integrated circuit, photovoltaic cells) [317] or food (edible film for food freshness conservation) [176]. The laters are made of liquid or gas, and have a dynamic behaviour that must be taken into account, understood and modeled. Note that solid films are sometimes manufactured from a liquid film deposition that is dried later. In the rest of this work, the focus is made on dynamic films.

Thin film flows are of prior importance in many scientific fields such as engineering, geophysics and biophysics [59]. Surprisingly, the mathematical formulation of thin films is valid on a wide range of length scales, from *nano-geometries* [75] to continental length scales [314]. Between those extrema, many authors have studied thin film flows in various applications: heat exchangers, microelectromechanical devices [100], gravity currents, snow avalanches, ice sheet models and lava flows. Films are of interest even in biology: the corneal thin film covering the eye (recasted at every blink), or lung linings [124] are examples among many others. In the aeronautical context, thin films have various applications: (i) thin films of oil are used to create lubricant layers in bearings, (ii) thin films of air generate a thermal shield around the combustion chamber walls and (iii) in airblast atomizers, the liquid fuel forms a thin film on the walls to increase the contact surface with the high speed air stream, promoting momentum transfers and enhancing liquid fragmentation.

3.1.2 Main characteristics of thin liquid films

Depending on the application field, some characteristics of the film are more important than others, and therefore are carefully monitored. Most of the time, the key element is the film thickness but it can also be the interface shear or flow rate. In film cooling technologies, the film has a role of thermal shelter as well as heat sink [113]: then its thickness sets the thermal resistance and its flow rate drives the heat removal out of the system. Film thickness regularity is also important: in coating processes where every part of a surface has to be regularly covered, it is mandatory to avoid film rupture or hydraulic jump that may be induced by a topography feature or a scratch [100].

Finally, the interface shear is sometime critical: in multiphase pipeline conveying, the film/gas interface modifies the pressure drop in a non negligible manner [33].

Those physical values are important to be described but also to be measured. The following paragraph introduces methods to characterize thin film main characteristics. In experiments, the mass flow rate is usually imposed and the first value to be measured is the film thickness, as shown in a great number of experiments [76, 94, 266, 343, 359]. Access to instantaneous recording of film thickness delivers many information: time averaging leads to mean film thickness, Fourier transform of the instantaneous signal displays the surface wave spectrum and derivatives of the signal (provided the wave velocity) convey the surface curvature that generates pressure jump through surface tension phenomenon. The difficulty in measuring thin film thickness is, in essence, its definition: when the film is very thin, about several dozen of micrometers, film thickness recording becomes a challenge. For further explanations, interested readers can consult the review by Tibiriçà *et al.* [342] on film thickness measurement devices.
The interface shear stress is another investigated value, through pressure drop measurements [343, 359]. This quantity is indeed difficult to accurately predict due to the complex phenomena occurring at the interface such as all types of waves, film stripping, droplet entrainment, and vaporization.

3.1.3 Origins of film motion

Given the large scalability of the film equations, many phenomena are potentially responsible for film motion. Craster [59] distinguishes several families of film flows with regards to their physical origin and driving mechanisms:

- **Film driven by body forces**

  Body forces are typically gravity and electromagnetism. It includes falling films, electrically charged films, and films evolving in non-Galilean referential, driven by centrifugal forces.

- **Film driven by surfactants**

  Surfactants are compounds that lower the surface tension at the film interface, and result in a non homogeneous surface tension distribution on the free surface. This surface tension gradient leads to interface stresses called Marangoni stresses. The output of the overall phenomenon is a tangential force that drives the film. Processes involving spreading of surfactants on thin films are key elements in various industrial and biological applications such as coating flows, microfluidics and drying of semiconductors.

- **Film driven by thermal effects**

  As surfactants, temperature inhomogeneities induce surface tension gradients and lead to Marangoni stresses. The difference between this class and the previous one is that thermocapillarity mainly produces constant stresses while films driven by surfactants present strong coupling between the surfactant concentration and the film flow, leading to a highly varying driving force.

- **Film driven by intermolecular forces**

  When the film thickness decreases to the value of 0.1 µm, intramolecular forces start to influence the flow dynamics and under certain conditions can lead to film rupture and dewetting. When the aim of a process is to cover a substrate by a thin layer (coating process), dewetting must be avoided and controlling instabilities generated by intramolecular forces is of prior importance.

- **Film driven by external surface stresses**

  This mechanism is essential in aeronautical applications since the thin film is surrounded by a viscous gas flowing at high velocity and the interface shearing induced by viscosity of both media is the predominant driving force.

3.2 Derivation of thin film equations

The flow within the film is ruled by the Navier-Stokes equations, with boundary conditions linked to the surrounding media: substrate roughness or ambient fluid viscosity may appear in the final set of equations. Thermal effects will be neglected in the following.

The general Navier-Stokes equations read:

$$\frac{\partial \rho}{\partial t} + \frac{\partial \rho u_i}{\partial x_i} = 0 \tag{3.1a}$$

$$\frac{\partial \rho u_i}{\partial t} + u_j \frac{\partial \rho u_i}{\partial x_j} = -\frac{\partial p}{\partial x_i} + \frac{\partial \tau_{ij}}{\partial x_j} + f_i \tag{3.1b}$$

Index notation has been adopted as well as Einstein summation rule for repeated indices. The above equations respectively represent the mass conservation and the momentum conservation. Assuming that the film does not breakup and no droplets impinge the film surface, there is no source or sink terms in the right-hand side of the mass conservation equation.

The stress tensor τ_{ij} is expressed from kinetical gas theory for Newtonian fluids [148] (Eq. A.2) and f_i denotes the volume forces. Since only non-charged fluids are considered, the volume forces reduce to gravity. In addition, flow length scales are small compared to Earth length scale so that gravity field g_i is taken uniform.

3.2.1 From Navier-Stokes to film equations

The following derivation follows the methodology of Thual [341] to obtain the general films equations, originally established by de Saint-Venant [62] who derived film equations for environmental fluid mechanics to predict flood or swell propagation. The major assumptions for deriving Saint-Venant equations are (a) incompressibility of the fluid, (b) negligible longitudinal gradients compared to normal ones, (c) negligible liquid/gas interface shear stress and (d) homogeneous exterior pressure (equal to atmospheric pressure). A bulk velocity is calculated by integrating the local Navier-Stokes equations over the *wall-normal* direction. The determination of an integration constant requires to model the liquid/gas interface shear stress. The assumption (b), also known as *lubrication theory*[1], *shallow water theory* or also *long-wave theory* [59] is widely used in other fields of fluid mechanics and allows many mathematical simplifications.

The above assumptions apply to thin film flows in aeronautical burners, except that gas/liquid shear stress is not negligible and exterior pressure is not homogeneous. Moreover, contrarily to Saint-Venant derivation, equations are not integrated over the film thickness.

Applying incompressibility ($\rho = cste$) to Eq. 3.1a leads to $\partial u_i / \partial x_i = 0$. As a consequence the stress tensor and its gradient simplify as:

$$\tau_{ij} = \mu \left(\frac{\partial u_i}{x_j} + \frac{\partial u_j}{x_i} \right) \tag{3.2}$$

$$\frac{\partial \tau_{ij}}{\partial x_j} = \mu \frac{\partial^2 u_i}{\partial x_j^2} \tag{3.3}$$

[1] lubrication theory embeds one additional assumption: negligible inertia of the film

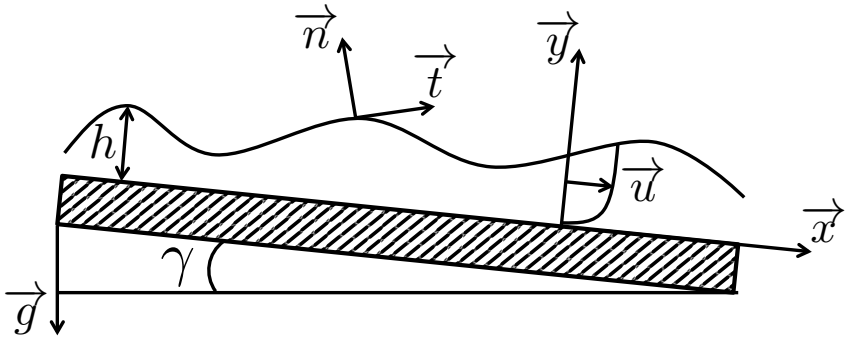

Figure 3.1 : *Sketch of a general film flow in a gravity field*

Following previous assumptions, Eqs. 3.1 may be written:

$$\frac{\partial u_i}{\partial x_i} = 0 \tag{3.4a}$$

$$\frac{\partial u_i}{\partial t} + u_j \frac{\partial u_i}{\partial x_j} = -\frac{1}{\rho}\frac{\partial p}{\partial x_i} + \nu\, \Delta u_i + g_i \tag{3.4b}$$

where ν and Δ denote respectively the kinematic viscosity and the Laplacian operator.

Boundary conditions

For the sake of clarity, the derivation is made in 2D geometry as sketched in Fig. 3.1. Let h be the thickness of the film, the free surface equation is expressed by $F(x,y,t) = z - h(x,t) = 0$, which excludes breaking waves. Writing the kinematic boundary condition as $dF/dt = 0$ and noting $u_x = u$ and $u_y = v$ leads to:

$$\frac{\partial h}{\partial t} + u\frac{\partial h}{\partial x} = v \qquad \text{for } y = h(x,t) \tag{3.5}$$

At the gas/liquid interface, the action of the stress tensor $\underline{\underline{\Gamma}}$ onto a surface of normal $\overrightarrow{n}$ is expressed by $\overrightarrow{n} \cdot \underline{\underline{\Gamma}}$. The dynamic boundary condition is thus determined by decomposing the stress tensor action into the normal and the tangential components, respectively, and writing jump conditions across the interface [202] leads to:

$$\left(\overrightarrow{n} \cdot \underline{\underline{\Gamma}}\right) \cdot \overrightarrow{n} - \left(\overrightarrow{n} \cdot \underline{\underline{\Gamma}}^{ext}\right) \cdot \overrightarrow{n} = \sigma\, \overrightarrow{\nabla} \cdot \overrightarrow{n} \tag{3.6a}$$

$$\left(\overrightarrow{n} \cdot \underline{\underline{\Gamma}}\right) \cdot \overrightarrow{t} - \left(\overrightarrow{n} \cdot \underline{\underline{\Gamma}}^{ext}\right) \cdot \overrightarrow{t} = \overrightarrow{\nabla\sigma} \cdot \overrightarrow{t} \tag{3.6b}$$

where $\overrightarrow{n}$ and $\overrightarrow{t}$ are the interface normal and tangential vectors as represented on Fig. 3.1, σ is the liquid surface tension. The stress tensor $\underline{\underline{\Gamma}}$ components write:

$$\Gamma_{ij} = -p \cdot \delta_{ij} + \tau_{ij} \tag{3.7}$$

The term Γ_{ij}^{ext} in Eqs. 3.6 is the gaseous stress tensor components at the interface. Equation 3.6a states that the jump in normal stress is the result of surface tension and surface curvature. Injecting the stress tensor expression Eq. 3.7 in Eq. 3.6a and considering a stationary flow ($\tau_{ij} = 0$), leads to the Laplace-Young equation that quantifies the pressure jump (also referred to as the Laplace pressure) across the interface for static fluids:

$$p_{ext} - p = \frac{\sigma}{R_1} \tag{3.8}$$

where R_1 is the interface radius of curvature. Note that on three dimensional surfaces, two principal radii (R_1 and R_2) must be defined and Eq. 3.8 writes:

$$p_{ext} - p = \sigma \left(\frac{1}{R_1} + \frac{1}{R_2} \right) \tag{3.9}$$

Equation 3.6b represents the tangential stress jump that can be generated by a surface tension gradient (often induced by non homogeneities in temperature or chemical composition fields). Using Eq. 3.7 for both the liquid and gas fluids:

$$\mu \left(\frac{\partial u_i}{\partial x_j} + \frac{\partial u_j}{\partial x_i} \right) - \mu^{ext} \left(\frac{\partial u_i^{ext}}{\partial x_j} + \frac{\partial u_j^{ext}}{\partial x_i} \right) = \frac{\partial \sigma}{\partial x_i} \cdot t_i \tag{3.10}$$

At the wall/liquid interface ($y = 0$), given the fact that the wall is stationary and not porous, the kinematic condition writes:

$$u_i = 0 \tag{3.11}$$

In addition the dynamic boundary condition writes:

$$n_i \cdot \Gamma_{ij} \cdot t_j = \tau_w \tag{3.12}$$

where τ_w is the shear stress applied by the liquid on the wall and depends on the liquid velocity and viscosity as well as the wall roughness. It must be either modeled by a phenomenological law (as it is done in environmental fluid mechanics) or computed from a prescribed velocity profile [90].

3.2.2 Nondimensionalization of the film equations

The above film equations are nondimensionalized as follows:

$$x = L_0 x^*, \quad y = h_0 y^*, \quad t = T_0 t^*, \quad u = U_0 u^*, \quad v = U_0 \frac{h_0}{L_0} v^*, \quad p = P_0 p^* \tag{3.13}$$

where L_0 is a longitudinal length scale, h_0 is a *wall-normal* length scale and T_0 is a characteristic time scale. The characteristic longitudinal velocity U_0 is *a priori* estimated from measurements, but an estimation of its expression, based on the following assumptions is derived in Section 6.1.4. The expression of characteristic pressure P_0 depends on the film driving force: when gravity is dominating, the reference pressure may be expressed as $P_0 = \rho g' \, h_0$ where $g' = g \cos\gamma$ (Fig. 3.1). In the configuration where pressure drop and wall shear balance, $P_0 = \mu U_0 L_0 / h_0^2$ might be relevant; if film inertia is preponderant $P_0 = \rho U_0^2$ is more appropriate. The choice of the reference time scale also depends on the driving phenomenon. For instance when gravity is leading, T_0 could be expressed as $\sqrt{h_0/g}$ while it may read h_0^2/ν when the film is driven by shear stress at the free surface.

Injecting Eqs. 3.13 into Eqs. 3.4 and fully expressing 2D components instead of using indices leads to:

$$\frac{\partial u^*}{\partial x^*} + \frac{\partial v^*}{\partial y^*} = 0 \tag{3.14a}$$

$$\tau_c \frac{\partial u^*}{\partial t^*} + u^* \frac{\partial u^*}{\partial x^*} + v^* \frac{\partial u^*}{\partial y^*} = -\mathrm{Eu} \frac{\partial p^*}{\partial x^*} + \frac{1}{\epsilon \mathrm{Re}} \Delta^* u^* + \frac{\tan\gamma}{\epsilon \mathrm{Fr}^2} \tag{3.14b}$$

$$\epsilon^2 \left(\tau_c \frac{\partial v^*}{\partial t^*} + u^* \frac{\partial v^*}{\partial x^*} + v^* \frac{\partial v^*}{\partial y^*} \right) = -\mathrm{Eu} \frac{\partial p^*}{\partial y^*} + \frac{\epsilon}{\mathrm{Re}} \Delta^* v^* - \frac{1}{\mathrm{Fr}^2} \tag{3.14c}$$

where Δ^* represents a modified non-dimensional Laplacian operator:

$$\Delta^* = \epsilon^2 \frac{\partial^2}{\partial x^{*2}} + \frac{\partial^2}{\partial y^{*2}} \tag{3.15}$$

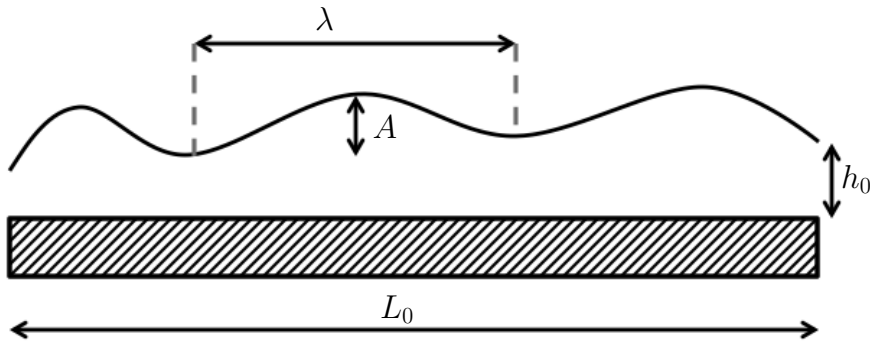

Figure 3.2 : *Lubrication theory hypothesis: the film size ratio $\epsilon = h_0/L_0$ (or lubrication parameter) is supposed far smaller than one. Moreover the free surface slope $2A/\lambda$ is supposed to be of the order of magnitude of ϵ*

Dimensionless parameters in Eqs. 3.14 are the film size ratio ϵ, the Froude number Fr, the Reynolds number Re, the gravity angle tangent tanγ, the Euler number Eu and the ratio of the convective time by the characteristic time of driving force τ_c. They are defined as:

$$\epsilon = \frac{h_0}{L_0}, \quad \text{Fr} = \frac{U_0}{\sqrt{g' h_0}}, \quad \text{Re} = \frac{h_0 U_0}{\nu}, \quad \text{tan}\gamma = \frac{g_y}{g_x}, \quad \text{Eu} = \frac{P_0}{\rho U_0^2}, \quad \tau_c = \frac{L_0}{U_0 T_0} \tag{3.16}$$

The film size ratio (Fig. 3.2) is the key parameter of the lubrication theory and is sometimes called 'lubrication parameter'. It is assumed to be small $\epsilon << 1$, allowing a Taylor expansion:

$$u_i = u_{i,0} + \epsilon\, u_{i,1} + ... \tag{3.17}$$

In this theory, the slope of the free surface (Eq. 3.2) is supposed to be of the order of magnitude of ϵ. Although it is verified very often, it happens that the free surface dramatically and sharply varies, violating the low slope assumption. However, Gaskell *et al.* [100] showed that lubrication theory is wrong by no more than 15% in the most extreme cases.

The Froude number is a dimensionless number defined for free surface flows that compares convection velocity to surface wave velocity. In Eq. 3.16 the velocity $c_0 = \sqrt{g' h_0}$ is the surface wave velocity for shallow waters. The Froude number can be interpreted as the ratio of inertial forces to gravitational ones. Its value determines the flow regime: subcritical, critical or supercritical:

- Subcritical regime (Fr < 1): the surface wave velocity is larger than the fluid velocity and consequently upstream traveling waves can propagate disturbances to the upstream flow.
- Critical regime (Fr $= 1$): surface wave and fluid convection have the same velocity.
- Supercritical regime (Fr > 1): fluid velocity is large enough to sweep upstream traveling waves away: surface information can not travel upstream and sharp surface level shifts may occur in front of downstream disturbances. This level change is called 'hydraulic jump' and can be seen as a 'shock wave for surface level'.

The Froude number and fluid thickness can be compared to the Mach number and pressure for compressible flow: depending on the Froude (resp. Mach) value, physical information (thickness or pressure) can travel upstream the main flow. A more detailed explanation has been made by Chanson [45]. The Froude number is of primary importance in

free surface flows where gravity plays a significant role. In pipe flows, the piezometric pressure $(p + \rho g z)$ is little influenced by gravity as the pressure can be set to any value, and in particular to a level such that $p >> \rho g \, \Delta z|_{max}$ where $\Delta z|_{max}$ is the maximum vertical length scale of the fluid. In free surface flows, pressure is set to the atmospheric pressure and the gravitational part of the piezometric pressure takes the lead [45].

In hydraulic engineering, the Euler number is also expressed as the ratio of pressure drop across the system to fluid inertia $(P_{out} - P_{in})/\rho U_0^2$, and is used to characterize the pressure drop in a fluid flow. With this expression, the Euler number is always lower than one, and equals one when wall friction is null.

Nondimensional boundary conditions

On free surfaces, the kinematic equation (Eq. 3.5) remains the same when non-dimensionalized:

$$\frac{\partial h^*}{\partial t^*} + u^* \frac{\partial h^*}{\partial x^*} = v^* \qquad \text{for } y^* = h^*(x^*, t^*) \tag{3.18}$$

Treating dynamic boundary conditions is more complicated because the free surface can be oriented in any direction, resulting in a different local coordinate system. Therefore a projection from the local to the original coordinate system is necessary to keep the original dimensionless number expressions. To avoid such projection, it is assumed that the surface local tangential plane is almost parallel to the wall. This assumption, previously called *long wave theory*, limits the following analysis to low slope waves, *i.e.* having an amplitude far smaller than wavelength.

Normal and tangent vectors of the interface can be expressed from the free surface derivative, yielding respectively in the original coordinate system:

$$\underline{N} = \begin{bmatrix} -\frac{\partial h}{\partial x} \\ 1 \end{bmatrix} \cdot \frac{1}{\sqrt{1 + \left(\frac{\partial h}{\partial x}\right)^2}} \qquad \text{and} \qquad \underline{T} = \begin{bmatrix} 1 \\ \frac{\partial h}{\partial x} \end{bmatrix} \cdot \frac{1}{\sqrt{1 + \left(\frac{\partial h}{\partial x}\right)^2}} \tag{3.19}$$

Then the matrix products conveying normal and tangential projections (first term of Eq. 3.6a and Eq. 3.6b) can be written (in 2D):

$$n_i \cdot \Gamma_{ij} \cdot n_j = N_x^2 \cdot \Gamma_{11} + N_x N_y \left(\Gamma_{12} + \Gamma_{21}\right) + N_y^2 \cdot \Gamma_{22} \tag{3.20a}$$

$$n_i \cdot \Gamma_{ij} \cdot t_j = N_x T_x \cdot \Gamma_{11} + N_x T_y \cdot \Gamma_{12} + N_y T_x \cdot \Gamma_{21} + N_y T_y \cdot \Gamma_{22} \tag{3.20b}$$

Invoking the long-wave hypothesis, the film thickness derivative is considered negligible compared to unity $(\partial h/\partial x << 1)$ and the normal and tangential vector components can be simplified at first order:

$$\underline{N} \approx \begin{bmatrix} -\frac{\partial h}{\partial x} \\ 1 \end{bmatrix} \qquad \text{and} \qquad \underline{T} \approx \begin{bmatrix} 1 \\ \frac{\partial h}{\partial x} \end{bmatrix} \tag{3.21}$$

Equations 3.20 then reduce to:

$$n_i \cdot \Gamma_{ij} \cdot n_j = \Gamma_{22} + \frac{\partial h}{\partial x} \left(\Gamma_{12} + \Gamma_{21}\right) \tag{3.22a}$$

$$n_i \cdot \Gamma_{ij} \cdot t_j = \Gamma_{21} + \frac{\partial h}{\partial x} \left(\Gamma_{22} - \Gamma_{11}\right) \tag{3.22b}$$

Substituting Eq. 3.22a together with Eq. 3.7 in the normal component of the dynamic boundary condition Eq. 3.6a leads to:

$$(p_e - p) + 2\left(\mu \frac{\partial v}{\partial y} - \mu_e \frac{\partial v_e}{\partial y_e}\right) + 2\,\frac{\partial h}{\partial x}\left[\mu\left(\frac{\partial u}{\partial y} + \frac{\partial v}{\partial x}\right) - \mu_e\left(\frac{\partial u_e}{\partial y} + \frac{\partial v_e}{\partial x}\right)\right] = \sigma \frac{\partial^2 h}{\partial x^2} \tag{3.23}$$

where the subscript e stands for the exterior (gaseous) variables at the interface. Nondimensionalizing with previously defined characteristic scales leads to:

$$\text{Eu}\,(p^*_{ext} - p^*) = \frac{\epsilon^2}{\text{We}}\frac{\partial^2 h^*}{\partial x^{*2}} - 2\frac{\epsilon}{\text{Re}}\left[\left(\frac{\partial v^*}{\partial y^*} - r\frac{\partial v^*_e}{\partial y^*_e}\right) + \frac{\partial h^*}{\partial x^*}\left[\left(\frac{\partial u^*}{\partial y^*} + \frac{\partial v^*}{\partial x^*}\right) - r\left(\frac{\partial u^*_e}{\partial y^*} + \frac{\partial v^*_e}{\partial x^*}\right)\right]\right] \tag{3.24}$$

where r and We are the ratio of viscosities and Weber number related to liquid thickness, respectively:

$$r = \frac{\mu_e}{\mu} \tag{3.25}$$

$$\text{We} = \frac{\rho\, h_0\, U_0^2}{\sigma} \tag{3.26}$$

Equation 3.24 states that the pressure jump across the interface is due to two contributions which are the two terms in the right-hand side. The first term expresses the role of surface tension while the second term represents the competition between viscosity and liquid inertia. It is worth noticing that for static fluids ($u_i = u_{e,i} = 0$), Eq. 3.24 reduces to the Laplace equation and the pressure jump is only due to surface tension.

Applying the same procedure to the tangential projection, *i.e.* injecting Eqs. 3.22b and 3.7 into Eq. 3.6b writes:

$$\left(\mu\frac{\partial u}{\partial y} - \mu_e\frac{\partial u_e}{\partial y}\right) + \frac{\partial h}{\partial x}\left[\mu\left(\frac{\partial v}{\partial y} - \frac{\partial u}{\partial x}\right) - \mu_e\left(\frac{\partial v_e}{\partial y} - \frac{\partial u_e}{\partial x}\right)\right] = \frac{1}{2}\left(\frac{\partial \sigma}{\partial x} + \frac{\partial h}{\partial x}\frac{\partial \sigma}{\partial y}\right) \tag{3.27}$$

Nondimensionalizing by using the same characteristic scales as before, and using previous results, leads to:

$$\left(\frac{\partial u^*}{\partial y^*} - \frac{\partial u^*_e}{\partial y^*}\right) + \epsilon^2\frac{\partial h^*}{\partial x^*}\left[\left(\frac{\partial v^*}{\partial y^*} - \frac{\partial u^*}{\partial x^*}\right) - \left(\frac{\partial v^*_e}{\partial y^*} - \frac{\partial u^*_e}{\partial x^*}\right)\right] = \frac{1}{2}\,\epsilon\,\frac{\text{Re}}{\text{We}}\left(\frac{\partial \sigma^*}{\partial x^*} + \frac{\partial h^*}{\partial x^*}\frac{\partial \sigma^*}{\partial y^*}\right) \tag{3.28}$$

The first term at the left-hand side expresses the jump of longitudinal velocity gradient due to fluid viscosities while the second term represents the stress induced by streamwise acceleration. The right-hand side accounts for surface tension gradients. Although Eqs.(3.24) and (3.28) seem difficult to integrate, they reduce to much more simple expressions in most of situations, thanks to nondimensional numbers comparison.

On the wall boundary, Eq. 3.11 simply delivers:

$$u^*_i = 0 \tag{3.29}$$

Considering a flat bottom wall, Eq. 3.12 reduces to:

$$\mu\frac{\partial u}{\partial y} = \tau_w \tag{3.30}$$

Writing $\tau_w = \mu U_0/h_0 \cdot \tau^*_w$ and using the previous characteristic scales, Eq. 3.30 reads:

$$\frac{\partial u^*}{\partial y^*} = \tau^*_w \tag{3.31}$$

3.2.3 Simplification of the equations in aeronautical combustion chambers

Considering the order of magnitude of all dimensionless numbers, it is possible to reasonably neglect some terms in equations of section (3.2.2). As Craster [59] states, discarding terms in a dimensionless equation can be seen as 'physics filtering': by evaluating the order of magnitude of physical phenomena and neglecting the smallest ones, some physics are not taken into account and only the predominant effects are described. In order to evaluate

Scale description	Variable name	Unit	Order of magnitude
Longitudinal length	L_0	$[m]$	10^{-2}
Film thickness	h_0	$[m]$	10^{-4}
Film velocity	U_0	$[m/s]$	1
Film density	ρ	$[kg/m^3]$	10^3
Film viscosity	μ	$[kg/ms]$	10^{-3}
Film surface tension	σ	$[kg/s^2]$	10^{-2}
Ambiant gas viscosity	μ_e	$[kg/ms]$	10^{-5}

Table 3.1 : *Order of magnitude of film scales in aeronautical burners*

dimensionless numbers, it is mandatory to know the order of magnitude of all scales in the concerned geometry at the targeted operating point. Characteristic scales related to film flows encountered in aeronautical burners are summarized in Table 3.1.

One important point is the choice of the scaling pressure P_0. As seen in section 3.2.2, several candidates exist for P_0 and their order of magnitude can be very different. The ambient gas pressure P_e may vary from 0.5 to 25 bars in aeronautical combustion chambers and choosing the proper order of magnitude is not straightforward. The scaling pressure is issued from the balance in pressure drop and shear stress within the film, and $P_0 = \mu U_0 L_0 / h_0^2$ is therefore preferred. With this setting, the Euler number transforms to the inverse of Reynolds number divided by the 'thickness-to-length' ratio:

$$\mathrm{Eu} = \frac{1}{\epsilon\,\mathrm{Re}} \tag{3.32}$$

Determination of the time scale ratio τ_c is based on the same consideration, *i.e.* the pressure drop/shear stress balance. This leads to:

$$\tau_c = \frac{1}{\epsilon\,\mathrm{Re}} \tag{3.33}$$

It is now possible to evaluate all dimensionless numbers that have been encountered so far and their value are listed in Table 3.2.

ϵ	Re	Fr^2	We	Eu	r
10^{-2}	10^2	10^3	10	1	10^{-2}

Table 3.2 : *Order of magnitude of dimensionless numbers used in film equations*

Replacing these numbers in Eqs. 3.14 helps to discriminate negligible terms:

$$\frac{\partial u^*}{\partial x^*} + \frac{\partial v^*}{\partial y^*} = 0 \tag{3.34a}$$

$$\frac{\partial u^*}{\partial t^*} + u^*\frac{\partial u^*}{\partial x^*} + v^*\frac{\partial u^*}{\partial y^*} = -\frac{\partial p^*}{\partial x^*} + 10^{-4}\,\frac{\partial^2 u^*}{\partial x^{*2}} + \frac{\partial^2 u^*}{\partial y^{*2}} + 10^{-1}\,\tan\gamma \tag{3.34b}$$

$$10^{-4}\left(\frac{\partial v^*}{\partial t^*} + u^*\frac{\partial v^*}{\partial x^*} + v^*\frac{\partial v^*}{\partial y^*}\right) = -\frac{\partial p^*}{\partial y^*} + 10^{-10}\,\frac{\partial^2 v^*}{\partial x^{*2}} + 10^{-4}\,\frac{\partial^2 v^*}{\partial y^{*2}} - 10^{-3} \tag{3.34c}$$

Applying the same procedure to dynamic boundary conditions on the free surface, Eqs. 3.24 and 3.28 yield:

$$(p^*_{ext} - p^*) = 10^{-5}\,\frac{\partial^2 h^*}{\partial x^{*2}} - 2\cdot 10^{-4}\left[\left(\frac{\partial v^*}{\partial y^*} - 10^{-2}\,\frac{\partial v^*_e}{\partial y^*_e}\right) + \frac{\partial h^*}{\partial x^*}\left[\left(\frac{\partial u^*}{\partial y^*} + \frac{\partial v^*}{\partial x^*}\right) - 10^{-2}\left(\frac{\partial u^*_e}{\partial y^*} + \frac{\partial v^*_e}{\partial x^*}\right)\right]\right] \tag{3.35a}$$

$$\left(\frac{\partial u^*}{\partial y^*} - \frac{\partial u^*_e}{\partial y^*}\right) = \frac{1}{2}\cdot 10^{-1}\,\left(\frac{\partial \sigma^*}{\partial x^*} + \frac{\partial h^*}{\partial x^*}\frac{\partial \sigma^*}{\partial y^*}\right) - 10^{-4}\frac{\partial h^*}{\partial x^*}\left[\left(\frac{\partial v^*}{\partial y^*} - \frac{\partial u^*}{\partial x^*}\right) - \left(\frac{\partial v^*_e}{\partial y^*} - \frac{\partial u^*_e}{\partial x^*}\right)\right] \tag{3.35b}$$

The order of magnitude of the predominant terms is unity. Terms in 10^{-1} in Eqs. 3.34b and 3.35b are of less importance but are kept. Liquid properties are supposed to be homogeneous so that surface tension gradients are considered to be negligible.

Finally, Eqs. 3.34 and 3.35 are simplified and transformed back into their dimensional formulation. Mass and momentum equations read in 2D:

$$\frac{\partial u}{\partial x} + \frac{\partial v}{\partial y} = 0 \tag{3.36a}$$

$$\frac{\partial u}{\partial t} + u\frac{\partial u}{\partial x} + v\frac{\partial u}{\partial y} = -\frac{1}{\rho}\frac{\partial p}{\partial x} + \nu\frac{\partial^2 u}{\partial y^2} + g\,\sin\gamma \tag{3.36b}$$

$$\frac{\partial p}{\partial y} = 0 \tag{3.36c}$$

Boundary conditions on the free surface are simplified to:

$$p_{ext} = p \tag{3.37a}$$

$$\mu\frac{\partial u}{\partial y} = \mu_e\frac{\partial u_e}{\partial y} \tag{3.37b}$$

And bottom wall conditions stay as originally expressed in Eqs. 3.11 and 3.30:

$$u_i = 0 \tag{3.38}$$

$$\mu\frac{\partial u}{\partial y} = \tau_w \tag{3.39}$$

From Eqs. 3.36c and 3.37a, it is deducted that the pressure within the film is independent of the y coordinate and is equal to the ambient gas pressure p_{ext}. The tangential projection of the free surface condition states that the discontinuity of longitudinal velocity slope is only due to the viscosity difference between the liquid and the surrounding gas.

In the following parts, additional assumptions will be made in order to further simplify the system of equations and be able to find an algebraic solution.

3.3 Overview of film modeling strategies

Depending on the application field, the length scales involved, different approaches are adopted in order to render a useful film description. As written in section 3.1, averaged and instantaneous film thicknesses and, to a less extent, film/gas shear are the most important physical quantities to describe.

In pipe geometries, some precise correlations for film/gas shear can be found in literature, based on global quantities such as the hydraulic diameter or the Reynolds number. However expressing the interface shearing with local variables such as film and gas velocities, strain rate and pressure gradient is difficult and lacks of universality due to the very complex behaviour of the free surface and the high number of controlling parameters [266].

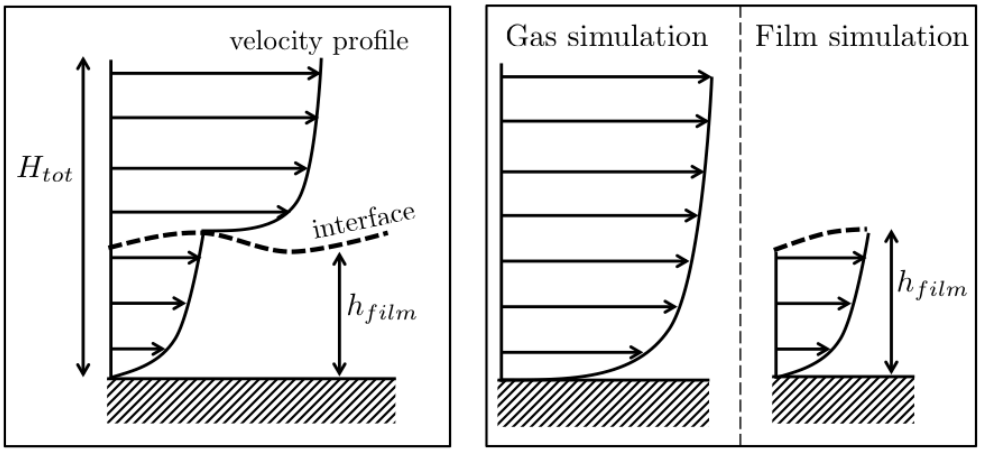

Figure 3.3 : *Thin film hypothesis. Left: real configuration. Right: decomposition of the flow into the gas and film parts. Film thickness being negligible compared to the gaseous wall-normal length, the gaseous velocity profile is supposed to be identical with or without film.*

3.3.1 Depth-Average Method

Integrating film equations over the film thickness simplifies the problem to an equation of film thickness h. This method is very popular and has been used in various engineering fields: environment, coating [100], internal combustion engine [90] as well as gas turbines [72]. One of the advantages of this method is to transform a 3D film problem into a 2D problem without reducing its physical representativeness, even when the film surface violates the lubrication theory. This finally decreases the computational costs.

Moreover, this approach is a stand-alone model. Not only it describes isolated film configurations such as free falling films or inertia driven films [100] but it also handles complex interactions with gas flows through coupling [73, 90]. In this coupled approach, the underlying assumption is the negligible film thickness compared to the *wall-normal* gaseous length scale, meaning that there is no blockage effect of the film on the gas flow (Fig. 3.3). The film/gas interface is seen by the gas as a boundary condition. As seen on Fig. 3.4, the coupling values that both solvers exchange are the interface shear (continuous across the interface) and the film roughness length scale. The interfacial shear is generally calculated by law-of-the-wall approach. For instance, Ebner *et al.* [73] used a differential description of the velocity profile $\partial u/\partial y$ with the mixing length damping proposed by Van Driest [68]. This modification allows to take in account several second order phenomena that alter the usual logarithmic law: pressure gradient, normal velocity component due to evaporation or blowing, and surface roughness. The film roughness length scale is calculated by the film solver using correlations that describe the roughness of a wavy film surface and is used in the gas solver to modify the boundary layer behaviour. Schöber *et al.* [313] correlated the film roughness length scale to the film Weber and Ohnesorge numbers.

During the last decade, advanced resolution techniques have been developed such as general Newton globally convergent solver [195], full approximation storage (FAS) and full multigrid (FMG) [354]. These methods have been tested in the context of painting, coating and semi-conductors technology.

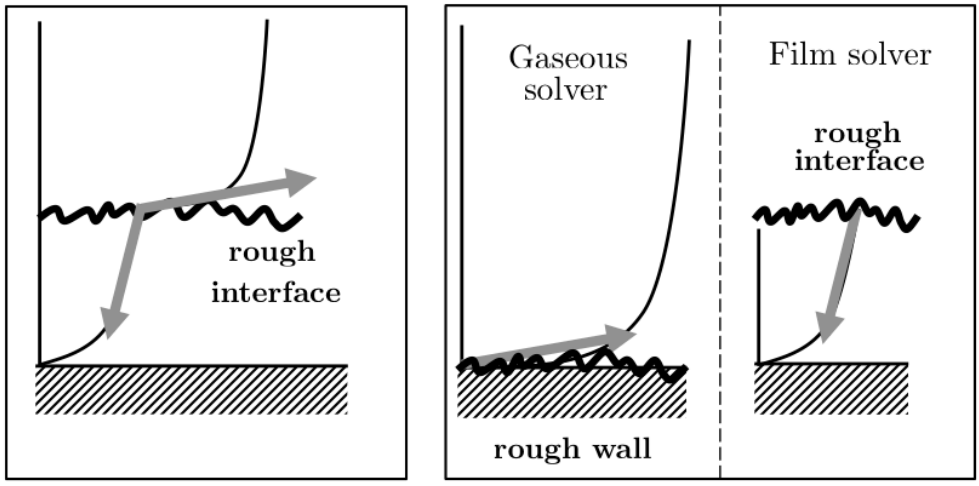

Figure 3.4 : *Film/gas coupling: continuity of shear stress (grey arrows) allows to set the liquid shear stress to the value computed in the gas simulation. Reversely the interface roughness is used to compute the gas flow.*

3.3.2 Interface tracking method

Interface tracking methods, presented in section 1.4.3, are broadly used in computational fluid dynamics for flows involving several non miscible phases. It is a very active research topic and many articles can be found in the literature, in various application fields.

3.3.2.a) Volume of Fluid method

In the context of thin liquid films, VOF methods have been applied for the evaporation of a falling and shear-driven film by Helbig *et al.* [141] and showed a good accuracy for the film thickness. Lan *et al.* [186] compared experiment and VOF model in the case of a 3D shear-driven film in a duct and obtained also reasonably good agreement for the film thickness and spreading. Still, Hashmi *et al.* [139] pointed out that large velocity gradients and property jumps across the interface yield inaccurate resolution of the velocity field within the gas phase. More precisely, velocity gradients are underestimated and the pressure drop is overestimated. This lack of accuracy was mainly connected to the turbulence model (RANS k-ϵ) and Hashmi *et al.* proposed an improvement of the turbulence model to obtain correct turbulent quantities in the interface neighbourhood.

3.3.2.b) Level Set method

In thin film configurations, the liquid layer may be too small to be discretized. The curvature computed from the gradient of ϕ (the function that localizes the interface) becomes noisy and the film ruptures too quickly [40]. In order to avoid such behaviours, improvements have been made in this area and allow to compute thin films formed at bubble surfaces [380].

3.3.3 Particles Model

The idea of the particles model is to represent a continuum medium by a large number of discrete objects, named particles. Using a particle approach to model thin film flows has been originally introduced by O'Rourke & Amsden

[257] in the context of spark-ignition engine taking into account film vaporization. The main advantage of particle versus continuous modeling is the possibility to describe sharp interfaces with particles whereas continuous formulations tend to naturally diffuse the interface. Particles contain the physical information that describe the film: mass, volume, velocity and temperature. This approach fits well to configurations where the film is generated by, or transforms into, 'discrete-like' objects. Typical examples are a film generated by droplets impinging a wall, or a film atomized at a sharp edge.

This approach could be qualified as 'hybrid' since Navier-Stokes fundamental equations are treated in different ways: mass conservation is ensured by particle number conservation while momentum is integrated over the film thickness and the mean film velocity is applied to particles. In their article, O'Rourke & Amsden supposed a quasi-steady state behaviour of the film momentum (i.e. steady state velocity is reached instantaneously) while the unsteadiness of film energy was taken in account. They also considered mass, momentum and energy transfers due to impinging droplets.

Coupling with the gaseous phase is achieved through interface shear stress and film equivalent roughness, as in the Depth-Averaged Method, and film mean temperature and heat flux for the energy equation.

As this model has been selected to be implemented in AVBP, it will be explained in more details in chapter 6.

3.4 Conclusion

This chapter proposes a qualitative overview of film phenomena and a list of film motion origins. Navier-Stokes equations were simplified in the particular configuration of 2D wall-bounded flow.

Using the strong assumption of the lubrication theory allowed to derive the film equations, and their non-dimensionalization exhibited several characteristic numbers. From the typical physical values encountered in aero-engines, only the predominant non-dimensional numbers were considered, leading to a physic filtering and simplification of the film equations. The remaining phenomena that drive the films are the pressure gradient, the gravity and the external gas shear stress.

Finally an overview of numerical strategies highlighted four methods to describe film flows, depending on the kinematic point of view (Lagragian or Eulerian) and the level of details (3D or Depth-Averaged films).

Chapter 4

Instabilities and Atomization

In an unstable flow configuration, a tiny disturbance, negligible from a macroscopic point of view, grows exponentially until it reaches a point where it locally modifies the mean flow. Then a complex and fully non-linear interaction occurs between the instability and the surrounding flow, leading sometimes to other type of instabilities and very often to a major change of the initial unperturbed flow (Fig 4.1).

Instabilities are of primary importance for free surface flows because they are the first step towards atomization. Jumps in physical properties at the interface are often the sources of instabilities: starting from an unperturbed flat state, the interface evolves to a wavy texture, presenting crests and troughs that modify the local flow conditions. This wavy texture is then even more distorted until it detaches from the liquid core and disintegrates into liquid blobs. This is called primary atomization. Then the liquid blobs are subject to other kind of instabilities and undergo a cascade fragmentation (namely the secondary atomization) until reaching a size where stabilizing and destabilizing phenomena are balanced.

The complexity of free surface instabilities is highlighted by the fact that depending on the situation a force (gravity or viscosity) can stabilize or destabilize the flow field [47].

Knowing and describing film instability is important for predicting atomization : the droplet population within a spray depends on how it has been generated. Different types of instability have different characteristic lengths (also

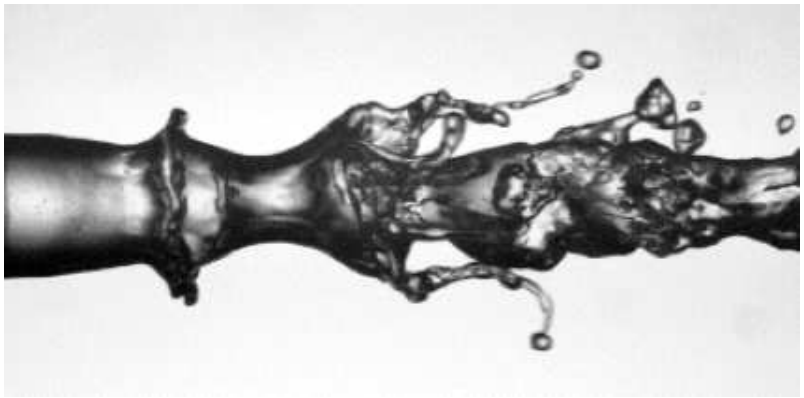

Figure 4.1 : *Visualization of instability mechanism leading to atomization, from Marmottant & Villermaux [220]*

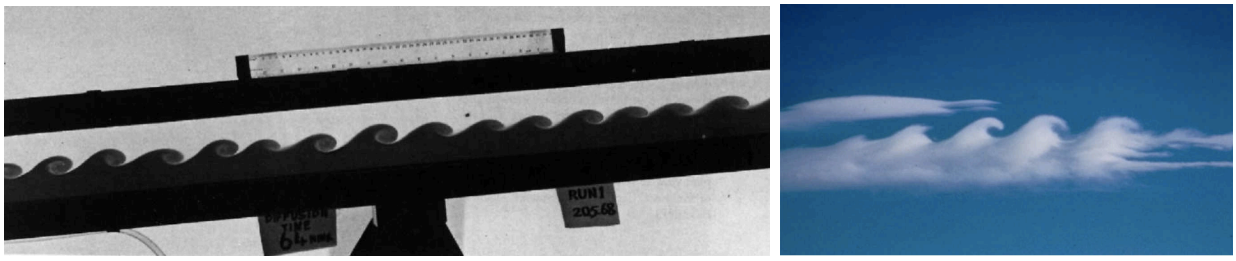

Figure 4.2 : *Illustration of Kelvin-Helmholtz instability at different length scales. Left: Kelvin-Helmholtz instability located at two different fluids interface, from [340] (scale* $\approx 1\,cm$*). Right: instability between different atmospheric layers, illustrated by clouds (scale* $\approx 1\,km$*).*

mentioned as 'wavelength' given the oscillatory nature of instabilities). These different length scales create blobs of different dimensions and finally generate sprays of different drop size spectra.

In this chapter, a theoretical study of instabilities is first summarized to highlight the basic phenomena, followed by the particular configuration of film instability. Then the primary atomization is presented in usual flow configurations of aeronautical atomizers. An overview of the numerical tools to compute the primary atomization is presented and finally secondary atomization is briefly tackled.

4.1 Hydrodynamic instabilities in parallel flows

This section briefly describes the mathematical study of hydrodynamic instability in parallel flow configurations. It follows and summarizes the rigorous derivation done by Charru [47].

4.1.1 Non viscous instabilities in parallel flows

This type of instability is mainly triggered by the fluid inertia (Kelvin-Helmholtz instability) or the pressure distribution (Couette-Taylor). The Kelvin-Helmholtz (KH) instability is a fundamental instability that develops in the presence of a velocity difference in a flow. It can occur within a single phase flow (shear layers, jets, high Reynolds wakes or boundary layers), but also in multiphase flows at the phases interface. Its wavelength, labeled λ_L in the following, presents a remarkably wide range in natural phenomena (Fig. 4.2). The viscosity only plays a minor role, damping the instability growth of short wavelength perturbations. The derivation of the general equation of a perturbation in non viscous parallels flow is proposed in the following as it allows to settle and understand the basis of an unstable flow. It starts with the incompressible Euler equations:

$$\frac{\partial u_i}{\partial x_i} = 0 \tag{4.1a}$$

$$\frac{\partial u_i}{\partial t} + u_j \frac{\partial u_i}{\partial x_j} = -\frac{\partial p}{\partial x_j} \tag{4.1b}$$

In the particular case of unidirectional mean flow as depicted on Fig. 4.3, the mean velocity components and pressure simplify to:

$$\overline{u}_x(\vec{x},t) = \overline{u}_x(y), \qquad \overline{u}_y(\vec{x},t) = \overline{u}_z(\vec{x},t) = 0, \qquad \overline{p}(\vec{x},t) = \overline{p} \tag{4.2}$$

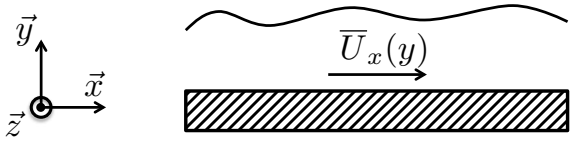

Figure 4.3 : *Unidirectional mean film flow configuration*

Considering the perturbed flow $\overline{u_i} + u_i''$, $\overline{p} + p''$, the linearized equations write:

$$\frac{\partial u_x''}{\partial x} + \frac{\partial u_y''}{\partial y} + \frac{\partial u_z''}{\partial z} = 0 \tag{4.3a}$$

$$\frac{\partial u_x''}{\partial t} + \overline{u}_x \frac{\partial u_x''}{\partial x} + u_y'' \frac{\partial \overline{u}_x}{\partial y} = -\frac{\partial p''}{\partial x} \tag{4.3b}$$

$$\frac{\partial u_y''}{\partial t} + \overline{u}_x \frac{\partial u_y''}{\partial x} + = -\frac{\partial p''}{\partial y} \tag{4.3c}$$

$$\frac{\partial u_z''}{\partial t} + \overline{u}_x \frac{\partial u_z''}{\partial x} + = -\frac{\partial p''}{\partial z} \tag{4.3d}$$

$$\tag{4.3e}$$

Given the invariance properties of the problem, the solution may be written with the form of normal modes of wave vector $\overrightarrow{k} = k_x\, e_x + k_z\, e_z$ and pulsation ω. For the longitudinal perturbation of the velocity, a normal mode writes:

$$u_x(\overrightarrow{x}, t) = \frac{1}{2}\, \hat{u}_x(y)\, \mathrm{e}^{i(k_x x + k_z z - \omega t)} + C \tag{4.4}$$

where C is a constant and $\hat{u}_x$ is the modulus of u_x''. Using similar expression for u_y'', u_z'' and p'' leads to the system of equations verified by $\hat{u}_x$,$\hat{u}_y$,$\hat{u}_z$ and $\hat{p}$:

$$i\, k_x\, \hat{u}_x + \frac{\partial \hat{u}_y}{\partial y} + i\, k_z\, \hat{u}_z = 0 \tag{4.5a}$$

$$i\, (k_x \overline{u}_x - \omega)\, \hat{u}_x + \frac{\partial \overline{u}}{\partial y}\, \hat{u}_y = -i\, k_x\, \hat{p} \tag{4.5b}$$

$$i\, (k_x \overline{u}_x - \omega)\, \hat{u}_y = -\frac{\partial \hat{p}}{\partial y} \tag{4.5c}$$

$$i\, (k_x \overline{u}_x - \omega)\, \hat{u}_z = -i\, k_z\, \hat{p} \tag{4.5d}$$

For an **infinite domain**, perturbations decrease at infinity, leading to the following boundary conditions:

$$\hat{u}_x,\, \hat{u}_y,\, \hat{u}_z \to 0, \qquad \text{for} \quad y \to \pm\infty \tag{4.6}$$

For a **bounded flow**, non permeability conditions at the wall surfaces (located at y_1 and y_2) read:

$$\hat{u}_y(y_1) = 0 \qquad \text{and} \qquad \hat{u}_y(y_2) = 0 \tag{4.7}$$

The set of equation 4.5-4.6 or 4.5-4.7 can be formally written as a linear system:

$$L\phi = \omega M \phi \tag{4.8}$$

where $\phi = (\hat{u}_x, \hat{u}_y, \hat{u}_z, \hat{p})$ and L and M are differential linear operators. The system is, for a given wave vector, a generalized eigenvalue problem that admits a non zero solution ϕ if the operator $L - \omega M$ is not invertible. This condition writes formally:

$$D(\overrightarrow{k}, \omega) = 0 \tag{4.9}$$

where D is the determinant operator. Equation 4.9 constitutes the dispersion relation of small amplitude perturbations. The Squires theorem states that any unstable tridimensional mode $(\overrightarrow{k}, w)$ of temporal growth rate ω can be related to a 2D mode $(\tilde{k}, \tilde{w})$. It is therefore possible to limit the study to 2D perturbations in a 3D flow. The main advantage of this transformation is to use the stream function ψ of the velocity perturbation defined by:

$$u_x = \frac{\partial \psi}{\partial y} \tag{4.10a}$$

$$u_y = -\frac{\partial \psi}{\partial x} \tag{4.10b}$$

Rewriting Euler equations (Eqs. 4.1) in 2D, canceling the pressure via cross differentiation, and injecting the normal modes of wave vector $\overrightarrow{k} = k\overrightarrow{e}_x$ and pulsation ω:

$$\psi(\overrightarrow{x}, t) = \frac{1}{2}\hat{\psi}(y)e^{i(k_x x - \omega t)} \tag{4.11}$$

leads to the Rayleigh equation:

$$(\overline{u}_x - c)\left(\frac{\partial^2}{\partial y^2} - k^2\right)(\hat{\psi}) - \frac{\partial^2 \overline{u}_x}{\partial y^2}\hat{\psi} = 0 \tag{4.12}$$

with associated boundary conditions for free or bounded flow:

$$\hat{\psi} \to 0 \quad \text{for} \quad y \to \pm\infty \qquad \text{or} \qquad \hat{\psi}(y_1) = \hat{\psi}(y_2) = 0 \tag{4.13}$$

For a real wave number k, if the eigen function $\hat{\psi}$ is associated to a real eigenvalue $c = k/\omega$ then the exponential term in Eq. 4.11 is purely imaginary and the perturbation is not amplified. On the contrary, if a real k leads to two complex conjugate eigenvalues, one of the mode is damped and the other is amplified: the flow is unstable.

Under simplifying assumptions on the velocity profile, the Rayleigh equation 4.12 can be formally solved, *e.g.* Raynal [280] supposed a piecewise linear velocity profile to derive the perturbation growth on two-phase flow interface and found a good agreement with experiments. More recently, Zaleski *et al.* [376] used this inviscid linearized stability theory to study a new fundamental 2D instability in a liquid/gas mixing layer.

In Eq. 4.12, if the velocity c of an eigenmode is equal to the fluid velocity $\overline{u}_c(y)$ at $y = y_c$, then the first term vanishes and the eigen function presents a singularity at $y = y_c$. The layer around y_c is called a *critical layer* and it has to be taken into account when considering film flows [247] as will be seen in sections 4.1.2 and 4.2.2.

4.1.2 Couette flow stabilty - continuous spectrum

In a non viscous Couette flow between two walls, the flow profile is linear in y and its second derivative is zero. This leads to the general solution:

$$\hat{\psi} = A\sinh(ky + \varphi) \tag{4.14}$$

where A and φ are two integration constants. The impermeability conditions at the wall ($\hat{\psi}(y_1) = \hat{\psi}(y_2) = 0$) would lead to $A = 0$ and no eigenmodes would be defined. In reality, some eigen modes are present, but they are associated to a critical layer, *i.e.* with a celerity equal to the flow speed. Solving the Rayleigh equation from both sides of the

critical layer shows that any normal mode of celerity between 0 and $2U_0$ is an eigen mode. The dispersion relation can therefore be written:

$$k\overline{u}_x(y_1) < \omega < k\overline{u}_x(y_2) \tag{4.15}$$

Equation 4.15 means that for any wave number k, the eigenvalue spectrum $\omega(k)$ is continuous. The flow is therefore linearly stable [42]. Taking into account viscous effects does not alter this assertion and the Couette flow is linearly stable for any Reynolds number [296].

4.1.3 Rayleigh and Fjørtoft theorems of stability

In parallel flows, Rayleigh theorem [279] states a necessary condition for having an unstable configuration: if the flow profile admits an inflection point, then the flow can be unstable. This criterion has been refined by Fjørtoft [88] by stating that the inflection point must correspond to a local maximum of the vorticity. This new theorem is still a necessary (but not sufficient) condition for having an unstable flow.

4.1.4 Viscous instabilities in parallel flows

The incompressible Navier-Stokes equations read:

$$\frac{\partial u_i}{\partial x_i} = 0 \tag{4.16a}$$

$$\frac{\partial u_i}{\partial t} + u_j \frac{\partial u_i}{\partial x_j} = -\frac{\partial p}{\partial x}_j + \frac{1}{\mathrm{Re}}\Delta u_i \tag{4.16b}$$

Following the same derivation as in subsection 4.1.1, normal modes are first sought, and the dispersion relation $D(\overrightarrow{k}, x, \mathrm{Re}) = 0$ is formally written. The Squires theorem is applied to use the stream function ψ. The *Orr-Sommerfeld* equation is finally found:

$$(\overline{u}_x - c)\left(\frac{\partial^2}{\partial y^2} - k^2\right)(\hat{\psi}) - \frac{\partial^2 \overline{u}_x}{\partial y^2}\hat{\psi} = \frac{1}{ik\mathrm{Re}}\left(\frac{\partial^2}{\partial y^2} - k^2\right)^2 \hat{\psi} \tag{4.17}$$

The difference between the Orr-Sommerfeld equation 4.17 and the Rayleigh equation 4.12 lies in the right-hand side that now accounts for viscosity. It rises the equation order from two to four. For a wall bounded flow, the boundary conditions are:

$$\frac{\partial \hat{\psi}}{\partial y}(y_1) = \hat{\psi}(y_1) = 0 \qquad \text{and} \qquad \frac{\partial \hat{\psi}}{\partial y}(y_2) = \hat{\psi}(y_2) = 0 \tag{4.18}$$

or in the case of a boundary layer at $y = 0$ and a perturbation decreasing at infinity:

$$\frac{\partial \hat{\psi}}{\partial y}\hat{\psi} = 0 \quad \text{for} \quad y = 0 \qquad \text{and} \qquad \frac{\partial \hat{\psi}}{\partial y}, \hat{\psi} \to 0 \text{ for } y \to \infty \tag{4.19}$$

The set of equations 4.17-4.18 or 4.17-4.19 can be formally written as:

$$L_A\hat{\psi} = cL_B\hat{\psi} \tag{4.20}$$

where L_A and L_B are differential operators. In a temporal stability study, the solution is found by imposing k real and the complex celerity c is calculated whereas a spatial resolution is achieved by imposing a real pulsation $\omega = ck$ and computing the wave number k. As Eq. 4.17 is linear with regards to the celerity while the wave number is elevated to the power four, the temporal study is easier and it is usually used for margin stability studies. For finite

wave number and Reynolds number, the right-hand side does not vanish and the problem induced by a critical layer (as in the Rayleigh equation) does not exist in this case. However the exact solution can be determined only in a few particular cases, and Eq. 4.17 is most often solved numerically. For instance, Yecko & Zaleski [371] used a Chebyshev colocation code to evaluate the eigenvalues of the Orr-Sommerfeld equation with an additional surface tension term, in the case of a two-phase mixing layer.

4.2 Film instabilities

Instabilities developing on the surface of a thin liquid film are a particular case of parallel flows instabilities. As liquid and gas are not miscible, their interface is well defined and surface tension effects are not negligible. In addition, the liquid/gas interface is dynamic and usually presents large jump conditions of density ($\rho_l/\rho_g \approx 1000$) and viscosity ($\mu_l/\mu_g \approx 100$). When the film is very thin, the diffusive role of viscosity is enhanced and the film thickness is to be compared to the wave length of the perturbation. When the film is sheared by a turbulent air stream, complex interactions between the surface instabilities and the gaseous turbulent boundary layer arise so that both media should be resolved and coupled for a complete prediction of the phenomenon. For these reasons, the study of thin liquid film instabilities is a complete research topic.

4.2.1 Intrinsic film stability

Oron [255] theoretically showed that when an isolated thin liquid film with zero surface tension is subjected to a constant shear stress, waves travel in the shear direction, and steepen as they go, but no instability is found. When accounting for a non-zero constant surface tension, the same waves appear with a delay, and in a long wave regime, they are damped. This is in accordance with the stabilizing influence of surface tension.

However when considering gravity, an unstable behaviour occurs if the heavier fluid is on top of the lightest one. This instability is known as Rayleigh-Taylor instability. It can also be triggered by any type of acceleration, not only gravity but also inertial or Coriolis acceleration. In a general case, when a continuum of fluid undergoes an acceleration a, the most amplified wavelength due to Rayleigh-Taylor instability expresses:

$$\lambda_{RT} = 2\pi\sqrt{\frac{3\sigma}{a\rho_l}} \tag{4.21}$$

This type of instability is essential in the atomization process, as seen in 4.3.1.

4.2.2 The origins of thin film instabilities

In the absence of gravity, or when the liquid is located below the gas layer, film instability is linked to the ambient gas flow. In a comprehensive review work, Boomkamp [31] highlights several origins of film disturbances when sheared by a turbulent flow:

1. In 1957, Miles [233] showed the occurrence of an energy transfer from the mean gas flow to the wave perturbation when a negative velocity profile curvature is present in the critical layer. This is called the *critical-layer instability*. It must be highlighted that if the critical layer is located in the viscous sublayer of the film, this mechanism can not occur.
2. In 1976, Yih [373] identified the *viscosity-contrast mechanism*. The viscosity jump across the phase interface is a cause of instability for long waves. The condition that the thinner layer is the most viscous one is sufficient. This phenomenon was studied in short waves excitation ($kh >> 1$) [146, 153], and non asymptotic situations (as $kh \approx 1$ or Re> 1) were numerically investigated by [284].

3. In 1957, Phillips [267] found out instabilities generated by a direct forcing due to turbulent pressure oscillations.

4. In 1997, Boomkamp [31] derived an *internal mode* when the bottom layer of the film is laminar. The energy feeding this instability comes from two different locations: the interface and the bulk bottom layer of the liquid film.

In a recent article, Náraigh *et al.* [247] present an analytical model to express the mean flow profile of a film sheared by a turbulent flow in a channel. They start from the incompressible 2D RANS equations:

$$\frac{\partial u_i}{\partial x_i} = 0 \tag{4.22a}$$

$$\frac{\partial u_i}{\partial t} + u_j \frac{\partial u_i}{\partial x_j} = -\frac{\partial p}{\partial x_j} + \frac{\partial \tau_{ij}}{\partial x_j} + \frac{\partial \tau_{ij}^{turb}}{\partial x_j} \tag{4.22b}$$

where τ_{ij} is the viscous stress tensor (Eq. A.2) and τ_{ij}^{turb} is the turbulent stress tensor, arising from Reynolds average. The turbulent stress tensor is expressed by:

$$\tau_{ij}^{turb} = \begin{pmatrix} n_1 & s \\ s & n_2 \end{pmatrix} \tag{4.23}$$

Terms n_1, n_2 denote the turbulent normal stresses and s is the turbulent shear stress. Expressing the velocity components with the stream function ψ and using the normal mode decomposition with pressure, stream function and turbulent normal and shear stresses leads to two Orr-Sommerfeld equations with additional terms, one for each phase:

$$(\overline{u}_x - c)\left(\frac{\partial^2}{\partial y^2} - k^2\right)(\hat{\psi_g}) - \frac{\partial^2 \overline{u}_x}{\partial y^2}\hat{\psi_g} = \frac{1}{ik\mathrm{Re}}\left(\frac{\partial^2}{\partial y^2} - k^2\right)^2 \hat{\psi_g} + \frac{\partial^2 \hat{n}}{\partial y^2} + \frac{1}{ik}\left(\frac{\partial^2}{\partial y^2} + k^2\right)\hat{s} \tag{4.24a}$$

$$(\overline{u}_x - c)\left(\frac{\partial^2}{\partial y^2} - k^2\right)(\hat{\psi_l}) - \frac{\partial^2 \overline{u}_x}{\partial y^2}\hat{\psi_l} = \frac{m}{ikr\mathrm{Re}}\left(\frac{\partial^2}{\partial y^2} - k^2\right)^2 \hat{\psi_l} \tag{4.24b}$$

where the subscripts g and l refer to the gas and liquid respectively, $m = \mu_g/\mu_g$ and $r = \rho_g/\rho_l$ denote the viscosity and density ratios, and $\hat{n} = \hat{n_1} - \hat{n_2}$. From Eqs. 4.24 turbulence is considered only in the gas phase, the film flow being laminar. Two turbulence models have been tested: the visco-elastic model expressed by a transport equation of the turbulent kinetic energy, and the eddy viscosity model based on the Boussinesq approach of the turbulent viscosity. This approach is interesting because it proposes to solve the Orr-Sommerfeld equation (Eq. 4.17) by taking the turbulence of the gaseous flow into account by adding extra terms (Eq. 4.24a).

From this study, Náraight *et al.* [247] found out that the turbulent stresses had a negligible impact on interfacial instability, promoting the *viscosity-contrast mechanism* of Yih. By an energy budget of the perturbation, they observed the predominance of the tangential stresses over other terms, ranking the interfacial mode (instability fed by tangential stresses) as the most important one. However they noticed the presence of a second mode, deriving from an energy transfer from the mean bulk region to the perturbation. This mode was called *internal* and can be the source of the instability when the *interfacial* mode is damped by surface roughness.

Náraigh *et al.* [247] also stated that Kelvin-Helmholtz type instabilities that are recorded in experimental studies arise in large amplitude waves and do not appear in the linearized problem wherein viscous effects are fully accounted. Moreover, Jurman & McCready [169] derived an equation for film thickness subjected to a two-dimensional wave via linear stabilty analysis. They found [168] good agreement between the predicted most amplified wave length and wave speed with experiments when the operating point was near the stabilty point, but an increasing deviation for higher velocity.

4.2.3 Evolution of film instabilities

In most cases, film instabilities evolve into waves arising at the film surface. There are no general procedures for predicting wave properties in cocurrent configurations, due to the complexity of the problem. For instance, when the film is coflowing with a high speed air stream, the high degree of shear makes flowing conditions far above the point of neutral stability of interfacial waves [168]. Consequently, arising waves are not periodic with a small amplitude, and the prediction of their wavelength and celerity greatly differs from linear stability theory.

Overview of wave regimes map

Peng *et al.* [266] established a map of wave regimes depending on the gaseous and film Reynolds numbers, for different liquid viscosities, shown on Fig. 4.4 (1 cP corresponds to 10^{-3} Pa.s). Different liquid viscosities lead to different regime maps, implying a strong impact of viscosity on wave formation. However on Fig. 4.4 the liquid viscosity is also present in the liquid Reynolds number (x axis). Consequently, liquid viscosity appears in two independent parameters (the liquid Reynolds number and itself), suggesting that either an additional dimensionless parameter is necessary to define the regime map completely, or the film Reynolds number may not be the appropriate dimensionless number to map the regimes. The various surface states identified in Fig. 4.4 are described below:

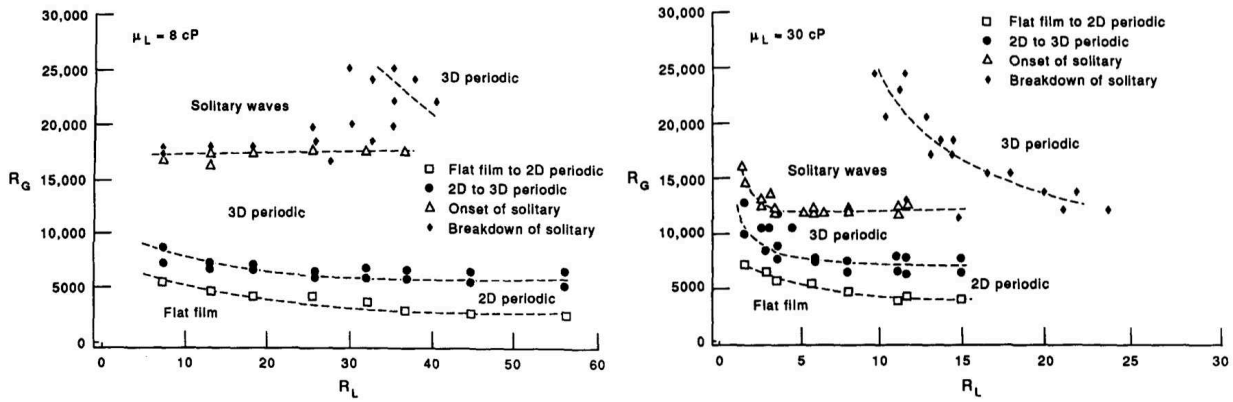

Figure 4.4 : *Wave regime maps, extracted from [266]*

- Flat film: the film surface shows little deviation from the unperturbed state. No significant periodic event is visible.
- 2D periodic: two dimensional waves, oriented and convected in the flow direction, arise on the film surface. As their amplitude is low and they frequency is regular, this regime is well described by the linear stability theory.
- 3D periodic: when the flow conditions are continuously changed (for instance an increase of the gas velocity), the 2D periodic waves evolve to a 3D pattern. Due to a variation in wave amplitude (Fig. 4.5), the convection velocity of the front varies locally (Fig. 4.6) and consequently leads to wave/wave interactions [2].
- Solitary waves: this regime produces quite asymmetric waves that, contrary to 2D and 3D periodic wave, occur irregularly. Thus they are named *solitary* waves. They are characterized by a continuous shape and well defined contours. Experiments show that these waves carry significant amount of liquid, which alters the base state so that the film thickness is significantly modified [266].

- Roll waves: these waves are similar to solitary waves, but due to different conditions (surface tension, gas shear, viscosity), they do not keep a clear contour and disrupt, or are shattered by the gas into droplets.

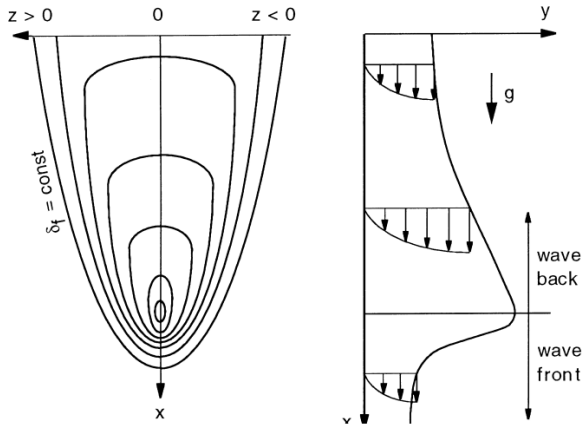

Figure 4.5 : *Contour lines of the film thickness of an idealized 3D-wave, from [2]*

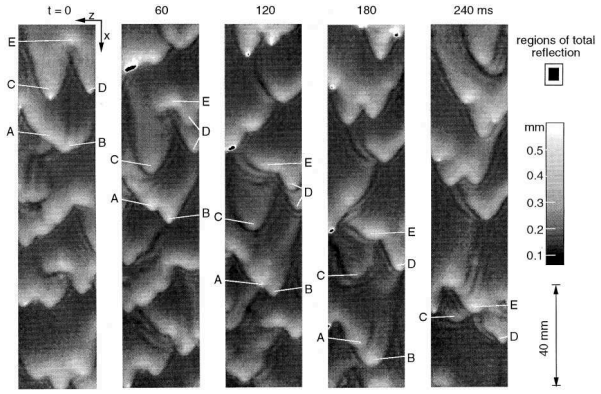

Figure 4.6 : *Temporal development of 3D-wave structures at Re_l=27, from [2]*

Transition to solitary and roll waves

The solitary and roll waves have a dominant effect compared to 2D periodic and 3D periodic waves. Indeed the low amplitude of the latter suggests a small deviation of the film from its unperturbed state and guarantees no droplet entrainment. Moreover their regular frequency allows to consider their influence on the gas as a global mean effect. Comparatively, solitary and roll waves have larger impact: they transport a significant amount of fluid with a velocity larger than the unperturbed film mean velocity, leading to a lower mean film thickness. In addition, due the gas shear, they lead to breakup and droplet entrainment. Therefore the characterization of the conditions leading to the onset of solitary and roll waves is more important.

Peng *et al.* [266] proposed a scenario for the rising of solitary and roll waves, based on their experiments and the work of [7, 37, 136, 234]. The triggering quantity is the wave amplitude to film thickness ratio a/h: if a periodic wave amplitude reaches a sufficiently large value (order of magnitude of the film thickness), the application of gas shear causes the wave to become asymmetric with a steeper front and a more shallow back. Depending upon fluid properties, such as viscosity and surface tension, they may either retain a continuous form (solitary waves) or break, producing roll waves [168].

For a thin layer (*i.e.* a low film Reynolds number) the most dominant 2D wavelength is large and weakly subject to dispersion. Therefore the waves close to the dominant wavelength are able to propagate and grow in a coherent manner, until reaching a large a/h ratio and transform into solitary waves. For larger film Reynolds numbers, the process is different. Waves with wavelengths close to the spectral peak cannot reach high a/h ratio. Peng *et al.* [266] suggest that because of a larger film thickness, the predominant waves are shorter and undergo a larger dispersion, keeping small a/h ratios. Bruno *et al.* [37] reported that for $\mathrm{Re}_l > 100$, roll waves are issued from disturbances that initially have wavelengths much longer than the film thickness (weakly subject to dispersion) and which grow slowly with distance. This could explain why solitary and roll waves occur less often in thicker films: the original disturbance needs a long distance to reach the adequate a/h ratio.

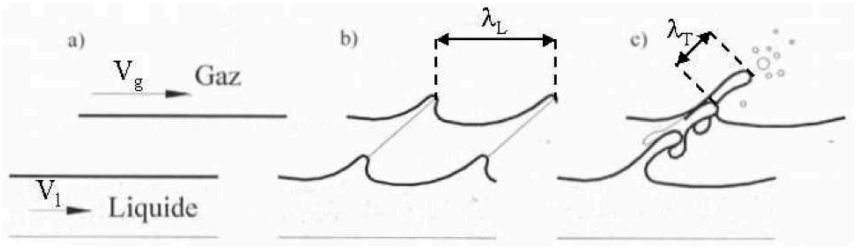

Figure 4.7 : *Illustration of 3D structures arising from a Kelvin-Helmholtz instability, in a thick film configuration, from [152]*

4.3 From a 2D instability to a 3D fragmentation process

In section 4.1, thanks to the Squires theorem, the instability phenomenon was reduced to a 2D problem characterized by one length scale. In section 4.2, it was shown that solitary and roll waves are mainly present 2D features. However in reality the breakup process is fully 3D: in many different configurations, experiments highlight the development of spanwise regular structures from the 2D longitudinal instabilities (figs. 4.1 and 4.7). Therefore it is necessary to consider additional effects to link the academic two-dimensional longitudinal instability to the fragmentation process.

4.3.1 The development of the secondary instability

Superposed to a 2D longitudinal wave, a 2D transverse regular pattern was observed in different configurations [86, 210] and leads to a surface marked with 3D features. During these last two decades, several scenarios were developed in particular configurations to find the origin of the transverse instability.

Capillarity instability

In the particular case of coaxial gas streams, Lasheras & Hopfinger [187] observed a capillarity instability for low to moderate Weber numbers (< 100 when defined with the liquid jet diameter). It leads to the transverse wavelength:

$$\lambda_T \propto \frac{\sigma}{\rho_g U_g^2} \tag{4.25}$$

where ρ_g and U_g stand for the surrounding gas density and mean velocity.

Faraday instability

Marmottant & Villermaux [219] stated that the wavy shape of the KH instability induces an acceleration of the fluid particles in the direction perpendicular to the gas flow. They compared the group velocity of the KH instability to the liquid velocity in a jet or sheet and found that the liquid flows much faster than the instability pattern. Therefore the liquid particles close to the interface evolve like in a wavy corridor, undergoing a normal acceleration as they follow the curved boundary. This acceleration leads to a Faraday (unsteady Rayleigh-Taylor) instability with a wavelength expressed by:

$$\lambda_T = C_\perp \delta_\omega \left(\frac{\rho_l}{\rho_g}\right)^{1/3} \mathrm{We}_{\delta_\omega}^{-1/3} \propto \sigma^{1/3} U_g^{-1} \tag{4.26}$$

where δ_ω is the vorticity thickness, and $C_\perp$ a constant prefactor measured at about 2.45 for coaxial configurations.

Rayleigh-Taylor instability

Hong [151] and Varga [353] stated that the transverse instability is triggered by an *axial* acceleration due to the aerodynamic drag of the gas onto the wave crests. This longitudinal acceleration leads to a Rayleigh-Taylor instability with a wavelength expressed as:

$$\lambda_T = 2\pi \sqrt{\frac{3\sigma}{a\rho_l}} \tag{4.27}$$

where a is the acceleration of the fluid particles located in the wave crest and can be expressed by the force exerted by the gas onto the crest divided by the mass of the accelerated structure. This mechanism is detailed in chapter 7. In the limit of $U_g \gg U_l$, Hong *et al.* showed that the scaling of λ_T with the surface tension and the gas velocity is:

$$\lambda_T \propto \sigma^{1/2} U_g^{-5/4} \tag{4.28}$$

that slightly differs from the Faraday instability.

Comparison of the three mechanisms with experiments

The transverse wavelength expression of the three mentioned mechanisms leads to different dependence on the gas velocity and surface tension. Experiments [151, 219] were conducted over a wide range of these parameters to discriminate the best expression. Considering that droplets are generated from the induced ligaments and assuming that their mean diameter (D_{10}) is proportional to the ligament size, Marmottant & Villermaux theory [219] gives reasonable D_{10} comparison and a good scaling of λ_T with $\sigma^{1/3}$, with a gas velocity increasing to 60 m/s. However Hong & Varga made observations on a wider velocity range (up to 180 m/s) and found that droplet size scales as $\sigma^{1/2}$ and not as $\sigma^{1/3}$ as predicted by Marmottant theory. They derived a second scenario which better fits with experiment [184]. In the following, the wavelength of the secondary instability is thus labeled λ_{RT} from Rayleigh-Taylor instability.

4.3.2 The ligament breakup

In primary breakup of parallel flows, many experimental observations report a ligament-induced breakup process. The 3D shape of the liquid surface is shattered into filiform structures that are elongated in the streamwise direction by the gas flow. This mechanism is known as *ligament breakup* and it has been theoretically and experimentally studied by Marmottant & Villermaux [220]. They defined the ligament size d_0 as the diameter of the equivalent sphere containing all the ligament volume, and linked its mean value $\langle d_0 \rangle$ to the transverse instability wavelength λ_T through experimental observations:

$$\lambda_T \approx 0.23 \langle d_0 \rangle \tag{4.29}$$

They physically interpreted the ligament breakup as a coalescence of several virtual layers included within the ligament itself, forming larger blobs (sometimes larger that the ligament diameter itself) due to the Laplace pressure (see Eq. 3.8), up to the rupture of the ligament. The authors state that, due to the random process of the virtual blob aggregation, the distribution of blob size inside the ligament is stable in shape by self convolution [357]. Therefore the probability function of the drop size p_B is written:

$$p_B(d) = p_1(d)^{\otimes n} \tag{4.30}$$

where $^{\otimes n}$ represents the nth-convolution of the elementary distribution p_1 representative of the blob size PDF in the ligament just after breakup:

$$p_1(d) = \frac{1}{\xi_b} \exp\left(-\frac{d}{\xi_b}\right) \tag{4.31}$$

where ξ_b is the thickness of the ligament at the breakup time. The authors indicate that the form of p_1 is of little importance given that the self convolution converges whatever the initial conditions are. The final distribution is a Gamma distribution [85]:

$$p_B(d) = \frac{n^n}{\Gamma(n)} s^{n-1} e^{-n\,s} \tag{4.32}$$

with $s = d/\langle d \rangle$ and $\langle d \rangle = n\,\xi_b$. The authors stated that *"the number of convolutions* $[n]$ *is, at most, such that the final average diameter* $\langle d \rangle$ *restores* d_0*, or a fraction of* d_0*"*, linking this theory to experimental observations. The parameter n is found to slightly increase with the gas velocity as $n \propto U_g^{1/2}$.

The whole sequence is labeled as the *coalescence cascade* [220]. It has been used to predict the drop size of a pressure swirl atomizer [346] where additional constant were added to Eq. 4.32 to match the experimental data.

Finally, in the context of real sprays, Marmottant & Villermaux [220] point out the importance of the ligament size dispersion for the drop size distribution. This leads to the convolution of $p_B(d)$ related to a ligament of one given initial size d_0, by the distribution of the ligament size $p_L(d_0)$. They observe a final drop size distribution $p(d)$ following:

$$p(d) \sim \exp\left(-\frac{n\,d}{\langle d_0 \rangle}\right) \tag{4.33}$$

4.4 Primary atomization in academic configurations

This section details primary breakup in academic configurations that aim to reproduce basic phenomena related to atomizing devices. Focus is made on devices that contain no moving parts. Rotary atomizers are therefore not treated. For a general overview of atomizers, the reader is referred to "Atomization and Sprays" by Lefebvre [196].

There are basically two families of atomizers in aero-burner devices : pressure swirl atomizers and air-blast atomizers (see Fig. 1.5). The first family consists in generating a pressurized swirling liquid flow passing through an orifice. The high pressure difference between the liquid chamber and the downstream cavity is converted into kinetic energy. The velocity difference between the liquid and the gas initiates the instability that leads to liquid breakup. The swirling motion of the liquid through the hole allows to retrieve a large spray angle that insures large liquid/gas contact area for a given penetration depth.

The second family uses the kinetic energy of a flowing airstream to shatter the liquid jet into ligaments. The liquid is injected at a low velocity and it is sheared by the high-speed gas. Most of those systems in service are of the *prefilming* type : the liquid is spread out in a thin film. The liquid/gas contact surface is increased in order to enhance the momentum transfer and therefore, in annular geometries, the liquid is injected at the periphery of the geometry and the gas is coflowing at the center. This type of atomizer enjoys the advantage of delivering a fine spray over a wide range of operating points, even at low liquid flow rate.

The academic flow configurations related to those categories of atomizers are illustrated on Fig. 4.8 and detailed in the following. In most cases, the geometry is a planar configuration assumed to be a 2D abstraction of an annular configuration. This allows to isolate the breakup phenomenon from macroscopic swirling effects and to enhance the optical access in experiments.

4.4.1 Liquid sheet configuration

A liquid layer is injected at a moderate velocity between two high-speed airstreams. The velocity difference between both phases induce a Kelvin-Helmholtz instability that initiates the breakup process. This configuration gives insight on the breakup process occurring in a typical airblast atomizer where a conical liquid sheet is generated downstream

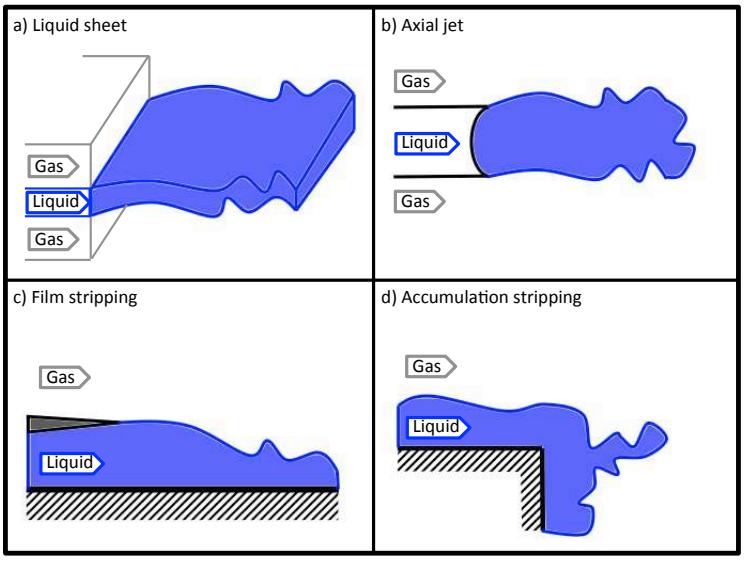

Figure 4.8 : *Illustration of main flow configurations encountered in aeronautical atomizers.*

the splitter-plate and fragmented by high velocity gas. The following briefly describes the mechanism of liquid sheet breakup. For further details, the reader is referred to the comprehensive review of Dumouchel [69].

Qualitative mechanisms in a quiescent atmosphere

In the absence of air stream, *i.e.* in a quiescent atmosphere, this configuration constitutes a 2D abstraction of the breakup phenomenon that occurs in pressure swirl atomizer. Carvalho *et al.* [41] observe two modes:

1. The **rim mode**: when the liquid is injected at low velocity, surface tension induces a force that contracts the shape of the liquid into a thick rim. This rim later disrupts similarly to a free jet, as illustrated on Fig. 4.9 a).

2. The **perforated-sheet disintegration**: holes randomly appear in the sheet (Fig. 4.9 b)). A thick rim is located at their periphery and contains the whole liquid originally included inside the holes. As the holes grow, their rim gets thicker and it coalesces with adjacent rim to form ligaments. This mode is promoted by sub-atmospheric pressure condition and highly viscous liquid [69]. Recently Lhuissier & Villermaux [201] observed that the disruption mechanism of a punctured soap film was very similar to the perforated-sheet disintegration mode.

Qualitative mechanisms in air-assisted configuration

In the presence of air stream, a significant shear develops at the interface, close to the nozzle. This triggers surface instabilities that end up in the sheet breakup and this regime is called the *wave mode*. It was theoretically studied by Mansour & Chigier [216] by considering the liquid sheet as a damped spring and applying linear stability analysis. They identified two fundamental regimes (*dilatational* and *sinusoidal*) that may combine. The *sinusoidal* mode corresponds to the in-phase oscillation of both sheet surfaces while their out-of-phase oscillation produces the *dilatational* mode.

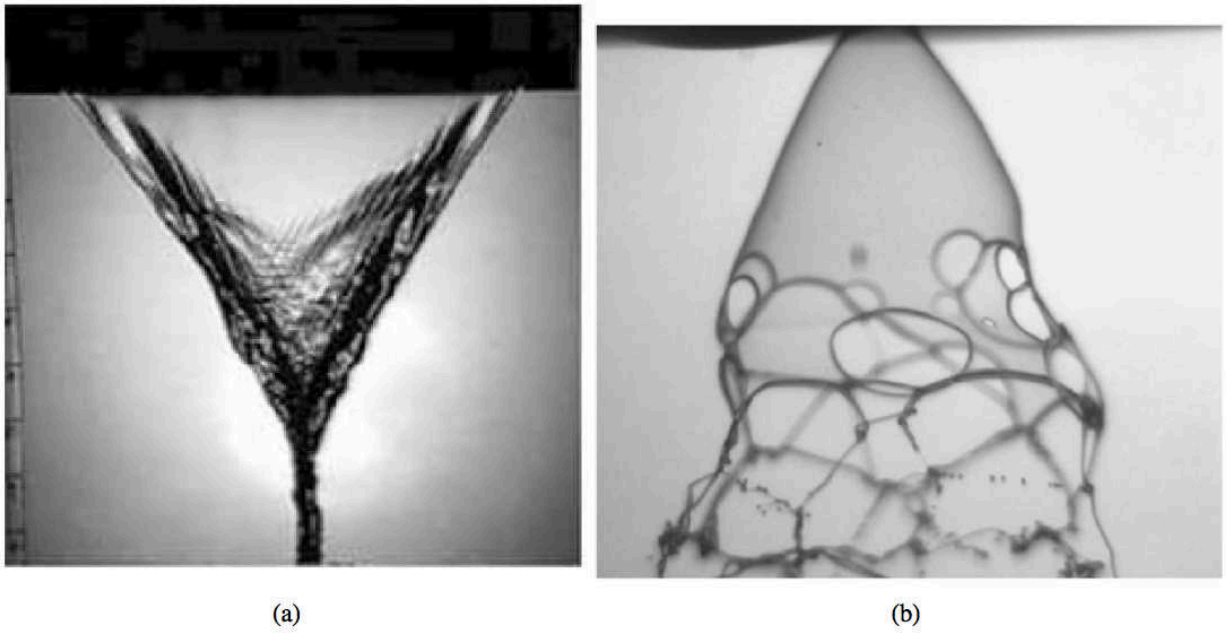

Figure 4.9 : *(a) Visualization of the rim disintegration mode from [41]. (b) Visualization of the perforation mode for a viscous conical sheet, from [323]*

Within the two last decades, experiments by Stapper & Samuelsen [334], Lozano *et al.* [209] and Fernández *et al.* [86] allowed to establish several macroscopic behaviours of liquid sheets disintegrated by the wave mode. The transition between those behaviours depends on the momentum flux ratio (also referred to as the *dynamic pressure ratio*):

$$M = \frac{\rho_g U_g^2}{\rho_l U_l^2} \tag{4.34}$$

The different regimes are depicted on Fig. 4.10:

1. For low gas velocity and/or high liquid velocity the dilatational mode can be expressed in combination with the sinusoidal mode, generating a two-dimensional pattern (cells). This disintegration behaviour is called the **cellular breakup** regime and finally leads to the formation of spanwise ligaments (Fig. 4.10a)). The generated spray presents a large penetration length and low spray angle.

2. As M increases the longitudinal mode disappears and the *sinusoidal* mode expression leads to streamwise ligaments. This regime is called **stretched ligament breakup**. The importance of the *sinusoidal* mode induces a large spray angle and decreases the breakup length. Mansour & Chigier [216] found out that the breakup length was proportional to the liquid velocity in this regime. Experimental visualizations exhibit the formation of liquid bags that are blown by the gas and finally burst into smaller droplets. (Figure 4.10b)).

3. For $M > 4$, the same type of liquid objects are observed (streamwise ligaments and bags) but the ligaments form directly at the nozzle tip. They present larger and more irregular dimensions, leading to a 'torn' profile. This regime is called the **torn-sheet breakup** (Figure 4.10c)).

4. Increasing the momentum flux ratio above 20 leads to the *membrane-sheet breakup* where no clear pattern is visible. The breakup length is lower than in the previous regime and the produced droplets distribution is very wide.

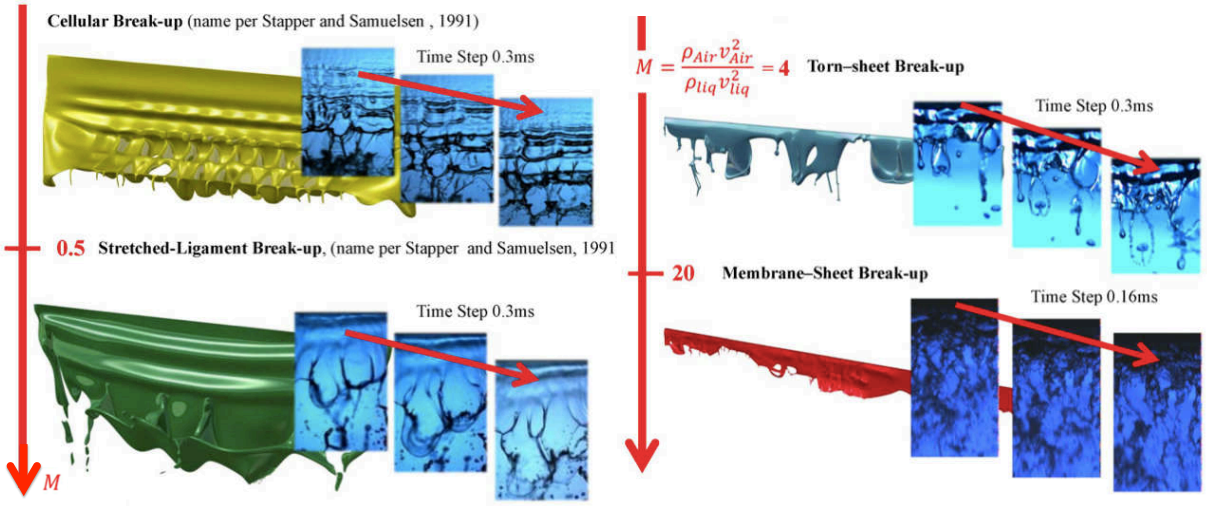

Figure 4.10 : *Mechanisms of liquid sheet atomization dominated by wave modes, adapted from [86]*

The frequency of the sheet oscillations can be associated to a Strouhal number $f\,L_c/(U_g - U_{min})$ ranging between 0.0067 and 0.01, depending on authors. The terms f, L_c, U_g correspond respectively to the oscillation frequency, a characteristic length and the mean gas velocity. The term U_{min} corresponds to the minimum air velocity that triggers a detectable sinusoidal oscillation in the liquid sheet. This may be related to the Strouhal number of the vortex shedding (≈ 0.21 for a Reynolds number based on the plate thickness ranging from $3{\cdot}10^2$ to 10^5), suggesting that the waves are initiated by the gaseous von Kármán street. The lower value in the liquid sheet case may be explained by the liquid inertia that decreases the flapping frequency.

From linear stability analysis, Lozano [208] found out the importance of the gas vorticity thickness as well as the fluid viscosity in the prediction of the instability wavelength.

4.4.2 Axial jet

This configuration consists in a cylindrical axial jet that can be surrounded by an annular gas flow (Fig. 4.11). In the literature this is often called *coaxial jet*. The liquid is injected through a circular orifice and the gas issues from a coaxial slit. Flow streams are parallel, separated by a thin wall usually called the splitter plate. The following discussion is mainly based on the reviews by Lasheras & Hopfinger [187] and Dumouchel [69]. The whole scope of breakup regimes is depicted on Fig. 4.12. It can be divided into two categories, depending on the presence, or not, of a co-axial airstream.

Axial liquid jet discharging in a quiescent atmosphere

When the liquid is injected into a stagnant gas, several regimes are noticeable, mainly depending on the Weber number. A detailed explanation of these regimes can be found in [69]. They are illustrated on Fig. 4.13 and summarized here:

1. The **dripping regime** (We < 8) corresponds to the situation where drops are directly emitted from the nozzle exit without formation of a continuous liquid column.

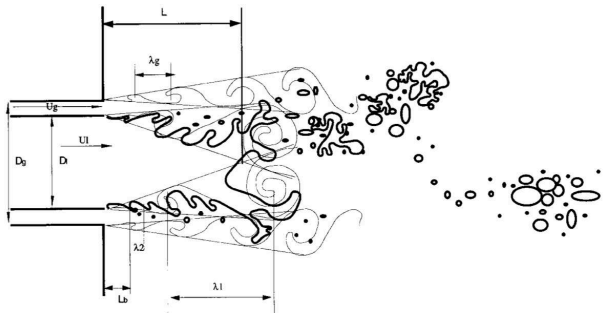

Figure 4.11 : *Schematic of the axial jet configuration, from [187]*

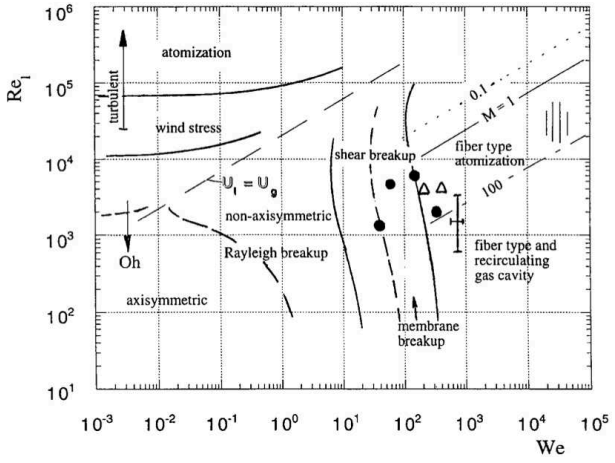

Figure 4.12 : *Map of the different breakup regimes in the air-assist axial jet configurations, from [154] and [187]*

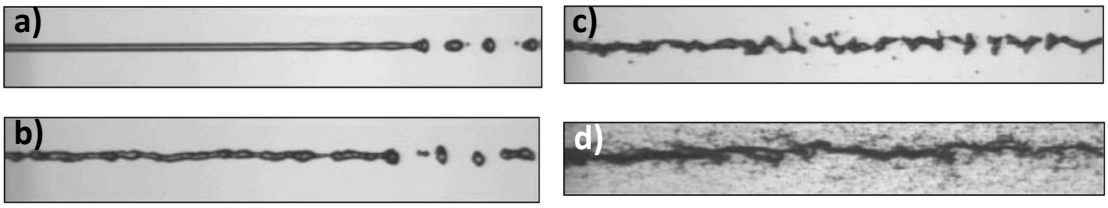

Figure 4.13 : *Atomization regimes for an axial liquid jet discharging in a stagnant atmosphere, adapted from [200]. a) Rayleigh regime, b) first-wind induced regime, c) second-wind induced regime, d) atomization regime.*

2. In the **Rayleigh regime** (We > 8, Fig. 4.13a), the jet is disturbed by a single axisymmetric perturbation with a wavelength of the same order of magnitude of the jet diameter. When the magnitude of the perturbation equals the jet diameter, it disrupts into droplets of the size of the jet. This phenomenon is called a *Rayleigh-Plateau* instability and it is driven by capillarity.

3. In the **first wind-induced regime** ($1.2 + 3.41\text{Oh}^{0.9} <$ We < 13, Fig. 4.13b, where Oh is the Ohnesorge number defined by eq 2.3), the liquid velocity is increased and the aerodynamic effects can be neglected. The drops detached in this regime are of the order of magnitude of the jet diameter.

4. In the **second wind-induced regime** ($13 <$ We < 40.3, Fig. 4.13c), the liquid jet column is perturbed directly at the nozzle exit and shows a very chaotic shape as the perturbations grow. The dispersion of produced droplet size is wide due to different mechanisms: near the nozzle exit, small droplets are peeled off the interface and farther downstream the remaining liquid flow breaks up into large liquid fragments.

5. The **atomization regime** (We > 40.3, Fig. 4.13d) is characterized by a complete jet disruption at the nozzle exit, and leads to droplets much smaller than the jet diameter. The atomization is triggered by short wavelength perturbations, rising from the velocity differential between the two phases.

Air-assisted axial liquid jet

In the presence of a high-speed coflowing gas stream, the fragmentation process is still driven by the velocity differential of the two phases, but in this case, the momentum is transferred from the gas to the liquid. This process is therefore called *air-assisted atomization*. Additional non dimensional numbers are introduced to describe and separate the different regimes. Following Lasheras & Hopfinger notations, the most influent numbers are the aerodynamic Weber number $\mathrm{We} = \rho_g U_g^2 D_l/\sigma$, the gas Reynolds numbers $\mathrm{Re}_g = U_g (D_g - D_l)/\nu_g$, the momentum flux ratio M and the mass flux ratio $m = \rho_g U_g A_g/\rho_l U_l A_l$, where A_i is the injection section of phase i. Diameters D_l and D_g are defined on Fig. 4.11.

Farago & Chigier [80] distinguished three atomization regimes: the Rayleigh-type breakup, the membrane-type breakup and the fiber-type breakup. Lasheras & Hopfinger [187] pointed out the influence of the M parameter in this classification.

1. The **Rayleigh-type breakup** is identified when drops are produced without any ligament shedding or liquid membrane. As in the quiescent atmosphere classification, the produced droplet diameters are of the order of the jet diameter. Two subregimes can be identified: the axisymmetric and non-axisymmetric regimes. In the former (We < 15) the gas flow accelerates the liquid jet, the breakup length is shorter than in still gaseous environment, and drops production results from the growth of an axisymmetric sinusoidal wave. In the latter (15 < We < 25, Fig. 4.14a), due to the acceleration by the gas, the jet diameter is reduced, and drops are still produced by the breakup of whole liquid jet.

2. The **membrane-type breakup** (25 < We < 70, Fig. 4.14b) is characterized by the development of thin liquid sheets of thickness δ that break into droplets of diameter of the order of δ, producing a finer spray than in the previous regime. The morphology of the jet becomes similar to that of a thin liquid sheet. As pointed out by [187], the difficulty lies in the prediction of δ.

3. The **digitation-type breakup regime** was later identified [187, 220]. This regime (visible on figs. 4.1 and 4.15a) presents the development of digitations (ligaments) on the crests of an axisymmetric perturbation and the subsequent disintegration of these ligaments by a non-axisymmetric Rayleigh-type regime. This regime was also studied by Hong *et al.* [151] and they suggested that the transverse instability leading to the ligament formation was of Rayleigh-Taylor type, as described in 4.3.1.

4. In the **fiber-type regime** (100 < We < 500), thin liquid fibers peel off the jet and disintegrate by a non symmetrical Rayleigh-type breakup. Farther downstream, the main liquid core presents large scale undulations and breaks into ligaments from which new fibers are peeled off. Resulting droplets are very small. Farago & Chigier [80] distinguish two subregimes: the pulsating and superpulsating modes. The former is the normal mode of atomization described above (Fig. 4.14c) while the latter (150 < We < 500) presents periodical changes of local volume fraction in the spray, as depicted on Fig. 4.14d.

Lasheras & Hopfinger [187] emphasized the importance of the gas vorticity thickness δ_ω for the membrane, digitation and fiber-type regimes, from the work of Raynal [280] (detailed in section 4.4.3). In these regimes, the gas is thus believed to impose both the velocity and the length scale of the instability. Consequently, surface tension effects become negligible on the onset of the primary instability.

Hopfinger & Lasheras [155] and Hardalupas & Whitelaw [137] highlighted the strong improvement of the gas swirling motion onto the atomization process when a critical swirl number S is exceeded. Hopfinger & Lasheras [155] found that the critical swirl number decreases when M increases and reaches an asymptotic value of about 0.4 at large M. An illustration of the effect of swirling gas is provided on Fig. 4.15.

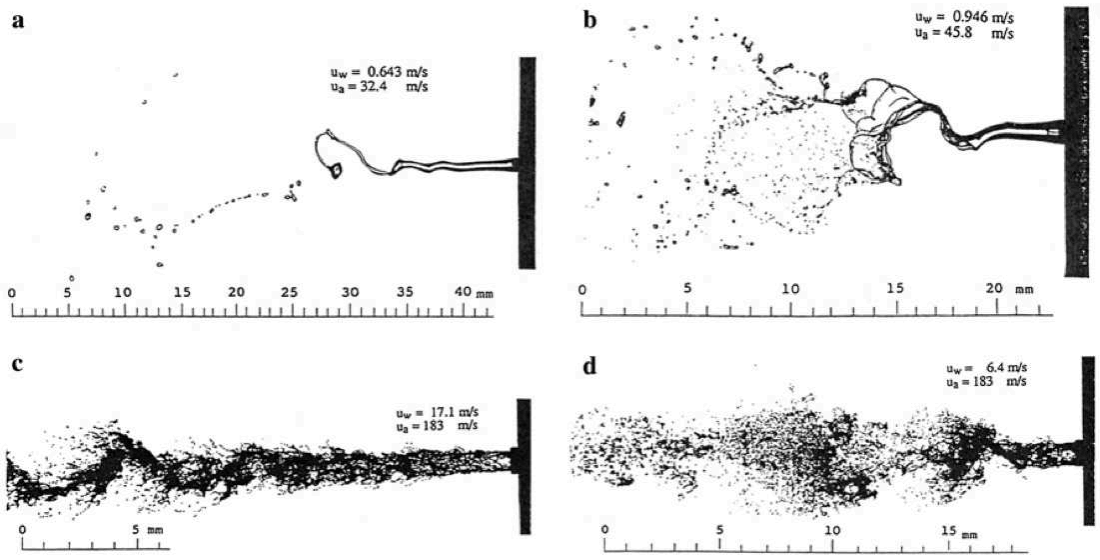

Figure 4.14 : *Atomization regimes for an axial liquid jet in the presence of a coflowing gas stream, adapted from [80]*

4.4.3 Thick film / Mixing layer

This flow configuration was studied to understand the fundamental liquid/gas interactions that occur at a *single* interface. In this experiment, the liquid and the gas are both injected trough separated channels of comparable dimensions (depending on the experiment, their order of magnitude ranges between 1 and 10 millimeters.), and they meet downstream a separating plate, as illustrated on Fig. 4.16. The gas usually flows with a velocity two orders of magnitude larger than the liquid: in [281], the gas velocity is between 10 and 100 m/s while the liquid flows from 0.1 to 1 m/s. This high velocity difference exerts a shearing of the liquid layer, inducing surface spanwise instabilities that further strip the film and entrain droplets. The liquid is then progressively shattered into finer structures that constitute the dense spray and its thickness decreases in the streamwise direction. The distance between the liquid injection to its complete atomization is called the *intact length* or *breakup length* L_b, and it is an important parameter for the design of injectors [280].

Contrary to the liquid sheet and jet configurations, only one 2D interface may be isolated and the bulk motion of the liquid phase (such as the flapping effect) does not interact with the atomization process. Furthermore, this configuration allows to avoid interferences between the two interfaces (*dilatational* and *sinusoidal* modes defined in 4.4.1) as in liquid sheets, as well as surface curvature effects in liquid jets. Finally the thickness of the liquid layer must be large enough to avoid the bottom wall influence.

The liquid layer primary breakup was studied by Raynal *et al.* [280, 281] and later by Ben Rayana [23]. It was shown by [281] that the mechanism responsible for primary instabilities at the liquid/gas interface is similar to shear layers of large density difference, and it is well described by a linear Kelvin-Helmholtz stability analysis. The influent parameters of this type of configuration are the momentum flux ratio M, the gaseous vorticity thickness δ_g depicted on Fig. 4.17 and the Weber number of the liquid film. Many correlations can be found for the prediction of the breakup length L_b. Raynal [280] derived:

$$\frac{L_b}{2\,H_1} = 0.5 + 307\,M^{-0.33}\,\mathrm{Re}_{\delta_g}^{-0.66} \tag{4.35}$$

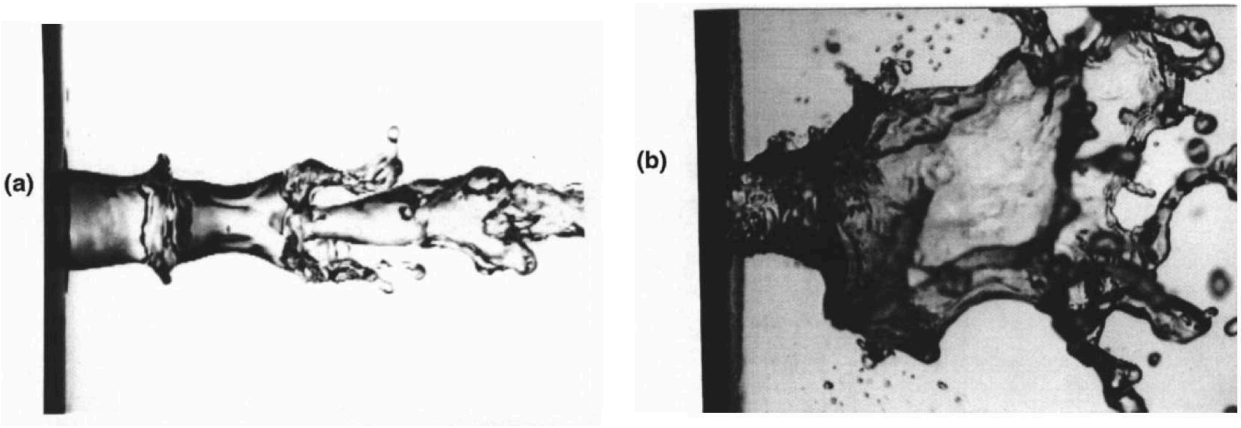

Figure 4.15 : *Images of water jet breakup with and without swirl of the coaxial gas jet. a) $S = 0$, b) $S = 1.27$, from [187]*

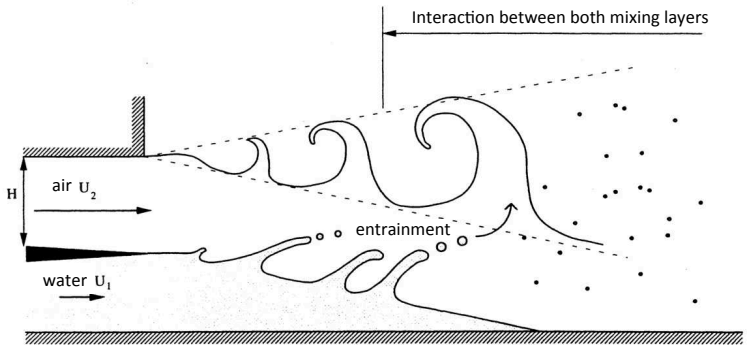

Figure 4.16 : *Schematic of the mixing layer configuration, adapted from [280]*

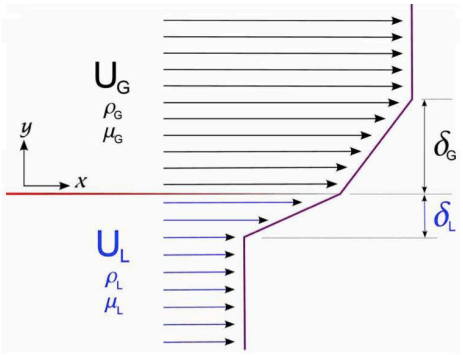

Figure 4.17 : *Assumed velocity profiles in Raynal analysis [280], from [23]*

where H_1 is liquid thickness at the separating plate. Raynal also investigated the convection velocity of the wavy structures triggered by surface instabilities and found out that it is well described by:

$$U_c = \frac{\sqrt{\rho_l}\,U_l + \sqrt{\rho_g}\,U_g}{\sqrt{\rho_l} + \sqrt{\rho_g}} \tag{4.36}$$

Equation 4.36 is due to Brown [36] and was later justified by Dimotakis [67] assuming the continuity of the pressure at the interface in a frame moving at the convection velocity. By conducting an inviscid temporal linear stability analysis of the interface, and assuming a simplified flow profile (Fig. 4.17), Raynal found out that the Kelvin-Helmhotz instabilitiy frequency showed good trends for the longitudinal wavelength prediction:

$$\lambda_L = C_{axi}\sqrt{\frac{\rho_l}{\rho_g}}\,\delta_g \tag{4.37}$$

where C_{axi} is a constant experimentally measured between 1 and 2 in coaxial geometry [218, 220] and between 1.5 and 1.8 in planar geometry [23], while the inviscid theory states $C_{axi} = 4$.

Yecko *et al.* [372] and Boeck & Zaleski [26, 27] took the fluid viscosities into account via temporal linear stability calculations based on the Orr-Sommerfeld equations. They found that the growthrate of the (viscous) most unstable mode is close to experiments, but the predicted frequency is too large.

Ben Rayana [23] investigated the mean drop size and found out that the Hong model [151] based on Rayleigh-Taylor instability was predicting accurately the Sauter Mean Diameter and the arithmetic diameter D_{10}. It was also observed that at low gas velocity, the primary breakup was modified due to disappearance of the transverse structures formation. This effect was seen by confronting the D_{10} evolution versus the gas velocity. Finally, the influence of the separator plate thickness was observed on the instability development.

Following Raynal's path, Matas [224] applied a linear stability analysis to a planar liquid layer with different velocity profiles. To better describe experiments, and in particular the influence of the splitter plate separating both phases, the interface velocity was set to zero. Comparisons with experiments showed a good agreement in the wave frequency but an over-predicted growth rate.

Recently, a major breakthrough in the understanding of this configuration has been brought by Fuster *et al.* [96]. Through spatiotemporal stability analysis, numerical simulations and experiments, several regimes are found for the generation of the surface instability. The main parameters are M and the ratio of the separator thickness h_a to the gaseous vorticity thickness δ_g defined as $\epsilon = h_a/\delta_g$. For $\epsilon < 1$ and $M < 8$, the surface instability is generated by the convection and amplification of tiny perturbances that arise directly downstream of the separator. This regime is usually named the *convective* regime, and a FFT treatment shows a noisy spectrum, corresponding to the noise convected from the injection. For $\epsilon < 1$ and $M > 10$, the instability does not depend on the upstream activity and this regime is called *absolute*. The FFT plot of this regime presents a clear peak corresponding to a single mode instability generation. For $\epsilon > 1$ the splitter plate thickness influence becomes significant. It increases the noise level in the *convective* mode and imposes another mode in the *absolute* regime (two peaks on the FFT plot).

4.4.4 Liquid accumulation at the atomizing edge

Recently, in the context of prefilming airblast atomizers, effort has been put on the understanding of the primary breakup of thin liquid films. An experiment was conducted at KIT-ITS by Gepperth *et al.* [102, 103, 104] aiming at reproducing the conditions of real prefilming airblast atomizer, in a simplified geometry. The primary breakup region was instrumented to gain deep insight of the mechanisms responsible for the film fragmentation. This experiment will be extensively detailed in chapters 7 and 8.

The primary breakup process was observed to be different from the liquid sheet configuration: the liquid phase does not propagate in the cavity in the form of a sheet, but it stays hooked in the wake region of the prefilmer, forming a liquid accumulation (Fig. 4.8d)). Due to the shearing action of the air stream, this liquid accumulation flaps and is torn apart into liquid blobs of the shape of ligaments and bags (Fig. 4.18), as in the *stretched ligament breakup* regime of the liquid sheet configuration.

From a comparison of the frequency of the different phenomena involved, it was found that the liquid film flow characteristic upstream the atomizing edge is of little importance for the fragmentation process and the drop size distribution, in accordance with the results of Wittig and co-workers [3, 307]. Furthermore it was observed that when the film thickness exceeds 5 times the atomizing edge height, the regime evolves to the liquid sheet configuration: the liquid accumulation disappears and the film has enough inertia to keep its longitudinal motion and propagates into the chamber[1].

From a qualitative point of view, this configuration has the advantage to limit atomization in a small and controlled area. Due to the sharp angle of the atomizing edge, the film undergoes a dramatic change in its boundary conditions that triggers accumulation and breakup. Thanks to this geometric feature, it is possible to instrument the configuration

[1] S. Gepperth, personnal communication, May 22, 2013

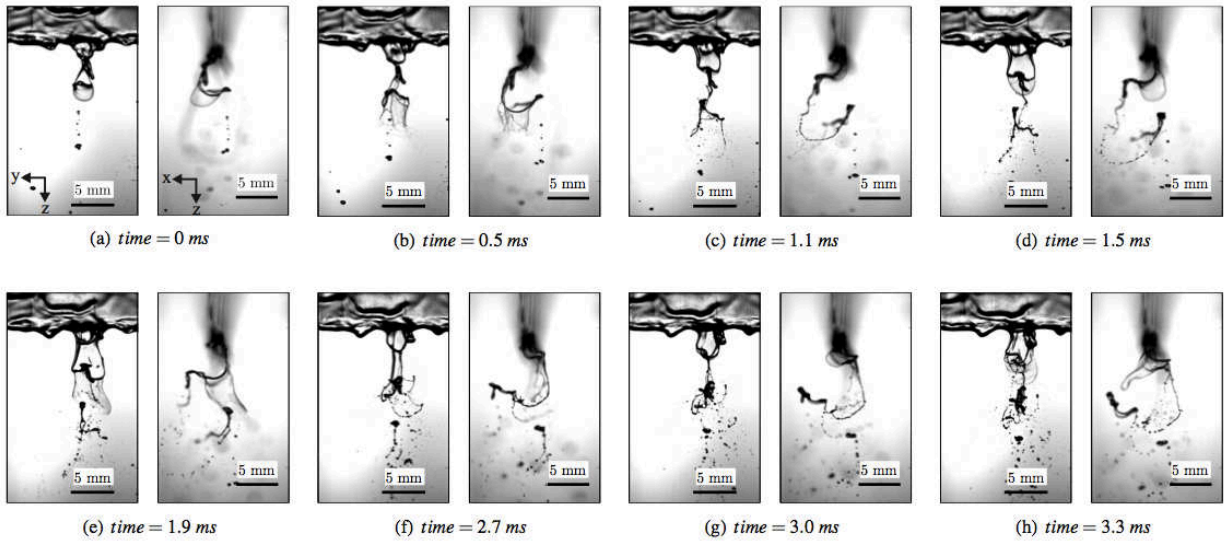

Figure 4.18 : *Time series of the accumulation breakup phenomenon, paired by top and side view, from [103]. The gas flows from the top to the bottom.*

to monitor precisely the atomization process. On the contrary, the breakup of liquid sheets or liquid jets starts at the injection and continues downstream to a distance that depends on the operating conditions. Consequently the volume to monitor is much larger that the breakup length scale, making it difficult to observe a single breakup event at a precise location. In addition, the liquid/gas interface can have a macroscopic motion due to flapping that can bring additional problems.

4.5 Overview of numerical methods for the prediction of primary breakup

As mentioned in the introduction, the interface capturing methods (Level Set and VOF) are the most appropriate approaches for the prediction of liquid instabilities thanks to their capacity to handle capillarity effects.

4.5.1 DNS and 'interface capturing' methods

This last decade, effort was put on developing robust numerical methods to tackle the simulation of multiphase flows presenting large fluid properties jumps.

Desjardins *et al.* [64] developed a level set method combined with high-order implicit transport schemes to counteract the former's main drawback: mass conservation. To improve handling of jump conditions at the interfaces, the Ghost Fluid (GF) method was used by several authors: Moureau & Desjardins [240] implemented a second-order GF method and Ménard *et al.* [231] coupled the GF method to a blend of level set and VOF methods, retrieving the advantages of both approaches (natural interface capturing for level set and mass conservation for VOF). A balanced force level set (BFLS) method [91] for two-phase flows on unstructured meshes was developed by Herrmann [142]. Popinet [275] developed an incompressible flow solver (GERRIS) able to handle dynamic grid refinement based on a quad/octree discretization and included the VOF method to describe two-phase flows [276].

These approaches showed good agreements with experiments. The BFLS method was applied to a jet in cross flow configuration [143, 145] (Fig. 4.19), Ménard *et al.* [231] model was validated on a Rayleigh instability of liquid jet and applied it to an axial turbulent liquid jet (fig 4.20). Shinjo & Umemura [320] also used a combination of level set and VOF for a DNS of an axial liquid jet. The very fine mesh (6 billion cell of size 0.35 µm) gave a deep insight into the coupling between propagating waves along the jet surface and the fragmentation of the liquid tip (Fig. 4.21). Fuster *et al.* [95] used GERRIS [275, 276] to simulate a mixing layer configuration (Fig. 4.22).

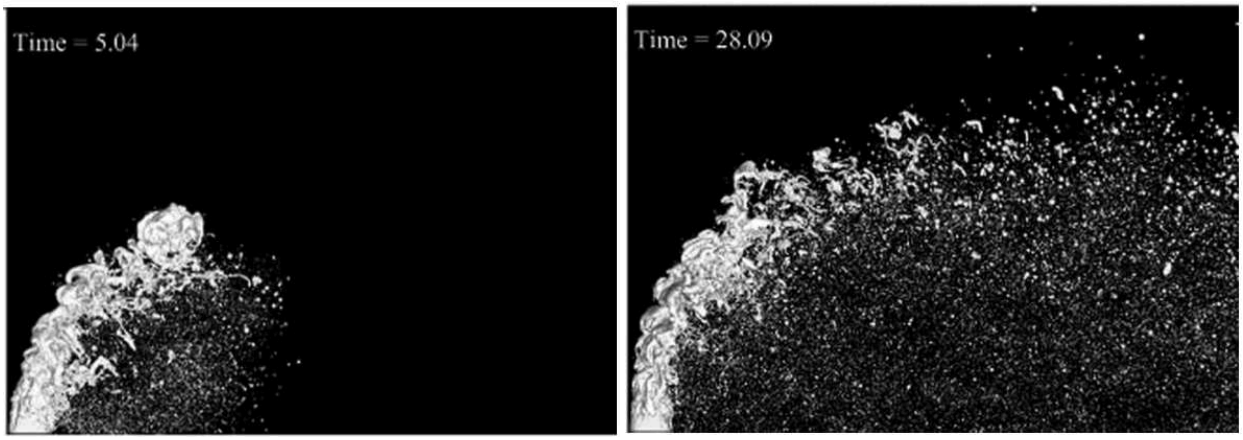

Figure 4.19 : *DNS of the primary breakup of a liquid jet in cross flow, from [145]*

As previously mentioned, interface capturing methods coupled to DNS allow to rank the numerical simulation as a 'numerical experiment' that can calibrate lower order models. From the work of Ménard *et al.* [231], Lebas *et al.* [190] calibrated the ELSA model, further described in section 4.5.2 .

The interface capturing methods suffer from the wide range of length scales encountered in atomization, especially when the simulation includes secondary atomization and spray generation. As the mesh size is imposed by the smallest liquid structure (at least two to five computational cells per droplets are needed [117]), the simulation of primary breakup requires an extremely high mesh resolution. Furthermore, in order to fully account for the interaction between turbulence and the interface, the DNS approach is generally preferred. It ends up in very CPU expensive methods that are employed for canonical experiments and are not applicable to industrial configurations. However, as small droplets are only present at the periphery of the liquid sheet, mesh adaptation techniques [5, 24, 336, 381] are promising to reduce the computational cost. Another strategy is to switched from an Eulerian formalism to a

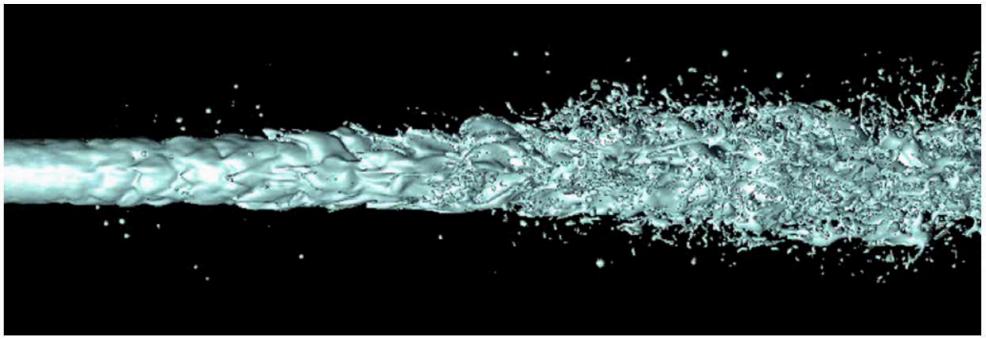

Figure 4.20 : *DNS of the primary breakup of a turbulent jet, from [231]*

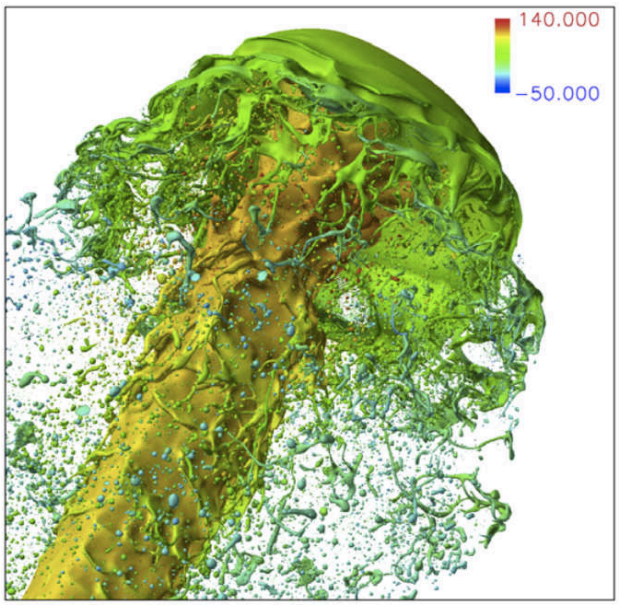

Figure 4.21 : *DNS of the primary breakup of a turbulent jet, from [320]*

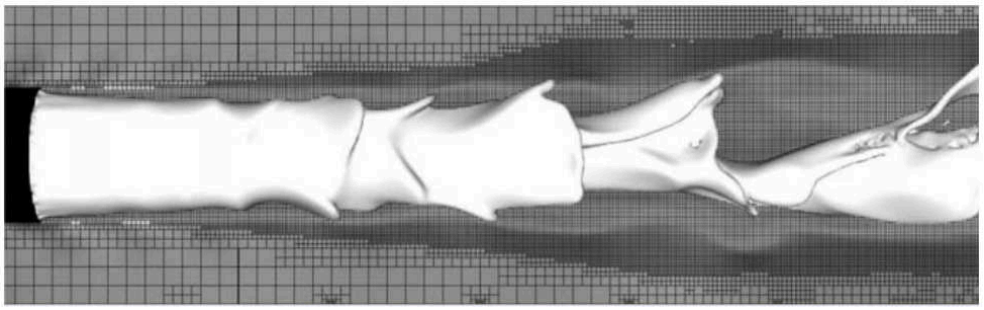

Figure 4.22 : *DNS of the primary breakup of a turbulent jet, from [95]*

Lagrangian one to describe small droplets. Tomar *et al.* [344] switch from VOF to a Lagrangian approach to predict the drop size distribution in a mixing layer configuration. Zuzio *et al.* [382] studied the liquid sheet configuration with a coupling between several codes developed at ONERA: CEDRE for the gas phase, SLOSH (solver based on a multifluid approach) for the liquid core and a Lagrangian solver for the generated droplets (Fig. 4.23).

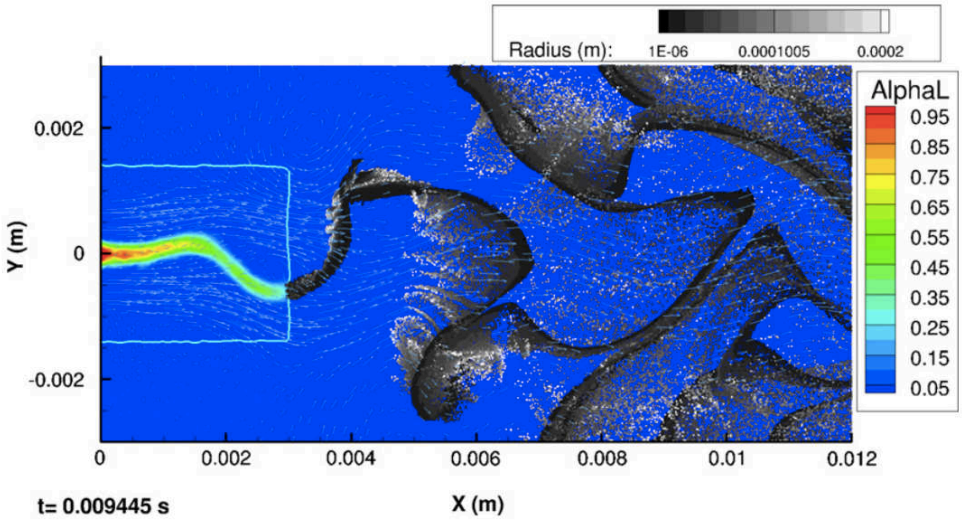

Figure 4.23 : *DNS of the primary breakup of a liquid sheet, from [382]*

4.5.2 Lower-order models

Direct Numerical Simulations of primary atomization remain extremely costly because of the large range of time and length scales involved. Therefore, simplifying approaches are necessary when considering the simulation of realistic configurations. Some approaches modify the whole treatment of the gas and liquid phase (Surface density / ELSA) while others are phenomenological models dedicated to one type of primary breakup configuration.

Surface density / ELSA

In order to describe the primary atomization within the RANS approach, Vallet & Borghi [350] and Vallet *et al.* [349] proposed a surface density based model. The spray is treated in an Eulerian formulation since the dense spray in the near-injector region forbids any Lagrangian approach. The two-phase flow is considered as a single flow with varying properties. For instance the density of this virtual fluid varies from the gaseous density ρ_g to the liquid one ρ_l, and the average density ρ writes:

$$\frac{1}{\rho} = \frac{Y_l}{\rho_l} + \frac{1 - Y_l}{\rho_g} \tag{4.38}$$

where Y_l is the liquid mass faction. Due to large density variations, the flow is described by Favre-averaged variables:

$$\overline{\rho u_i''} = \overline{\rho}\,\widetilde{u_i''} \tag{4.39}$$

In the RANS framework, in addition to the mass, momentum and energy transport equations of the mixture, the turbulent kinetic energy $\widetilde{k}$ and its dissipation rate $\widetilde{\epsilon}$ are transported, following the classical $k - \epsilon$ model. In addition, similar to a classical turbulence model stating that the Reynolds number is so large that it does not control the large-scale mixing (*i.e.* the liquid dispersion), it is supposed here that the Weber number based on the length scale of high energy eddies does not intervene in the liquid dispersion. However the viscosity and the surface tension influence the dissipation of small scales so they control the liquid fragment size (through a balance between turbulent stretching and capillarity force). They must be taken into account. For more details on the transport equations and modeled terms, the reader is referred to [21, 350, 349].

Finally the size of the ligaments and ejected liquid lumps is described through a mean interfacial surface area per unit volume $\overline{\Sigma}$. This framework is adapted from flame surface density methods in turbulent combustion [140]. The mean interfacial surface area is solved via:

$$\frac{\partial \overline{\Sigma}}{\partial t} + \frac{\partial \widetilde{u_j}\overline{\Sigma}}{\partial x_j} = \frac{\partial}{\partial x_j}\left(D_\Sigma \frac{\partial \overline{\Sigma}}{\partial x_j}\right) + \frac{\overline{\Sigma}}{\tau_{prod}} - \frac{\overline{\Sigma}^2}{\overline{\Sigma}_{eq}\,\tau_{destr}} \tag{4.40}$$

where τ_{prod} and τ_{destr} are respectively the production (surface stretching) and destruction (coalescence) characteristic times. The equilibrium surface Σ_{eq} is reached when the production is balanced by the destruction and when $\tau_{prod} = \tau_{destr}$. Knowledge of local $\overline{\Sigma_{eq}}$ allows to estimate the mean radius of spherical liquid lumps $r = 3\overline{\rho}\widetilde{Y_l}/\rho_l\overline{\Sigma}$. This information can be coupled to a Lagrangian solver in a dilute region to render the entire spray evolution, yielding the so-called Euler Lagrange approach for Spray and Atomization (ELSA)

This approach was applied to simulations of the primary atomization of a Diesel spray [21] (showing a good agreement with DNS [190]) and air-blast atomizers [165].

Stochastic primary atomization under scaling symmetry

The stochastic approach was initially applied to the simulation of secondary atomization in high Reynolds and Weber number configurations [9, 116, 118, 291, 300, 358]. It has been extended to primary air-blast atomization by

Gorokhovki *et al.* [115, 120]. Its general principle is overviewed in the following.

Statistical universalities in fragmentation under scaling symmetry

In 1941, Kolmogorov [179] considered that the fragmentation of solid particles was a random discrete process. He assumed that the number and size of children droplets was independent of the size of the parent droplet. After a large number of breakup events and using the central limit theorem, he predicted that the drop size distribution should result in a log-normal function. This process can be formulated by $r_p \Rightarrow \alpha\, r_c$ where r_p and r_c are the parent and child drop size respectively. The independent random multiplier α is governed by the so-called fragmentation spectrum $q(\alpha)$, having the property $\int_0^1 q(\alpha)\mathrm{d}\alpha = 1$. In the case of constant fragmentation frequency f_{bu}, the kinetic fragmentation equation for the normalized distribution function $f(r,t)$, *i.e.* the probability to find a droplet of radius r, has the following form [118, 119]:

$$\frac{1}{f_{bu}}\frac{\partial f(r)}{\partial t} = \int_0^1 \frac{1}{\alpha} f\left(\frac{r}{\alpha}\right) q(\alpha)\,\mathrm{d}\alpha - f(r) \tag{4.41}$$

The steady state solution of Eq. 4.41 is the delta function $f(r) = \delta(r)$, meaning that after a long time, the breakup process reduces droplets to infinitely small particles. Obviously this steady state is never reached in reality and the transient state is to be resolved, requiring the knowledge of $q(\alpha)$. Noting that the first term of the right-hand side in Eq. 4.41 is invariant under the scaling symmetry $\alpha \to \alpha\, r$, Gorokhovski & Saveliev [119] showed that the asymptotic solution of Eq. 4.41 in the long-time limit (*i.e.* for a large breakup frequency f_{bu}) writes:

$$r\, f(r,t) = \frac{1}{\sqrt{2\pi\langle \ln^2\alpha\rangle f_{bu} t}} \exp\left(-\frac{\langle \ln\alpha\rangle^2}{2\,\langle \ln^2\alpha\rangle} f_{bu} t\right) \exp\left(-\frac{\ln^2(r/R)}{2\,\langle \ln^2\alpha\rangle f_{bu} t}\right) \left(\frac{r}{R}\right)^{\frac{\langle \ln\alpha\rangle}{\langle \ln^2\alpha\rangle}} \tag{4.42}$$

where R denotes the initial length scale and $< \ln^i\alpha >= \int_0^1 \ln^i\alpha\, q(\alpha)\,\mathrm{d}\alpha$ is the ith logarithmic moment of $q(\alpha)$. By increasing time further, one can see that the log-normal multiplier in Eq. 4.42 tends towards unity. The long-time particle-size distribution is thus determined by a power law with just one universal parameter $\langle \ln\alpha\rangle / \langle \ln^2\alpha\rangle$:

$$r\, f(r, t\to\infty) \propto \left(\frac{r}{R}\right)^{\langle \ln\alpha\rangle / \langle \ln^2\alpha\rangle} \tag{4.43}$$

This equation implies a fractal distribution for the particle size. It can be shown [119] that the first logarithmic moment of of the solution of Eq. 4.41 evolves as:

$$\langle \ln r\rangle \sim f_{bu}\, t\, \langle \ln\alpha\rangle \tag{4.44a}$$

$$\langle (\ln r - \langle \ln r\rangle)^2\rangle \sim f_{bu}\, t\, \langle \ln^2\alpha\rangle \tag{4.44b}$$

Therefore the fragmentation parameter defined by the ratio:

$$\frac{\langle \ln r\rangle}{\langle (\ln r - \langle \ln r\rangle)^2} = \frac{\langle \ln\alpha\rangle}{\langle \ln^2\alpha\rangle} \tag{4.45}$$

is constant in time and does depend on the dispersion of $f(r,t)$, confirming the result prescribed in Eq. 4.43. The fragmentation parameter is an important input of the primary breakup model, as shown later.

Another interesting result of Eq. 4.42 is that the fragmentation spectrum $q(\alpha)$ intervenes in the long-time limit behaviour only by its two first logarithmic moments. Therefore the required knowledge of $q(\alpha)$ is limited to $\langle \ln\alpha\rangle$ and $\langle \ln^2\alpha\rangle$ for this asymptotic behaviour. The kernel $\frac{1}{\alpha} f\left(\frac{r}{\alpha}\right)$ of Eq. 4.41 is thus expanded into logarithmic series:

$$\frac{1}{\alpha} f\left(\frac{r}{\alpha}\right) = \sum_{n=0}^{\infty} (-1)^n \frac{1}{n!} \left(\frac{\partial}{\partial r} r\right)^n f(r) \ln^n\alpha \tag{4.46}$$

and injected in Eq. 4.41. Since only the two first logarithmic moments appear in Eq. 4.42, the logarithmic expansion (Eq. 4.46) can be limited up to the second term and Eq. 4.41 takes the form of a Fokker-Planck differential equation:

$$\frac{1}{f_{bu}}\frac{\partial f(r)}{\partial t} = -\langle \ln \alpha \rangle \frac{\partial r f(r)}{\partial r} + \frac{1}{2}\langle \ln^2 \alpha \rangle \frac{\partial}{\partial r}\left[r \frac{\partial r f(r)}{\partial r} \right] \tag{4.47}$$

Equation 4.47 describes the log-Brownian stochastic process. The corresponding stochastic equation is:

$$\dot{r} = f_{bu}\langle \ln \alpha \rangle r + r\,\Gamma(t)\sqrt{\frac{1}{2} f_{bu}\langle \ln^2 \alpha \rangle} \tag{4.48}$$

where $\Gamma(t)$ is the Langevin process yielding $\langle \Gamma(t) \rangle = 0$ and $\langle \Gamma(t)\,\Gamma(t+\tau) \rangle = 2\,\delta(\tau)$. Integrating Eq. 4.48 from the initial distribution $f(r_0, t_0)$ allows to know $f(r, t)$ in the long-time limit.

Modeling primary breakup of an axial liquid jet

In the context of LES of primary breakup of an axial liquid jet, this method is named the *stochastic model of liquid jet depletion* [115, 120]. The gas flow is resolved with a LES solver conditioned by the presence of liquid blobs. Those liquid blobs are dragged along and may undergo secondary atomization or coalescence [358]. Contrary to the description of the secondary breakup, the fragmentation process is not applied to the evolution of the drop size distribution, but to the evolution of the liquid jet radius. Therefore the one-point distribution $f(x, t; r)dr$ is the probability that the radial location of the liquid core interface r at axial position x and time t lies in the element dr around r. Gorokhovski & Herrmann [117] underline the fact that experimental observation favors the axial jet breakup as a fractal process, promoting the validity of Eq. 4.43. The fragmentation parameter (Eq. 4.45) is expressed by [115] as:

$$\frac{\langle \ln \alpha \rangle}{\langle \ln^2 \alpha \rangle} = \ln\left(\frac{\lambda_{KH}}{\lambda_{RT}} \right) \tag{4.49}$$

The interface is located by stochastic particles injected at the initial liquid boundaries, as depicted on Fig. 4.24. The radial motion of a stochastic particle is governed by Eq. 4.48 and their axial velocity is taken as the convection velocity of Kelvin-Helmholtz structures *i.e.* the Dimotakis velocity (Eq. 4.36). Finally the statistics of the core surface are used to express the size and position of the generated droplets around the liquid core.

Figure 4.25 shows a comparison of the present model with the experiment of Werquin [365] consisting in an axial jet atomized by a high velocity coflowing air-stream. The qualitative agreement is good.

However, high spatial resolution DNS of atomizing diesel jets by Gorokhovski & Herrmann [144] tends to limit the validity of the stochastic model of the liquid jet depletion. The authors state that the primary breakup process is not a cascade process from large scales to small scales, but *"small-scale drops can be ripped out of the liquid directly via ligament-formation processes, bypassing any cascade process for the phase interface geometry"* [144]. This observation gives credit to the approach of Marmottant & Villermaux and ligament fragmentation. Nevertheless, the statistical universality in fragmentation has shown an applicability to turbulence and some stochastic subgrid models were developed for LES [121, 299, 377].

4.6 Secondary breakup

After the ejection of liquid blobs due to primary atomization, the aerodynamic stresses start to compete with surface tension. If the drag force of the gas is larger than the surface tension force, the blobs disintegrate into smaller droplets. It is worth noticing that secondary breakup is a more *universal* process than primary breakup: the latter is closely connected to the geometrical configuration of both the flow field and the liquid phase while the former can be generally described as a liquid structure immersed in a flow field. There are still particular features that may induce

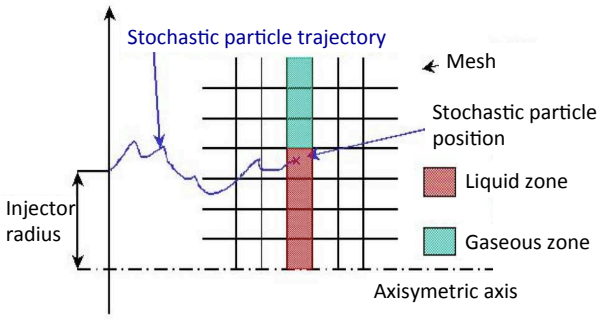

Figure 4.24 : *Schematic of the phase reconstruction from the stochastic particle position, adapted from [167]*

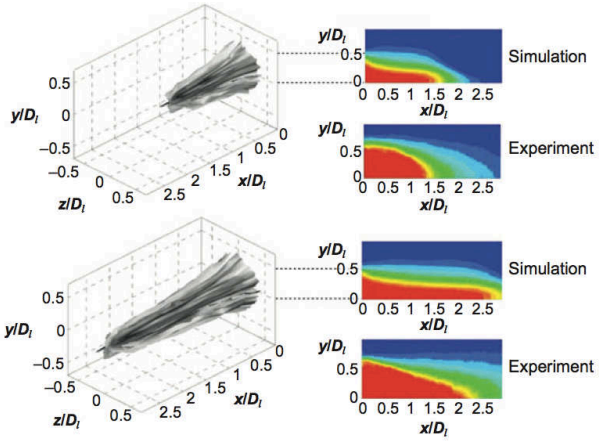

Figure 4.25 : *Modeling liquid core geometry and averaged liquid fraction field [115], compared to measurements from Werquin [365], from [117]*

deviation from canonical cases, such as sphericity of the liquid blobs, blob characteristic lengths compared to the local flow scales or turbulent intensity, but most phenomena are common.

In this general description, secondary atomization is well characterized by the Weber number based on the droplet diameter d_p and its velocity relative to the gas ΔU:

$$\mathrm{We} = \frac{\rho_l \, d_p \, \Delta U^2}{\sigma} \tag{4.50}$$

Krzeczkowski [180] as well as Pilch & Erdmann [268] classified secondary breakup mechanisms in five distinct regimes:

- vibrational breakup ($We < 12$), where the particle oscillates with the characteristic frequency of the vortex tail forming in the wake of the particle.
- bag breakup ($12 < We < 50$), identified by a hollow bag-shaped membrane surrounded by a ring torus, analogous to soap bubbles blown from a ring.
- bag-stamen breakup, also called multimode breakup ($50 < We < 100$), similar to bag breakup but with the presence of a stamen in the middle of the bag.
- particle stripping ($100 < We < 350$), characterized by the stripping of small fragments from the particle surface layer.
- catastrophic breakup ($We > 350$), where the drop is desintegrated by long wavelength amplitudes, creating several large fragments which generally undergo stripping.

As an illustration, Fig. 4.26 from Pilch & Erdmann [268] presents a sketch of the listed breakup mechanisms. Pilch & Erdmann [268] argue that fragments from secondary breakup undergo further desintegrations as long as their Weber number exceeds a critical value. They propose the following formula for the critical Weber number (based on the diameter):

$$\mathrm{We}_c = 12(1 + 1.077\mathrm{Oh}^{1.6}) \tag{4.51}$$

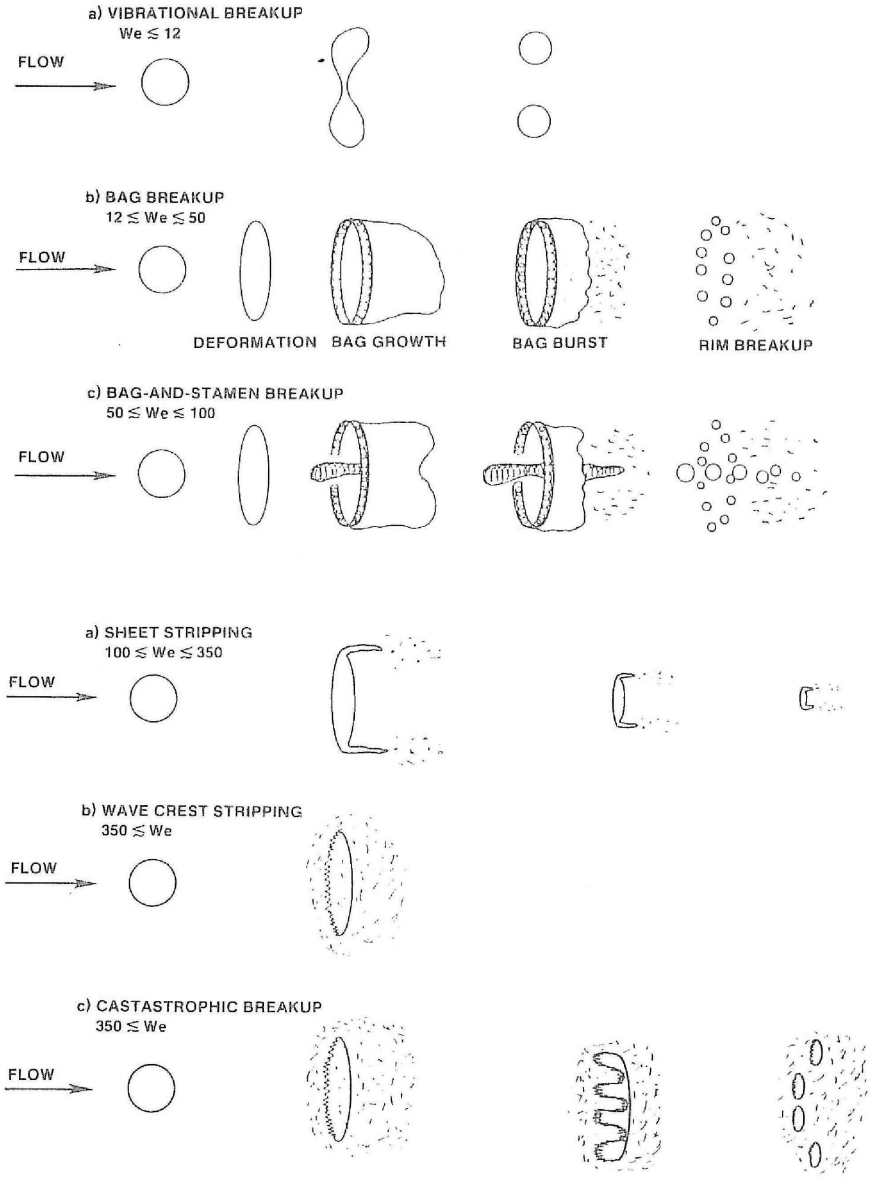

Figure 4.26 : *Classification of secondary breakup regimes by Pilch & Erdmann [268]*

Due to the difficulty of observing particles after secondary breakup, there is little experimental information available about the outcome of the breakup process, in particular the characteristic size and size distributions resulting from the different breakup regimes. Simmons [321] made the useful observation that sprays produced by a wide range of nozzle designs have similar particle size distributions when compared in a root/normal graph, *i.e.* a $(d_p/\bar{d_p})^{1/2}$ abscissa (with $\bar{d_p}$ the mean particle diameter) and an ordinate with a normal distribution scale. However, Hsiang & Faeth [156] found that the Simmons distribution failed to reproduce particle size distributions after stripping breakup which exhibited a clear bimodal character due to the stripping of small particles from the boundary layer at the particle surface. Hsiang & Faeth [156] also provide a relationship for the Sauter Mean Diameter D_{32} after bag, bag-stamen, and stripping breakup:

$$D_{32} = 6.2 \left(\frac{\rho_l}{\rho_g}\right)^{1/4} \left(\frac{\mu_l \, d_p}{\rho_l \|u_{p,i} - u_i\|}\right)^{1/2} \tag{4.52}$$

where d_p is the diameter of the parent particle.

4.7 Conclusion

This chapter gave an overview of atomization with a focus on thin film instabilities and primary breakup in academic experiments. It started with a theoretical study of instabilities in parallel flows derived by Charru [47] and led to the Rayleigh equation in the inviscid case and to the Orr-Sommerfeld equation in the viscous case. Those equations can be formally solved in few configurations were simplifying assumptions can be made, and require to be solved numerically otherwise. It was seen that instabilities arising in parallel flows are always of two dimensional type.

As a particular and complex configuration of parallel flow instabilities, thin liquid films were tackled. In the absence of exterior forces, no interface instability can arise. It is thus necessary to take into account exterior influences (gravity, interface shear and gaseous turbulence) as well as the coupling between the two phases to observe film instabilities. Therefore, deriving an analytical model is a complicated task and a phenomenological approach would be more appropriate, especially in engineering-oriented applications. For instance, the regimes maps drawn by McCready *et al.* (Fig. 4.4) depending on the liquid and gaseous Reynolds number would be a good starting point. From a macroscopic point of view, especially when considering the mean film thickness, the 2D and 3D periodic waves have limited effects as they only modify the apparent roughness of the film surface. On the other hand, for high gaseous Reynolds number, the onset of solitary and roll waves have a considerable influence on the mean film thickness as they convect at their velocity a significant amount of liquid. A modeling approach would be to increase the mean film velocity to account for these waves. In the context of aeroengines where the gaseous Reynolds number is large, these waves should considered.

The development of a 2D instability to a 3D process, through a spanwise instability was then presented. Several potential scenarios were described and the one from Hong [152] & Varga [353] showed the best scaling with experiments. It is therefore selected for further work on primary atomization in the following. The *coalescence cascade* [220] was briefly presented, leading to a drop size distribution described by the Gamma function. Note that to compare this mechanism with experiments, it is preferable to use the total PDF (Eq. 4.33), *i.e.* the Gamma distribution convoluted with the ligament size distribution.

Academic experiments highlighting primary breakup encountered in aeroegine atomizers were discussed. The four majors types are liquid sheets, cylindrical jets, mixing layers and finally liquid accumulation breakup. Common characteristic parameters are (sorted by decreasing influence): the momentum flux ratio M, the Weber number We (based on either aerodynamic or liquid inertia), the Reynolds number Re, the Ohnesorge number Oh and the film thickness to atomizing edge thickness ratio h/h_a. In the context of airblast atomizer, the KIT-ITS experiment provides interesting information: when $h/h_a \lesssim 5$ the film does not detach from the atomizing edge and feed the liquid accumulation that undergoes stretched ligament breakup. Consequently the film behaviour and especially its

surface state (waves onset) has a weak influence on the breakup and the drop size distribution. In this case, the liquid accumulation sheared by the gas can be considered as the *mixing layer* academic case, and the parameters related to the later, especially the Dimotakis velocity U_c (Eq. 4.36) can be used. For $h/h_a \gtrsim 5$, the film goes on its trajectory into the chamber, mimicking the *liquid sheet* academic case.

An overview of the numerical methods to compute primary atomization was presented. The DNS/interface capture methods allow to recover early instabilities that degenerate to fragmentation. However due to a considerable demand on computational resources, they do not suit to engineering-oriented applications, and lower-order models focusing on first-order spray characteristics (liquid volume fraction, number of droplets, drop size distribution) are generally preferred. As the primary breakup mechanisms are strongly related to the geometry, there are no universal lower-models that accurately describe primary atomization. The ELSA method is an Eulerian approach designed for RANS (which is out of the context of this work) and the stochastic breakup of Gorokhovski was originally developed for secondary breakup in a cascade process (high Weber number), which is not observed for primary breakup. In this context emerges the necessity to develop a phenomenological model dedicated to primary breakup occurring in airblast injectors, presented in Chapter 8.

Part II

Developments

Chapter 5

General purpose Lagrangian developments

5.1 Lagrangian module

The Lagrangian module of AVBP has been developed and implemented by García [98] and it has already demonstrated its ability to simulate dilute sprays [162, 316] and two-phase combustion [134]. As presented in Appendix B, the Lagrangian module solves the kinematic (Eq. B.1) and dynamic (Eq. B.14) equations of a particle immersed in a flow and subject to gravity. Its main steps are listed below, in the execution order:

- Particle injection
- Interpolation of gas physical values at particle location
- Computation of source terms for particle equations (drag and evaporation)
- Computation of source terms for the gaseous phase (in case of two-way coupling)
- Time and space advancement
- Particle tracking (relocalization)

The coupling with the gaseous phase requires to compute Eulerian values of the liquid phase, such as volume fraction, mean volume diameter (D_{30}), or enthalpy. The whole flowchart of the Lagrangian module and its dialog with the Eulerian gaseous solver is depicted on Fig. 5.1. In the following, the successive steps are briefly described.

5.1.1 Particle injection

From a modeling point of view, injection is a critical operation because it generates regions of large liquid volume ratio, compromising the dilute spray assumption necessary to the point source approximation (presented in section B.3.1). Consequently the coupling between the liquid and the gaseous phase is strong, in particular the momentum exchange, and injected liquid momentum has to be carefully modeled.

Particles are injected inside the computational volume according to the user inputs. Several parameters are taken into account to describe a realistic spray:

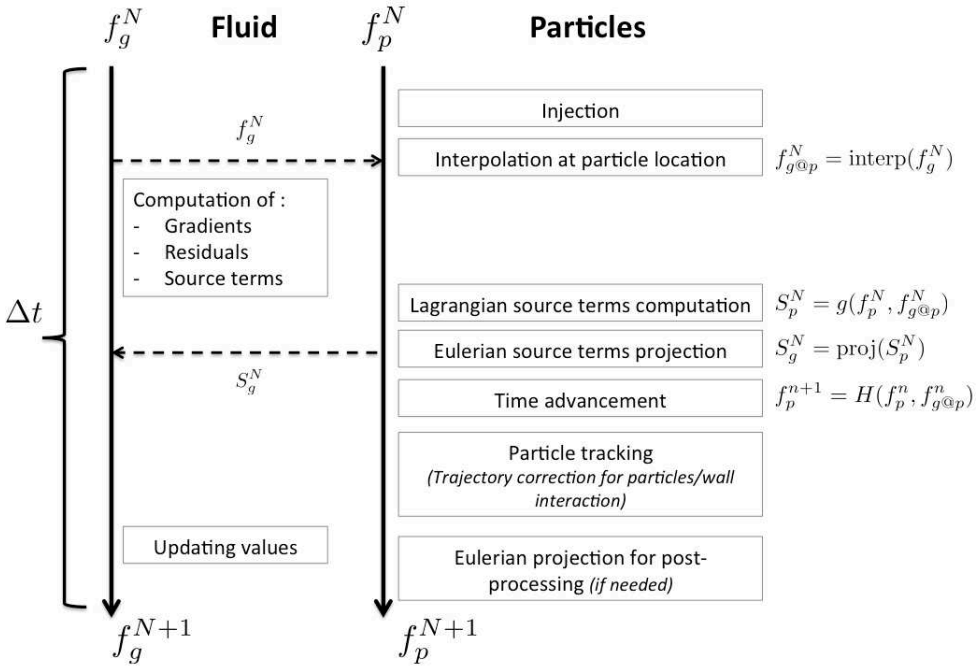

Figure 5.1 : *Flowchart of the Lagrangian module of AVBP.*

- Mass flow rate: the injected mass during one time step is computed as the sum of particle mass injected in the computational volume during the same time step

- Drop size distribution: in order to describe a polydisperse spray, diameters are randomly chosen following a given probability density function. Several classical functions are available in AVBP. They can be expressed either as a numerical density (the probability density represents the number of particles) or as a volume density (the probability function represents the volume of particles).

- Surface injection geometry: basic geometries are available such a point, disk, line or crown injection.

- Particle velocity: from a macroscopic point of view the droplet velocity corresponds to the liquid momentum injected in the system and is strongly related to the injection geometry. In the context of piston engines where the injection is achieved through a pressurized device, a plain or hollow cone are generated.
  A more sophisticated injection model called FIM-UR (for Fuel Injection Method by Upstream Reconstruction) was developed in the context of pressure swirl atomizer (*simplex*) by Sanjosé [304] and Senoner [316]. In this model, a developed spray is directly injected at the atomizer orifice, neglecting the effects of liquid disintegration on spray dynamics. Velocity profiles are determined by the model and used for the injected droplets. Both Euler/Lagrange and Euler/Euler formalisms are supported.

The injected particle is randomly placed in a volume determined from the injector geometrical characteristics and flow conditions. This method allows an homogenous space distribution and avoids the formation of clusters of particles at every $u_p \Delta t$.

5.1.2 Interpolation of gas physical values at particle location

The calculation of the coupling terms between the carrier and dispersed phase (presented in B.3) requires the determination of both phases quantities at the same location. Therefore the gaseous values are interpolated from the Eulerian grid to the particle position $x_{p,i}$. The expression for an arbitrary quantity f at the particle location $x_{p,i}$ is obtained as:

$$f_{g@p,i} = \sum_{j \in K_e} w(x_{p,i}, x_{n,i}) f \tag{5.1}$$

The term $w(x_{p,i}, x_{n,i})$ describes a generic interpolation function which defines the weights associated to the nodal coordinates $x_{n,i}$ of the cell K_e inside which the particle is located. Three different interpolation methods are available in AVBP:

- an interpolation based on a first-order Taylor expansion of f:

$$f(x_i) = f(x_{n,i}) + f'(x_{n,i})(x_i - x_{n,i}) \tag{5.2}$$

  where $x_{n,i}$ denotes the coordinates of the node n and $f'(x_{n,i})$ the first derivative of f at the node n. As pointed out by García [98], this interpolation method reduces the computational overhead to a strict minimum as the first derivatives of gaseous quantities at the nodes are directly available in the solver. On the contrary, chosing a second-order interpolation would require the computation and storage of second derivatives at all nodes.

- a linear-least squares method which reconstructs polynomials. This leads to an overdetermined systems and the coefficients of the linear polynomials are minimized in a least-squares sense:

$$\min ||Ax - b|| = 0 \tag{5.3}$$

  The matrix A contains the nodal coordinates, the vector x the unknown coefficients of the linear polynomes and the vector b the nodal values of the scalars to interpolate.

- an interpolation based on Lagrangian polynomials. A Lagrange polynomial $P(x_i)$ is constructed as the function of degree (n-1) passing through the N nodal values $f(x_{n,i})$ of the quantity f in the computational cell K_e:

$$P(x_i) = \sum_{j=1}^{N} \prod_{i=1}^{n_d} P_j^i(x_i) \qquad \text{with} \qquad P_j^i(x_i) = f(x_{j,i}) \prod_{\substack{k=1 \\ k \neq j}}^{N} \left(\frac{x_i - x_{k,i}}{x_{j,i} - x_{k,i}} \right) \tag{5.4}$$

García [98] observed very similar accuracy for the three methods in particle laden homogeneous isotropic turbulence simulations, but important differences in computational cost. Taylor and Lagrange interpolations were computationally much faster than the Linear Least Squares method. For this reason, Taylor interpolation is used in the present work.

5.1.3 Discretization

In a first approach, the time advancement of the Lagrangian solver relies on a first-order explicit Euler method:

$$f_p^{N+1} = f_p^N + H(f_p^N, f_{g@p}^N) \tag{5.5}$$

where $H(\cdot)$ denotes a function depending on both properties of the particle f_p^N and properties of the gas interpolated at the particle position $f_{g@p}^N$. The term f_p^{N+1} stands for particle properties at the next time step. However, the particle

velocity is computed through a semi-implicit method that guarantees a higher robustness: the velocity equation is expressed with an implicit formulation, but contrarily to a pure implicit method, no loop within the time step is achieved. Neglecting the gravity for clarity sake, Eq. B.14 yields:

$$\frac{du_{p,i}}{dt} = \frac{1}{\tau_p}(u_{i,g@p} - u_{i,p}) \tag{5.6}$$

Adopting a semi-implicit formulation leads to:

$$\frac{u_{i,p}^{N+1} - u_{i,p}^{N}}{\Delta t} = \frac{1}{\tau_p^N}(u_{i,g@p}^{N} - u_{i,p}^{N+1}) \tag{5.7}$$

In Eq. 5.7 the particle relaxation time τ_p as well as the gas velocity $u_{i,g@p}$ are considered at the previous time step for two different reasons. First, in the code execution order, the gas velocity is interpolated at the particle location before it is updated by momentum flux. Second, the particle relaxation time τ_p does not linearly depend on the gas velocity. As the purpose of Eq. 5.7 is to directly express $u_{i,p}^{N+1}$ ($u_{i,p}^{N+1} = f$(other parameters)), it would not be mathematically possible to transfer the dependence of τ_p on $u_{i,p}^{N+1}$ on the left-hand side of Eq. 5.7.

Equation 5.7 leads to a direct expression for the updated particle velocity:

$$u_{i,p}^{N+1} = \frac{u_{i,p}^{N} + \aleph \cdot u_{i,g@p}^{N}}{1 + \aleph} \tag{5.8}$$

where $\aleph$ stands for the ratio of the numerical time step to the particle relaxation time:

$$\aleph = \frac{\Delta t}{\tau_p^{N+1}} \tag{5.9}$$

Theoretically, the barycentric nature of Eq. 5.8 guarantees a stable behaviour: whatever the value of $\aleph > 0$, Eq. 5.8 is still defined and the value is comprised between $u_{i,p}$ and $u_{i,g@p}$. If the time step is very small compared to the particle relaxation time ($\aleph << 1$) and gaseous and particle velocity are of the same order of magnitude then Eq. (5.8) degenerates to $u_{i,p}^{N+1} \approx u_{i,p}^{N}$ and the updated particle velocity is mainly influenced by its history. Contrarily for $\aleph >> 1$ we obtain $u_{i,p}^{N+1} \approx u_{i,g@p}^{N}$ and the particle velocity stick to the gaseous one. However this expression is not stable in practice: the time delay between particles and gas (the updated particle velocity is equal to the previous gaseous velocity) leads to spurious oscillations.

Finally, as previously stated, the semi-implicit formulation of Eq. 5.6 is more robust than a full explicit formulation: an explicit formulation would lead to:

$$u_{i,p}^{N+1} = (1 - \aleph) \cdot u_{i,p}^{N} + \aleph \cdot u_{i,g@p}^{N} \tag{5.10}$$

and clearly shows an oscillating behaviour for $\aleph > 1$.

Once the new velocity is calculated, the particle coordinates are updated by integrating Eq. B.1 with an Euler method:

$$x_{i,p}^{N+1} = x_{i,p}^{N} + u_{i,p}^{N+1} \cdot \Delta t \tag{5.11}$$

Note that particle coordinates are updated after the wall-impact management routine that can further modify the particle velocity in case of rebound, splashing or filming.

5.1.4 Particle tracking

In order to interpolate the gaseous values as well as compute the Lagrangian source terms to the gas, a particle must localized within the mesh grid *i.e.* it must know the identity of its containing cell. As particles travel within the domain, they move from one cell to another and it is mandatory to keep their cell location updated. The first generation of particle tracking algorithm in AVBP was of 'known-vicinity' type: it was supposed that particles elementary motion is always smaller than the minimum cell size:

$$u_p \cdot \Delta t < \Delta x \tag{5.12}$$

As AVBP is an compressible, explicit in time solver, relation 5.12 is always fulfilled. Indeed the CFL condition for compressible flow is based on the speed of sound and the time step order of magnitude is about:

$$\Delta t \approx \frac{\Delta x}{u_g + c} \tag{5.13}$$

Combining 5.12 and 5.13 leads to a "CFL-like" condition for particle tracking with a known-vicinity algorithm:

$$u_p < u_f + c \tag{5.14}$$

which is always the case in classical applications. However, this type of algorithm is blind to particle trajectory and presented some limitations in case of advanced particle/wall interaction. Moreover, in the optics of using an implicit solver *i.e.* much larger time steps, Eq. 5.12 would not be valid and this algorithm would not apply.

Recently a new algorithm has been implemented by Paulhiac [265] based on the work of Haselbacher [138]. This algorithm is based on particle trajectory, and tracks each cell face crossed by the particle during its journey. There is no CFL-like condition and particle/wall interaction is naturally embedded (Fig. 5.2).

This algorithm is robust, *i.e.* no particles are lost, but is more CPU expensive, especially for massively parallel computation: if a particle crosses several partitions, it requires an inter-partition communication for each crossing.

5.2 Eulerian projection of Lagrangian fields

As previously mentioned, it is necessary to interpolate the carrier phase quantities to the particle location in order to compute the influence of the former onto the latter. The reverse operation *i.e.* interpolating the particle physical quantities onto the mesh grid, is necessary to compute the retro action of the scattered phase on the carrier (two-way coupling). In the present work, this interpolation is called *projection* and its related mathematical object is called a *projector*. Furthermore the projection of Lagrangian fields is useful for post-processing purpose: the Eulerian representation of the scattered phase gives access to interesting analysis objects such as gradients, volume or mass averages, etc. In addition, as AVBP embeds a two-phase flow solver based on the mesoscopic Euler/Euler approach, the comparison between the two formalisms is of interest and requires the same fields. Therefore this section also tackles the conversion of an AVBP Euler/Lagrangian solution into an AVBP Euler/Euler solution. The projection is performed through several steps that are detailed in the following.

5.2.1 Variable conversion

Depending of their use and their properties, the Lagrangian variables (parcel number, diameter, velocity, temperature) must be converted into different forms, leading to a different treatment.

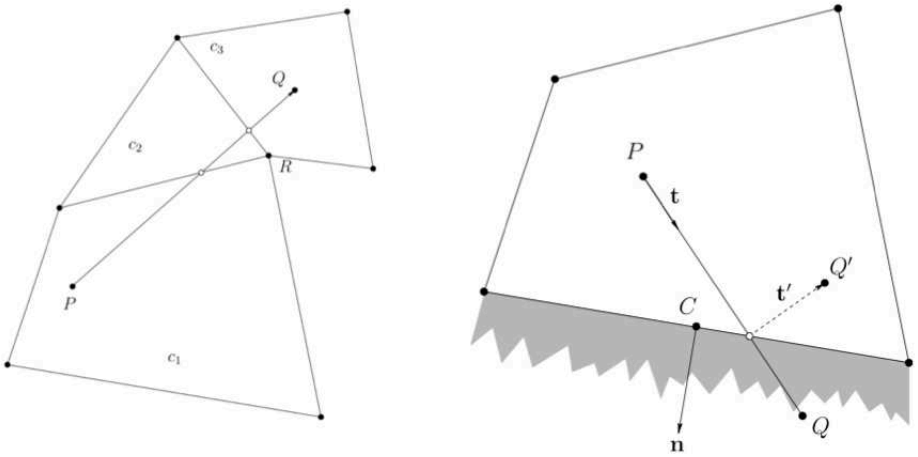

Figure 5.2 : *Illustration of Haselbacher's algorithm, from [138]. Left: particle is initially located at point P and it travels to point Q. This algorithm tests every face of cell c_1 to check which one is crossed by PQ segment. Once the proper face is discriminated, the same process is applied to cell c_2, and cells are iteratively tracked to Q position. Right: when the trajectory crosses a wall boundary, the trajectory is changed following an appropriate behaviour (from Q to Q′) and the remaining path to achieve is updated.*

Extensive quantitites

When they are used as input for source terms (two-way coupling), they are converted into conservative variables that are solved by the flow solver (mass, momentum and energy). Theses variables are extensive: for a homogenous system, their values are proportional to the volume of the system. Consequently when considering two different subsystems, an extensive variable ϕ of the subsystem union is equal to the sum of each subsystem variable:

$$\phi(S_1 \cup S_2) = \phi(S_1) \cup \phi(S_2) \tag{5.15}$$

The following rules convert a Lagrangian particle characterized by a parcel number N_p, diameter d_p, density ρ_p, velocity $u_{p,i}$, mass heat capacity c_p and temperature T_p, into extensive quantities that correspond to a number of particles n_p with an overall volume v_p, mass m_p, momentum $M_{p,i}$ and enthalpy h_p:

$$n_p = N_p \tag{5.16a}$$
$$v_p = \frac{\pi}{6} d_p^3 \, n_p \tag{5.16b}$$
$$m_p = \rho_p \, v_p \tag{5.16c}$$
$$M_{p,i} = m_p \, u_{p,i} \tag{5.16d}$$
$$h_p = m_p \, c_p(T_p) \, T_p \tag{5.16e}$$

Note that Eqs. 5.16 are invertible and Lagrangian variables can be extracted from conservative quantities.

Lagrangian variables are then split among the nodes of the containing cell using a geometric projector g that must be conservative, *i.e.* the sum of the nodes coefficients must be equal to one:

$$\sum_{n \in \mathcal{N}(\mathcal{C}_\mathrm{p})} g(p,n) = 1 \tag{5.17}$$

where $\mathcal{C}_p$ and $\mathcal{N}(\mathcal{C}_p)$ represent the cell containing the particle p and the nodes of $\mathcal{C}_p$, respectively. The coefficient $g(p,n)$ corresponds to the projection of the particle p on the node n. Projecting all the particles to nodes is then straightforward by summing all the extensive quantities. Let ϕ be an extensive value, the quantity $\mathcal{P}_e$ represents the projected value of ϕ using the projector g at the node n:

$$\phi(n) = \sum_p g(p,n)\phi(p) \equiv \mathcal{P}_e(\phi, g, n) \tag{5.18}$$

Non-extensive quantities

Contrary to extensive variables, intensive variables are independent of the system volume. A physical value ϕ is intensive if and if only it is equal in any subsystems S_k of a *homogeneous* system S:

$$\forall k, \phi_{S_k} = \phi_S \tag{5.19}$$

Note that some physical quantities can be neither extensive nor intensive: the drop diameter is not proportional to the volume, but the cubic root of the volume through $d_p = \sqrt[3]{6v_p/\pi n_p}$. Lagrangian variables as the density, velocity, temperature, mass heat capacity are intensive. Projecting non-extensive quantities requires a normalization by the sum of the coefficients $w(p,n)$ at the end of the process. Let ϕ be a non-extensive value, the quantity $\mathcal{P}_{ne}$ represents the projected value of ϕ using the normalization w at the node n:

$$\phi(n) = \frac{\sum_p w(p,n)\phi(p)}{\sum_p w(p,n)} \equiv \mathcal{P}_{ne}(\phi, w, n) \tag{5.20}$$

where the coefficients $w(p,n)$ correspond to the weight of the particle p on the node n. This weighting function may have different forms:

1. $w_1(p,n) = g(p,n)$ is the pure geometric weighting that corresponds to the projector used for extensive values.
2. $w_2(p,n) = g(p,n) \cdot N_p$ is the geometric projector weighted by the parcel number.
3. $w_3(p,n) = g(p,n) \cdot \frac{\pi}{6} d^3$ is the geometric projector weighted by the volume of the particle.
4. $w_4(p,n) = g(p,n)\rho_p$ is the geometric projector weighted by liquid density.

Note that combination of different weight is possible, for instance $g(p,n) \cdot N_p \cdot \frac{\pi}{6} d^3$ represents the total volume of the parcel. The choice of the weighting function influences the final projected quantity and it must be accounted for when analyzing the results. Therefore when extracting a non-extensive quantity from extensive fields, there is no guarantee that the results are equal. For instance, considering the velocity extracted from mass and momentum:

$$u_i^{(1)}(n) = \frac{\mathcal{P}_e(M_i, g, n)}{\mathcal{P}_e(m, g, n)} \tag{5.21}$$

and the velocity obtained by projecting the particle velocity using the filter w_2:

$$u_i^{(2)}(n) = \mathcal{P}_{ne}(u_{p,i}, w_2, n) \tag{5.22}$$

The two projected velocity are *a priori* different $u_i^{(1)}(n) \neq u_i^{(2)}(n)$. In addition, only the velocity $u_i^{(1)}(n)$ is representative of the momentum conservation computed at the node n together with the mass.

A lack of representativeness arises with non-extensive quantities when the scattered phase is not present in a cell. Since extensive values are proportional to the volume, no particles in the cell leads to extensive quantities equal to zero (*e.g.* no mass/momentum/enthalpy). However non-extensive values (mainly velocity or temperature) that are not related to a concentration cannot be translated into a zero value. For instance setting the velocity (or the temperature) to zero in the absence of particle could be mistaken with the presence of stationary particles (or zero temperature particles). This problem occurs for both values extracted from extensive values (*e.g.* $u_i(n) = M_i(n)/m(n)$) and projected values (*e.g.* $u_i(n) = \mathcal{P}_{ne}(u_{p,i}, w, n)$) and when analyzing such fields, it is important to superimpose a 'presence' variable such as $n_p(n)$ to check if a zero value is meaningful or linked to the absence of particles.

Time averaged quantities

The intermittent presence of the liquid in a cell can lead to erroneous interpretations of mean fields. Considering a cell that contains a particle of m = 1 g, c_p = 1000 J/K/kg and T = 300 K, during three time steps over one hundred. The basic time averaging process for the mass m and temperatpure T (n dependence is dropped for clarity sake):

$$\langle m \rangle_t = \frac{1}{\tau_{avg}} \sum_{t_i} m(t_i)\Delta t \tag{5.23a}$$

$$\langle h \rangle_t = \frac{1}{\tau_{avg}} \sum_{t_i} h(t_i)\Delta t \tag{5.23b}$$

leads to a mean mass of 0.03 g and mean enthalpy of 9 J. Those value must be not interpreted as the mean mass and enthalpy of droplets belonging to the considered cell but as a mean liquid mass and enthalpy in time at this space location. In order to determine mean extensive quantities of the scattered phase and taking into account its presence, it would be necessary to define an averaging time τ_{avg} that depends on the node location and the scattered phase presence:

$$\tau_{avg}(n) = \sum_{t_i} P(n, t_i)\Delta t(t_i) \tag{5.24}$$

with P a presence indicator of the scattered phase:

$$P(n,t) = \begin{cases} 1 & \text{if } n_p(n,t) > 0 \\ 0 & \text{otherwise} \end{cases}$$

The ratio $\tau_{avg}(n)/\tau_{tot}$ can therefore be understood as a 'in time' presence probability. It ranges from 0 when no particles are located in the cell during the whole simulation, to 1 when the cell contains continuously at least one droplet. Note that when proceeding to a 'extensive to non-extensive' extraction (*e.g.* extracting temperature from enthalpy and mass) the intermittency problem disappears. With the same example, the extracted temperature would be $T = h/(mc_p) = 300$ K.

Non-extensive variable are subject to the same phenomenon, but they can lead to non-physical values. Using the basic time averaging process (Eq. 5.23) onto the previous example for computing the mean liquid temperature:

$$\langle T \rangle_t = \frac{1}{\tau_{avg}} \sum_{t_i} T(t_i)\Delta t \tag{5.25}$$

would lead to a non realistic value of 9 K. The solution is the same as for extensive quantities, *i.e.* to compute a local 'presence time' $\tau_{avg}(n)$ for each node (Eq. 5.24).

5.2.2 Projecting quantities onto the mesh grid

The aim of this subsection is to assess the quality of different projectors. The projection operation can lead to two types of error. The first type occurs only for non locally conservative projectors: for a finite number of particles, the overall mass (or volume) is not conserved in the containing cell; but when the number of particles tends to infinity, the mass is conserved. This is called the *statistical error* and it can be reduced by increasing the filter control volume, leading to a larger number of samples. The second type of error has been pointed out by Boivin *et al.* [30]. Projection is equivalent to a low-pass filtering of the spatial frequencies, with the cutoff frequency equals to the inverse of filter characteristic length (*i.e.* the control volume). Therefore high spacial gradients are filtered out by the projection. In order to counteract this effect, the length scale has to be decreased. Therefore a compromise has to be found to minimize the superposition of both type of bias, as detailed in 5.2.2.c).

However in the simulation, as the number of particle is limited, the statistical error has no guarantee to decrease, especially in very diluted regions where only few droplets cruise. In addition, the characteristic length scale on unstructured meshes is usually taken as the cell characteristic length (*e.g.* LES implicit filter) and defining a larger filter length can be CPU costly in massively parallel simulations. For those reasons, only *conservative* projectors with *compact stencil* (*i.e.* limited to the cell size) are discussed in the following. This ensures that the first type of error is zero and focus is made on the second type of error, *i.e.* gradient rendering.

Three projectors have been selected: the **closest node** method, the **inverse distances** method and the **normalized gaussian filter** method. They are first presented and the gradient rendering is assessed through a Fourier Transform comparison.

5.2.2.a) Closest node method

The particle data is projected on the closest node of the belonging cell. The corresponding weight function can be expressed by:

$$w(p,n) = \begin{cases} 1 & \text{if } n \text{ is the closest node of the containing cell} \\ 0 & \text{otherwise} \end{cases} \tag{5.26}$$

This projector delivers sharper results than the two others: if the particle total number is too low, the result of the projection presents some 'value gaps' as illustrated on Fig. 5.3. The conservativeness is naturally ensured by Eq. 5.26. If the unstructured mesh presents some stretched cells, there is a risk that the closest node of the belonging cell is not the absolute closest node (Fig. 5.4).

5.2.2.b) Inverse distances method

The particle data is projected on all nodes of the belonging cell thanks to a geometric weight formulation [98]. The weight of the projector is constructed to be inversely proportional to the distance d_n between the particle p and the node n, as illustrated on Fig. 5.5:

$$w(p,n) = \frac{1/d_n}{\sum_{i \in \mathcal{N}(\mathcal{C}_\mathrm{p})} 1/d_i} \tag{5.27}$$

The conservativeness is straightforward by summing Eq. 5.27 over the cell nodes. The projector can be considered as a 'conservative' large volume filter with an adaptive characteristic length [175].

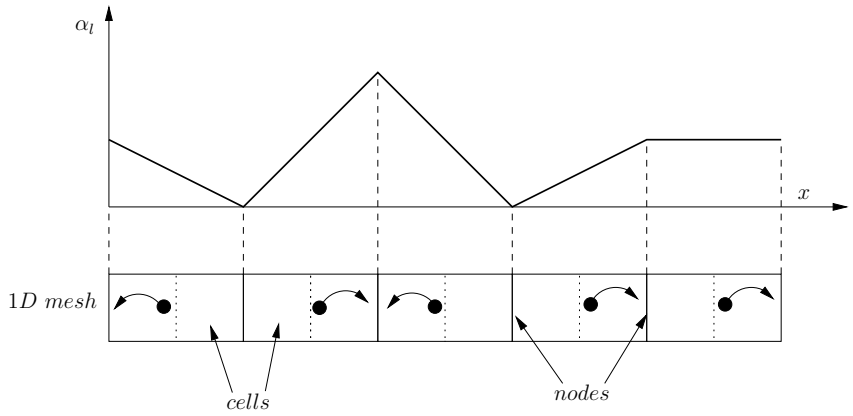

Figure 5.3 : *Projection on a 1D mesh of particles slightly shifted from regular spatial repartition using the closest node method*

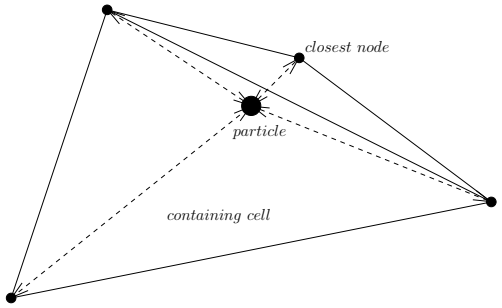

Figure 5.4 : *On highly stretched mesh, the closest node may not belong to the containing cell*

5.2.2.c) Normalized gaussian filter

In order to minimize both the statistical and spatial gradients errors, Kauffmann *et al.* [175] proposed to use a Gaussian type filter on a large volume control with a smaller characteristic length. On a structured mesh made of quadrilateral elements, the control volume of this filter is set to the cell containing the particle, leading to:

$$w(p,n) = \left[\sqrt{\frac{6}{\pi}}\frac{1}{\text{erf}\left(\sqrt{6}\right)}\right]^{\text{D}} \exp\left(-6\,\frac{d_p^2}{{L_c}^2}\right) \tag{5.28}$$

with D the dimensions number of the case and L_c the cell characteristic length of the cell. In this present case of squared cells, L_c is equal to the length of an edge. The preexponential factor in (5.28) ensures the conservativeness in case of statistical convergence, *i.e.* for an infinite number of particles randomly located within a regular cell, the average sum of the nodes coefficient is equal to unity. This projector is not locally conservative: the sum of the nodes weight depends on the location of the particle within the cell and thus it is not always equal to one (see Fig. 5.6 a)). Therefore in diluted regions, the number of particles per cell can reach very low values, the statistical convergence hypothesis may not hold, leading to an inaccurate projection. Furthermore it was demonstrated (but not presented in this thesis) that in case of non isotropic cells (*e.g.* in 2D, a rectangle instead of a square) the projector looses its statistical conservativeness. The use of this projector on unstructured grid in aeronautical applications is strongly not recommended.

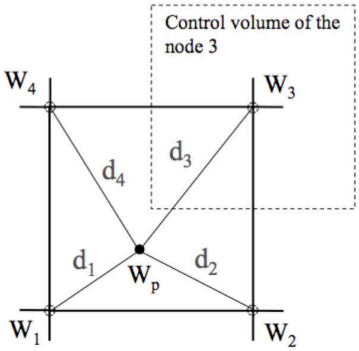

Figure 5.5 : *Illustration of the particle p contribution onto the nodes of a quadrilateral cell, from [98]*

Nevertheless, it is possible to make it fully conservative by normalizing the weights $w(p,n)$ of the cells by their summation over the cell. This leads to a readjustment of the preexponential factor in Eq. 5.28 by a preliminary loop of the weight calculation over the cells nodes:

$$w(p,n) = \frac{1}{S} \exp\left(-6\,\frac{d_p^2}{{L_c}^2}\right) \tag{5.29a}$$

$$S = \sum_{n \in \mathcal{N}(\mathcal{C}_p)} w(p,n) \tag{5.29b}$$

This renormalization ensures then a local conservativeness, independently of the statistical convergence (see Fig. 5.6 b)). It is close to the inverse distances method, except that the kernel is not inversely proportional to the distance, but follow a gaussian distribution. However note that the filter still depends on a characteristic length L_c that is questionable in case of highly stretched cells (large skewness ratio).

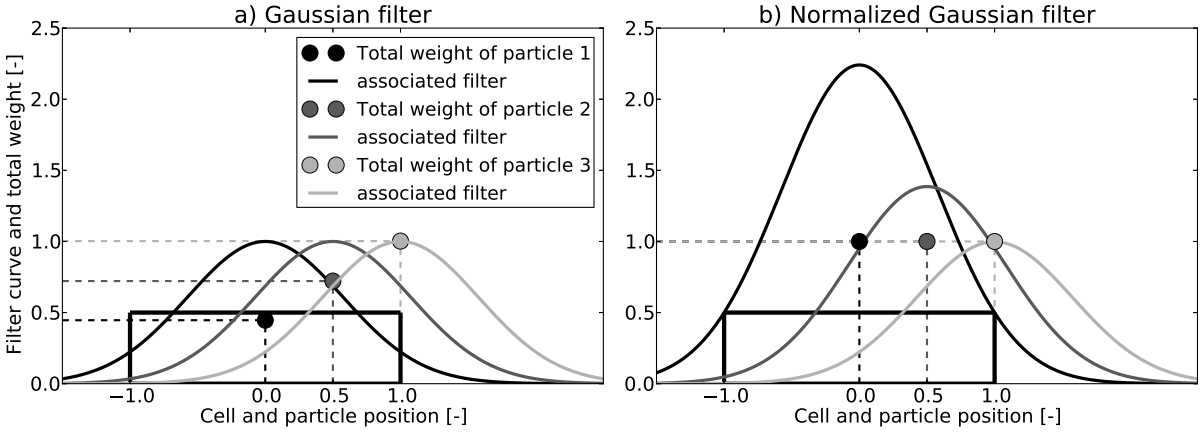

Figure 5.6 : *Illustration of the total weight of three particles located at the center, three quarter and the boundary of the cell in a 1D case, for a) the Gaussian filter and b) the Normalized Gaussian filter. The thick rectangle represents the cell location. The y coordinate of the particles corresponds to the sum of the coefficients of the two nodes of the 1D cell ($w(p, x = -1) + w(p, x = 1)$).*

5.2.2.d) Fourier Transform study of different projection methods

As the three projectors mentioned above are conservative, they do not suffer from any statistical error, and their efficiency relies of how they minimize the second type error. A spatial Fourier Transform study is therefore performed in a 1D case, to estimates their filtering properties. Two signals are studied: $\mathcal{S}_1$ is the sum of two sinus functions of different amplitude with a non zero mean value, and $\mathcal{S}_2$ is a Gaussian function:

$$\mathcal{S}_1(x) = 1 + \sin(2\pi\,\sigma_1\,x) + 0.01\sin(2\pi\,\frac{\sigma_1}{2}\,x) \tag{5.30a}$$

$$\mathcal{S}_2(x) = \exp\left(-[x-5]^2\right) \tag{5.30b}$$

The signal $\mathcal{S}_1$ aims to estimates the ability of the projector to separate two different wave number (σ_1 = 10) of different amplitudes and $\mathcal{S}_2$ mimic a sudden change that can occur to a particle, *e.g.* when crossing a flame front. The signals can represent any quantities carried by the particle like parcel number, diameter, velocity, temperature or evaporation rate.

Figure 5.7 depicts a part of the test configuration: a large number of particles (2^{16}) are regularly distributed over a spatial dimension and the carried property is represented by $\mathcal{S}_1$ and $\mathcal{S}_2$. It corresponds to the so-called input signal and has a large sampling frequency. A Fourier transform of this input signal is performed and is used as a reference for the projectors. Different meshes are tested in order to observe the influence of the cutoff frequency induced by the cell size.

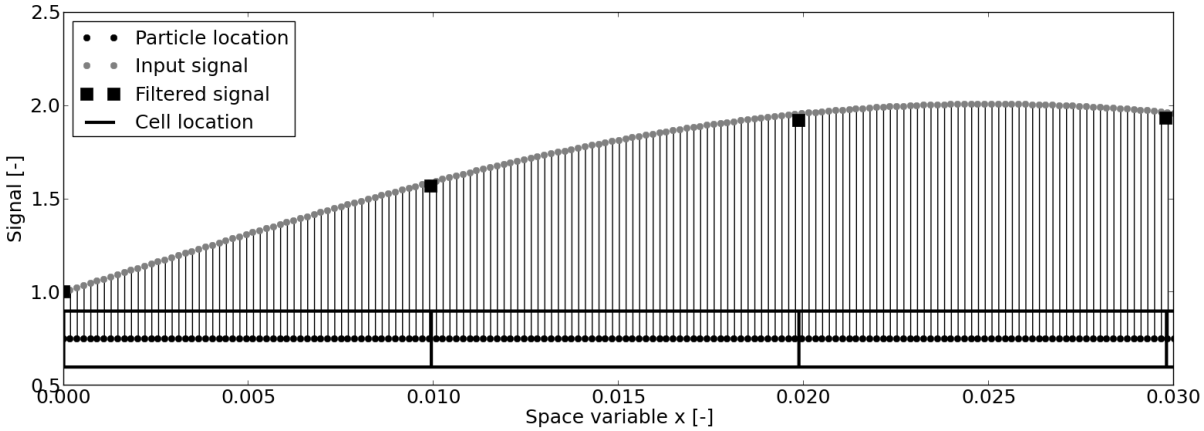

Figure 5.7 : *Schematics of the particles and filtering cells location in the case of signal* $\mathcal{S}_1$

Figure 5.8 displays the space signal $\mathcal{S}_1$ and its Fourier Transform with different mesh resolutions, characterized by the ratio of the cell size by the wavelength $\sigma_1\Delta x \approx 0.3$ (*top*), 0.1 (*middle*) and 0.01 (*bottom*). The input signal FT is best visible on the *top*: the two peaks and their relative amplitude are clearly marked. With this low resolution (Shanon principle imposes $\sigma_1\Delta x < 0.5$) the three projectors have the same frequency behaviour, and they capture the two sinus signal with acceptable amplitudes, even if the spacial signal is highly distorted. For $\sigma_1\Delta x \approx 0.1$ (*middle*), the closest node projector presents a larger noise amplitude than the two other, but still allows to capture the two peaks. For the lowest frequency ($\sigma_1\Delta x \approx 0.01$, *bottom*), the peaks are well resolved by the three projectors but the inverse distances projector present a significant lower noise amplitude. The space signal reconstructed by the closest node projector shows a high frequency distortion at the crest of the sinus function. This may be due to the regular spacing of the particles that produces a Moiré pattern and it may be occurs in a real turbulent configuration. The partial conclusion on signal $\mathcal{S}_1$ is a slight advantage of the inverse distances method and significant weakness of the closest node method.

Figure 5.9 shows the space signal $\mathcal{S}_2$ and its FT with mesh resolution characterized by 6 (*top*), 12 (*middle*) and 120 (*bottom*) data points in the half of the peak. The theoretical FT curve is superimposed on each frequency graphs. The FT of the input signal matches the theoretical curve up to $\sigma \approx 1.8$. With 6 points in the gradient zone, the three projector have the same behaviour and accurately extract the Gaussian FT up to $\sigma = 1/2\Delta x$ imposed by Shannon principle. With 12 points (*middle*) the projectors show deviation from the theory at different locations. The sooner (with regards to σ) deviation arises with the closest node method and the latest with the inverse distances method. For a high resolution (120 points, *bottom*) the presents secondary peaks at higher frequency but their amplitude still remain relatively low in the "noise" range, except for the closest node method that displays a peak at 10^{-2}. This peak at higher frequency maybe related to the space signal particular behaviour at the crest of the Gaussian peak, as for $\mathcal{S}_1$.

To conclude this assessment, the frequency response of the inverse distances method is the most accurate, with a little advantage over the Gaussian filter. This study was performed on a regular 1D mesh. On a 2D irregular grid with stretched cells, the Gaussian projector is expected to behave less precisely, due its dependence to only one characteristic length L_c. As a first order method, the closest node projector provides a low accurate prediction.

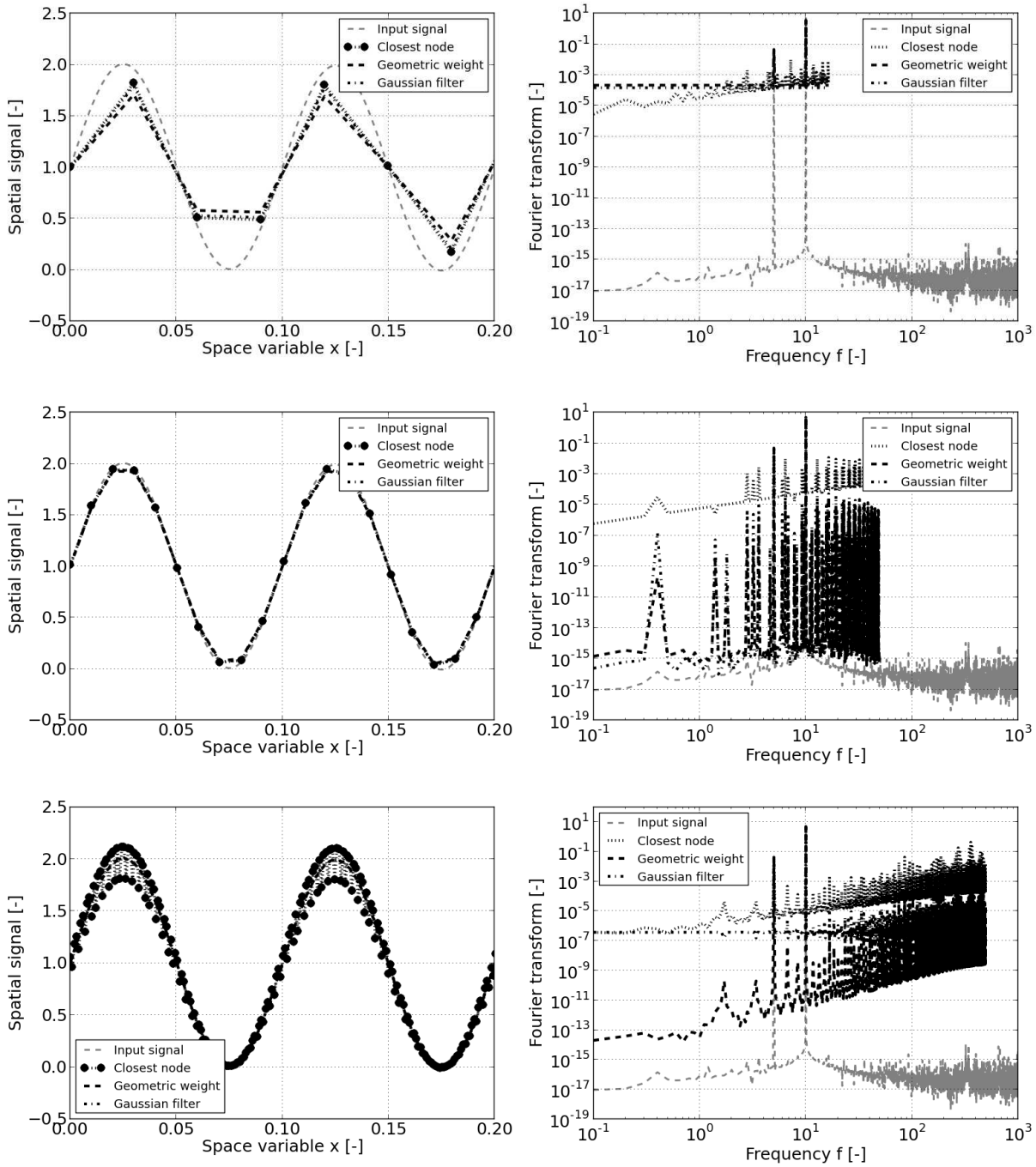

Figure 5.8 : *Fourier Transform of signal $\mathcal{S}_1$ filtered by different projectors for different mesh resolutions*

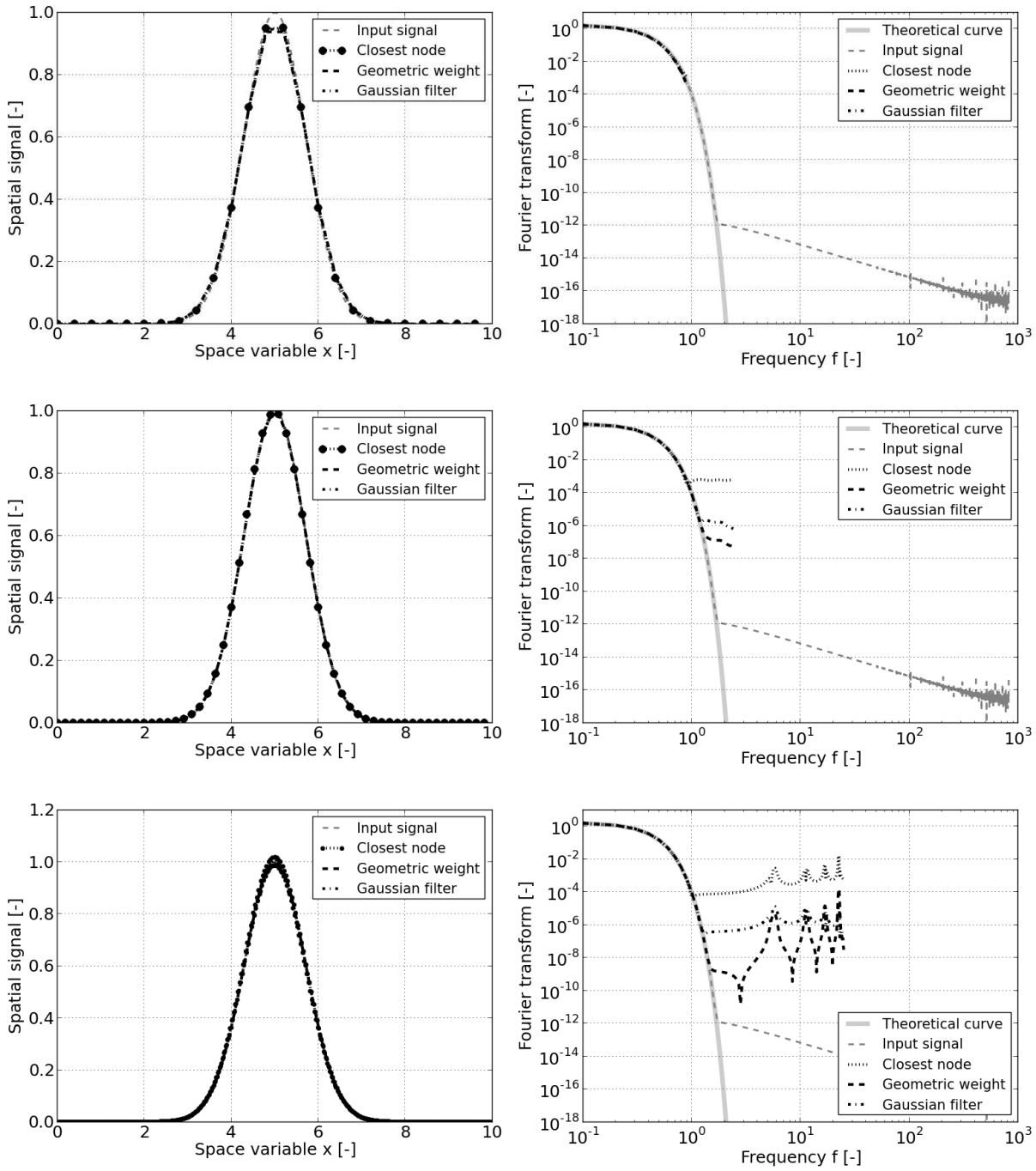

Figure 5.9 : *Fourier Transform of signal $\mathcal{S}_2$ filtered by different projectors for different mesh resolutions*

5.2.3 EL → EE Projection rules

In the Euler/Euler AVBP solver, the liquid phase is described by the following field:

- n_l : particle volume density
- $\alpha_l \rho_l$: mean liquid density
- $\alpha_l \rho_l u_i$: mean liquid volume momentum
- $\alpha_l \rho_l \delta q_p^2$: Random Uncorrelated Energy
- $\alpha_l \rho_l h_l$: mean liquid volume enthalpy

Except for $\alpha_l \rho_l \delta q_p^2$, all quantities are volume concentration expressed by the ratio of an extensive quantity divided a local volume. In AVBP, every physical quantity is stored at the nodes and thus the local volume is the nodal volume $V(n)$. Therefore Euler/Euler fields are obtained by dividing Eq. 5.31 by $V(n)$:

$$\phi^{E/E}(n) = \frac{1}{V(n)} \sum_p g(p,n)\phi(p) \tag{5.31}$$

where ϕ an extensive quantity described by Eqs. 5.16 in 5.2.1 and g is a geometric projector described in 5.2.2.

Particle density

The particle volume density is constructed from the total particle number in the local volume.

$$n_l(n) = \frac{1}{V(n)} \sum_p g(p,n) n_p(p) \tag{5.32}$$

Mean liquid density

The mean liquid density is defined as the integral volume of the liquid density ρ_l weighted by its presence function χ_l [174]:

$$\{\alpha_l \rho_l\}(n) = \frac{1}{V(n)} \int_{V(n)} \chi_l \, \rho_l \, \mathrm{d}V(n) \tag{5.33}$$

In a discrete Lagrangian context associated to projectors, it corresponds to:

$$\{\alpha_l \rho_l\}(n) = \frac{1}{V(n)} \sum_p g(p,n) \, m_p \tag{5.34}$$

Note that $\alpha_l \rho_l$ is the normalizing factor for the extraction of a Favre-averaged liquid quantity.

Momentum components

As an extensive quantity, the momentum is computed as:

$$\{\alpha_l \rho_l u_{l,i}\}(n) = \frac{1}{V(n)} \sum_p g(p,n)\, M_{p,i} \tag{5.35}$$

The Favre-average of the liquid velocity is thus recovered by:

$$u_{l,i}(n) = \frac{\{\alpha_l \rho_l u_{l,i}\}(n)}{\{\alpha_l \rho_l\}(n)} \tag{5.36}$$

Random Uncorrelated Energy

The Random Uncorrelated Energy (RUE) is a value derived from the mesoscopic average of the Euler formulation of sprays. Many details of this physical signification can be found [87, 289, 322] but only the decomposition of the liquid phase kinetic energy q_p^2 into a correlated $\breve{q}_p^2$ and uncorrelated δq_p^2 term will be used:

$$q_p^2 = \underbrace{\breve{q}_p^2}_{correlated} + \underbrace{\delta q_p^2}_{uncorrelated} \tag{5.37}$$

The correlated term derives from a statistical average on an (idealy) infinite number of particle configurations with the same flow configuration. The uncorrelated term can be expressed as the difference between the instantaneous liquid phase kinetic energy and instantaneous correlated term.

As it is a not an extensive quantity, the total particle kinetic energy is projected onto nodes using Eq. 5.20, weighted by the particle number n_p:

$$q_p^2(n) = \mathcal{P}_{ne}(u_{p,i}^2, w_2, n) \equiv \overline{u_{p,i}^2} \tag{5.38}$$

As in [175], the correlated term is taken as the squared *in node* ensemble average of the particles velocity:

$$\breve{q}_p^2(n) = \left[\mathcal{P}_{ne}(u_{p,i}, w_2, n)\right]^2 \equiv \overline{u_{p,i}}^2 \tag{5.39}$$

Injecting Eqs. 5.39 and 5.38 into Eq. 5.37 leads to the expression of the RUE:

$$\delta q_p^2(n) = \overline{u_{p,i}^2} - \overline{u_{p,i}}^2 \tag{5.40}$$

And

$$\left\{\alpha_l \rho_l \delta q_p^2\right\}(n) = \{\alpha_l \rho_l\}(n) \left(\overline{u_{p,i}^2} - \overline{u_{p,i}}^2\right)(n) \tag{5.41}$$

Note that with this projection method, the RUE can be seen as the sum of components variance of the particle velocity:

$$\delta q_p^2(n) = \sum_{i=1}^{\text{dim}} \text{var}[u_{i,p}(n)] \tag{5.42}$$

Enthalpy

As for the mass fraction and the momentum, the liquid phase enthalpy is reconstructed by a canonical projection:

$$\{\alpha_l \rho_l h_l\}(n) = \frac{1}{V(n)} \sum_p g(p,n)\, h_p \tag{5.43}$$

5.3 Implementation of Particle/Wall treatment

This section details the Spray/Wall Interaction (SWI) model implemented in AVBP. It was developed and implemented by Habchi [128].

5.3.1 Simplification of the regime map

The different regimes of the map of Fig. 2.8 are simplified down to four main regimes. The driving parameters are the impacting droplet Weber number and the wall temperature. The simplification is shown on Fig. 5.10. In cold conditions, the impacting droplet can splash if its impact energy is large enough, otherwise it is deposited on the wall and forms a film. For hot conditions and large Weber numbers, the droplet splashes with a different behaviour than in cold conditions. Low Weber number droplets end up in a rebound with a slight kinetic energy loss.

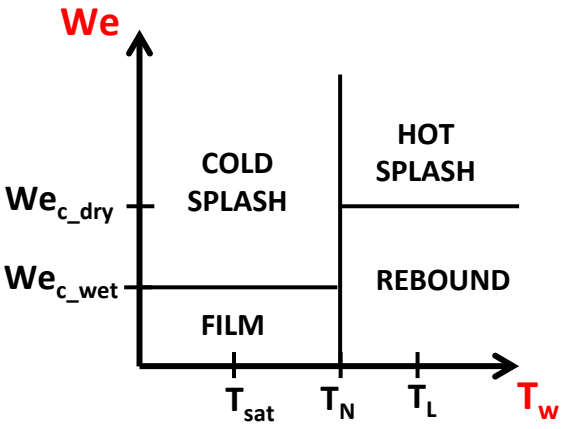

Figure 5.10 : *Simplified SWI regime map*

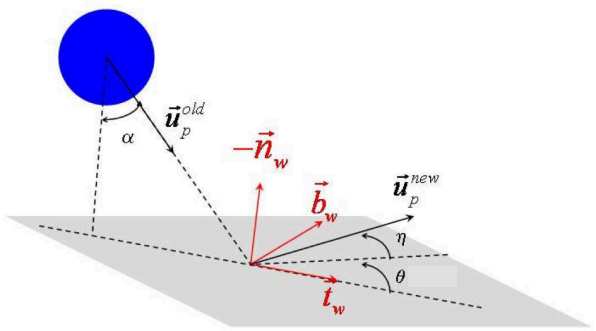

Figure 5.11 : *Definition of the local referential and angles involved in the SWI model, from [128]*

5.3.2 Threshold criteria

Wall temperature

Due to the absence of a film boiling model, the temperature transition between the cold and hot regime is set to the Nukiyama temperature T_N [128]. It is approximated by [81, 127] the arithmetic mean of the saturation T_{sat} and Leidenfrost T_L temperature:

$$T_N = \frac{T_{sat} + T_L}{2} \tag{5.44}$$

where the Leidenfrost temperature is estimated by [127] proportional to the critical temperature T_c:

$$T_L = \frac{27}{32} T_c \tag{5.45}$$

Impact Weber number

From experimental observation [245, 360], the threshold Weber number on hot surfaces ($T_w > T_N$) is roughly constant:

$$\mathrm{We}_{c,dry} \approx 30 \tag{5.46}$$

However, when the wall surface temperature is below T_N, the critical Weber number depends on the surface roughness to drop diameter ratio R^* (Eq. 2.8) as well as the drop Reynolds number [56, 133]. Based on these observations and their associated correlations, Habchi [125, 126] proposes:

$$\mathrm{We}_{c,wet} = C_{spray} \frac{1500 + 650/R^{*\,0.42}}{\sqrt{\mathrm{Re}_d}} \tag{5.47}$$

where Re_d is the impacting droplet Reynolds number:

$$\mathrm{Re}_d = \frac{u_{p,i}^{old}\, d_p}{\nu_l} \tag{5.48}$$

and C_{spray} is a constant calibrated in [128] to 0.05 to fit experiments from Mathews *et al.* [225]. However, the criterion 5.47 has been modified to take the film thickness into account, as suggested by [133] (Eq. 2.12). This leads to a wet Weber number criterion:

$$\mathrm{We}_{c,wet} = C_{spray} \frac{1500 + 650/R^{*\,0.42}}{\sqrt{\mathrm{Re}_d}} \cdot \left[1 + 0.1\sqrt{\mathrm{Re}_d} \cdot \min(\delta, 0.5)\right] \tag{5.49}$$

where δ (Eq. 2.6a) is the film thickness normalized by the impacting droplet diameter. Qualitatively, Eq. 5.49 states that in the presence of a liquid film on the surface, the droplet needs a larger Weber number in order to splash.

5.3.3 Regime outcomes

Applying the above criteria to the wall temperature and the impacting Weber number, the regime of the impinging droplet behaviour is determined. In each regime it is assumed that the droplet/wall interaction is sufficiently fast to avoid any thermal transfer and the droplet temperature is kept constant.

Film regime

The droplet spills on the surface and forms a film. It is flagged as a film particle and its velocity magnitude is given the film mean velocity. This regime is extensively detailed in chapter 6.

Rebound regime

The droplet rebounds on the wall without fragmentation. The new velocity (u_i^{new}, defined on Fig. 5.11) is computed by supposing an inelastic rebound [114]:

$$u_{i,p}^{new} = u_{i,p}^{old} - \left(u_{i,p}^{old} \cdot n_{w,i}\right)(1 + \phi)\, n_{w,i} \tag{5.50}$$

where ϕ is the damping factor of the rebound, expressed by [360] as the velocity magnitude ratio of the outcoming and incoming droplets:

$$\phi = \frac{\|u_{i,p}^{new}\|}{\|u_{i,p}^{old}\|} = 0.678 \exp\left(-0.044\, \mathrm{We}^{old}\right) \tag{5.51}$$

Cold splash regime

In this regime the droplet is fragmented into several child droplets that are re emitted oppositely to the wall. In this regime, a fraction of the droplet mass can spill on the wall and be brought to the film model. The correlations involved in this model mainly derive from the experimental work of [133, 258].

Experiments conducted by [370] showed that a fraction of the mass remains on the wall. Based on their observation, Habchi derived [125]:

$$\frac{M_{spl}}{M_0} = \min\left[2.9\,10^{-4}\sqrt{\mathrm{Re}_n}(\mathrm{We}-\mathrm{We}_{c,wet}), 0.75\right] \tag{5.52}$$

To avoid a too high number of numerical particles, no new particle is created during the splash. The liquid deposition is treated in a stochastic way by a random draw X between 0 and 1. If $X > M_{spl}/M_0$ the droplet is totally deposited on the wall and becomes a film particle. If $X < M_{spl}/M_0$ the droplet splashes. Its child droplets are given a diameter and velocity described in the following paragraphs. This procedure statistically converges to experimental observations.

The size distribution of the child droplets is based on experiments [245, 370]. O'Rourke & Amsden [258] suggest to employ a Nukiyama-Tanasawa distribution. The following distribution [125] is used in AVBP:

$$f(r) = \frac{4r^4}{\sqrt{\pi}r_{max}^5}\exp\left(-\frac{r^2}{r_{max}^2}\right) \tag{5.53}$$

where r_{max} is the peak droplet radius of the distribution. Similarly to [258], its value is related to the the impacting drop radius by:

$$\frac{r_{max}}{r_{old}} = \max\left[\left(\frac{\mathrm{We}_{c,crit}}{\mathrm{We}}\right)^{1/4}, \frac{6}{\mathrm{We}}, 0.06\right] \tag{5.54}$$

The exponent $1/4$ was calibrated by [125] based on experimental results of [225]. In order to conserve the droplet volume, the new parcel number N_p is changed so that:

$$r_p^{old,3}\,N_p^{old} = r_p^{new,3}\,N_p^{new} \tag{5.55}$$

The velocity of child droplets is computed from:

$$u_{i,p}^{new} = w'\,n_{i,w} + (0.8\,\nu_0 + 0.12\,w_0)(t_{i,w}\cos\psi + b_{i,w}\sin\psi) + v'(t_{i,w}\cos\theta + b_{i,w}\sin\theta) \tag{5.56}$$

where $(-n_{i,w}, t_{i,w}, b_{i,w})$ defines the local referential at the impact location, as defined on Fig. 5.11, and v_0 and w_0 are the projection of the impacting droplet velocity onto $(t_{i,w}, n_{i,w})$. Angles ψ and θ lie in the interval $[-\pi, +\pi]$, following respectively the Naber & Reitz distribution [246] and a normal disribution. Finally, v' and w' are the tangential and normal fluctuating components of the splashed droplet velocity. They are randomly determined by a normal distribution:

$$G(u') = \frac{1}{\delta\sqrt{\pi}}\exp\left(-\frac{u'^2}{\delta^2}\right) \tag{5.57}$$

where $\delta = 0.1w_0\sqrt{2}$ for v' and $\delta = 0.2w_0$ for w'.

Hot splash regime

In the hot splash regime, it is assumed that no liquid is deposited onto the wall. In addition, no new particles are created and the parcel number is changed to ensure mass conservation (Eq. 5.55). The droplet velocity after the impact is chosen as:

$$u_{i,p}^{new} = |u_{i,p}^{old}| \left(-n_{i,w}\text{sin}\eta + t_{i,w}\text{cos}\eta\,\text{cos}\psi + b_{i,w}\text{cos}\,\eta\text{sin}\psi\right) \tag{5.58}$$

The angle ψ is between $-\pi$ and $+\pi$ and it follows the distribution suggested by Naber & Reitz [246]:

$$\psi = -\text{sign}(X)\,\frac{\pi}{\beta}\,\ln\left[1 - X(1 - e^{-\beta})\right] \tag{5.59}$$

where X is an equipossible random number betwen -0.5 and 0.5. The parameter β is linked [246] to the impact angle α defined on Fig. 5.11 by:

$$\sin\alpha = \frac{e^{\beta}+1}{e^{\beta}-1}\,\frac{\beta^2}{\beta^2+\pi^2} \tag{5.60}$$

The angle η in Eq. 5.58 is assumed between $0°$ and $30°$, and the radius ratio r_p^{new}/r_p^{old} is set between 0.2 and 1 [128]. Both quantities are determined by an equipossible random draw X between 0 and 1, such as $X = 1$ leads to $r_p^{new}/r_p^{old} = 0.2$ and $\eta = 30°$, and $X = 0$ leads to $r_p^{new}/r_p^{old} = 1$ and $\eta = 0°$.

5.4 Frozen gas approach

On the cost of multiscale simulation in the Lagrangian framework

One drawback of the Lagrangian approach is the low statistical convergence. When studying ignition phenomenon in a real combustion chamber, it is necessary to fill in the chamber with a sufficient amount of particles to ensure (i) a minimum gaseous equivalence ratio for the ignition to start, and (ii) a minimum global equivalence ratio that will allow the flame to propagate by evaporating the droplets. This filling of the chamber is called *carburation* and it can take a much longer time than the gaseous characteristic timescale. In addition, when the gaseous solver is compressible and explicit in time, the statistical convergence is even more worrying. As previously mentioned, in such a solver, the CFL condition relies on the speed of sound, and the time step decreases even further.

The same problem arises when simulating thin film flow: the very small thickness leads to a large and prohibitive convective time. For instance in chapter 8, the film steady state was reached after between 0.1 and 1s, depending on the case. With a mesh composed of several millions of elements and a time step of ≈ 0.1µs, a parametric study becomes out of reach.

Freezing the gas to vanish the CFL condition

A solution is therefore required to speedup the physical time advancement of the simulation. The parcel approach (one numerical particle represent N_p identical physical particles) as well as the Lagrangian subcycling (particles are treated every N_{ite} iterations) allow to decrease the numerical expense but they don't increase the time step of the simulation, and the overall speedup is 'linear'. In the optic of filling the domain with particles, a more pragmatic approach is presented here, and labeled the *frozen gas* approach: the gaseous field is leaved unperturbed, and only the particles are treated and time-advanced. Consequently, there is no CFL condition based on the gas flow, but the time step is only restricted by the particle motion. This method allows to increase the time step by two or three orders of magnitude. As the gaseous field is frozen, no fluctuations nor unsteady gaseous effect can be captured: this method is only used to seed the domains with particles. Once the domain is filled, it is mandatory to switch to the regular (labeled here *dynamic*) approach to compute vaporization, dispersion, or combustion. The particles undergo

the gas effect via the coupling terms in the mass, momentum and energy equations, but obviously no retro-coupling is possible. In principle the particle can be evaporated (decrease of the particle diameter), but it has not been tested. One requirement is to provide a gaseous solution representative of the usual flow field. In the following, a time-averaged solution is given as the representative solution. It is also possible to input an instantaneous solution, but since it is a snapshot of the flow field, it can enhance the influence of small fluctuations and lower the mean flow pattern influence onto particle distribution.

Time step imposed by the particles motion

When computing the motion of a particle with an explicit or semi-implicit time integration, the numerical time step must be lower than the particle relaxation time τ_p in order to properly predict the particle trajectory, as mentioned in 5.1.3. If not, the particle is subject to oscillations that (i) have no physical meanings and (ii) can lead to a numerical divergence. It is therefore still necessary to choose the time step carefully.

Figure 5.12 displays the particle relaxation time τ_p versus the particle diameter d_p, superimposed with Δt_{AVBP} a time step related to a typical simulation. The calculation of τ_p accounts for the Schiller-Neumann correction and supposed a relative velocity of 1 m/s. It was observed that in the context of aeroengines, τ_p does not change much with the relative velocity. Two typical cumulative volume distributions of typical sprays are superimposed on Fig. 5.12. It allows to estimate the maximum time step Δt to compute properly a considered mass fraction of the spray. For instance, as $\tau_p(d_p = 20\mu m) \approx 10^{-5}$ s means that a time step of 10^{-5} s predicts accurate trajectories for particles larger than $\approx$ 20 µm, because in this case $\aleph < 1$. From the spray curves, a diameter lower than 20 µm corresponds to $\approx$ 35 and 5% of the total mass of spray 1 and 2, respectively. Therefore a time step of 10^{-5} s is accurate for the largest particles that compose $\approx$ 65 and 95% of the sprays. An additional result shown on Fig. 5.12 is that a typical time step in AVBP is small enough to properly handle more than 99% of the mass of the finest spray.

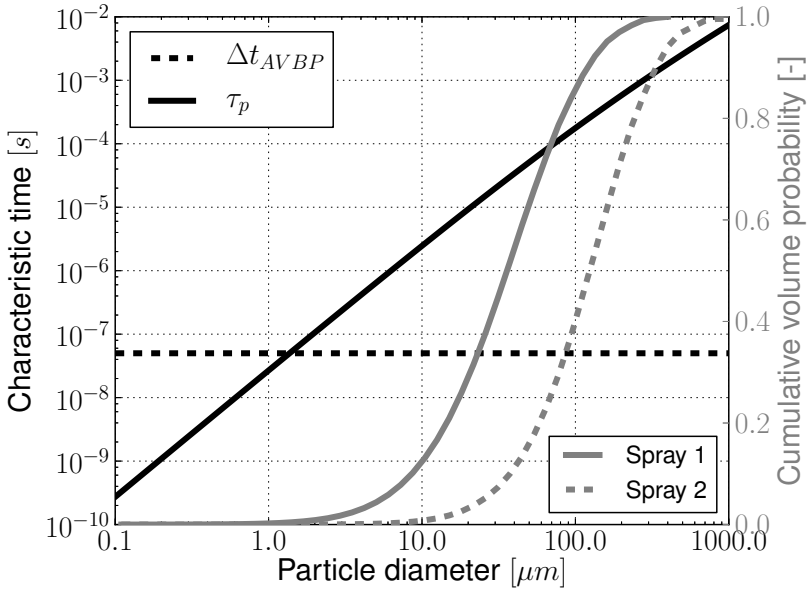

Figure 5.12 : *Particle relaxation time versus the particle diameter, superimposed with typical spray cumulative volume distribution*

The time step requirement for film particles is different. As it is explained in chapter 6, they are assumed to reach the steady state instantaneously, dictated by the wall shear stress. Therefore the distance they travel during one time step must be lower than the varying length scale of the wall shear stress L_{c,τ_w}, expressed by its gradient:

$$u_f \cdot \Delta t < \frac{\tau_w}{\frac{\partial \tau_w}{\partial x_i}} \tag{5.61}$$

To illustrate Eq. 5.61, let us consider a typical thin film flowing with a velocity of 1 m/s in a geometry where the wall shear stress evolves from 20 to 60 Pa over 10 mm. The length scale of the wall shear stress is $\approx 20/(40/0.01)m \approx 5mm$, leading to a maximum time step of $\approx 5\,10^{-3}$ s. The limiting factor in the time step is therefore the droplet motion.

Modification of the code

The principle of this method is easy to implement: it simply consists in by-passing the gaseous routines except for the first iteration. Indeed, it is necessary to compute the gaseous fields in order to derive the coupling term in the Lagrangian equation. Skipping the gaseous routines presents an additional advantage of avoiding expensive parallel reductions, and it leads to a faster execution for one time step.

Test case

A test is performed on the KIT-ITS case presented in Chapter 8. It consists in a film developing on a prefilming surface and being atomized at the trailing edge of this surface. A *dynamic* run is started from a preliminary established film and the simulation is run for 76 ms (that corresponds to less than a film convective time). The *frozen gas* run starts from a purely mean gaseous solution and runs for 705 ms. Figure 5.13 shows a scatter plot of the particles position. No physical interpretations are presented here but just a global sketch: the *frozen gas* method associated to a time averaged gaseous solution generates a spray 'smooth' in space. This may be a serious limitation for an accurate filling in of a combustion chamber.

Speedup

The speed up of this method is assessed on the KIT-ITS case presented in chapter 8. It is a highly unbalanced case as a film is simulated. Nevertheless, it can give an idea of the possible improvement of the code efficiency to fill in a film. Table 5.1 summarizes the characteristics of the two comparative runs. The *dynamic* run is started from an established film, and the *frozen gas* case was run from a empty film. The speedup of the *frozen gas* method is considerable. Note that the speedup is larger than the time step ratio, meaning that skipping the gaseous routines accelerates significantly the code. Since the time step ratio is ≈1760 and the total speedup ≈2487, it can be stated that skipping the gas treatment leads to a speedup of 1.413. Of course, this last estimation is bounded to the total number of particles and the load balancing.

Improvement

It must be highlighted that this method was only developed to speedup the filling of the film and little attention was paid to the accurate prediction of the spray topology. There are thus several possibilities of improvement for this approach:

1. **Implicit loop for particle advancement**: In order to have $\aleph < 1$ for every particles without decreasing the time step, the implicit loop sub-iterates the particle motion along its path depending on the particle size.

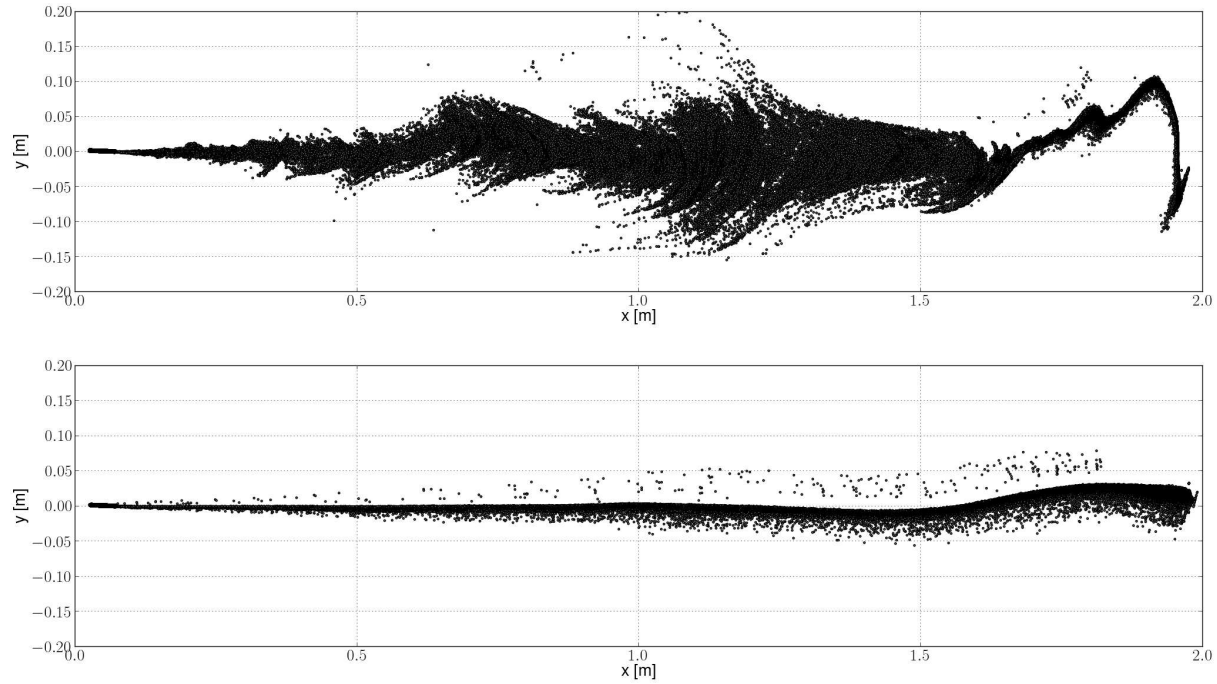

Figure 5.13 : *Scatter plot of spray droplets with the* dynamic *(top) and* frozen gas *approach (bottom)*

Therefore large particles would require only one loop whereas small ones (larger ℵ) would need several sub-iterations to follow the right trajectory.

2. **Random velocity fluctuation from kinetic turbulent energy**: When the gaseous field is a well-converged time average, gaseous fluctuations are smoothed out. Therefore no turbulence dispersion can be captured. A random drag could be applied to the particle, deriving from the viscous dissipation of the turbulent kinetic energy combined with the Stokes time of the considered particle. This would perturb the particle from its time-average trajectory and mimic the turbulent dispersion for a more realistic realization.

	Unit	*Dynamic*	*frozen gas*
Δt	$[s]$	5.7 10^{-8}	10^{-4}
Max ptcl / partition	$[-]$	184 098	271 011
Mean total ptcl number	$[-]$	273 870	312 206
Physical time	$[s]$	0.076	0.705
CPU time	[hCPU]	5.836 10^4	249
CPU / Physical time*	$[-]$	2.779 10^9	1.117 10^6
Time step ratio *frozen gas* / *dynamic*	$[-]$	-	1760
Speedup *frozen gas* / *dynamic*	$[-]$	-	2487

Table 5.1 : *Comparison between the* dynamic *and* frozen gas *approaches for a film simulation. (*value of* frozen gas *approach was multiplied by the particle number ratio to ensure a proper comparison)*

Chapter 6

Development, implementation and partial validation of the film model

This chapter explains the derivation of a simple model for the description of a film flow, in the framework of LES. It also details how this model is implemented in the AVBP solver. A first comparison with the analytical solution of a 2D Poiseuille flow is performed. Then a Large Eddy Simulation is conducted in a simple academic geometry with a turbulent flow.

6.1 Equations of motion

6.1.1 Simplifying the local equations

In Chapter 3, film equations were derived from the Navier-Stokes equations parametrized by non-dimensional numbers. In the context of aeronautical burners, additional assumptions allows further simplification. The film equations derived in Chapter 3 are recalled:

$$\frac{\partial u}{\partial x} + \frac{\partial v}{\partial y} = 0 \tag{6.1a}$$

$$\frac{\partial u}{\partial t} + u\frac{\partial u}{\partial x} + v\frac{\partial u}{\partial y} = -\frac{1}{\rho}\frac{\partial p}{\partial x} + \nu\frac{\partial^2 u}{\partial y^2} + g\,\sin\gamma \tag{6.1b}$$

$$\frac{\partial p}{\partial y} = 0 \tag{6.1c}$$

A sketch of the film flow and the associated notation is available on Fig. 6.1. Driven by shear, the film characteristic time scale is imposed by momentum diffusion and reads:

$$\tau_{carac} = \frac{h^2}{\nu} \tag{6.2}$$

where h is the film thickness. With a film thickness h of $0.1\,mm$ and a liquid kinematic viscosity ν of $\approx 1 \cdot 10^{-5}$ m^2/s, the characteristic time is about 10 ms. With a mean velocity of 1 m/s, the film requires a distance of ≈ 1 cm to reach a steady state. This characteristic length is comparable to the length of the path traveled by the film in aeronautical burners and the assumption of steady-state can be made. The time derivative consequently vanishes in Eq. 6.1b.

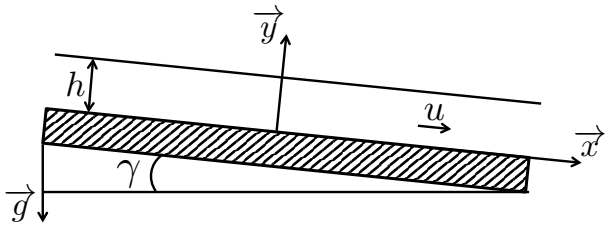

Figure 6.1 : *Sketch of a general film flow in a gravity field. Definition of wall-tangential ($\vec{x}$) and wall-normal ($\vec{y}$) directions.*

The steady-state assumption allows then to consider the film flow as uniform along the x direction, meaning that there is no source of variation along x once the film is stabilized. This is not exactly true in reality, as the wall geometry and the surrounding gas flow change, but this means that thin film flows adapt instantaneously to these changes. As a consequence the velocity derivative in x disappears and the final set of equations reduces to:

$$\frac{dv}{dy} = 0 \tag{6.3a}$$

$$v\frac{du}{dy} = -\frac{1}{\rho}\frac{\partial p}{\partial x} + \nu\frac{d^2u}{dy^2} + g\,\sin\gamma \tag{6.3b}$$

$$\frac{\partial p}{\partial y} = 0 \tag{6.3c}$$

Mass conservation (Eq. 6.3a) states that the wall normal velocity is constant over the film thickness. As non porous walls impose that v is zero at the wall surface, this leads to:

$$v = 0 \tag{6.4}$$

Equation 6.3c shows that pressure is a function of x only. Finally, the film motion is described by the longitudinal momentum equation 6.3b that writes:

$$\nu\frac{d^2u}{dy^2} = \frac{1}{\rho}\frac{dp}{dx} - g\,\sin\gamma \tag{6.5}$$

6.1.2 Integration and Depth-Averaging

Double integration in y of Eq. 6.5 leads to:

$$u(y) = \frac{1}{2}\left(\frac{1}{\mu}\frac{dp}{dx} - \frac{g}{\nu}\,\sin\gamma\right)y^2 + A\,y + B \tag{6.6}$$

where A and B are two integration constants that are determined from boundary conditions. The no-slip boundary condition imposes $u(0) = 0$ so $B = 0$. Using Eq. 3.37b from chapter 3, the slope of the velocity profile may be linked to the shear stress at the film/gas interface:

$$\mu\left.\frac{du}{dy}\right|_h = \tau_{fg} \tag{6.7}$$

leading to:

$$A = \frac{\tau_{fg} - h\,\frac{dp}{dx} + \rho g h\,\sin\gamma}{\mu} \tag{6.8}$$

And u finally writes:

$$u(y) = \left[\left(\frac{dp}{dx} - \rho g \sin\gamma\right)\left(\frac{y}{2} - h\right) + \tau_{fg}\right] \frac{y}{\mu} \tag{6.9}$$

The obtained film velocity profile has a parabolic shape, the square term comes from the pressure gradient and/or gravity. When these two terms are negligible, the profile is linear and the slope is only imposed by the interface shear stress.

In a first modeling approach, the local expression of velocity is averaged over the film thickness. This is a consequence of the thin film assumption where the film internal flow is neglected. This approximation has been widely used [73, 90] and was presented in section 3.3.1 (Depth-Average Method). Averaging the film velocity profile over its thickness gives:

$$\overline{u}_f = \frac{1}{h}\int_0^h u(y)\,\mathrm{d}y = \tau_{fg} \cdot \frac{h}{2\mu} + \left(\rho g \sin\gamma - \frac{dp}{dx}\right) \cdot \frac{h^2}{3\mu} \tag{6.10}$$

As the film thickness h is small, Eq. 6.10 shows that the film flow is dominated by the interfaces shear stress and that the impact of pressure gradient and gravity is smaller. This assessment will be later confirmed.

The film motion imposes a boundary condition to the gas flow velocity, equal to the interface velocity u_{fg}:

$$u_{fg} = u(h) = \tau_{fg} \cdot \frac{h}{\mu} + \left(\rho g \sin\gamma - \frac{dp}{dx}\right) \cdot \frac{h^2}{\mu} \tag{6.11}$$

6.1.3 Expressing the interface shear stress

The liquid/gas shear stress at the interface is of primary interest in many engineering applications, in particular in piping domain [33], because it is directly linked to pressure drop. As the liquid/gas interface is not resolved in our approach, the shear stress has to be modeled. One possibility is to use one of the many correlation available in the literature [33]. This large variety of expression is linked to the fact that interface shear stress strongly depends on the geometry and physical quantities such as gaseous velocity, turbulent kinetic energy, pressure losses, etc. It must also be highlighted that correlations are always expressed in terms of macroscopic quantities such as bulk velocity or hydraulic diameter. In aeronautical burners such quantities are not appropriate due to the highly heterogeneous flow and the complexity of geometric features. For instance in annular chambers, the presence of diffusors and convergents exclude the use of a constant hydraulic diameter. Moreover correlations derived in the context of pipe flows assume axisymetry that is never reached in burner configurations. In addition the use of the bulk velocity is improper because of the strong swirling motion of the flow in aeronautical burners: the gaseous velocity at the wall has a large azimuthal component that is not taken into account in the bulk velocity. For all these reasons, empirical correlation based on global quantities will not be used.

As a first approximation, the interface shear stress is locally determined using the wall shear stress calculated by the gas flow solver (either directly or through a law-of-the-wall approach), assuming a 'one way coupling' hypothesis, *i.e.* there is no retroaction of the film on the shear stress. This approximation leads to the mean film velocity $\overline{u}_f$:

$$\overline{u}_f = \frac{h}{2\mu} \cdot \tau_w + \frac{h^2}{3\mu} \cdot \left(\rho g \sin\gamma - \frac{dp}{dx}\right) \tag{6.12}$$

6.1.4 Film characteristic velocity

Equation 6.12 allows to estimate the characteristic velocity scale U_0 for a sheared thin film as:

$$U_0 = \frac{h_0}{2\,\mu_0} \cdot \tau_{w,0} - \frac{h_0^2}{3\,\mu_0} \cdot \left.\frac{\partial p}{\partial x}\right|_0 + \frac{h_0^2}{3\,\mu_0} \cdot (\rho g \sin\gamma)_0 \tag{6.13}$$

Assuming that the wall shear stress balances the pressure gradient and the gaseous channel characteristic length is equal to the film longitudinal length L_0, one can write:

$$\tau_{w,0} \sim L_0 \left.\frac{\partial p}{\partial x}\right|_0 \tag{6.14}$$

The third term of the right-hand side in Eq. 6.13 corresponds to the gravity influence and is expressed as:

$$(\rho g \sin\gamma)_0 = \frac{\sin\gamma}{3\,\mathrm{Fr}^{*2}\,\mathrm{Eu}\,\epsilon} \tag{6.15}$$

where $Fr^* = U_0/\sqrt{g\,h_0}$, and Eu and ϵ are the Euler number and the film size ratio as defined in Eq. 3.16. Equation 6.13 thus writes:

$$U_0\left[1 - \frac{1}{3}\frac{\sin\gamma}{\mathrm{Fr}^{*2}\,\mathrm{Eu}\,\epsilon}\right] = \frac{h_0\,\tau_{w,0}}{\mu_0}\left[\frac{1}{2} + \frac{1}{3}\epsilon\right] \tag{6.16}$$

Using orders of magnitude of Table 3.2, and maximizing $\sin\gamma$ to 1, Eq. 6.16 writes:

$$U_0\left[1 - \frac{1}{3}10^{-1}\right] \approx \frac{h_0\,\tau_{w,0}}{\mu_0}\left[\frac{1}{2} + \frac{1}{3}10^{-2}\right] \tag{6.17}$$

leading to:

$$U_0 \sim \frac{h_0\,\tau_{w,0}}{\mu_0} \tag{6.18}$$

Equation 6.18 states that in sheared thin films where the longitudinal pressure gradient is balanced by the wall shear stress, the characteristic velocity scale is proportional to the gaseous wall shear stress and the film thickness.

6.2 Implementation in AVBP

This section gives details on the numerical development and code implementation of the film model expressed through a Lagrangian formalism.

6.2.1 Lagrangian formalism choice

Liquid film being a continuous medium, the natural way to handle it is with an Eulerian approach. However Eulerian approach does not allow an easy description of impacting droplets on walls: this requires to use of the method of moments or the multifluid approach (described in Sections 1.4.3.d) and 1.4.3.e)) that can be very complex and computationally costly. Therefore a particle film model is chosen, following the pioneering work of Amsden & O'Rourke [257]. Details on this approach were given in Section 3.3.3 and focus is made on numerical aspects.

The other advantage of a film discrete description is numerical, as Lagrangian particle tracking is not subject to numerical diffusion while Eulerian methods are naturally bound to the mesh resolution and the numerical scheme. On the other hand the main concern with particle film model is linked to parallel computations [98, 131]. Since all partitions synchronize at the end of each time step, partitions containing many particles impose a delay to particles-free partitions. As thin films lead to droplet accumulation on particular zones, they may dramatically enhance load imbalance, as detailed in Appendix C.

6.2.2 Film particles

Film particles are Lagrangian particles with a particular treatment. Following the film behaviour, they are given a bulk film velocity along the film flow direction that follow the wall (Eq. 6.10). The bulk film velocity uses dp/dx and τ_w that are related to the gas flow and must be interpolated at the particle location. Because of the thin film hypothesis, the interpolation is made at the wall surface and not in the particle-containing cell volume.

6.2.3 Scenario for a droplet impacting a wall

When a droplet impacts a wall, several sequential steps are used to account for the particle as a film. For clarity purpose every step is detailed in following subsections. The explanation starts when the particle impinges a wall face and is detected by the particle tracking module. As splashing and bouncing regimes was presented in section 5.3, only the film regime is detailed here.

6.2.3.a) Reseting particle position and trajectory

As explained in subsection 5.1.4, when a particle crosses a wall surface, the particle tracking algorithm checks the impacting regime and gives the proper behaviour to the droplet. This implies that a particle enters the film only when it hits the wall and not when it is located below the fictive film surface, leading to a small delay in the film feeding compared to reality. Taking usual values of film thickness (100 µm) and droplet velocity (10 m/s), this delay is about 10 µs and it is negligible compared to the film time scale.

When the impacting droplet becomes a film particle, a special treatment is applied as follow:

1. Due to a numerical issue encountered when the film particle is located exactly on wall surface and switches to another cell, the particle is arbitrarily relocated to 1 nm above the wall surface. As the film thickness order of magnitude is 100 µm, this short distance of 1 nm has a negligible impact on the film behaviour.
2. During one time step, a particle is supposed to travel a distance of $U_p\,\Delta t$ (velocity multiplied by the time step), corresponding to, *e.g.* , the path $\overrightarrow{P_1^N P_1^{N+1}} = l_A + l_B$ on Fig. 6.2. When the particle impacts the wall and is relocated at 1 nm above the wall surface, it traveled only a part (l_A) of the expected trajectory and the remaining part (l_B) is converted into a time $t_B = l_B/U_p$. Times $t_A = \Delta t - t_B$ and t_B correspond to the time while the particle was a droplet and film particle, respectively.
3. The magnitude of the film particle velocity is set to the mean film velocity $\overline{u}_f$ (Eq. 6.10) and its direction is set tangential to the wall.
4. The remaining trajectory (l'_B) of the film particle corresponds to the distance traveled by a film particle during t_B, and is set to:
$$l'_B = \overline{u}_f \cdot t_B \tag{6.19}$$
The particle is finally located at the position $P_1^{'N+1}$.

Figure 6.2 provides several examples of different scenarios illustrating the special treatment. At $t = t^N$, particle P_1 was located to a distance greater than the film thickness h_f. As its expected position is beyond the wall, it is converted to a film particle, relocated to 1 nm above the wall surface and advanced over a distance $l'_B = \overline{u}_f\, t_B$. Particle P_2 was located to a distance lower than the film thickness, but since it did not cross the wall surface during the previous iteration, it was still considered as a droplet. It is applied the same treatment as P_1. Particle P_3 was located to a distance greater than the film thickness h_f. At $t = t^{N+1}$ its new location is *below the film fictive surface level* but as it did not crossed the wall, it is still considered as a droplet and no special treatment is applied.

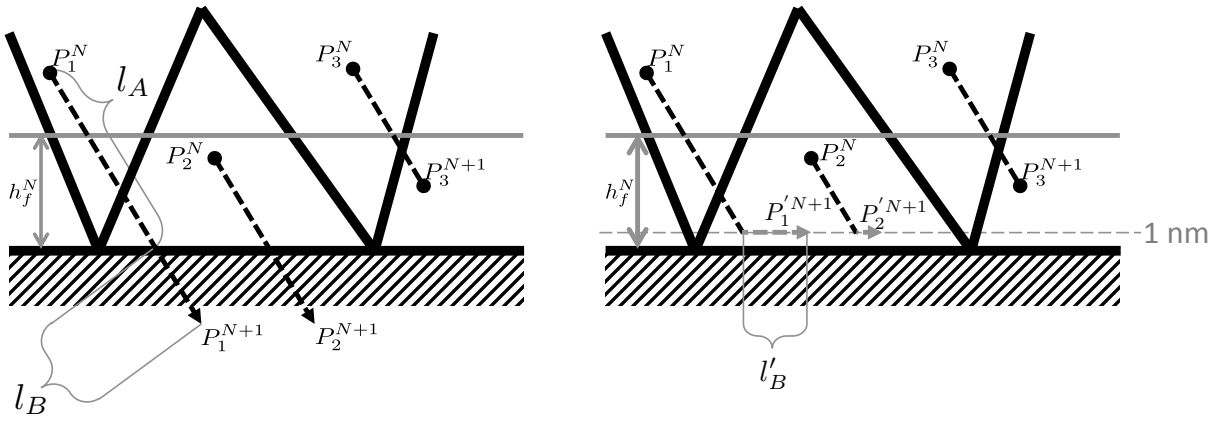

Figure 6.2 : *Illustration of particle treatment in filming regime. Superscript ^{N} stands for the current iteration and $^{N+1}$ for the next one. Left: particle trajectory without wall treatment. Right: particles trajectories with wall treatment.*

6.2.3.b) Eulerian projection

In order to compute the film thickness, the total volume of film particles contained in a control volume is divided by the area of this volume in contact with the wall. The resulting length represents the thickness of the film in the current cell. The underlying assumption of this method is that the liquid totally wets the surface, which is consistent with experimental observations, the low surface tension of the fuel and the low roughness height of prefilmer walls.

In a cell-vertex solver such as AVBP, values are stored at the nodes and the default control volume is bound to the nodes. Therefore a particular operation is necessary to compute the film thickness as illustrated on Fig. 6.3: the 'in-cell' liquid film volume is projected to the surface nodes. This operation is called surface *scattering* where extensive values are distributed over wall surface nodes. It induces a diffusion error on the film thickness but it smoothes geometrical perturbations that could arise from mesh variations.

An example of film thickness calculation *without scattering* is given here in the case of tetrahedra to illustrate the error committed with this method. Calculating the film thickness *without scattering*, *i.e.* by dividing the in-cell liquid volume divided by the face area ($h = V_l/A_{face}$), as depicted on Fig. 6.4 is subject to several problems: first, cells with no wall faces have a zero face area $A_{face} = 0$ and consequently the volume of liquid included in these cells cannot by converted into a thickness h. Second, when the wall cell is not a prism (*i.e.* a normal extrusion of the wall face) but for instance a tetrahedra or a pyramid, the film thickness would be subject to a geometrical deviation, as illustrated on Fig. 6.4. It is possible to estimate the deviation that induces a regular tetrahedron (*i.e.* all edges of same length) compared to a hexahedron, by volume consideration. The approximated film thickness h^{approx} represents the film thickness computed by $h = V_l/A_{face}$ as if the cell was a regular hexahedra and h^{exact} is the exact film thickness that results from the liquid volume inside the tetrahedra (Fig. 6.4). These two film thicknesses are linked by:

$$h^{approx} = h^{exact}\left[1 + \sqrt{\frac{2}{3}}\frac{h^{exact}}{a} - \frac{1}{2}\left(\frac{h^{exact}}{a}\right)^2\right] \tag{6.20}$$

where a stands for the edge length of the tetrahedron. For typical values of a ranging between 0.5 and 1 mm and a film thickness of 100 µm, the approximated film thickness would be overestimated between 7 and 15 %, which is

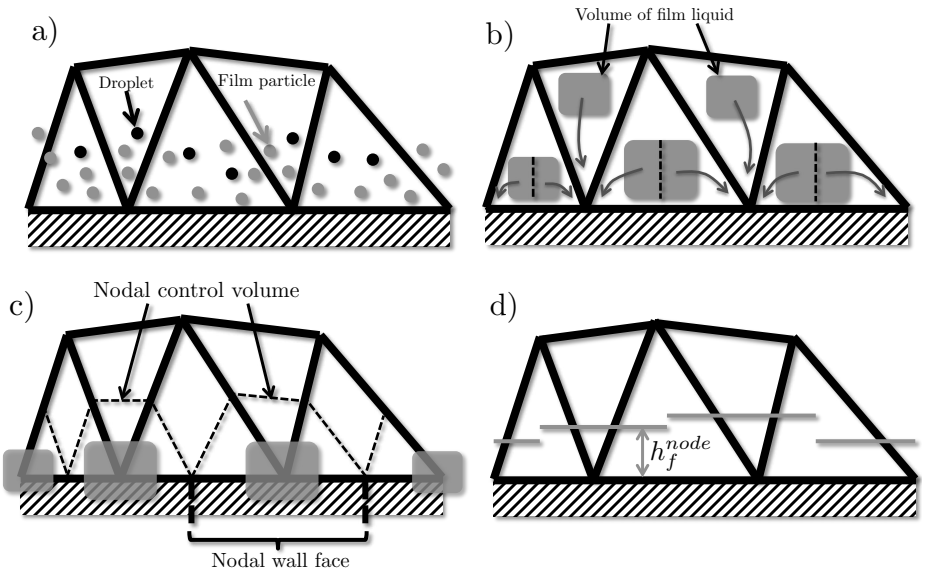

Figure 6.3 : *Illustration of film thickness computation with scattering. a) Only film particles are accounted for the film liquid volume. b) Film liquid volume calculated in a) is equally distributed to surface nodes. c) Film volume at surface node (calculated in b)) is divided by the nodal wall surface. d) Resulting film thickness value is attributed at surface node.*

a significant deviation. This error is linked to the *non scattering* method and therefore *scattering* the liquid volume cancel it.

When the mesh is irregular, *i.e.* made of elements of different size, an additional error arises due to the size ratio. To go further into accuracy estimation, the two methods (with and without scattering) are tested in a 2D case for irregular tetrahedra. The situation is depicted on Fig. 6.5. A cluster of three wall cells (C_1, C_2 and C_3) is examined. Their geometry is characterized by the wall edge (a_1 and a_2) and their edge angle to the wall (θ_1, θ_2, θ_3 and θ_4). It is supposed that the film droplets are regularly distributed on the surface, generating an ideally constant film thickness h_e. The 'in-cell' liquid volume (a surface in 2D) is denoted by S_1, S_2 and S_3. It is proposed here to compute the film thickness with and without scattering and to analyze the deviation. The film thickness in cells C_1 and C_3 without scattering are denoted h_1 and h_3, respectively. The film thickness h_N at the common node of the three cells is computed with scattering. Geometrical considerations lead to the expression of film thicknesses:

$$h_1 = h_e \left[1 - \frac{h_e}{a_1}\left(\frac{1}{\tan\theta_1} + \frac{1}{\tan\theta_2}\right)\right] \tag{6.21a}$$

$$h_3 = h_e \left[1 - \frac{h_e}{a_2}\left(\frac{1}{\tan\theta_3} + \frac{1}{\tan\theta_4}\right)\right] \tag{6.21b}$$

$$h_N = h_e \left[1 + \frac{h_e}{4\,\overline{a_{12}}}\left(\frac{1}{\tan\theta_2} - \frac{1}{\tan\theta_1} + \frac{1}{\tan\theta_3} - \frac{1}{\tan\theta_4}\right)\right] \tag{6.21c}$$

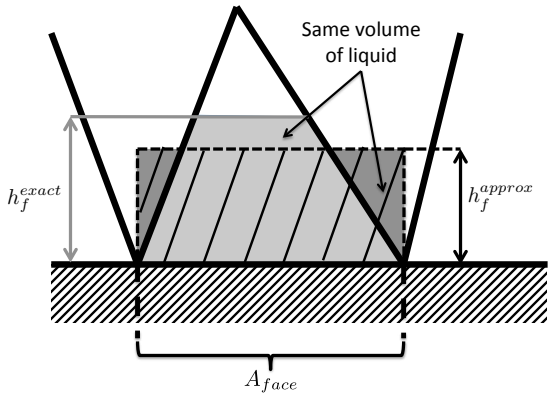

Figure 6.4 : *Error associated to the no-scattering method on a regular mesh*

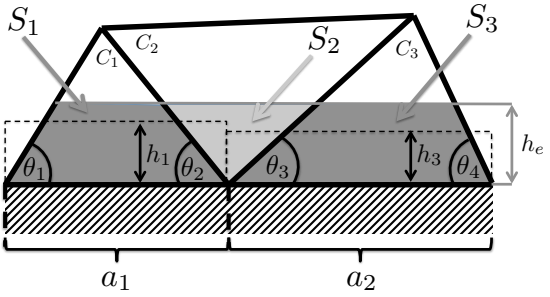

Figure 6.5 : *Error associated to the no-scattering and scattering methods on an irregular mesh*

where $\overline{a_{12}}$ is the arithmetic average of a_1 and a_2. By expressing deviation from the exact thickness $D_i = h_i/h_e - 1$, Eqs. 6.21 lead to:

$$D_1 = -\frac{h_e}{a_1}\left(\frac{1}{\tan\theta_1} + \frac{1}{\tan\theta_2}\right) \tag{6.22a}$$

$$D_3 = -\frac{h_e}{a_2}\left(\frac{1}{\tan\theta_3} + \frac{1}{\tan\theta_4}\right) \tag{6.22b}$$

$$D_N = \frac{h_e}{4\,\overline{a_{12}}}\left(\frac{1}{\tan\theta_2} - \frac{1}{\tan\theta_1} + \frac{1}{\tan\theta_3} - \frac{1}{\tan\theta_4}\right) \tag{6.22c}$$

Eqs. 6.22a and 6.22b show that no-scattering leads to an error proportional to h_e/a_1 while this error is divided by four with scattering (Eq. 6.22c). On top of that, the expression of D_N shows a difference of the angle terms while D_1 and D_3 exhibit a summation. For irregular meshes with a low distortion, it is expected that angles of elements are not too different so that the bracketed term on the right-hand side of Eq. 6.22c may be of second order importance. On the contrary, expression of D_1 and D_3 do not decrease. In order to see the influence of angle difference on D_N, Eq. 6.22c is rewritten as:

$$D_N = f \cdot \frac{h_e}{\overline{a_{12}}} \tag{6.23}$$

where f is a factor of deviation related to the angle difference. An estimation of f is displayed on Fig. 6.6. For clarity purposes, only one angle pair, (θ_1, θ_2), has been investigated and f is doubled to account for the other pair. When the angle difference is about 10%, $f \approx 0.1$. With a ratio $h_e/\overline{a_{12}}$ of 0.2, the total deviation is about 2%.

To conclude, scattering the liquid volume on the surface nodes showed several advantages compared to the no-scattering method.

6.2.3.c) Surface interpolation of gaseous values

In order to determine the mean film velocity (Eq. 6.10), the wall shear stress and the gas pressure gradient are interpolated on the wall surface, at the position of the particle orthogonal projection. This is done in accordance with the thin film hypothesis, that allows to consider only wall nodes to describe the gas flow at film surface. The chosen projector is the inverse distance method presented in section 5.2.2.b).

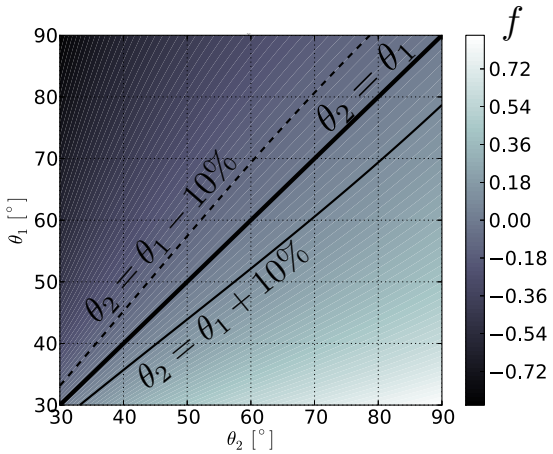

Figure 6.6 : *Error of the scattering approach as a function of cell angle pair*

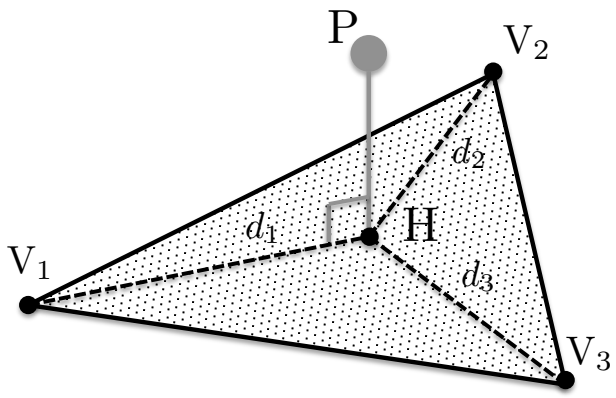

Figure 6.7 : *Sketch of surface projection of particle location. Particle P is orthogonally projected onto the wall face to the point H. Then distances d_i are used to compute geometric weights w_i*

The location of the particle orthogonal projection is depicted on Fig. 6.7, where H coordinates are expressed by:

$$\overrightarrow{HP} = r\overrightarrow{N} \quad \Leftrightarrow \quad x_i^H = x_i^P - r\, n_i \tag{6.24}$$

where r is the normal distance to the wall and $\overrightarrow{N}$ is the face normal expressed as:

$$\overrightarrow{N} = \overrightarrow{V_1V_2} \times \overrightarrow{V_1V_3} \quad \text{and} \quad r = \frac{\overrightarrow{V_1P} \cdot \overrightarrow{N}}{\|\overrightarrow{N}\|^2} \tag{6.25}$$

6.3 Validation on a laminar analytically test case

The aim of this first validation is to verify that the implementation of the model has been achieved correctly, and to prove that the model follows the basic physics that it aims to describe. In the very simple case of a 2D Poiseuille flow

configuration, it is possible to solve analytical the equations that determine the system evolution and specifically the film thickness. Moreover, this configuration allows to quantify the error induced by the 'one way coupling' hypothesis. The geometry is visible on Fig. 6.8. It is a rectangular channel composed of an inlet (left) that provides a gas flow to the system, an outlet (right) for both gas and liquid film, a wall on which a liquid film is formed (bottom), and a no-slip wall (top). Liquid is injected in the system with a very low velocity so that it brings no additional momentum to the gas. The injection point is located in the first wall cell and the droplets are given a velocity normal to the wall so that they impact the wall and becomes film particles.

In the following we will only focus on the steady state of the system, and will focus the analysis on the right part of the geometry close to the outlet, supposing a sufficiently long channel for the validity to reach a steady state motion. In a first part, the exact solution of the problem is derived for reference. In a second part the additional 'one way coupling' hypothesis is made. A comparison with numeric results is made in the third part.

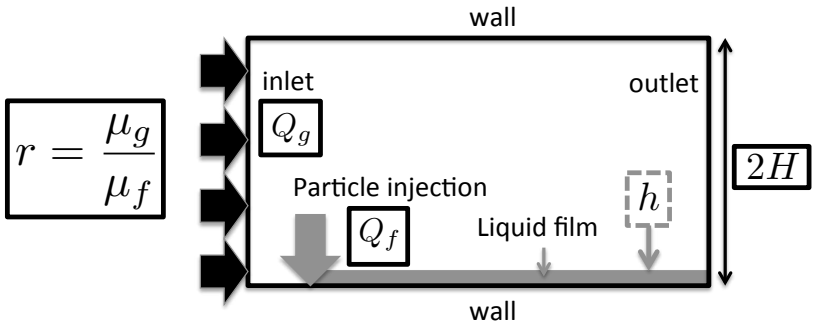

Figure 6.8 : *Sketch of the 2D channel geometry. In this Poiseuille configuration, the liquid film thickness is determined from four (black line framed) dimensional parameters: liquid and gas volume flow rates, channel height and viscosity ratio.*

6.3.1 Derivation of the exact solution

The resolution of the Navier-Stokes equations in this particular case of Poiseuille flow leads to a parabolic shape for both gaseous and film velocity profiles:

$$u(y) = -\frac{K}{2\mu} \cdot y^2 + B \cdot y + A \tag{6.26}$$

where $K = \partial p/\partial x$ is the pressure gradient and is positive in this case: the pressure gradient is the driving force of this flow and balances the losses induced by the shear stress on the wall and at the film/gas interface. A and B are two constants determined by boundary conditions. These boundary conditions are the ones derived in Chapter 3, in addition to the velocity and shear stress continuity at the interface:

$$u_f(y=0) = 0 \tag{6.27a}$$

$$u_f(y=h) = u_g(y=h) \tag{6.27b}$$

$$\tau_{fg} = \mu_f \left.\frac{\partial u_f}{\partial y}\right|_{y=h} = \mu_g \left.\frac{\partial u_g}{\partial y}\right|_{y=h} \tag{6.27c}$$

Velocities then read:

$$u_f(y) = -\frac{K}{2\mu_f}y^2 + \left(\frac{\tau_{fg} + Kh}{\mu_f}\right) y \tag{6.28a}$$

$$u_g(y) = -\frac{K}{2\mu_g}\left[y^2 + (m-1)\,h^2\right] + \left(\frac{\tau_{fg} + Kh}{\mu_g}\right)\left[y + (r-1)\,h\right] \tag{6.28b}$$

where r is the viscosity ratio μ_g/μ_f. On the channel wall top boundary, the velocity is zero:

$$u_g(y = 2H) = 0 \tag{6.29}$$

Combined to Eqs. 6.28, this leads to the definitions of two functions φ_0 and φ_1:

$$\tau_{fg} = KH \cdot \frac{1 - \eta - \frac{\eta^2}{4}(r-1)}{1 + \frac{\eta}{2}(r-1)} \equiv KH \cdot \varphi_0(r,\eta) \tag{6.30a}$$

$$\tau_{fg} + K\,h = KH \cdot \frac{1 + \frac{\eta^2}{4}(r-1)}{1 + \frac{\eta}{2}(r-1)} \equiv KH \cdot \varphi_1(r,\eta) \tag{6.30b}$$

where η is the non-dimensional film thickness:

$$\eta = h/H \tag{6.31}$$

It can be verified that the denominators of φ_0 and φ_1 are never zero: as $\eta \in [0,2]$ and $m \in]0,\infty[$, the product $\eta/2\,(r-1) \in]-1,+\infty[$. The expression of φ_0 is consistent for $\eta = 0$ that leads to $\tau_{lg} = KH = \tau_w$ [294]. When r = 1, setting η to 1 leads to a zero shear stress at the centerline, which is coherent with the symmetric configuration.

In Eqs. 6.28, the pressure gradient K is still unknown. Expressing the gaseous bulk velocity U_0 from the gas velocity profile and assuming that the gas flow is incompressible leads to:

$$Q_g = 2U_0H = \int_h^{2H} u_g(y)\,\mathrm{d}y \tag{6.32}$$

Equation 6.32 leads to the definition of a new function φ_2 expressing the pressure gradient as a function of case parameters:

$$K \equiv \frac{U_0\mu_g}{H^2} \cdot \frac{1}{\varphi_2(r,\eta)} \tag{6.33}$$

where $\varphi_2(r,\eta)$ is a fourth order polynomial fraction:

$$\varphi_2(r,\eta) = \frac{\frac{\eta^2}{4}(r-1) + \eta\,(1-2r) - 1}{1 + \frac{\eta}{2}(r-1)} \cdot \frac{(\eta-2)^2}{12} \tag{6.34}$$

As φ_2 has the same denominator as φ_0 and φ_1, it is always defined. The consistency of φ_2 expression can be verified by setting the film thickness to zero: then φ_2 is equal to $-1/3$ and the pressure gradient reads $K = -3\,U_0\mu_g/H^2$ which is a well-known result for laminar 2D Poiseuille flows. Equation 6.33 states that to obtain a constant gaseous flow rate, the pressure gradient to impose depends on the film thickness. This is a clear proof of a retroaction of the film on the gas, but its influence is expected to be negligible. For the sake of clarity φ_1 and φ_2 dependence on (r,η) will be omitted in the following. Velocities then rewrite:

$$u_f(\kappa) = \frac{U_0 m}{\varphi_2}\left[-\frac{1}{2}\kappa^2 + \varphi_1\,\kappa\right] \qquad \text{for } 0 \le \kappa \le \eta \tag{6.35a}$$

$$u_g(\kappa) = \frac{U_0}{\varphi_2}\left[-\frac{\kappa^2 + (m-1)\,\eta^2}{2} + \varphi_1\,\left[\kappa + (m-1)\,\eta\right]\right] \qquad \text{for } \eta \le \kappa \le 2 \tag{6.35b}$$

where $\kappa = \dfrac{y}{H}$ is the non-dimensional vertical coordinate. Expressing the liquid flow rate:

$$Q_l = \int_0^h u_f(y)\,\mathrm{d}y \tag{6.36}$$

leads to a non-dimensional equation that links the flow rate ratio $Q^* = \dfrac{Q_l}{Q_g}$, the viscosity ratio r and the non-dimensional film thickness η:

$$Q^* = \frac{r}{4\,\varphi_2}\left[-\frac{\eta^3}{3} + \varphi_1\,\eta^2\right] \tag{6.37}$$

In Eq. 6.37, the unknown is the non-dimensional film thickness η and it is solved numerically by a least square method. The non-dimensional film thickness is then expressed in terms of two non-dimensional numbers Q^* and r. Equivalently, the film thickness directly depends on four parameters:

$$\eta = g(Q^*, r) \Leftrightarrow h = f(Q_l, U_0, H, r) \tag{6.38}$$

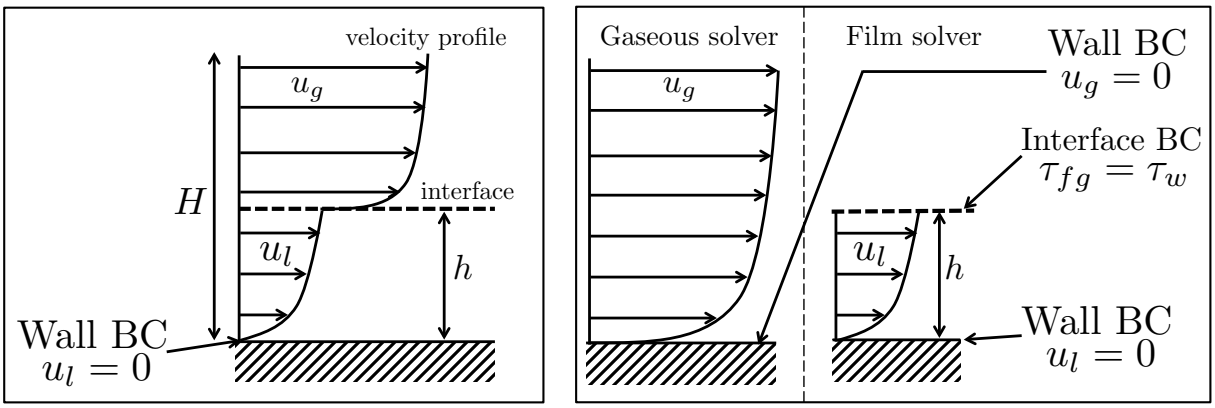

Figure 6.9 : *One way coupling approximation. Left: configuration of the exact solution. Right: configuration of the approximate solution. (Scales are not in accordance with the thin film assumption for the sake of clarity)*

6.3.2 Derivation of the 'one-way coupled' solution

As mentioned in section 3.3.1, neglecting the retroaction of the film on the gas results in three assumptions. First, the blockage due to film volume is supposed to be negligible as the film thickness is much lower than the cavity characteristic length. Second, the interface velocity seen by the gas is considered far lower than the gaseous bulk velocity and thus the interface is stationary. Third the interface is considered as plane, without waves or ripples. These assumption allow to split the film/gas problem into two sub-problems, as illustrated on Fig. 6.9: the gas only sees a modified boundary condition at the wall while the liquid velocity is driven by τ_w. Under these assumptions, the derivation of the film thickness follows the same development as for the exact solution, introducing a new expression for the shear stress at the film/gas interface and the gaseous velocity profile:

- the liquid/gas interface shear stress is considered equal to the gaseous wall shear stress in the absence of liquid:

$$\tau_{fg} = \tau_{w,gas\ only} = KH = 3\frac{U_0\mu_g}{H} \tag{6.39}$$

- the resulting film velocity profile then writes:

$$u_f(\kappa) = 3\,r\,U_0\left[-\frac{1}{2}\kappa^2 + \kappa\,(1+\eta)\right] \tag{6.40}$$

Finally solving for the film thickness is equivalent to solve the following third-order equation:

$$\frac{1}{2}\eta^3 + \frac{3}{4}\eta^2 = \frac{Q^*}{r} \tag{6.41}$$

6.3.3 Computational setup and operating points

The computational domain is 2D channel of length 8 cm and height ($2H$) 8 mm, and is meshed with 41 000 quadrilateral cells, leading to space steps of Δx = 0.2 mm and Δy = 80 µm. The fine vertical mesh resolution allow to accurately resolve the boundary layer of the gaseous flow. The inlet inject air at ambient temperature (300 K) with a bulk velocity U_0 is 0.5 m/s and the outlet is set to atmospheric pressure (1 atm). In these condition, the air has a density ρ_g of 1.2 kg/m^3 and a dynamic viscosity μ_g of 1.8×10^{-5} Pa.s, leading to a gaseous Reynolds number Re_g of 267, ensuring a laminar flow. The liquid has a density ρ_l of 792 kg/m^3 and a dynamic viscosity μ_g of 1.56×10^{-3} Pa.s. The liquid flow rates are chosen to cover a wide range of non-dimensional flow rate Q^*, as summarized in Table 6.1.

Parameter	Case 1	Case 2	Case 3	Case 4	Case 5
Q_l [m^3/s]	3.08×10^{-5}	3.08×10^{-4}	3.08×10^{-3}	3.08×10^{-2}	3.08×10^{-1}
Q^* [-]	10^{-5}	10^{-4}	10^{-3}	10^{-2}	10^{-1}

Table 6.1 : *Dimensional and non-dimensional liquid flow rates*

6.3.4 Results

The third-order polynomials Eqs. 6.37 and 6.41 were solved for a large range of fuel/air flow rate ratio (Q^*). A snapshot of the velocity magnitude inside the channel obtained with AVBP is shown on Fig. 6.10. Results are plotted on Fig. 6.11, where the film thickness calculated with AVBP and the film model is also reported for five cases.

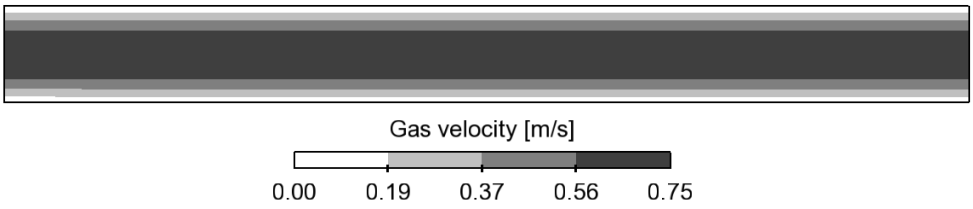

Figure 6.10 : *Gas velocity magnitude in the channel obtained with AVBP*

As expected, AVBP closely matches the results of the approximate solution, proving a correct model implementation. The discrepancy between approximate and exact solutions increases with the fuel/air flow rate ratio mainly because the film gets thicker relatively to the channel height. This induces a growing blockage effect that discredites the 'thin' film hypothesis. However in aeronautical combustors, fuel/air flow rate ratio Q^* lays between 10^{-5} and

10^{-4}, leading to a relative deviation between AVBP and theoretical case below 5%. Moreover as the flow is highly turbulent in real combustors, the wall shear stress increases and, it is expected that for the same Q^* the film thickness will be thinner leading to a less significant blockage effect. Note that the theoretical curve of the approximate solution can exceed the channel height (8 mm) because the film *top* boundary condition is a constant shear stress τ_w independent of the film thickness. This is a consequence of neglecting the blockage effect of the approximate approach.

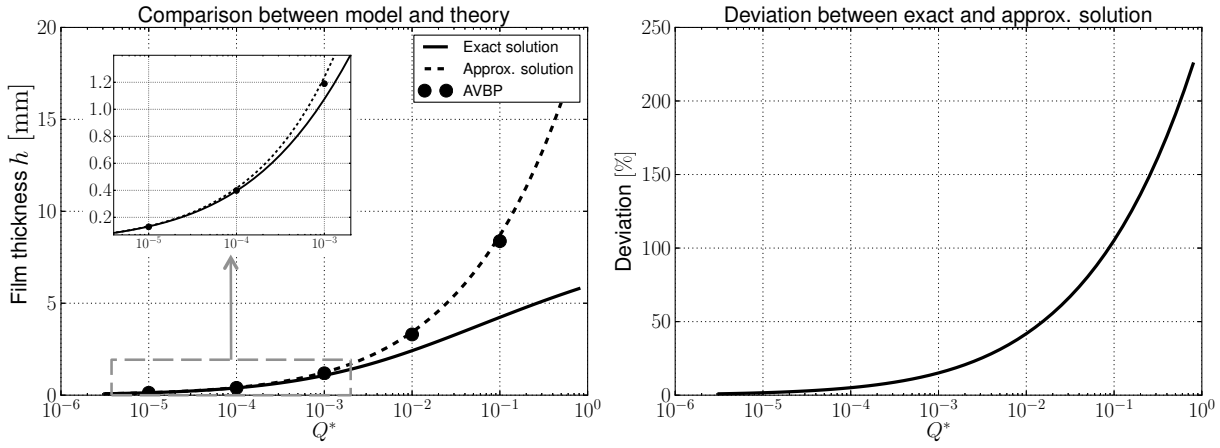

Figure 6.11 : *Left: Film thickness comparison between exact, approximated model and AVBP. Right: deviation induced by the 'one way coupling' approach.*

6.4 Validation in a turbulent lab scale test case

The next step for the model validation is to consider a turbulent flow. The experimental configuration of Ebner *et al.* [72, 73] is chosen, for which experimental measurements of film thickness is available. Ebner *et al.* also simulated the case, using a RANS approach and including apparent film roughness in the coupling with the gas.

6.4.1 Experimental setup

The experiment consists in a rectangular channel of two different sections leading to an accelerated gas flow. The width b is constant (190 mm) while the height varies from 90 mm at the inlet to 30 mm at the outlet. The section restriction is ensured by a nozzle or radius 60 mm which is adjustable in x so that the acceleration point can move upstream and downstream, as illustrated on Fig. 6.12. This particular set-up allows to fix measurement devices at one location and to measure the flow at varying longitudinal locations. Velocity measurement was performed by a high resolution Laser Doppler Velocimetry system (LDV). The film thickness was measured using a non-intrusive optical system called LFDM (for Laser Focus Displacement Meter) with a spatial resolution of about 2 microns [71, 313].

A suction side blower allows an inlet velocity U_0 up to 25 m/s, leading to 75 m/s in the restricted section. The liquid flow rate is express in term of the *film loading* $\Lambda_f = Q_f/b$ with Q_f the film volume flow rate, and varies from 10 to 100 mm^2/s. The experiment is performed with air at atmospheric pressure (998 mbar) and temperature (20°C). The physical properties of the film liquid are listed in Table 6.2.

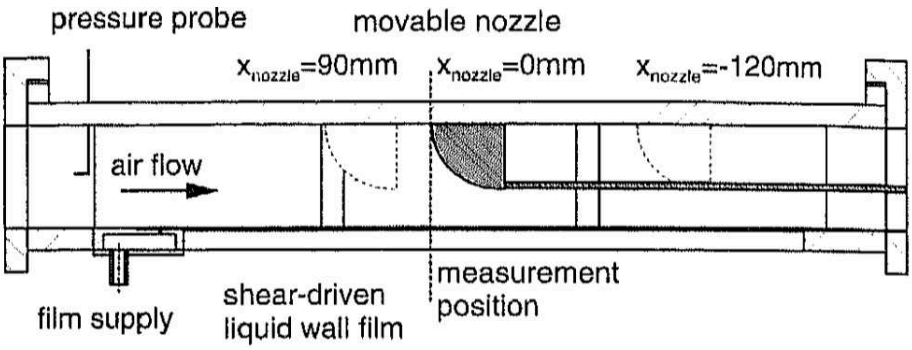

Figure 6.12 : *Sketch of the experiment of Ebner et al. [73]*

Density	Dynamic viscosity	Surface tension
ρ_f = 781 kg/m^3	μ_f = 1.17$\times$10^{-3} Pa.s	σ = 0.026 N/m

Table 6.2 : *Physical properties of the film liquid*

The aim of this experiment was to reproduce aeronautical combustor flow conditions, especially the gas acceleration due to a section reduction that is typically found in airblast atomizers. In their paper, Ebner *et al.* also provided film model inputs, from their simulation. This allows first to apply the film model without simulating the flow (Section 6.4.2) before performing a full simulation with AVPB and the film model (Section 6.4.3).

6.4.2 Validation of film model using given inputs

The wall shear stress and longitudinal pressure gradient delivered by Ebner's *et al.* simulations are plotted on Fig. 6.13. As τ_w and $\partial p/\partial x$ are of the same order of magnitude, it appears that for a thin film ($h \approx 0.5$ mm), the influence of the pressure gradient is negligible compared to the shear stress: ($\tau_w \gg dp/dx\, h$). Mass conservation leads to:

$$u_f\, h = \frac{Q_f}{b} = \Lambda_f \tag{6.42}$$

Then, when the pressure gradient is neglected, the film thickness is easy to determine by combining Eqs. (6.10) and (6.42):

$$h = \sqrt{\frac{2\,\mu_f\,\Lambda_f}{\tau_w}} \tag{6.43}$$

Equation 6.43 states that the film thickness is inversely proportional to the square root of the wall shear stress. In simple configurations where wall shear correlations are available, this means that the film thickness can be estimated, providing that pressure gradient is negligible and above all, providing that the one-way coupling hypothesis holds. In this study, as the pressure gradient is not negligible, Eq. 6.42 is solved numerically by a least square method.

Figure 6.14 displays the results of the film model fed with Ebner's inputs. The trend of the accelerated film thickness is well recovered, as well as the absolute values. The agreement is very good between Ebner *et al.* [73] simulation and the present film model. This implies that both film models follow the same behaviour although Ebner's model expresses momentum conservation with a differential equation while the present film model uses an algebraic mean film velocity. The maximum deviation between models and experiment (30%) appears downstream the nozzle for $0.05 < x < 0.1$. Ebner *et al.* explain it by the neglected inertia in the film model: after being accelerated

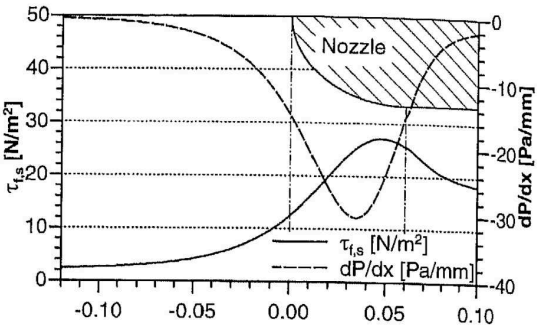

Figure 6.13 : *Wall shear stress and longitudinal pressure gradient profiles in the acceleration region, from [73]*

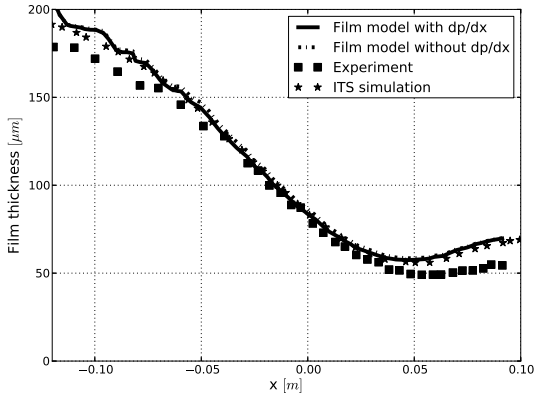

Figure 6.14 : *Comparison of film model only, with and without the pressure gradient (U_0 = 20 m/s and Λ_f = 0.4 cm^2/s)*

to a higher velocity, the film tends to keep flowing at the same velocity because of its inertia. One of the film model assumption is an instantaneous equilibrium with the exterior, leading in the present case to an unrealistic deceleration (*i.e.* a too sharp increase of film thickness). Finally, Fig. 6.14 shows that the pressure gradient is negligible in this configuration.

6.4.3 Validation of the film model coupled to the flow solver

A Large Eddy Simulation of the above geometry has been performed with AVBP and the film model developed in the previous chapter.

6.4.3.a) Computational details

Two unstructured meshes (ITS1 and ITS2) were used to assess the impact of the domain spatial resolution onto the film thickness. They contain approximately 2 and 26 millions of tetrahedral cells. The characteristic mesh size in the acceleration region is 1 mm for ITS1, and 0.3 mm in the wall region and 0.5 mm in the center zone for ITS2. A mid-plane cross section of the meshes through the acceleration zone is shown on Fig. 6.15. In order to have a statistically established flow in the acceleration zone, the first part of the channel is 0.9 meter long, equivalent to ten times the channel height. The width is 80 mm. Turbulence is injected at the inlet with a level of 10% following [326, 351].

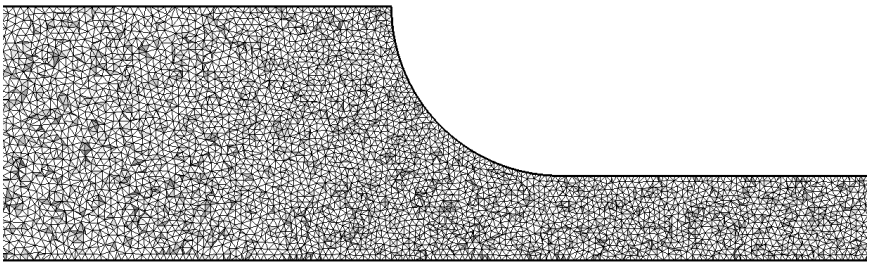

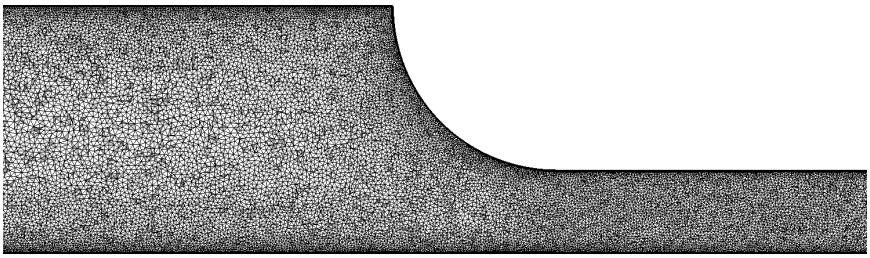

Figure 6.15 : *Mid-plane cut of the mesh zoomed in the acceleration region. Top: ITS1. Bottom: ITS2.*

To avoid 3D side effects as well as a transverse confining of the flow, lateral boundary condition are set periodic. The outlet and the horizontal walls are modeled by a non reflective pressure outflow condition and adiabatic law of the wall [312], respectively. Special care as put on set the first grid point, placed in the logarithmic zone of the boundary layer. However due to flow acceleration, this constraint is difficult to fulfill *a priori*. Gaseous phase equations are solved via the second-order Lax-Wendroff scheme. Turbulent viscosity is computed from the Dynamic Smagorinsky subgrid scale model, and a slight amount of artificial viscosity is added using the Colin sensor [54] (second and fourth order coefficients are respectively 0 and 0.005 for ITS1, and 0.001 and 0.005 for ITS2). Air is injected in the same condition as Ebner *et al.* experiment with a bulk velocity of 20 m/s. The outlet is imposed an atmospheric pressure. The inlet and outlet Reynolds numbers are both equal to 300 000.

6.4.3.b) Gaseous results

ITS1 and ITS2 simulations have been run for 7 and 0.25 seconds of physical time, respectively. Time average has been computed with an approximate sampling frequency of 17.5 and 97 kHz. Figure 6.16 displays a snapshot of the velocity magnitude on mid-plane cut for ITS2. Velocity fluctuations are visible upstream the nozzle and decrease downstream. A recirculation zone is located in front of the top part of the nozzle.

Figure 6.17 presents several velocity profiles in the convergent flow region for the coarse and fine meshes. The mesh size influence can be noticed by sharper velocity gradients with the fine mesh. Far upstream the nozzle, the 'turbulent-like' channel velocity profile is clearly visible on the fine mesh. On the contrary, the profile is closer to a laminar flow (parabolic profile) on the coarse mesh. The recirculation zone is visible on both meshes. Directly downstream the nozzle, the flow is not symmetric and exhibits a larger velocity in the top part of the channel, due to the amount of gas coming from the top part of the nozzle. However the flow symmetry is recovered approximately three diameters downstream.

To illustrate the quality of the LES performed here, the Pope criterion [274] is shown in Fig. 6.17. This criterion estimates the amount of turbulent kinetic energy that is explicitly resolved by the solver, the rest being modeled by the subgrid scale model:

$$C_{Pope} = \frac{k_{res}}{k_{res} + k_{sgs}} \tag{6.44}$$

where k_{res} is the resolved turbulent kinetic energy, calculated via:

$$k_{res} = \frac{1}{2}\left(u_{rms} + v_{rms} + w_{rms}\right) \tag{6.45}$$

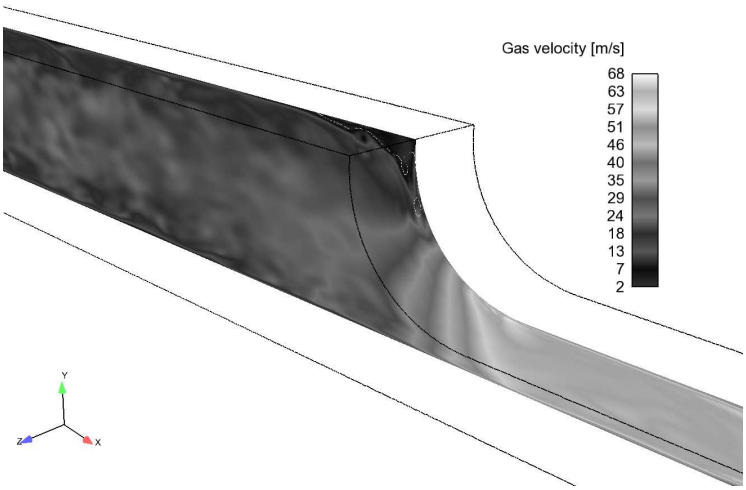

Figure 6.16 : *Gas velocity magnitude on a mid-plane cut superimposed with a white iso-contour of zero axial velocity for ITS2*

Estimating k_{res} thus requires to know the RMS values and therefore estimating the Pope criterion is limited averaged fields. The subgrid scale turbulent kinetic energy k_{sgs} is estimated by Sagaut [302] as :

$$k_{sgs} = \left(\frac{\nu_t}{C_s \, \Delta} \right)^2 \tag{6.46}$$

where C_s is the Smagorinsky constant and Δ the LES filter size. In the case of implicit filter LES, Δ is equal to the cube root of the local cell volume.

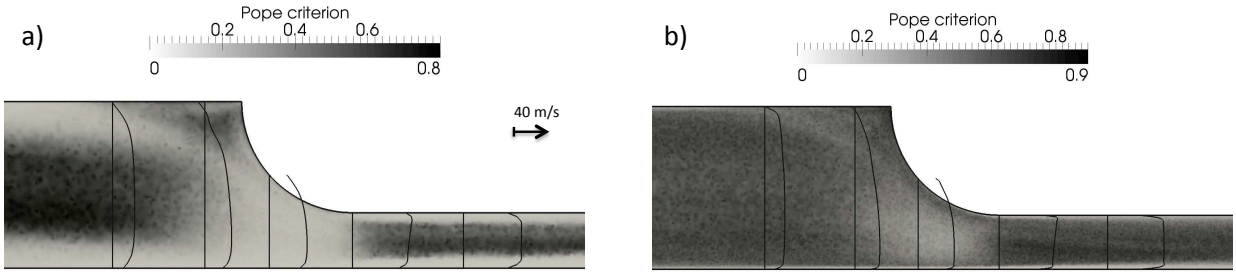

Figure 6.17 : *Longitudinal velocity profile and Pope criterion from a mean solution. Left: ITS1. Right: ITS2.*

Pope [274] states that a LES can be considered of good quality when 80% of the turbulent kinetic energy is resolved. The confrontation of this statement with Fig. 6.17 indicates that turbulence in ITS1 is not well resolved close to the wall and in the whole acceleration region. ITS2 presents a more homogeneous distribution of the Pope criterion, and its average value is close to the value of 80% of the resolved turbulent kinetic energy.

The distribution of turbulent-to-laminar viscosity ratio is another estimator of the quality of the LES performed. As the ratio is close to one, it means that the energy is equally dissipated between laminar viscosity (resolved energy dissipation) and turbulent viscosity (modeled energy dissipation). As the ratio increases it means that more energy

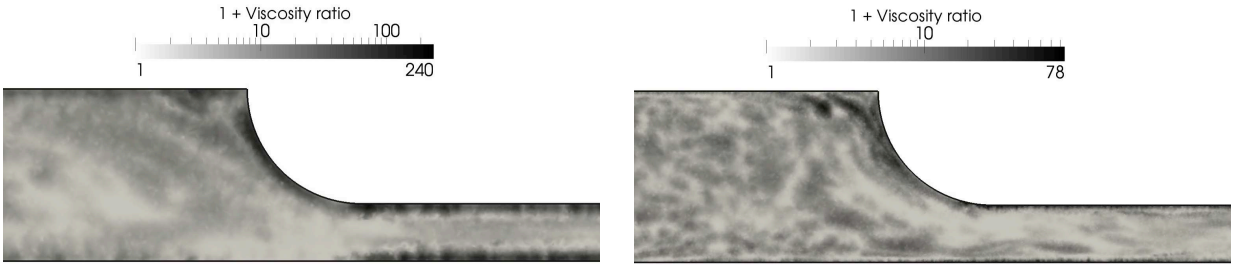

Figure 6.18 : *Ratio of turbulent to laminar viscosity from an instantaneous solution in a mid-plane cut of ITS1 (left) and ITS2 (right)*

dissipation is modeled and thus subject to model limitations. To the contrary a ratio decreasing to zero indicates that most of the energy is dissipated by laminar viscosity. The limit behavior is a DNS where there is no turbulent viscosity model.

The turbulent-to-laminar viscosity ratio is depicted on Fig. 6.18, with logarithmic scale. The coarse mesh presents a global ratio of 50 which is acceptable. In the near wall region, this ratio increases above 100 and the mesh low resolution in this region is confirmed. The fine mesh shows a global ratio of the order of magnitude of ten, meaning a fairly well-resolved LES. As for the coarse mesh, the near wall region suffers from higher modeled energy dissipation.

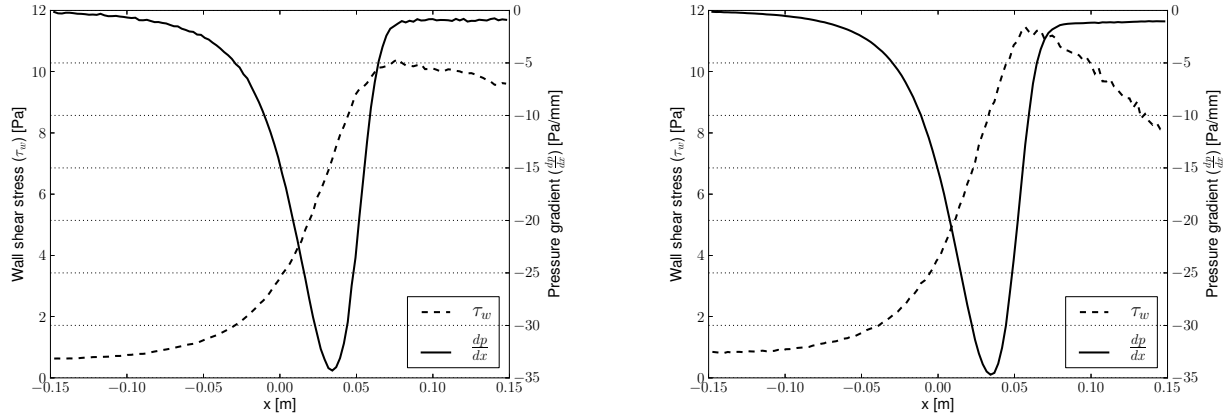

Figure 6.19 : *Longitudinal profile of the wall shear stress and pressure gradient computed by AVBP on ITS1 (left) and ITS2 (right)*

Figure 6.19 plot the profile of the wall shear stress at the bottom wall and the centerline pressure gradient, in the acceleration region. Despite the large difference of mesh resolution between both cases, the pressure and wall shear stress are sensibly equal. The main difference is the wall shear stress peak (10 versus 11.5 Pa) and its behavior directly downstream the nozzle. The coarse mesh records a lower decrease (to 9 Pa) while the wall shear stress computed onto the fine mesh reaches 8 Pa. Comparison with Fig. 6.13 shows that AVBP delivers the same pressure gradient as in [73]. Wall shear stresses in the upstream channel are comparable, approximately equal to 1 Pa. In the convergent zone, although the trend is similar in both cases, AVBP predicts a very low peak value compared to [73] (25 Pa). As the wall shear stress is the predominant effect for the film motion in this configuration (seen in subsection

6.4.2), an under-prediction of the wall shear stress leads to an under-prediction of the film mean velocity that, in turn, generates an over-prediction of the film thickness.

6.4.3.c) Steady film thickness from frozen gas simulation

Due to the timescale separation between the gas and the film, and in accordance with the 'one-way' coupling, the steady state of the film flow (*i.e.* a stable in time film thickness) is reached using a frozen gas time-averaged distribution as described in the previous chapter.

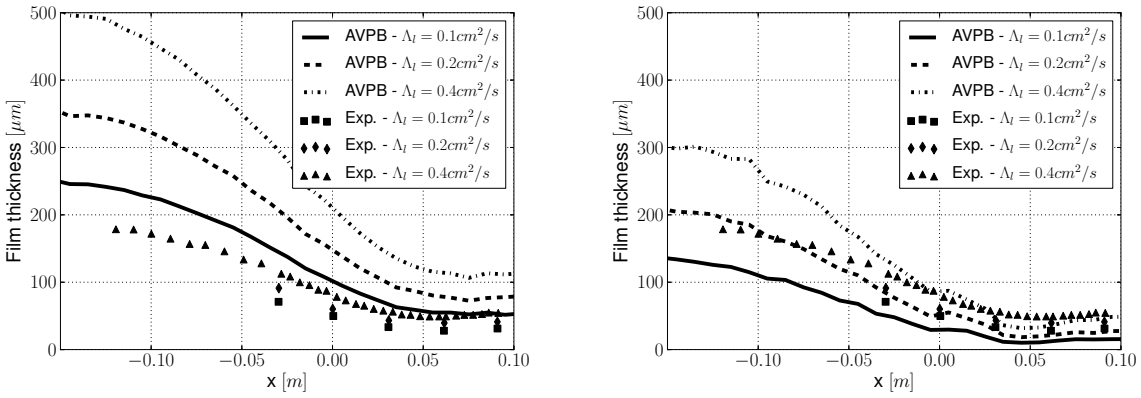

Figure 6.20 : *Comparison between AVBP and measurements with ITS1 (left) and ITS2 (right)*

Figure 6.20 compares AVBP and experimental film thickness. Both meshes show a good trend, *i.e.* a decreasing film thickness when the gas is accelerated. However, the quantitative comparison presents a significant deviation between the simulations and the experiment, especially for large liquid flow rates. The deviation is larger for the coarse mesh with between 150% and 230% in the upstream channel and $\approx 50\%$ in the downstream channel. The fine mesh presents a deviation of $\approx 100\%$ and 50% in the upstream and downstream channel respectively.

6.5 Conclusion

As a conclusion, the presented film model has proven to be well incorporated within the Lagrangian module of AVBP. In the laminar test case, it provides precisely the film thickness predicted by theory. However in turbulent experimental test cases, the model appears to significantly deviates from the measurements. This is explained in the first place by the difficulty to accurately predict the wall shear stress with the law-of-the-wall approach in LES of complex geometry. It was seen that inputing a shear stress computed by a RANS flow solver led to better results. Secondly, the 'one-way coupling' hypothesis have shown its limits and Ebner *et al.* [73] have proposed a way to model a momentum retro coupling from the film to the gas without resolving the film surface. This model implies a differential expression of the law-of-the-wall and it is expected to increase CPU overheads. From a numerical point of view, the strongly located essence of thin film configuration generates an extreme load imbalance that diminishes the overall performances of the code. Finally, in the context of aeronautical combustion chamber, heat transfers may be considered. They have been neglected at the beginning because they do not dramatically modifies the film dynamics. Nevertheless, film evaporation can provide gaseous fuel in the prefilming region of the combustor. It may whether shift the main flame upstream, or create a diffusion flame above the film surface.

To conclude, the film model improvements road map could be the following:

- Enhance film dynamics estimation by developing a retro coupling from the film to the gas flow solver. This implies to implement a differential formulation of the law of the wall in the flow solver, stable in the LES framework. A numerical communication is necessary to input the film thickness from the film model to the differential formulation.
- Imbed a multi-constraints partitioning tool with regard to the Lagrangian phase, with 'strong' or 'weak' option (see Appendix C). The first step would be to ensure a static load balancing, and it is currently underway at CERFACS. Nevertheless, in a near future, dynamic load balancing will be the standard and it will be necessary to develop this method.
- Develop an evaporation model. The first step would be to derive a simple evaporation model based on film temperature estimated from droplet temperature. To go further in details, it would be necessary to compute the real film temperature. This would require to account for heat transfers and thermal dynamics within the film. The tedious point is the necessary wall temperature knowledge for proper estimations, that implies to also account for heat conduction within the combustor walls.

Chapter 7

Modeling prefilming airblast atomization

This chapter details the development of a primary atomization model for prefilming airlbast atomizers. It is called PAMELA for "**P**rimary **A**tomization **M**odel for pr**E**filming airb**LA**st injectors" and aims at predicting the drop size probability density function. The model is developed on the basis of experimental results obtained by Gepperth *et al.* [102, 103, 104], in a configuration representative of airblast atomization.

From the experimental observations of Gepperth *et al.* , it is shown that the drop size probability density function is always well fitted by a Rosin-Rammler function, under their experimental conditions. Following these observations, the model derives a parametrization of the Rosin-Rammler constants based on influencing physical quantities (gaseous velocity, surface tension and atomizing edge thickness) that leads to good predictions in a large range of conditions. This parametrization relies on the description of a spanwise liquid instability (Rayleigh-Taylor instability) from the work of Hong [151] and Varga [353] for coaxial jets. First, a *global* approach, based on the bulk velocity of the gas, is presented and compared to the experiment. Then a *local* approach is derived, based on experimental observation and an estimation of the characteristic time scale. Both local and global approaches have the same expression but use different parameter values determined from experimental fitting.

The sensitivity of the model is tested with regards to the gaseous velocity as well as model parameters. The model is also confronted to an *ad-hoc* correlation [104]. Finally its implementation into the AVBP solver is detailed.

7.1 Reference experiment

The experimental device was designed and manufactured at the Institut für Thermische Strömungmaschinen (ITS) from the Karlsruhe Institute of Technology (KIT). Details may be found in [102, 104]. It is dedicated to the study of the filming and primary breakup processes in operating conditions close to airblast atomizers in real aeroengines.

7.1.1 Geometry and diagnostic

The geometry consists in a planar wing-shaped prefilmer (Fig. 7.1), through which liquid is injected via fifty equidistantly distributed holes. Due to high gas velocity, the injected liquid forms a thin film homogeneously wetting the prefilmer, and is finally atomized at the prefilmer edge. No film stripping is observed upstream the atomizing edge. Measurements combine particle and ligament tracking velocimetry, and blacklight illumination (shadowgraphy) showing the fragmentation mechanism. More details may be found in [102]. All experiments have been performed at ambient conditions, summarized in Table 7.2. The air and liquid flow rates were varied, and two dif-

ferent liquids were tested to measure the impact of their transport properties on the film and atomization behaviours: (i) Shellsol D70, referred to as *ShellsolD70* or simply *D70* in the following and (ii) a volume mixture of 50% of Propanediol and 50% of water, referred to as *Propanediol* or simply *Prop.* in the following.

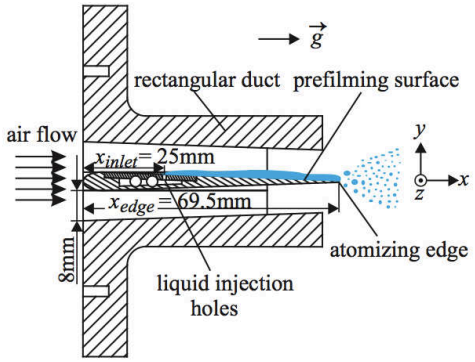

Figure 7.1 : *Schematics of the KIT-ITS experiment, from [102]*

Mean air velocity	U_0	$30 - 70$ m/s
Air temperature	T	298 K
Air density	ρ_g	1.2 kg/m^3
Air kinematic viscosity	ν_g	$1.5 \cdot 10^{-5}$ m^2/s
Liquid density	ρ_l	770*, 1008** kg/m^3
Liquid surface tension	σ	0.0275*, 0.0466** kg/s^2
Liquid flow rate	Λ_f	$12.5 - 75$ mm^2/s
Atomizing edge thickness	h_a	1, 2.5 mm

Figure 7.2 : *Operating conditions, from [102]. *Shellsol D70, **Propanediol*

7.1.2 Observation of the primary atomization process at the atomizing edge

After injection, the liquid homogeneously wet the prefilmer and flows down in a sheared film to the atomizing edge, where it accumulates before atomization. This accumulation acts as a liquid reservoir feeding a atomized process described by Müller *et al.* [243] and illustrated on Fig. 7.3: first, aerodynamic stresses create a transverse wave that deforms the liquid surface. The crest of the wave is blown by the airstream, leading to a bubble framed by a thicker rim of liquid. The bubble-like part of the structure bursts following a bag breakup process and generates fine droplets. The rim is stretched and splits into two elongated ligaments that fragment into larger drops.

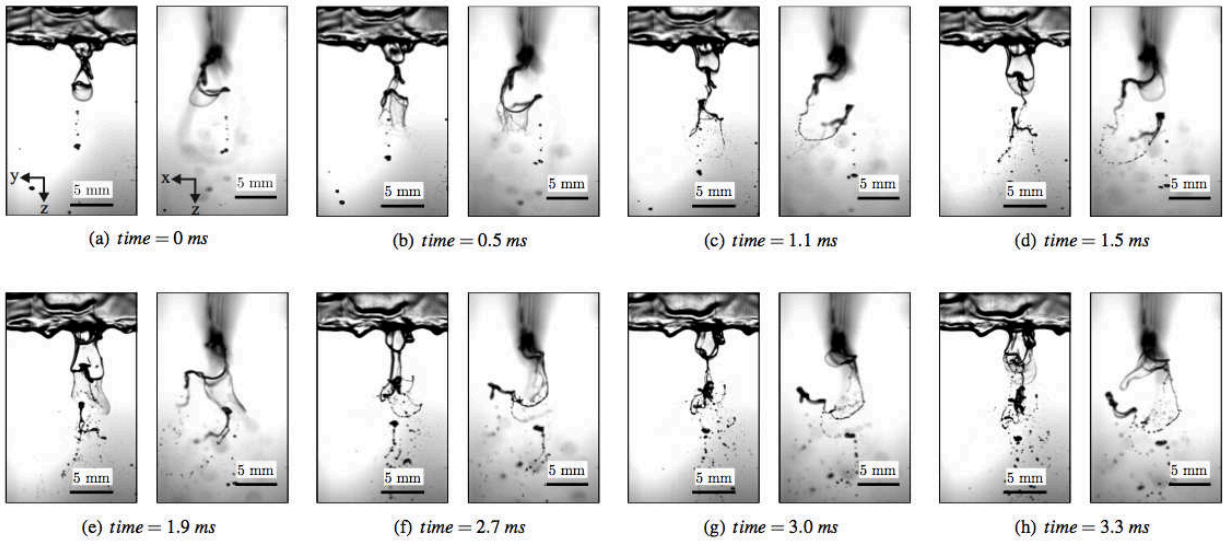

Figure 7.3 : *Time series of the accumulation breakup phenomenon, paired by top and side view (U_0 = 20 m/s, Λ_f = 25 mm^2/s, h_a = 1 mm), from [103]. The gas flows from the top to the bottom.*

Gepperth *et al.* [104] identified three important parameters controlling the drop size distribution after atomization:

- The atomizing edge thickness h_a that partly controls the volume of accumulated liquid
- The surface tension of the liquid σ, that influences the dimensions of the liquid accumulation as well as the ligaments size
- The momentum flux of the gas $M = \rho_g u_g^2$, that control the quantity of momentum transferred from the gas to the liquid.

Under the investigated conditions, the fragmentation of the liquid accumulation is not correlated to the film flow: the frequency of incoming film waves is one order of magnitude lower than the frequency of the atomization process, implying different time scales. This means that the film thickness and film loading (or film velocity) have a weak influence on the spray topology.

Shadowgraphy and high speed visualization allowed to measure diameter in the primary atomization zone. From this set of data, a droplet number and volume probability density function is established for different gas velocities, liquid properties and atomizing edge thicknesses. For each operating condition, the resulting PDF is compared to the Rosin-Rammler functions [14]:

$$F_0(d) = \int_0^d f_0(u)\mathrm{d}u = 1 - \exp\left[-\left(\frac{d}{m}\right)^q\right] \tag{7.1}$$

$$f_3(d) = d^3 f_0(d) \tag{7.2}$$

where $F_0(d)$ and $f_0(d)$ are the Number Cumulative Distribution Function and Number Probability Density Function (NPDF) respectively, and $f_3(d)$ is the Volume Probability Density Function (VPDF) of the spray. Rosin-Rammler functions present the advantage of having only two parameters: the *scale* m and the *shape* q parameters. These parameters have been fitted versus experimental data.

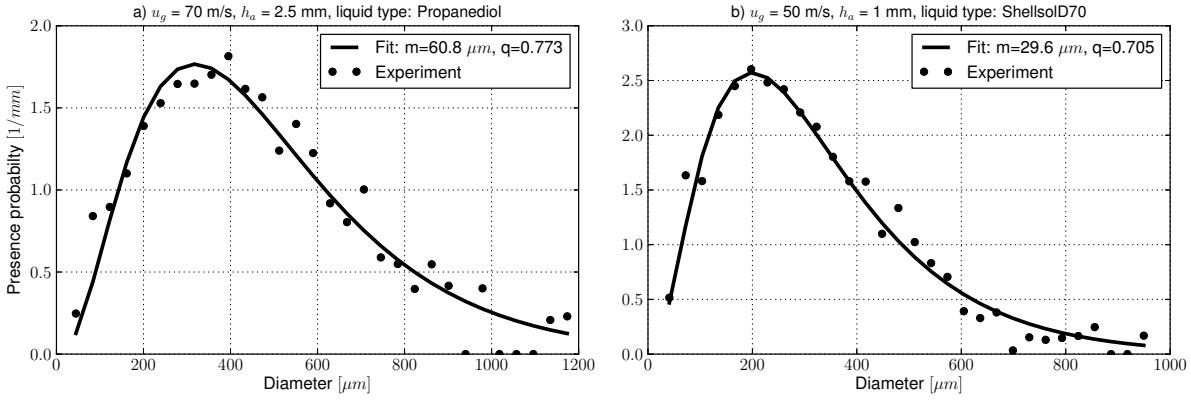

Figure 7.4 : *Experimental VPDF for two different operating conditions, fitted by numeric Rosin-Rammler functions (Eq. 7.1)*

An example is given on Fig. 7.4 for two cases. In the first case shown, m = 60.8 µm and q = 0.773 while in the second case m = 29.6 µm and q = 0.705. Therefore, the shape of the Rosin-Rammler function seems always adapted

and the parameters change with each operating point. It is then necessary to derive expressions for m and q using the influencing flow quantities. This is the objective of this chapter. First the mechanisms of atomization are described and analyzed as is done in the literature. From this analysis, expression for m and q are proposed.

Note that in the context of dilute sprays encountered in aeronautical combustors, PAMELA only provides the spray PDF downstream the accumulation, and dense regime phenomena (mainly coalescence due to particles collisions) are neglected. Moreover no description of the phenomena occurring in the liquid accumulation is considered in this work: liquid structure acceleration, Rayleigh-Taylor instability, bag breakup or ligament dynamics are not resolved.

7.2 Fragmentation mechanism at the atomizing edge

Atomization is described following the approach of Hong [151] and Varga [353] introduced below.

7.2.1 Summary of Hong & Varga's approach

It is widely admitted [23, 151, 219, 280] that primary breakup is the result of several sequential instabilities: a Kelvin-Helmholtz 2D instability arises at the liquid surface, and the deformed surface undergoes a secondary instability that generates a 3D pattern. This pattern degenerates into ligaments that are stretched and fragmented into droplets. Hong [151] and Varga [353] suggested that the secondary instability was triggered by the *streamwise* acceleration of the 2D wave crest, due to aerodynamic drag (see Fig. 4.7).

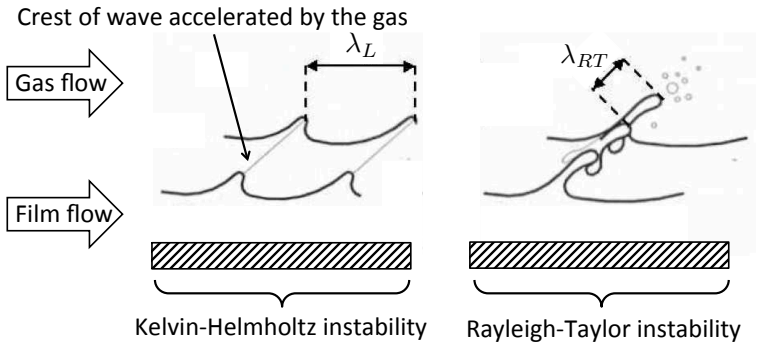

Figure 7.5 : *Illustration of 3D structures arising from a Kelvin-Helmholtz instability, in a thick film configuration, adapted from [152]*

This results in a Rayleigh-Taylor instability whose most amplified wavelength is expressed as:

$$\lambda_{RT} = 2\pi\sqrt{\frac{3\sigma}{\rho_l a}} \tag{7.3}$$

where a stands for the crest acceleration, expressed as the ratio of the drag force F by the mass of the wave m:

$$F = \frac{1}{2} C_d \, A_f \, \rho_g (U_0 - u_c)^2 \tag{7.4}$$

$$m = A_f \, b \, \rho_l \tag{7.5}$$

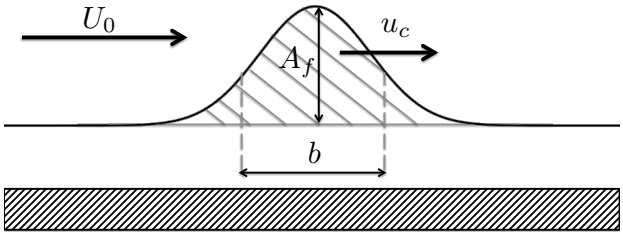

Figure 7.6 : *Sketch of the wave accelerated by the gas*

where C_d is the drag coefficient of the wave (considered equal to 1 in the following), A_f is the wave front area and b the thickness of the wave, as depicted on Fig. 7.6. U_0 is the mean gas velocity and u_c the crest velocity expressed by Dimotakis *et al.* [67] and Raynal *et al.* [280] as:

$$u_c = \frac{\sqrt{\rho_l}\, u_l + \sqrt{\rho_g}\, U_0}{\sqrt{\rho_l} + \sqrt{\rho_g}} \tag{7.6}$$

The crest acceleration a then writes:

$$a = \frac{F}{m} = \frac{1}{2}\frac{C_d}{b}\frac{\rho_g}{\rho_l}(U_0 - u_c)^2 \tag{7.7}$$

Finally Eq. 7.3 results in:

$$\lambda_{RT} = 2\pi\sqrt{\frac{6\, b\, \sigma}{C_d \rho_g (U_0 - u_c)^2}} \tag{7.8}$$

In the case of a liquid sheet or axial jet, b is expressed as a fraction of the Kelvin-Helmholtz wavelength λ_L by [219, 281] as:

$$\lambda_L = C_{axi}\sqrt{\frac{\rho_l}{\rho_g}}\,\delta_g \tag{7.9}$$

where C_{axi} is constant between 1 and 2 and δ_g is the gaseous vorticity thickness (see Eq. 4.37 in Section 4.4.3).

The Sauter Mean Diameter was found to be proportional to the transverse wavelength λ_{RT} in planar liquid sheet [23, 280] and axial jet [151, 219] atomization.

7.2.2 Application to breakup at an atomizing edge

As already described, liquid accumulates at the atomizing edge before atomizing. A behaviour similar to the mechanism described by Hong & Varga is assumed in the present case of breakup of the accumulated liquid, justified by the observation of transverse waves and longitudinal ligaments.

To express λ_{RT} with the Hong & Varga's approach, it is necessary to estimate the amount of liquid accelerated by the gas, represented by b in Eq. 7.8. Contrary to the liquid sheet and coaxial configurations, b is not linked to a Kelvin-Helmholtz instability: when calculating λ_L in Gepperth *et al.* experiment (assuming $\delta_g \approx 100$ µm), one obtains $\lambda_L \approx 4$ mm. As the longitudinal dimension of the liquid accumulation is below or equal to 1 mm, the Kelvin-Helmholtz instability cannot arise on its surface. This means that waves arising on the liquid accumulation surface do not derive from a Kelvin-Helmholtz instability and therefore the parameter b (the amount of liquid subject to the gas acceleration) cannot be expressed as a fraction of λ_L.

Therefore, it is assumed that b is proportional to the atomizing edge thickness h_a independently of the gas flow, for two reasons: (i) the length h_a scales the size of the liquid accumulation and (ii) it was observed experimentally that h_a was an influent parameter of the drop size distribution. Therefore b is expressed as:

$$b = C_A\, h_a \tag{7.10}$$

where C_A is a constant between 0 and 1. Injecting Eq. 7.10 into Eq. 7.8 leads to an expression of the most amplified transverse wavelength for a prefilmer of thickness h_a:

$$\lambda_{RT}^{h_a} = 2\pi\sqrt{\frac{6\, C_A\, h_a\, \sigma}{C_d\, \rho_g (U_0 - u_c)^2}} \tag{7.11}$$

As the accumulated liquid does not move, the liquid velocity is considered negligible compared to the gas velocity ($u_l \ll U_0$) and the term $(U_0 - u_c)$ reduces to:

$$U_0 - u_c = U_0 \frac{\sqrt{\rho_l}}{\sqrt{\rho_l} + \sqrt{\rho_g}} \equiv U_0\, r_\rho \tag{7.12}$$

where r_ρ is a dimensionless parameter that represents the liquid/gas density ratio. Finally Eq. 7.11 simplifies to:

$$\lambda_{RT}^{h_a} \;=\; \frac{2\pi}{r_\rho\, U_0}\sqrt{\frac{6\, C_A\, h_a\, \sigma}{C_d\, \rho_g}} \;=\; \frac{2\pi}{U_0}\sqrt{\frac{6\, C_A\, h_a\, \sigma}{C_d}}\left(\frac{1}{\sqrt{\rho_g}} + \frac{1}{\sqrt{\rho_l}}\right) \tag{7.13}$$

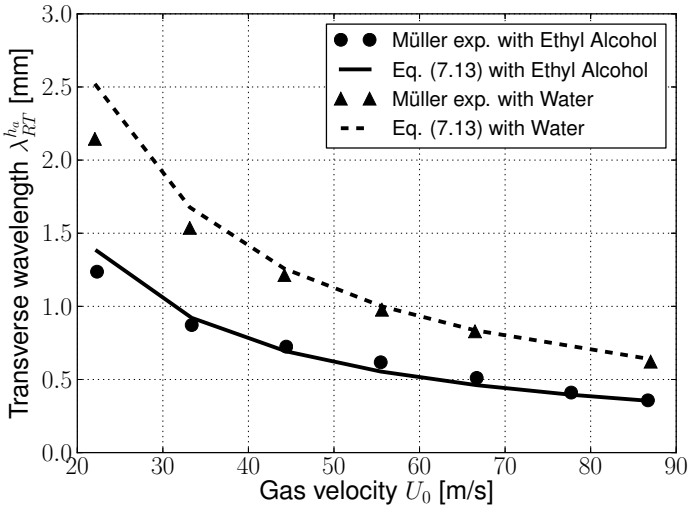

Figure 7.7 : *Comparison of experimental and predicted transverse wavelength from Eq. 7.13 versus gas velocity for two different liquids*

The constant C_A, that estimates the size of liquid accumulated volume, is determined from the experimental results of Müller *et al.* [243] who provided a measurement of the transverse wavelength in a similar configuration as the one of Gepperth *et al.* , with different gas velocities and liquid properties, and an atomizing edge thickness of 0.5 mm. Fitting C_A from Ethyl Alcohol measurements leads to $C_A \approx 0.801$. Results are reported on Fig. 7.7,

showing that Eq. 7.13 describes the correct dependence with U_0. Keeping this value of C_A and applying Eq. 7.13 to water gives good results, demonstrating that C_A is little dependent on liquid properties.

By normalizing Eq. 7.13 with h_a, one may express the dimensionless transverse wavelength as:

$$\frac{\lambda_{RT}^{h_a}}{h_a} = \frac{K}{\sqrt{\mathrm{We}_{h_a}}} \tag{7.14}$$

where K is a non-dimensional constant and We_{h_a} the Weber number based on the atomizing edge thickness:

$$K = 4\pi\sqrt{\frac{3\,C_A}{2\,C_d}} \tag{7.15a}$$

$$\mathrm{We}_{h_a} = \frac{\rho_g\, h_a\, (r_\rho\, U_0)^2}{\sigma} \tag{7.15b}$$

Figure 7.8 displays the D_{32} measured by Gepperth *et al.* [102] experiment normalized by the atomizing edge thickness h_a versus $1/\sqrt{\mathrm{We}_{h_a}}$.

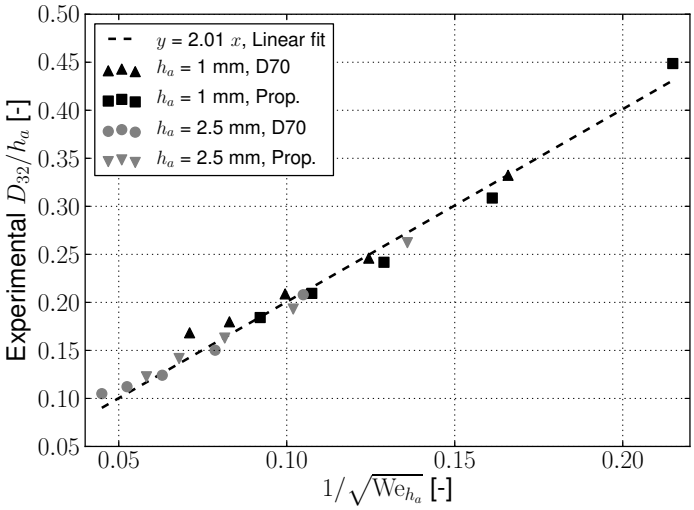

Figure 7.8 : *Experimental D_{32} normalized by h_a versus $1/\sqrt{We_{h_a}}$*

The experimental database is composed of several different prefilmer thicknesses, gas velocities and liquid properties (see Table 7.2). A strong linear correlation between D_{32}/h_a and $1/\sqrt{\mathrm{We}_h}$ is observed, that is well fitted by the equation $y = 2.01\,x$. The correlation error lies within the measurement uncertainty of about 7% [104]. This leads to an *a priori* estimation of the D_{32} from the bulk boundary conditions:

$$\frac{D_{32}}{h_a} = \frac{C_1}{\sqrt{\mathrm{We}_{h_a}}} \tag{7.16}$$

where C_1 is the fitting constant equal to 2.01. Identifying Eqs. 7.14 and 7.16 allows to express D_{32} proportionally to the transverse wavelength:

$$D_{32} = C_B \cdot \lambda_{RT}^{h_a} \tag{7.17}$$

where $C_B = C_1/K$ is a constant evaluated at 0.146. This linear expression was already observed in other configurations with comparable proportionality factor: C_B = 0.1 $\pm$ 10% in liquid planar sheets [23] and C_B = 0.28 in axial jets [219]. Note that the constant C_1 is related to C_A and C_B through:

$$C_1 = 4\pi \sqrt{\frac{3\,C_A}{2\,C_d}}\,C_B \tag{7.18}$$

7.3 Parametrization of the Rosin-Rammler distribution from global quantities

7.3.1 Expressing m parameter

When the numerical drop size distribution of the spray is described by a Rosin-Rammler distribution (Eq. 7.1), the SMD (D_{32}^{RR}) is expressed as:

$$D_{32}^{RR} = m\,\frac{\Gamma(3/q+1)}{\Gamma(2/q+1)} \tag{7.19}$$

where $\Gamma(x)$ is the Gamma function:

$$\Gamma(x) = \int_0^\infty u^{x-1}\,\mathrm{e}^{-u}\mathrm{d}u \tag{7.20}$$

Combining Eqs. 7.16 and 7.19 yields:

$$m = C_1\,\frac{h_a}{\sqrt{\mathrm{We}_{h_a}}}\,\frac{\Gamma(2/q+1)}{\Gamma(3/q+1)} \tag{7.21}$$

Equivalently m can be expressed in term of $\lambda_{RT}^{h_a}$:

$$m = C_B\,\lambda_{RT}^{h_a}\,\frac{\Gamma(2/q+1)}{\Gamma(3/q+1)} \tag{7.22}$$

Note that Eqs. 7.21 and 7.22 still depend on the q parameter.

7.3.2 Expressing q parameter

The q parameter in the Rosin-Rammler distribution is related to the width of the peak, *i.e.* the dispersion of the drop size in the spray. Contrary to m, q cannot be formally linked to a single measurable value. Therefore each experimental drop size distribution is fitted with a Rosin-Rammler distribution using a Least-Square Method, and the resulting q parameter is considered as the *experimental* q^{exp}, subjected to a fitting uncertainty. These values of q are compared to the aerodynamic Weber number We_δ based on the boundary layer thickness δ at the atomizing edge:

$$\mathrm{We}_\delta = \frac{\rho_g\,\delta\,U_0^2}{\sigma} \tag{7.23}$$

The thickness δ, introduced by Gepperth *et al.* [104], is determined from [366] as:

$$\delta = 0.16 \cdot \frac{L_{surf}}{\mathrm{Re}^{1/7}} \tag{7.24a}$$

$$\text{with} \quad \mathrm{Re} = \frac{U_0\,L_{surf}}{\nu_g} \tag{7.24b}$$

Fitting form	h_a	a	b	Pearson correlation
$y = a\,x + b$	1 mm	9.74	$4.56 \cdot 10^{-2}$	≈ 0.99
$y = a\,x + b$	2.5 mm	8.73	0.268	0.880
$y = 9.74\,x + b$	2.5 mm	–	0.192	0.880

Table 7.1 : *Fitting coefficients of the q linear regression and resulting Pearson correlation for h_a = 1 and 2.5 mm*

where L_{surf} is the prefilmer length.

Figure 7.9 displays q^{exp} versus $1/\sqrt{\text{We}_\delta}$. Two different linear trends are clearly visible, depending on the prefilmer thickness. For low values of We_δ (empty symbols), q reaches a plateau around $q \approx 1.2$. A linear regression (summarized in Table 7.1) is applied to each dataset, taking into account the linear part only. The slope of the linear fitting shows a slight difference (9.74 and 8.73) between the two atomizing edge thickness. This deviation may be explained by a more scattered data for h_a = 2.5 mm compared to h_a = 1 mm. Therefore the same slope (9.74) is assumed for h_a = 2.5 mm and the additive constant is fitted with this slope constraint (grey dashed line). The resulting Pearson correlation (equal to one when the data matches perfectly the linear fit, and decreasing to zero when the data is scattered) is identical (0.880) to the unconstraint fitting and therefore it provides an acceptable trend. Consequently, q can be expressed as:

$$q(\text{We}_\delta, h_a) = \frac{C_2}{\sqrt{\text{We}_\delta}} + g(h_a) \tag{7.25}$$

where C_2 is a constant equal to 9.74 and $g(h_a)$ is an additive constant that depends on the atomizing edge thickness only.

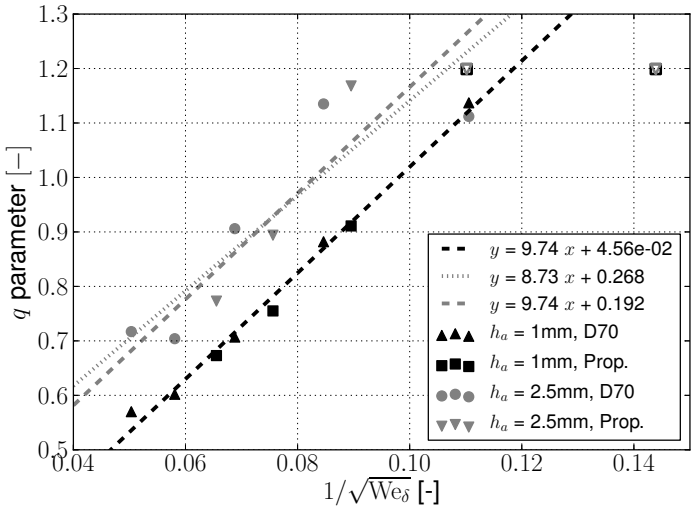

Figure 7.9 : *Scatter plot of q^{exp} values versus $1/\sqrt{We_\delta}$. Black dashed and grey dotted lines correspond to linear regressions for h_a = 1 and 2.5 mm respectively. The grey dashed line correspond to linear fitting for h_a = 2.5 mm keeping the slope to the value 9.74 obtained for h_a = 1 mm*

In order to determine an appropriate form for $g(h_a)$ in Eq. 7.25, it is assumed that the fragmentation process becomes independent of h_a for low values of h_a and any values of We_δ. Consequently the shape of the distribution,

and thus q, are supposed constant when $h_a \to 0$. This yields:

$$\frac{\partial q}{\partial h_a} \to 0 \quad \text{when} \quad h_a \to 0 \tag{7.26}$$

Expressing q with Eq. 7.25 leads to:

$$g'(h_a) \to 0 \quad \text{when} \quad h_a \to 0 \tag{7.27}$$

Therefore the function $g(h_a)$ may reach a constant as $h_a \to 0$. As two different values of h_a are available in the experimental database, g is chosen to depend on two parameters only. The form of g is arbitrarily chosen as:

$$g(h_a) = \left(\frac{h_a}{C_3}\right)^2 + C_4 \tag{7.28}$$

where C_3 and C_4 are determined from the additive constants of the linear regressions to C_3 = 5.99 mm and C_4 = 1.77 10^{-2}. Figure 7.10 depicts the evolution of g versus h_a. The value $g(h_a = 0)$ remains positive, ensuring a positive q parameter at small h_a for any values of We_δ.

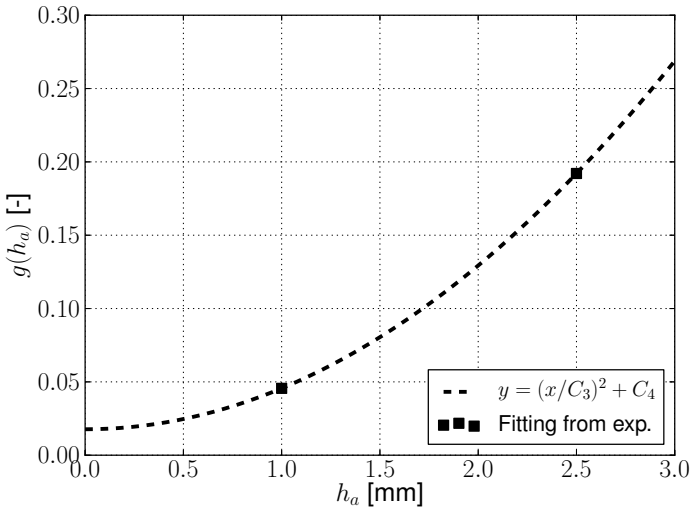

Figure 7.10 : *Function $g(h_a)$ versus h_a, superimposed with $y = (h_a/C_3)^2 + C_4$*

7.4 Parametrization of the Rosin-Rammler distribution from local quantities

In real airblast configurations, the flow field distribution is heterogeneous and unsteady. For instance in the case of a swirled annular flow, the Precessing Vortex Core (PVC) creates a precessing center recirculation zone that dramatically increases the velocity magnitude at the atomizing edge. The bulk velocity at the swirler outlet is thus not representative of the velocity seen by the liquid accumulated at the edge. In addition, in a reactive case, due to the heating of the liquid by the flame, the surface tension at the atomizing edge may be different from its value at lower temperature. Therefore a local expression of the parametrization of Rosin-Rammler distribution is required

to accurately predict the atomizing conditions at the atomizing edge in unsteady and heterogeneous configurations. Note also that a local expression is easier to include in numerical solvers.

The gas velocity being the most fluctuating quantity involved in the present model, all efforts are made to describe its local behaviour.

7.4.1 Characteristic time scales

Numerical simulation, especially LES or DNS provide access to local instantaneous values of physical properties, leading to a good description of velocity fluctuations and flow heterogeneities. Before including the flow variation in the model, it is useful to evaluate time scales ratios.

At the liquid accumulation location, the gaseous characteristic time scale is given by the vortex shedding frequency. It mainly depends on the gas velocity and was measured from 4 to 18 kHz in the present experiment at 0.2 mm downstream the atomizing edge, for a bulk velocity ranging from 20 to 70 m/s. Therefore the time scale of the gaseous flow τ_g in the vicinity of the atomizing edge ranges from 0.05 to 0.25 ms.

As it is based on a transverse structure triggered by a Rayleigh-Taylor instability, the breakup time scale is of the same order of magnitude than the instability time scale, derived by dimensional considerations and linear stability analysis [47]. The characteristic time of the Rayleigh-Taylor instability is estimated from the capillarity time $\tau_c = \sqrt{l_c/a}$ where l_c is the *capillarity length* defined by:

$$l_c = \sqrt{\frac{\sigma}{a|\rho_l - \rho_g|}} \tag{7.29}$$

where a is the local acceleration. The capillarity time scale hence yields:

$$\tau_c = \left(\frac{\sigma}{a^3|\rho_l - \rho_g|}\right)^{1/4} \tag{7.30}$$

Using Eq. 7.7 with $b = C_A\, h_a$ and a mean gas velocity from 20 to 70 m/s to determine the local acceleration leads to a capillarity time between 0.15 and 1 ms.

The capillarity time τ_c estimated from the Rayleigh-Taylor instability is not equal to the characteristic time of the most amplified mode τ_{RT}. A linear stability analysis is performed to determine τ_{RT}, following Charru [47]: when two fluids are in contact in an acceleration field (Fig. 7.11), linearizing Navier-Stokes equation with a small perturbation hypothesis at the interface, leads to the dispersion relation:

$$(\rho_g + \rho_l)\omega^2 - \left[(\rho_g - \rho_l)\; a\; k + k^3\; \sigma\right] = 0 \tag{7.31}$$

where k and ω are respectively the wave number and the pulsation of the fundamental perturbation. When the acceleration points from light to heavy fluid, the system is unconditionally stable. With the opposite direction, the configuration is unstable for length scales larger than the *capillarity* length, *i.e.* when $kl_c > 1$ (Fig. 7.11).

The dispersion relation (Eq. 7.31) admits thus pure imaginary roots:

$$\tau_c\, \omega_\pm = \pm i\sqrt{-\mathrm{At}\, k\, l_c\, (1 - k^2 l_c^2)} \tag{7.32}$$

where At is the Atwood number [112] (or the density parameter), negative when the acceleration points from the heavier fluid to the lighter one, and positive otherwise. In the present case, it is expressed as:

$$\mathrm{At} = \frac{\rho_g - \rho_l}{\rho_g + \rho_l} \tag{7.33}$$

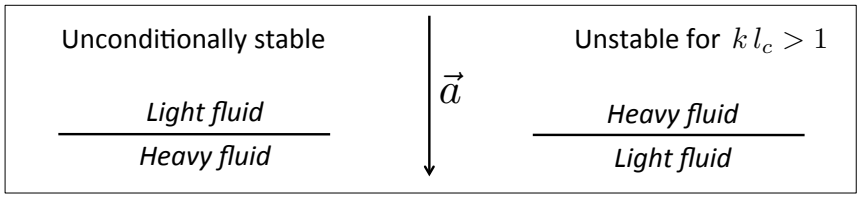

Figure 7.11 : *Rayleigh-Taylor instabilty for stationary fluids in an acceleration field* $\vec{a}$

The two modes defined by Eq. 7.32 correspond to a stable damped wave and a diverging, unstable perturbation, respectively. The most amplified wavelength is defined by the wavenumber k_M that maximizes the growth rate ω, and corresponds to $k_M\, l_c \approx 0.6$. The corresponding pulsation ω_M is found by injecting k_M into Eq. 7.32, leading to $\omega_M \approx 0.62/\tau_c$ and the corresponding time scale writes:

$$\tau_{RT} = \frac{2\pi}{\omega_M} \approx 10 \cdot \tau_c \tag{7.34}$$

The time scale of the most amplified wave for the Rayleigh-Taylor instability, assumed here as the generating phenomenon for the accumulation breakup, ranges from 1.5 to 10 ms.

Finally, the ratio τ_{RT}/τ_g lies between 30 and 40. This means that during the phase of linear growth, the instability undergoes several 'cycles' of gas fluctuations, and is subject to the gas velocity averaged over several turbulent time scales. Consequently the transverse wavelength and the SMD of the resulting spray do not depend on instantaneous quantities, but on quantities averaged over τ_{RT}. Nevertheless, the Rayleigh-Taylor instability is influenced by long time variations of the gas velocity: suppose that the gaseous field undergoes fluctuations over a time scale $\tau_1 > \tau_{RT}$ (*e.g.* pulsated flow, low frequency PVC, etc), the instability (and consequently the spray SMD) will follow these fluctuations. As the SMD is not proportional to the gas velocity, its average over a time τ_1 will be different from the SMD calculated with the gas velocity averaged over τ_1. As a consequence, when the gas flow is subject to *low frequency fluctuations*, the use of the bulk velocity would lead to a wrong estimation of the spray SMD.

7.4.2 Local gas velocity at the atomizing edge

Morris & Foss' experiment [239] (referred to as the *M-F experiment* in the following) provides useful information for the present study. They investigated the transition from a turbulent boundary layer to a single-stream shear layer in the particular geometry of a backward facing step (Fig. 7.12).

In particular, they built a map of the different flow regimes in the wake zone of the step (Fig. 7.13) and showed that the canonical turbulent boundary layer extends beyond the detachment point. Given the similarities of the geometrical features between an atomizing edge and a backward facing step, the conclusions of the M-F experiment are supposed to hold in the present case. The extension of the canonical turbulent boundary layer beyond the detachment point allows to consider that the velocity of the turbulent boundary layer (computed for instance by a law-of-the-wall approach) as the characteristic velocity in the atomizing edge region.

In Gepperth *et al.* experiment, observations indicate that the liquid/gas shearing zone of interest lies betwen $0 < x/\theta_0 < 5$ and $0.5 < y/\theta_0 < 2$ where θ_0 is the momentum thickness of the canonical boundary layer, and (x, y) origin located at the top of the atomizing edge (see Fig. 7.12). The momentum thickness θ_0 is estimated at 200 µm using the turbulent boundary layer formula from Cousteix [58] :

$$\frac{\theta_0}{L_{surf}} = \frac{(A_1+1)\,A_2}{\mathrm{Re}_{\theta_0}^{A_1}}, \qquad \mathrm{Re}_{\theta_0} = \frac{u_\infty\,\theta_0}{\nu} \tag{7.35}$$

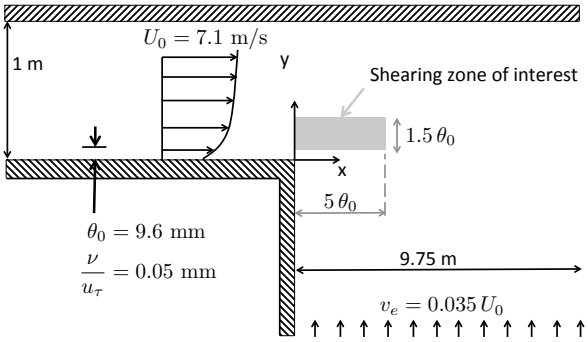

Figure 7.12 : *Geometry of the M-F experiment. The bottom entrainment velocity v_e provides the correct entrainment rate for a shear layer at zero pressure gradient*

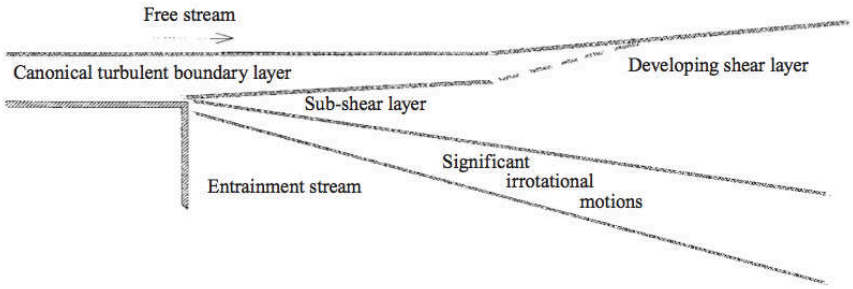

Figure 7.13 : *Map of different flow regimes, from [239]*

with $A_1 = 1/5$ and $A_2 = 0.0086$. L_{surf} is the prefilmer length, equal to 70.9 mm in this experiment, and u_∞ is the velocity outside the boundary layer.

Figure 7.14 displays the mean velocity profiles along the y axis for different x positions in the M-F experiment. In the liquid/gas shearing zone, the velocity magnitude varies little with x and y, between $0.6\,U_0$ and $0.75\,U_0$. The gas velocity seen by the liquid is thus acceptably estimated by a fraction of the bulk velocity in this particular configuration. Integrating the average velocity over $0.5 < y/\theta_0 < 2$ leads to 70% of the bulk velocity and it is referred to as u_{70}:

$$u_{70} = 0.7\,U_0 \tag{7.36}$$

To express u_{70} in a local form, Eq. 7.36 is formulated in terms of boundary layers variables. In boundary layer flows theory, the friction velocity u_τ is a characteristic scale for viscous sub-layer phenomena and is defined as:

$$\tau_w = \rho\,u_\tau^2 \tag{7.37}$$

The friction velocity and the laminar kinematic viscosity ν allow to define the length scale of the viscous sub-layer δ_v and the non-dimensional wall distance y^+:

$$y^+ = \frac{y}{\delta_v} = \frac{y\,u_\tau}{\nu} \tag{7.38}$$

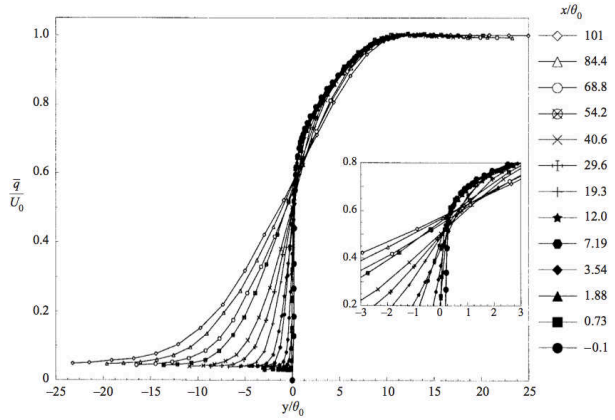

Figure 7.14 : *Mean velocity magnitude normalized with the free stream velocity U_0 a plane versus the vertical position, for several horizontal locations, from [239]*

In turbulent boundary layer flows, for $30 < y^+ < 600$, the velocity profile follows a logarithmic law (referred to as the *law-of-the-wall* in the following) that expresses the tangential velocity magnitude in wall unit:

$$u^+ = \frac{u}{u_\tau} = \frac{1}{\kappa}\ln(y^+) + B \tag{7.39}$$

where κ and B are two constants experimentally determined to be equal to 0.41 and 5.2 respectively. κ is called the von Kàrmàn constant, due to the instigator of the log law.

In their paper, Morris & Foss indicated that U_0/u_τ = 25.5, leading to the local expression of u_{70}:

$$u_{70} = 17.9\,u_\tau \iff u^+_{70} = 17.9 \tag{7.40}$$

According to [239], the corresponding vertical position is located in the logarithmic zone of the turbulent boundary layer. Therefore y^+_{70} is found by inverting Eq. 7.39:

$$y^+_{70} = \exp\left[\left(u^+_{70} - B\right)\kappa\right] \tag{7.41}$$

leading to:

$$y_{70} = 183\,\delta_\nu \iff y^+_{70} = 183 \tag{7.42}$$

In the M-F experiment, θ_0 and δ_ν were found to be equal to 9.6 mm and 0.05 mm respectively, allowing to express y_{70} in terms of the momentum thickness:

$$y_{70} = 0.953\,\theta_0 \tag{7.43}$$

To conclude, the velocity seen by the accumulated liquid u_{70} and the associated vertical position y_{70} were independently expressed in terms of the momentum thickness θ_0 and of wall units u_τ and δ_ν.

Note that the M-F experiment investigated a purely gaseous flow and it can be expected that the presence of liquid modifies the flow distribution. However in the present case the film thickness is small enough compared to the gaseous length scale upstream the atomizing edge, to assume a negligible effect. Moreover, visualizations show that the liquid accumulation interface is aligned with the prefilmer, with a mean deviation angle of $11°$ over a distance of $\approx 10\,\theta_0$. This small angle suggests that the outer part of the boundary layer extension is left unchanged over $10\,\theta_0$. These two reasons are in favor of the validity of the flow map of Fig. 7.13 in the presence of a thin liquid film.

Estimating τ_{RT} with u_{70} instead of U_0 leads to a time scale ratio between 25 and 32, and the assumption that primary breakup depends on a *time-averaged* velocity still holds.

7.4.3 Expressing Rosin-Rammler parameters

Using u_{70} instead of U_0 in Eq. 7.13 leads to modified constant C_A for the transverse wavelength estimation, found to be 0.670 from the same experiment data of Müller *et al.* [243]. The Weber number We_{h_a} (Eq. 7.15b) is also expressed with u_{70}:

$$\mathrm{We}_{h_a} = \frac{\rho_g \, h_a \, (r_\rho \, u_{70})^2}{\sigma} \tag{7.44}$$

leading to C_1 = 1.40 in Eqs. 7.16 and 7.21 and C_B = 0.111. The parametrization of q is finally expressed with the Weber number based on u_{70} and y_{70}:

$$\mathrm{We}_{70} = \frac{\rho_g \, y_{70} \, u_{70}^2}{\sigma} \tag{7.45}$$

This leads to a constant C_2 (Eq. 7.25) equal to 1.83. The function $g(h_a)$ (Eq. 7.28) is thus expressed with C_3 = 5.99 mm and C_4 = 8.15 10^{-3}.

7.4.4 Constants summary

The constants of the global approach are summarized in Table 7.2. The basic formulation, expressed with We_{h_a}, requires four constants and it is referred to as *4C*. The alternative formulation requires five constants, and gives access to the transverse instability wavelength $\lambda_{RT}^{h_a}$ that can be experimentally measured for further validation of the model. It is referred to as *5C* in the following. These two formulations are linked by expressing C_1 in terms of C_A and C_B (Eq. 7.18). In both cases, q depends on We_δ, the Weber number based on the boundary layer thickness.

<table>
<tr><td rowspan="2">Expression with
We_{h_a} (Eq. 7.15b)</td><td colspan="2">C_1 from Eq. 7.21</td><td>C_2 from Eq. 7.25</td><td>C_3 from Eq. 7.28</td><td>C_4 from Eq. 7.28</td></tr>
<tr><td colspan="2">2.01</td><td rowspan="3">9.74</td><td rowspan="3">5.99 mm</td><td rowspan="3">1.77 10^{-2}</td></tr>
<tr><td>Expression with
$\lambda_{RT}^{h_a}$ (Eq. 7.13)</td><td>C_A from Eq. 7.13</td><td>C_B from Eq. 7.22</td></tr>
<tr><td></td><td>0.801</td><td>0.146</td></tr>
</table>

Table 7.2 : *Model constants with the global approach.*

The constants of the local expression are summarized in Table 7.3. As for the global approach, the PAMELA model can be locally expressed by the transverse instability wavelength $\lambda_{RT}^{h_a}$ with five constants. If the use of We_{h_a} is preferred, only four constants are necessary.

<table>
<tr><td rowspan="2">Expression with
We_{h_a} (Eq. 7.44)</td><td colspan="2">C_1 from Eq. 7.21</td><td>C_2 from Eq. 7.25</td><td>C_3 from Eq. 7.28</td><td>C_4 from Eq. 7.28</td></tr>
<tr><td colspan="2">1.40</td><td rowspan="3">1.83</td><td rowspan="3">5.99 mm</td><td rowspan="3">8.15 10^{-3}</td></tr>
<tr><td>Expression with
$\lambda_{RT}^{h_a}$ (Eq. 7.13)</td><td>C_A from Eq. 7.13</td><td>C_B from Eq. 7.22</td></tr>
<tr><td></td><td>0.670</td><td>0.111</td></tr>
</table>

Table 7.3 : *Model constants with the local approach.*

7.5 Preliminary results

In this section are presented the results of PAMELA applied to reference experiment of Gepperth *et al.* , with global approach using the $5C$ formulation. A maximum deviation of 0.7% was found on mean diameters between the three methods described in Tables 7.2 and 7.3. Therefore all comments in this section apply to the other expressions.

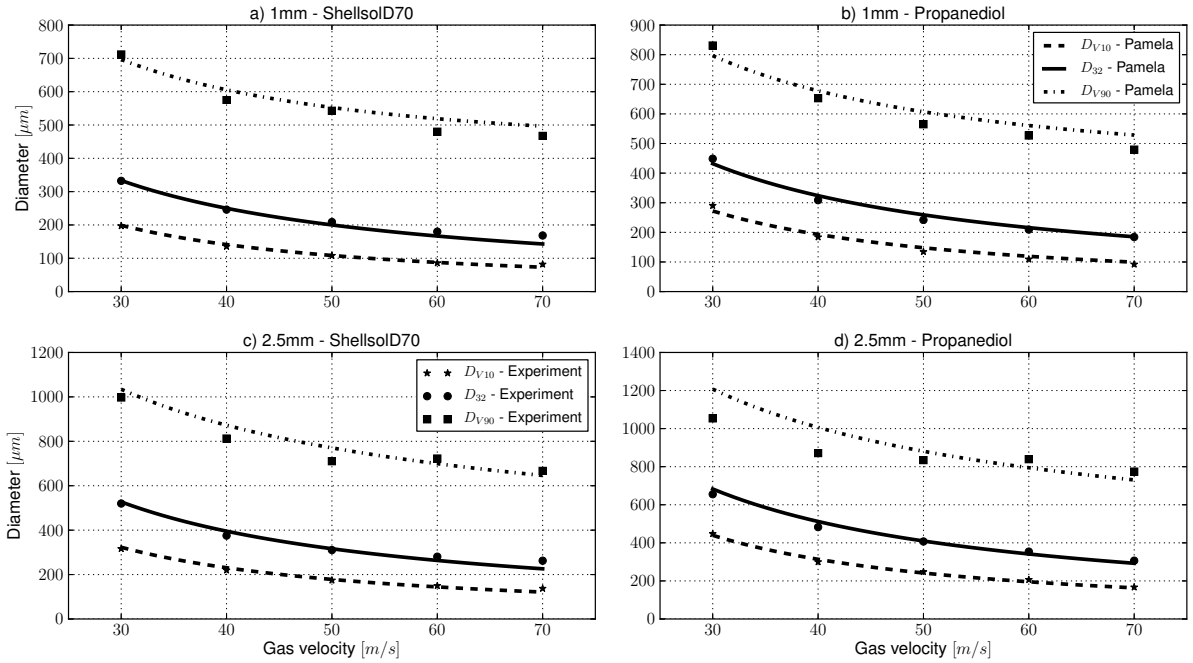

Figure 7.15 : *Evolution of D_{V10}, D_{32}, D_{V90} versus mean gas velocity for different prefilmer thicknesses and liquid properties.*

Figure 7.15 presents three mean diameters of the drop size distribution for the investigated conditions. D_{32} is the Sauter Mean Diameter, D_{V10} and D_{V90} represent the diameter at which the cumulative spray volume represent respectively 10% and 90% of the total spray volume V_{tot}:

$$F_3(D_{V10}) = \frac{1}{V_{tot}} \int_0^{D_{V10}} f_3(d)\,\mathrm{d}d = 0.1 \tag{7.46a}$$

$$F_3(D_{V90}) = \frac{1}{V_{tot}} \int_0^{D_{V90}} f_3(d)\,\mathrm{d}d = 0.9 \tag{7.46b}$$

D_{V10} provides information on the lower bound of the spray droplet size while D_{V90} exhibits the upper size range of the produced droplets. The accuracy of the proposed approach can be directly measured: since constants are fitted on experiment, both model and experiment data should perfectly match. However, this ideal behaviour encounters two limitations. First, the fitting of experimental data on a Rosin-Rammler function may lead to deviations. Second, low velocities are more difficult to match because of a less statistically converged dataset.

In all cases, predicted SMD and D_{V10} are in excellent agreement with the experiment, with a deviation below 10% even at low air velocities. This ensures an accurate prediction of the drop size probability density function in the low diameter range, and for all investigated conditions. However, the model slightly over predicts D_{V90} with an average deviation between 15% and 25% for low velocity. This over prediction is attributed to a too sharp decrease of the Rosin-Rammler function with large diameters, that 'pushes forward' the upper bound to integrate 90% of the spray volume.

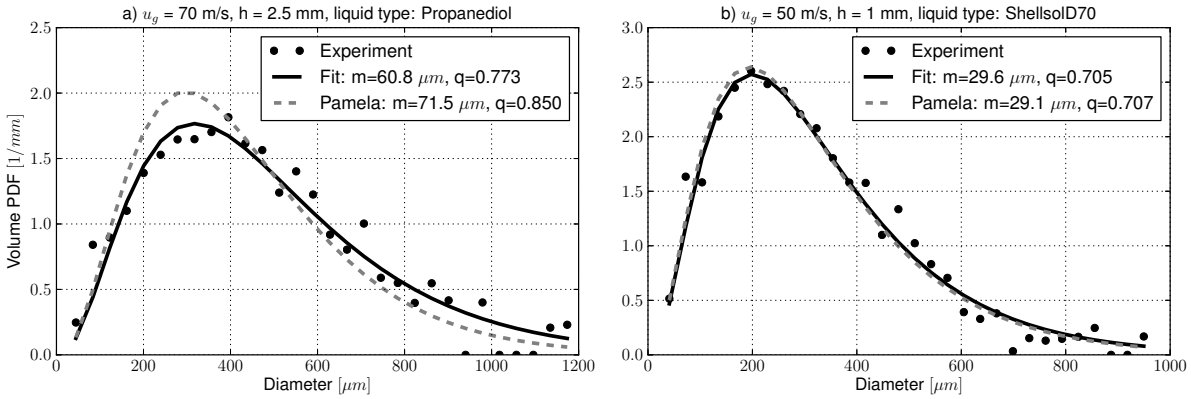

Figure 7.16 : *Comparison of the modeled, the fitted, and the experimental VPDF in two different configurations*

Figure 7.16 a) illustrates the results of the PAMELA model for the drop size PDF of a spray generated with h_a = 2.5 mm. The deviation between the model and the fitted curve is mainly attributed to errors on q. This is explained by the dispersion of q along the the fitting line on Fig. 7.9 with h_a = 2.5 mm. Moreover, as q takes part in the expression of m (Eq. 7.22), an error on q also alters the accuracy of m. Figure 7.16 b) exhibits a better agreement between the model and the fitted curve: as the atomizing edge thickness of 1 mm led to less scattered values of q (Fig. 7.9), the estimation of q is closer to the data.

7.6 PAMELA sensitivity

As PAMELA includes many sources of uncertainties, it is natural to evaluate its sensitivity to them. The first subsection details the model behaviour with regards to fluctuating air velocity. Second, the influence of the fitting constants is studied.

7.6.1 Sensitivity to velocity fluctuations

When used in a LES solver, the PAMELA model calculates the velocity u_{70} averaging the local velocity over τ_{RT}. The result is therefore subject to fluctuations. The purpose of this subsection is to evaluate the impact on the output PDF and mean diameters, and to check that PAMELA does not produce unrealistic distributions. As both local methods (described in Table 7.3) have a very similar behaviour, only the $5C$ formulation is presented here. The tested reference conditions are: bulk velocity of 60 m/s, atomizing edge thickness of 1 mm and liquid properties of Shellsol D70. Two situations are tested: (i) a bulk velocity deviation of 10% without fluctuations and (ii) an exact bulk velocity with fluctuations.

Assuming a bulk velocity deviation of $\pm 10\%$ with no fluctuation leads to U_0 = 54 and 66 m/s. The resulting seen velocity u_{70} is 37.8 and 46.2 m/s. Estimating y_{70} with Eq. 7.43 leads to y_{70} = 19.0 and 19.8 µm. The deviations are presented in Table 7.4 and referred to as $U_0 + 10\%$ and $U_0 - 10\%$.

For the second situation (*i.e.* exact bulk velocity with fluctuations), the gas velocity is supposed to fluctuate according to a distribution function. The resulting drop size PDF, assuming that statistical convergence is reached, is equal to a convolution product of the Rosin-Rammler function with the velocity distribution. The Rosin-Rammler

function is rewritten in terms of model inputs:

$$f_0(d, m, q) = f_0(d, U_0, \sigma, h) \tag{7.47}$$

For clarity purpose, f_0 dependence on σ and h_a is dropped in the following: $f_0(d, U_0)$. Suppose that the velocity follows a distribution $\mathcal{G}(c)$ verfiying:

$$\int_{-\infty}^{\infty} \mathcal{G}(c)\,\mathrm{d}c = 1 \tag{7.48}$$

The drop size number and volume distribution functions are respectively given by:

$$\overline{f_0}(d) = \int_{-\infty}^{\infty} f_0(d, c)\,\mathcal{G}(c)\,\mathrm{d}c \tag{7.49}$$

and:

$$\overline{f_3}(d) = \int_{-\infty}^{\infty} f_3(d, c)\,\mathcal{G}(c)\,\mathrm{d}c = \int_{-\infty}^{\infty} d^3\, f_0(d, c)\,\mathcal{G}(c)\,\mathrm{d}c = d^3\,\overline{f_0}(d) \tag{7.50}$$

As is classical in sensitivity analysis, the gas velocity is supposed to follow a normal distribution expressed by:

$$\mathcal{G}(c) = \frac{1}{\nu\sqrt{2\pi}} \exp\left(-\frac{1}{2}\left[\frac{c-\mu}{\nu}\right]^2\right) \tag{7.51}$$

where μ and ν respectively represent the mean and the standard deviation. The mean value is set to 60 m/s and several standard deviations are chosen to 3, 7 and 10 m/s, referred to as $\nu = 3m/s$, $\nu = 7m/s$ and $\nu = 10m/s$ respectively. The corresponding probability density functions are depicted on Fig. 7.17 a). Increasing the standard deviation of the gas velocity is equivalent to model flows with increasing turbulent intensity: the velocity range in the flow is wider, implying higher fluctuations. Turbulent intensity may be evaluated by the ratio of the standard deviation by the mean value

$$I_t = \frac{\nu}{\mu} \tag{7.52}$$

and leads to turbulent intensities of 5, 11.7 and 16.7%. The resulting VPDF are displayed on Fig. 7.17 b).

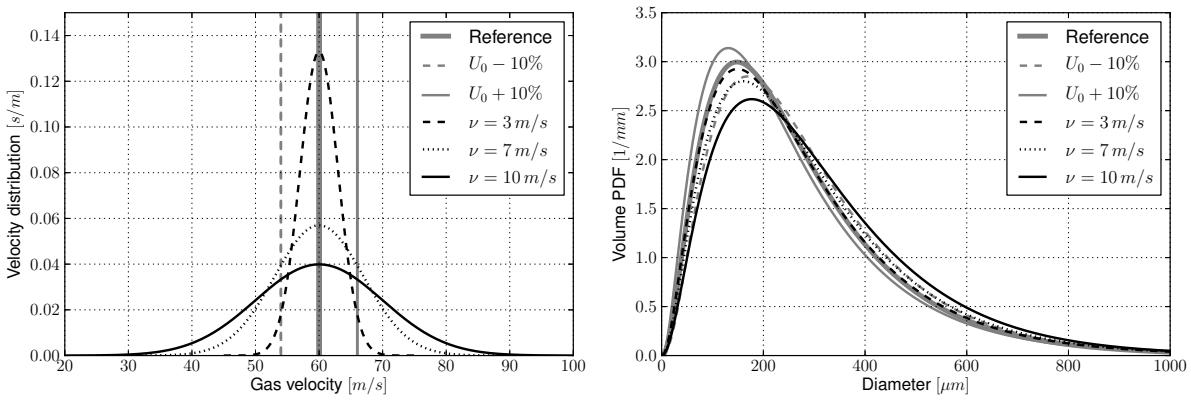

Figure 7.17 : *Left: Gaseous velocity distributions. Right: Resulting Volume PDF*

As expected, imposing a constant velocity 10% lower than the reference shifts the droplet volume PDF peak towards larger diameters while the contrary happens for a 10% larger velocity. However, this shift mainly impacts small diameters and leaves the 'decreasing part' of the PDF slightly unchanged. This phenomenon is quantitatively visible on Table 7.4 where the deviation is of the order of 10% for D_{V10} and D_{32}, and is less than 4% for D_{V90}. It is important to highlight that, for D_{V10} and D_{32}, the lower velocity induces a larger absolute deviation (13% and 11%) than the larger velocity (10 and 9%). This may be explained by the fact that increasing the number of larger droplets (resulting from lower air velocity) lead to a much higher increase of liquid volume.

When the gas velocity follows a normal distribution, the resulting droplet volume PDF peak is slightly moved towards larger diameters. This result is surprising because in the case of a normal distribution, lower and larger gas velocities are symmetrically distributed around the mean. Consequently, the peak of the volume PDF should be located at the same diameter with a larger width. However, as previously pointed out, lower velocities have a stronger impact on volume density function than larger velocities, which may explain this trends towards larger diameters.

Qualitatively, in a weak turbulent flow ($I_t \approx 5\%$), assuming that turbulence and primary breakup time scales are close, the spray generated by PAMELA will be close to a spray generated in constant flow conditions. When turbulent intensity increases to 10%, spray mean diameters are over predicted from 7% (small and medium diameters) to less than 2% (D_{V90}). For stronger turbulent flows the deviation varies between +6 and +15%.

Diameter	D_{V10}		D_{32}		D_{V90}	
Data type	Val.	Dev.	Val.	Dev.	Val.	Dev.
Unit	$[\mu m]$	$[\%]$	$[\mu m]$	$[\%]$	$[\mu m]$	$[\%]$
U_0- 10%	98	13.14	184	11.11	534	3.54
U_0+ 10%	78	-10.50	151	-9.09	501	-2.75
$\nu = 3\,m/s$	88	0.94	167	0.61	509	-1.23
$\nu = 7\,m/s$	93	6.96	175	5.89	523	1.41
$\nu = 10\,m/s$	100	15.51	188	13.62	547	6.12

Table 7.4 : *Mean diameters of the spray modulated by velocity fluctuation*

7.6.2 Sensitivity to model constants

PAMELA is defined by constants that have been fitted in a particular experiment under several conditions. A single deviation of 10% of each of these parameters is studied in the following. The uncertainty is quantified by the deviation of D_{V10} and D_{V90} compared to the reference case. Observation of D_{32} deviation is meaningless because it is proportional to C_1 (Eq. 7.16) or $\sqrt{C_A}$ and C_B (Eq. 7.17) and does not depend on the three other constants. Thus, the predicted Sauter Mean Diameter sensitivity directly follows the one of $\sqrt{C_A}$, C_B or C_1.

Results are depicted on Fig. 7.18. Both global and local formulations have a very similar behaviour. The most sensitive variables are C_1 and C_B: since the *scale* parameter m of the Rosin-Rammler function is proportional to C_1 (Eq. 7.16) or C (Eq. 7.17), the PDF and therefore D_{V10} and D_{V90} follows their variation. The second most critical constants are C_A and C_2, and C_3 and C_4 are the less sensitive constants. The tail of the PDF (*i.e.* large diameters) is more sensitive to the model constants. It may be explained by the fact that D_{V90} results from an integration over a wide range of diameters, from the smallest to the largest, and a discrepancy on small and medium diameters prediction will result in a discrepancy on D_{V90}.

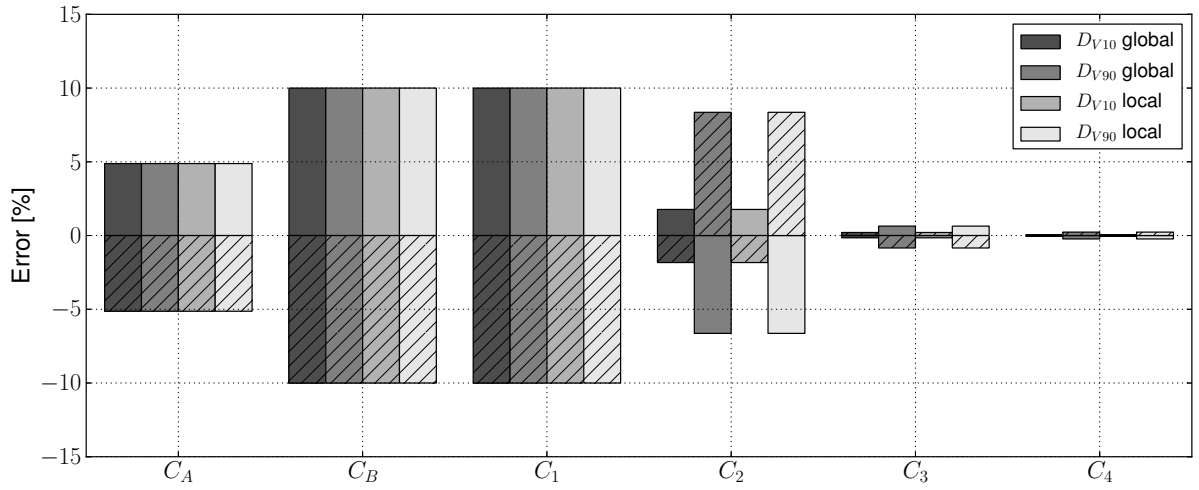

Figure 7.18 : *Deviation of D_{V10} and D_{V90} for both global and local formulations, with regards to the model constant variations. Blanked and hatched bars correspond to an increase and decrease of 10% respectively.*

7.7 Comparison with *ad hoc* correlation

Based on approximately 300 test cases, Gepperth *et al.* [104] derived correlations for the SMD, the Strouhal number and the droplet velocity, expressed with four non-dimensional parameter groups: Reynold number, Weber number, the density ratio and the ratio between the prefilmer thickness and the boundary layer thickness. In order to validate the present model, the SMD calculated from Eq. 7.16 is compared to the *ad hoc* correlation that reads:

$$\frac{D_{32}}{\delta_{x_{edge}}} = 4.96 \cdot \left(\frac{\rho_g \ \overline{u}_g \ \delta_{x_{edge}}}{\mu_g} \right)^{-0.17} \cdot \left(\frac{\rho_g \ \overline{u}_g^2 \ \delta_{x_{edge}}}{\sigma} \right)^{-0.36} \cdot \left(\frac{\rho_l}{\rho_g} \right)^{-0.013} \cdot \left(\frac{h_a}{\delta_{x_{edge}}} \right)^{0.46} \tag{7.53}$$

where $\delta_{x_{edge}}$ is the turbulent boundary layer thickness at the atomizing edge expressed by [366]:

$$\delta_{x_{edge}} = 0.16 \cdot \frac{L_{surf}}{\left(\frac{\rho_g \ \overline{u}_g \ L_{surf}}{\mu_g} \right)^{1/7}} \tag{7.54}$$

and L_{surf} is the prefilmer length. Examining Eq. 7.53, allows first to check the scaling of the PAMELA model: the atomizing edge thickness h_a appears with a power of 0.46 while PAMELA shows a dependence in 0.5, which is very close. On the contrary, the surface tension exponent is more questionable: it is equal to 0.36 ($\approx 1/3$) in Eq. 7.53 whereas it is 0.5 in PAMELA. Additional tests should be conducted on a large range of surface tension values in order to test the robustness of both approaches (correlation and PAMELA).

Finally, Fig. 7.19 shows a comparison of the *ad hoc* correlation of Gepperth *et al.* and PAMELA. Dashed lines represent a deviation of 10%. It appears that the model tends to overestimate the SMD for large values, *i.e.* for low velocities. The overall behaviour of PAMELA is however in a reasonably good agreement with the *ad hoc* correlation and the data.

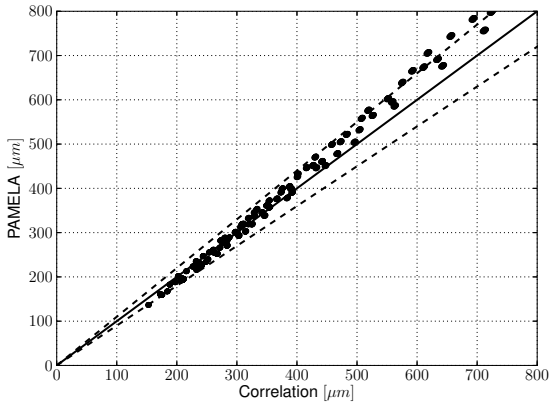

Figure 7.19 : *SMD comparison of Gepperth et al. correlation and PAMELA*

Varying parameter	Range	Units
U_0	20 - 70	m/s
σ	0.0255 - 0.0466	kg/s^2
ρ_l	742 - 1071	kg/m^3
u_l	0.5 - 2.5	m/s
h_a	1 - 2.5	mm
L_{surf}	43 - 70.9	mm

Figure 7.20 : *Varying parameters for correlation comparison*

7.8 Implementation of PAMELA in the AVBP solver

The implementation of PAMELA in AVBP implies a number of technical difficulties that are presented here. As the film model presented in Chapter 6 provides some inputs to PAMELA, both models are implemented in the same framework and use a Lagrangian formulation. This choice seems appropriate since it allows to naturally describe the polydispersity of the spray. As shown in subsection 7.4.1, the RT instability is sensitive to an averaged gaseous velocity, and it is necessary to compute a local time average during the atomization process.

The overall strategy consists in several successive steps that describe the life of a fluid particle from film to spray state. The scenario, illustrated on Fig. 7.21, takes place as follow:

1. A particle belonging to the liquid film arrives at the atomizing edge, its velocity is set to zero and its numerical state changes from 'film particle' to 'accumulation particle'.
2. An accumulation particle is stationary and does not interact with the gaseous flow nor with the other droplets. It only records the gaseous velocity at this location during a period corresponding to half of the RT instability Eq. (τ_{RT}).
3. Once the averaging period is over, the accumulation particle feeds the atomization model with its liquid mass and averaged gaseous velocity.
4. A random diameter is determined following the Rosin-Rammler function, provided by the local parameters and the averaged velocity.
5. The mass of the droplet to be injected is compared to the available liquid in the liquid reservoir:
   - If the available mass is not sufficient, the accumulation droplet disappears and its mass is added to the reservoir mass of the current cell.
   - If the contained mass is sufficient, a new droplet is generated with the diameter determined randomly at step #4.
6. The newborn droplet is injected directly at the 'accumulation particle' location, by a one-step shift to the neighbouring cell downstream, with a zero velocity.

7. The newly injected liquid droplet starts its spray life.

In order to ensure the robustness of the above scenario, some steps are treated in a particular manner, as detailed in the following.

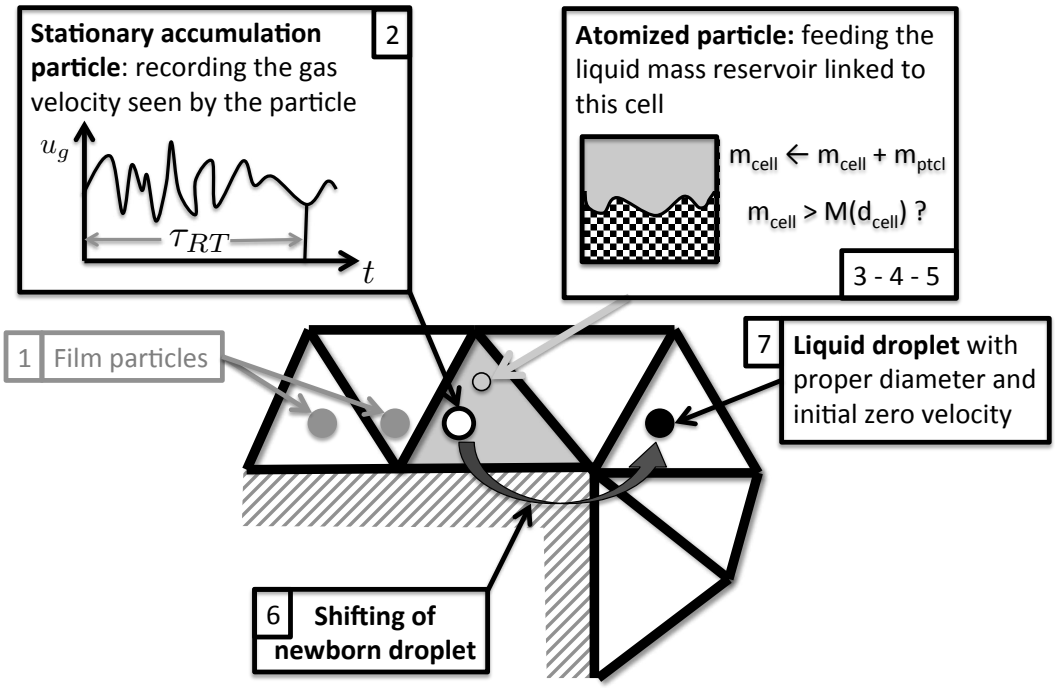

Figure 7.21 : *Description of PAMELA general procedure*

7.8.1 Film particle detachment

Three ways have been selected to detach a film particle, *i.e.* to change the particle from a 'film' state to another one, depending on three possible stuations: (i) the particle ends up in a non-wall cell, (ii) the particle normal velocity changes and its virtual inertia is higher than a given criterion, (iii) the particle sees a sharp change in wall surface orientation. The two firsts lead to a simple particle detachment with no change of particle diameter while the third one feeds the liquid accumulation reservoir. Additional details are given below.

7.8.1.a) Detachment in non-wall cell

This type of detachment is not related to a physical phenomenon but is a numerical trick to enhance the robustness on irregular meshes. When a film particle changes of cell, it can end up in an interior cell if the mesh size sharply decreases, as depicted on Fig. 7.22. The particle can not be considered as a film particle anymore, and it is given a droplet state without any modification. Given the usual values of particle velocitiy and mesh size, this scenario is highly unlikely.

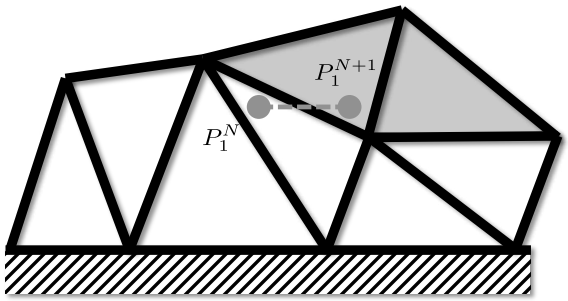

Figure 7.22 : *First type of detachment: the film particle located originally at P_1^N travels to the position P_1^{N+1} in the direction of the wall surface. Since the new containing cell is not connected to the wall, the particle is detached.*

7.8.1.b) Inertia criterion

In order to account for the film inertia effect when it flows over a sharp edge with a certain angle variation (figure 7.23, left), O'Rourke & Amsden [257] derived a criterion based on the competition between film inertia and pressure drop induced by a separation: *"As the liquid film approaches the corner surface, it will tend to keep its direction of flow and separate because of its inertia [...]. A low pressure region forms at the wall-side of the film, and the resulting pressure difference between the pressure in the gas-side, which is the gas pressure, and that on the wall-side, causes the flow to run and remain attached to the corner. If, however, the liquid inertia is so large that the wall-side pressure drops to zero, then the liquid and wall no longer are pushing against each other, and the liquid film separates"*. The translation of these considerations leads to:

$$c_s \, \rho_l \, u_f^2 \, \frac{\sin\theta}{1+\cos\theta} > p_{gas} \tag{7.55}$$

where θ is the wall angle, c_s is a constant parameter set to 3 by O'Rourke & Amsden and that depends on the shape of the pressure profile along the wall. This condition (Eq. 7.55) has never been validated experimentally. If the criterion is satisfied, droplets are detached without any diameter modification. The angle θ is calculated by the angle difference between the wall face normals of the previous cell and the current (Fig. 7.23, right). It implies that the normal of the previous wall face seen by any film particle has to be stored.

7.8.1.c) Detachment on a right angle edge

In thin film flows, the inertial criterion (Eq. 7.55) is not sufficient to detach film particles. Even with a right angle ($\theta = 90°$), typical film inertia ($\rho \, u_f^2 \approx 1000 \times 1^2$ = 1000) is too low in comparison to ambient pressure ($p_{gas} \approx$ 10 bars). Therefore an additional criterion is added to force film particle atomization when it encounters an angle (formed by two consecutive face normals) larger than a critical angle θ_c:

$$\theta > \theta_c \Leftrightarrow \cos\theta = \overrightarrow{n}_{old} \cdot \overrightarrow{n}_{new} < \cos\theta_c \tag{7.56}$$

where $\overrightarrow{n}_{old}$ and $\overrightarrow{n}_{new}$ are the wall face normals of the previous and the current cells, respectively. This criterion is purely geometrical and the critical angle θ_c is arbitrary chosen to $45°$, leading to:

$$\overrightarrow{n}_{old} \cdot \overrightarrow{n}_{new} < \sqrt{2}/2 \tag{7.57}$$

When this condition is satisfied, the film particle is considered as entering the liquid accumulation reservoir and its state is set to 'accumulation particle'.

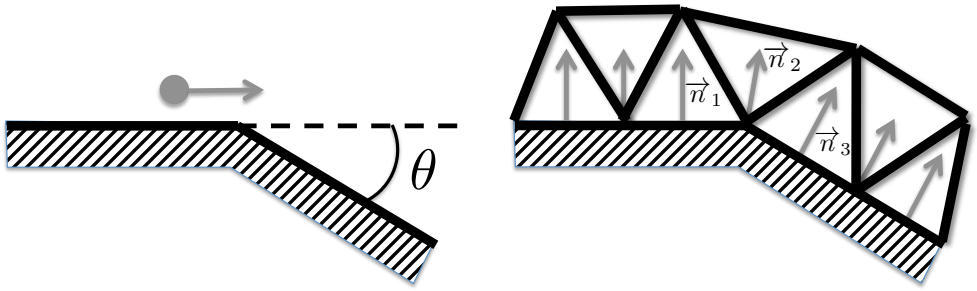

Figure 7.23 : *Illustration of the detachment on a sharp edge. Left: the film particle moves with a trajectory parallel to the wall surface and goes beyond a sharp edge. Right: wall normals specifically built for film particles. Cells sharing at least one node with a wall are accounted as potential filming cells, and their normal are computed as the average of the neighboring cell normals, e.g.* $\vec{n}_2 = (\vec{n}_1 + \vec{n}_3)/2$.

7.8.2 Accumulation droplet steady behaviour

In this state, the particle is stationary and records gas velocity for a period of τ_{RT}.

7.8.2.a) Estimating u_{70} and y_{70} from the law-of-the-wall

Ideally, the detached particle should be at the accumulation location, just downstream the atomizing edge, and record the gas velocity at this location. However, Morris & Foss [239] observed that the flow profile in this region can be assimilated to a turbulent boundary layer profile, which is non linear. This may lead to a problem: the gas velocity seen by the particle is computed by a linear interpolation from the mesh nodes to the particle location. In AVBP, all the available interpolation schemes are linear or isotropic and cannot describe the anisotropic behaviour of a boundary layer. Therefore the gas velocity seen by the particle computed that way is highly mesh dependent.

In order to circumvent this problem, the choice has been made to do an 'upstream shift' of the detachment point inside the boundary layer linked to the prefilmer, as seen in subsection 7.4.2. The use of law-of-the-wall reduces the mesh dependency as soon as the first off-wall node lies in the log layer.

Preliminary tests were performed with AVBP in a turbulent channel to verify the robustness of the expressions of u_{70} and y_{70} in terms of wall units (Eq. 7.40 and 7.42). A turbulent channel was simulated, with a law-of-the-wall approach. Equation 7.40 was compared to 70% of the maximum velocity, and a strong overestimation was observed.

A calibration step was thus necessary to ensure a good estimation of u_{70}: single phase flow runs were conducted and averaged to determine the mean friction velocity upstream the atomizing edge for different bulk velocity. It was found that when the first off-wall node lies in the log law region *i.e.* ($y^+ > 30$), u_{70} was recovered for $y^+ \approx 23$. Similarly, the determination of y_{70} (Eq. 7.43) in term of wall units was found to $y^+_{70} \approx 35$. The local gaseous velocity seen by the accumulation and the vertical location of the gas/liquid interface thus yield:

$$u_{70} = 12.8\, u_\tau \tag{7.58a}$$

$$y_{70} = 35\, \delta_v \tag{7.58b}$$

Equation 7.58a shows a deviation of 28% compared to Eq. 7.40. The large deviation ($\approx 80\%$) between Eqs. 7.58b and 7.42 is due to the determination of y_{70} via Eq. 7.41 that involves an exponential function.

7.8.2.b) Upstream shifting of the detachment

An additional constraint appears here due to the discretization scheme of AVBP (cell-vertex). The wall shear stress is computed on faces and its value is scattered and stored at the nodes. Consequently, the wall shear stress stored on the sharp edge nodes (N_0 on Fig. 7.24) is biased by the recirculation zone directly downstream the atomizing edge. It is therefore necessary to use values of τ_w located upstream the atomizing edge nodes (N_{-1} on Fig. 7.24). On Fig. 7.25 the time-averaged wall shear stress is plotted versus the transverse coordinate. With a Relative Standard Deviation (RSD) of 24% the node N_0 records a very noisy signal whereas the signal is much smoother on node N_{-2} with a RSD of 4.1%. The trade-off is taken at node N_{-1} where the RSD is 13%.

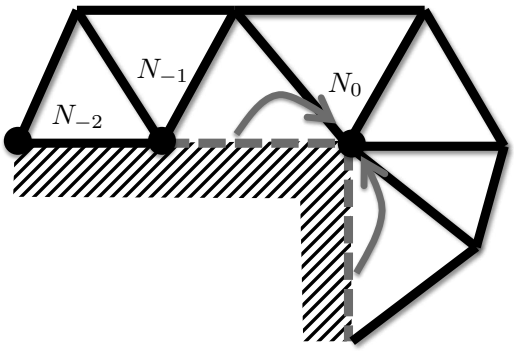

Figure 7.24 : *Nodes receive the wall shear stress computed from all connected faces*

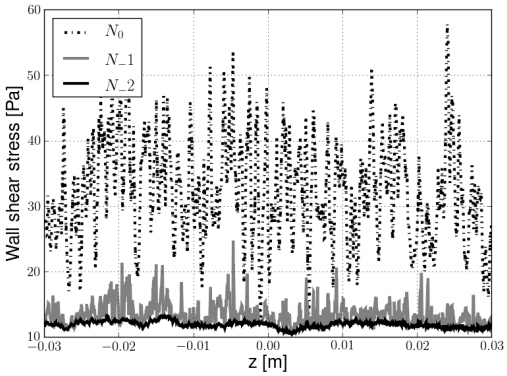

Figure 7.25 : *Time average of the wall shear stress computed on nodes N_0, N_{-1} and N_{-2} (Fig. 7.24)*

7.8.3 Cell-bound mass tank for atomization

The mass of the accumulation particle is transmitted to a virtual liquid tank connected to the cell where atomization takes place. A diameter is randomly chosen following the parametrized Rosin-Rammler distribution. The randomly generated diameter is converted to a mass and compared to the liquid mass available in the virtual reservoir. If the liquid mass is sufficient, a newborn droplet is injected and the available mass is updated. The overall process is illustrated on Fig. 7.26.

Generating a random number following a Rosin-Rammler law is straightforward since its Cumulative Distribution Function can be directly inverted [345]. The random diameter d is computed as:

$$d = X_{\text{PDF}} = -m \ln \left[(1 - X_{[0,1]})^{1/q} \right] \tag{7.59}$$

where m and q are the *scale* and *shape* parameters of the Rosin-Rammler function respectively, and $X_{[0,1]}$ an equiprobable random variable between 0 and 1. Note that extreme values of X (*e.g.* X = 0.999999) lead to very large droplets that may be unrealistic. It is therefore necessary to set an upper bound diameter.

Finally the parcel number N_p of the injected droplet is kept constant to avoid any influence of N_p variation on the generated distribution.

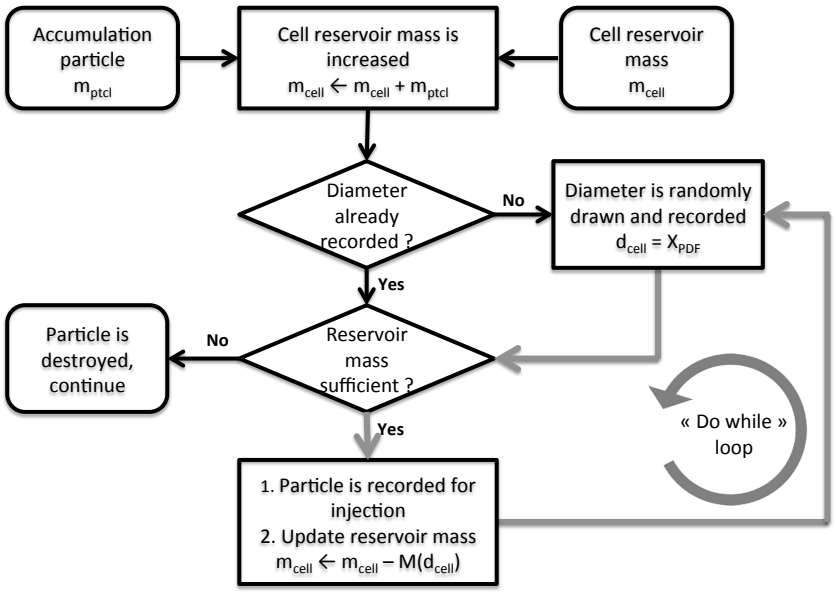

Figure 7.26 : *Flowchart of the PAMELA atomization procedure*

7.8.4 Shifting the newborn droplet

Atomized droplets are injected at the location of the last 'accumulation particle' accounted, *i.e.* at a distance of approximately the cell size upstream the atomizing edge. This can lead to non realistic behaviour such as an early momentum exchange between the gas and liquid phase and above all, a 're-filming' process : because of wall normal fluctuations of the gas velocity, the droplet can re-impact the prefilmer and create a film. The same scenario may happen in swirling flows, because of centrifugal effects. It is thus necessary to move the droplet downstream the prefilmer immediately after it is injected. Therefore the distance of the particle to the atomizing edge is evaluated with the longest edge of containing cell and the film particle velocity direction. In swirling flow, the film particle reaches the atomizing edge with a helicoidial trajectory. This behaviour is illustrated on Fig. 7.27 by a planar projection. The film velocity presents an angle θ compared to the atomizing edge normal, and the shifting distance l_t is longer than the cell characteristic length. In order to properly handle this situation, the longest edge of the containing cell is taken as the reference length. The shifting distance is then expressed by:

$$l_t = \frac{l_c}{\cos\theta} \tag{7.60}$$

and the angle θ is determined by

$$\cos\theta = \frac{\overrightarrow{n}_a \cdot \overrightarrow{u}_f}{\|\overrightarrow{n}_a\| \, \|\overrightarrow{u}_f\|} \tag{7.61}$$

The newborn droplet is imposed a velocity that moves it to the right position in one time step. Given the very small time step compared to the mesh size, the velocity is unrealistically large and no interaction with the gas is considered during the journey. The imposed velocity is expressed by:

$$\overrightarrow{u}_f^{new} = \frac{l_t}{\Delta t} \frac{\overrightarrow{u}_f^{old}}{\|\overrightarrow{u}_f^{old}\|} = \frac{l_c}{\Delta t} \frac{\overrightarrow{u}_f^{old}}{\overrightarrow{u}_f^{old} \cdot \overrightarrow{n}_a} \tag{7.62}$$

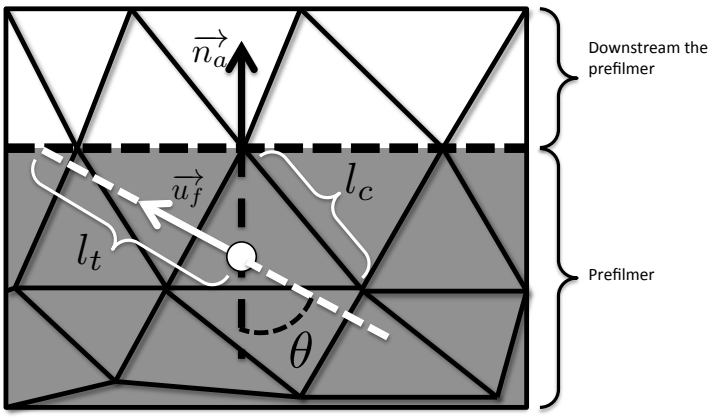

Figure 7.27 : *Top view of the prefilmer configuration in the case of swirling flow*

7.9 Conclusion

In this chapter we have proposed a mechanism to statistically predict the drop size probability density function of a spray generated by a prefilming atomization in the context of airblast injectors. It is based on the mechanism described by Hong [151] and Varga [353], and it is described by a Rosin-Rammler function that depends on influent parameters identified by Gepperth *et al.* [102, 104], namely the gaseous velocity, the surface tension and the atomizing edge thickness. The agreement of both local and global approaches with experiment is good and exhibits promising trends. The results of the overall model show an accurate determination of the drop size probability function over a wide range of operating conditions. It is expected that this accuracy will be reproduced in industrial configurations, as soon as the atomization process remains the same as in Gepperth's experiment. The particularity of this model is the rendering of the whole probability density function of the drop diameter, and not only a correlation on the arithmetic or Sauter Mean diameter. Therefore an accurate prediction of the PDF enables to recover every moments of the distribution, including all mean diameters.

This model has been implemented into AVBP in order to provide a polydisperse spray to the downstream models chain (drag, evaporation), up to the combustion process. Its implementation uses the already existing Lagrangian module and is embedded within the film framework developed and explained in chapter 6. Additional assumptions have been made in order to shift the injection point, and the work of Morris & Foss [239] provides the necessary justifications. The delay-inducing effect of the liquid accumulation is mimicked through an averaging procedure. This time-average operation is justified by accounting for the time scale of the atomization process, that mainly depends on the development of the Rayleigh-Taylor instability and the elongation of the ligament. During the atomization process, in order to ensure a right Number PDF and, at the same time, a right Volume PDF, the parcel number is kept constant and a system of virtual local liquid tanks has been built. Finally the injected droplets are instantaneously shifted to their physical position downstream the atomizing edge where they interact with the gaseous phase through drag and evaporation, up to the flame.

All the necessary models are now ready to perform a full Large Eddy Simulation of realistic (academic or industrial) configurations, as presented in the following parts.

Part III

Application to an academic configuration

Chapter 8

The KIT-ITS experiment

This chapter presents the simulation of an academic configuration representative of real systems, using the models developed in this thesis. The objective is to evaluate the accuracy and impact of these models by comparison with experiment. The geometry and the experimental apparatus are described in a first part, followed by the results of the purely gaseous simulation and finally the two-phase flow simulation.

8.1 Configuration

8.1.1 Geometry and operating conditions

The experimental device has been designed by Müller *et al.* [243] and Gepperth *et al.* [102] and manufactured at the Institut für Thermische Strömungmaschinen (ITS) from the Karlsruhe Institute of Technology (KIT). It is dedicated to study the filming and primary breakup processes in conditions close to airblast atomizers. It consists in a wing-shaped prefilmer, placed in a high velocity air stream channel (see Fig. 8.1). With a height e of 21.6 mm and a width w of 96 mm, the duct has a wide aspect ratio to ensure a two-dimensional air flow and avoid interfering corner vortices. The liquid is injected on one side of the prefilmer through fifty equidistantly distributed holes, located 45 mm upstream the atomizing edge. The holes spacing is 1 mm leading to an injection patch width b of 50 mm, meaning that the film does not fully cover the duct width. The prefilmer length L_{surf} is 70 mm long and the thickness h_a at the atomizing edge is 1 mm. To enhance accessibility for measurements, and to reduce the configuration complexity, the prefilmer and the channel walls are planar, but still considered representative of the annular geometry encountered in real systems.

The high gas velocity entrains the liquid towards the atomizing-edge of the prefilmer, *i.e.* in the z-direction, by inducing a high shear at the film surface. A thin film forms, that wets homogeneously the prefilmer, before full atomization at the prefilmer trailing edge. No film stripping is observed from the film surface before reaching the atomizing edge.

In order to determine the parameters influencing the primary breakup process, many conditions were experimentally varied:

- the liquid type with different viscosities and surface tensions;
- the gas flow with different velocities and operating pressures;
- the geometry with different prefilmer lengths and thicknesses.

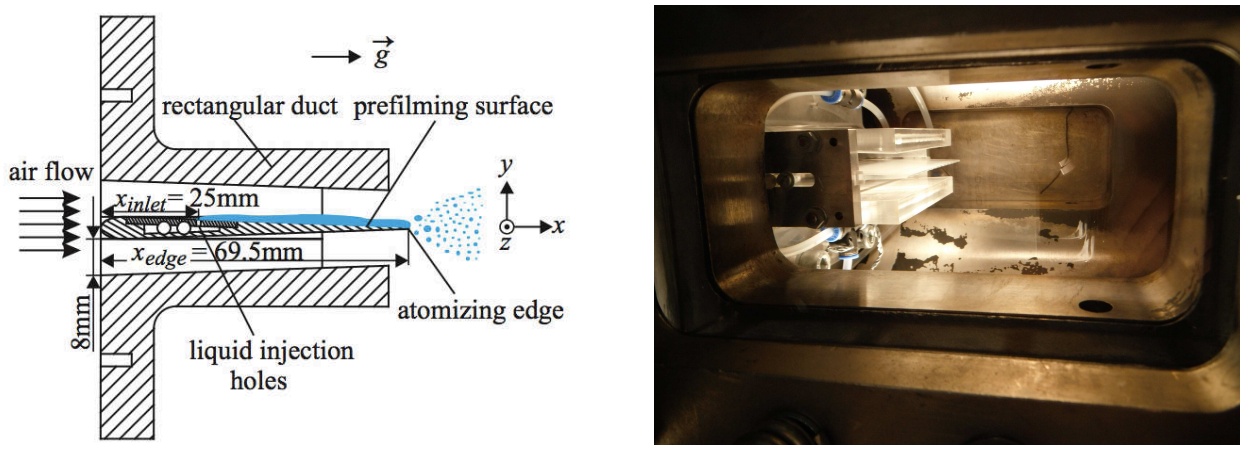

Figure 8.1 : *Illustration of the KIT-ITS experiment. Left: schematic, from [102]. Right: Picture of the atomizing edge region in the high pressure test rig.*

In this chapter, the prefilmer length is not investigated because it has no influence on the spray and does not appear in the PAMELA model. Similarly, the atomizing edge thickness is not studied because it influences the Sauter Mean Diameter (SMD) as the surface tension: h_a and σ appear in the product $h_a \cdot \sigma$ in the expression of the transverse wavelength λ_{RT} (Eq. 7.13) and the SMD is proportional to λ_{RT} (Eq. 7.22). Thus, when considering the SMD, modifying σ is equivalent to modify h_a.

Three parameters are then tested: the gas velocity, the liquid type and the liquid flow rate. The gas velocity is arbitrarily calculated at the location where the section is minimum (Fig. 8.4 *right*) of height e, leading to different mass flow rates and inlet velocities as summarized in Table 8.1.

Exp. bulk velocity	$[m/s]$	20	40	60	70
Inlet mass flow rate	$[g/s]$	37.32	74.65	112.0	130.6
Inlet mean velocity	$[m/s]$	6.392	12.78	19.18	22.37

Table 8.1 : *Inlet physical boundary conditions*

Two types of liquid are investigated: Shellsol D70 whose physical properties are close to kerosene and a equi-volume mix of 1,2-Propanediol and water, to test the model behaviour with different surface tensions. For clarity sake, the Shellsol D70 and the iso-volume mix of 1,2-Propanediol and water are respectively labeled *Shellsol* (or *D70*) and *Propanediol* (or *Prop.*) in the following. Their characteristics are listed in Table 8.2. The liquid mass flow rate ($\dot{m}_{15}$ and $\dot{m}_{50}$) is converted to 2D volume flow rate Λ_f by:

$$\Lambda_f = \frac{\dot{m}}{\rho_l \, b} \tag{8.1}$$

where b is the injection patch width. This leads to two 2D volume flow rates of 15 and 50 mm^2/s, as summarized in Table 8.2.

The matrix of the different cases and their label is summarized in Table 8.3. For single phase experiment or computations, cases will be simply referred to as their velocity: **U20**, **U40**, **U60** and **U70**.

To characterize the flow features, two Reynolds numbers may be employed. First, the Reynolds number in the channel Re_c gives information about the form of the velocity profile, the boundary layer flow and the shear stress on

Property	Unit	**Shellsol D70**	**Propanediol**
Density ρ_l	$[kg/m^3]$	770	1008
Dynamic viscosity μ_l	$[kg/m/s]$	$1.56 \cdot 10^{-3}$	$6.06 \cdot 10^{-3}$
Surface tension σ	$[kg/s]$	$27.5 \cdot 10^{-3}$	$46.6 \cdot 10^{-3}$
Mass flow rate $\dot{m}_{15}$	$[g/s]$	0.5775	0.756
Mass flow rate $\dot{m}_{50}$	$[g/s]$	1.925	2.520

Table 8.2 : *Physical properties of investigated liquid, from [104]*

Liquid type	2D flow rate Λ_f [mm^2/s]	Gas velocity [m/s] 20	40	60	70
D70	15	**U20L15D70**	**U40L15D70**	**U60L15D70**	**U70L15D70**
	50	**U20L50D70**	**U40L50D70**	**U60L50D70**	**U70L50D70**
Prop.	15	**U20L15Prop**	**U40L15Prop**	**U60L15Prop**	**U70L15Prop**
	50	**U20L50Prop**	**U40L50Prop**	**U60L50Prop**	**U70L50Prop**

Table 8.3 : *Test case matrix*

the prefilmer. It is calculated from the hydraulic diameter D_h of the channel, defined as

$$D_h = \frac{4\mathcal{S}}{\mathcal{P}} \tag{8.2}$$

where $\mathcal{S}$ and $\mathcal{P}$ are respectively the flow section and its related perimeter. As the geometry has a high aspect ratio, the flow in the center place can be considered two dimensional and therefore the hydraulic diameter is equal to:

$$D_h = 2\,e \tag{8.3}$$

The second Reynolds number Re_a is based on the atomizing edge thickness h_a and it is used to determine the vortex shedding frequency through experimental correlations. Both Reynolds numbers values are summarized in Table 8.4 and it appears that the channel flow is fully turbulent.

Case	U20	U40	U60	U70
Re_c	21600	43200	64800	75600
Re_a	1304	2609	3913	4565

Table 8.4 : *Reynolds number corresponding to different gas cases*

8.1.2 Measurement methods

The test-rig is equipped with different measurement devices briefly described in the following. The measured values are:

- the gas velocity, through 3D LDA;
- the film thickness, using a LFDM;

- the ligaments and the primary blob size and velocity in the atomizing edge region, using PIV and shadowgraphy;
- the mean droplet diameter, 50 mm downstream the atomizing edge, with PDA technique;
- the breakup mechanism through high-speed videos.

The **LDA** (for Laser Doppler Anemometry) technique uses a pair of coherent laser beams that cross at the velocity measurement location. In this region, the coherent beams form interference fringes with a regular and known inter-fringe distance. The flow is seeded with reflecting tracers, *i.e.* particles of very low Stokes number that closely follow the flow. When the particle travels through the dark and bright fringes, its reflective property produces a light signal with a frequency given by the ratio of the particle velocity by the inter-fringe distance u_p/d_i. Note that classical LDA only measures the velocity perpendicular to the fringes, and the measurement must be repeated with tilted fringes pattern to obtain other velocity components. The **3D** LDA uses 3 lasers of different wavelength to distinguish each velocity component at the same time.

In a **LFDM** (for Laser Focal Displacement Meter), the laser beam is oriented normal to the film surface and its focusing lens vibrates with a known displacement. As the lens moves, the focal point of the laser beam follows a shift proportional to the lens displacement. It is assumed that the backscattered light intensity is maximum when the laser focal point coincides with the film surface. The intensity is recorded as a function of time, and the peaks are related to the focal displacement *i.e.* the film surface shift. In this experiment the measurement range was 1 mm with a resolution of 0.1 µm. Further details on this device and its application on film surface height measurement are available in [71].

The **shadowgraphy** measurement technique consists in placing a homogeneous light source behind the object to measure. The shadow created by the object contrasts with the lighten up background. Both photography and video can be combined with this technique. One requirement is to measure sufficiently opaque materials. In this experiment shadowgraphy was used in concordance with a high resolution CCD camera to measure the size of the large droplets and blobs produced by the primary breakup. The diameter (or area equivalent diameter of ellipsoid or spheroid) was reconstructed by the use of a MATLAB image processing code [171, 244]. Coupled with a high speed camera, shadowgraphy was used to obtain high speed videos of the basic mechanisms responsible for this particular primary breakup.

Finally, it is important to note that a Depth of Field correction (DoF) is applied to the droplets measured with the CCD camera [104, 192]. If the droplet diameter is large compared to the focal plane thickness, the droplet gets blurred when it moves out of the focal plane. To overcome the measurement uncertainties coupled to this phenomena a calibration is mandatory. This yields a size correction for droplets that are larger than 70 µm.

The **PDA** (for Phase Doppler Anemometry) is an improvement of the LDA technique that uses two detectors for the light scattered by the particle. It allows to measure at the same time the velocity and the diameter of the particle. The principle of the diameter measurement relies on the phase shift between two different scattered beams. When it reflects (or refracts) a laser beam, a droplet diffuses the scattered light around its main direction of reflection (or refraction). The slight difference of angle in the light path induce a phase shift. Placing two detectors at different angles allows to measure this phase shift, that is translated into the droplet diameter. Note that this technique only works for nearly spherical objects or dual PDA setup. Further details can be found in [70, 347].

8.1.3 Spray visualization

Figures 8.2 and 8.3 show the experimental visualization of the spray shape for a bulk velocity of 20, 40 and 60 m/s. For a low gas velocity, the spray angle is much larger than for 40 m/s. This is a consequence of a significant flapping behaviour of the liquid accumulation coupled with the large size of the ejected liquid lumps that are characterized by a large Stokes number and a large momentum. The low velocity of the gas provides a low drag that operates in much

slower manner. Therefore the decreases of the gas velocity has a double 'in-phase' influence on the spray angle: (i) it increases the droplet size, leading to droplets of larger vertical momentum and (ii) it decreases the axial momentum transfer from the gas to the liquid.

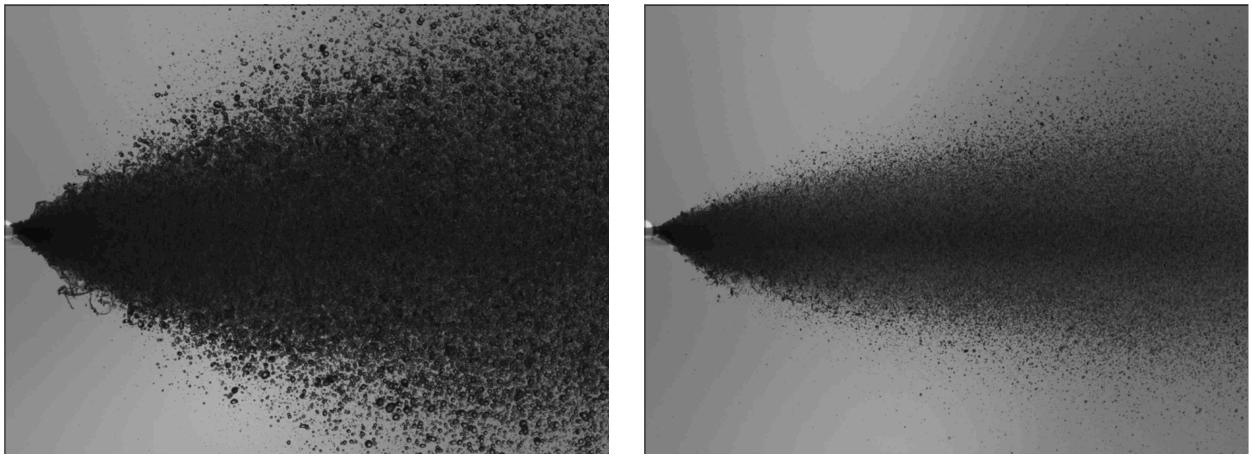

Figure 8.2 : *Experimental spray visualization for Shellsol D70, U_0 = 20 m/s (left) and U_0 = 40 m/s (right) (source: S. Gepperth from KIT-ITS).*

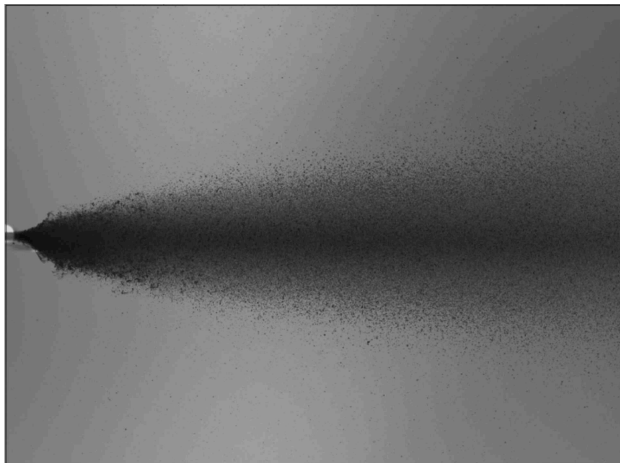

Figure 8.3 : *Experimental spray visualization, U_0 = 60 m/s, Shellsol D70 (source: S. Gepperth from KIT-ITS)*

8.2 Numerical setup

8.2.1 Computational mesh

The computational domain represents a part of the real test-rig and focuses on the prefilmer. It is composed of an inlet nozzle, the prefilming device, illustrated on Fig. 8.4 (*right*), and an atmosphere. The dimension of the atmosphere is much larger than the prefilmer length (Fig. 8.4 *left*) in order to avoid any back flow effect at the outlet.

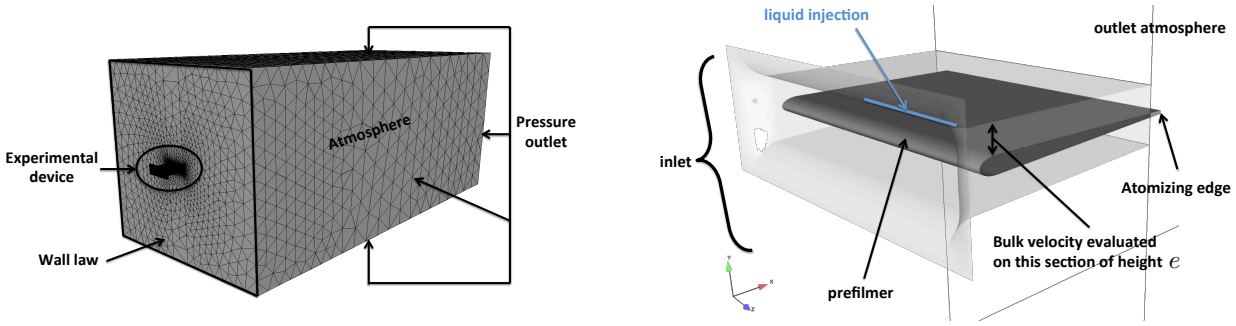

Figure 8.4 : *Computational domain. Left: superimposed with COARSE surface mesh. Right: zoomed on the prefilmer*

Three mesh resolutions were tested in order to evaluate the quality of LES and the grid refinement on the models developed in this thesis. Their characteristics are summarized in Table 8.5. The coarser mesh is labeled COARSE and is displayed on Fig. 8.5. It contains 4.8 millions of cells and allows to test the film and breakup models in case of low mesh resolution. The characteristic mesh size is 0.5 mm in both the film and the atomizing edge region. A finer mesh (labeled REF) is more representative of the typical cell size in nowadays realistic configurations and accounts 8.8 million elements. It is the reference mesh (Fig. 8.5). The film and atomizing edge region have a spatial resolution of 0.5 and 0.1 mm respectively. The third mesh (labeled FINE) aims at checking the mesh convergence of the simulation with a very small space step. Since the geometry has a large aspect ratio the meshing of the whole channel would be prohibitive. Therefore REF is refined to $\Delta x = 0.1$ mm in the center plane of the whole channel and downstream the atomizing edge (Fig. 8.6). The width of the refined layer is 1 mm, as displayed on Fig. 8.7 and leads to 28.7 million of cells. Although a full of hexahedral mesh was possible, tetrahedral cells were used as commonly done in industrial complex geometries.

Approximately five channel heights downstream the prefilmer, the mesh resolution is coarsened in order to reduce the computational expense and because an accurate capture of the flow field in this region is out of interest.

Parameter	Unit	COARSE	REF	FINE
Number of cells	$[-]$	4 750 983	8 757 443	28 782 397
Number of nodes	$[-]$	864 287	1 561 936	5 009 365
Film region mesh size	$[mm]$	0.5	0.5	0.1 (on the center plane)
Atomizing edge region mesh size	$[mm]$	0.5	0.1	0.1
Smallest element size	$[mm^3]$	$4.1 \cdot 10^{-3}$	$5.65 \cdot 10^{-5}$	$3.32 \cdot 10^{-5}$
Time step (CFL = 0.7)	$[\mu s]$	0.25	0.057	0.046

Table 8.5 : *Parameters of mesh resolution*

8.2.2 Numerical parameters

Numerical parameters are listed in Table 8.6. Convective and diffusive fluxes are resolved via the TTGC scheme [55] and the 2Δ diffusion operator [53] respectively. The main flow feature of the present experiment is a shearing layer due to the recirculation zone in the wake region in the prefilmer. Therefore, the *dynamic* Smagorinsky model [106] has been preferred for its better behaviour in pure shear region.

The inlet and outlet boundaries are set with characteristic method (NSCBC [272]). A turbulent velocity profile is imposed at the inlet, with a turbulent intensity of 10%, generated from a turbulent spectrum [325]. The different

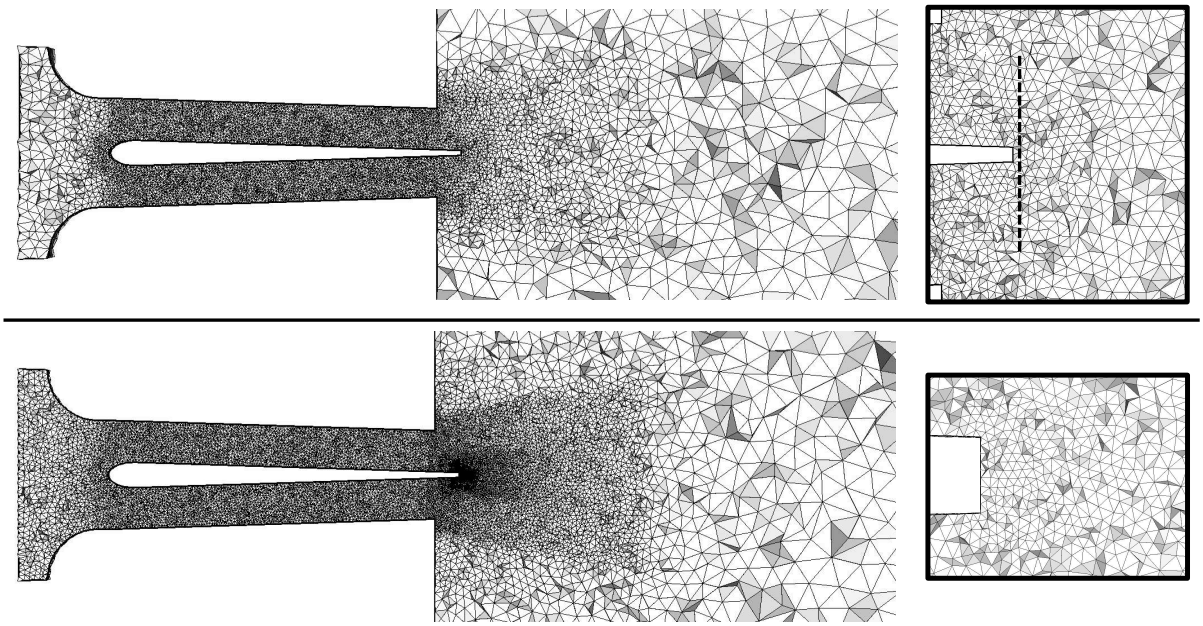

Figure 8.5 : *Mid-plane cut of the mesh with a zoom in the atomizing edge region. Top: COARSE, the dashed line in the zoom box corresponds to the location of the experimental measurement presented in 8.3.5. Bottom: REF.*

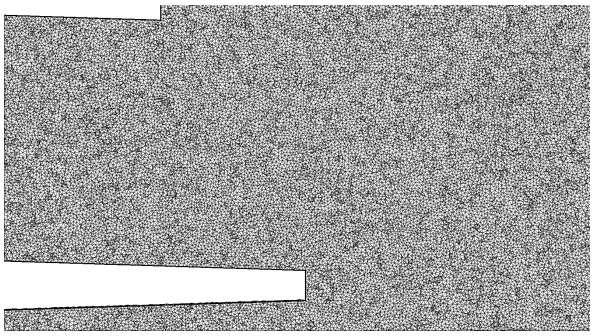

Figure 8.6 : *Part of the mid-plane cut zoomed in the atomizing region for the FINE mesh*

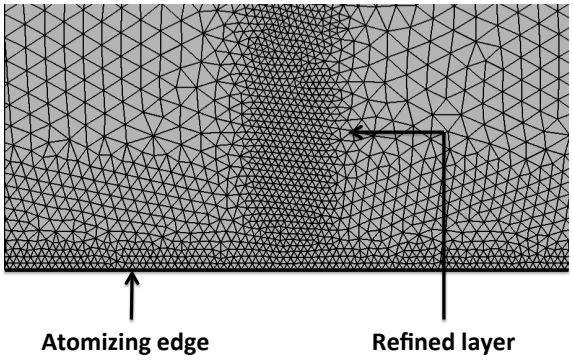

Figure 8.7 : *Top view of the prefilmer surface mesh showing the FINE refined layer*

inlet mean velocities, enumerated in Table 8.1, were imposed to match the experimental bulk velocity of 20, 40, 60 and 70 m/s at the lowest section of the channel (Fig. 8.4 *right*). The inlet temperature was constant (300 K) for all simulations. The outlet is controlled by a static pressure of 1 atm (103 748 Pa). All solid boundaries use the adiabatic law of the wall approach, except the atomizing edge where a slip velocity condition is imposed.

Contrarily to the experiment, the liquid is injected as droplets in the channel. The injection location is a spanwise line of 50 mm, 0.2 mm above the prefilmer surface, at the same x coordinates as in the experiment. The droplet velocity is oriented towards the wall surface with a magnitude of 1 m/s so that droplets impact the prefilmer and

Convection scheme	TTGC
Diffusion operator	2Δ
Subgrid scale model	Dynamic Smagorinsky
Artificial viscosity	Colin sensor [55]
2^{nd} order coefficient	0.05
4^{th} order coefficient	0.005

Table 8.6 : *Numerical parameters used thorough the simulations*

form a film at t = 0.2 ms after injection. Two-way coupling is deactivated in this zone to avoid any influence of these droplets on the gas flow. Considering the small angle ($11°$) between the prefilmer surface and the horizontal, gravity is neglected in this chapter.

8.3 Results from the purely gaseous flow simulations

In this section are presented the results of purely gaseous simulations for case U60. Instantaneous fields are first presented, followed by the mean fields. Finally an assessment of the quality of the LES performed is presented.

8.3.1 Instantaneous fields

The instantaneous fields are presented and compared for the REF and the FINE cases.

The global behaviour of the configuration is presented on Fig. 8.8. The flow is accelerated through the convergent nozzle and the front part of the wing-shaped prefilmer. Downstream the prefilmer "bump", the turbulent flow begins to establish. Then the gas flows downstream to the channel opening and the atomizing edge. The sudden change in hydraulic diameter due to the geometrical features (the channel opening and the atomizing edge) generates four shear layers (best visible on Fig. 8.9) that do not interact with each other in the atomizing edge region. The jet opens as it penetrates deep into the quiescent atmosphere. Large recirculation zones are created around the jet.

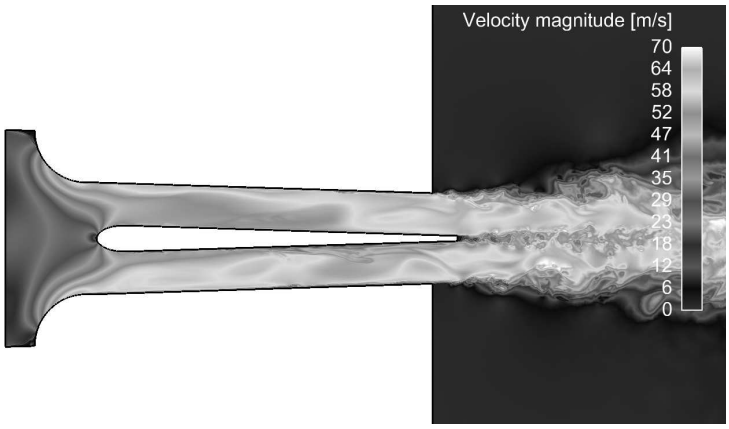

Figure 8.8 : *Instantaneous velocity magnitude in a mid-plane cut, FINE case*

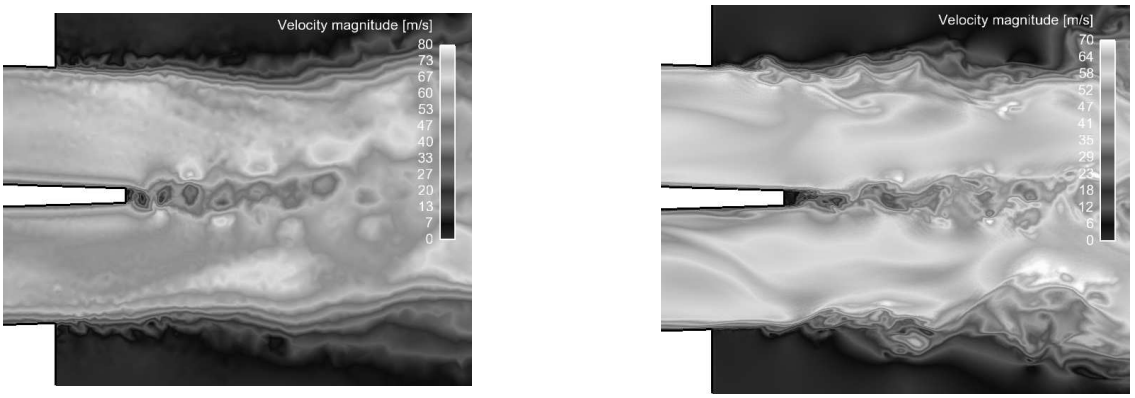

Figure 8.9 : *Velocity magnitude in a mid-plane cut in the atomizing edge region. Left: REF case. Right: FINE case.*

Atomizing edge region

A zoom of the flow in the atomizing region is visible on Fig. 8.9. The REF case is able to capture the velocity fluctuations in the wake region of the prefilmer, but with a lower resolution than the FINE case. The fluctuations induced by the shear layer at the outer part of the jet are not well resolved. Nevertheless this lack of resolution is not of primary importance for the simulation of the primary breakup and the vortex shedding, as they do not interact with the outer shear layers. Figure 8.10 displays a comparison of the transverse vorticity component. The REF case captures the von Kármán street that develops downstream the prefilmer. The coarsening of the mesh in the streamwise direction decreases the vorticity transverse component through numerical diffusion. In addition, comparison with FINE case clearly shows the influence of space filtering on the vortical structures. It is expected that this filtering has an impact on the prediction of the vortex frequency, as discussed in section 8.3.3.

As the vorticity is sensitive to velocity gradients, it is high close to the walls because of the wall normal velocity gradients, but it is not meaningful in these regions. The Q criterion is then proposed [130] as a better evidence of coherent turbulent structures:

$$Q = \frac{1}{2}\left(\Omega_{ij}\Omega_{ij} - s_{ij}s_{ij}\right) > 0 \tag{8.4}$$

with s_{ij} the strain rate and Ω_{ij} the vorticity tensor:

$$\Omega_{ij} = \frac{1}{2}\left(\frac{\partial u_i}{\partial x_j} + \frac{\partial u_j}{\partial x_i}\right) \tag{8.5}$$

Qualitatively, the REF case is able to capture the longitudinal variation of the vortex street, as illustrated on Fig. 8.11 via the isosurface of the Q criterion.

Time scales of the flow field

Two characteristic times can be defined for this experiment, related to the Reynolds numbers defined in Table 8.4. The convective time of the channel is defined by the time needed to fully renew the air of the channel. It is expressed by the ratio of the channel length (70 mm) by the bulk velocity:

$$\tau_c = \frac{L_c}{U_0} \tag{8.6}$$

The second characteristic time scale τ_a is linked to the vortex shedding and corresponds to the time period of the von Kármán street. As for the channel flow, it can be interpreted as the time required to renew the air in the wake

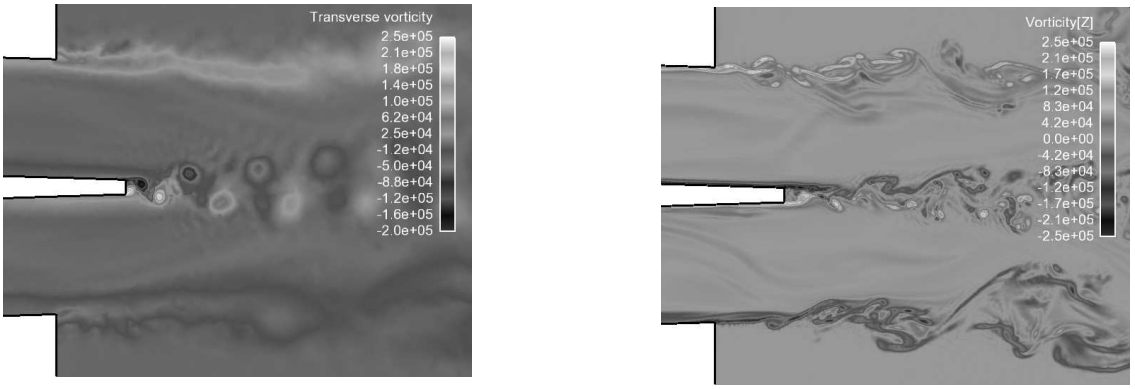

Figure 8.10 : *Transverse vorticity in a mid-plane cut in the atomizing edge region. Left: REF case. Right: FINE case.*

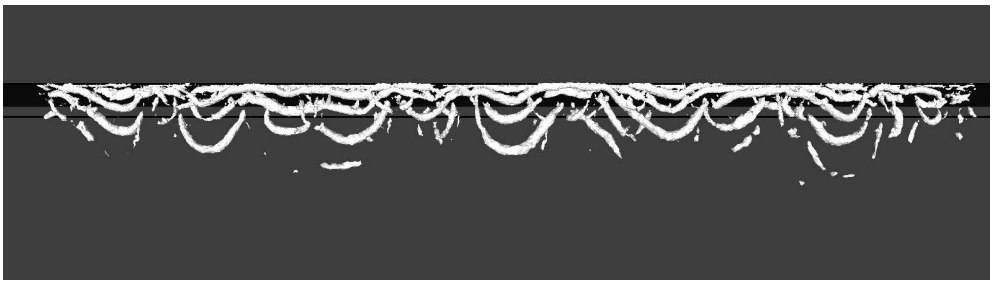

Figure 8.11 : *Top view of the prefilmer and atomizing edge region, superimposed with an isosurface of the Q-criterion ($Q = 5 \cdot 10^9\ s^{-2}$). The gas is flowing from the top of the picture.*

region, and it is equal to the inverse of the vortex shedding frequency (estimated from Fig. 8.15). Both time scales are evaluated for the various test cases in Table 8.7.

Case	Unit	U20	U40	U60	U70
τ_c	$[ms]$	3.5	1.8	1.2	1
τ_a	$[ms]$	0.24	0.10	0.06	0.05

Table 8.7 : *Time scales corresponding to different gas velocities*

8.3.2 Time-averaged fields

The global picture of the configuration presents a regular flow in the channel with no boundary layer detachment, and mixing layers developing at the trailing edge and the channel outlets.

Figure 8.12 shows the mean axial velocity in the trailing edge region. The outer shear layers are clearly visible and their opening angle is the same in the REF and FINE cases, even if the REF case has a lower space resolution in this region. In the wake region of the prefilmer, both meshes capture the recirculation zone although the FINE case predicts a slightly larger zone. The turbulent boundary layer presents a particular behaviour as it goes beyond the atomizing edge, as marked on Fig. 8.12 by a '*striped zone*' referred to as *zone A*. With the chosen banded color preset, the velocity gradient of the boundary layer is marked by stripes. These stripes are constant over the prefilmer

(*i.e.* a boundary layer of constant thickness), but when they goes beyond the sharp angle of the atomizing edge, they show a constriction over the recirculation zone, and then re-expands to their original height. For a given gaseous fluid particle located at a constant distance to the prefilmer surface, this pattern represents an acceleration and deceleration as it passes the edge and the recirculation zone. However, since the flow section increases at the atomizing edge location, the volume conservation implies a decrease of the axial velocity. Therefore the shrinking and expansion of these stripes in zone A are non physical effects that might be related to the use of wall functions, as discussed by Jaegle [162].

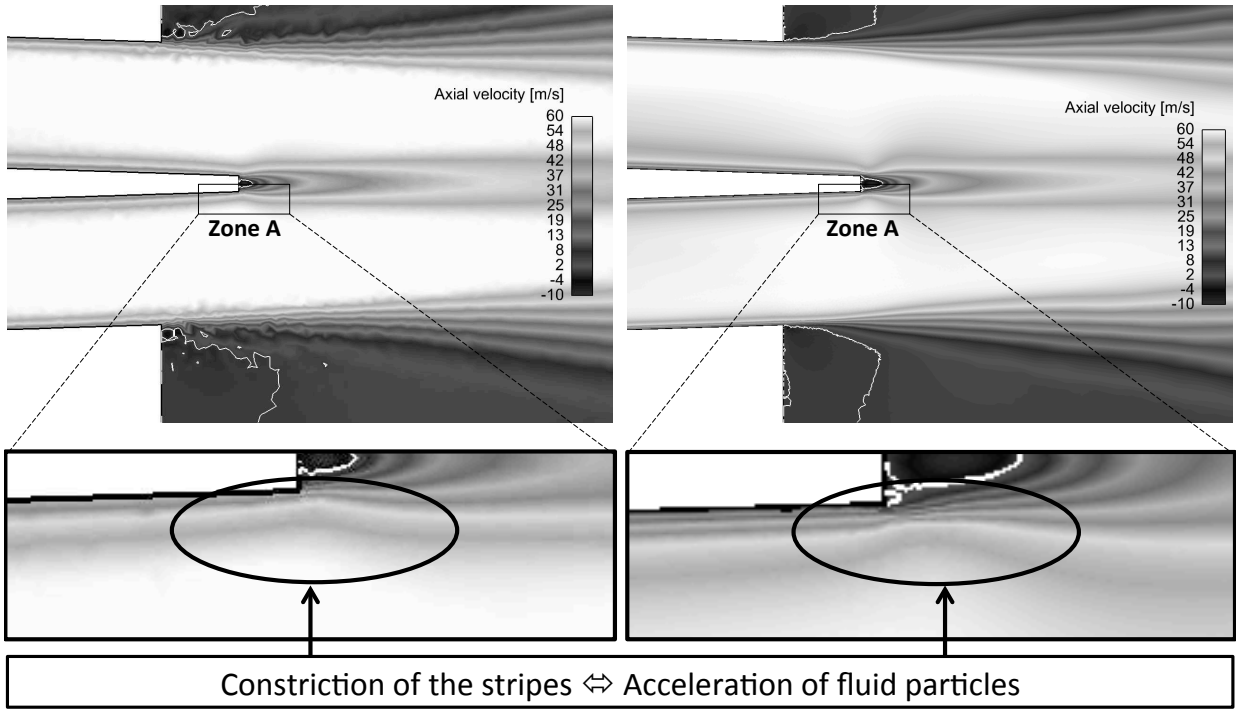

Figure 8.12 : *Axial velocity in a mid-plane cut in the atomizing edge region, superimposed with a zero velocity isocontour. Left: REF case. Right: FINE case.*

Figure 8.13 displays the 2D velocity vectors in a mid-plane cut zoomed in the wake region of the prefilmer. Over a distance smaller than h_a downstream the atomizing edge, two stationary contra-rotative vortices are visible. They constitute the time-averaged print of the vortices created by the high speed gas stream; and their alternative detachment leads to the vortex shedding phenomenon. The contra rotative vortices, and in turn, the recirculation zone, are smaller in the REF case. These vortices, and especially the one on the side of the film, have an impact on the turbulent dispersion of the particles and the width of the generated spray, as it will be seen in section 8.4.3.

Turbulent Kinetic Energy (TKE), that represents the mean kinetic energy deriving from the fluctuating velocity $\vec{u'}$, is defined as:

$$k = \frac{1}{2}\langle u_i' u_i' \rangle \tag{8.7}$$

where $\langle \cdot \rangle$ represents the time averaging process. Note that TKE represents half of the sum of the velocity components variance. In the LES context, the velocity is written as the sum of a filtered term and subgrid term:

$$u_i = \overline{u_i} + u_i'' \tag{8.8}$$

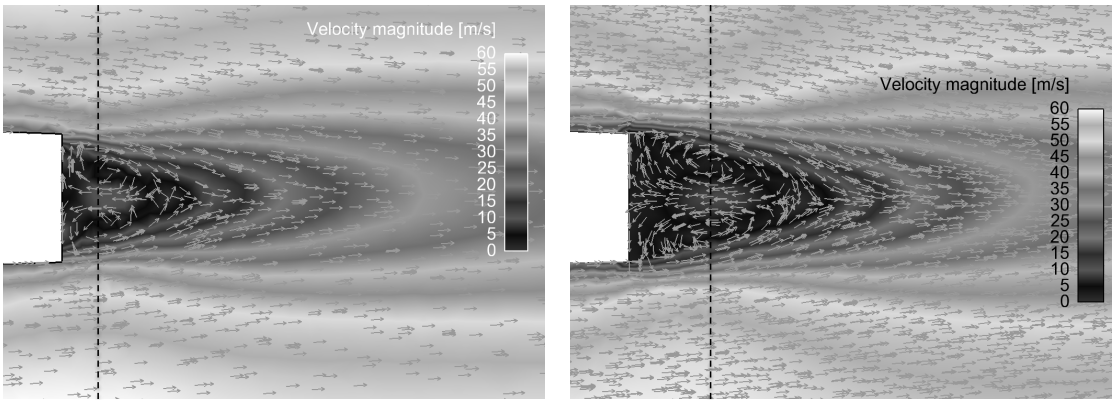

Figure 8.13 : *Velocity magnitude superimposed with velocity vectors projected on the mid-plane cut. Vectors size is constant. The dashed vertical line coincides with the vortices center. Left: REF. Right: FINE.*

and the TKE may be expressed as:

$$k = \underbrace{\frac{1}{2}\left[\langle \overline{u}_i^2 \rangle - \langle \overline{u}_i \rangle^2\right]}_{\text{RES}} + \underbrace{\frac{1}{2}\left[\langle u_i^2 - \overline{u}_i^2 \rangle + \langle \overline{u}_i \rangle^2 - \langle \overline{u}_i - u_i'' \rangle^2\right]}_{\text{SGS}} \tag{8.9}$$

The term RES in Eq. 8.9 corresponds to the kinetic energy of the filtered velocity and can be directly computed. The term SGS corresponds to the kinetic energy of the subgrid velocity. If the LES filter size is small enough, $u_i'' \ll \overline{u}_i$ and TKE reduces to:

$$k = \underbrace{\frac{1}{2}\left[\langle \overline{u}_i^2 \rangle - \langle \overline{u}_i \rangle^2\right]}_{\text{RES}} + \underbrace{\frac{1}{2}\left[\langle u_i^2 - \overline{u}_i^2 \rangle\right]}_{\text{SGS}} \tag{8.10}$$

The subgrid term in Eqs. 8.9 and 8.10 cannot be directly calculated since it involves the non-filtered velocity u_i, but it can be evaluated through the turbulent viscosity (Eq. 6.46). However in the following only the resolved part will be displayed and discussed: since the subgrid turbulent dispersion of droplets is not taken into account in this simulation, the droplet spatial distribution is not directly sensitive to the subgrid TKE.

The resolved TKE is displayed on Fig. 8.14. It highlights the presence of the shear layers and the vortex street where velocity fluctuations reach an important level compared to the rest of the domain. The spatial evolution of the boundary layer and the wake is opposite. The shear layer zones at the outer part of the jet show an increase of the TKE in the direction of the flow whereas the TKE level in the wake zone is maximum at a distance of $\approx h_a$ downstream the atomizing edge, and then decreases. This is because the vortices that seed the vortex street are generated close to the prefilmer (high TKE) and loose their angular kinetic energy as they interact with the main stream, leading to lower velocity fluctuations. The TKE pattern is comparable between the REF and FINE cases, with slight differences in opening angle of the shear layers. The location of maximum TKE in the prefilmer recirculation zone is also slightly shifted upstream in REF case.

8.3.3 Frequency analysis

In this section, the vortex shedding is studied through a frequency analysis. As the PAMELA model injects atomized droplets with a zero velocity, the spray angle fully depends on the gaseous velocity fluctuations that are high in the wake zone. Therefore the capacity of AVBP to predict the vortex shedding is critical to retrieve the spray angle in this particular configuration. The vortex shedding is characterized by an alternate periodic detachment of vortices

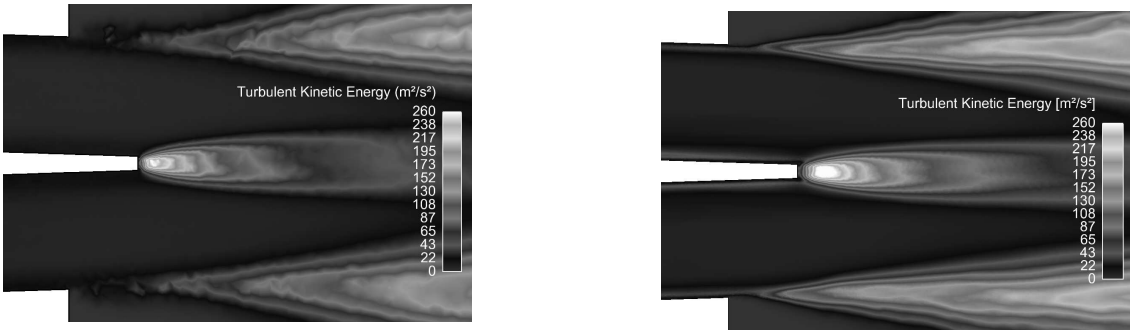

Figure 8.14 : *Turbulent kinetic energy in a mid-plane cut in the atomizing edge region. Left: REF case. Right: FINE case.*

with a regular frequency f_{vs}. The flow pattern of this phenomenon is populated with regularly spaced eddies that constituted the so called 'von Kármán street'. In the present study, the vertical velocity v is monitored with a series of probes and a sampling frequency of ≈ 100 kHz. The probes P_1 are immersed in the vortex street, 4 mm downstream the atomizing edge as illustrated on Fig. 8.15.

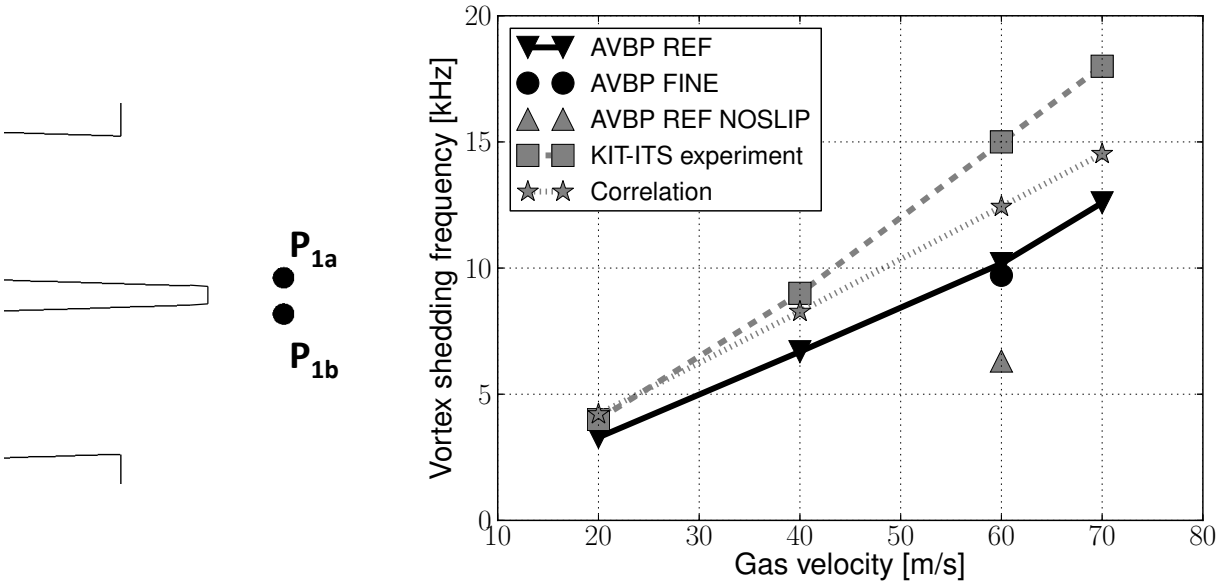

Figure 8.15 : *Left: Location of probes. Right: Comparison of the vortex shedding frequency between AVBP, experimental measurements and a correlation from [213]*

A Fast Fourier Transform (FFT) is applied to the signals monitored by the probes. A particular treatment was applied in order to strengthen the results, following the practical advices of [262], and automatically processed via an in-house tool developed by T. Livebardon:

1. The signal is interpolated onto a regular time axis, with a time step equal to the mean time step of the overall signal.

2. Multi-windowing is applied: the total signal is split into 4 subsets. It allows to smooth the spectral signal.
3. Overlapping: the overlap length is one fourth of the subset, leading to 13 sub-signals in total. This procedure is supported by the stationary and ergodic properties of the vortex street.
4. The cross spectrum of $P_{1,a}$ and $P_{1,b}$ is computed for each sub-signal and averaged.

The cross spectrum χ of $(P_{1,a}, P_{1,b})$ can be expressed as the product:

$$\chi = \mathcal{F}[P_{1,a}(t)] \cdot \mathcal{F}[P_{1,b}(t)]^* \tag{8.11}$$

where $\mathcal{F}$ represent the Fourier Transform (FT) and * is the conjugate. The cross spectrum therefore filters out the frequency peaks that are not shared by the two probes. It is useful to highlight the phenomena 'seen' by both probes.

The four test cases were computed on the COARSE and the REF meshes, while only U60 was computed on the FINE mesh. In addition, a case labeled NO SLIP, was also made on the REF mesh with a *no slip* condition on the prefilmer surface (*i.e.* no use of the law-of-the-wall and imposing a zero velocity at the wall) to quantify the impact of the law-of-the-wall. Figure 8.15 displays the peak frequency evolution with the gas velocity, in comparison with the experiment and a correlation from [213], expressed with the Strouhal number:

$$\mathrm{St} = f_{vs} \frac{h_a}{U_0} \approx 0.2 \tag{8.12}$$

Results on the COARSE mesh are not displayed because they did not show any peak frequency: the very low mesh resolution in the wake region of the prefilmer completely filters out the vortex shedding. For the REF and FINE case, the vortex shedding frequency is in good agreement with the experiment and the correlation, increasing with velocity. However, the slope of the curve deviates by 37% and 12% with the experiment and the correlation respectively. Unexpectedly, the FINE mesh does not provide a better result than the REF mesh. It may be explained by an inadequate wall treatment in the FINE case, as it will be seen in subsection 8.3.4. The deviation of the REF case, initially attributed to the use of wall function on the prefilmer surface was checked on the NO SLIP test case. However the insufficient wall resolution of the REF case with the no-slip condition leads to a strong under-estimation of the vortex shedding frequency. Finally the deviation between the correlation and the KIT-ITS experiment may be related to measurement and manufacturing uncertainties in the atomizing edge thickness.

8.3.4 Wall treatment

In wall flows modeling using the law-of-the-wall approach, it is preferred to have to wall resolution (y^*) between 30 and 100. As the wall unit strongly depends on the flow, the wall resolution is a function of the bulk velocity. To further investigate the wall treatment, Fig. 8.16 displays the wall flow resolution y^+ for the REF cases. The grey, black and white isolines represent y^+ = 10, 30 and 100. The main part of the prefilmer lies between 30 and 100 for all velocities. The refined mesh over the film region is clearly visible. With a $y^+ < 30$, the wall resolution is too fine in the atomizing edge region for a correct application of the law-of-the-wall for U20 and U40. A less accurate prediction of the velocity and the shear stress is expected in this region. For U60, the area below $y^+ = 30$ is reduced to a few nodes upstream the atomizing edge, and for U70, only one node is concerned. This highlights another meshing complexity of this type of geometry: it is preferred to have an accurate resolution in the atomizing edge region and a 'not too fine' mesh on the filming wall surface to stay in the validity range of the law-of-the-wall models. As two consecutive cells size ratio may not exceed 1.2, satisfying both conditions may be difficult for low velocity configurations.

On the other hand, the COARSE mesh (depicted on Fig. 8.17) is regularly meshed over the whole prefilmer, including in the atomizing edge region. This is due to the uniform mesh size of 0.5 mm for both the channel and the

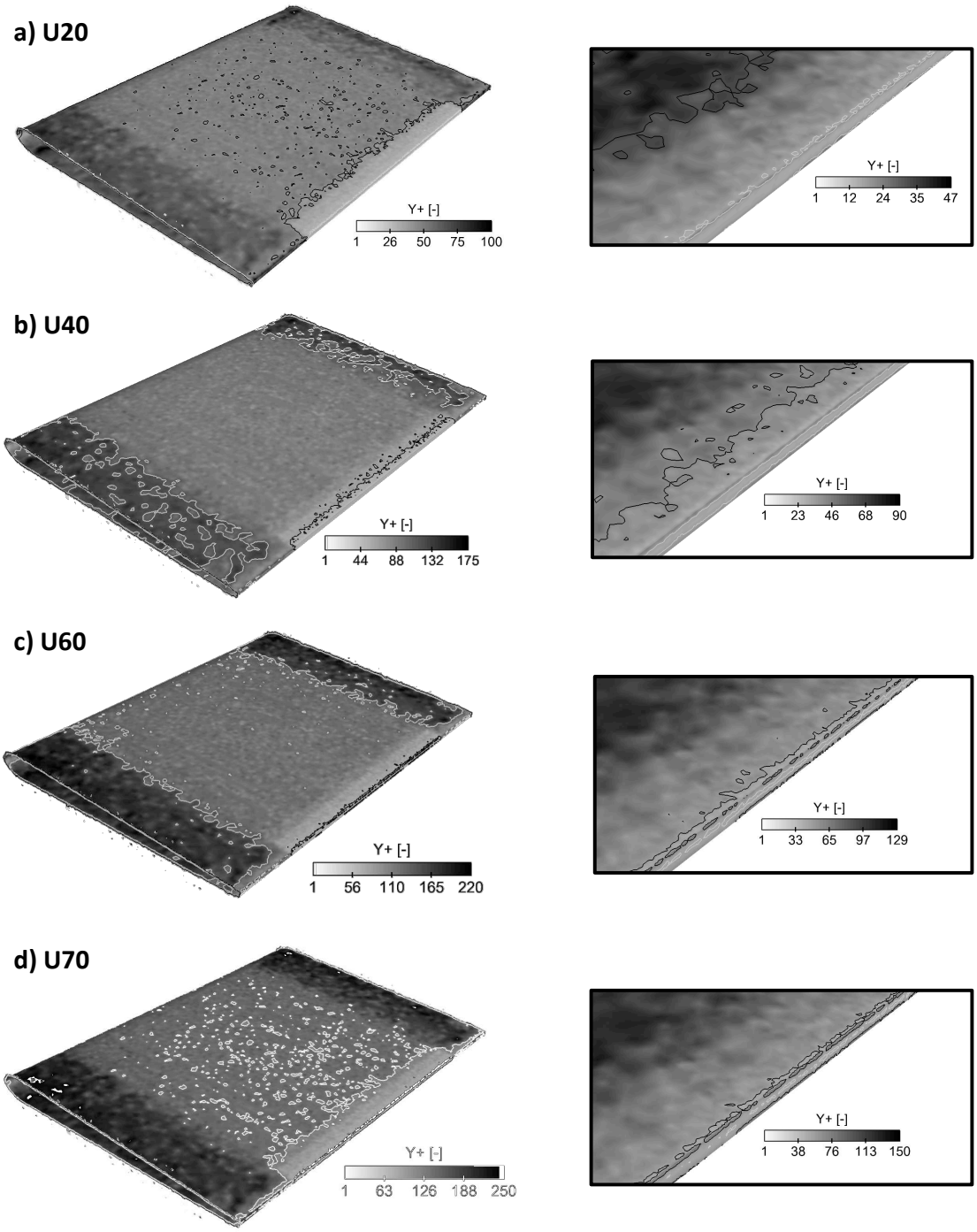

Figure 8.16 : *First wall cell height in wall units (y^+) from a REF time-averaged solution. The grey, black and white contours mark respectively y^+ = 10, 30 and 100.*

atomizing edge regions. This is an advantage for the film flow because it guarantees a more constant y^+ and shear stress prediction close to the atomizing edge. The COARSE mesh globally outputs a y^+ between 30 and 100. It decreases slightly under 30 for low velocity and increases to 130 for U7. For U20, longitudinal fringes of low y^+ are distributed in the spanwise direction. Given that $y^+ = y_{\text{first node}}\, u_\tau/\nu_g$ and that ν_g and $y_{\text{first node}}$ are roughly constant in this region, the origin of this pattern is linked to u_τ. Finally even if the COARSE mesh presents an acceptable y^+ distribution for all cases, the low resolution in the atomizing edge region that completely filters out the vortex shedding phenomenon makes it unadapted for the purpose of this study.

The y^+ mean value of the FINE mesh in the refined layer is between 10 and 20, which corresponds to the so-called 'buffer layer'. Contrary to the log law, this layer lacks of universal phenomenological law and a first off-wall node located in this zone is not recommended. This may explain the large deviation in the vortex shedding frequency, despite an enhanced mesh resolution.

From the previous comments, the deviation of the vortex shedding frequency f_{vs} with the experiment and the correlation can not be solely linked to the wall treatment on the prefilmer surface: in the REF case, the largest velocity case (U70) provides the most appropriate y^+ but also the largest deviation on f_{vs} at the same time, while it is the contrary for low velocity case (U20).

Figure 8.18 displays the wall shear stress on the prefilmer surface, computed from the time average solutions. The coarser mesh on the external parts is visible on both meshes by the saturated values. On the COARSE mesh, some longitudinal fringes appear in the same way as for y^+ (Fig. 8.17). However in this case, they are accentuated with medium and large velocities, contrary to y^+. It is observed that τ_w slightly increases along the x axis, on both meshes. In turn, the film thickness is expected to slightly increase as it is convected closer to the atomizing edge. As noticed with the observation of y^+, the wall shear stress presents a sharp increase in the atomizing edge region for large velocities on the REF case, due the to mesh refinement.

The distribution of τ_w over the prefilmer surface is not as smooth as it could be expected from a converged time average. However simulations were averaged over a duration of 13, 26, 38 and 40 convective times (increasing velocity) for the REF case and 31, 42, 84 and 69 for COARSE cases, and those averaging periods are usually sufficient to obtain converged statistics.

The wall shear stress averaged on the top face of the prefilmer, from the prefilmer bump to the atomizing edge over its whole width, for the COARSE and REF cases, is summarized in Table 8.8. The coarse mesh presents an over-prediction of $\approx 5\%$ in all cases. The deviation may be related to the different mesh size in the atomizing edge region, as discussed above, but also to the *dry* part of the surface, where the mesh size is larger.

Case	Unit	U20	U40	U60	U70
τ_w for COARSE mesh	$[Pa]$	1.71	6.04	13.0	17.3
τ_w for REF mesh	$[Pa]$	1.59	5.74	12.3	16.5
Deviation from COARSE to REF	$[\%]$	7.5	5.2	5.7	5.0

Table 8.8 : *Space average in the prefilmer surface of the wall shear stress for the different cases on different meshes.*

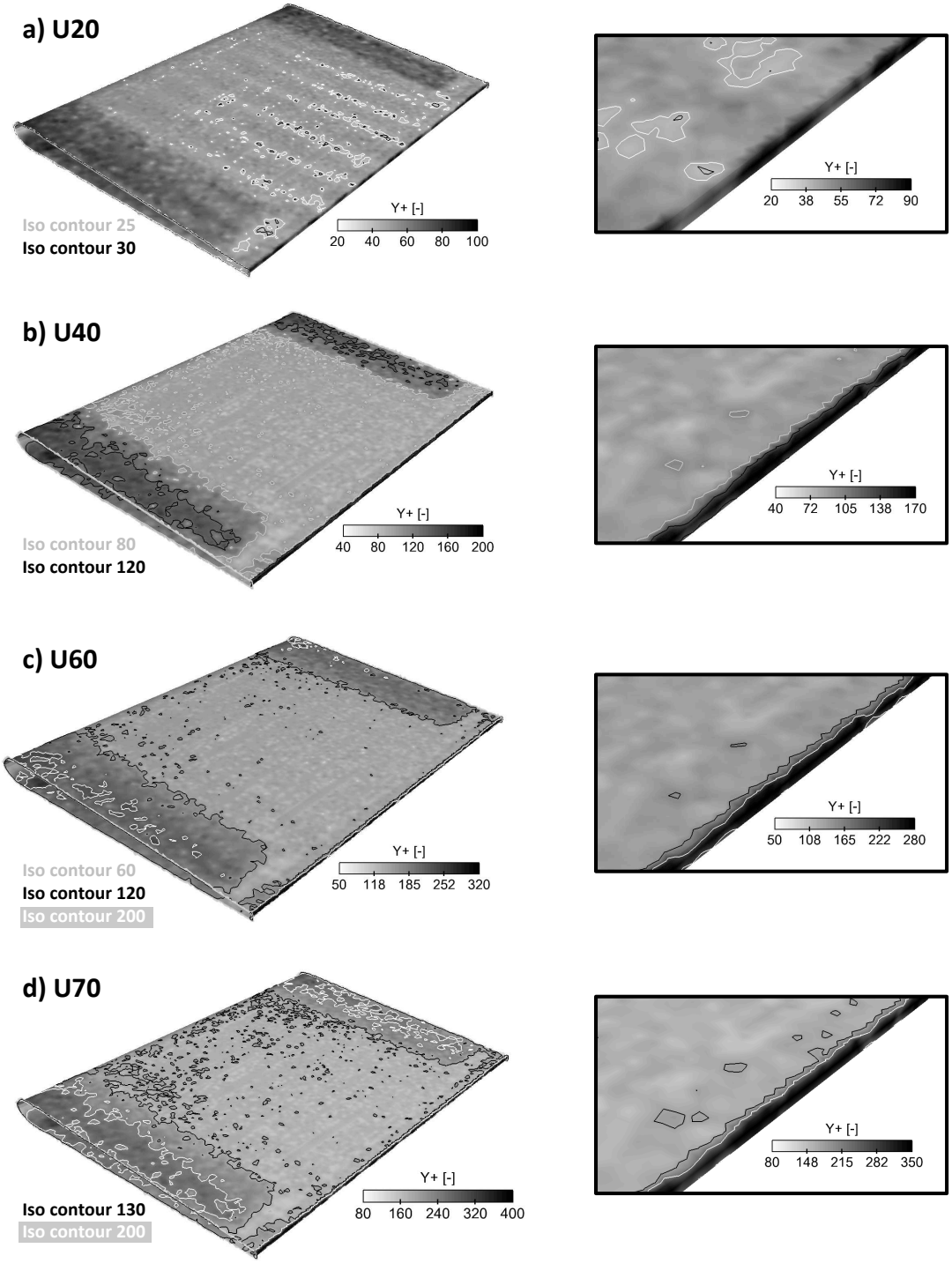

Figure 8.17 : *First wall cell height in wall units (y^+) from a COARSE time-averaged solution. The contours depend on the gas velocity.*

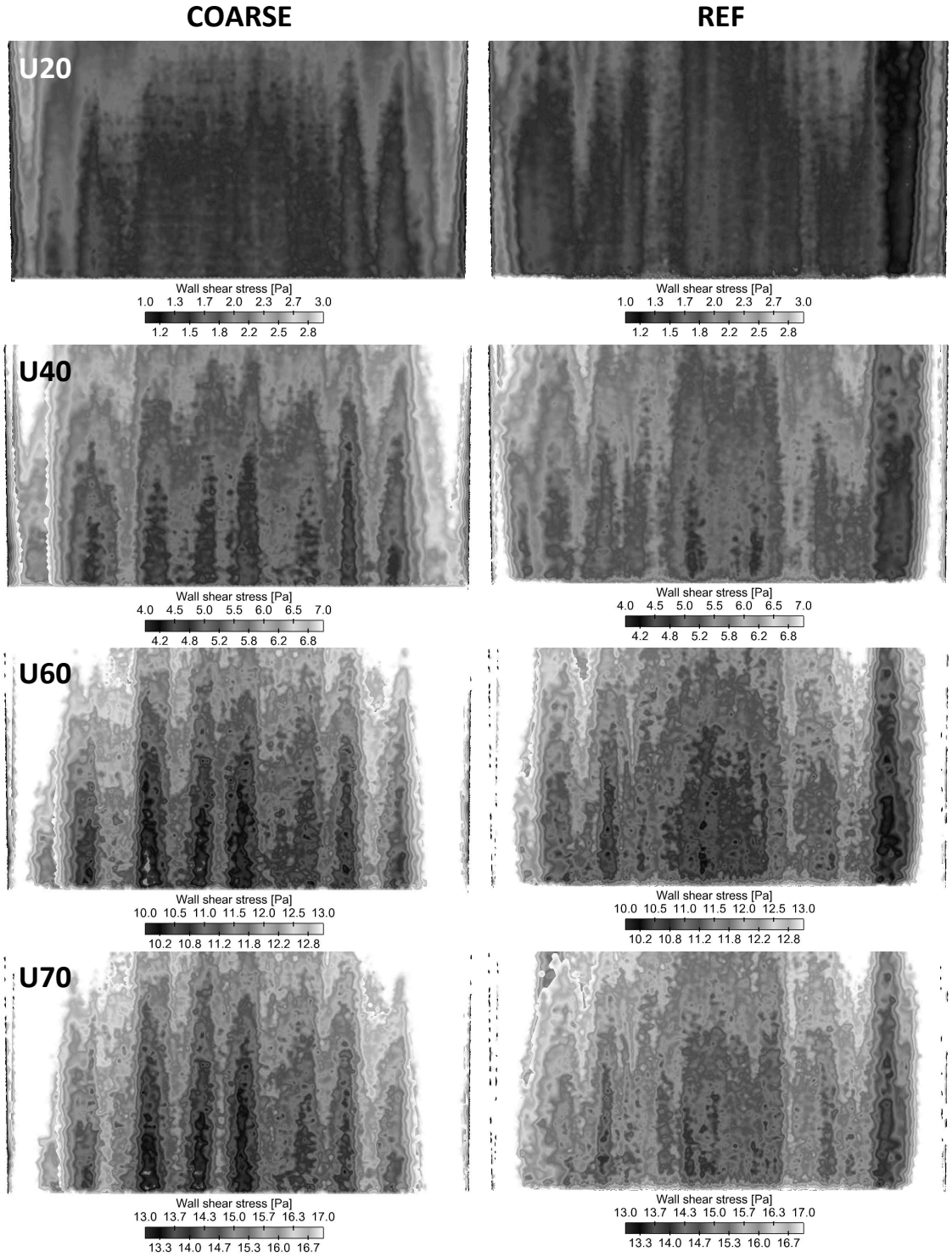

Figure 8.18 : *Time averaged wall shear stress on the top face of the prefilmer.*

8.3.5 Comparison of velocity profiles with the experiment

Axial and vertical mean velocity profiles on COARSE and REF meshes are compared with measurements on Fig. 8.19. The velocity is probed over a vertical line of 12 mm, 0.2 mm downstream the atomizing edge. This virtual line is marked on Fig. 8.5. For the REF case, the axial velocity prediction is very good for the three cases U20, U40 and U60 while the low space resolution of the COARSE mesh is already visible. The vertical velocity is also well predicted by the REF case but shows small discrepancies in the prefilmer wake region: the velocity sign changes several time in the simulation while it is rather monotonic in the experiment. This may be explained by the size of the stationary vortices visible on the time-average solution, as marked on Fig. 8.13 and sketched on Fig. 8.20: the black dashed line is set on the center of the vortices. Upstream this line in the wake region, when traveling downwards on a vertical line, the vertical velocity is sequentially *negative*, *positive*, *negative* and *positive*. Downstream this line, the vertical velocity is *negative* then *positive*. The upstream and downstream behaviour of the vertical velocity corresponds on Fig. 8.19 to the simulation and the experimental curves, respectively. Therefore for a constant distance downstream the prefilmer, the size of the vortices controls the vertical velocity behaviour. As this size is mesh dependent, the vertical velocity is difficult to predict accurately. In addition, taking into account the uncertainty of the experimental measurement location $\pm$ 0.1 mm, a slight shift in x can switch from one behaviour to another.

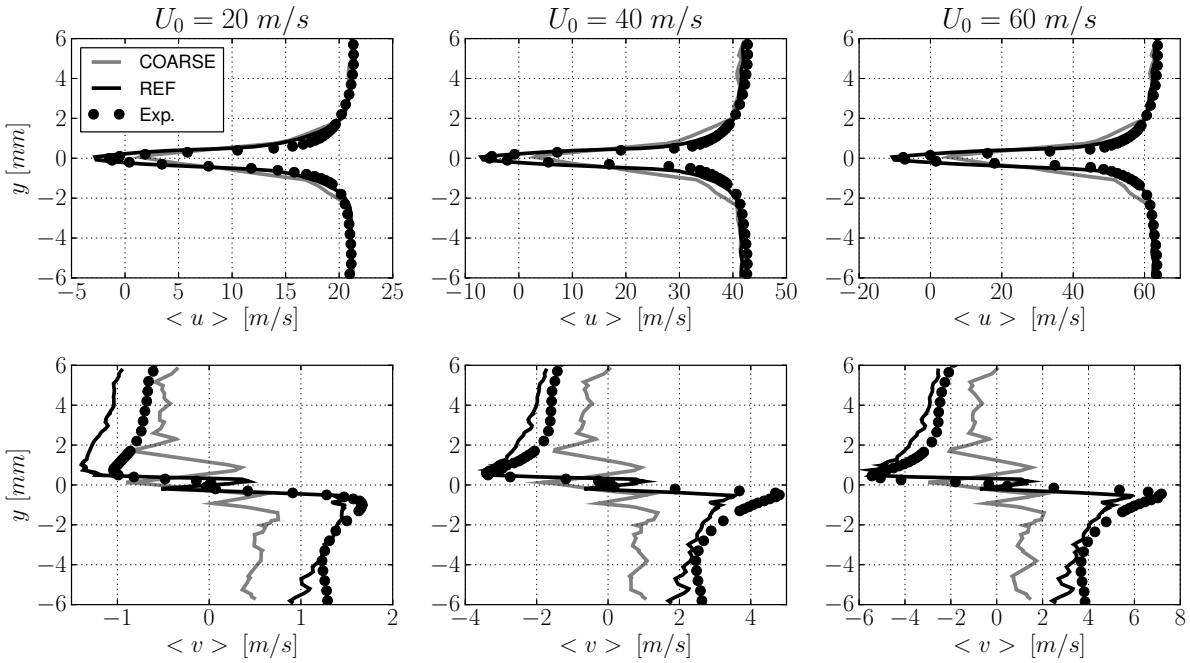

Figure 8.19 : *Comparison with experiment of axial (top) and vertical (bottom) mean velocity profile of the COARSE and REF cases*

The vertical velocity profile of the COARSE mesh is very distorted. It is not related to a too short time averaging period because simulations were run for a physical time of 110, 74 and 98 ms, (for U20, U40 and U60 respectively) corresponding to at least 31 convective times. A similar pattern appears in the three cases, that prefigures an effect of the too coarse mesh and confirms the necessity of increasing the mesh resolution in the von Kármárn street region.

The RMS velocity profiles are displayed on Fig. 8.21. The COARSE case profiles globally show the inability of a low resolution mesh to capture the turbulent phenomena in the wake region of the prefilmer. The REF case

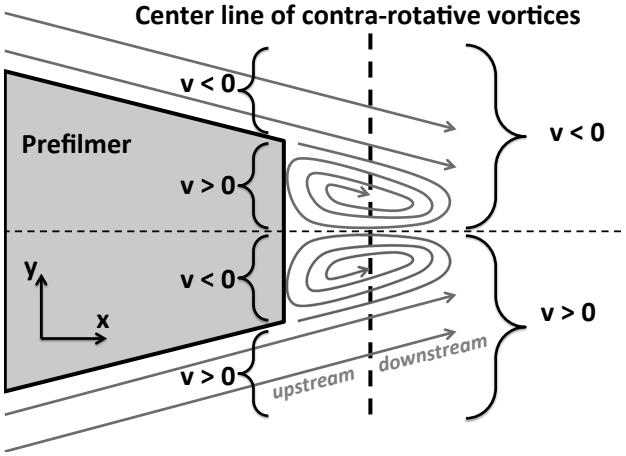

Figure 8.20 : *Schematic of contra-rotative vortices in the prefilmer recirculation zone. Prefilmer angle is increased for the sake of clarity.*

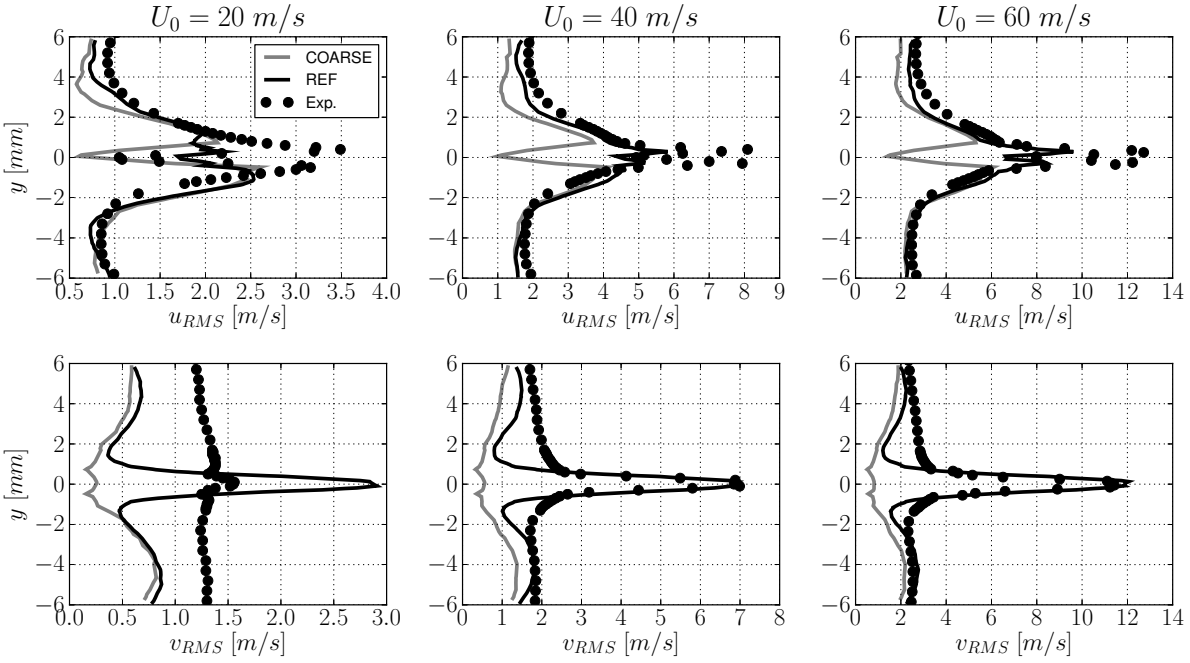

Figure 8.21 : *Comparison with experiment of axial (top) and vertical (bottom) RMS velocity profile of the COARSE and REF cases*

predictions are satisfactory: the axial RMS velocities follow the experimental trends with a low fluctuation point at the centerline and two surrounding peaks within the prefilmer thickness. Quantitatively, the value of the low fluctuation point is acceptable while the two peaks are lower than the experiment. It is representative of a lower fluctuation level that may derive from either the use of law-of-the-wall, or a too high momentum diffusion. Note that

the peaks are not symmetrical, suggesting an insufficient convergence, or as for the mean vertical velocity profile for the COARSE case, a mesh impact.

The experimental vertical velocity fluctuation (v_{RMS}) presents two distinct zones: a very flat profile in the channel and a peak in the wake region. The REF cases is able to capture the peak, but it shows a wavy profile in the channel zone while the experiment exhibits a flat one. From a quantitative point of view, the peak and the free stream ($y \approx \pm$ 6 mm) RMS are accurately predicted for U40 and U60. For U20 the experimental profile is very regular and the wake region presents a small peak. The observation of the experimental vertical *mean* velocity profile for U20 on Fig. 8.21 at $y \approx \pm$ 6 mm shows a non symmetrical profile. This may suggest that this experimental profile is not fully converged.

To conclude, comparisons of mean and RMS velocities with the experiment are good at medium (U40) and large (U60) velocities, where the wall treatment is better, *i.e.* where y^+ shows more adequate values, suggesting a link between velocity fluctuation and wall treatment. Furthermore the large discrepancy of u_{RMS} (Fig. 8.21) in the wake zone of the prefilmer for U40 and U60 may be related to the deviation of the vortex shedding frequency f_{vs} with the experiment (Fig. 8.15).

8.4 Results for the two-phase flow simulations

The main steps of the liquid phase flow are illustrated on Fig. 8.22. Note that in this figure, the film particles simply detach from the prefilmer edge and no primary breakup is activated, leading to an unchanged diameter. It is interesting to observe that during the film establishment, the front of the film is not regular and presents fluctuations in the propagation. This wrinkled film front is due to wall shear stress turbulent fluctuations.

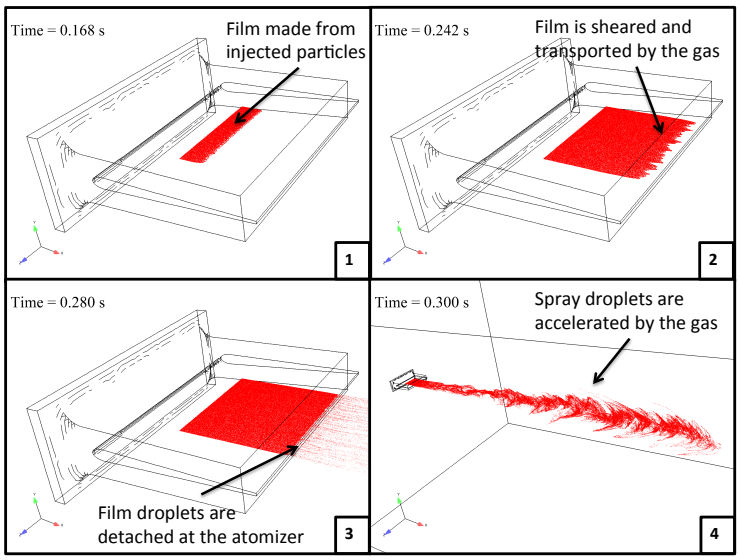

Figure 8.22 : *Main steps of film shearing, particle detachment and transport.*

8.4.1 Film flow

Predominant effect of the shear stress

In order to estimate the predominant phenomenon responsible for film motion, the mean wall shear stress τ_w and mean longitudinal pressure gradient $\partial p/\partial x$ are estimated from the purely gaseous simulations. Since there is no retro action of the film on the gas, these estimated values correspond to the ones seen by the film. In the film velocity expression (Eq. 6.10), the wall shear stress and pressure gradient terms appear as $\tau_w/2$ and $h/3 \cdot \partial p/\partial x$ respectively. The quantity A defined as the proportion of the shear stress and pressure gradient effects is expressed in $[\%]$ by:

$$A = 100 \cdot \frac{\tau_w/2}{\tau_w/2 + |h/3\,\frac{\partial p}{\partial x}|} \tag{8.13}$$

As the film thickness appears in the pressure gradient term, A is computed for several film thicknesses representative of typical flows in aeroengines: 50, 100 and 500 µm, leading to the quantities A_{50}, A_{100}, A_{500}. Values are summarized in Table 8.9: in this configuration, the pressure gradient has a minor effect on the film velocity. Expressing the

Case	τ_w	$\frac{\partial p}{\partial x}$	A_{50}	A_{100}	A_{500}
$[m/s]$	$[Pa]$	$[Pa/m]$	$[\%]$	$[\%]$	$[\%]$
U20	1.59	-519.8	99.46	98.92	94.83
U40	5.74	-1906	99.45	98.91	94.76
U60	12.3	-4134	99.44	98.88	94.70

Table 8.9 : *Order of magnitude of the effects responsible for the film motion, from the REF cases*

film thickness through the 2D volume flow rate Λ_f and the film velocity u_f (volume conservation, Eq. 6.42):

$$h = \frac{\Lambda_f}{u_f} \tag{8.14}$$

leads to the uncertainty expression of film thickness:

$$\frac{\Xi(h)}{h} = \frac{\Xi(\Lambda_f)}{\Lambda_f} + \frac{\Xi(u_f)}{u_f} \tag{8.15}$$

where $\Xi(\phi)$ stands for the uncertainty of the quantity ϕ. As Λ_f is an input value, $\Xi(\Lambda_f) = 0$ and the relative film thickness uncertainty is thus equal to the relative velocity uncertainty:

$$\frac{\Xi(h)}{h} = \frac{\Xi(u_f)}{u_f} \tag{8.16}$$

Note that additional error in the film thickness prediction can arise from the Eulerian projection of particle volume, as discussed in section 6.2.3.b). Equation 8.16 means that neglecting the pressure gradient in the film velocity leads to an error of at least (100-A)% on the film thickness, which is acceptable for the targeted accuracy of this study. Therefore the pressure gradient is neglected in the following and the film velocity (Eq. 6.10) simplifies to:

$$u_f = \frac{h}{2\mu}\,\tau_w \tag{8.17}$$

Estimation of the time needed to reach steady state

The film steady state establishment is a critical step, especially in explicit compressible Large Eddy Simulation where the time step is dictated by the acoustic CFL. As the film is mainly driven by the wall shear stress, the film thickness and mean velocity are evaluated from Eq. 6.43 and 6.10 with the mean value of the wall shear stress from the purely gaseous simulation. Results are given in Table 8.10, with a distance of L_c = 45 mm to travel from the injection to the atomizing edge, the convective time τ_c is between 101 and 1014 ms. This time period is prohibitive with regards to the number of cases to run on the REF mesh. Therefore a *frozen gas* approach described in subsection 5.4 is employed to establish the film from a mean gaseous solution. Tests were made to compare the film thickness between the classical and the *frozen gas* approach with U60L15 REF and U60L50 REF (2D volume flow rate of 15 and 50 mm^2/s respectively). The space-averaged film thickness deviation between both methods was 0.08% and 1% respectively for the low and high liquid flow rate. This method thus brings low deviation in the film thickness prediction and consequently is used for the present study.

In order to decrease the computational cost of the film simulation, the number of particles is decreased through a parcel approach. On another hand, the number of particles per cell must be sufficiently large to ensure a correct description. The parcel number N_p and the resulting number of particles that represent the film are listed in Table 8.11.

Physical value	Unit	$U_0 = 20m/s$			$U_0 = 40m/s$			$U_0 = 60m/s$		
Liquid type	–	D70		Prop.	D70		Prop.	D70		Prop.
2D volume flow rate Λ_f	$[mm^2/s]$	50	15		50	15		50	15	
Wall shear stress τ_w	$[Pa]$	1.59			5.74			12.3		
Film thickness h_f	$[\mu m]$	313	172	338	165	90.3	178	113	61.7	122
Film velocity u_f	$[mm/s]$	160	87.4	44.4	303	166	84.3	444	243	123
Convective time τ_c	$[ms]$	282	515	**1014**	148	271	534	**101**	185	365

Table 8.10 : *Estimated characteristic scales from the mean wall shear stress of single phase REF cases*

Physical value	Unit	$U_0 = 20m/s$			$U_0 = 40m/s$			$U_0 = 60m/s$		
Liquid type	$[-]$	D70		Prop.	D70		Prop.	D70		Prop.
2D volume flow rate Λ_f	$[mm^2/s]$	50	15		50	15		50	15	
Parcel number N_p	$[-]$	50	20	20	40	20	20	30	20	20
Number of particles	$[\times 1000]$	223	306	598	147	334	319	133	109	436

Table 8.11 : *Parcel number and number of film particles for each cases*

Film thickness

Longitudinal profiles of the film thickness with several air velocities and liquid types are displayed on Figs. 8.23 and 8.24. They are computed by projecting the film particles volume onto a longitudinal 1D grid. The projector is a rectangular function (that corresponds to a histogram of particles x position) and the mesh size is 0.5 mm like in the LES mesh. The profile is averaged over the spanwise direction. This post-processing is applied to a snapshot which partly explains the sharp fluctuation of the profiles. These correspond to the square projector applied to an

instantaneous particle field and are not numerical wiggles. The film thickness presents a slight increase with x, which is directly connected to the decreasing wall shear stress profile (Fig. 8.18). For moderate and high gas velocities, at the injection point, the liquid film is thin in the first cell and reaches its steady state thickness in the next cell. With the REF mesh at low velocity, the film thickness sharply drops in the atomizing edge region. This is due to an over prediction of the wall shear stress, where the mesh refinement leads to a y^+ in the buffer layer, as depicted on Figs. 8.16 and 8.18.

To visualize the transverse variation of the film, the particles are projected on a 2D cartesian mesh of 0.5 mm spacing (Fig. 8.25). The film thickness is very irregular in both axial and transverse directions. Axial fringes are visible in all cases, as if the film particles gather on constant z locations. The wavelength of these fringes is larger than the mesh size so it may be not related to it. These fringes are not visible at injection and their contour becomes more distinct as the particles moves along the prefilmer. This precludes any injection numerical artifact, and promotes the hypothesis of gas effect on the film particles. As thicker zones carry more volume to atomize, the presence of the fringes will bring heterogeneity in the primary breakup location.

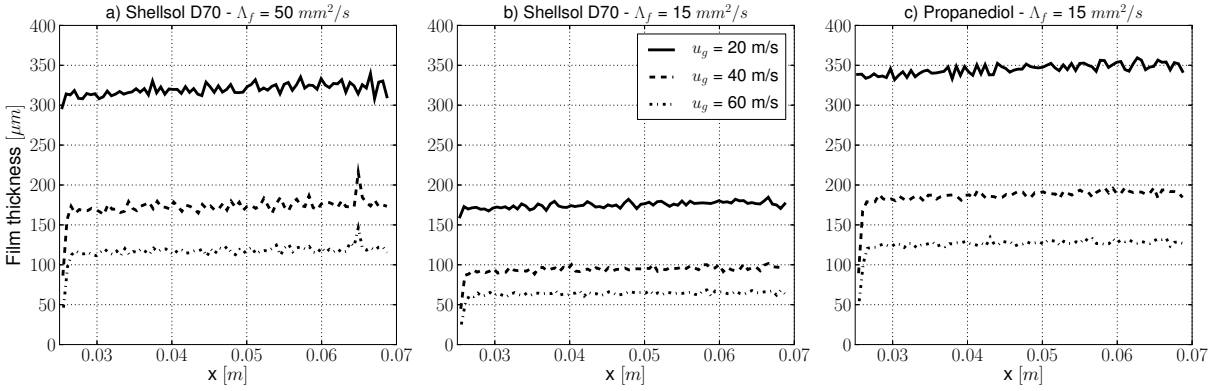

Figure 8.23 : *Profile of the transverse averaged film thickness along the prefilmer for the COARSE case*

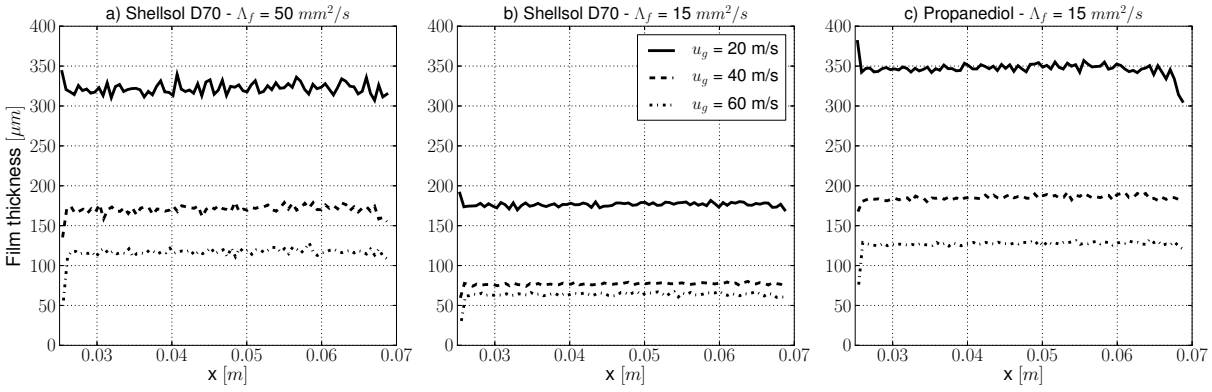

Figure 8.24 : *Profile of the transverse averaged film thickness along the prefilmer for the REF case*

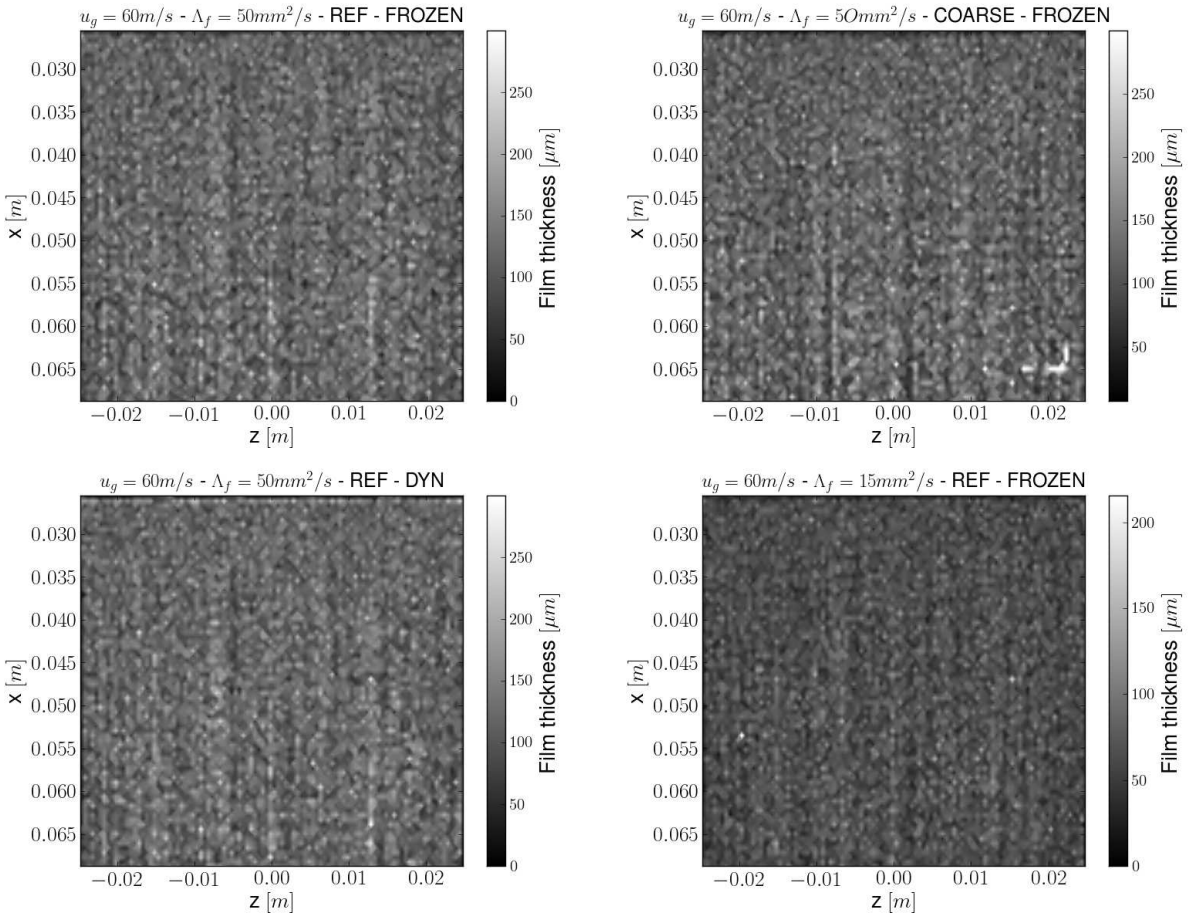

Figure 8.25 : *Film thickness computed from film particles volume and projected on a 2D cartesian mesh. The film is flowing from the top.*

Figure 8.26 compares the film thickness from the COARSE and REF cases with the experiment. Unexpectedly, both cases output the same numerical film thickness. As the COARSE mesh presents a mean wall shear stress higher by 5% (see Table 8.8), the film thickness was expected to be lower by $\approx 2.5\%$. However as stated above, the mean shear stress calculated in Table 8.8 is averaged over the whole top surface of the prefilmer, and the deviation may derive from the coarser mesh of zones not covered by the film.

The comparison with experimental data shows good trends with regards to the investigated parameters. The film becomes:

- thinner as the gas velocity increases;
- thicker for a more viscous liquid;
- thicker for a larger liquid volume flow rate.

However, the value of the film thickness is not well predicted, except for one set of parameters (U60L15D70). There are several possible origins for the deviation. First, the film model does not account for any roll waves that may appear at the interface, as observed in the experiment. Due to its shape, the roll wave is accelerated by the air stream leading to faster thus thinner film. In addition, the mean film velocity expression (Eq. 6.10) has been derived with the assumption of a flat interface, that does not hold in the presence of roll waves. Another possible reason is the retro action of the film on the gas, that may in turn increase the gas shear stress and thus decrease the film thickness. The last possible explanation is the unsufficiently accurate prediction by LES of the wall shear stress [18, 162] in real configurations.

From the 2D projection of the film thickness (Fig. 8.25), the standard deviation h_f^{RMS} is computed and displayed on Fig. 8.27 for the COARSE and the REF meshes. When normalized by the mean thickness, the standard deviation is between 20 and 30% which is a high level of fluctuation compared to the turbulent intensity ($\approx 10\%$) in the channel. This is mostly explained by the longitudinal fringes that appear at the end of the film: when the film thickness is averaged in the transverse direction, the fluctuation level is much lower, as visible on Figs. 8.23 and 8.24. As stated above, this heterogenous thickness is not critical for the breakup model but it can lead to heterogeneities in the liquid loading in the primary breakup region.

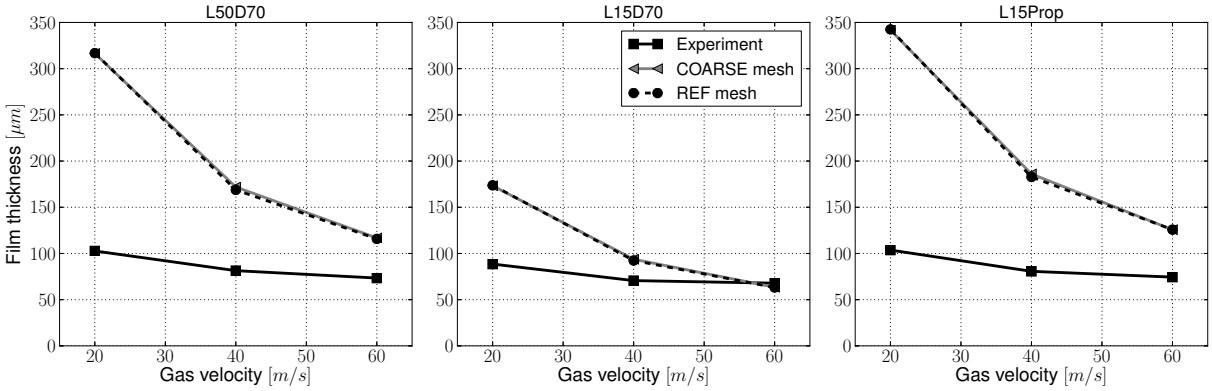

Figure 8.26 : *Comparison of the mean film thickness with experimental data*

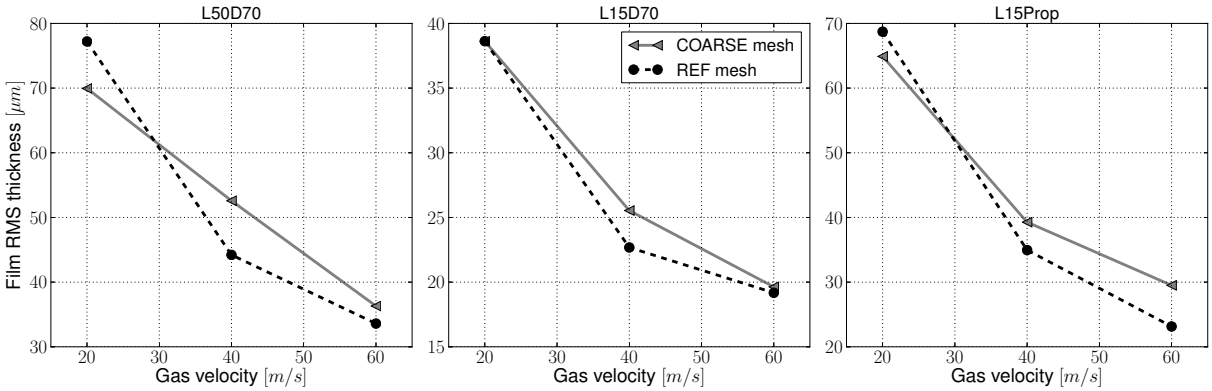

Figure 8.27 : *Film thickness standard deviation versus the gas velocity*

Velocity of film particles

The film velocity (Eq. 8.17) is the result of two fluctuating values: the wall shear stress and the film thickness. The wall shear stress undergoes time and space variations while the film thickness fluctuates mainly in space. Figure 8.28 is a scatter plot of axial and transverse film particles velocity components. It is extracted from a standard simulation (opposite to *frozen gas*) on the U60L50D70 REF case. The axial velocity starts from zero in the injection region, that is to be related to the low film thickness in this region (Fig. 8.24), and sharply increases to the steady state velocity. Its mean value is approximately constant over x but the dispersion seems to increase regularly, up to the atomizing edge where the fluctuations show a clear augmentation. Globally, the transverse velocity is not correlated with x: the mean value varies continuously in the flow direction. However the dispersion seems slightly larger in the injection and the atomizing edge regions. On Fig. 8.28, some peaks of the transverse velocity are regularly distributed. On Fig. 8.29 (*left*) is displayed the histogram of the axial film velocity. It has a global Gaussian shape, the width resulting from a combination of wall shear stress and film thickness fluctuation. A histogram of the transverse velocity is shown on Fig. 8.29 (*right*). The Gaussian shape is also visible and the mean value is unexpectedly non zero, but slightly negative. As this histogram is taken from one snapshot, it means that the instantaneous spatial mean of the transverse velocity is not zero. As the film globally moves in the longitudinal direction, it can be expected that the time and space averaged transverse velocity is zero.

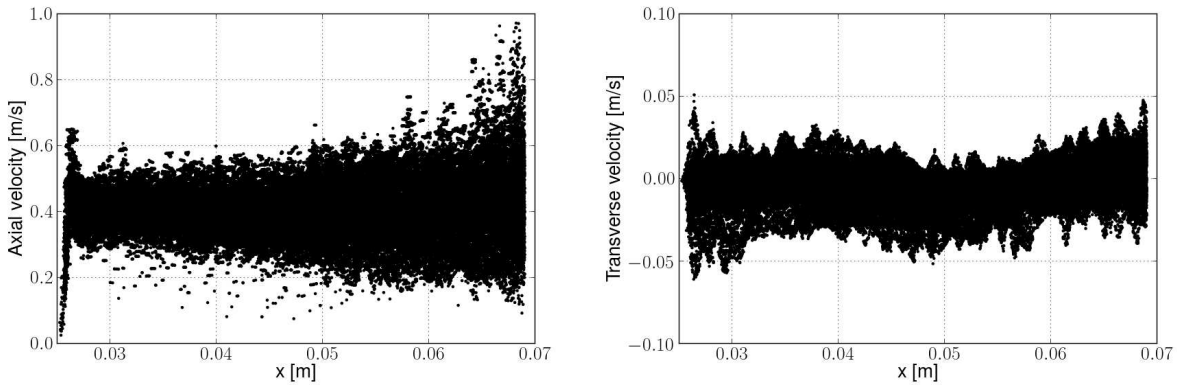

Figure 8.28 : *Scatter plot of the axial and transverse velocity components versus x coordinate, for U60L50D70 REF*

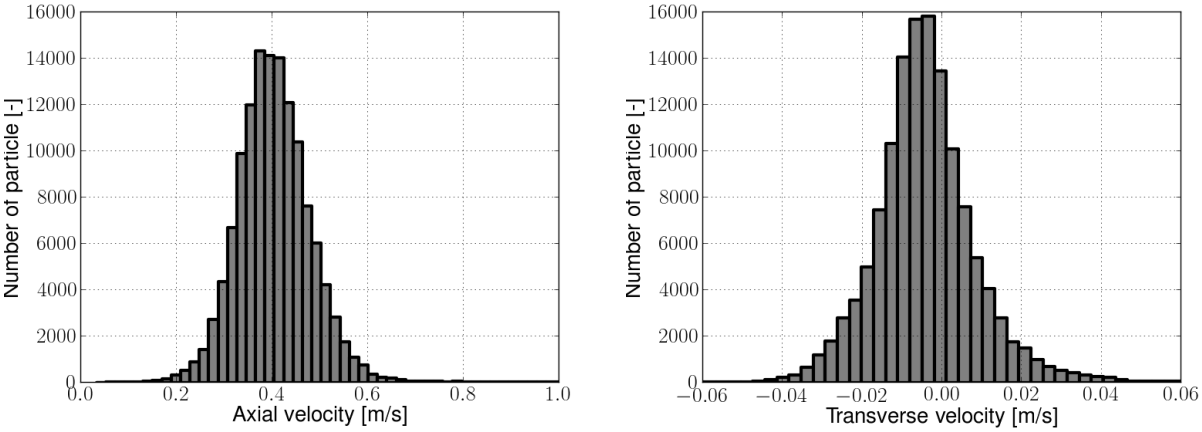

Figure 8.29 : *Histograms of film particles axial (left) and transverse (right) velocity component, for U60L50D70 REF*

Steady state establishment

In this section, the time to reach the steady state is measured from the *frozen gas* simulation by monitoring the volume of the film V_f versus physical time. For a more intuitive handling, the volume is converted into a thickness through a division by a constant surface. This surface is defined as the surface covered by the film when the steady state is reached:

$$S_f = b \cdot L_f \tag{8.18}$$

where b and L_f are respectively the width and length of the film. It leads to the monitoring thickness

$$h^{mon}(t) = \frac{V_f(t)}{b \cdot L_c} = \frac{\Lambda_f \cdot t}{L_c} \tag{8.19}$$

When the film reaches steady state, h^{mon} follows a plateau at the mean film thickness depicted on Fig. 8.26. Using non-dimensional variables t^* and h^* defined as:

$$t = t^* \cdot \frac{L_c}{u_f} \tag{8.20a}$$

$$h^{mon} = h^* \cdot \frac{\Lambda_f}{u_f} \tag{8.20b}$$

Equation 8.19 reduces to:

$$h^* = t^* \tag{8.21}$$

This expression corresponds to the filling of a reservoir with a constant mass flow rate. Figure 8.30 (*left*) displays $h^*(t^*)$ for different cases on the REF mesh with the *frozen gas* approach while Fig. 8.30 (*right*) compares the *frozen gas* approach with the dynamic one on the COARSE mesh. The unity slope (Eq. 8.21) is well recovered for each case, but the final film thickness is slightly larger than expected. This deviation is due to the estimation of the wall shear stress used to derive characteristic scales. Since it is a space average over the whole top surface of the prefilmer, it includes the very coarse dry zones where the shear stress prediction is less accurate. However, this result shows that the steady state establishment time can be estimated correctly from the mean value of the wall shear stress, when the pressure gradient is negligible. Furthermore it is observed here that the filling time of the film computed from a time averaged wall shear stress in combination with the *frozen gas* approach or with the dynamic approach are

identical. This is explained by the large film-to-gas convective timescale ratio $\tau_f/\tau_g = U_0/u_f \approx 100$: the influence of the high frequency gas fluctuations on the film are smoothed out by the traveling time of the film front along the prefilmer.

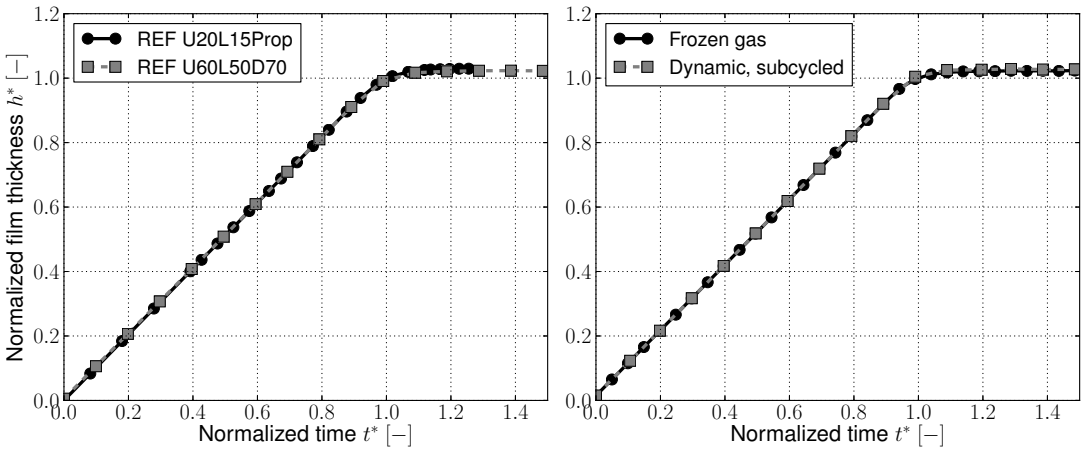

Figure 8.30 : *Non dimensional film monitoring thickness versus non-dimensional physical time. Left: REF,* frozen gas *approach. Right: U60L50D70 COARSE ,* frozen gas *and dynamic approaches.*

Conclusion

Two meshes, two types of liquid, three gas velocities and two liquid flow rates were extensively tested and compared with experiment. The use of the *frozen gas* approach with a time averaged gaseous solution accelerates the film steady state. It leads to a maximum film thickness deviation of 1% between the *frozen gas* and the classical approach with a speedup of ≈ 2000. The low value of the film thickness allows to neglect the longitudinal pressure gradient within the film. Consequently, *a priori* estimations are easily accessible with converged averages of the gaseous flow fields. The estimation of the steady state establishment times (Table 8.10) is in good agreement with the *frozen gas* approach as well as with the classical approach. As the film particles evolve on the prefilmer surface, they tend to gather, forming longitudinal fringes of thicker film. This effect is not critical but may bring heterogeneities in the generated spray downstream the atomizing edge. The velocity of film particles is distributed following a normal distribution that is a consequence of wall shear stress fluctuations and film thickness heterogeneities.

Finally, the quantitative prediction of the film thickness is poor at low gas velocity, and medium at higher gas velocities. The main reasons for this deviation are the absence of interface deformation modeling such as Kelvin-Helmholtz instabilities or roll-waves, and the one-way coupling approach between the gas and the film. However, comparison with experiment of the film thickness shows that the model has the proper dependencies with the influent parameters. In addition, the film thickness is not an influent parameter for primary atomization.

8.4.2 Atomization process

This section focuses on the primary breakup model presented in Chapter 7 (PAMELA) at the atomizing edge and especially the droplet size distribution of the generated spray. In this chapter, PAMELA is applied in a LES context, therefore the local $5C$ formulation of the model is used with the quantities u_{70} (Eq. 7.58a) and y_{70} (Eq. 7.58b) defined in section 7.4.2 and expressed in section 7.8.2.a). Three gas velocities are tested: 40, 60 and 70 m/s. For a low gas velocity (U20) the droplets are very large and a converged experimental PDF could not be obtained. The

two liquids described in subsection 8.4.1 and one atomizing edge thickness of 1 mm are investigated. All case are labeled in Table 8.12. The 2D volume liquid flow rate was kept to 50 mm^2/s and does not appear in the case names.

Liquid type	Gas velocity [m/s]		
	40	60	70
D70	**U40D70**	**U60D70**	**U70D70**
Prop.	**U40Prop**	**U60Prop**	**U70Prop**

Table 8.12 : *Test case matrix for the simulation of primary atomization*

In order to reduce the CPU costs of the film model, the liquid is injected 0.8 mm upstream the atomizing edge. The modification of the injection location does not create any deviation with the full film simulation since PAMELA does not rely on the film thickness. The film particles are convected by the gas to the atomizing edge where they feed the atomization model. As described in Chapter 7, they are converted into accumulation particles and record the gas velocity. After a period determined by the time scale of the Rayleigh-Taylor instability, their mass fills in a virtual reservoir connected to their cell, and they transmit the average gas velocity to the Rosin-Rammler parametrization. If enough mass is available, a droplet is created and placed in the first cell downstream the atomizing edge with a zero velocity. The turbulent mixing is in this case the unique responsible of the spray shape.

Accumulation particles

When a film particle passes from a cell to the next one, the model checks the angle between the normal vectors. If this angle is superior to 60°, then the breakup model is activated and the particle becomes an *accumulation* particle. The gaseous velocity u_{70} is estimated from the wall shear stress and calibrated value of y^+ as detailed in 7.8.2.a), and is used to determine the characteristic time scale of the Rayleigh-Taylor instability τ_{RT} (Eq. 7.34) that corresponds to the time during which the particle records the gas velocity.

Figure 8.31 (*left*) shows the value of τ_{RT} averaged over all the accumulation particles. According to theory, as the bulk velocity becomes larger, the characteristic time scale of the instability decreases. The difference between Shellsol and Propanediol comes from the surface tension which is a parameter of the Rayleigh-Taylor instability. The deviation between the COARSE and the REF cases is explained by the lower estimated velocity for the COARSE case, leading to a longer time scale τ_{RT}. This effect is visible on Fig. 8.31 (*right*) where the estimated gaseous velocity seen by the liquid accumulation u_{70} is normalized by the bulk velocity. This value is is approximately 10% lower on the COARSE mesh and accordingly to expression of Eq. 7.34, it is little influenced by the liquid type. As seen in Chapter 7 the mean value of u_{70} should be 70% of the bulk velocity. The calibration of the model onto $U_0 = 60\ m/s$ with the REF case is clearly visible. The deviation from 70% for $U_0 = 40$ and $70\ m/s$ is low, about 3%.

A more detailed analysis of u_{70} is displayed on Fig. 8.32. Its two first statistical moments are compared with different meshes, liquid types and gas velocities. The mean value of $\langle u_{70} \rangle$ increases linearly with the bulk velocity, but Fig. 8.31 (*right*) shows a slight variation in the proportionality factor. The standard deviation is representative of u_{70} fluctuations. It may be interesting to link the fluctuations of the estimated gas velocity seen by the liquid accumulation to the fluctuations of the gas velocity computed from the solver. Due to its expression ($u_{70} = cste \cdot u_\tau$, Eq. 7.40), u_{70} fluctuations directly derive from the shear velocity u_τ fluctuations:

$$\sigma(u_{70}) = cste \cdot \sigma(u_\tau) \tag{8.22}$$

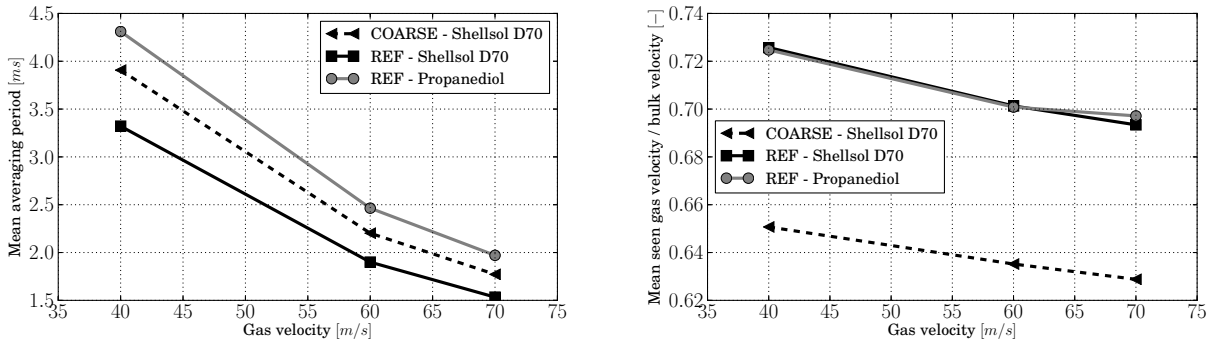

Figure 8.31 : *Left: mean averaging time τ_{RT} of accumulation particles. Right: mean gas velocity seen by the accumulation particles divided by the bulk velocity*

where σ stands for the standard deviation operator. Unfortunately it is not simple to quantify the standard deviation of u_τ from the bulk velocity fluctuation, as shown in the expression recalled below:

$$u(y) = u_\tau \left[\frac{1}{\kappa} \ln\left(\frac{y\, u_\tau}{\nu} \right) + B \right] \tag{8.23}$$

As u_τ appears twice in Eq. 8.23, there is no direct expression of $\sigma(u_\tau)$ with $\sigma(u)$. However Eq. 8.23 clearly states that fluctuations of u_{70} are correlated to the fluctuations of $u(y)$ but the shape of the distribution is changed and cannot be easily foreseen.

The standard deviation graph of Fig. 8.32 shows a constant shift between the Shellsol and Propanediol curves for the REF case. This is because the larger surface tension of the Propanediol imposes a longer averaging period τ_{RT}, and thus a less fluctuating output.

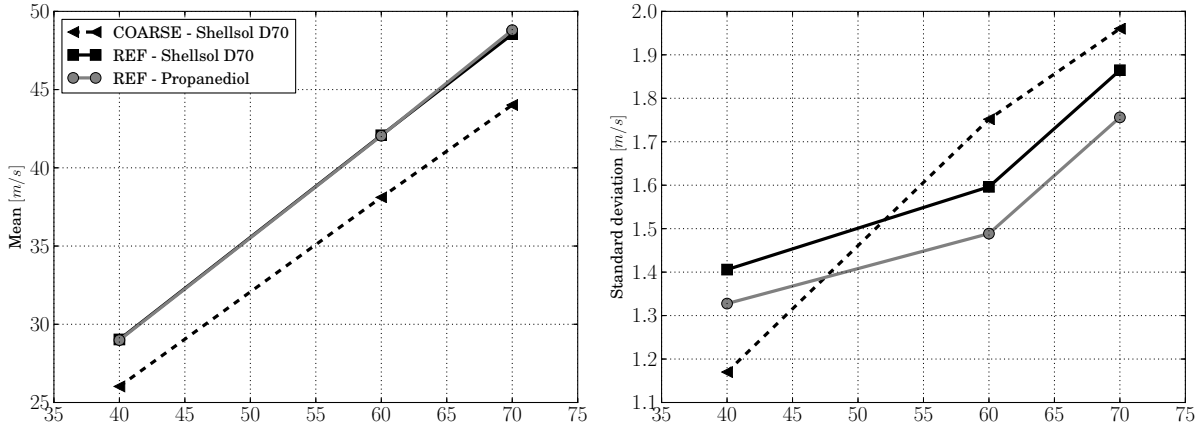

Figure 8.32 : *Mean (left) and standard deviation of u_{70} versus the bulk velocity*

Figure 8.33 shows some histograms of u_{70}, averaged over a period τ_{RT}, for U40 and U60. A dissymmetrical distribution is clearly visible for the U40D70 on the REF mesh (top left). The COARSE mesh (top right) is more symmetrical but presents a peak shifted to $\approx$ 38.5 m/s while it is 42 m/s for REF cases (bottom line: U60Prop REF and U60D70 REF) which show an overall shape close to a normal distribution.

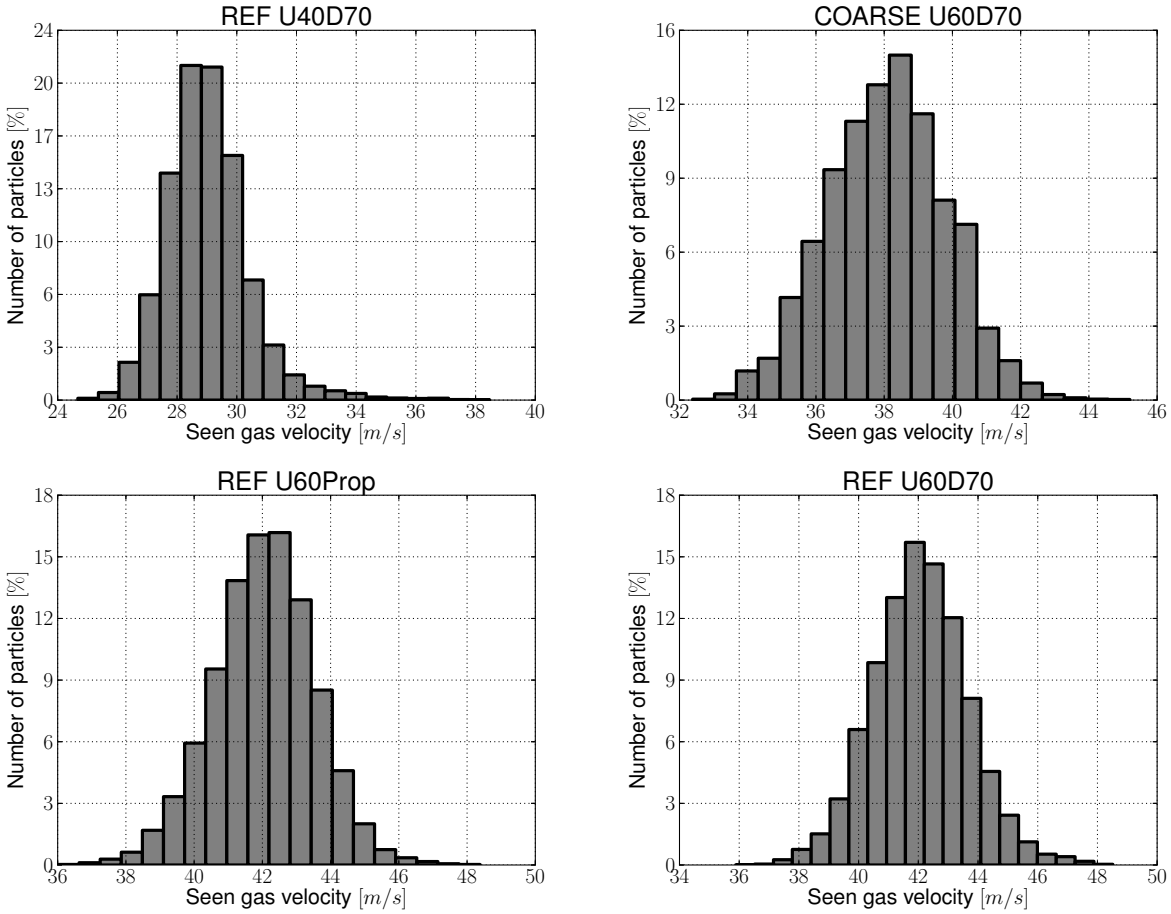

Figure 8.33 : *Histogram of the gaseous velocity seen by the accumulation particles* u_{70}

The error quantification of the primary breakup model due to fluctuations of the input velocity was assessed in section 7.6 by comparing the output mean diameters with a reference case of constant input velocity. Table 7.4 presented the deviation of mean diameters with a mean velocity difference of $\pm$ 10 % (labeled case A in the following), and when the gas velocity was described by a Gaussian PDF with a non zero standard deviation (labeled case B in the following). In the present simulation, u_{70} is not always equal to 0.7 U_0, as illustrated on Fig. 8.31 (*right*), and constitutes the case A. In addition, as the velocity seen by the liquid accumulation fluctuates, the case B is automatically triggered for each simulations. The relative deviation D_m and the relative standard deviation (labeled I_t to recall the turbulent intensity) between a targeted mean velocity ($\langle u \rangle_{tar}$) and a recorded mean velocity ($\langle u \rangle_{rec}$) is expressed:

$$D_m(u) = \frac{\langle u \rangle_{rec} - \langle u \rangle_{tar}}{\langle u \rangle_{tar}} \tag{8.24a}$$

$$I_t(u) = \frac{\sigma(u)}{\langle u \rangle_{tar}} \tag{8.24b}$$

As U_0 and u_{70} are proportional, they yield the same relative deviation and the same relative standard deviation:

$$D_m(U_0) = D_m(u_{70}) \tag{8.25a}$$
$$I_t(U_0) = I_t(u_{70}) \tag{8.25b}$$

Equations 8.24 and 8.25 allow to link to D_m and I_t of this experiment to the error quantification of section 7.6. In section 7.6 Case A with a mean velocity difference of $\pm$ 10% leads to $D_m(u_70) = \pm 10\%$ and $I_t(u_{70}) = 0\%$, and case B with velocity fluctuations of 3 m/s lead to $D_m(u_70) = 0\%$ and $I_t(u_70) = 5\%$. Consequently deviations of cases A and B in section 7.6 can be compared to the results obtained with LES.

Table 8.13 summarizes the value of D_m and I_t for tested cases. By comparison with Table 7.4 for D_m, the COARSE case roughly corresponds to $U_0 - 10\%$ (case A) and, according to Table 7.4, the COARSE case is expected to deliver a D_{V10} and a D_{32} 10% larger than expected. The REF cases present deviations lower than 10% and the diameter prediction discrepancy cannot be precisely assessed but is lower than 10%. The turbulent intensity parameter I_t is lower than 5% for every cases, leading to the line corresponding to $\sigma = 3\,m/s$ in Table 8.13. Consequently the expected error due to fluctuations is below 1% for the D_{V10} and a D_{32}, and about -2% for the D_{V90}.

Physical value	Unit	$U_0 = 40m/s$			$U_0 = 60m/s$			$U_0 = 70m/s$		
Liquid type	[–]	D70		Prop.	D70		Prop.	D70		Prop.
Mesh type	[–]	COARSE	REF		COARSE	REF		COARSE	REF	
$D_m(u_{70})$	[%]	-7.0	3.7	3.5	-9.2	0.19	0.12	-10	-0.94	-0.41
$I_t(u_{70})$	[%]	4.2	5.0	4.7	4.2	3.8	3.5	4.0	3.8	3.6

Table 8.13 : *Deviation of u_{70} statistics from the constant targeted value*

Diameter distribution

In order to compare the diameter volume distribution of the generated spray with the experiment, each droplet injected with PAMELA is included into a statistical set. The large experimental data sets contain between ten and one hundred thousands of samples. The convergence of these sets were checked by computing their mean, variance, skewness and kurtosis for a growing number of samples gradually by 10%. The same process was applied to the data set from the numerical simulation.

Figures 8.34 to 8.36 summarize the results and compare them with experimental data. For each figure, the top left graph represents the mean diameters of the distribution versus the bulk gas velocity. The other graphs display the volume distribution for U40 (top right), U60 (bottom left) and U70 (bottom right). The squares symbols stand for the experiment, while the simulation is represented by a line with circles.

The low and medium mean diameters (D_{V10} and D_{32}) are well predicted and the D_{V90} is overestimated, due to the lower statistical quality of the large diameter classes. In addition this effect is amplified by the conversion to the *volume* PDF: as the volume is proportional to d^3, a droplet ten times larger than another is one thousand times more important when converted into volume. The predicted volume PDF is in very good agreement with the experimental data for all cases, suggesting an appropriate determination of the PAMELA constants in Chapter 7. The lower statistical convergence for large diameters is also observable: the tail of the distribution is always less smooth than around the peak. The increased weight of large diameters in the volume distribution is clearly visible for U70 on Fig. 8.34 at 700 µm. For low velocity (40 m/s) on both meshes, the peak is slightly under predicted. This is because the q parameter of the Rosin-Rammler function fitted from experiment is more scattered, and its correlation

from experimental data is less accurate, as seen on Fig. 7.9: lower velocities induce smaller Weber numbers and more scattered data.

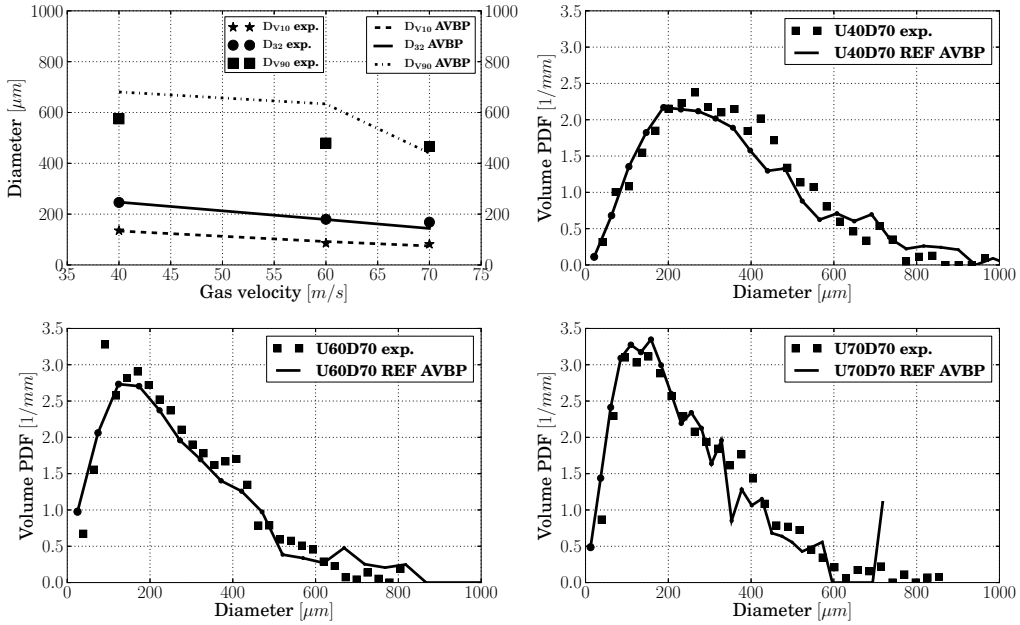

Figure 8.34 : *Characterization of the generated spray for the REF case and Shellsol D70. Top left: mean diameters comparison. Top right: U40D70, Bottom left: U60D70. Bottom right: U70D70*

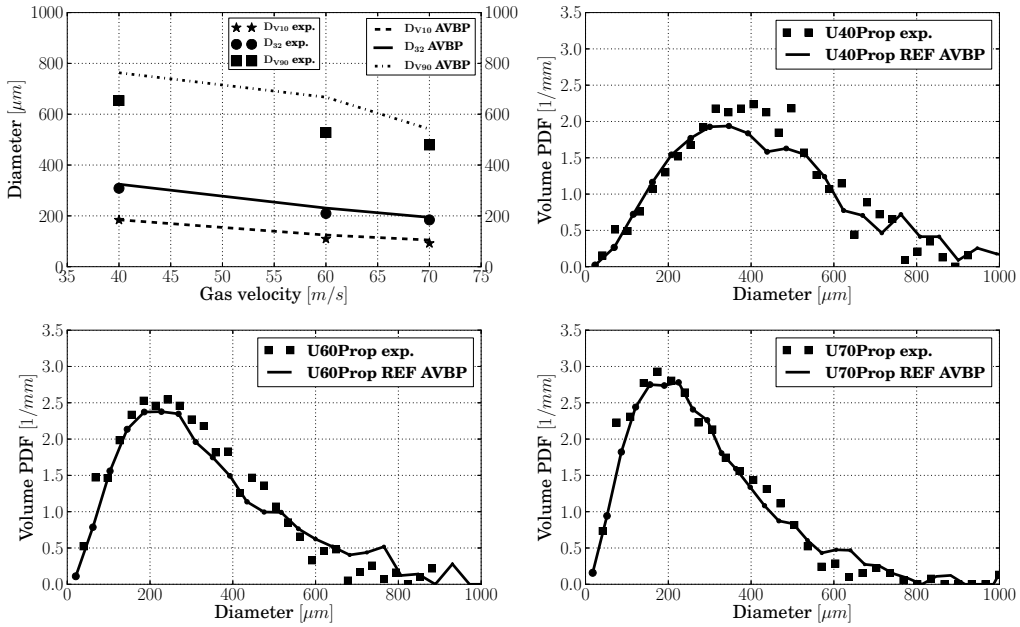

Figure 8.35 : *Characterization of the generated spray for the REF case and Propanediol. Top left: mean diameters comparison. Top right: U40Prop, Bottom left: U60Prop. Bottom right: U70Prop*

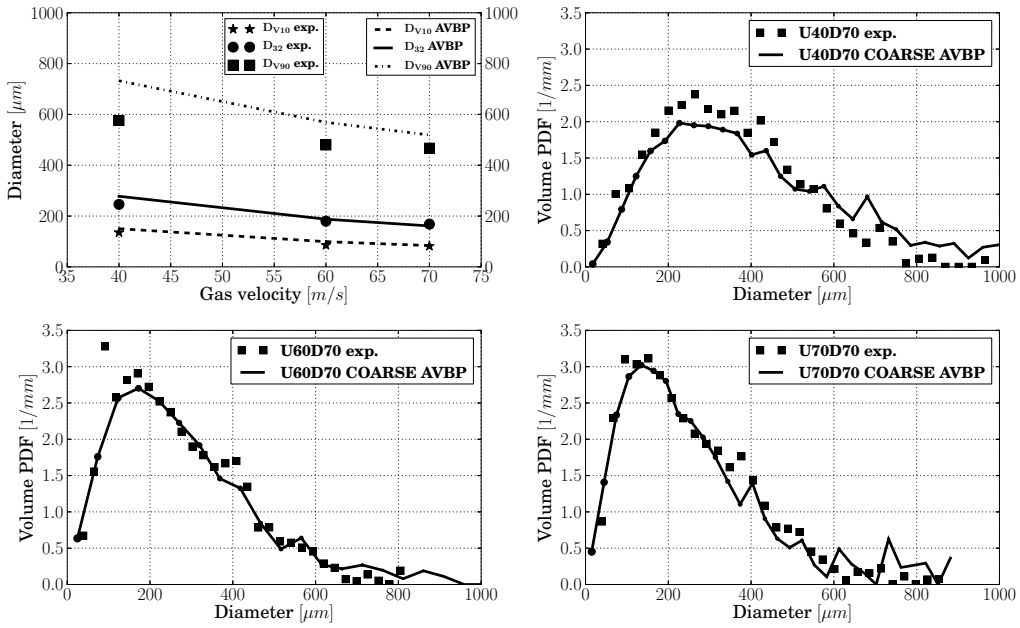

Figure 8.36 : *Characterization of the generated spray for the COARSE case and Shellsol D70. Top left: mean diameters comparison. Top right: U40D70, Bottom left: U60D70. Bottom right: U70D70*

Special attention is required to compare the *number* droplet distribution between simulation and experiment. Because of experimental measurement limitations, very small droplets are not accounted for. In the experiment, the smallest measurable diameter is $d_{min}^{exp} \approx 25$ µm. On the contrary, in the simulation, there is no small diameter limitation and the breakup model is able to generate droplets below 1 µm. In addition, due to the shape of the Rosin-Rammler distribution, many small droplets smaller than d_{min}^{exp} are generated, as depicted on Fig. 8.37 (*left*). When comparing the arithmetic mean diameter (D_{10}) between simulation and experiment, the deviation is about 50%, because of the large number of droplets smaller than 25 µm. Note that when working with volume statistics such as the *volume* PDF, or the volume diameters (D_{V10}, D_{V90}, D_{32}, D_{30}, etc), this effect is not visible due to the multiplication by d^3: the volume created by small droplets is negligible, even when they are numerous.

The special treatment required by the *number* droplet distribution is to filter out particles smaller than d_{min}^{exp} in the simulation. This method ensures that both the model and the experiment account for the same range of diameters. The effect of filtering is depicted on Fig. 8.37 (*right*). For this experiment, filtering droplets lower than ≈ 25 µm reduces the total number of particles by 49% and 84% for small and large gas velocities respectively. For instance, the first class on Fig. 8.37 (*left*) represents droplet smaller that 25 µm. As this filter is a post-treatment, the numerical simulation still keeps all particles. However creating a large number of small particles is CPU costly. As droplets below ≈ 1 µm are insignificant for the volume distribution, they are filtered out during the simulation by setting a low diameter limit.

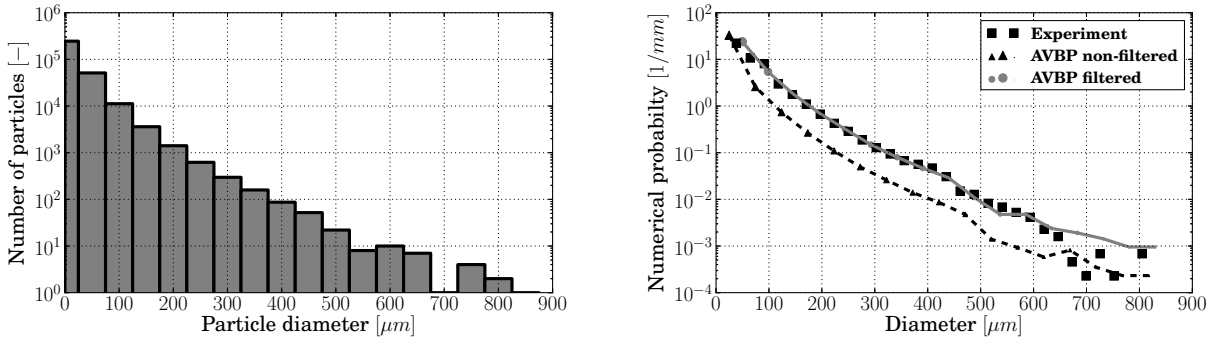

Figure 8.37 : *Left: Number of particles per diameter classes from PAMELA for U60D70 REF. Right: number PDF, effect of filtering the small diameters for U60D70 REF*

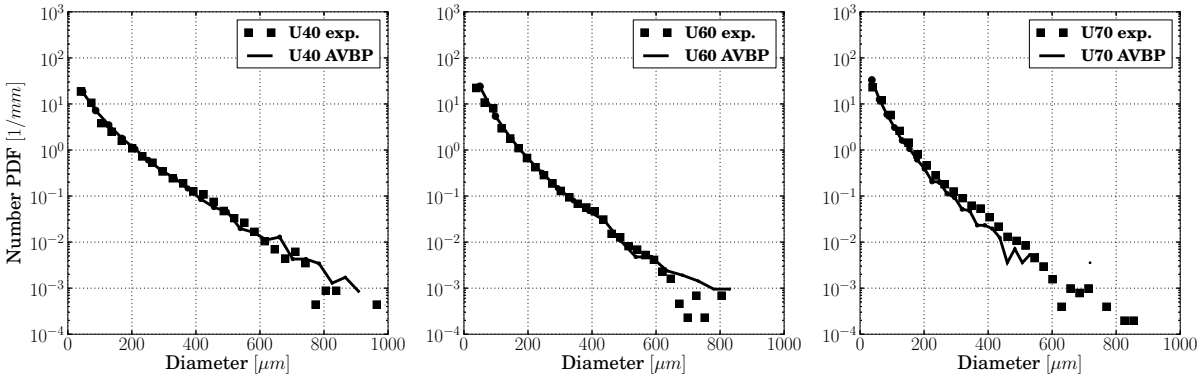

Figure 8.38 : *Number distribution of the generated spray for the REF D70 case*

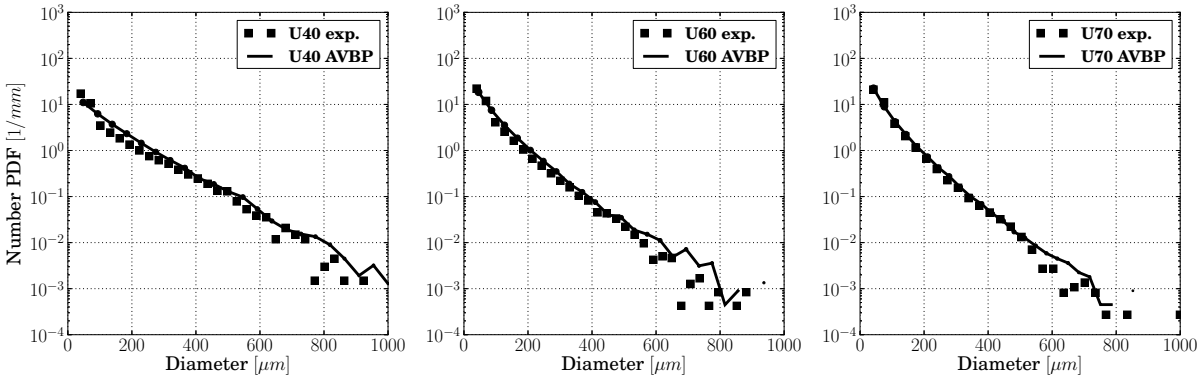

Figure 8.39 : *Number distribution of the generated spray for the REF Prop case*

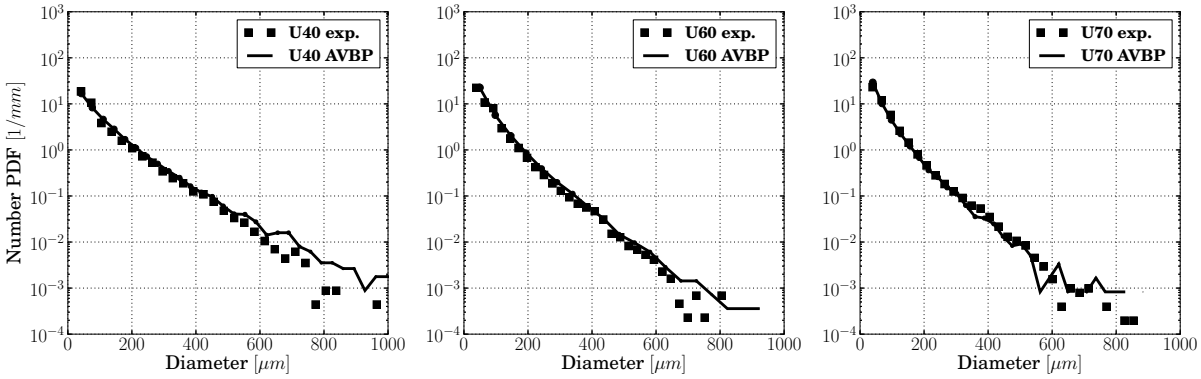

Figure 8.40 : *Number distribution of the generated spray for the COARSE D70 case*

Figures 8.38 to 8.40 compare the number PDF from AVBP with experimental data. Up to d = 500 µm all cases are in very good agreement with experiment except U40Prop REF (for d < 200 µm) and U70D70 REF (for d > 300 µm) where a slight deviation is visible. Above a diameter of 500 µm, all cases show a larger deviation due to the low statistical convergence of both experimental and simulation data.

Table 8.14 quantifies the deviation of mean diameter prediction from experiment. As discussed above, the D_{V90} is the less accurate prediction. Note that it is overestimated in all cases except U60D70 REF. This case is curiously poorly predicted in terms of all diameters, while the same conditions with Propanediol provide a better agreement. The reason could be that the averaging period τ_{RT} is too short and the seen gas velocity u_{70} fluctuates to much. It would not be the case with Propanediol because of a larger surface tension inducing a larger τ_{RT}. However, the standard deviation of u_{70} in this case is not significantly larger than the Propanediol case (Table 8.13).

From Table 8.13 and the results of the error quantification (subsection 7.6 of Chapter 7), it was expected that the COARSE case would provide a D_{V10} and a D_{32} about 10% larger than the experiment. It is the case for U40, but no clear trend can be observed for other cases. The point is that error quantification assumed a fully converged pdf, *i.e.* an infinite number of particles, which is not the case with the numerical simulation, especially for large diameters. Another element is the fact that in subsection 7.6, the computed deviations are below, or of the order of magnitude of, 10% which is quite low, regarding the complexity of the breakup phenomenon in combination with the complexity

of the model. Therefore the quantification of error is useful to assess the global behaviour of the model, but the implementation of the model into AVBP brings more complexity and uncertainty that sweeps away the theoretical error prediction.

Case	U40D70		U40Prop	U60D70		U60Prop	U70D70		U70Prop
Mesh type	COARSE	REF		COARSE	REF		COARSE	REF	
ΔD_{V10} [%]	11	-1.3	0.32	16	7.5	14	2.3	-8.8	14
ΔD_{10} [%]	9.3	-0.70	22	-4.2	-9.9	9.7	-9.5	-14	1.3
ΔD_{32} [%]	13	0.46	5.1	4.4	-0.51	10	-4.2	-15	5.4
ΔD_{V90} [%]	27	18	17	19	32	27	11	-5.8	13

Table 8.14 : *Deviation of predicted mean diameters from experiment*

Conclusion

The output of PAMELA, *i.e.* the dropsize distribution is in good agreement with the experiment. Note that the constants of the model were calibrated on the present experiment in Chapter B.48 were kept constant over all cases. The good agreement is therefore a proof that the model is well formulated for Large Eddy Simulation, well implemented into AVBP, and brings no major distortion to the predictions (below 10%). The COARSE case provides results as accurate as the REF case and this is a half-surprising result. On one hand, the COARSE mesh showed a proper boundary layer resolution (y^+) in the atomizing edge region for all velocities, contrarily to the REF case. This suggested that the COARSE mesh might be more accurate. On the other hand, the gas velocity seen by the accumulation particles (u_{70}) showed a significant deviation (10%) with the COARSE mesh, and it was expected a significant deviation of the mean diameters, which is not observed here. So in conclusion, the prediction of the dropsize distribution is robust in terms of mesh dependence. Finally, the atomization model is able to predict more than mean diameters: the comparison of *numeric* and *volume* PDF with the experiment proved that the whole polydispersity was recovered.

8.4.3 Spray topology

This subsection presents the global shape of the generated spray compared to the experiment. Since the atomized droplets are injected downstream the atomizing edge with a zero velocity, the shape of the spray is totally dictated by the flow pattern and the turbulent mixing. Because of the polydispersity of the spray, a segregation occurs with regards to the Stokes number of the particles.

Figures 8.42 to 8.45 show the 2D distribution of (i) the probability presence of droplets, (ii) the liquid volume fraction α_l and (iii) the Sauter Mean Diameter, for several numerical simulations. The gas is flowing from the top to the bottom of the figures and the film is created on the right side of the prefilmer (the black rectangle), which is labeled as the *film side*, oppositely to the *no film side*. The investigated parameters are the surface tension, the gas velocity and the mesh resolution.

Projection procedure

In order to compare with the experiment, a similar procedure is applied to the numerical solutions. Several successive snapshots of the Lagrangian phase are treated to compute a mean value. They are projected onto a 2D cartesian mesh that mimics the pixels array of the CCD camera used in the experiment. In order to increase the number of samples,

the whole spray is projected on the 2D slice, and not only the droplets that belong to the mid-plane layer. The pixels size is 43 µm.

The probability of presence is computed as follow: when a droplet is found in a cell, its diameter is compared to the pixel size. If the droplet is smaller than the pixel, the containing pixel is set to the value 1, corresponding to the presence of liquid. If the droplet is larger than the pixel, its shape is assimilated to the square inscribed into the droplet contour and the covered pixels are set to 1, as depicted on Fig. 8.41. The reason to consider the inscribed square and not the total circle is to avoid to account for too many pixels: from the experiment point of view, because of the sensor threshold, if a pixel 'partially detects' some liquid it is not guaranteed to be activated. The probability of presence map is then averaged over the number of snapshots and it outputs a value between 0 and 1.

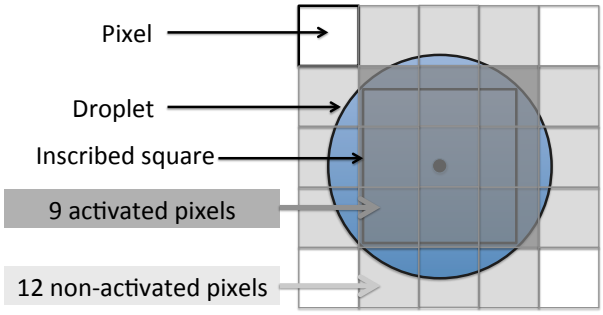

Figure 8.41 : *Schematic of the detection algorithm*

The computation of the volume fraction $\alpha_l = V_{liq}/V_{tot}$ follows the same principle. The liquid volume is equally distributed among the activated pixels. For particles larger than a pixel, it induces a loss of accuracy: accounting for the third dimension, the pixel at the center of the droplet should 'receive' a liquid volume approximately equal to the pixel surface A_p multiplied by the droplet diameter d_p whereas the periphery pixels should record a smaller volume:

$$V_{liq,\text{pixel center}} \approx A_p \cdot d_c \tag{8.26a}$$

$$V_{liq,\text{pixel periphery}} \approx A_p \cdot d_c \cdot \epsilon \tag{8.26b}$$

where $0 < \epsilon < 1$ is related to the distance of the pixel center from the droplet center. However for simplicity sake, all activated pixels receive the same volumes of liquid. The total volume V_{tot} is computed by the pixel surface A_p multiplied by the fixed width of the spray $w_s = 50\,mm$. This procedure is applied to each snapshot and it is averaged over the number of snapshots.

The SMD calculation does not require to take the pixel size into account, nor the number of snapshots. The droplet volume is added to the pixel containing its center, for every droplets of every snapshot. The same procedure is applied to the droplet surface. The SMD distribution is the ratio of the volume map by the surface map.

Discussion

From the observation of Figs. 8.42 to 8.45 it can be stated that:

- For all cases, the spray is deflected on the no film side. This is due to the injection point of the atomized particles, located in a region where the mean flow pattern is directed towards the symmetry plane (see Fig. 8.13). Particles therefore undergo an acceleration towards the no film side.

- The distribution of probability of presence shows a central core at the value one and decreases sharply to zero for Propanediol. With Shellsol, the transition from 0 to 1 is smoother.
- The liquid volume fraction presents a center core larger than 10^{-3}, that (i) weakens the hypothesis of isolated droplet and (ii) may lead to droplet collision and coalescence. As a consequence, the perturbation of gaseous velocity by the particle is under-predicted, leading to an inaccurate momentum exchange between the phase. In evaporating conditions, the mass and energy exchange terms would show the same kind of inaccuracy. In addition, due to the large volume of the liquid occupation, a blockage effect may accelerate the gas in this region, and lead to larger mean gaseous flow perturbation, which is not accounted for in the point source approximation.
- Observations of Sauter Mean Diameter clearly show that the liquid core is composed of large particles (large Stokes number) that weakly follow the gas resolved velocity fluctuations. The dispersion effect on small particles is clearly visible at the outer part of the spray, mainly composed of the smallest particles of the PDF. However no preferential concentration zone is visible because of the time average effect.
- Surface tension acts on the spray dispersion through the droplets size: in this study there is no modulation of drag due to droplet deformation. Therefore the surface tension only impacts the dropsize. When the surface tension is larger, the generated droplets are larger, inducing a larger Stokes. The particles have a more 'ballistic motion' and are insensitive to turbulence, resulting in a less dispersed spray. For the low velocity (U40), the difference is clearly visible between Shellsol and Propanediol, and it decreases with increasing gas velocity.
- The gas velocity has a minor influence on the dispersion of the Shellsol spray: its shape remains approximately constant. However, its effect is clearer onto the Propanediol spray, especially between 40 and 60 m/s.
- The spray angle is not symmetrical in the near-prefilmer region. This is visible on the three fields, especially for U_0 = 70 m/s on the REF mesh. On the no-film side, the spray angle is larger and the spray yields a more curved contour. On the film side, the spray contour is a straight line with a lower angle. A qualitative comparison with experiment is possible on Fig. 8.2 (*right*).
- The mesh resolution in the wake of the prefilmer is of primary importance for all velocities. It was seen that the drop size distributions of the COARSE and REF meshes were similar, so the difference of the spray shape is explained by the turbulent mixing. The incapacity of the COARSE mesh to capture the von Kármán street is undoubtedly responsible of the very low spray angle.

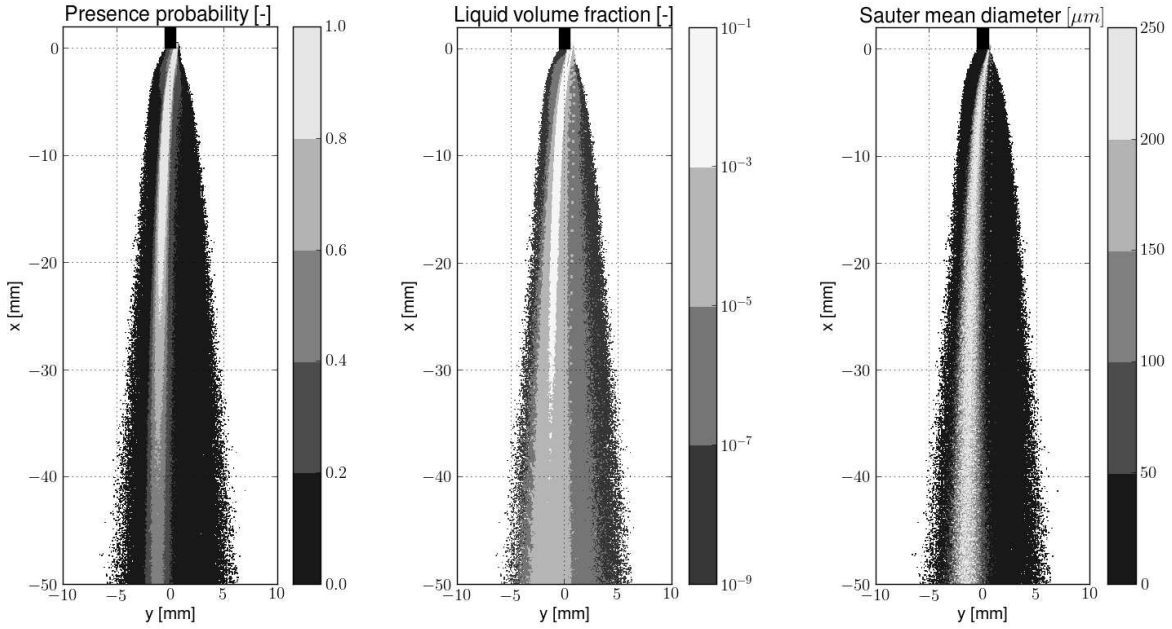

Figure 8.42 : *Projection of spray characteristics for U60D70 REF*

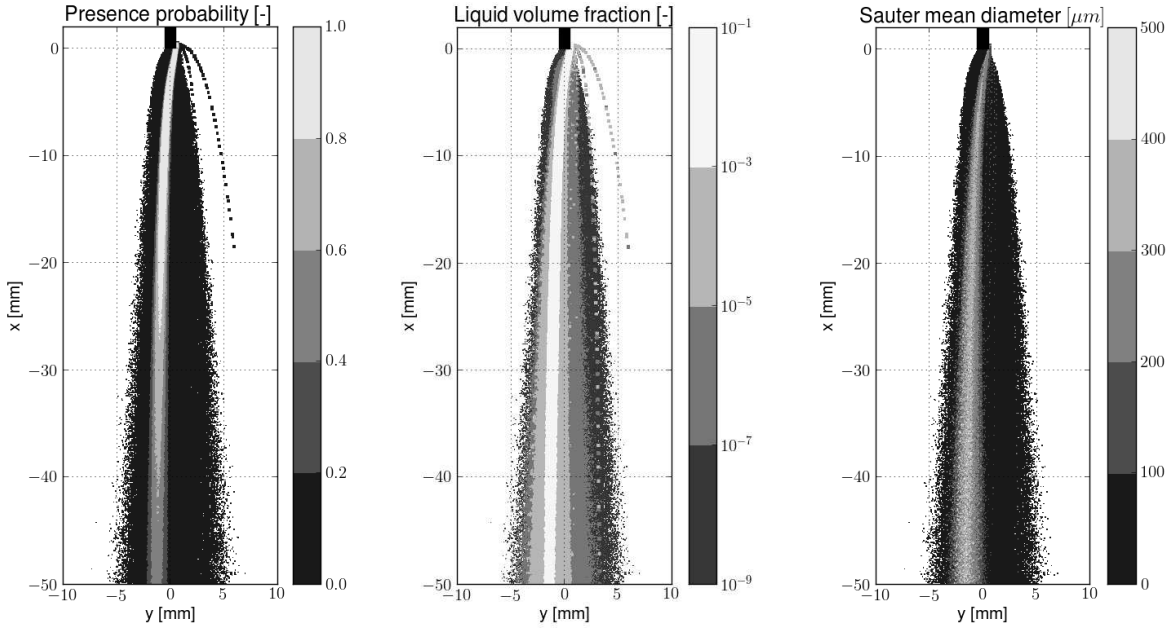

Figure 8.43 : *Projection of spray characteristics for U40D70 REF*

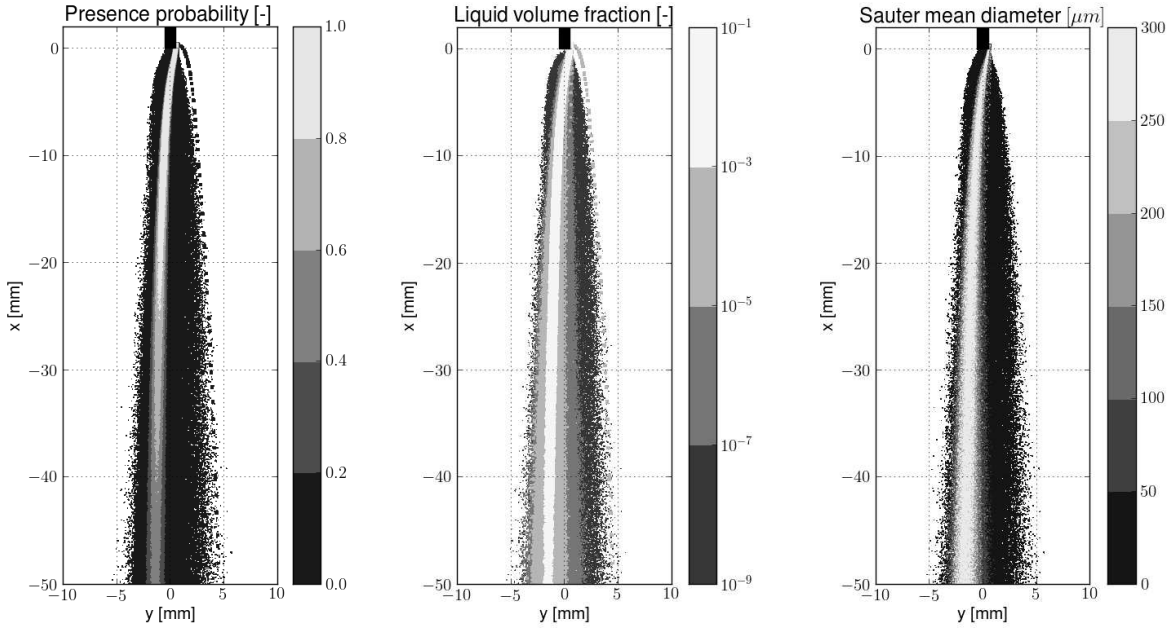

Figure 8.44 : *Projection of spray characteristics for U60Prop REF*

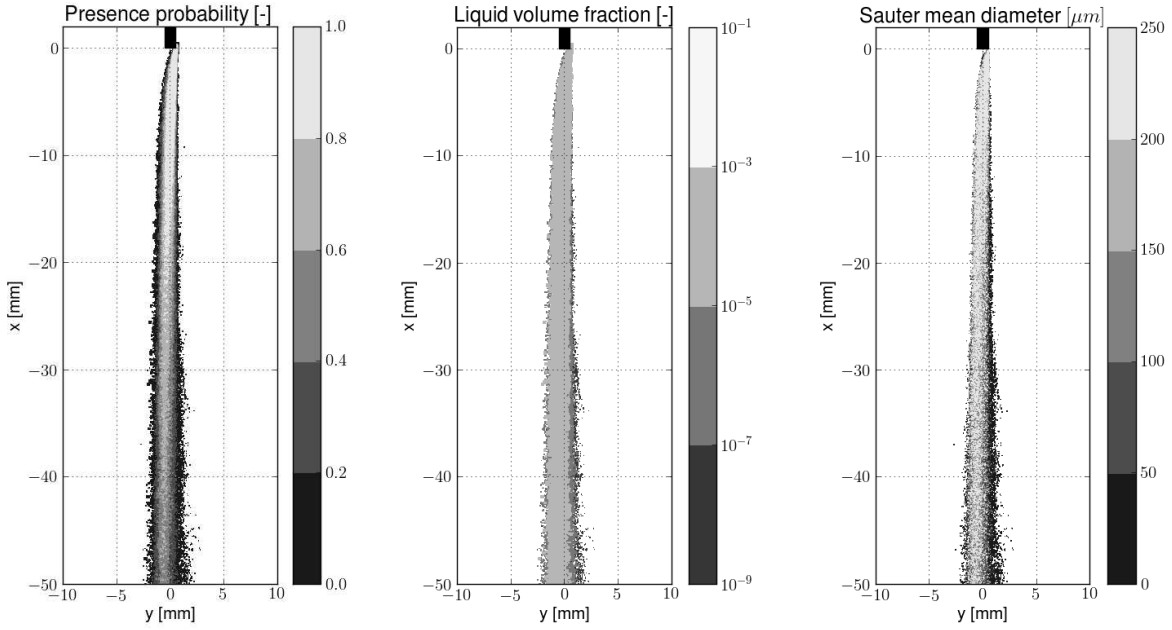

Figure 8.45 : *Projection of spray characteristics for U60D70 COARSE*

Comparison with experiment

Figure 8.46 shows a qualitative comparison between experiment and simulation. The experimental plot is made of 200 superimposed snapshots with a recording frequency of 10 Hz. The simulation contains approximately the same number of snapshots, but the sampling frequency is $\approx$ 10 **k**Hz and the whole spray is projected onto the slice.

Directly downstream the prefilmer, the simulated spray is narrower than in the experiment. This is explained by the flapping motion of the liquid accumulation, that is not represent in the simulation. Far downstream the prefilmer, the shape of the simulated spray is less scattered. The main reasons for this discrepancy are: (i) secondary atomization is not activated in the simulation while it naturally takes place in reality, generating smaller droplets of smaller Stokes number, more sensitive to turbulent mixing; (ii) the mesh rapidly coarsens in the streamwise direction, decreasing the resolved turbulent kinetic energy. Since there is no subgrid model for particle/turbulence interaction, the particle are less sensitive to turbulent dispersion on low resolution grids.

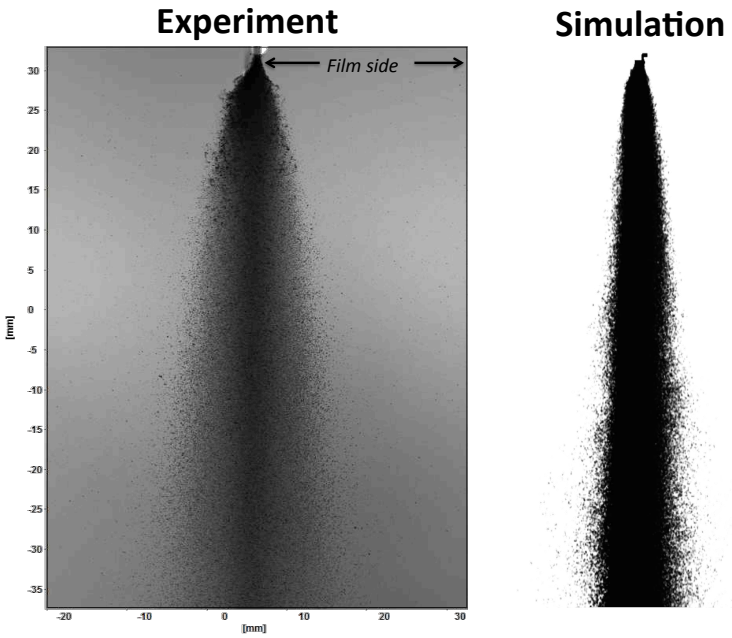

Figure 8.46 : *Qualitative comparison with the experiment (source: S. Gepperth from KIT-ITS), U60D70 REF*

On Fig. 8.47 the probability of presence is compared. Both experiment and simulation exhibit a deviation of the spray towards the no film side. The predicted span of the spray at x = -60 mm is in good agreement with the simulation. However, the shape of the "50$\rightarrow$90%" and ">90%" zones are erroneous. While they are more symmetrical and more localized in the wake region for the experiment, these zones are deflected to the no film side and are largely convected by the gas in the simulation. Here also the main explanations for this deviating behaviour are (i) the neglect of the liquid accumulation flapping and (ii) the damped turbulence due to the coarsening of the grid.

Conclusion

The spray dynamics are reasonably well described by the simulation. Special care has to be brought to the mesh resolution in the wake region in order to accurately resolve the turbulent length scales. However the whole predicted

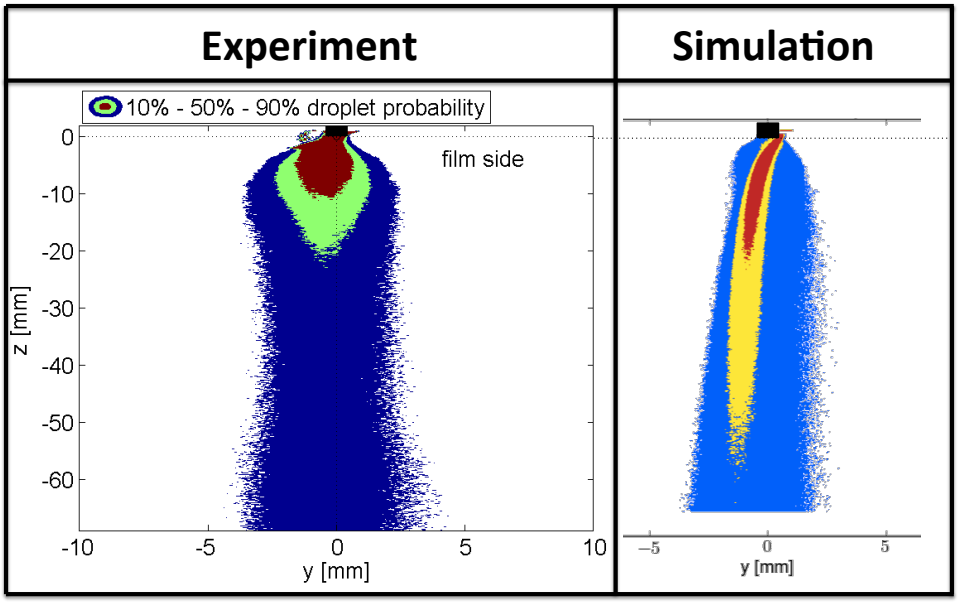

Figure 8.47 : *Comparison of presence probability with the experiment (source: S. Gepperth from KIT-ITS), REF, U_0 = 60 m/s, Shellsol D70. The blue, green/yellow and red colors represent a presence probability between 10 and 50%, 50 and 90%, and above 90% respectively.*

behaviour suffers from the lack of flapping motion description of the liquid accumulation. Even if it cannot be resolved with the present Lagrangian approach, this flapping phenomenon could be modeled by imposing a fluctuating normal velocity to the generated droplets, based on a correlation of the flapping frequency derived by Gepperth *et al.* [104]. In addition, the activation of the secondary atomization in the simulation is believed to bring a better agreement to the spray shape, further downstream the atomizing edge.

It is worth noticing that this configuration is academic and largely 'unidirectional', in terms of flow pattern. In a real combustion chamber the flow is highly disturbed by large scale hydrodynamic instabilities such as the Precessing Vortex Core. It can be expected that the generated droplets are totally dragged by these large scale flow features, and therefore neglecting the accumulation flapping may lead to lower-ranking errors. In addition, in a real combustion chamber the flame is generally stabilized close to the atomizing edge. The question of secondary atomization is raised in this case: "Is the distance between the primary breakup zone and the flame front large enough to allow secondary atomization ?"

8.5 Conclusion

This chapter allows to draw several conclusions about the modeling and description of the liquid phase in dense region of prefilming airblast atomizers. The gaseous phase is resolved in the LES formalism which captures the largest energetic fluctuations influencing the liquid phase motion. In particular, for a sufficiently good and affordable spatial resolution, the code is able to capture the vortex shedding that appears downstream the atomizing edge. Although the frequency of vortex detachment presents some discrepancy with the experiment, it still allows a good mixing process of particles. In order to properly estimate the wall shear stress, that is assumed to be equal to the film/gas interfacial stress, a law-of-the-wall (wall functions) is applied to the prefilmer surface. This creates a slight

unrealistic acceleration of the gas at the atomizing edge. However it is shown that the proper use of wall functions provides less deviation in the Strouhal number prediction than no special wall treatment at all. One difficulty of the wall treatment in such configurations is to provide sufficiently large wall cells on the prefilmer and a refined grid downstream the atomizing edge. This implies high mesh size gradients that are not advised in practice. The comparison with the experimental RMS velocity profile in the wake region of the prefilmer shows that even if the Strouhal number is not well predicted, the amount of Turbulent Kinetic Energy is well recovered, insuring a realistic amount of fluctuations.

Concerning the two-phase flow, it is shown that the pressure gradient is negligible in this particular configuration. This may be not the case in the industrial burner where the geometric features enhance the pressure losses and thus the overall pressure gradient. The *frozen gas* approach has proven its efficiency and reliability to provide a film steady state solution from a mean gaseous solution. The film thickness prediction shows good trends but quantitatively wrong results. Note that the film model embeds no surface tension effect (contrarily to VOF/LevelSet or SPH approaches) and there is no retro action of the film on the gas. In this context, surface instabilities such as Kelvin-Helmholtz or roll-waves cannot be predicted by the present model. However as it is stated by Gepperth *et al.* [104] and Wittig and co-workers [3, 307], the film flow is not correlated to the primary breakup process, and it does not influence the film model. When thermal effects will be considered, the film may act has thermal resistance between the wall and the gas, and its thickness may be of primary importance. In the simulation, the film thickness presents some longitudinal fringes that could not be explained, but their presence is believed to be enhanced because of the unidirectional flow of this configuration. In real annular geometries with the presence of a PVC, the flow main direction is more unsteady, and these fringes are not expected to be as visible as here.

The atomization model and its implementation shows a high robustness with regards to the gas velocity, surface tension, and above all, on mesh resolution. As the model constants were calibrated onto this experiment, this does not constitute a formal validation of the model. But as the model relies on all influent parameters that Gepperth *et al.* [102, 104] have identified, it is believed that it will output accurate results in other realistic configurations as soon as the breakup process is similar. As mentioned above, this primary breakup model is able to predict the whole PDF of the spray and not only a few moments.

The study of the spray topology demonstrates the necessity of capturing the vortex shedding phenomenon. However, discrepancies are visible in the spray core, due to the neglect of the liquid accumulation flapping. In the far-field of the atomizer, the spray shape is narrower than in the experiment and may originate from a very coarse mesh and the neglecting of the secondary breakup. In industrial annular configurations, the resolved swirling motion as well as the PVC generated a strong mixing which is believed to create a more realistic spray topology.

Several paths of improvement can be drawn for the future. First, the film thickness prediction must be more accurate. This may be achieved by (i) the modeling of solitary and roll waves effects onto the mean film velocity, (ii) the retro action of the film on the gas, in terms of momentum transfer through, for example an apparent sand roughness [73]. In order to reduce the computational expense of the small particles, a clipping diameter could be prescribed. However, depending on the operating conditions, the SMD can vary from 10 to 500 μm and setting a constant minimum diameter could be inaccurate and requires special attention: it should be an input of the model filled in by the user. The primary breakup model (PAMELA) can be improved by imposing a fluctuating vertical velocity, in order to mimic the liquid accumulation flapping and widen the spray distribution in the atomizing edge near-field.

General conclusion

In the present work, Large-Eddy Simulations of the evaporating two-phase flow in a realistic geometry were conducted using the Euler-Lagrange approach. The presentation of the global context and the expected changes for the XXIst century was first introduced, followed by an overview of the liquid phase phenomena in airblast injectors and the state of art in simulating two-phase combustion in realistic aeroengines.

In the first part, a bibliographic study of the liquid phenomena from fuel injection to atomization is presented, describing the academic experiments, the identified mechanisms and the methods of modeling. In a second part, developments for the liquid phase were presented. The Lagrangian library was first detailed, followed by the projection method to computed Eulerian quantities from a Lagrangian description of the liquid phase. It was seen that efficient projectors on regular cartesian meshes were biased when the mesh becomes irregular. Therefore conservative projectors of lower order were preferred. In addition, the accent was set on the necessity to manipulate extensive quantities when performing projection and averaging. The detail of the SWI models implemented in AVBP conjointly with Habchi [128] were presented. The Frozen Gas concept was introduced and the results were exhibited on a simple test case. The dynamic of the spray is weakly predicted and the droplet dispersion is totally filtered out by the use of a mean gaseous solution. However, the main purpose of the Frozen Gas approach is the filling of the film, and as no dispersion is to take into account for this task, this new approach provides satisfactory results for a tremendous speedup.
The film model is then tackled. Equations are integrated over the film thickness to derive a mean film velocity, arising the necessity to express the film/gas shear stress. From considerations on the film geometry and the usual operating conditions, the interface shear stress is assimilated to the wall shear stress computed by the gaseous solver. The Lagrangian approach is chosen to transport the film mass: film particles are convected along the wall with a mean film velocity. The film thickness is computed from the liquid volume contained in wall cells, implying a total wetting of the cell by the liquid. It is seen that this method may lead to low deviation on smoothly varying tetrahedral grids. Comparison with an analytical solution showed that the model behaves as expected over a wide range of liquid to gas mass flow rate. The deviation with the exact solution is low within the usual mass flow rate range in aeroengines. The comparison with an academic test case of a convergent channel [72, 73] shows that the film formulation delivers the right behaviour, but the wall shear stress prediction from the LES flow solver is poorly predicted, leading to a wrong thickness. Therefore the wall shear stress is a sensitive key element in the present film model. The large numerical imbalance due to the film particles is assessed and the necessity of multi constraint partitioning is pointed out. The perspective of film model improvements are too account for the retro coupling of the film to the gas, the development of an automated multi-constraints partitioning and a film evaporation model [160].
The primary breakup model (called PAMELA) aims to predict the drop size distribution of the spray generated by an airblast atomization. It is based on experimental KIT-ITS observations [102, 104] stating that the sheared film feeds a liquid accumulation hooked downstream of the atomizing edge in the wake region. In the present work, the liquid accumulation is assumed to be torn apart by the high gas shearing, following the Hong-Varga mechanism [151, 353]: the gas axially accelerates the top part of the liquid accumulation, leading to a transverse Rayleigh-Taylor instability that evolves into elongated ligaments. From experimental observations the liquid accumulation is sheared at a height between half and twice the momentum thickness of the turbulent boundary layer developed on the prefilmer. This

leads to a velocity seen by the liquid accumulation of $\approx 70\%$ of the bulk velocity. The pdf of the spray is described by a Rosin-Rammler distribution whose coefficients depends on the influent parameters identified by experimenters: the gas velocity seen by the accumulation, the liquid surface tension and the atomizing edge thickness. The shape parameter q of the Rosin-Rammler function is expressed by two different methods, the *Weber number* and the *length scale* based methods. The *Weber number* based method seems valid on a wider range because of the use of a non dimensional number, however it requires the knowledge of the boundary layer thickness on the prefilmer and therefore is subject to a larger uncertainty. The model depends on four constants, calibrated with the KIT-ITS experimental data over several gas velocities, surface tensions and atomizing edge thicknesses. The *a posteriori* comparison with the experiment shows that mean statistical diameters prediction is accurate for the whole range of investigated operating conditions. To go further, the whole predicted pdf matches the experiment with a satisfactory agreement. The primary breakup therefore prove its ability to recover the whole polydispersity of a spray, and it is not limited to a mean diameter prediction. An error quantification is assessed from the variation of the input parameters as well as from the model constants. The mean velocity seen by the accumulation is the most critical input parameter, and an error of 10% leads to a deviation of $\approx 10\%$ as well. The velocity fluctuation (*i.e.* the turbulence intensity) has a low impact on the predicted pdf. Concerning the model constants impact, C is the most critical, closely followed by κ. The details of PAMELA implementation shows that several choices are necessary in order to code a proper model. In particular it is shown the necessity to (i) predict the wall shear stress on the first node upstream the atomizing edge to avoid the noise generated at the corner, and to (ii) keep a constant parcel number during the atomization process in order to keep both a realistic numeric and volume drop size distribution.

In a third part, the film and primary breakup models are tested and compared with real experiments. First, a LES of the KIT-ITS experiment is performed on several meshes and operating conditions. Due to the large dimension of the experiment, the law of the wall approach is employed for the prefilmer surface. In many case, especially at low gas velocity, the film model overestimates the thickness up to a deviation of 200%. The most probable reasons are (i) the neglect of the film surface phenomena such as roll-waves that considerably modify the mean film velocity and (ii) the neglected influence of the film onto the gas flow that locally impact the wall shear stress. The predictions of the primary breakup model in terms of drop size distribution is in good agreement with the experiment over the whole range of investigated parameters. The mesh size has little influence on the predicted pdf, ensuring a robust formulation and implementation. On the other hand, the space distribution of the spray strongly depends on the mesh resolution downstream of the atomizing edge. This is because the droplets generated by the primary breakup model are injected with a zero velocity, and the spray angle and shape are controlled by the gaseous turbulent mixing. A way of improvement is to impose an injection fluctuating velocity perpendicular to the main flow direction in order to mimic the flapping behaviour of the liquid accumulation. Finally the *frozen gas* method has proved its efficiency for accelerating the film steady state.
During this thesis, simulations of a realistic airblast atomizer were preformed, but not presented here because of confidentiality reasons. Still, the comparison between the measurements of the drop size pdf and the numerical simulation show a good agreement. As the four constants of the primary breakup model where kept constant since the validation on the KIT-ITS case, these good results for a real industrial case with different operating conditions (gas velocity, prefilmer thickness) strengthens the primary breakup model fidelity.
The use of the developed models in a real combustion chamber, and the comparison with usual methods, showed that injection method have a major impact on the flame structure, the main parameter being the spray SMD.

To summarize, the models developed in this thesis extend the prediction capability of two-phase flow LES in the case of realistic gas turbines fueled by airblast atomizers. The numerical simulation of the KIT-ITS experiment as well as a real aeroengine allowed to identify several points of improvement such as a dynamic multi-constraint grid partitioner, an advanced description of momentum transfer between the film and the gas (roll-waves and other interface instabilities), and a thermal model linking the film, the surrounding gas and the solid (film boiling, thermal transfers at droplet impact). In the context of thickened-flame approach, a correction of the drag and the evaporation of Lagrangian droplet is still required [316]. Finally, when large droplets cross the flame front and are scattered enough to burn in single-droplet regime, the current combustion models associated with the usual mesh resolution

cannot accurately predict the real heat released by this diffusion flame. Hence a subgrid scale model for single-droplet combustion may bring considerable accuracy to the overall reactive simulation [265].

Bibliography

[1] E. Abo-Serie, M. Gavaises, and C. Arcoumanis. Spray/wall interaction in direct-injection spark ignition engines equipped with multi-hole injectors. In *Proc. 9th Int. Conf. on Liquid Atomisation and Spray Systems (ICLASS), Sorrento*, 2003. cited p. 28

[2] P. Adomeit and U. Renz. Hydrodynamics of three-dimensional waves in laminar falling films. *International journal of multiphase flow*, 26(7):1183–1208, 2000. cited p. 62, 63

[3] M. Aigner and S. Wittig. Swirl and counterswirl effects in prefilming airblast atomizers. *Journal of engineering for gas turbines and power*, 110(1):105–110, 1988. cited p. 74, 205

[4] S. Akhtar and A. Yule. Droplet impaction on a heated surface at high weber numbers. *ILASS-Europe, Zurich*, 2001. cited p. 37

[5] A. S. Almgren, J. B. Bell, P. Colella, L. H. Howell, and M. L. Welcome. A conservative adaptive projection method for the variable density incompressible navier–stokes equations. *Journal of computational Physics*, 142(1):1–46, 1998. cited p. 76

[6] C. Amiel, P. Le Clercq, O. Ravel, G. Lavergne, P. Berthoumieu, and J. A. Farre. Use of an infrared detector to analyze the temperature evolution of a droplet impacting on a heating wall. In *Aerospace/Defense Sensing, Simulation, and Controls*, pages 13–20. International Society for Optics and Photonics, 2001. cited p. 27, 37

[7] P. Andreussi. The onset of droplet entrainment in annular downward flows. *The Canadian Journal of Chemical Engineering*, 58(2):267–270, 1980. cited p. 63

[8] C. Angelberger, T. Poinsot, and B. Delhaye. Improving near-wall combustion and wall heat transfer modelling in si engine computations. In S. P. 972881, editor, *Int. Fall Fuels & Lub. Meeting & Exposition*, Tulsa, 1997. cited p.

[9] S. V. Apte, M. Gorokhovski, and P. Moin. Large-eddy simulation of atomizing spray with stochastic modeling of secondary breakup. *International Journal of Multiphase Flow*, 29:1503–1522, 2003. cited p. 16, 18, 20, 79

[10] S. V. Apte, K. Mahesh, M. Gorokhovski, and P. Moin. Stochastic modeling of atomizing spray in a complex swirl injector using large eddy simulation. *Proceedings of the Combustion Institute*, 32:2257–2266, 2009. cited p. 18

[11] S. V. Apte, K. Mahesh, P. Moin, and J. C. Oefelein. Large-eddy simulation of swirling particle-laden flows in a coaxial-jet combustor. *International Journal of Multiphase Flow*, 29(8):1311–1331, 2003. cited p. 18

[12] K. Araki and A. Moriyama. Deformation behaviour of a liquid droplet impinging on a hot metal surface. *ICLASS1982, Madison, Wisconsin*, pages 389–396, 1982. cited p. 36

[13] C. Arcoumanis and J.-C. Chang. Heat transfer between a heated plate and an impinging transient diesel spray. *Experiments in Fluids*, 16(2):105–119, 1993. cited p. 41

[14] E. Babinsky and P. Sojka. Modeling drop size distributions. *Progress in Energy and Combustion Science*, 28:303–329, 2002. cited p. 24, 135

[15] C. Bai and A. Gosman. Development of methodology for spray impingement simulation. In *SAE Technical Paper 950283*, 1995. cited p. 30, 32, 33, 36, 37, 38

[16] C. Bai, H. Rusche, and A. Gosman. Modelling of gasoline spray impingement. *Atom. Sprays*, 12:1–27, 2002. cited p. 37, 38

[17] S. Balachandar and J. K. Eaton. Turbulent dispersed multiphase flow. *Annual Review of Fluid Mechanics*, 42:111–133, 2010. cited p. 8

[18] D. Barré, M. Kraushaar, G. Staffelbach, V. Moureau, and L. Gicquel. Compressible and low mach number LES of a swirl experimental burner. *Comptes Rendus de l'Académie des Sciences - Mécanique*, 341(1-2):277–287, 2013. cited p. 186

[19] A. B. Basset. *Treatise on Hydrodynamics*, volume 2. Deighton Bell, London, 1888. cited p. 237

[20] F. Z. Batarseh. *Spray generated by an airblast atomizer: atomization, propagation and aerodynamic instability*. PhD thesis, Technische Universität Darmstadt, 2008. cited p. 28

[21] P. Beau. *Modélisation de l'atomisation d'un jet liquide - Application aux sprays Diesel*. PhD thesis, Université de Rouen, 2007. cited p. 79

[22] J. Becker and C. Hassa. Breakup and atomization of a kerosene jet in crossflow at elevated pressure. *Atomization and Sprays*, 12(1-3):49–68, 2002. cited p. 20

[23] F. Ben Rayana, A. Cartellier, and E. Hopfinger. Assisted atomization of a liquid layer: investigation of the parameters affecting the mean drop size prediction. In *Proceedings of the international conference on Liquid Atomization and Spray Systems (ICLASS)*, volume 27, 2006. cited p. 72, 73, 74, 136, 137, 140

[24] M. J. Berger and J. Oliger. Adaptive mesh refinement for hyperbolic partial differential equations. *Journal of computational Physics*, 53(3):484–512, 1984. cited p. 76

[25] J. D. Bernardin and I. Mudawar. A Leidenfrost point model for impinging droplets and sprays. *ASME Journal of Heat Transfer*, 126(2):272–278, 2004. cited p. 31

[26] T. Boeck and S. Zaleski. Instability of two-phase mixing layers: analysis of exact and approximate base flows from boundary layer theory. *Journal of Non-Equilibrium Thermodynamics*, 30(3):215–224, 2005. cited p. 74

[27] T. Boeck and S. Zaleski. Viscous versus inviscid instability of two-phase mixing layers with continuous velocity profile. *Physics of fluids*, 17:032106, 2005. cited p. 74

[28] M. Boileau, S. Pascaud, E. Riber, B. Cuenot, L. Gicquel, T. Poinsot, and M. Cazalens. Investigation of two-fluid methods for Large Eddy Simulation of spray combustion in Gas Turbines. *Flow, Turbulence and Combustion*, 80(3):291–321, 2008. cited p. 19

[29] M. Boileau, G. Staffelbach, B. Cuenot, T. Poinsot, and C. Bérat. LES of an ignition sequence in a gas turbine engine. *Combustion and Flame*, 154(1-2):2–22, 2008. cited p. 19

[30] M. Boivin, O. Simonin, and K. D. Squires. On the prediction of gas-solid flows with two-way coupling using large eddy simulation. *Physics of Fluids*, 12(8):2080–2090, 2000. cited p. 95

[31] P. Boomkamp and R. Miesen. Classification of instabilities in parallel two-phase flow. *International Journal of Multiphase Flow*, 22, Supplement(0):67 – 88, 1996. cited p. 60, 61

[32] R. Borghi and M. Destriau. *Combustion and Flames, chemical and physical principles*. Editions TECHNIP, 1998. cited p. 8

[33] S. Boulesteix. *Cisaillement d'une interface gaz-liquide en conduite et entraînement de gouttelettes*. PhD thesis, Université de Toulouse / MEGeP, 2010. cited p. 43, 114

[34] J. Boussinesq. *Théorie Analytique de la Chaleur*, volume 2. Ecole Polytechnique, Paris, 1903. cited p. 237

[35] R. Brodkey and H. Hershey. *Transport Phenomena: A Unified Approach*. McGraw-Hill chemical engineering series. Brodkey, 1988. cited p.

[36] G. L. Brown and A. Roshko. On density effect on large structure in turbulent mixing layer. *Journal of Fluid Mechanics*, 64(Part 4):775–816, 1974. cited p. 73

[37] K. Bruno and M. McCready. Origin of roll waves in horizontal gas-liquid flows. *AIChE journal*, 34(9):1431–1440, 1988. cited p. 63

[38] M. Burger, R. Schmehl, R. Koch, S. Wittig, and H.-J. Bauer. DNS of droplet-vortex interaction with a Karman vortex street. *International Journal of Heat and Fluid Flow*, 27(2):181 – 191, 2006. cited p. 8

[39] T. D. Butler and P. J. O'Rourke. A numerical method for two-dimensional unsteady reacting flows. *Proceedings of the Combustion Institute*, 16(1):1503 – 1515, 1977. cited p. 11

[40] K. Byungmoon, L. Yingjie, L. Ignacio, and R. J. R. Simulation of bubbles and liquid films. Gvu technical report;git-gvu-06-10, Georgia Institute of Technology, 2006. cited p. 53

[41] I. S. Carvalho, M. V. Heitor, and D. Santos. Liquid film disintegration regimes and proposed correlations. *International Journal of Multiphase Flow*, 28(5):773–789, 2002. cited p. 67, 68

[42] K. Case. Stability of inviscid plane couette flow. *Physics of Fluids*, 3:143, 1960. cited p. 59

[43] G. Castanet, T. Liénart, and F. Lemoine. Dynamics and temperature of droplets impacting onto a heated wall. *International Journal of Heat and Mass Transfer*, 52(3):670–679, 2009. cited p. 33, 36, 38

[44] G. P. Celata, M. Cumo, A. Mariani, and G. Zummo. Visualization of the impact of water drops on a hot surface: effect of drop velocity and surface inclination. *Heat and Mass Transfer*, 42(10):885–890, 2006. cited p. 31

[45] H. Chanson. *The Hydraulics of Open Channel Flow: An Introduction ; Basic Principles, Sediment Motion, Hydraulic Modelling, Design of Hydraulic Structures*. Elsevier Butterworth Heinemann, 2004. cited p. 47, 48

[46] F. Charlette, D. Veynante, and C. Meneveau. A power-law wrinkling model for LES of premixed turbulent combustion: Part I - non-dynamic formulation and initial tests. *Combustion and Flame*, 131:159–180, 2002. cited p.

[47] F. Charru. *Instabilités hydrodynamiques*. Savoirs actuels. EDP Sciences, 2007. cited p. 55, 56, 84, 143

[48] J. Chen, C. Wilson, and B. Tapley. Satellite gravity measurements confirm accelerated melting of greenland ice sheet. *Science*, 313(5795):1958–1960, 2006. cited p. 3

[49] H. H. Chiu and E. J. Croke. Group combustion of liquid fuel sprays. Energy Technology Lab 81-2, University of Illinois, Chicago, 1981. cited p. 8

[50] H. H. Chiu, H. Y. Kim, and E. J. Croke. Internal group combustion of liquid droplets. In *19th Symp. (Int.) on Combustion*, pages 971–980. The Combustion Institute, Pittsburgh, 1982. cited p. 8, 9

[51] R. Clift, J. R. Grace, and M. E. Weber. *Bubbles, Drops, and Particles*. Academic Press, 1978. cited p. 239

[52] O. Colin. *Simulations aux grandes échelles de la combustion turbulente prémélangée dans les statoréacteurs*. Phd thesis, INP Toulouse, 2000. cited p.

[53] O. Colin. A finite element operator for diffusion terms in avbp. *IFP-Division Techniques d'Applications Énergétiques*, 2003. cited p. 166

[54] O. Colin, F. Ducros, D. Veynante, and T. Poinsot. A thickened flame model for large eddy simulations of turbulent premixed combustion. *Physics of Fluids*, 12(7):1843–1863, 2000. cited p. 11, 128

[55] O. Colin and M. Rudgyard. Development of high-order taylor-galerkin schemes for unsteady calculations. *Journal of Computational Physics*, 162(2):338–371, 2000. cited p. 166, 168

[56] G. Cossali, A. Coghe, and M. Marengo. The impact of a single drop on a wetted solid surface. *Experiments in fluids*, 22(6):463–472, 1997. cited p. 29, 35, 36, 105

[57] G. E. Cossali, M. Marengo, and M. Santini. Single-drop empirical models for spray impact on solid walls: a review. *Atomization and Sprays*, 15(6), 2005. cited p. 30, 34

[58] J. Cousteix. *Turbulence et couche limite*. Cépaduès-éditions, 1989. cited p. 144

[59] R. V. Craster and O. K. Matar. Dynamics and stability of thin liquid films. *Rev. Mod. Phys.*, 81:1131–1198, Aug 2009. cited p. 42, 43, 44, 49

[60] C. Crowe, M. Sommerfeld, and Y. Tsuji. *Multiphase Flows with Droplets and Particles*. 1998. cited p. 238

[61] S. de Chaisemartin, L. Fréret, D. Kah, F. Laurent, R. O. Fox, J. Réveillon, and M. Massot. Turbulent combustion of polydisperse evaporating sprays with droplets crossing: Eulerian modeling and validation in the infinite Knudsen limit. In *Proceedings of the Summer Program*. Center for Turbulence Research, NASA Ames/Stanford Univ., 2008. cited p. 16

[62] A.-J.-C. B. de Saint-Venant. Théorie du mouvement non-permanent des eaux, avec application aux crues des rivières et à l'introduction des marées dans leur lit. *C.R. Académie des Sciences*, pages 147–154; 238–240, 1871. cited p. 44

[63] P. Dellenback, D. Metzger, and G. Neitzel. Measurement in turbulent swirling flows through an abrupt axisymmetric expansion. *AIAA Journal*, 13(4):669–681, 1988. cited p.

[64] O. Desjardins, V. Moureau, and H. Pitsch. An accurate conservative level set/ghost fluid method for simulating turbulent atomization. *Journal of Computational Physics*, 227:8395–8416, 2008. cited p. 75

[65] J. Dewitte, P. Berthoumieu, and G. Lavergne. An experimental study of droplet–hot wall interactions and a survey of the splashing regime. In *5th International Symposium on Multiphase Flow, Heat Mass Transfer and Energy Conversion, ISMF*, volume 5, 2005. cited p. 34

[66] D.G.Goodwin. *Cantera C++ Users Guide*. http://sourceforge.net/pro jects/cantera, 2002. cited p.

[67] P. E. Dimotakis. Two-dimensional shear-layer entrainment. *AIAA journal*, 24(11):1791–1796, 1986. cited p. 73, 137

[68] E. R. V. Driest. On turbulence flow near a wall. *Journal of the Aeronautical Sciences*, 23(11):1007–1011, 1036, 1956. cited p. 52

[69] C. Dumouchel. On the experimental investigation on primary atomization of liquid streams. *Experiments in Fluids*, 45:371–422, 2008. cited p. 67, 69

[70] F. Durst, G. Brenn, and T. Xu. A review of the development and characteristics of planar phase-doppler anemometry. *Measurement Science and Technology*, 8(11):1203, 1997. cited p. 164

[71] J. Ebner, M. Gerendas, O. Schäfer, and S. Wittig. Droplet entrainment from a shear-driven liquid wall film in inclined ducts: Experimental study and correlation comparison. *Journal of engineering for gas turbines and power*, 124:874, 2002. cited p. 125, 164

[72] J. Ebner, O. Schafer, P. Schober, and S. Wittig. Modeling of shear-driven liquid wall films on curved surfaces - effect on accelerated air flow and variable film load. In *9th International Conference on Liquid Atomization and Spray Systems (ICLASS)*, 2003. cited p. 52, 125, 206

[73] J. Ebner, P. Schober, O. Schafer, R. Koch, and S. Wittig. Modelling of shear-driven liquid wall films: effect of accelerated air flow on the film flow propagation. *Progress in Computational Fluid Dynamics*, 4:183–190, 2004. cited p. 52, 114, 125, 126, 127, 130, 131, 205, 206

[74] J. E. Eckhause and R. D. Reitz. Modeling heat transfer to impinging fuel sprays in direct-injection engines. *Atomization and Sprays*, 5(2), 1995. cited p. 41

[75] J. C. T. Eijkel and A. v. d. Berg. Nanofluidics: what is it and what can we expect from it? *Microfluidics and Nanofluidics*, 1:249–267, 2005. 10.1007/s10404-004-0012-9. cited p. 42

[76] A. Elsäßer. *Fuel Preparation of Internal Combustion Engines: Fundamentals of the Flow of Shear-Driven Liquid Films (in german)*. PhD thesis, Department of Thermal Turbomachinery, University Karlsruhe, Germany, 1998. cited p. 43

[77] K. Emanuel. Increasing destructiveness of tropical cyclones over the past 30 years. *Nature*, 436(7051):686–688, 2005. cited p. 3

[78] G. Faeth. Spray combustion phenomena. In *Symposium (International) on Combustion*, volume 26, pages 1593–1612. Elsevier, 1996. cited p. 8

[79] M. Falese, L. Gicquel, and T. Poinsot. LES of bifurcation and hysteresis in confined annular swirling flows. *Journal of Computational Physics*, 2013. cited p.

[80] Z. Farago and N. Chigier. Morphological classification of disintegration of round liquid jets in a coaxial air stream. *Atomization and Sprays*, 2:137–153, 1992. cited p. 71, 72

[81] D. Fardad and N. Ladommatos. Evaporation of hydrocarbon compounds, including gasoline and diesel fuel, on heated metal surfaces. *Proceedings of the Institution of Mechanical Engineers, Part D: Journal of Automobile Engineering*, 213(6):625–645, 1999. cited p. 31, 104

[82] P. Fede, P. Février, and O. Simonin. Numerical study of the effect of the fluid turbulence microscales on particle segregation and collision in gas-solid turbulent flows. In *5th International Conference on Multiphase Flow*, Yokohama, Japan, 2004. ICMF. cited p. 5

[83] P. Fede and O. Simonin. Numerical study of the subgrid fluid turbulence effects on the statistics of heavy colliding particles. *Physics of Fluids*, 18(045103), 2006. cited p. 16

[84] P. Fede, O. Simonin, P. Villedieu, and K. D. Squires. Stochastic modeling of the turbulent subgrid fluid velocity along inertial particle trajectories. In *Proceedings of the Summer Program*, pages 247–258. Center for Turbulence Research, NASA Ames/Stanford Univ., 2006. cited p. 16

[85] W. Feller. *An introduction to probability theory and its applications*. Wiley series in probability and mathematical statistics: Probability and mathematical statistics. Wiley, 1971. cited p. 66

[86] V. G. Fernández, P. Berthoumieu, and G. Lavergne. Liquid sheet disintegration at high pressure. In *International Conference on Liquid Atomization and Spray Systems (ILASS)*, 2008. cited p. 64, 68, 69

[87] P. Février, O. Simonin, and K. Squires. Partitioning of particle velocities in gas-solid turbulent flows into a continuous field and a spatially uncorrelated random distribution: Theoretical formalism and numerical study. *Journal of Fluid Mechanics*, 533:1–46, 2005. cited p. 14, 15, 103

[88] R. Fjortoft. Application of integral theorems in deriving criteria of stability for laminar flows and for the baroclinic circular vortex. *Geofys. Publ*, 17(6):1–52, 1950. cited p. 59

[89] J. W. Forrester. World dynamics. 1971. cited p. 1

[90] H. Foucart. *Modélisation tridimensionnelle des films liquides pariétaux dans les moteurs à combustion interne = Development of a Three Dimensional Model of Wall Fuel Liquid Film for Internal Combustion Engines*. PhD thesis, Université de Rouen, 1998. cited p. 46, 52, 114

[91] M. M. Francois, S. J. Cummins, E. D. Dendy, D. B. Kothe, J. M. Sicilian, and M. W. Williams. A balanced-force algorithm for continuous and sharp interfacial surface tension models within a volume tracking framework. *Journal of Computational Physics*, 213(1):141–173, 2006. cited p. 75

[92] B. Franzelli, E. Riber, M. Sanjosé, and T. Poinsot. A two-step chemical scheme for Large-Eddy Simulation of kerosene-air flames. *Combustion and Flame*, 157(7):1364–1373, 2010. cited p. 11

[93] R. P. Fraser, N. Dombrowski, and J. H. Routley. The Atomisation of a liquid sheet by an impinging air stream. *Chemical Engineering Science*, 18:339–353, 1963. cited p. 23

[94] Q.-f. Fu, L.-j. Yang, and Y.-y. Qu. Measurement of annular liquid film thickness in an open-end swirl injector. *Aerospace Science and Technology*, 15(2):117–124, 2011. cited p. 6, 43

[95] D. Fuster, A. Bagué, T. Boeck, L. Le Moyne, A. Leboissetier, S. Popinet, P. Ray, R. Scardovelli, and S. Zaleski. Simulation of primary atomization with an octree adaptive mesh refinement and vof method. *International Journal of Multiphase Flow*, 35(6):550–565, 2009. cited p. 76, 77

[96] D. Fuster, J.-P. Matas, S. Marty, S. Popinet, J. Hoepffner, A. Cartellier, and S. Zaleski. Instability regimes in the primary breakup region of planar coflowing sheets. *Journal of Fluid Mechanics*, 736:150–176, 2013. cited p. 74

[97] L. Gao and T. J. McCarthy. The "lotus effect" explained: two reasons why two length scales of topography are important. *Langmuir*, 22(7):2966–2967, 2006. PMID: 16548542. cited p. 32

[98] M. García. *Développement et validation du formalisme Euler-Lagrange dans un solveur parallèle et non-structuré pour la simulation aux grandes échelles*. PhD thesis, Université de Toulouse - Ecole doctorale : Mécanique, Energétique, Génie civil, Procédés, 2009. cited p. 20, 87, 89, 95, 97, 115, 246, 248

[99] N. García Rosa. *Phénomènes d'allumage d'un foyer de turbomachine en conditions de haute altitude*. PhD thesis, Toulouse, ISAE, 2008. cited p. 18

[100] P. H. Gaskell, P. K. Jimack, M. Sellier, H. M. Thompson, and M. C. T. Wilson. Gravity-driven flow of continuous thin liquid films on non-porous substrates with topography. *Journal of Fluid Mechanics*, 509:253–280, 2004. cited p. 42, 47, 52

[101] R. Gatignol. The faxén formulae for a rigid particle in an unsteady non-uniform stokes flow. *Journal de Mécanique Théorique et Appliquée*, 1(2):143–160, 1983. cited p. 238

[102] S. Gepperth, D. Guildenbecher, R. Koch, and H. Bauer. Pre-filming primary atomization: Experiments and modeling. ILASS-Europe, 2010. cited p. 74, 133, 134, 139, 159, 161, 162, 205, 206

[103] S. Gepperth, R. Koch, and H.-J. Bauer. Analysis and comparison of primary droplet characteristics in the near field of a prefilming airblast atomizer. In *ASME Turbo Expo 2013: Turbine Technical Conference and Exposition*. American Society of Mechanical Engineers, 2013. cited p. 74, 75, 133, 134

[104] S. Gepperth, A. Müller, R. Koch, and H. Bauer. Ligament and droplet characteristics in prefilming airblast atomization. *ICLASS*, 2012. cited p. 74, 133, 135, 139, 140, 152, 159, 163, 164, 204, 205, 206

[105] M. Germano. Turbulence: the filtering approach. *Journal of Fluid Mechanics*, 238:325–336, 1992. cited p. 235, 236

[106] M. Germano, U. Piomelli, P. Moin, and W. Cabot. A dynamic subgrid-scale eddy viscosity model. *Physics of Fluids*, 3(7):1760–1765, 1991. cited p. 166, 235

[107] S. Ghosal and P. Moin. The basic equations for the large eddy simulation of turbulent flows in complex geometry. *Journal of Computational Physics*, 118:24 – 37, 1995. cited p. 233

[108] O. Gicquel, D. Thevenin, M. Hilka, and N. Darabiha. Direct numerical simulation of turbulent premixed flames using intrinsic low-dimensional manifolds. *Combustion Theory and Modelling*, 3(3):479–502, 1999. cited p. 11

[109] E. Giffen and A. Muraszew. *Atomization of liquid fuels*. Chapman & Hall, London, 1953. cited p. 6

[110] R. Gingold and J. Monaghan. Smoothed particle hydrodynamics-theory and application to non-spherical stars. *Monthly notices of the royal astronomical society*, 181:375–389, 1977. cited p. 16

[111] V. Giovangigli. *Multicomponent Flow Modeling*. Modeling and Simulation in Science, Engineering and Technology. Birkhauser, Boston, 1999. cited p. 228, 229

[112] J. Glimm, J. Grove, X. Li, W. Oh, and D. Sharp. A critical analysis of Rayleigh-Taylor growth rates. *Journal of Computational Physics*, 169(2):652–677, 2001. cited p. 143

[113] R. J. Goldstein. Film cooling. In T. F. Irvine and J. P. Hartnett, editors, *Advances in Heat Transfer*, volume 7 of *Advances in Heat Transfer*, pages 321 – 379. Elsevier, 1971. cited p. 42

[114] M. Gonzalez D, G. L. Borman, and R. D. Reitz. A study of diesel cold starting using both cycle analysis and multidimensional calculations. *SAE transactions*, 100(3):189–208, 1991. cited p. 105

[115] M. Gorokhovski, J. Jouanguy, and A. Chtab. Simulation of air-blast atomization:'floating guard'statistic particle method for conditioning of les computation; stochastic models of break-up and coalescence. In *Proc. Int. Conf. Liq. Atom. Spray Syst., 10th (ICLASS-2006)*, 2006. cited p. 80, 81, 82

[116] M. Gorokhovski. The stochastic Lagrangian model of drop breakup in the computation of liquid sprays. *Atomization and Sprays*, 11:505–519, 2001. cited p. 79

[117] M. Gorokhovski and M. Herrmann. Modelling primary atomization. *Annual Review of Fluid Mechanics*, 40:343–366, 2008. cited p. 12, 13, 20, 76, 81, 82

[118] M. Gorokhovski and V. Saveliev. Analyses of Kolmogorov's model of breakup and its application into Lagrangian computation of liquid sprays under air-blast atomization. *Physics of Fluids*, 15(1):184–192, 2003. cited p. 20, 79, 80

[119] M. Gorokhovski and V. Saveliev. Statistical universalities in fragmentation under scaling symmetry with a constant frequency of fragmentation. *Journal of Physics D: Applied Physics*, 41(8):085405, 2008. cited p. 80

[120] M. Gorokhovski, J. Jouanguy, and A. Chtab-Desportes. Stochastic model of the near-to-injector spray formation assisted by a high-speed coaxial gas jet. *Fluid dynamics research*, 41(3):035509, 2009. cited p. 80, 81

[121] M. Gorokhovski, R. Zamansky, I. Vinkovic, et al. Channel flow les with stochastic modeling of the subgrid acceleration. *Studying Turbulence Using Numerical Simulation Databases-XII: Proceedings of the Summer Program 2008*, pages 377–386, 2008. cited p. 81

[122] N. Gourdain, L. Gicquel, M. Montagnac, O. Vermorel, M. Gazaix, G. Staffelbach, M. Garcia, J. Boussuge, and T. Poinsot. High performance parallel computing of flows in complex geometries: I. methods. *Comput. Sci. Disc.*, 2:015003, 2009. cited p. 20

[123] J. Greenberg, D. Alibagli, and Y. Tambour. An opposed jet quasi-monodisperse spray diffusion flame. *Combustion science and technology*, 50(4-6):255–270, 1986. cited p. 16

[124] J. B. Grotberg. Pulmonary Flow and Transport Phenomena. *Annual Review of Fluid Mechanics*, 26(1):529–571, 1994. cited p. 42

[125] C. Habchi. Modélisation de l'interaction spray-film liquide par une approche lagrangienne incluant splashing et évaporation. Technical report, IFPEN, 2005. cited p. 105, 106

[126] C. Habchi. Modélisation de l'interaction spray/paroi dans les moteurs à combustion interne. Technical Report 59166, IFPEN, 2006. cited p. 105

[127] C. Habchi. A comprehensive model for liquid film boiling in internal combustion engines. *Oil & Gas Science and Technology–Revue de l'Institut Français du Pétrole*, 65(2):331–343, 2010. cited p. 104

[128] C. Habchi. Développement de modèles d'atomisation secondaire et d'intéractions spray-paroi en les décrits par une approche lagrangienne dans avbp. Technical report, Institut Français du Pétrole, 2010. cited p. 20, 29, 37, 38, 104, 105, 107, 206

[129] E. H. P. A. Haeckel. *Generelle Morphologie der Organismen: allgemeine Grundzüge der organischen Formen-Wissenschaft, mechanisch begründet durch die von Charles Darwin reformirte Descendenz-Theorie*, volume 2. G. Reimer, 1866. cited p. 1

[130] G. Haller. An objective definition of a vortex. *Journal of Fluid Mechanics*, 525:1–26, 2005. cited p. 169

[131] F. Ham, S. V. Apte, G. Iaccarino, X. Wu, M. Herrmann, G. Constantinescu, K. Mahesh, and P. Moin. Unstructured LES of reacting multiphase flows in realistic gas turbine combustors. In *Annual Research Briefs*, pages 139–160. Center for Turbulence Research, NASA Ames/Stanford Univ., 2003. cited p. 18, 115, 246, 248

[132] Z. Han, R. D. Reitz, F. E. Corcione, and G. Valentino. Interpretation of $k - \epsilon$ computed turbulence length scale predictions for engine flows. In *26th Symp. (Int.) on Combustion*, pages 2717–2723. The Combustion Institute, Pittsburgh, 1996. cited p.

[133] Z. Han, Z. Xu, and N. Trigui. Spray/wall interaction models for multidimensional engine simulation. *International Journal of Engine Research*, 1(1):127–146, 2000. cited p. 27, 29, 35, 36, 37, 38, 105, 106

[134] G. Hannebique. *Etude de la structure des flammes diphasiques dans les brûleurs aéronautiques*. PhD thesis, Institut National Polytechnique de Toulouse - MeGeP - Dynamique des Fluides, 2013. phd. cited p. 15, 18, 19, 20, 87, 247

[135] G. Hannebique, P. Sierra, E. Riber, and B. Cuenot. Large eddy simulation of reactive two-phase flow in an aeronautical multipoint burner. *Flow, turbulence and combustion*, 90(2):449–469, 2013. cited p. 19

[136] T. J. Hanratty and A. Hershman. Initiation of roll waves. *AIChE Journal*, 7(3):488–497, 1961. cited p. 63

[137] Y. Hardalupas, A. Selbach, and J. Whitelaw. Aspects of oscillating flames. *Journal of Visualization*, 1(1):79–85, 1998. cited p. 71

[138] A. Haselbacher, F. M. Najjar, and J. P. Ferry. An efficient and robust particle-localization algorithm for unstructured grids. *Journal of Computational Physics*, 225(2):2198–2213, 2007. cited p. 91, 92, 246

[139] A. A. Hashmi, K. Dullenkopf, R. Koch, and H.-J. Bauer. Cfd methods for shear driven liquid wall films. *ASME Conference Proceedings*, 2010(43994):1283–1291, 2010. cited p. 53

[140] E. R. Hawkes and S. R. Cant. A flame surface density approach to large eddy simulation of premixed turbulent combustion. In *28th Symp. (Int.) on Combustion*, pages 51–58. The Combustion Institute, Pittsburgh, 2000. cited p. 11, 79

[141] K. Helbig, A. Alexeev, T. Gambaryan-Roisman, and P. Stephan. Evaporation of falling and shear-driven thin films on smooth and grooved surfaces. *Flow, Turbulence and Combustion*, 75:85–104, 2005. 10.1007/s10494-005-8582-5. cited p. 53

[142] M. Herrmann. A balanced force refined level set grid method for two-phase flows on unstructured flow solver grids. *Journal of Computational Physics*, 227(4):2674 – 2706, 2008. cited p. 75

[143] M. Herrmann. The influence of density ratio on the primary atomization of a turbulent liquid jet in crossflow. *Proceedings of the Combustion Institute*, 33(2):2079–2088, 2011. cited p. 76

[144] M. Herrmann and M. Gorokhovski. An outline of a LES subgrid model for liquid/gas phase interface dynamics. In *Proceedings of the Summer Program*, page 171, 2008. cited p. 81

[145] M. Herrmann. Detailed numerical simulations of the primary atomization of a turbulent liquid jet in crossflow. *Journal of Engineering for Gas Turbines and Power*, 132(6):061506–10, 2010. cited p. 76

[146] E. Hinch. A note on the mechanism of the instability at the interface between two shearing fluids. *Journal of Fluid Mechanics*, 144(1):463–465, 1984. cited p. 60

[147] H. Hiroyasu and T. Kadota. Fuel droplet size distribution in diesel combustion chamber. *SAE Technical paper 740715*, 1974. cited p. 18, 20

[148] J. O. Hirschfelder, F. Curtiss, and R. B. Bird. *Molecular theory of gases and liquids*. John Wiley & Sons, 1964. cited p. 44, 228

[149] C. Hirt and B. Nichols. Volume of fluid (VOF) method for the dynamics of free boundaries. *Journal of Computational Physics*, 39(1):201 – 225, 1981. cited p. 13

[150] C. Hoefler, S. Braun, R. Koch, and B. H.-J. Modeling spray formation in gas turbine - a new meshless approach. *ASME Conference Proceedings*, 2012. cited p. 17

[151] M. Hong, A. Cartellier, and E. Hopfinger. Atomisation and mixing in coaxial injection. In *Proc. 4th Int. Conference on Launcher Technology" Space Launcher Liquid Propulsion", Liège, Belgique*, pages 3–6, 2002. cited p. 65, 71, 74, 133, 136, 137, 159, 206

[152] M. Hong, A. Cartellier, E. Hopfinger, et al. Atomisation mechanism in coaxial injectors. In *5th Euromech Fluid Mechanics Conference*, 2003. cited p. 64, 84, 136

[153] A. Hooper and W. Boyd. Shear-flow instability at the interface between two viscous fluids. *Journal of Fluid Mechanics*, 128(1):507–528, 1983. cited p. 60

[154] E. Hopfinger. Liquid jet instability and atomization in a coaxial gas stream. In *Advances in Turbulence VII*, pages 69–78. Springer, 1998. cited p. 70

[155] E. Hopfinger and J. Lasheras. Explosive breakup of a liquid jet by a swirling coaxial gas jet. *Physics of Fluids*, pages 1696–1698, 1996. cited p. 71

[156] L. P. Hsiang and G. M. Faeth. Near-limit drop deformation and secondary breakup. *International Journal of Multiphase Flow*, 18(5):635–652, 1992. cited p. 84

[157] X. Hu and N. Adams. A multi-phase sph method for macroscopic and mesoscopic flows. *Journal of Computational Physics*, 213(2):844–861, 2006. cited p. 16

[158] G. L. Hubbard, V. E. Denny, and A. F. Mills. Droplet evaporation: effects of transient and variable properties. *International Journal of Heat and Mass Transfer*, 18:1003–1008, 1975. cited p. 242

[159] H. Hulburt and S. Katz. Some problems in particle technology: A statistical mechanical formulation. *Chemical Engineering Science*, 19(8):555–574, 1964. cited p. 16

[160] N. Iafrate. *Etude LES des effets d'injection à la paroi en moteur essence downsizé [Work in progress]*. PhD thesis, INP Toulouse, 20015. cited p. 206

[161] J. Jacobsson. *Thin film technologies: April 20-22, 1983, Geneva, Switzerland*. Proceedings of SPIE Series. SPIE–the International Society for Optical Engineering, 1983. cited p. 42

[162] F. Jaegle. *LES of two-phase flow in aero-engines*. PhD thesis, Université de Toulouse - Ecole doctorale MEGeP, CERFACS - CFD Team, Toulouse, December 2009. cited p. 18, 20, 87, 171, 186, 240

[163] F. Jaegle, J.-M. Senoner, M. Garcia, F. Bismes, R. Lecourt, B. Cuenot, and T. Poinsot. Lagrangian and eulerian simulations of evaporating fuel spray in an aeronautical multipoint injector. *Proceedings of the Combustion Institute*, 33:2099–2107, 2011. cited p. 18

[164] S. Jauré. *Méthodologies pour le couplage Simulation aux Grandes Echelles/Thermique en environnement massivement parallèle*. PhD thesis, Université de Toulouse - Ecole doctorale : Mécanique, Energétique, Génie civil, Procédés - Dynamique des Fluides - December, 13, 2012. cited p. 248

[165] S. Jay, F. Lacas, and S. Candel. Combined surface density concepts for dense spray combustion. *Combustion and Flame*, 144(3):558–577, 2006. cited p. 79

[166] P. Jenny, D. Roekaerts, and N. Beishuizen. Modeling of turbulent dilute spray combustion. *Progress in Energy and Combustion Science*, 2012. cited p. 8, 9

[167] J. Jouanguy. *Modélisation phénoménologique de pulvérisation de sprays couplée à une approche LES pour la phase gazeuse.* PhD thesis, Université de Rouen, 2007. cited p. 82

[168] L. Jurman, K. Bruno, and M. McCready. Periodic and solitary waves on thin, horizontal, gas-sheared liquid films. *International journal of multiphase flow*, 15(3):371–384, 1989. cited p. 61, 62, 63

[169] L. Jurman and M. McCready. Study of waves on thin liquid films sheared by turbulent gas flows. *Physics of Fluids A: Fluid Dynamics*, 1:522, 1989. cited p. 61

[170] D. Kalantari and C. Tropea. Spray impact onto flat and rigid walls: Empirical characterization and modelling. *International Journal of Multiphase Flow*, 33(5):525 – 544, 2007. cited p. 32, 36, 37, 40

[171] R. Kapulla, J. Tuchtenhagen, A. Müller, K. Dullenkopf, and H.-J. Bauer. Droplet sizing performance of different shadow sizing codes. *Lasermethoden in der Strömungsmesstechnik*, 16:38–1, 2008. cited p. 164

[172] G. Karypis and V. Kumar. A fast and high quality multilevel scheme for partitioning irregular graphs. *SIAM Journal on Scientific Computing*, 20(1):359–392, 1998. cited p. 247

[173] G. Karypis, K. Schloegel, and V. Kumar. *Parmetis: Parallel Graph Partitioning and Sparse Matrix Ordering Library*. Univ. of Minnesota, Department of Computer Science and Engineering, USA, 2003. (version 3.1). cited p. 247

[174] A. Kaufmann. *Vers la simulation des grandes échelles en formulation Euler/Euler des écoulements réactifs diphasiques*. Phd thesis, INP Toulouse, 2004. cited p. 14, 15, 102

[175] A. Kaufmann, M. Moreau, O. Simonin, and J. Hélie. Comparison between lagrangian and mesoscopic eulerian modelling approaches for inertial particles suspended in decaying isotropic turbulence. *Journal of Computational Physics*, 227(13):6448–6472, 2008. cited p. 95, 96, 103

[176] J. J. Kester. Edible films and coatings: a review. *Food technology*, (40):47–59, 1987. cited p. 42

[177] T. R. Knutson, J. J. Sirutis, S. T. Garner, G. A. Vecchi, and I. M. Held. Simulated reduction in atlantic hurricane frequency under twenty-first-century warming conditions. *Nature Geoscience*, 1(6):359–364, 2008. cited p. 3

[178] A. N. Kolmogorov. The local structure of turbulence in incompressible viscous fluid for very large reynolds numbers. *Comptes rendus de l'Académie des sciences, USSR*, 30:301, 1941. cited p. 231

[179] A. Kolmogorov. On the log-normal distribution of particles sizes during break-up process. In *Dokl. Akad. Nauk SSSR*, volume 31, page 99, 1941. cited p. 80

[180] S. A. Krzeczkowski. Measurement of liquid droplet disintegration mechanisms. *International Journal of Multiphase Flow*, 6:227–239, 1980. cited p. 82

[181] V. Kumar. Graph partitioning for dynamic, adaptive and multi-phase computations. In *Workshop Resource Recovery*, 2000. Material from IMA Talks. cited p. 246

[182] M. Kunihide and I. Michiyoshi. Effects of the initial size of water droplet on its evaporation on heated surfaces. *International Journal of Heat and Mass Transfer*, 22(6):979–981, 1979. cited p. 31

[183] K. K. Kuo. *Principles of combustion*. John Wiley & Sons, Inc., Hoboken, New Jersey, 2005 Second Edition. cited p. 8

[184] M. Lalo. *Atomisation d'un film liquide mince par action combinée des instabilités de Kelvin-Helmholtz et de Faraday. Application aux injecteurs aérodynamiques des turbomachines aéronautiques*. PhD thesis, Ecole Nationale Supérieure de l'Aéronautique et de l'Espace, 2006. cited p. 65

[185] N. Lamarque. *Schémas numériques et conditions limites pour la simulation aux grandes échelles de la combustion diphasique dans les foyers d'hélicoptère*. Phd thesis, INP Toulouse, 2007. cited p. 20

[186] H. Lan, M. Friedrich, B. Armaly, and J. Drallmeier. Simulation and measurement of 3d shear-driven thin liquid film flow in a duct. *International Journal of Heat and Fluid Flow*, 29(2):449 – 459, 2008. cited p. 53

[187] J. C. Lasheras and E. J. Hopfinger. Liquid jet instability and atomisation in a coaxial gas stream. *Annual Review of Fluid Mechanics*, 32:275–308, 2000. cited p. 64, 69, 70, 71, 73

[188] F. Laurent and M. Massot. Multi-fluid modeling of laminar poly-dispersed spray flames: origin, assumptions and comparison of the sectional and sampling methods. *Combustion Theory and Modelling*, 5:537–572, 2001. cited p. 16

[189] J. Lavedrine. *Simulations aux grandes échelles de l'écoulement diphasique dans des modèles d'injecteur de moteurs aéronautiques*. Phd thesis, INP Toulouse, 2008. cited p. 18

[190] R. Lebas, T. Menard, P. Beau, A. Berlemont, and F. Demoulin. Numerical simulation of primary break-up and atomization: Dns and modelling study. *International Journal of Multiphase Flow*, 35(3):247–260, 2009. cited p. 76, 79

[191] R. Lecourt, G. Linassier, and G. Lavergne. Detailed characterisation of a swirled air/kerosene spray in reactive and non-reactive conditions downstream from an actual turbojet injection system. In *ASME 2011 Turbo Expo: Turbine Technical Conference and Exposition*, pages 185–194. American Society of Mechanical Engineers, 2011. cited p. 19

[192] S. Y. Lee and Y. D. Kim. Sizing of spray particles using image processing technique. *KSME international journal*, 18(6):879–894, 2004. cited p. 164

[193] S. Y. Lee and S. U. Ryu. Recent progress of spray-wall interaction research. *Journal of mechanical science and technology*, 20(8):1101–1117, 2006. cited p. 32, 33, 36, 39

[194] S. H. Lee and H. S. Ryou. Development of a new spray/wall interaction model. *International journal of multiphase flow*, 26(7):1209–1234, 2000. cited p. 37

[195] Y. Lee, H. Thompson, and P. Gaskell. Three-dimensional thin film and droplet flows over and past surface features with complex physics. *Computers & Fluids*, 46(1):306 – 311, 2011. 10th ICFD Conference Series on Numerical Methods for Fluid Dynamics (ICFD 2010). cited p. 52

[196] A. H. Lefebvre. *Atomization and Sprays*. Combustion (Hemisphere Publishing Corporation). Taylor & Francis, 1989. cited p. 5, 66

[197] A. H. Lefebvre. Airblast atomization. *Progress in Energy and Combustion Science*, 6(3):233–261, 1980. cited p. 23, 25

[198] A. H. Lefebvre. Fifty years of gas turbine fuel injection. *Atomization and Sprays*, 10(3-5), 2000. cited p. 5

[199] J.-P. Légier, T. Poinsot, and D. Veynante. Dynamically thickened flame LES model for premixed and non-premixed turbulent combustion. In *Proceedings of the Summer Program*, pages 157–168. Center for Turbulence Research, NASA Ames/Stanford Univ., 2000. cited p. 11

[200] S. Leroux. *Stabilité d'un jet liquide cylindrique. Influence de fortes pressions ambiantes*. PhD thesis, 1996. cited p. 70

[201] H. Lhuissier and E. Villermaux. Destabilization of flapping sheets: The surprising analogue of soap films. *Comptes Rendus Mecanique*, 337(6):469–480, 2009. cited p. 67

[202] B. Li. *Discontinuous Finite Elements in Fluid Dynamics And Heat Transfer*. Computational Fluid and Solid Mechanics. Springer, 2006. cited p. 45

[203] T. Li, K. Nishida, and H. Hiroyasu. Droplet size distribution and evaporation characteristics of fuel spray by a swirl type atomizer. *Fuel*, 90(7):2367–2376, 2011. cited p. 8

[204] P. A. Libby and F. A. Williams. Turbulent combustion: fundamental aspects and a review. In *Turbulent Reacting Flows*, pages 2–61. Academic Press London, 1994. cited p. 11

[205] D. K. Lilly. A proposed modification of the germano sub-grid closure method. *Physics of Fluids*, 4(3):633–635, 1992. cited p. 236

[206] E. Longmire and J. Eaton. Structure of a particle-laden round jet. *Journal of Fluid Mechanics*, 236(1):217, 1992. cited p. 8

[207] E. Loth. Numerical approaches for motion of dispersed particles, droplets and bubbles. *Progress in Energy and Combustion Science*, 26:161–223, 2000. cited p. 13

[208] A. Lozano and F. Barreras. Experimental study of the gas flow in an air-blasted liquid sheet. *Experiments in fluids*, 31(4):367–376, 2001. cited p. 69

[209] A. Lozano, C. Call, C. Dopazo, and A. Garcia-Olivares. Experimental and numerical study of the atomization of a planar liquid sheet. *Atomization and Sprays*, 6(1):77–94, 1996. cited p. 68

[210] A. Lozano, F. Barreras, G. Hauke, and C. Dopazo. Longitudinal instabilities in an air-blasted liquid sheet. *Journal of Fluid Mechanics*, 437:143–173, 2001. cited p. 64

[211] O. Lucca-Negro and T. O'Doherty. Vortex breakdown: a review. *Progress in Energy and Combustion Science*, 27:431–481, 2001. cited p.

[212] L. Lucy. A numerical approach to the testing of the fission hypothesis. *The astronomical journal*, 82:1013–1024, 1977. cited p. 16

[213] H.-Y. Ma and M.-D. Zhou. *Vorticity and vortex dynamics*. Springer, 2006. cited p. 173, 174

[214] U. Maas and S. B. Pope. Implementation of simplified chemical kinetics based on low-dimensional manifolds. *Proceedings of the Combustion Institute*, 24:719–729, 1992. cited p. 11

[215] K. Mahesh, G. Constantinescu, S. Apte, G. Iaccarino, and P. Moin. Large-eddy simulation of gas turbine combustors. In *Annual Research Briefs*, pages 3–17. Center for Turbulence Research, NASA Ames/Stanford Univ., 2001. cited p. 18

[216] A. Mansour and N. Chigier. Dynamic behavior of liquid sheets. *Physics of Fluids A*, 3(12):2971–2980, December 1991. cited p. 67, 68

[217] D. L. Marchisio and R. O. Fox. Solution of population balance equations using the direct quadrature method of moments. *J. Aerosol Sci.*, 36:43–73, 2005. cited p. 16

[218] P. Marmottant. *Atomisation d'un liquide par un courant gazeux*. PhD thesis, Université de Grenoble, 2001. cited p. 73

[219] P. Marmottant and E. Villermaux. Mécanismes d'atomisation primaire dans les jets coaxiaux. In *Combustion dans les moteurs fusées - Acte du Colloque de Synthèse du groupe de Recherche CNES*, 2001. cited p. 64, 65, 136, 137, 140

[220] P. Marmottant and E. Villermaux. On spray formation. *Journal of Fluid Mechanics*, 498:73–111, 2004. cited p. 55, 65, 66, 71, 73, 84

[221] F. Mashayek. Droplet-turbulence interactions in low-Mach number homogeneous shear two-phase flows. *Journal of Fluid Mechanics*, 367:163–203, 1998. cited p. 237

[222] E. Mastorakos, T. A. Baritaud, and T. J. Poinsot. Numerical simulations of autoignition in turbulent mixing flows. *Combustion and Flame*, 109:198 – 223, 1997. cited p. 11

[223] E. Mastorakos. Ignition of turbulent non-premixed flames. *Progress in Energy and Combustion Science*, 35(1):57–97, 2009. cited p. 8

[224] J. Matas, S. Marty, and A. Cartellier. Experimental and analytical study of the shear instability of a gas-liquid mixing layer. *Physics of Fluids*, 23:094112, 2011. cited p. 74

[225] W. Mathews, C. Lee, and J. Peters. Experimental investigations of spray/wall impingement. *Atomization and Sprays*, 13(2-3):223–242, 2003. cited p. 105, 106

[226] M. Maxey and J. Riley. Equation of motion for a small rigid sphere in a nonuniform flow. *Physics of Fluids*, 26(4), 1983. cited p. 237, 238

[227] M. R. Maxey and B. K. Patel. Localized force representations for particles sedimenting in Stokes flow. *International Journal of Multiphase Flow*, 27(9):1603–1626, 2001. cited p. 243, 244

[228] R. McGraw. Description of aerosol dynamics by the quadrature method of moments. *Aerosol Science and Technology*, 27(2):255–265, 1997. cited p. 16

[229] D. L. Meadows, W. W. Behrens, D. H. Meadows, R. F. Naill, J. Randers, and E. Zahn. *Dynamics of growth in a finite world*. Wright-Allen Press Cambridge, MA, 1974. cited p. 2

[230] D. H. Meadows, D. H. Meadows, J. Randers, and W. W. Behrens III. *The Limits to Growth: A Report to The Club of Rome (1972)*. Universe Books, New York, 1972. cited p. 1, 2

[231] T. Menard, S. Tanguy, and A. Berlemont. Coupling level set/VOF/ghost fluid methods: Validation and application to 3d simulation of the primary break-up of a liquid jet. *International Journal of Multiphase Flow*, 33:510–524, 2007. cited p. 14, 75, 76

[232] M. Might. What is a ph.d.? what is research? and, tips for success. Programming Languages Mentoring Workshop, Rome, January 2013. cited p. 2, 3

[233] J. W. Miles. On the generation of surface waves by shear flows. *Journal of Fluid Mechanics*, 3(02):185–204, 1957. cited p. 60

[234] M. Miya, D. E. Woodmansee, and T. J. Hanratty. A model for roll waves in gas-liquid flow. *Chemical Engineering Science*, 26(11):1915–1931, 1971. cited p. 63

[235] P. Moin and S. V. Apte. Large-eddy simulation of realistic gas turbine combustors. *AIAA Journal*, 44(4):698–708, 2006. cited p. 18

[236] J. Monaghan. Simulating free surface flows with SPH. *Journal of computational physics*, 110(2):399–406, 1994. cited p. 16

[237] S. Moon, E. Abo-Serie, and C. Bae. Liquid film thickness inside the high pressure swirl injectors: Real scale measurement and evaluation of analytical equations. *Experimental Thermal and Fluid Science*, 34(2):113–121, 2010. cited p. 6

[238] A. Moreira, A. Moita, and M. Panão. Advances and challenges in explaining fuel spray impingement: How much of single droplet impact research is useful? *Progress in Energy and Combustion Science*, 36(5):554–580, 2010. cited p. 27, 30, 31, 35, 36, 40, 41

[239] S. C. Morris and J. F. Foss. Turbulent boundary layer to single-stream shear layer: the transition region. *Journal of Fluid Mechanics*, 494(1):187–221, 2003. cited p. 144, 145, 146, 156, 159

[240] V. Moureau and O. Desjardins. A second-order ghost-fluid method for the primary atomization of liquid fuel in air-blast type injectors. In *Proceedings of the Summer Program*, volume 143, 2008. cited p. 75

[241] V. Moureau, P. Domingo, and L. Vervisch. From large-eddy simulation to direct numerical simulation of a lean premixed swirl flame: Filtered laminar flame-pdf modeling. *Combustion and Flame*, 158(7):1340–1357, 2011. cited p. 10

[242] V. Moureau, P. Domingo, and L. Vervisch. Design of a massively parallel CFD code for complex geometries. *Comptes Rendus Mécanique*, 339(2):141–148, 2011. cited p. 248

[243] A. Müller, R. Meier, O. Schäfer, and S. Wittig. The influence of unsteady flow conditions on liquid sheet atomisation. In *Atomization and Spray Processes*, 2004. cited p. 134, 138, 147, 161

[244] A. Müller, F. Schumann, K. Dullenkopf, and H. Bauer. Analysis of droplet wall interaction using advanced image processing techniques. *Proc. 21st ILASS Europe, Muğla, Turkey*, 2007. cited p. 164

[245] C. Mundo, M. Sommerfeld, and C. Tropea. Droplet-wall collisions: experimental studies of the deformation and breakup process. *International journal of multiphase flow*, 21(2):151–173, 1995. cited p. 28, 29, 35, 37, 38, 104, 106

[246] J. D. Naber. Hydrodynamics of droplet impingement on a heated surface. 1993. cited p. 31, 106, 107

[247] L. Ó. Náraigh, P. Spelt, O. Matar, and T. Zaki. Interfacial instability in turbulent flow over a liquid film in a channel. *International Journal of Multiphase Flow*, 37(7):812 – 830, 2011. cited p. 58, 61

[248] F. Nicoud and F. Ducros. Subgrid-scale stress modelling based on the square of the velocity gradient. *Flow, Turbulence and Combustion*, 62(3):183–200, 1999. cited p. 236

[249] F. Nicoud, H. B. Toda, O. Cabrit, S. Bose, and J. Lee. Using singular values to build a subgrid-scale model for large eddy simulations. *Physics of Fluids (1994-present)*, 23(8):085106, 2011. cited p. 236

[250] S. Nishio and M. Hirata. Direct contact phenomenon between a liquid droplet and high temperature solid surface. In *6th International Heat Transfer Conference*, volume 1, pages 245–250, 1978. cited p. 31

[251] S.-Y. No. Breakup length of conical emulsion sheet discharged by pressure-swirl atomizer. *International journal of automotive technology*, 2(3):103–107, 2001. cited p. 6

[252] S. Nukiyama and Y. Tanasawa. Experiments in on the atomization of liquids in air stream. report 3: on the droplet-size distribution in an atomized jet. *Trans. Soc. Mech. Eng. Japan*, 5:62–67, 1939. cited p. 23

[253] T. Okawa, T. Shiraishi, and T. Mori. Production of secondary drops during the single water drop impact onto a plane water surface. *Experiments in fluids*, 41(6):965–974, 2006. cited p. 37

[254] T. Okawa, T. Shiraishi, and T. Mori. Effect of impingement angle on the outcome of single water drop impact onto a plane water surface. *Experiments in Fluids*, 44(2):331–339, 2008. cited p. 37

[255] A. Oron, S. H. Davis, and S. G. Bankoff. Long-scale evolution of thin liquid films. *Rev. Mod. Phys.*, 69:931–980, Jul 1997. cited p. 60

[256] P. J. O'Rourke and A. A. Amsden. The TAB method for numerical simulations of spray droplet breakup. *Society of automotive engineers*, 96, 1987, Paper 872089. cited p. 12

[257] P. O'Rourke and A. A. Amsden. A particle numerical model for wall film dynamics in port-injected engines. *SAE Technical Paper*, 1996. cited p. 54, 115, 155

[258] P. J. O'Rourke and A. Amsden. A spray/wall interaction submodel for the KIVA-3 wall film model-3 wall film model. *SAE transactions*, 109(3):281–298, 2000. cited p. 106

[259] C. W. Oseen. *Hydrodynamik*. Leipzig, 1927. cited p. 237, 239

[260] S. Osher and R. P. Fedkiw. Level set methods: An overview and some recent results. *Journal of Computational Physics*, 169(2):463 – 502, 2001. cited p. 14

[261] S. Osher and J. A. Sethian. Fronts propagating with curvature-dependent speed: algorithms based on Hamilton-Jacobi formulations. *Journal of Computational Physics*, 79(1):12 – 49, 1988. cited p. 14

[262] T. L. P. P. H. Wirsching and K. Ortiz. *Random Vibrations : Theory and Practice*. Dover publications, 2006. cited p. 173

[263] R. K. Pachauri and A. Reisinger. Climate change 2007: Synthesis report. contribution of working groups i, ii and iii to the fourth assessment report of the intergovernmental panel on climate change. *Intergovernmental Panel on Climate Change*, 1, 2007. cited p. 3

[264] M. Panão and A. Moreira. Interpreting the influence of fuel spray impact on mixture preparation for HCCI combustion with port-fuel injection. *Proceedings of the Combustion Institute*, 31(2):2205–2213, 2007. cited p. 41

[265] D. Paulhiac. *Extension des méthodes LES diphasique aux moteurs d'hélicoptères [Work in progress]*. PhD thesis, INP Toulouse, 2014. cited p. 18, 20, 91, 208, 246

[266] C.-A. Peng, L. Jurman, and M. McCready. Formation of solitary waves on gas-sheared liquid layers. *International Journal of Multiphase Flow*, 17(6):767 – 782, 1991. cited p. 43, 51, 62, 63

[267] O. M. Phillips. On the generation of waves by turbulent wind. *Journal of Fluid Mechanics*, 2(05):417–445, 1957. cited p. 61

[268] M. Pilch and C. A. Erdman. Use of breakup time data and velocity history data to predict the maximum size of stable fragments for acceleration-induced breakup of a liquid drop. *International Journal of Multiphase Flow*, 13(6):741–757, 1987. cited p. 82, 83

[269] U. Piomelli, W. H. Cabot, P. Moin, and S. Lee. Subgrid-scale backscatter in turbulent and transitional flows. *Physics of FluidsA*, 3(7):1766–1771, July 1991. cited p. 235

[270] H. Pitsch and L. D. de la Geneste. Large eddy simulation of premixed turbulent combustion using a level-set approach. *Proceedings of the Combustion Institute*, 29:2001–2008, 2002. cited p. 11

[271] C. Poelma, J. Westerweel, and G. Ooms. Particle-fluid interactions in grid-generated turbulence. *Journal of Fluid Mechanics*, 589(1):315–351, 2007. cited p. 8

[272] T. Poinsot and S. Lele. Boundary conditions for direct simulations of compressible viscous flows. *Journal of Computational Physics*, 101(1):104–129, 1992. cited p. 20, 166

[273] T. Poinsot and D. Veynante. *Theoretical and Numerical Combustion*. Third Edition (www.cerfacs.fr/elearning), 2011. cited p. 11, 12

[274] S. B. Pope. *Turbulent flows*. Cambridge University Press, 2000. cited p. 10, 128, 129

[275] S. Popinet. Gerris: a tree-based adaptive solver for the incompressible euler equations in complex geometries. *Journal of Computational Physics*, 190(2):572 – 600, 2003. cited p. 75, 76

[276] S. Popinet. An accurate adaptive solver for surface-tension-driven interfacial flows. *Journal of Computational Physics*, 228(16):5838 – 5866, 2009. cited p. 75, 76

[277] M. J. Radzicki and R. A. Taylor. Origin of system dynamics: Jay W. Forrester and the history of system dynamics". cited p. 1

[278] W. E. Ranz and W. R. Marshall. Evaporation from drops. *Chem. Eng. Prog.*, 48(4):173, 1952. cited p. 241

[279] L. Rayleigh. On the stability, or instability, of certain fluid motions. *Proceedings of the London Mathematical Society*, 1(1):57–72, 1879. cited p. 59

[280] L. Raynal. *Instabilite et entrainement a l'interface d'une couche de melange liquide-gaz*. PhD thesis, Universite Joseph Fourier, 1997. cited p. 58, 71, 72, 73, 136, 137

[281] L. Raynal, E. Villermaux, J. Lasheras, and E. Hopfinger. Primary instability in liquid-gas shear layers. In *Symposium on Turbulent Shear Flows, 11 th, Grenoble, France*, pages 27–1, 1997. cited p. 72, 137

[282] M. Rein. Phenomena of liquid drop impact on solid and liquid surfaces. *Fluid Dynamics Research*, 12(2):61–93, 1993. cited p. 32

[283] M. Rein. Interactions between drops and hot surfaces. *Courses and lectures - International centre for mechanical sciences*, pages 185–218, 2002. cited p. 33

[284] Y. Renardy. Instability at the interface between two shearing fluids in a channel. *Physics of Fluids*, 28(12):3441, 1985. cited p. 60

[285] J. Reveillon and F. Demoulin. Evaporating droplets in turbulent reacting flows. *Proceedings of the Combustion Institute*, 31(2):2319–2326, 2007. cited p. 8

[286] J. Réveillon and L. Vervisch. Accounting for spray vaporization in turbulent combustion modeling. In *Proceedings of the Summer Program*, pages 25–38. Center for Turbulence Research, NASA Ames/Stanford Univ., 1998. cited p. 8

[287] J. Réveillon and L. Vervisch. Analysis of weakly turbulent diluted-spray flames and spray combustion regimes. *Journal of Fluid Mechanics*, 537:317–347, 2005. cited p. 8, 9

[288] O. Reynolds. On the dynamical theory of incompressible viscous fluids and the determination of the criterion. *Phil. Trans. R. Soc. London A*, 186:123–164, 1895. cited p. 231

[289] E. Riber. *Développement de la méthode de simulation aux grandes échelles pour les écoulements diphasiques turbulents*. Phd thesis, INP Toulouse, 2007. cited p. 103

[290] E. Riber, V. Moureau, M. García., T. Poinsot, and O. Simonin. Evaluation of numerical strategies for LES of two-phase reacting flows. *Journal of Computational Physics*, 228:539–564, 2009. cited p. 16

[291] N. Rimbert and O. Séro-Guillaume. Log-stable laws as asymptotic solutions to a fragmentation equation: application to the distribution of droplets in a high Weber-number spray. *Physical Review E*, 69(5):056316, 2004. cited p. 79

[292] N. K. Rizk and A. H. Lefebvre. Influence of liquid film thickness on airblast atomization. *Journal of Engineering for Gas Turbines and Power*, 102:706–710, 1980. cited p. 25

[293] N. K. Rizk and A. H. Lefebvre. Internal Flow Characteristics of simplex swirl atomizers. *Journal of Propulsion and Power*, 1(3):193–199, May-June 1985. cited p. 6

[294] D. F. Rogers. *Laminar flow analysis*. Cambridge University Press, 1992. cited p. 122

[295] I. Roisman, K. Horvat, and C. Tropea. Spray impact: Rim transverse instability initiating fingering and splash, and description of a secondary spray. *Physics of Fluids*, 18:102104, 2006. cited p. 28, 34, 35, 37, 38

[296] V. Romanov. Stability of plane-parallel couette flow. *Functional analysis and its applications*, 7(2):137–146, 1973. cited p. 59

[297] N. G. Rosa, P. Villedieu, J. Dewitte, and G. Lavergne. A new droplet-wall interaction model. In *Proceedings of the 10th International Conference on Liquid Atomization and Spray Systems, Tokyo, Japan*, 2006. cited p. 29, 32, 33, 34, 35, 36, 37, 38, 39, 40

[298] J. R. Rybicki and I. Mudawar. Single-phase and two-phase cooling characteristics of upward-facing and downward-facing sprays. *International Journal of Heat and Mass Transfer*, 49(1):5–16, 2006. cited p. 41

[299] V. Sabel'nikov, A. Chtab, and M. Gorokhovski. The coupled LES-subgrid stochastic acceleration model (LES-SSAM) of a high reynolds number flows. In *Advances in Turbulence XI*, pages 209–211. Springer, 2007. cited p. 81

[300] V. Sabel'Nikov, M. Gorokhovski, and N. Baricault. The extended iem mixing model in the framework of the composition pdf approach: applications to diesel spray combustion. *Combustion Theory and Modelling*, 10(1):155–169, 2006. cited p. 79

[301] P. Saffman. On the settling speed of free and fixed suspensions. *Stud. Appl. Math*, 52(2):115–127, 1973. cited p. 243

[302] P. Sagaut. *Introduction à la simulation des grandes échelles*. Springer, mathématiques & applications edition, 1998. cited p. 129

[303] W. Samenfink, A. Elsäßer, K. Dullenkopf, and S. Wittig. Droplet interaction with shear-driven liquid films: analysis of deposition and secondary droplet characteristics. *International journal of heat and fluid flow*, 20(5):462–469, 1999. cited p. 37, 38

[304] M. Sanjosé. *Evaluation de la méthode Euler-Euler pour la simulation aux grandes échelles des chambres à carburant liquide*. PhD thesis, Institut National Polytechnique de Toulouse, 2009. cited p. 88

[305] M. Sanjosé, J. Senoner, F. Jaegle, B. Cuenot, S. Moreau, and T. Poinsot. Fuel injection model for euler–euler and euler–lagrange large-eddy simulations of an evaporating spray inside an aeronautical combustor. *International Journal of Multiphase Flow*, 37(5):514–529, 2011. cited p. 20

[306] F. Sarghini, U. Piomelli, and E. Balaras. Scale-similar models for large-eddy simulations. *Physics of Fluids A*, 11(6):1596 – 1607, 1999. cited p. 234

[307] T. Sattelmayer and S. Wittig. Internal flow effects in prefilming airblast atomizers: mechanisms of atomization and droplet spectra. *Journal of engineering for gas turbines and power*, 108(3):465–472, 1986. cited p. 74, 205

[308] R. Scardovelli and S. Zaleski. Direct numerical simulation of free-surface and interfacial flow. *Annual Review of Fluid Mechanics*, 31(1):567, 2003. cited p. 14

[309] L. Schiller and A. Nauman. A drag coefficient correlation. *VDI Zeitung*, 77:318–320, 1935. cited p. 239

[310] H. Schlichting. *Boundary layer theory*. McGraw-Hill, New York, 1955. cited p.

[311] K. Schloegel, G. Karypis, and V. Kumar. Graph partitioning for high-performance scientific simulations. In J. Dongarra, I. Foster, G. Fox, W. Gropp, K. Kennedy, L. Torczon, and A. White, editors, *Sourcebook on Parallel Computing*, chapter 18, pages 491–541. Morgan Kaufmann, San Francisco, CA, 2002. cited p. 246

[312] P. Schmitt. *Simulation aux grandes échelles de la combustion étagée dans les turbines à gaz et son interaction stabilité-polluants-thermique*. Phd thesis, INP Toulouse, 2005. cited p. 128

[313] P. Schober, J. Ebner, O. Schäfer, and S. Wittig. Experimental study on the effect of a strong negative pressure gradient on a shear-driven liquid fuel film. *Proceedings of 9th ICLASS, Sorrento, Italy*, 2003. cited p. 5, 52, 125

[314] C. Schoof and R. C. A. Hindmarsh. Thin-film flows with wall slip: An asymptotic analysis of higher order glacier flow models. *Q J Mechanics Appl Math*, 2010. cited p. 42

[315] J. Senda and H. Fujimoto. Multidimensional modeling of impinging spray on the wall. *Appl. Mech. Rev.*, 52(4):119–138, 1999. cited p. 37, 38

[316] J.-M. Senoner. *Simulation aux grandes échelles de l' écoulement diphasique évaporant dans un brûleur aéronautique par une approche Euler-Lagrange*. PhD thesis, Institut National Polytechnique de Toulouse - Dynamique des Fluides, 2010. cited p. 8, 18, 20, 87, 88, 207, 227, 237

[317] K. Seshan. *Handbook of Thin Film Deposition*. William Andrew Publishing. Elsevier Science Limited, 2012. cited p. 42

[318] J. A. Sethian and P. Smereka. Level set methods for fluid interfaces. *Annual Review of Fluid Mechanics*, 35:341–372, 2003. cited p. 14

[319] H. T. Shen, J. Su, and L. Liu. SPH simulation of river ice dynamics. *Journal of Computational Physics*, 165(2):752 – 770, 2000. cited p. 16

[320] J. Shinjo and A. Umemura. Simulation of liquid jet primary breakup: Dynamics of ligament and droplet formation. *International Journal of Multiphase Flow*, 36(7):513 – 532, 2010. cited p. 76, 77

[321] H. Simmons. The correlation of drop-size distributions in fuel nozzle sprays. *Journal of Engineering for Power*, 99(3):309–319, 1977. cited p. 84

[322] O. Simonin, P. Fevrier, and J. Lavieville. On the spatial distribution of heavy particle velocities in turbulent flow: from continuous field to particulate chaos. *Journal of Turbulence*, 3, 2002. cited p. 15, 103

[323] D. Sindayihebura and C. Dumouchel. Pressure atomiser: hole break-up of the sheet. *Journal of Visualization*, 4(1):5–5, 2001. cited p. 68

[324] W. A. Sirignano. *Fluid dynamics and transport of droplets and sprays*. Cambridge University Press, 1999. cited p. 8, 240

[325] A. Smirnov, S. Shi, and I. Celik. Random flow simulations with bubble dynamics model. In *Proceedings of FEDSM00, ASME 2000 Fluids Egineering Division Summer Meeting*, volume FEDSM2000-11215, June 11-15, Boston, Massachusetts, USA, 2000. cited p. 166

[326] A. Smirnov, S. Shi, and I. Celik. Random flow generation technique for large eddy simulations and particle-dynamics modeling. *Trans. ASME. Journal of Fluids Engineering*, 123:359–371, 2001. cited p. 127

[327] M. Sommerfeld and H. H. Qiu. Detailed measurements in a swirling particulate two-phase flow by a phase-doppler anemometer. *International Journal of Heat and Fluid Flow*, 12(1), 1991. cited p. 18

[328] M. Sommerfeld and H. H. Qiu. Characterisation of particle-laden, confined swirling flows by phase-doppler anemometry ad numerical calculation. *International Journal of Multiphase Flow*, 19(6):1093–1127, 1993. cited p. 18

[329] M. Sommerfeld and H. H. Qiu. Experimental studies of spray evaporation in turbulent flow. *International Journal of Heat and Fluid Flow*, 19:10–22, 1998. cited p. 8

[330] D. B. Spalding. The combustion of liquid fuels. In *4th Symp. (Int.) on Combustion*, pages 847–864. The Combustion Institute, Pittsburgh, 1953. cited p.

[331] K. D. Squires and J. K. Eaton. Particle response and turbulence modification in isotropic turbulence. *Physics of FluidsA*, 2(7):1191–1203, 1990. cited p. 8

[332] K. D. Squires and J. K. Eaton. Preferential concentration of particles by turbulence. *Physics of Fluids*, 3(5):1169–1178, 1991. cited p. 8

[333] D. W. Stanton and C. J. Rutland. Modeling fuel film formation and wall interaction in diesel engines. Technical report, Society of Automative Engineers, 1996. cited p. 36, 37, 38

[334] B. E. Stapper and G. S. Samuelsen. An experimental study of the breakup of a two-dimensional liquid sheet in the presence of co-flow air shear. In *Proceedings of the American Insitute for Aeronautics and Astronautics*, volume 90, 1990, paper 0461. cited p. 68

[335] C. Stow and M. Hadfield. An experimental investigation of fluid flow resulting from the impact of a water drop with an unyielding dry surface. *Proceedings of the Royal Society of London. A. Mathematical and Physical Sciences*, 373(1755):419–441, 1981. cited p. 29

[336] M. Sussman, A. S. Almgren, J. B. Bell, P. Colella, L. H. Howell, and M. L. Welcome. An adaptive level set approach for incompressible two-phase flows. *Journal of Computational Physics*, 148(1):81–124, 1999. cited p. 76

[337] N. Syred. A review of oscillation mechanims and the role of the precessing vortex core in swirl combustion systems. *Progress in Energy and Combustion Science*, 32(2):93–161, 2006. cited p.

[338] A. M. Tartakovsky and P. Meakin. A smoothed particle hydrodynamics model for miscible flow in three-dimensional fractures and the two-dimensional Rayleigh-Taylor instability. *Journal of Computational Physics*, 207(2):610 – 624, 2005. cited p. 17

[339] C.-M. Tchen. *Mean Value and Correlation Problems connected with the Motion of Small Particles supended in a turbulent fluid*. Phd thesis, Technical University of Delft, Netherlands, 1947. cited p. 237

[340] S. Thorpe. Experiments on the instability of stratified shear flows: miscible fluids. *Journal of Fluid Mechanics*, 46(02):299–319, 1971. cited p. 56

[341] O. Thual. *Hydrodynamique de l'environnement*. Ecole Polytechnique, 2010. cited p. 44

[342] C. B. Tibiriçà, F. J. do Nascimento, and G. Ribatski. Film thickness measurement techniques applied to micro-scale two-phase flow systems. *Experimental Thermal and Fluid Science*, 34(4):463 – 473, 2010. cited p. 43

[343] T. A. N. Timothy A. Shedd. Characteristics of the liquid film and pressure drop in horizontal, annular, two-phase,flow through round, square and triangular tubes. *Journal of Fluids Engineering*, 126:807 – 817, 2004. cited p. 43

[344] G. Tomar, D. Fuster, S. Zaleski, and S. Popinet. Multiscale simulations of primary atomization. *Computers & Fluids*, 39(10):1864 – 1874, 2010. cited p. 78

[345] K. E. Train. *Discrete choice methods with simulation*. Cambridge university press, 2003. cited p. 157

[346] A. Tratnig and G. Brenn. Drop size spectra in sprays from pressure-swirl atomizers. *International Journal of Multiphase Flow*, 36:349–363, 2010. cited p. 6, 66

[347] C. Tropea. Optical particle characterization in flows. *Annual Review of Fluid Mechanics*, 43:399–426, 2011. cited p. 164

[348] G. M. Turner. A comparison of 'The Limits to Growth' with 30 years of reality. *Global Environmental Change*, 18(3):397–411, 2008. cited p. 2, 3

[349] A. Vallet, A. A. Burluka, and R. Borghi. Development of a Eulerian model for the atomization of a liquid jet. *Atomization and Sprays*, 11(6):619–642, 2001. cited p. 79

[350] A. Vallet and R. Borghi. Modélisation eulerienne de l'atomisation d'un jet liquide. *Comptes Rendus de l'Académie des Sciences-Series IIB-Mechanics-Physics-Astronomy*, 327(10):1015–1020, 1999. cited p. 79

[351] E. van Kalmthout, T. Poinsot, and S. Candel. Turbulence 2d – théorie et simulations directes. Technical report, 1995. cited p. 127

[352] R. L. Vander Wal, G. M. Berger, and S. D. Mozes. The combined influence of a rough surface and thin fluid film upon the splashing threshold and splash dynamics of a droplet impacting onto them. *Experiments in fluids*, 40(1):23–32, 2006. cited p. 31

[353] C. Varga, J. Lasheras, and E. Hopfinger. Initial breakup of a small-diameter liquid jet by a high-speed gas stream. *Journal of Fluid Mechanics*, 497(1):405–434, 2003. cited p. 65, 84, 133, 136, 159, 206

[354] S. Veremieiev, H. Thompson, Y. Lee, and P. Gaskell. Inertial thin film flow on planar surfaces featuring topography. *Computers & Fluids*, 39(3):431 – 450, 2010. cited p. 52

[355] O. Vermorel, B. Bédat, O. Simonin, and T. Poinsot. Numerical study and modelling of turbulence modulation in a particle laden slab flow. *Journal of Turbulence*, 4, 025, 2003. cited p. 237

[356] A. Vié, S. Jay, B. Cuenot, and M. Massot. Accounting for polydispersion in the eulerian large eddy simulation of the two-phase flow in an aeronautical-type burner. *Flow, turbulence and combustion*, 90(3):545–581, 2013. cited p. 19

[357] E. Villermaux, P. Marmottant, and J. Duplat. Ligament-mediated spray formation. *Physical review letters*, 92(7):074501, 2004. cited p. 65

[358] I. Vinkovic, C. Aguirre, S. Simoëns, and M. Gorokhovski. Large eddy simulation of droplet dispersion for inhomogeneous turbulent wall flow. *International Journal of Multiphase Flow*, 32(3):344–364, 2006. cited p. 79, 81

[359] N. Vlachos, S. Paras, and A. Karabelas. Liquid-to-wall shear stress distribution in stratified/atomization flow. *International Journal of Multiphase Flow*, 23(5):845 – 863, 1997. cited p. 43

[360] L. Wachters and N. Westerling. The heat transfer from a hot wall to impinging water drops in the spheroidal state. *Chemical Engineering Science*, 21(11):1047–1056, 1966. cited p. 36, 104, 105

[361] C. Walshaw and M. Cross. JOSTLE: Parallel multilevel graph-partitioning software – an overview. In F. Magoules, editor, *Mesh Partitioning Techniques and Domain Decomposition Techniques*, pages 27–58. Civil-Comp Ltd., 2007. (Invited chapter). cited p. 247

[362] A.-B. Wang, C.-H. Lin, and C.-C. Chen. The critical temperature of dry impact for tiny droplet impinging on a heated surface. *Physics of Fluids*, 12:1622, 2000. cited p. 31

[363] L.-P. Wang and M. R. Maxey. Settling velocity and concentration distribution of heavy particles in homogeneous isotropic turbulence. *Journal of Fluid Mechanics*, 256:27–68, 1993. cited p. 8

[364] J. Warnatz, U. Maas, and R. W. Dibble. *Combustion: physical and chemical fundamentals, modeling and simulation, experiments, pollutant formation*. Springer, 2006. cited p. 229

[365] O. Werquin. *Diagnostics de scalaires par plan laser dans des jets diphasiques denses*. PhD thesis, 2001. cited p. 81, 82

[366] F. M. White. *Viscous fluid flow*. McGraw-Hill, New-York, 1991. cited p. 140, 152

[367] F. A. Williams. *Combustion Theory*. Benjamin Cummings, Menlo Park, CA, 1985. cited p. 8, 11

[368] H. Yamashita, M. Shimada, and T. Takeno. A numerical study on flame stability at the transition point of jet diffusion flame. In *26th Symp. (Int.) on Combustion*, pages 27 – 34. The Combustion Institute, Pittsburgh, 1996. cited p.

[369] S.-C. Yao and K. Y. Cai. The dynamics and Leidenfrost temperature of drops impacting on a hot surface at small angles. *Experimental Thermal and Fluid Science*, 1(4):363–371, 1988. cited p. 36

[370] A. Yarin and D. Weiss. Impact of drops on solid surfaces: self-similar capillary waves, and splashing as a new type of kinematic discontinuity. *Journal of Fluid Mechanics*, 283(1):141–173, 1995. cited p. 29, 106

[371] P. Yecko and S. Zaleski. Transient growth in two-phase mixing layers. *Journal of Fluid Mechanics*, 528:43–52, 2005. cited p. 60

[372] P. Yecko, S. Zaleski, and J.-M. Fullana. Viscous modes in two-phase mixing layers. *Physics of Fluids*, 14:4115, 2002. cited p. 74

[373] C.-S. Yih. Instability due to viscosity stratification. *Journal of Fluid Mechanics*, 27(02):337–352, 1967. cited p. 60

[374] S. S. Yoon and P. E. DesJardin. Modelling spray impingement using linear stability theories for droplet shattering. *International Journal for Numerical Methods in Fluids*, 50(4):469–489, 2006. cited p. 37, 38, 39

[375] Z. Yuan and E. Michaelides. Turbulence modulation in particulate flows—a theoretical approach. *International Journal of Multiphase Flow*, 18(5):779–785, 1992. cited p. 8

[376] S. Zaleski, A. Cartellier, D. Fuster, J. Hoepffner, J.-P. Matas, et al. A new mechanism for atomization and the primary instability in liquid-gas mixing layers. *Bulletin of the American Physical Society*, 56, 2011. cited p. 58

[377] R. Zamansky. *Simulation numérique directe et modélisation stochastique de sous-maille de l'accélération dans un écoulement de canal à grand nombre de Reynolds*. PhD thesis, Ecole Centrale de Lyon, 2011. cited p. 81

[378] B. Zamuner, P. Gilbank, D. Bissières, and C. Berat. Numerical simulation of the reactive two-phase flow in a kerosene/air tubular combustor. *Aerospace Science and Technology*, 6(7):521 – 529, 2002. cited p.

[379] Y. Zhao, H. H. Tan, and B. Zhang. A high-resolution characteristics-based implicit dual time-stepping vof method for free surface flow simulation on unstructured grids. *Journal of Computational Physics*, 183(1):233 – 273, 2002. cited p. 13

[380] W. Zheng, J.-H. Yong, and J.-C. Paul. Simulation of bubbles. *Graphical Models*, 71(6):229–239, November 2009. cited p. 53

[381] D. Zuzio and J.-L. Estivalezes. A parallel adaptive projection method for incompressible two phase flows. In *Computational Fluid Dynamics 2010*, pages 841–846. Springer, 2011. cited p. 76

[382] D. Zuzio, J.-L. Estivalezes, P. Villedieu, and G. Blanchard. Numerical simulation of primary and secondary atomization. *Comptes Rendus Mécanique*, 341(1–2):15 – 25, 2013. cited p. 78

Part IV

Appendices

Appendix A

Equations for the gaseous phase

This appendix recalls the compressible Navier-Stokes equations with chemical reactions and coupling terms between carrier and dispersed phases. It then introduces the concept of filtering in the framework of Large-Eddy Simulations and presents the different modeling assumptions and the closures of the unresolved terms. It mainly derives from the PhD thesis of Senoner [316].

A.1 Conservation equations

The system of conservation laws describing the evolution of a compressible fluid with chemical reactions and coupling between phases writes:

$$\frac{\partial \rho u_i}{\partial t} + \frac{\partial}{\partial x_j}\rho u_i u_j = -\frac{\partial p}{\partial x_i} + \frac{\partial \tau_{ij}}{\partial x_j} + \rho f_i + s_{m,i}^{l-g} \tag{A.1a}$$

$$\frac{\partial \rho E}{\partial t} + \frac{\partial}{\partial x_j}\rho E u_j = \frac{\partial}{\partial x_j}(-p u_j + u_i \tau_{ij} - q_j) + \dot{\omega}_T + \rho f_i u_i + s_e^{l-g} \tag{A.1b}$$

$$\frac{\partial \rho_k}{\partial t} + \frac{\partial}{\partial x_j}\rho_k u_j = -\frac{\partial}{\partial x_j} J_{j,k} + \dot{\omega}_k + s_{v,k}^{l-g} \qquad \text{for k = 1, N} \tag{A.1c}$$

Index notation has been adopted and Einstein's summation rule over repeated indices holds except for the index k which denotes species of the mixture. The above equations respectively state the conservation of momentum, total non-chemical energy and partial density over N species. f_i denotes a volumetric force, s^{l-g} the source terms due to the coupling with the dispersed phase. The latter are detailed in section B.3.2. In order to close the above equation system, material laws for the the stress tensor τ_{ij}, the pressure p, the specific energy e_s, the diffusive species flux $J_{j,k}$, the diffusive heat flux q_j and the chemical source terms $\dot{\omega}$ are required and detailed in the following.

A.1.1 Stress tensor

For Newtonian fluids, the stress tensor τ_{ij} may be derived from kinetical gas theory as:

$$\tau_{ij} = 2\mu s_{ij} + \left(\mu_b - \frac{2}{3}\mu\right) s_{ll}\delta_{ij} \tag{A.2}$$

with μ and μ_b respectively the dynamic and bulk viscosities. The bulk viscosity accounts for internal friction effects of molecules at strong fluid expansions. Such expansions are not expected in the present applications and the bulk

viscosity is therefore neglected. s_{ij} is the symmetric part of the velocity gradient tensor:

$$s_{ij} = \left(\frac{\partial u_i}{\partial x_j} + \frac{\partial u_j}{\partial x_i} \right) \tag{A.3}$$

A.1.2 Equation of state

The equation of state for an ideal gas writes:

$$p = \rho R T \tag{A.4}$$

R represents the gas constant of the mixture given by:

$$R = \frac{\mathcal{R}}{W} \tag{A.5}$$

$\mathcal{R}$ is the universal gas constant and W the molar fraction of the mixture:

$$W = \left(\sum_k \frac{Y_k}{W_k} \right)^{-1} \tag{A.6}$$

A.1.3 Specific energy and thermodynamic relations

The assumption of a thermically ideal gas is made, the caloric relation thus reduces to:

$$e_{s,k} = \int_{T_0}^{T} c_{v,k}(\theta) d\theta - \frac{R T_0}{W} \tag{A.7}$$

with $c_{v,k}$ the specific heat capacity at constant volume of the species k. The subscript 0 denotes a thermodynamical reference state. In AVBP, the pressure and temperature at the reference state are respectively $P_0 = 1\,\text{bar}$ and $T_0 = 0\,\text{K}$. The sensible energy of the mixture is given as:

$$\rho e_s = \sum_k Y_k e_{s,k} \tag{A.8}$$

The sensible enthalpy writes:

$$h_{s,k} = \int_{T_0}^{T} c_{p,k}(\theta) d\theta \tag{A.9}$$

with $c_{p,k}$ the calorific capacity at constant pressure of the species k.

A.1.4 Diffusive species flux

The species diffusion velocity $V_{k,i}$ is approximated by the Hirschfelder-Curtis relation [148]:

$$Y_k V_{k,i} = -D_k \frac{W_k}{W} \frac{\partial X_k}{\partial x_i} \tag{A.10}$$

Effects of temperature or pressure gradients on the species diffusion velocity [111] are neglected. Mass conservation states that the sum of all species diffusions be zero. This is not guaranteed by eq. A.10 for mixtures of more than two species. Thus, a correction velocity V_i^c ensuring mass conservation is added:

$$J_{i,k} = -\rho \left(D_k \frac{W_k}{W} \frac{\partial X_k}{\partial x_i} - Y_k V_{k,i}^c \right) \tag{A.11}$$

with:

$$V_{i,k}^{c} = \sum_{k} D_k \frac{W_k}{W} \frac{\partial X_k}{\partial x_i} \tag{A.12}$$

The diffusion coefficients for species D_k are specified in section A.1.7.

A.1.5 Heat flux

The heat flux vector is composed of two distinct contributions:

$$q_i = -\lambda \frac{\partial T}{\partial x_i} + \sum_{k} J_{i,k} h_{s,k} \tag{A.13}$$

with $J_{i,k}$ defined by eq. A.11. The first term on the right-hand side of eq. A.13 denotes heat conduction while the second represents the heat flux through species diffusion. The Dufour effect, which accounts for the heat flux induced by a chemical potential gradient [111], is neglected in eq. A.13.

A.1.6 Chemical source terms

A system of M chemical reactions involving N species may be summarized as follows:

$$\sum_{k=1}^{N} \nu'_{kj} \mathcal{M}_{kj} \rightleftharpoons \sum_{k=1}^{N} \nu''_{kj} \mathcal{M}_{kj} \qquad \text{for j = 1, M} \tag{A.14}$$

$\mathcal{M}_{kj}$ denotes the reacting species k in the reaction j. ν'_{kj} and ν''_{kj} are the stoechiometric coefficients of the products and reactants respectively. The progression rate $\mathcal{Q}_j$ is composed of a forward and a backward contribution:

$$\mathcal{Q}_j = K_{f,i} \prod_{k=1}^{N} \left(\frac{\rho Y_k}{W_k} \right)^{\nu'_{kj}} - K_{r,i} \prod_{k=1}^{N} \left(\frac{\rho Y_k}{W_k} \right)^{\nu''_{kj}} \tag{A.15}$$

The forward reaction constant $K_{f,j}$ is modelled by an Arrhenius-law:

$$K_{f,j} = A_{f,j} \exp\left(-\frac{E_{a,j}}{\mathcal{R}T} \right) \tag{A.16}$$

The backward reaction constant $K_{r,j}$ is obtained from a thermodynamic equilibrium:

$$K_{r,j} = \frac{K_{f,j}}{K_{eq}} \tag{A.17}$$

The equilibrium constant K_{eq} is derived from the minimization of the Gibbs free energy G combined with the equation of state for ideal gases [364]:

$$K_{eq} = \left(\frac{p_0}{\mathcal{R}T} \right) \exp\left(\frac{\Delta S_j^0}{\mathcal{R}} \right) - \left(\frac{\Delta H_j^0}{\mathcal{R}T} \right) \tag{A.18}$$

ΔS_j^0 and ΔH_j^0 respectively denote the entropy and enthalpy variations:

$$\Delta S_j^0 = \sum_{k=1}^{N} \nu_{kj} s_k(T) \tag{A.19}$$

$$\Delta H_j^0 = \sum_{k=1}^{N} (\nu''_{kj} - \nu'_{kj}) \int_{T_0}^{T} c_{p,k}(\theta) d\theta + \Delta h_{f,k}^0 \tag{A.20}$$

From eqs. A.15-A.20, the species reaction rates may be determined:

$$\dot{\omega}_k = \sum_{j=1}^{M} \dot{\omega}_{k,j} = W_k \sum_{j=1}^{M} \nu_{kj} \mathcal{Q}_j \tag{A.21}$$

The heat release is directly deduced from eq. A.21 as:

$$\dot{\omega}_T = -\sum_{k=1}^{N} \dot{\omega}_k \Delta h^0_{f,k} \tag{A.22}$$

$\Delta h^0_{f,k}$ is the formation enthalpy of the species k at the thermodynamical reference state.

A.1.7 Transport properties

For ideal gases, the dynamic viscosity μ is relatively independent of the species composition. A standard power law is used to account for its temperature dependence:

$$\mu = \mu_0 \left(\frac{T}{T_0} \right)^b \tag{A.23}$$

where b depends on the gaseous mixture and ranges between 0.6 and 1.0. The subscript 0 denotes a thermodynamical reference state.

The species diffusion coefficients D_k are estimated by assuming constant Schmitt numbers Sc_k for all species:

$$D_k = \frac{\mu}{\rho \mathrm{Sc}_k} \tag{A.24}$$

The heat conduction coefficient λ is computed from the viscosity μ as:

$$\lambda = \frac{\mu c_p}{\mathrm{Pr}} \tag{A.25}$$

Pr is the Prandtl number which is assumed constant.

A.2 Large-Eddy Simulation

This section presents the derivation of the filtered governing equations in the framework of Large-Eddy Simulation. First, a few concepts related to turbulent flows are introduced. Then, the different resolution levels in numerical simulations of turbulent flows are presented. Finally, the filtered Navier-Stokes equations are derived and the approximations related to the closure of subgrid terms are described.

A.2.1 Basic aspects of turbulence

The transition from a laminar flow, for which the trajectories of single fluid elements are parallel, to a turbulent flow is characterized by the Reynolds number:

$$\mathrm{Re} = \frac{ul}{\nu} \tag{A.26}$$

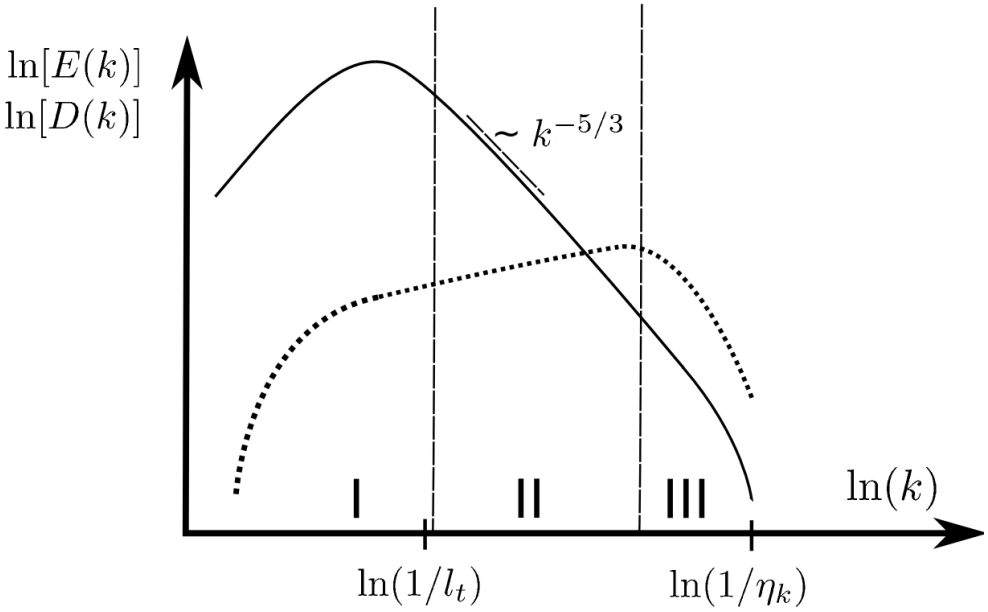

Figure A.1 : *Sketch of energy spectrum E(k) in solid lines and dissipation spectrum D(k) in dashed lines. Distinction between energy containing (I), inertial (II) and dissipation ranges (III). The abscissa of the integral (l_t) and Kolmogorov (η_k) length scales are indicated*

where u and l are respectively the characteristic velocity and length scales of the flow field. The Reynolds number represents the ratio of inertial to viscous forces and may be interpreted as a gauge of the competition between destabilizing (inertia) and stabilizing (viscosity) effects. Turbulent flows exhibit significant and irregular variations of fluid velocity in both space and time. An essential aspect of turbulent flows is the presence of a continuous spectrum of vortical structures, the so called *eddies*. These eddies strongly interact with each other through a cascade process first stated in 1941 by Kolmogorov [178].

The largest eddies display characteristic length and velocity scales of the order of magnitude of the global geometry and are thus very little affected by viscous effects. The large eddies become unstable and break down into smaller eddies. These smaller eddies become in turn unstable, they are also stretched and distorted through shear forces and interactions with larger eddies. The cascade process is repeated up to scales where viscous effects become predominant so that the eddy motion is stable and viscosity is effective in dissipating the eddy's energy. Therefore, turbulence is also intrinsically a dissipative phenomenon which converts kinetic energy into heat. In terms of length scales, the largest turbulent structures are related to the integral length scale l_t whereas the smallest dissipative structures define the Kolmogorov scale l_k. The energetic density spectrum $E(k)$ of the turbulent eddies may be displayed in a diagram over the wave number k, which is proportional to the inverse of the eddy length scale. For isotropic steady turbulence, an inertial range characterized by a constant $k \sim -5/3$ slope is observed in the energetic density spectrum, which is displayed in fig. A.1.

Given the random nature of turbulence, statistical averaging appears as an adequate tool to describe turbulent flows. If the existence of a statistical mean is assumed, a deviation from this mean immediately follows, yielding the splitting:

$$u_i = \langle u_i \rangle + u_i'' \tag{A.27}$$

where $\langle \cdot \rangle$ denotes an averaging operator. This decomposition was first introduced by Osborne Reynolds [288]. The most general averaging operator $\langle \cdot \rangle$ corresponds to an *ensemble* average: an arithmetic average over a large number

of realizations N of the same experiment:

$$\langle u_i \rangle(x_i, t) = \frac{1}{N} \sum_{k=1}^{N} u_i(x_i, t) \tag{A.28}$$

If the flow field is statistically steady or homogeneous in certain directions, statistical averaging may be performed in time or in space over the homogeneous directions. Instead of eq. A.28, short-time averages are often defined:

$$\langle u_i \rangle(x_i, t) = \frac{1}{T} \int_{-T/2}^{T/2} u_i(x_i, t + \tau) d\tau \tag{A.29}$$

T represents the averaging time interval, it must be small compared to the timescales of the statistically unsteady turbulence and large compared to the integral scales of the fluctuations.

A.2.2 Resolution levels in turbulence simulations

A first possibility when performing numerical simulations of turbulent flows is to average the Navier-Stokes equations according to eq. A.27. This yields the Reynolds-averaged Navier-Stokes (RANS) equations. Due to the non-linearity of the Navier-Stokes equations, unclosed higher order terms appear (closure problem of turbulence). The unclosed terms represent the effect of the entire turbulence spectrum on the mean flow field. It appears that the largest scales of turbulent motion mainly depend on the simulated configuration and RANS closure models are thus expected to lack universality.

The opposite approach to RANS consists in performing resolved turbulence simulations without any averaging procedure. This approach is referred to as Direct Numerical Simulation (DNS). It requires the explicit resolution of all turbulent structures down to the Kolmogorov scale l_k on the numerical grid. From dimensional analysis, it appears that the number of mesh points required for the simulation of a three dimensional cubic domain of side lengths $L = 5l_t$ is a pure function of the turbulent Reynolds number Re_t:

$$N^3 = \left(\frac{L}{l_k} \right)^3 \approx 27\, \mathrm{Re}_t^{9/4} \tag{A.30}$$

with:

$$\mathrm{Re}_t = \frac{(2k)^{1/2}\, l_t}{\nu} \tag{A.31}$$

where $k = 1/2 \langle u_i'' u_i'' \rangle$ denotes the turbulent kinetic energy. Equation A.30 indicates that the Direct Numerical Simulation of realistic configurations is computationally very intensive.

An intermediate approach between RANS and DNS consists in filtering the Navier-Stokes equations so as to remove the smallest scales of motion while explicitly resolving the largest scales. This approach is called Large-Eddy Simulation (LES). Explicitly resolving geometry dependent large structures, LES also appears advantageous in that smaller turbulent scales are assumed to exhibit a more universal behaviour. LES filtered quantities are defined as the convolution product of the non-filtered scalar quantity f with a filter G of characteristic width $\overline{\Delta}$:

$$\overline{f}(x_i, t) = \int f(x_i, t) G_{\overline{\Delta}}(x_i - x_i') dx_i \tag{A.32}$$

The unresolved or *subgrid* scale contribution is denoted as:

$$f'(x_i, t) = f(x_i, t) - \overline{f}(x_i, t) \tag{A.33}$$

For variable density flows it appears advantageous to weigh filtered quantities by the volumetric mass in order to avoid the appearance of additional terms when filtering the Navier-Stokes equations. Favre filtering is defined as:

$$\overline{\rho} \widetilde{f} = \overline{\rho f} \tag{A.34}$$

A.2.3 Filtered equations

Applying Favre filtering to the compressible Navier-Stokes equations with chemical source terms and coupling between phases yields:

$$\frac{\partial \overline{\rho}\widetilde{u_i}}{\partial t} + \frac{\partial \overline{\rho}\widetilde{u_i}\widetilde{u_j}}{\partial x_j} = -\frac{\partial}{\partial x_i}\overline{p} + \frac{\partial}{\partial x_j}[\overline{\tau}_{ij} + \overline{\tau}_{ij}^{sgs})] + \overline{\dot{s}}_{m,i} + \overline{\rho}\widetilde{f_i} \tag{A.35a}$$

$$\frac{\partial \overline{\rho}\widetilde{E}}{\partial t} + \frac{\partial \overline{\rho}\widetilde{E}\widetilde{u_j}}{\partial x_j} = -\frac{\partial}{\partial x_j}[\overline{pu_j} - \overline{\tau_{ij}u_i} + \overline{q}_j + \overline{q}_j^{sgs}] + \overline{\rho}\widetilde{f_i u_i} + \overline{\dot{\omega}}_T + \overline{\dot{s}}_q \tag{A.35b}$$

$$\frac{\partial \overline{\rho_k}}{\partial t} + \frac{\partial \overline{\rho_k}\widetilde{u_i}}{\partial x_i} = \frac{\partial}{\partial x_i}[\overline{J_{i,k}} - \overline{J}_{i,k}^{sgs}] + \overline{\dot{\omega}}_k + \overline{\dot{s}}_{v,k} \qquad \text{for k = 1, N} \tag{A.35c}$$

The superscript sgs (for subgrid-scale) denotes unclosed terms appearing through the filtering operation due to the nonlinearity of the Navier-Stokes equations, they are explicited in section A.2.4. In the derivation of eqs. A.35, it has been tacitly assumed that the order of filtering and differenciation operations may be exchanged. However, Ghosal & Moin [107] show that this permutation is only valid for constant filter widths. The error associated with the permutation for varying filter widths is of second order in the filter width. It is thus only tolerable for numerical schemes with at most second-order spatial accuracy. The permutation error may be included in the subgrid closure terms, but this seems rarely done in practice.

The viscous stress tensor is approximated as follows:

$$\overline{\tau}_{ij} = \overline{2\mu s_{ij} - \frac{2}{3}\mu s_{ll}\delta_{ij}} \tag{A.36}$$

$$\overline{\tau}_{ij} \approx 2\overline{\mu}\widetilde{s_{ij}} - \frac{2}{3}\overline{\mu}\widetilde{s_{ll}}\delta_{ij} \tag{A.37}$$

This assumes that dynamic viscosity is constant across the filter width and that it can be extracted from the filtering operator. For the dynamic viscosity as for all other material properties, it is assumed that:

$$\overline{\mu} \approx \mu(\widetilde{T}) \tag{A.38}$$

This approximation may induce large errors for strongly nonlinear behaviors of the given material property, but such behaviors are not expected in the present applications.

Similar simplifications to the derivation of the viscous stress tensor are made for the species diffusive fluxes:

$$\overline{J_{i,k}} = -\overline{\rho\left(D_k\frac{W_k}{W}\frac{\partial X_k}{\partial x_i} - Y_k V_{k,i}^c\right)} \tag{A.39}$$

$$\overline{J_{i,k}} \approx -\overline{\rho}\left(\overline{D_k}\frac{W_k}{W}\frac{\partial \widetilde{X_k}}{\partial x_i} - \widetilde{Y_k}\widetilde{V_{k,i}}^c\right) \tag{A.40}$$

For the heat flux, one obtains:

$$\overline{q}_j = -\overline{\lambda\frac{\partial T}{\partial x_j} + \sum_k J_{j,k}h_{s,k}} \tag{A.41}$$

$$\overline{q}_j \approx -\overline{\lambda}\frac{\partial \widetilde{T}}{\partial x_j} + \sum_k \overline{J_{j,k}}\widetilde{h_{s,k}} \tag{A.42}$$

with:

$$\overline{\lambda} \approx \frac{\overline{\mu}\,\overline{c_p}}{\mathrm{Pr}} \tag{A.43}$$

A.2.4 Subgrid closures

Many closure models rely on the observation that turbulent flows mix fluid much more effectively than laminar flows. A basic modelling idea then consists in representing the unclosed terms as diffusive contributions with an associated turbulent viscosity μ_t. Under this assumption, the subgrid stress tensor may be rewritten as:

$$\overline{\tau}_{ij}^{sgs} = -\overline{\rho}(\widetilde{u_i u_j} - \widetilde{u}_i\widetilde{u}_j) = 2\overline{\mu}_t\widetilde{s_{ij}} - \frac{2}{3}\overline{\mu}_t\widetilde{s_{ll}}\delta_{ij} \tag{A.44}$$

This supposes that the principal axes of the strain rate tensor are aligned with those of the subgrid stress tensor which is not fulfilled in general [306]. The turbulent viscosity may be derived from algebraic relations or through the resolution of additional transport equations. A few models to determine the turbulent viscosity are detailed in subsection A.2.5.

The subgrid species flux is modelled in an analogous manner to the subgrid stress tensor:

$$\overline{J}_{i,k}^{sgs} = \overline{\rho}\left(\widetilde{u_i Y_k} - \widetilde{u}_i\widetilde{Y_k}\right) \tag{A.45}$$

$$\overline{J}_{i,k}^{sgs} = -\overline{\rho}\left(D_k^t\frac{W_k}{W}\frac{\partial\widetilde{X_k}}{\partial x_i} - \widetilde{Y_k}\widetilde{V_{k,i}}^{c,t}\right) \tag{A.46}$$

with:

$$\widetilde{V_{k,i}}^{c,t} \approx \sum_k D_k^t\frac{W_k}{W}\frac{\partial\widetilde{X_k}}{\partial x_i} \tag{A.47}$$

The turbulent species diffusions are deduced from a turbulent Schmidt number Sc_k^t:

$$D_k^t = \frac{\nu_t}{\mathrm{Sc}_k^t} \tag{A.48}$$

The constant value $\mathrm{Sc}_k^t = 0.7$ is chosen for all species.

For the subgrid heat flux, one obtains:

$$\overline{q}_j^{sgs} = \overline{\rho}\left(\widetilde{u_i E} - \widetilde{u}_i\widetilde{E}\right) \tag{A.49}$$

$$\overline{q}_j^{sgs} = -\overline{\lambda_t}\frac{\partial\widetilde{T}}{\partial x_j} + \sum_k \overline{J}_{i,k}^{sgs}\widetilde{h_{s,k}} \tag{A.50}$$

with:

$$\lambda_t = \frac{\nu_t\overline{c_p}}{\mathrm{Pr}_t} \tag{A.51}$$

The turbulent Prandtl number $\mathrm{Pr}_t = 0.6$ is also assumed constant.

A.2.5 Subgrid scale models

The main task of the subgrid scale model is to correctly reproduce the energy fluxes between resolved and unresolved turbulent scales. This involves interactions among the whole turbulence spectrum and the subgrid scale model must ideally account for interactions between turbulent structures of different sizes ('non-local interactions') as well as between structures of comparable sizes ('local interactions'). This is a difficult task and one may only expect subgrid scale models to be correct in the statistical sense.

Viscosities are the product of characteristic length and velocity scales. As the most energetic unresolved scales are found at the cut-off frequency k_c of the LES filter, the filter width $\overline{\Delta}$ is a natural choice for the length scale. The characteristic velocity scale is determined from the subgrid scale energy. The models based on an eddy viscosity assumption make different levels of simplification to obtain an estimate for this energy.

A.2.5.a) The Smagorinsky model

The Smagorinsky model is among the most popular subgrid scale models due to its simplicity. It assumes equilibrium between production and dissipation of turbulent kinetic energy at the subgrid scale. This assumption is justified in regions of isotropic turbulence for which the Smagorinsky model reproduces correct dissipation levels. In regions of anisotropy however, the model shows to be overdissipative as it cannot predict the occurence of backscatter, which describes the instantaneous and localized backflow of turbulent energy from smaller to larger scales. Piomelli et al. [269] showed that the failure to reproduce this phenomenon may result in wrong prediction of perturbation growth in transitional flows. Furthermore, it appears that the Smagorinsky model does not accurately distinguish between zones of pure shear and turbulence. It writes:

$$\nu_t = \left(C_S \overline{\Delta}\right)^2 \sqrt{2\widetilde{s_{ij}}\widetilde{s_{ij}}} \tag{A.52}$$

Smagorinsky determined an analytical value of 0.18 for the constant C_S. However, C_S is often adjusted to the given application case and values ranging between 0.1 and 0.18 may be found in literature.

A.2.5.b) Dynamic Smagorinsky model

The dynamic Smagorinsky model [106] relies on the same expression as eq.A.52 with the notable difference that the Smagorinsky constant is now evaluated from a dynamic procedure:

$$\nu_t = \left(C_S^{dyn} \overline{\Delta}\right)^2 \sqrt{2\widetilde{s_{ij}}\widetilde{s_{ij}}} \tag{A.53}$$

An additional high-pass filter of characteristic width $\widehat{\Delta}$ is introduced, yielding two distinct filter scales which are parametrized in a similar manner:

$$\overline{\tau}_{ij}^d = -2C_S^{dyn}\overline{\Delta}^2\sqrt{2\widetilde{s_{ij}}\widetilde{s_{ij}}} = -2C_S^{dyn}\alpha_{ij} \tag{A.54a}$$

$$\widehat{\overline{\tau}}_{ij}^d = -2C_S^{dyn}\widehat{\Delta}^2\sqrt{2\widehat{\widetilde{s_{ij}}}\widehat{\widetilde{s_{ij}}}} = -2C_S^{dyn}\beta_{ij} \tag{A.54b}$$

A scale-similarity assumption is made for both filter scales, which implies that C_S^{dyn} takes the same value in eqs. A.54. τ_{ij}^d denotes the anisotropic part of the stress tensor:

$$\tau_{ij}^d = \tau_{ij} - \frac{1}{3}\delta_{ij}\tau_{kk} \tag{A.55}$$

The dynamic constant C_S^{dyn} may be determined from eqs. A.54a and A.54b using the Germano identity [105]:

$$L_{ij} = \widehat{\widetilde{u}_i\widetilde{u}_i} - \widehat{\widetilde{u}}_i\widehat{\widetilde{u}}_i = -2C_S^{dyn}\beta_{ij} + 2\widehat{C_S^{dyn}\alpha_{ij}} \tag{A.56}$$

Eq. A.56 presents two major difficulties. First, C_S^{dyn} is under the filter operator in the second term on the right-hand side of eq. A.56, which implies that it must be determined with specific numerical methods. A first approach uses the Germano identity in an integral manner and minimizes an associated error function. A second approach considers

eq. A.56 as implicit in C_S^{dyn} and solves it through an iterative process. An second difficulty of eq. A.56 arises from the fact that it provides 5 independent equations for a single unknown. Germano [105] proposes to multiply eq. A.56 with $\widetilde{s_{ij}}$, which reduces the relation to a single equation for C_S^{dyn}. Lilly [205] proposes to minimize eq. A.56 in a least squares sense in order to obtain C_S^{dyn}. The dynamic Smagorinsky model is capable of predicting backscatter which manifests itself through locally negative values of the turbulent viscosity. Negative values of the turbulent viscosity favor numerical oscillations that are difficult to handle in practice.

A.2.5.c) The Wale model

The Wale model was designed by Ducros & Nicoud [248] to recover the correct y^3 scaling of turbulent viscosity close to walls for wall resolved simulations. The turbulent viscosity ν_t is defined as:

$$\nu_t = (C_w\overline{\Delta})^2 \frac{(\widetilde{s}_{ij}^d \widetilde{s}_{ij}^d)^{3/2}}{(\widetilde{s}_{ij}\widetilde{s}_{ij})^{5/2} + (\widetilde{s}_{ij}^d \widetilde{s}_{ij}^d)^{5/4})} \tag{A.57}$$

$C_w = 0.4929$ is a model constant. $\widetilde{s}_{ij}^d$ is the traceless symmetric part of the square of the velocity gradient tensor:

$$\widetilde{s}_{ij}^d = \frac{1}{2}(\widetilde{g}_{ij}^2 + \widetilde{g}_{ji}^2) - \frac{1}{3}\widetilde{g}_{kk}^2\delta_{ij} \tag{A.58}$$

$\widetilde{g}_{ij}$ represents the resolved velocity gradient:

$$\widetilde{g}_{ij} = \frac{\partial \widetilde{u}_i}{\partial x_j} \tag{A.59}$$

An advantage of the Wale model is its improved behavior in zones of pure shear compared to the Smagorinsky model. However, it exhibits a non accurate behaviour when employed with the law-of-the-wall approach, and for this reason the Wale model is not used in the present work.

A.2.5.d) The σ-model

The σ-model developped by Nicoud *et al.* [249] aims to recover several properties assessed for a practical/physical turbulence model: (i) expressed from local variables (locality) and delivering a positive viscosity (positiveness), (ii) a correct y^3 scaling of turbulent viscosity close to walls, (iii) a zero viscosity in case of two dimensional (2D) and/or two components (2C) flow and (iv) a zero viscosity for axisymmetric or isotropic expansion/contraction. It is based on the singular values of the resolved velocity gradient tensor. The turbulent viscosity ν_t is thus defined as:

$$\nu_t = (C_\sigma\overline{\Delta})^2 \, \frac{\sigma_3(\sigma_1 - \sigma_2)(\sigma_2 - \sigma_3)}{\sigma_1^2} \tag{A.60}$$

where $\sigma_1 > \sigma_2 > \sigma_3 > 0$ are the singular values of the velocity gradient tensor and $C_\sigma = 1.35$ is a model constant. In addition, the σ-model is easy to implement and shows a low computational cost compared to the classical Smagorinsky model.

Appendix B

Equations for the dispersed phase

This appendix provides a general overview of the Lagrangian approach. Focus is made on the deterministic approaches, where each numerical particle represents a physical particle [221, 355]. First, the forces acting upon an isolated rigid spherical particle are derived. Then, the evaporation model employed in the present work is presented and this appendix concludes with the interphase exchange terms. It mainly derives from the PhD thesis of Senoner [316].

B.1 Lagrangian equations of motion for an isolated particle

B.1.1 Generalized Basset-Boussinesq-Oseen equations

Basset [19], Boussinesq [34] and Oseen [259] examined the flow of a settling particle under gravity in a quiescent fluid flow and derived an analytical expression for the forces acting upon a particle in such flow. Tchen [339] extended their work to the motion of a rigid sphere in a nonuniform flow. More recently, Maxey and Riley [226] corrected certain inconsistencies in Tchen's derivations. The following derivations follow those of Maxey and Riley [226].

The tracking of an isolated rigid spherical particle in its own frame of reference is considered. Particle rotation is excluded and only the translatory motion of the particle is taken into account. The kinematic equation writes:

$$\frac{dx_{p,i}}{dt} = u_{p,i} \tag{B.1}$$

The momentum balance is obtained as:

$$m_p \frac{du_{p,i}}{dt} = \int_{S_p} (-p\delta_{ij} + \tau_{ij}) n_j dS = F_{p,i} \tag{B.2}$$

The subscript p denotes particle properties. The force $F_{p,i}$ exerted upon the particle is obtained by integrating the fluid pressure and the fluid viscous stresses over the particle surface S_p. This force may be decomposed in two distinct contributions:

$$F_{p,i} = F^u_{p,i} + F^d_{p,i} \tag{B.3}$$

$F^u_{p,i}$ denotes the force acting upon a fluid element coinciding with the particle. $F^d_{p,i}$ represents the force exerted upon the particle resulting from the perturbation of the fluid flow field by the particle. In order to derive both contributions,

Maxey and Riley [226] split the fluid flow field into an undisturbed component $\breve{u}_i$ and a disturbed component set by the particle. The authors assume that the particle diameter is small compared to the smallest flow field length scale, for example the Kolmogorov scale in a turbulent flow:

$$d_p \ll \eta_k \tag{B.4}$$

With these simplifications, the force contribution resulting from the undisturbed flow component writes:

$$F^u_{p,i} = \frac{\pi d_p^3}{6}\left[\rho \frac{D\breve{u}_i}{Dt}\bigg|_{x_i=x_{p,i}} - (\rho_p - \rho)g_i\right] \tag{B.5}$$

where g_i is the gravity vector. $\breve{u}_i$ denotes the undisturbed fluid velocity at the particle location and D/Dt represents the total derivative along the undisturbed fluid trajectory:

$$\frac{D}{Dt} = \frac{\partial}{\partial t} + \breve{u}_j \frac{\partial}{\partial x_j} \tag{B.6}$$

Through the total derivative of the undisturbed fluid velocity, eq. B.5 accounts for the pressure and viscous forces acting upon a fluid element coinciding with the particle. In order to analytically derive the unsteady disturbance flow set by the particle, a low particle Reynolds number is assumed in addition to the previous hypotheses:

$$\mathrm{Re}_p = \frac{d_p \| \overrightarrow{\breve{u}} - \overrightarrow{u_p} \|}{\nu} \ll 1 \tag{B.7}$$

The forces arising from the unsteady disturbance flow set by the particle may be obtained from a temporal Laplace transform of the disturbed flow field momentum equation (see Maxey and Riley [226]) for more details. One obtains:

$$F^d_{p,i} = \frac{\pi d_p^3}{6}\left[\frac{18\rho\nu}{d_p^2}(\breve{u}_i - u_{p,i}) + \frac{\rho}{2}\frac{d}{dt}(\breve{u}_i - u_{p,i}) + \frac{9\rho}{d_p}\sqrt{\frac{\nu}{\pi}}\int_{-\infty}^{t}\frac{d}{d\tau}(\breve{u}_i - u_{p,i})\frac{d\tau}{\sqrt{t-\tau}}\right] \tag{B.8}$$

The first term on the right-hand side of eq. B.8 represents the Stokes drag force. The second term denotes the added mass force, which accounts for the acceleration/ deceleration of fluid by the particle. The third term is the Basset history force and originates from the lagging development of the boundary layer on the surface of an accelerated particle [60]. Gatignol [101] generalizes the previous derivations to a particle diameter comparable to the smallest flow field lengthscale, partly relaxing the assumption expressed in eq. B.4. The expressions obtained for the forces $F^u_{p,i}$ and $F^d_{p,i}$ remain unchanged in eqs. B.5 and B.8, except that the undisturbed fluid velocity $\breve{u}_i$ at the particle location is replaced by an undisturbed fluid velocity averaged either over the particle surface $\breve{u}^s_i$ or the particle volume $\breve{u}^v_i$, depending on the considered force.

B.1.2 Generalized drag force

The drag term in eq. B.8 corresponds to the force originally derived by Stokes in a steady viscous fluid flow for small particle Reynolds numbers. Introducing the drag coefficient C_d, this force may be rewritten as:

$$F^{drag}_{p,i} = \frac{1}{8}\rho\pi d_p^2 C_d \| \overrightarrow{u_p} - \overrightarrow{\breve{u}} \| (u_{p,i} - \breve{u}_i) \tag{B.9}$$

with:

$$C_d = \frac{24}{\mathrm{Re}_p} \tag{B.10}$$

This assumption of a small particle Reynolds number allows to neglect inertial effects of the fluid flow in the derivation of the drag force. Oseen [259] accounted for a linearized inertial term and obtained the following correction to the Stokes drag coefficient:

$$C_d = \frac{24}{\mathrm{Re}_p}\left(1 + \frac{3}{16}\mathrm{Re}_p\right) \tag{B.11}$$

Equation B.11 is valid for particle Reynolds numbers up to 5. More general analytical solutions for the evolution of the drag coefficient have not been derived to this date. Instead, empirical correlations are used to cover the large range of particle Reynolds numbers encountered in practical applications. In this study, the correlation proposed by Schiller and Naumann [309] is used:

$$C_d(\mathrm{Re}_p) = \frac{24}{\mathrm{Re}_p} f(\mathrm{Re}_p) \qquad \text{for} \qquad \mathrm{Re}_p \leq 1000 \tag{B.12a}$$

$$f(\mathrm{Re}_p) = \left(1 + 0.15\mathrm{Re}_p^{0.687}\right) \tag{B.12b}$$

The validity of eqs. B.12 ranges up to particle Reynolds numbers of approximately 1000 with a maximum deviation of 5% from experimental data. In some of the presented applications, the values of the particle Reynolds number may exceed 1000. In this case, the drag coefficient is evaluated according to Clift et al. [51]:

$$C_d = 0.44 \qquad \text{for} \qquad \mathrm{Re}_p > 1000 \tag{B.13}$$

Note that similar empirical corrections need to be applied to all previously enumerated forces when the assumption of small particle Reynolds number no longer holds.

B.1.3 Momentum equation implemented in AVBP

In order to simplify the momentum equations for the isolated particle, the following assumptions are made:

- H1: particle diameters are small compared to unity ($d_p \ll 1$).
- H2: dense particles are considered and the density ratio between particles and fluid is large compared to unity $\left(\rho_p/\rho \sim \mathcal{O}(10^3)\right)$.
- H3: the perturbation of the fluid flow field induced by a single particle is negligible compared to the perturbations arising from the remaining particles in the fluid flow.

The first assumption allows to neglect all forces but drag from a dimensional analysis since it is the only force scaling with the square of the inverse particle diameter. Under the second assumption, the expression for the gravity force may be simplified. Finally, the third assumption allows to approximate the unperturbed fluid velocity $\breve{u}_i$ at the particle location by the fluid velocity perturbed by the particle u_i. Therefore, the momentum equation simplifies to:

$$\frac{du_{p,i}}{dt} = \frac{1}{\tau_p}(u_i - u_{p,i}) + g_i \tag{B.14}$$

τ_p is the particle relaxation time, which is defined as:

$$\tau_p = \frac{\rho_p\, d_p^2}{18\,\mu_g\, f(\mathrm{Re}_p)} \tag{B.15}$$

with $f(\mathrm{Re}_p)$ given by eq. B.12b. The relaxation time scale τ_p defines a characteristic time scale of particle acceleration. The behavior of the particle in a fluid flow field is therefore dictated by the ratio of the particle relaxation time scale τ_p to a characteristic convective fluid flow time scale τ_{cv}. This ratio defines the Stokes number St:

$$\mathrm{St} = \frac{\tau_p}{\tau_{cv}} \tag{B.16}$$

For large Stokes numbers ($\mathrm{St} \gg 1$), the particle is insensitive to fluid flow perturbations and follows the trajectory dictated by its inertia. On the contrary, a particle with small Stokes number ($\mathrm{St} \ll 1$) follows the fluid flow like a tracer. In a turbulent flow field, effects of preferential concentration (see section 1.3) are most pronounced for a unitary Stokes number ($\mathrm{St} \approx 1$).

B.2 Evaporation of an isolated particle

A Spalding type evaporation model based [324] on an equilibrium law was implemented in the Lagrangian solver by Jaegle [162] and is briefly described in the following. The equations for particle evaporation are derived from the conservation equations of mass, vapor and energy of a single particle. The following assumptions are made:

- H1: the particle is isolated and effects of particle interactions on evaporation are neglected.
- H2: the atmosphere around the particle is at rest and the problem is quasi-steady, which implies that equations are independent of time
- H3: the particle is at equilibrium with the surrounding gas.
- H4: the thermal conductivity inside the particle is considered infinite, which leads to a uniform particle temperature.

The problem is treated in spherical coordinates and due to spherical symmetry, only the radial coordinate is considered. The gaseous conservation laws between the particle's surface (denoted by the subscript ζ) and the far-field (denoted by the subscript ∞) write:

$$\rho u r^2 = \text{constant} = \frac{\dot{m}_v}{4\pi} \tag{B.17a}$$

$$\rho u r^2 \frac{dY_v}{dr} = \frac{d}{dr}\left(r^2 [\rho D_v] \frac{dY_v}{dr} \right) \tag{B.17b}$$

$$\rho u r^2 \frac{dh}{dr} = \frac{d}{dr}\left(r^2 \frac{\lambda}{c_p} \frac{dh}{dr} \right) \tag{B.17c}$$

where the vapor species is denoted by the subscript v. Note that since the equations are written in spherical coordinates, a flux directed away from the particle is positive.

B.2.1 Mass transfer

Integrating eq. B.17b twice between the particle surface and the far-field, an expression for the vapor mass flux as a function of the vapor mass fractions may be derived:

$$\dot{m}_p = 4\pi r_\zeta [\rho D_v] \ln(\mathrm{B}_M + 1) \tag{B.18}$$

B_M denotes the Spalding mass number:

$$\mathrm{B}_M = \frac{Y_{v,\zeta} - Y_{v,\infty}}{1 - Y_{v,\zeta}} \tag{B.19}$$

Considering the evolution of the particle mass over time, eq. B.18 may be rewritten as:

$$\dot{m}_p = \pi d_p \mathrm{Sh}[\rho D_v] \ln(\mathrm{B}_M + 1) \tag{B.20}$$

The Sherwood number Sh represents a ratio of convective to conductive mass transfer and takes the value 2 in a quiescent atmosphere. However, the flow field around the particle is generally not quiescent in practical applications and the Sherwood number is modified using empirical correlations to account for the relative velocity between the particle and the surrounding gas. Ranz and Marshall [278] propose the following correction:

$$\mathrm{Sh} = 2 + 0.55 \mathrm{Re}_p^{1/2} \mathrm{Sc}_v^{1/3} \tag{B.21}$$

Sc_v denotes the Schmidt number of the vapor species. Finally, the vapor mass fraction at the particle surface is deduced from the Clausius-Clapeyron law:

$$p_{v,\zeta} = p_{cc} \exp\left(\frac{W_v L_{ev}(T_{ref})}{\mathcal{R}} \left(\frac{1}{T_{cc}} - \frac{1}{T_\zeta}\right)\right) \tag{B.22}$$

with the subscript cc designating an arbitrary reference point on the saturation curve. $\mathcal{R}$ is the universal gas constant and $L_{ev}(T_{ref})$ the latent heat of vaporization at the reference temperature T_{ref}. The vapor partial pressure $p_{v,\zeta}$ directly yields the molar fraction $X_{F,\zeta}$ and in turn allows to obtain the vapor mass fraction at the particle's surface $Y_{v,\zeta}$. The Clausius-Clapeyron law assumes a thermodynamic equilibrium at the particle's surface during the evaporation process, which is consistent with assumption H3.

B.2.2 Heat transfer

The evolution of the particle's temperature is derived from eq. B.17c. Since no enthalpy can be stored at the interface between the particle and the surrounding gas ζ, an equilibrium can be stated for the conductive and convective heat fluxes, respectively Φ^c and Φ^{cv}, on both sides of the interface:

$$\Phi_l^{cv} + \Phi_l^c + \Phi_g^{cv} + \Phi_g^c = 0 \tag{B.23}$$

The liquid and gaseous convective fluxes may be equated to the latent heat of vaporization L_{ev}:

$$\Phi_l^{cv} + \Phi_g^{cv} = -\dot{m}_v h_{s,p}(T_\zeta) + \dot{m}_p h_{s,v}(T_\zeta) = \dot{m}_v L_{ev}(T_\zeta) \tag{B.24}$$

The liquid conductive contribution writes:

$$\Phi_l^c = \left(4\pi r_p^2 \lambda \frac{dT_p}{dr}\right)_{\zeta^-} \tag{B.25}$$

with the supersript ζ^- denoting quantities measured on the "particle side" of the interface. The gaseous conductive flux is written in an analogous manner:

$$\Phi_g^c = \left(4\pi r_p^2 \lambda \frac{dT_p}{dr}\right)_{\zeta^+} \tag{B.26}$$

with the subscript ζ^+ denoting quantities measured on the "gaseous side" of the interface.

Considering the temporal evolution of the particle enthalpy [1], one may write:

$$\frac{d}{dt}(m_p h_{s,l}(T_p)) = \Phi_l^c + \Phi_l^{cv} \tag{B.27}$$

Splitting the right hand-side of eq. B.27 through partial differentiation, using the relation $dh_{s,l}(T_p) = c_{p,l}dT_p$ together with eqs. B.23 and B.24, an equation for the evolution of the particle temperature is obtained:

$$\frac{dT_p}{dt} = \frac{1}{m_p c_{p,l}}(-\Phi_g^c + \dot{m}_v L_{ev}(T_\zeta)) \tag{B.28}$$

Finally, the conductive flux on the gaseous side needs to be determined. More specifically, an expression for the temperature gradient on the gaseous side of the particle's surface must be derived. This is done by integrating the enthalpy conservation equation (eq. B.17c) twice between the particle's surface and infinity. This yields:

$$\Phi_g^c = \lambda d_p \mathrm{Nu}(T_\zeta - T_\infty)\frac{\ln(B_T + 1)}{B_T} \tag{B.29}$$

The Nusselt number Nu represents a ratio of convective to conductive heat transfer at the particle's surface and assumes a value of 2 in a quiescent gaseous environment. It is expressed in an analogous manner to the Sherwood number in order to account for the relative velocity between the particle and the surrounding gas:

$$\mathrm{Nu} = 2 + 0.55\mathrm{Re}_p^{1/2}\mathrm{Pr}_v^{1/3} \tag{B.30}$$

B_T is the Spalding number for the temperature:

$$\mathrm{B}_T = \frac{(T_\infty - T_\zeta)\dot{m}_p c_{p,l}}{T_\zeta - T_\infty} \tag{B.31}$$

A relation between the Spalding number for mass B_M and temperature B_T may be derived by equating the mass flow rates in eqs. B.18 and B.31:

$$\mathrm{B}_T = (1 + \mathrm{B}_M)^{\mathrm{Sh}/(\mathrm{Nu}\,\mathrm{Le}_v)} - 1 \tag{B.32}$$

with Le_v the Lewis number of the vapor species, which represents a ratio of thermal to mass diffusivities.

B.2.3 Determination of thermodynamic quantities over the integration path

Integrating eqs. B.17b and B.17c from the particle surface to the far-field requires the knowledge of averaged thermodynamic quantities over the integration path, for instance the dynamic viscosity $\bar{\mu}$ and the heat capacity $\bar{c}_p$ of the gaseous mixture. These average quantities are evaluated by interpolating the temperature and the mixture fractions between the droplet surface and the far-field with the so called "$1/3^{rd}$" rule [158]:

$$T_{int} = T_\zeta + \frac{1}{3}(T_\infty - T_\zeta) \tag{B.33a}$$

$$Y_{v,int} = Y_{v,\zeta} + \frac{1}{3}(Y_{v,\infty} - Y_{v,\zeta}) \tag{B.33b}$$

[1] in order to avoid confusion, the particle enthalpy and particle constant heat capacity are denoted with the subscript 'l' for liquid

B.3 Interaction between fluid and particle phase

The interaction of particles with the fluid phase is twofold. First, direct coupling occurs through the perturbation of the fluid phase induced by the presence of the particles, it is accounted for through interphase exchange terms.

The exact evaluation of the coupling terms between a particle and the surrounding gas would require the explicit numerical resolution of the interface between them and lead to excessive computational costs. Instead, the point-force approximation of Saffman [301] is used. It allows to represent the interphase exchange terms by punctual source terms coinciding with the particle location. The derivation of the point-force approximation is given in the following.

B.3.1 Point source approximation

The motion of N_p rigid spherical particles in a steady viscous flow is considered. The volumetric concentration of particles is low and the fluid density constant. Under these assumptions, the mass and momentum conservation equations for the fluid write:

$$\frac{\partial u_i}{\partial x_i} = 0 \tag{B.34a}$$

$$\mu \frac{\partial^2 u_i}{\partial x_j^2} - \frac{\partial p}{\partial x_i} = -F_{p,i}^n \tag{B.34b}$$

The coupling between both phases is accounted for through the no-slip conditions on the particle surfaces S_p:

$$u_i = u_{p,i}^n \qquad \text{for} \qquad x \in S_p^n, \qquad n = 1, N_p \tag{B.35}$$

The force acting upon the particle n writes:

$$F_{p,i}^n = \int_{S_p} (-p\delta_{ij} + \tau_{ij}) n_j dS \tag{B.36}$$

According to the *actio = reactio* principle, the particle exerts the opposite force upon the flow field:

$$-F_{p,i}^n = \int_{S_p} (p\delta_{ij} - \tau_{ij}) n_j dS \tag{B.37}$$

Therefore, the derivation of the coupling force between phases requires knowledge of the flow field on the particle's surface. In order to avoid this tedious evaluation, Saffman [301] introduced the point-force approximation which specifies a distribution of force singularities centered on each particle and allows to roughly fulfill the boundary conditions of eq. B.35 [227]. The forces acting upon the particles are rewritten as multipole expansions:

$$\mu \frac{\partial^2 u_i}{\partial x_j^2} - \frac{\partial p}{\partial x_i} = \sum_{n=1}^{N_p} \left[F_i^n \delta(\overrightarrow{x} - \overrightarrow{x_p}) + F_{ij}^n \frac{\partial}{\partial x_j} \delta(\overrightarrow{x} - \overrightarrow{x_p}) + F_{ijk}^n \frac{\partial^2}{\partial x_j \partial x_k} \delta(\overrightarrow{x} - \overrightarrow{x_p}) \right] \tag{B.38}$$

The coefficients F_i^n, F_{ij}^n and F_{ijk}^n respectively denote the force monopole, dipole and quadripole. They are related to the fluid force and torque on the n-th particle. Due to the linearity of the Stokes flow, the local fluid velocity

may be obtained by a linear superposition of the flows induced by each multipole force term. This allows to use the fundamental solution for the perturbation velocity induced by the motion of an isolated particle in a fluid at rest:

$$u_i = T_{ij} F_j \tag{B.39}$$

T_{ij} denotes the Oseen tensor:

$$T_{ij} = \frac{1}{8\pi\mu}\left(\frac{\delta_{ij}}{r} + \frac{r_i r_j}{r^3}\right) \tag{B.40}$$

The perturbation velocity induced by a force dipole may be obtained from the derivative of the Oseen tensor, the perturbation velocity induced by a force quadrupole from the second-order derivative and so forth. The forces acting upon an isolated spherical particle of diameter d_p in a fluid at rest are drag and a degenerate force quadrupole [227]:

$$F_i = F_{p,i} = 3\pi d_p \mu (u_i - u_{p,i}) \tag{B.41}$$

$$F_{ijk} = \frac{d_p^2}{24} F_{p,i} \delta_{jk} \tag{B.42}$$

The perturbed fluid velocity due to an isolated particle in a Stokes flow is then obtained as:

$$u_i = \breve{u}_i + \frac{1}{8\mu\pi} F_{p,j}\left(\frac{\delta_{ij}}{r} + \frac{r_i r_j}{r^3}\right) + \frac{d_p^2}{96\mu\pi} F_{p,j}\left(\frac{\delta_{ij}}{r^3} + 3\frac{r_i r_j}{r^5}\right) \tag{B.43}$$

The perturbation of the velocity field by the particle is composed of a long range contribution induced by the force monopole, proportional to the inverse of the particle radius. The second contribution is a short range contribution induced by the force quadripole, proportional to the inverse of the cube of the particle radius. For particles which are small compared to all flow field length scales, only the long range contribution needs to be taken into account as the perturbation induced by the particle is rapidly dissipated by viscous fluid effects. This allows to truncate the multipole expansion after the first term. Thus, the perturbation of the flow field by N_p particles in a steady viscous fluid flow may be represented by the sum of punctual forces centered on the particles:

$$\mu \frac{\partial^2 u_i}{\partial x_j^2} - \frac{\partial p}{\partial x_i} = -\sum_{n=1}^{N_p} F_{p,i} \delta(\overrightarrow{x} - \overrightarrow{x_p}) \tag{B.44}$$

This result is strictly speaking only valid for a steady viscous fluid flow but extended to more general flow fields in practice.

B.3.2 Expressions for the source terms

This section derives the interphase exchange terms of mass, momentum and energy between fluid and particle phase. According to the point source approximation, all interphase exchange terms are treated as the sums of source terms centered on the particles. The evaporated mass of the particles appears as a positive source term in the conservation equation of the evaporating species:

$$s_{ev,k}^{p-f}(x_i) = -\sum_{p=1}^{N} \dot{m}_p \delta(\overrightarrow{x} - \overrightarrow{x_p}) \delta_{kv} \tag{B.45}$$

The subscript v denotes the index of the evaporating species. When considering an evaporating particle, the momentum exchange term between phases writes:

$$s_{m,i}^{p-f}(x_i) = -\sum_{p=1}^{N} \left[\frac{dm_p}{dt} u_{p,i} + F_{p,i}\right] \delta(\overrightarrow{x} - \overrightarrow{x_p}) \tag{B.46}$$

The energy exchange term gathers the contributions of the work done by the particles and the enthaply fluxes due to evaporation.The work done by the particles is the product between the forces acting upon the particles and the gaseous velocity at the particle surface. Since a no-slip condition must be fulfilled at the particles' surfaces, the gaseous velocity at the particle location is equal to the particle velocity. The exchanged enthalpy fluxes are retrieved from the particle temperature evolution equation, see eqs. B.28 and B.29. This yields:

$$s_e^{p-f}(x_{p,i}) = \sum_{p=1}^{N} \left[-F_{p,i}u_{p,i} - \dot{m}_p(L_{ev} + \frac{1}{2}u_{p,i}^2) - \Phi_g^c \right] \delta(\overrightarrow{x} - \overrightarrow{x_p}) \tag{B.47}$$

In the context of Large-Eddy Simulation, these source terms are filtered, which involves replacing all the fluid quantities by their filtered counterparts:

$$\begin{aligned}
\overline{s}_{v,k}^{p-f}(x_i) =& -\sum_{p=1}^{N} \overline{\dot{m}}_p \delta(\overrightarrow{x} - \overrightarrow{x_p})\delta_{kv} \\
&= \pi d_p \mathrm{Sh}[\overline{\rho}\overline{D}_v] \ln\left[\left(\frac{\widetilde{Y}_{v,\zeta} - \widetilde{Y}_{v,\infty}}{1 - \widetilde{Y}_{v,\zeta}} \right) + 1 \right] \delta(\overrightarrow{x} - \overrightarrow{x_p})\delta_{kv} && \text{(B.48a)} \\
\overline{s}_{m,i}^{p-f}(x_i) =& -\sum_{p=1}^{N} \left[\frac{dm_p}{dt} u_{p,i} + F_{p,i} \right] \delta(\overrightarrow{x} - \overrightarrow{x_p}) \\
&= \sum_{p=1}^{N} \left[-\overline{\dot{m}}_p u_{p,i} - \frac{m_p}{\tau_p} \left(\widetilde{u}_i - u_{p,i} \right) \right] \delta(\overrightarrow{x} - \overrightarrow{x_p}) && \text{(B.48b)} \\
\overline{s}_e^{p-f}(x_{p,i}) =& \sum_{p=1}^{N} \left[-F_{p,i}u_{p,i} - \dot{m}_p(L_{ev} + \frac{1}{2}u_{p,i}^2) - \Phi_g^c \right] \delta(\overrightarrow{x} - \overrightarrow{x_p}) \\
&= \sum_{p=1}^{N} \left[-F_{p,i}u_{p,i} - \overline{\dot{m}}_p(L_{ev} + \frac{1}{2}u_{p,i}^2) - \lambda d_p \mathrm{Nu}(\widetilde{T}_\zeta - \widetilde{T}_\infty) \frac{\ln(\overline{\mathrm{B}_T} + 1)}{\overline{\mathrm{B}_T}} \right] \delta(\overrightarrow{x} - \overrightarrow{x_p}) && \text{(B.48c)}
\end{aligned}$$

Appendix C

Load balancing issues

C.1 General context

The following section presents the issue of load balancing encountered in Eulerian/Lagrangian simulations, in a qualitative manner. For a more detailed overview of load balancing and partitioning methods, one can read the PhD thesis of García [98]. For deeper technical insights, the articles of Kumar [181] and Schloegel [311] are advised.

As the liquid phase is described by a Lagrangian formalism, its coupling with the gas phase (described by another formalism) is a tedious problem that was discussed in chapter 5. To compute the gaseous influence on the liquid phase, it is necessary to interpolate the gaseous quantities at the particle location and reciprocally the particles variables must be projected onto the mesh grid. This imposes to track the particles, *i.e.* to keep a dictionary that link all particles to their containing cells. In AVBP, this topic has been improved by the work of Paulhiac [265] for the implementation of the new particle tracking from Haselbacher [138] that avoid particles leakage as seen in section 5.1.4.

Another difficulty derives from the spatial distribution of Lagrangian particles, especially in massively parallel simulations. The mesh can be seen as the geometric base of Eulerian elements, where local quantities are calculated and stored. Partitioning of the mesh is achieved in a way to, *a)* balance the number of cells treated by each processor and, *b)* minimize the inter-processors surface. This method may be labelled as *mono-constraint* method because it is solely based on a optimization of the cells balance among the processors. For an Euler/Lagrange simulation with a mono-constraint partitioning, when particles additionally evolve within the domain, their treatment induces an extra CPU cost [98, 131]. This cost is roughly proportional to the number of particles when particle-to-particle interactions are neglected. If Lagrangian elements are not equally distributed among the CPUs, it creates a misbalanced in processing time that decreases the efficiency of the code. The tedious point lies in the necessary interaction between both formalisms. As mentioned above, since particles must interact with the gas, they require to have access to gaseous values of the containing cells. Consequently, they must be located on the same processor as the containing cell otherwise it would generate extra interpartition communication. This 'cell access' requirement translates from a particles *'in physical space'* heterogeneous distribution to a *'in-CPU'* heterogeneous distribution. Therefore when Lagrangian formalism is applied to configurations that present a high heterogeneity in liquid space distribution, a CPU load imbalance is likely. This problem is negligible in homogeneous (relatively to the partition lenght scale) liquid distribution. However, when the number of partitions increases for given fixed geometrical dimensions, the characteristic length of the partition decreases. Problems arise when it goes below the length scale of particles clusters imposed by a segregation phenomenon as illustrated on fig. C.1. Then increasing the number of partition in a balanced simulation can lead to load imbalance. Furthermore, configurations where the particle distribution is not homogeneous are always subject to load imbalance. As an example, one can cite the space heterogeneity generated

by a point-wise spray injection, as illustrated on fig. C.4: droplets are injected in a relatively small volume and due to turbulent mixing the droplet cloud grows. This induces a decreases of particle concentration downstream the injection, and load imbalance may occur (fig. C.4 b)). Film flows described by a Lagrangian approach is an extreme situation of load imbalance, as film particles are located on a surface corresponding to layer thick by one cell only (fig. C.2).

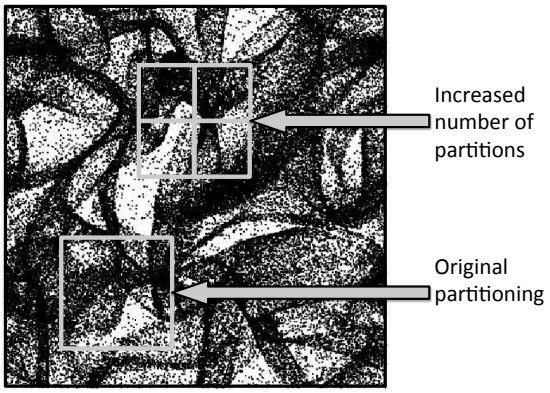

Figure C.1 : *Preferential concentration impact on load balancing in a Homogeneous Isotropic Turbulence case, adapted from [134]*

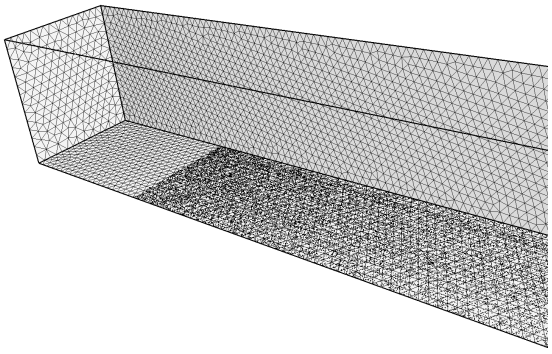

Figure C.2 : *Particle space distribution in filming configuration*

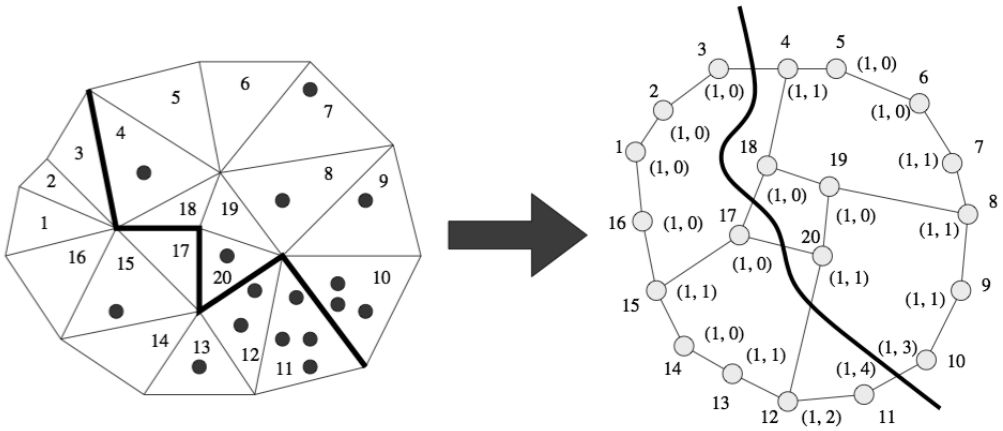

Figure C.3 : *A dual graph with vertex weight vectors of size two (right) is constructed from particle-in-cell mesh (left). A multi-constraint partitioning has been computed for this graph, and this partitioning has been projected back to the mesh. From [173]*

Applying a 'multi-constraints' partitioning constitutes a solution: in addition to the cell distribution constraint previously mentioned, a particle distribution constraint is imposed. The partitioning algorithm thus tries to distribute to every partitions approximately the same number of cells *and* particles (fig. C.3). Such partitioning algorithms exist in the literature and are readily pluggable into AVBP, such as Jostle [361] and METIS [172]. This method is applicable in steady state configurations where the particle number and its space distribution have reach a stable

'in-time' value (HIT, steady state dilute spray configuration) as shown in [98]. However, its benefit decreases in transient situations where the particle distribution continuously evolves during the simulation. For instance, in ignition configuration, as depicted on fig. C.4, the combustion chamber is initially empty, free of particles. Then it is filled with evaporating droplets, and when the flame develops, it heats up all droplets located in the hot gases. This results in a steady state where no droplet is present downstream the flame, which corresponds to a particle distribution different from the initial condition. Nevertheless, it is possible to apply a multi-constraint partitioning method to transient simulations by resplitting the domain every N iterations, or when an imbalance criterion is exceeded. This running procedure is called 'dynamic partitioning'. It has shown a significant efficiency by Ham *et al.* [131]. For massively parallel simulations where the size of the mesh imposes a distributed memory management [164, 242], the use of parallel partitioning algorithm is preferred. The application of the two above-mentioned partitioning code in distributed paradigm is possible via their parallel version: PJostle and ParMETIS.

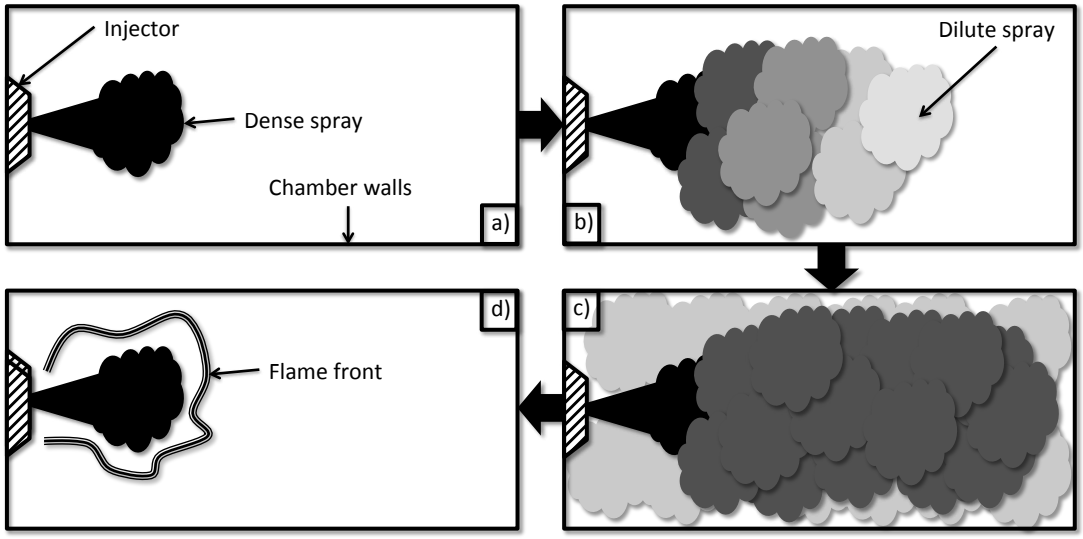

Figure C.4 : *Illustration of load imbalance in space and time, in case of ignition simulation. Black to white colors represent high to low particle concentration. a) Early injection in the empty chamber. b) Intermediate stage of carburation. c) End of carburation stage d) Steady state flame.*

The previously described multi-constraints splitting method could be labelled by 'strong' multi-constraint partitioning because the balance is achieved for the number of cells and particles, independently of their relative computational cost. Although this strong method may be efficient in moderate segregated situations, it happens to be impossible in thin film configuration where the particle number density ratio presents too high extrema and too high spatial variance. Figure C.2 illustrates the situation where film particles are only located on the bottom layer of wall cells while the rest of the domains is empty.

There exists another type of multi-constraint approach that could be qualified of 'weak' partitioning. Its principle is to account for the number of particles per cell and to derive a virtual weight that estimates the CPU cost of each cells. The partitioning algorithm therefore splits the domain in a manner that balances the overall partition weight. It is necessary to preliminary determine the computational weight of processing a particle compared to a gaseous cell. This relative weight depends on the level of physics described by the particle: momentum two-way coupling, thermal evolution or evaporation increase the computational weight of a particle.

As it optimizes the combined computational weight of cells and particles, the weak partitioning requires a code execution sequence without any parallel reductions (or any types of CPU-waiting instruction) in between the Eulerian and Lagrangian treatment. A parallel reduction synchronizes every processor because they all need the same reduced value. In a parallel code it is common to perform parallel reductions at the beginning or the end of a time step. In the case of a parallel reduction call in between both formalisms treatment, processors with a low number of cells will have to wait for the others at the mid-point reduction. It will be the contrary at the reduction located at the end of the time step: partitions with a low number of particles will be faster compared to particle heavily loaded processors. This will result in a loss of efficiency that, may be worse that mono-constraint partitioning.

C.2 Computational expense of Lagrangian models in AVBP

C.2.1 Numerical setup

In order to compare the computation weight of a cell and a particle, a 3D rectangle channel of length 0.1 m and cross section 1×1 cm is simulated. The mesh is made of $\approx$ 450 000 tetrahedral cells tessellated in 84 000 nodes (Fig. C.5 a), partitioned into 16 balanced domains (Fig. C.5 b). Gas velocity (20 m/s) and pressure (1 atm) are imposed at inlet and outlet, respectively, and a law-of-the-wall approach is used to describe the four walls, leading to classical velocity distribution inside the channel (Fig. C.5 c). Turbulence is modeled through the Smagorinsky model and the convective numerical scheme is Lax-Wendroff. In order to asses for the computational weight of a particle, the gaseous flow solver is by-passed through the *frozen gas* approach described in section 5.4.

The computational weight of a particle depend on the models activated (momentum two-way coupling, vaporization) and also of the type (droplet or film particle). Two different two-phase flow cases were thus tested: the liquid phase is exclusively made of (i) droplets or (ii) film particles, referred to as the *droplet* or *film* configuration respectively. In the droplet configuration, the momentum two-way couping is alway activated. Droplets are injected on a point, 1 mm downstream the inlet, at the center of the cross section (Fig C.5 d) while film particles are injected on a transverse line, 1 mm downstream the inlet and 1 mm above the bottom wall, with a velocity oriented towards the wall (Fig. C.5 e).

Five test cases were tested, summarized in Table C.1: (i) a single-phase reference simulation, (ii) non-evaporating droplets, (iii) evaporating droplets, (iv) non-evaporating droplets in *frozen gas*, (v) film configuration in *frozen gas*.

	REF	NONEVAP	EVAP	FROZENDROP	FROZENFILM
Gas solver	normal	normal	normal	*frozen gas*	*frozen gas*
Liquid phase configuration	–	droplet	droplet	droplet	film
Momentum two-way coupling	–	yes	yes	no	no
Evaporation	–	no	yes	no	no

Table C.1 : *Main parameters of the different cases*

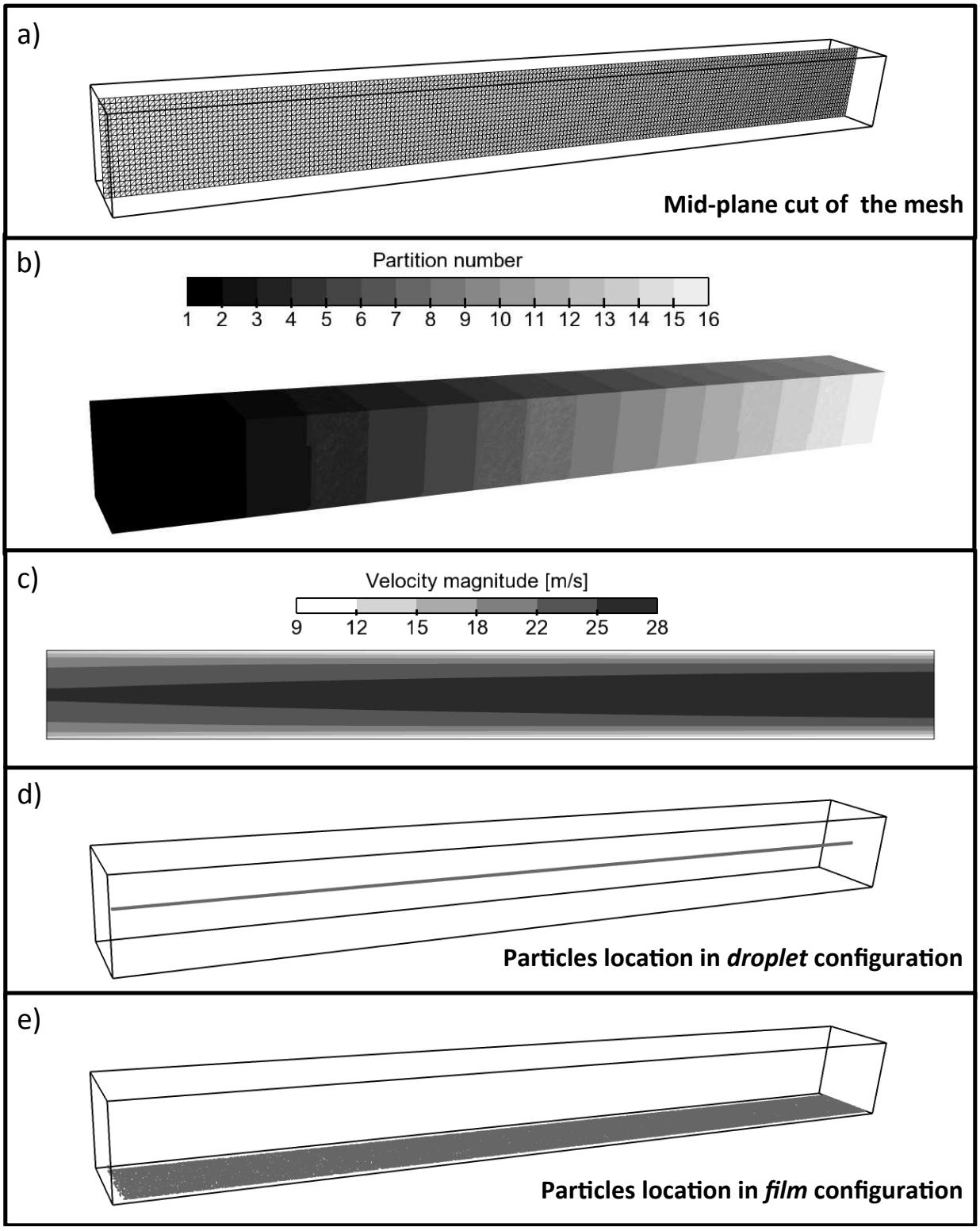

Figure C.5 : *Geometrical details of the test case*

C.2.2 Results

All cases were run twelve times, their averaged statistics are summarized in Table C.2. The reference case has a mean time per iteration per cell $\tau_{i,c}$ of 3.59 µs. With ≈ 11 600 particles, the NONEVAP and EVAP case increase $\tau_{i,c}$ to 3.61 and 3.77 µs, leading to an increase of 0.72 and 5.1% respectively. As expected the evaporation brings additional CPU expenses but the ratio EVAP/NONEVAP cannot be determined yet. The mean CPU time per iteration per particle $\tau_{i,p}$ of FROZENDROP and FROZENFILM is 16.3 and 38.9 µs respectively. This means that a film particle is 2.4 more expensive that a non-evaporating droplet.

	Units	REF	NONEVAP	EVAP	FROZENDROP	FROZENFILM
Number of cells n_c	$[-]$	453 720	453 720	453 720	NA	NA
Number of particles n_p	$[-]$	0	11 615	11 606	10 693	62 601
Time/iteration τ_{tot}	[s]	1.627	1.639	1.711	0.178	2.437
Total CPU time	[h]	95.17	95.11	95.20	95.06	95.09
Time/iteration/cell $\tau_{i,c}$	[µs]	3.59	3.61*	3.77*	NA	NA
Time/iteration/particle $\tau_{i,p}$	[µs]	NA	141*	147*	16.3	38.9

Table C.2 : *Mean computational expenses. *Due to the activation of both gas and liquid solvers for EVAP and NONEVAP, these numbers are not correct, but give an idea of the difference between both cases*

Table C.3 gives more detailed number on the difference between the EVAP and NONEVAP cases. The CPU time of purely gaseous simulation τ_{gas} was estimated from the number of iterations (N_{ite}) of EVAP and NONEVAP, and from the mean time per iteration per cell $\tau_{i,c}$ of the REF case. For instance, with the EVAP case:

$$\tau_{gas}^{\text{EVAP}} = N_{ite}^{\text{EVAP}} \cdot \tau_{i,c}^{\text{REF}} \tag{C.1}$$

For the total CPU time τ_{tot}, the remaining time is attributed to the Lagrangian solver τ_{ptcl}. In the case of EVAP:

$$\tau_{ptcl}^{\text{EVAP}} = \tau_{tot}^{\text{EVAP}} - \tau_{gas}^{\text{EVAP}} \tag{C.2}$$

This results in a $\tau_{i,p}$ equal to 1.01 and 7.20 µs for NONEVAP and EVAP. Note that $\tau_{i,p}^{\text{NONEVAP}}$ = 1.01 µs is much lower than $\tau_{i,p}^{\text{FROZENDROP}}$ = 16.3 µs, suggesting an under estimation of $\tau_{i,p}$ with this method. However, this method is applied to NONEVAP and EVAP and it is expected that relative comparisons are valid. Hence, this shows that an evaporating droplet is 7.2 times more expensive than a non-evaporating droplet.

	Units	NONEVAP	EVAP
Total CPU time τ_{tot}	[h]	95.11	95.20
Estimated* CPU time for gas phase τ_{gas}	[h]	94.44	90.55
Remaining CPU time attributed to liquid phase τ_{ptcl}	[h]	0.678	4.65
Time/iteration/particle	[µs] $\tau_{i,p}$	1.01	7.20

Table C.3 : *Repartition of CPU time among gas and liquid solvers for NONEVAP and EVAP. *Estimated from the number of iterations of NONEVAP and EVAP, and from the time/iteration/cell of the REF case*

As a conclusion, it can be stated that the CPU cost of particles can be sorted as:

$$\tau_{i,p}^{\text{NONEVAP}} < \tau_{i,p}^{\text{FILM}} < \tau_{i,p}^{\text{EVAP}} \tag{C.3}$$

$$\tau_{i,p}^{\text{NONEVAP}} = \frac{\tau_{i,p}^{\text{FILM}}}{2.4} = \frac{\tau_{i,p}^{\text{EVAP}}}{7.2} \tag{C.4}$$